Electrochemical Dinitrogen Splitting and Nitride Transfer to Nitric Oxide with Rhenium Pincer Complexes

Dissertation

Zur Erlangung des mathematisch-naturwissenschaftlichen Doktorgrades

DOCTOR RERUM NATURALIUM

der Georg-August-Universität Göttingen

Im Promotionsprogramm der Georg-August University School of Science (GAUSS)

vorgelegt von

M. Sc. Lukas Alig

aus Hanau

Göttingen, 2022

Betreuungsausschuss

Prof. Dr. Sven Schneider
Institut für Anorganische Chemie, Georg-August-Universität Göttingen

Prof. Dr. Franc Meyer
Institut für Anorganische Chemie, Georg-August-Universität Göttingen

Dr. Markus Finger
Institut für Anorganische Chemie, Georg-August-Universität Göttingen

Mitglieder der Prüfungskommission

Referent: Prof. Dr. Sven Schneider
Institut für Anorganische Chemie, Georg-August-Universität Göttingen

Korreferent: Prof. Dr. Franc Meyer
Institut für Anorganische Chemie, Georg-August-Universität Göttingen

Weitere Mitglieder der Prüfungskommission

Prof. Dr. Inke Siewert
Institut für Anorganische Chemie, Georg-August-Universität Göttingen

Prof. Dr. Manuel Alcarazo
Institut für Organische und Biomolekulare Chemie, Georg-August-Universität Göttingen

Dr. Michael John
Institut für Organische und Biomolekulare Chemie, Georg-August-Universität Göttingen

Dr. Daniel Janssen-Müller
Institut für Organische und Biomolekulare Chemie, Georg-August-Universität Göttingen

Tag der mündlichen Prüfung: 24.03.2022

Acknowledgments

There are many people for which I want to express my genuine gratitude accompanying and supporting me throughout the last couple of years. Without all of you this would have not been possible!

First, and certainly among the most important ones I want to thank my supervisor Prof. Dr. Sven Schneider. Thank you for giving me the freedom to pursue my (sometimes crazy) ideas, providing me with excellent research conditions and encourage critical thinking in the scientific context and beyond. You have a huge impact on how I developed over the years and I appreciate every day I could work under your supervision.

I want to thank Prof. Dr. Franc Meyer not only for taking the time of being my second supervisor, but also for valuable input regarding my research topic. The co-use of some of your instrumentation and crucial chemicals like nitric oxide was an important cornerstone of the NO project and I really appreciate your support.

The further examiners Prof. Dr. Inke Siewert, Prof. Dr. Manuel Alcarazo, Dr. Michael John and Dr. Daniel Janssen-Müller are acknowledged for their time, patience and uncomplicated communication in the entire examination process.

I would like to thank several people, who taught me important chemistry related skills:

- Dr. Christian Würtele for being an awesome and patient mentor in crystallography and Dr. Regine Herbst-Irmer for teaching me the crystallography basics and beyond.
- Dr. Markus Finger for his uncomplicated help with various DFT-related problems and Till Schmidt-Räntsch for introducing me to DFT calculations.
- Dr. Michael John for the informative and very useful NMR courses, with early hands-on measuring experience at the spectrometers.
- Dr. Claudia A. Stückl for introducing me to using the X-band EPR spectrometer.

The AK Schneider has to be mentioned as a very enjoyable group to work in, which (mostly) tried to solve problems in a pragmatic manner. Especially lab and office colleagues like Maximilian Fritz, Yaroslava Zelenkova, Katharina Wenderoth, Dr. Jian Sun, Dr. Sebastian J. K. Forrest, Dr. Arne Glüer, Dr. Bastian Schluschass, Dr. Richt van Alten and Sebastian Kopp were a pleasure to work with. I thank Dr. Arne Glüer for introducing me in an exceptionally friendly and patient manner to the lab at the very beginning of my PhD. Furthermore, I want to

particularly highlight Dr. Sebastian J. K. Forrest as a general mentor for chemistry- and life-related things, for your time and input and your genuine helpfulness.

I want to thank my students Sotirios Pavlidis, Amir Kharrazizadeh, Sven Rosendahl and Sophie Groß for their motivation, contributions to the projects and coping with my working times and moods. It was always a pleasure to help you develop and give you a perspective how the life of a PhD student could (or should not?) look like.

Our collaboration partners from Frankfurt, Prof. Dr. Max C. Holthausen and Kim Eisenlohr are thanked for their integral contributions to the NO project and for the many NO meetings.

I also want to highlight the analytical facilities:

- The NMR department of Dr. Michael John and especially Martin Weitemeyer, Christiane Siebert and Ralf Schöne for the numerous long-term measurements and the friendly and problem-oriented atmosphere.
- The mass department of Dr. Holm Frauendorf for measuring a vast amount of samples and trying to simulate possible species.
- The analytical lab with Angelika Wraage, Diana Kumpart and Susanne Petrich for the numerous elemental analyses they measured.

A special thanks goes to Yaroslava Zelenkova, Till Schmidt-Räntsch, Katharina Wenderoth, Dr. Farheen Fatima Khan, Dr. Marvin Lübcke, Patrick Swolana and Kim Eisenlohr for proofreading various parts of this thesis.

Coming to an end, I want to thank my family, which supported me throughout all the years without any pressure at all. I can not really express how much this helped me over the years, but I hope you are all aware that this would have not been possible without you.

Finally, I have to particularly thank Yaroslava Zelenkova for her exceeding help and for the time she spent caring for me. You made my life in the last year so much easier and I am deeply grateful for everything.

Danke!

Table of Contents

Abbreviations

BDFE	bond dissociation free energy
HOMO	highest occupied molecular orbital
LUMO	lowest unoccupied molecular orbital
PCET	proton coupled electron transfer
TON	turnover number
TOF	turnover frequency
FMO	frontier molecular orbital
TMS	trimethylsilyl
EXAFS	extended X-ray absorption fine structure
Mes	mesityl
TIP	temperature independent paramagnetism
DFT	density functional theory
rRaman	resonance Raman
py	pyridine
$BArF_{18}$	$B(C_6H_3(CF_3)_2)_3$
$BArF_{24}^-$	$[B(C_6H_3(CF_3)_2)_4]^-$
$[AcFc]^+$	acetylferrocenium
$Fc^{+/0}$	ferrocenium / ferrocene
NMR	nuclear magnetic resonance
NIR	near IR
IC	interconfigurational
IT	intervalence
OTf^-	triflate
PPN^+	$[N(PPh_3)_2]^+$
COSY	correlation spectroscopy
HSQC	heteronuclear single quantum coherence
HMBC	heteronuclear multiple bond correlation
HAT	hydrogen atom transfer
SQUID	superconducting quantum interference device
Cp	cyclopentadienyl
Cp^*	pentamethylcyclopentadienyl-
CASSCF	complete active space self consistent field
QDPT	quasi-degenerate perturbation theory
***m*CPBA**	*meta*-chlorperbenzoic acid
NBS	*N*-bromosuccinimide
CV	cyclic voltammetry
PDI	pyridinediimino
SOMO	singly occupied molecular orbital
Tp	hydro*tris*(1-pyrazolyl)borate)
terpy	terpyridine
NOR	nitric oxide reductase
OAT	oxygen atom transfer
EPR	electron paramagnetic resonance
TEMPO	(2,2,6,6-tetramethylpiperidin-1-yl)oxyl
Cy	cyclohexyl
HFI	hyperfine interaction
LIFDI	liquid injection field desorption ionization
ESI	electrospray ionization
Zora	zeroth order relativistic approximation
HYSCORE	hyperfine correlation spectroscopy
ENDOR	electron nuclear double resonance
CPE	controlled potential electrolysis
NBO	natural bond orbital
NEVPT2	*n*-electron valence state perturbation theory
NCS	*N*-chlorosuccinimide
SEC	spectroelectrochemistry
ATR	attenuated transmission
UCO	unrestricted corresponding orbitals
MLC	metal-ligand cooperativity
***i*Pr**	*iso*propyl
***t*Bu**	*tert*butyl
HMDS	hexamethyldisilazan
IMes	*bis*(2,4,6-trimethylphenyl)imidazole-2-ylidene
FWHM	full width at half maximum
INEPT	insensitive nuclei enhanced by polarization transfer
DOSY	diffusion-ordered NMR spectroscopy
Ad	adamantyl
WBI	Wiberg bond index

List of Complexes and Ligands

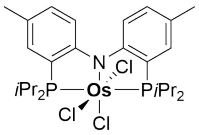

1

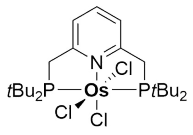

2

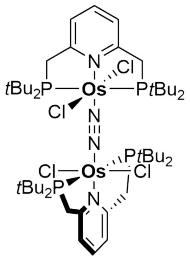

3

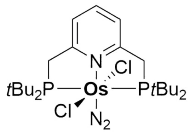

4

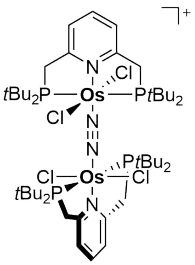

5^{+}

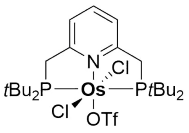

6

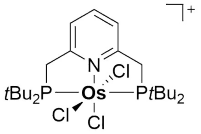

7^{+}

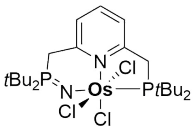

8

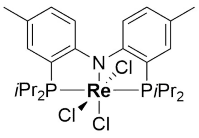

9

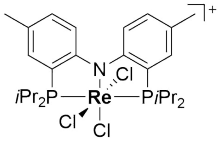

10^{+}

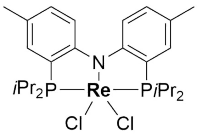

11

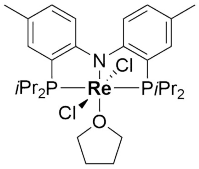

12

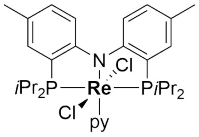

trans-**13**

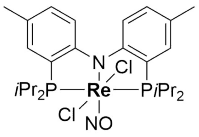

cis-/*trans*-**14**

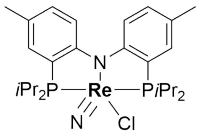

15

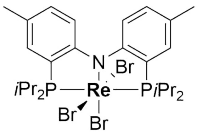

16

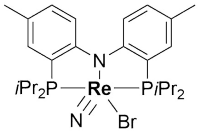

17

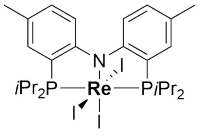

18

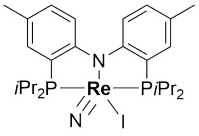

19

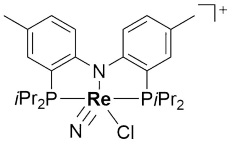

20^{+}

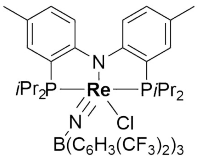

21

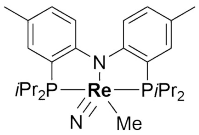

22

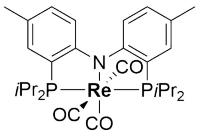

23

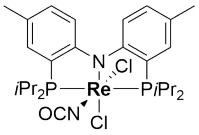

cis-**24**

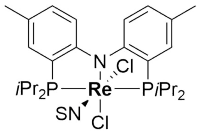

cis-**25**

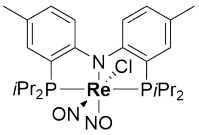

cis-/*trans*-**26**

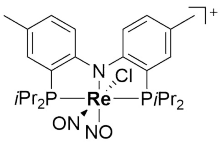

cis-**27**$^{+}$

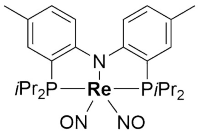

28

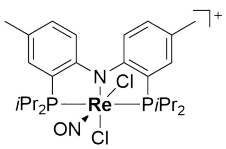

cis-**29**$^{+}$

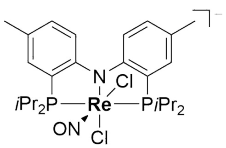

cis-**30**$^{-}$

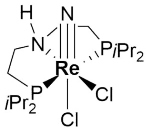

cis-**31**

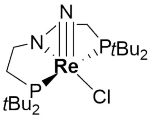

32

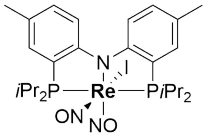

cis-**33**

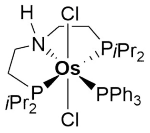

trans-**34**

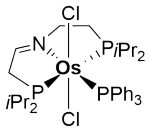

trans-**35**

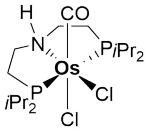

cis-**36**

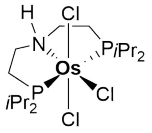

37

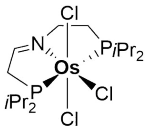

38

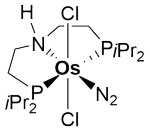

trans-**39**

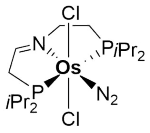

trans-**40**

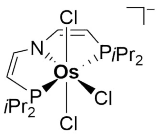

41^{-}

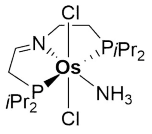

42

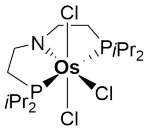

43

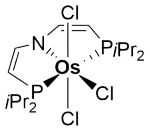

44

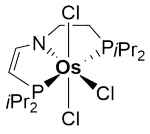

45

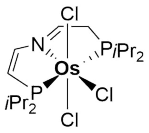

46

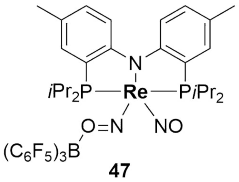

47

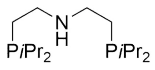

$^{i\mathrm{Pr}}$P$^{\mathrm{H}}$NP

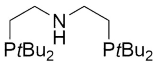

$^{t\mathrm{Bu}}$P$^{\mathrm{H}}$NP

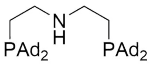

$^{\mathrm{Ad}}$P$^{\mathrm{H}}$NP

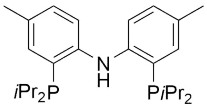

$^{\mathrm{Ph}}$P$^{\mathrm{H}}$NP

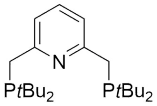

$^{\mathrm{Py}}$PNP

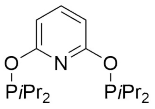

PONOP

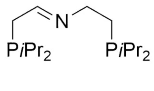

$^{\mathrm{Imine}}$PNP

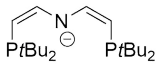

$^{t\mathrm{Bu}}$P=N=P

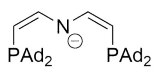

$^{\mathrm{Ad}}$P=N=P

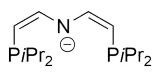

$^{i\mathrm{Pr}}$P=N=P

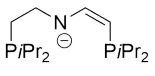

$^{i\mathrm{Pr}}$P=NP

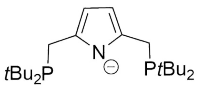

$^{\mathrm{Pyrr}}$PNP

Part I: Dinitrogen Activation with Osmium and Rhenium Pincer Complexes

1.1 Associative Dinitrogen Activation

Dinitrogen is the most abundant element in the atmosphere (>70%, ~$4 \cdot 10^9$ Tg N)[1–3] and is consequently physically almost ubiquitously available. On the contrary, it is one of the most limiting nutritients in any ecosystem.[4] This contradiction can be explained by the chemical properties of the dinitrogen molecule, which limit its bioavailability significantly.[5] The N≡N triple bond is among the strongest chemical bonds known (BDE = 941 kJ·mol^{-1}) and is only exceeded by the triple bonds in acetylene (BDE = 962 kJ·mol^{-1}) and carbon monoxide (BDE = 1070 kJ·mol^{-1}).[6] In combination with the lack of a dipole moment and a large HOMO-LUMO gap, the N_2 molecule is consequently thermodynamically stable and kinetically inert. Strategies involving activation of dinitrogen rely on binding of N_2 to a specific substrate (most often a metal center), which reduces the barrier for functionalization/cleavage or increases the thermodynamic driving force. Based on the subsequent steps a categorization of dinitrogen activation into associative and dissociative mechanisms is possible (Scheme 1.1). In the associative mechanism, dinitrogen binds (terminally) to a metal, followed by functionalization of the N_2, accompanied by successive reduction of the N-N bond order. In the dissociative mechanism, initial complete cleavage of the N≡N triple bond yields metal nitride complexes, which can subsequently be functionalized.

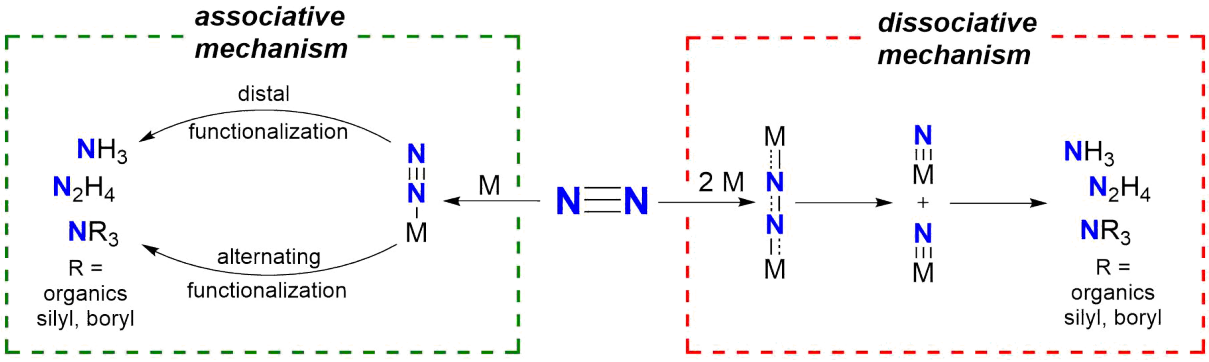

Scheme 1.1: Comparison of associative and dissociative dinitrogen activation mechanisms.[7]

Nature developed sophisticated enzymes to render the gaseous, inert dinitrogen molecule bioavailable. The nitrogenase enzyme family is capable of catalyzing the nitrogen reduction reaction (N_2RR) to form ammonia from dinitrogen, as well as proton and electron equivalents

at ambient conditions.[8] Until broad application of the Haber-Bosch process the vast majority of bioavailable nitrogen was fixed by the select group of microorganisms,[9,10] which contain nitrogenase enzymes. Even today the Haber-Bosch process and biological, nitrogenase enzyme catalyzed N_2RR contribute in comparable quantities to the global N_2 fixation.[11,12] The MoFe protein of the most abundant nitrogenase enzymes contains two metal clusters: The P cluster, a Fe_8S_7 cluster that acts as an electron relay, and the iron-molybdenum cofactor (M cluster, FeMo-co), which contains the active site for binding and reduction of N_2.[8,13] The actual catalytic mechanism[14,15] together with spectroscopic[16] and structural characterization[17–19] of the active site and reaction intermediates are very active areas of research, yet a seemingly essential part like the interstitial carbon atom in the center of the FeMo-co was just recently discovered.[20,21] Overall, the FeMo nitrogenase catalyzes the stepwise proton coupled electron transfer (PCET) of N_2 to ammonia according to the following equation:

$$N_2 + 8\,H^+ + 8\,e^- + 16\,MgATP \longrightarrow 2\,NH_3 + 16\,MgADP + 16\,P_i + H_2$$

In the simplified, commonly accepted mechanism dinitrogen binds to a highly reduced FeMo-co upon reductive elimination of H_2.[8] Subsequent PCET steps deliver hydrogen atoms to the dinitrogen ligand and release of ammonia regenerates the resting state of the FeMo-co. Iron is the essential metal of all nitrogenases and additionally, molybdenum- (FeMo nitrogenase) or in shortage of Mo, vanadium- (VFe nitrogenase) or iron-based (FeFe nitrogenase) co-factors are biosynthesized to sustain N_2 fixation under different environmental conditions.[15,22,23] Moreover, it was found that the enzymes are capable of reducing other small, nonphysiological molecules like nitrite, nitrous oxide, hydroxylamine, alkynes, CO and CO_2 as well.[15,23–28]

The early report of *Bortels* in 1930 established the recognition of molybdenum as an essential element in biological nitrogen fixation.[29] Biomimetic approaches for nitrogen activation were therefore initially focused on dinitrogen complexes of Mo and its heavier congener W.[30–32] However, the first isolated and characterized terminal dinitrogen complex $[Ru(NH_3)_5(N_2)]^{2+}$, with a central Ruthenium atom, was reported by *Allen* and *Senoff* in 1965.[33,34] Since then, terminal dinitrogen complexes of numerous transition metals were discovered and η^1-N_2 is in general the most abundant coordination mode found in dinitrogen coordination complexes.[35–37] The simplified frontier MO scheme of an octahedral, terminally η^1-N_2 coordinated complex of idealized C_{4v} symmetry is shown in Figure 1.1.

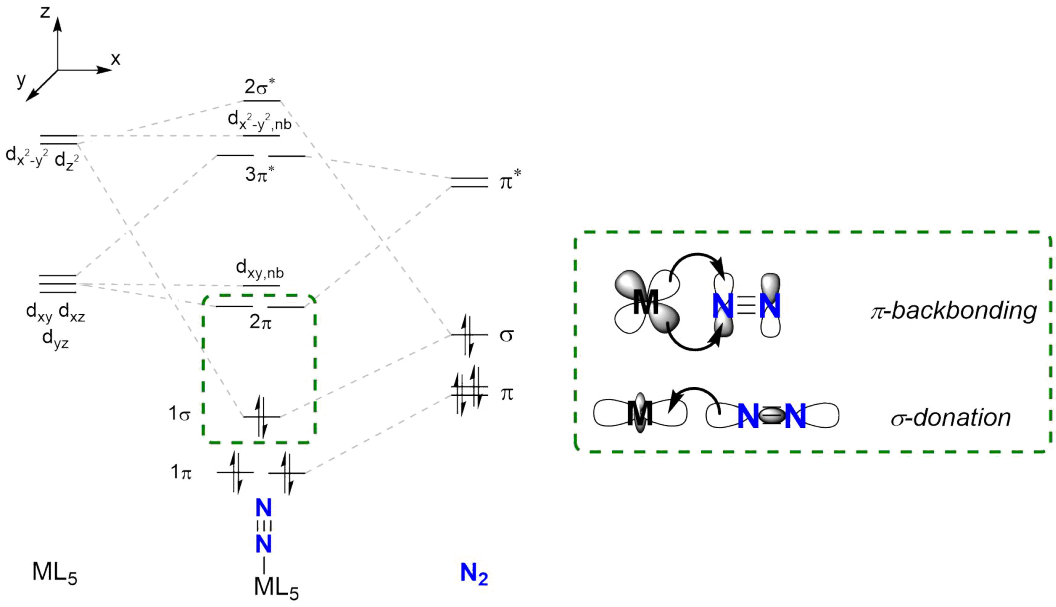

Figure 1.1: Simplified frontier MO scheme of a hypothetical d^0 octahedral η^1-N_2 complex (left) and major metal-ligand orbital interactions evolving from population of the 1σ and 2π orbitals (green box, right).[7,38],[a]

The bonding metal-ligand interaction can be split into two main contributions: The σ-bonding interaction of the filled dinitrogen σ-orbital with an empty d-orbital of the metal (e.g. d_z^2) and the π-backbonding of filled metal d-orbitals with the antibonding π^*-orbital of N_2 (Figure 1.1, green box).[7] The σ-bonding interaction (1σ) is of M-N bonding character and the molecular orbital has a high nitrogen contribution. The π-backbonding (2π) is of M-N bonding and N-N antibonding character, but due to the very large HOMO-LUMO gap of N_2 (10.82 eV)[7] the overlap of $\pi^*(N_2)$ with the filled metal d-orbitals is poor. In first consequence the two resulting degenerate MOs (2π) are significantly lifted in energy, making them essentially nonbonding and weakening the π-backbonding in terminal N_2 complexes substantially. Thus, the terminal dinitrogen ligand is considered a weak σ-donor and a weak to moderate π-acceptor.[39]

Associative dinitrogen splitting is generally divided into two major mechanistic scenarios after binding of dinitrogen in the η^1-N_2 coordination mode to a metal.[40] In the distal mechanism, atoms and / or electrons are initially delivered to the terminal nitrogen atom, until the newly formed NR_3 (R = H, organics, silyl, boryl) is eliminated and the remaining terminal metal nitride is further functionalized (Scheme 1.2, left). This mechanism was mainly influenced by work of *Chatt* and coworkers, who found as early as 1975 that terminally coordinated dinitrogen can be protonated to release ammonia in yields up to 90% for $[W(PMe_2Ph)_4(\eta^1\text{-}N_2)_2]$.[41,42] In the

[a] Own computations on the prototypical $[Ru(NH_3)_5(N_2)]^{2+}$ complex can be found in the computational appendix.

following years numerous terminal nitrogen ligands with different degree of protonation were isolated, which added up to what is known today as the Chatt cycle.[43–48]

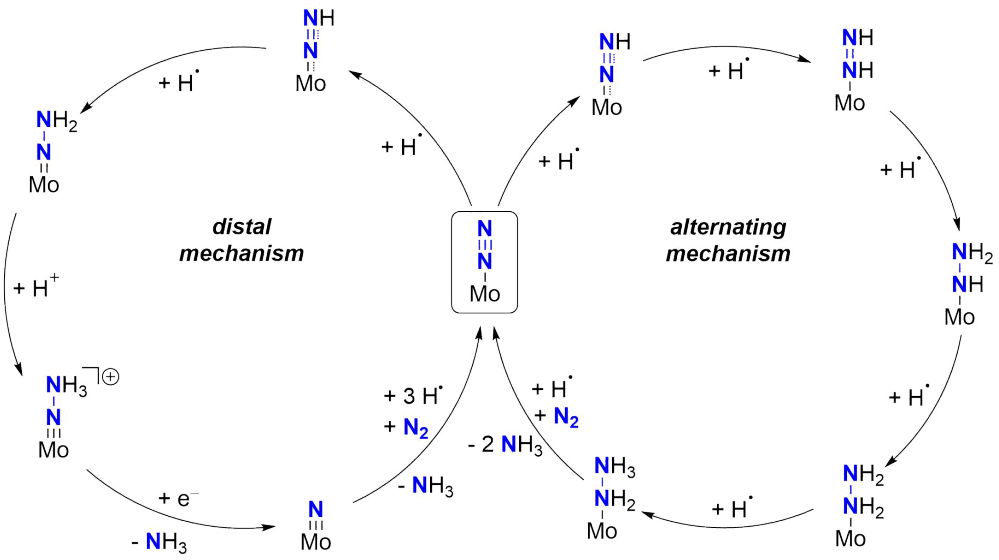

Scheme 1.2: Simplified distal (Chatt cycle) and alternating mechanisms for the nitrogen reduction to ammonia at a molybdenum metal center.[40]

An alternative mechanistic scenario evolved from observations that species like $M(NHNH_2)$ or $M(NH_2NH_2)$, which are not part of the distal mechanism, can form ammonia and that ammonia formation of certain complexes does not involve a terminal nitride complex.[49–52] In the alternating mechanism, atoms and/or electrons are delivered in an alternating fashion to the terminal and metal-bound dinitrogen atom (Scheme 1.2, right), followed by ammonia release of the former terminal nitrogen atom and final PCET to the metal amide ligand. Notably, formation of hydrazine can only proceed *via* the alternating mechanism, given that hydrazido intermediates are only part of this particular mechanism. Furthermore, hybrid mechanisms were proposed, in which for example the complex $[Cp^*W(Me)_3(NNH_3)]^+$, which would be considered a distal intermediate, isomerized to the alternating intermediate $[Cp^*W(Me)_3(\eta^2\text{-}NHNH_2)]^+$.[53]

Guided by these mechanistic investigations of associative N_2 splitting and NH_3 formation, efficient metal catalysts for the ammonia formation from N_2 were explored. The first well-defined metal complex that showed catalytic conversion of dinitrogen to ammonia was reported by *Schrock* and coworkers in 2003.[54] Slow addition of excess Cp^*_2Cr (36 eq.) and $[LutH][BArF_{24}]$ (48 eq.) to the sterically demanding Mo^{III} complex **I** (Figure 1.2) furnished approximately 8 equivalents of NH_3 per molybdenum center. The molybdenum complex and possible intermediates of the catalytic cycle were in the following years thoroughly investigated

experimentally and with the aid of DFT calculations, suggesting that **I** engages in a distal mechanism of ammonia formation.[55–61] Compliant with these findings was the isolation of the corresponding terminal molybdenum nitride complex and its comparable potency in catalytic ammonia formation.[54] Despite considerable efforts, the catalytic activity of the system could neither be improved by ligand modifications,[62–65] nor by utilizing other group 5 or 6 metals.[66,67]

In 2010 *Nishibayashi* and coworkers demonstrated catalytic ammonia formation from a dinuclear molybdenum PNP pincer complex **II**, which is ligated by two terminal η^1-N_2 ligands per molybdenum and additionally exhibits a bridging μ-η^1:η^1 dinitrogen ligand between the two metal centers.[68] The addition of excess [LutH][OTf] (266 eq.) and Cp_2Co (288 eq.) to **II** produced 23.2 equivalents of NH_3 (11.6 eq. per Mo). In this study, the crucial influence of the acid counterion was highlighted, with chloride and $BArF_{24}^-$ anions producing significantly less ammonia (0.7 and 2.7 eq. NH_3, respectively). Interestingly, related mononuclear pincer complexes with a phosphine ligand instead of the N_2 bridge proved to be significantly less active, producing (sub)stoichiometric amounts of NH_3.[69,70] The reaction was proposed to proceed *via* a distal reaction mechanism with formation of a terminal molybdenum nitride complex, which was found to be catalytically active as well.[71] Notably, only the terminally coordinated dinitrogen ligands are involved in the catalysis.

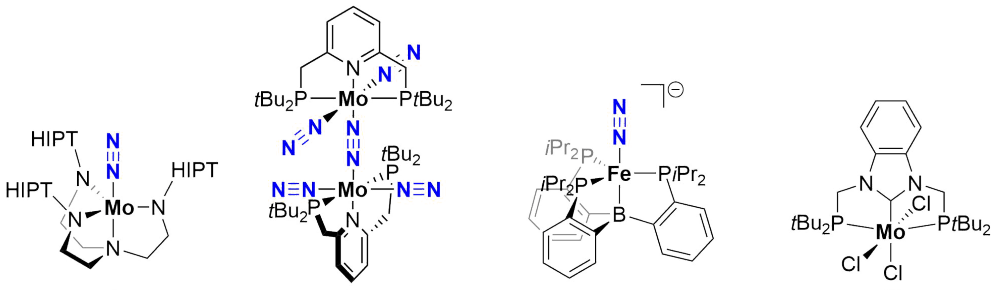

Figure 1.2: Selected examples of nitrogen reduction (pre)catalysts. HIPT = hexaisopropylterphenyl.

Efforts to realize catalytic ammonia formation at the abundant first-row metal iron were promoted by publications of *Peters* and coworkers starting in 2013. They reported trigonal bipyramidal boratrane complexes like **III** (Figure 1.2), which are capable of catalytic nitrogen fixation.[72–74] The flexibility of the Fe-B interaction was pointed out as one of the decisive

factors, stabilizing a wide range of intermediates, for example a distorted tetragonal Fe^{IV} terminal nitride complex.[40,75] The intermediacy of the terminal nitride complex is, in contrast to earlier proposals of a hybrid mechanism, based on the disproportionation of [Fe=N-NH_2] and [Fe=N-NH_2]$^+$ to [Fe-N_2] and [Fe-NH_2-NH_2]$^+$. With excess of the strong acid [H(OEt_2)$_2$][$BArF_{24}$] (1500 eq.) and KC_8 (1800 eq.) at −78 °C high amounts of ammonia (59 eq. NH_3 per Fe) were obtained.[76] Related anionic silatrane N_2 complexes of Ru and Os were also demonstrated to be catalytically active (up to 120 eq. NH_3 per Os).[77] Interestingly, *Peters* and coworkers found that metallocene reductants like decamethylcobaltocene can be protonated by acids at low temperatures and the resulting complex can act as a PCET reagent (BDE_{CH} = 31 kcal·mol^{-1}).[78,79]

The choice of reductant / proton source combination is crucial for high ammonia yields, as demonstrated in the application of the SmI_2 / H_2O couple as PCET reagent by *Nishibayashi* and coworkers in 2019.[80] The significantly weakened O-H bond ($BDFE_{OH}$ = 26 kcal·mol^{-1}) upon coordination of H_2O or alcohols to SmI_2 was exploited in the reduction of organic substrates,[81–84] and adaption to the N_2RR improved the ammonia yield significantly. Excess SmI_2 (14400 eq.) and H_2O (14400 eq.) with Mo^{III} PCP pincer complex **IV** as precatalyst furnished an impressive amount of 4350 equivalents of ammonia at ambient conditions.[80] Additionally, 150 equivalents of H_2 were formed from competing proton reduction. The catalytic activity upon using ethylene glycol as proton source (turnover frequency, TOF = 117 min^{-1}) is the first well-defined metal complex that reaches the activity levels observed from the nitrogenase enzyme (TOF = 40 – 120 min^{-1})[85]. The reaction mechanism is not fully elucidated yet, but the involvement of a terminal nitride complex was implied by its independent synthesis and successful reactivity with SmI_2 and ethylene glycol. Notably, this does not rule out dinuclear dinitrogen splitting *via* a dissociative pathway.

Terminal dinitrogen complexes are – beyond ammonia formation – also involved in synthesis of other (organic) nitrogenous products.[86] Direct formation of nitrogenous products from N_2 avoids the energy-demanding initial formation of ammonia and is therefore highly desirable to reduce their carbon footprint. Nitrogen-element bond formation usually occurs at the terminal nitrogen atom with initial retention of the N-N bond. Alkylation of the terminal nitrogen atom with reductive release of amines was reported as early as 1972.[87–90] One remarkable example was described by *Cummins* and coworkers utilizing the Mo^{III} *tris*amide complex **V** (Scheme 1.3A).[91]

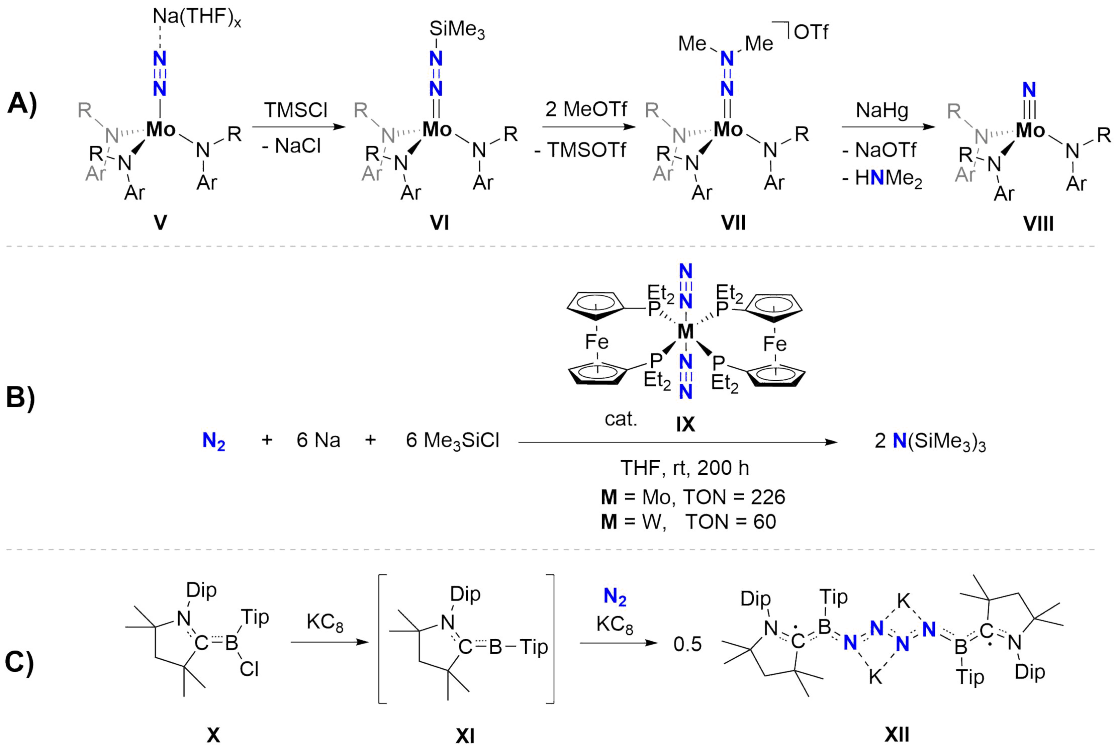

Scheme 1.3: Examples of N-C- (A), catalytic N-Si- (B) and N-B (C) bond formation from terminally bound dinitrogen.

Silylation of the anionic dinitrogen complex **V** produced silylhydrazido complex **VI**, which was treated with MeOTf to obtain the dialkylated complex **VII**. Final reduction with sodium amalgam in the presence of a proton source released dimethylamine and terminal Mo^{VI} nitride **VIII**. Catalytic silylation of N_2 using a molybdenum dinitrogen complex was achieved by *Nishibayashi* and coworkers using Mo^0 and W^0 *bis*nitrogen complexes **IX** as catalysts, TMSCl as silyl source and sodium metal as reductant.[92] The highest catalyst durability was achieved using the molybdenum complex (turnover number, TON = 226). Complex **IX** remains one of the most durable silylation catalysts, although numerous other N-Si bond formations are reported by now.[93–97] N-B bond formation exploits the inherent electron deficiency of most boron compounds and leads to adduct formation of nucleophilic dinitrogen complexes with $B(C_6F_5)_3$.[98,99] Recently, *Braunschweig* and coworkers extended dinitrogen activation to main group p-block chemistry.[100,101] With the aid of a transient CAAC-borylene (CAAC = cyclic alkylaminocarbene) intermediate, which was formed by reduction of a stable precursor (**X**) with KC_8, a B=N=N=N=N=B structural motif (**XII**) was obtained upon dinitrogen coupling.[102] These functionalizations of terminally coordinated N_2 beyond ammonia highlight the potential of associative N_2 activation to shortcut established industrial processes.

1.2 Dissociative Dinitrogen Activation

Full cleavage of N_2 to obtain (terminal) nitride complexes is the initial step of dissociative dinitrogen activation (c.f. Scheme 1.1). The associated large barrier for direct splitting of the stable triple bond is the main drawback of this methodology and delayed development of well-defined metal complexes capable of splitting dinitrogen into nitrides significantly. Ironically, the most prominent and impactful application was already found in the early 20th century when *Fritz Haber* (Nobel prize 1918) and *Carl Bosch* (Nobel prize 1931) developed the Haber-Bosch process for the reduction of dinitrogen to ammonia on an industrial scale. It is hard to overstate the historical and present impact of its application: The Haber-Bosch process allowed sustained growth of the human population (quadrupeled in the 20th century) by providing large quantities of ammonia, which are further processed to fertilizers. Approximately 1–2% of the annual global energy consumption is associated with the ammonia production, consuming 4% and 60% of the global methane and hydrogen production, respectively.[4,40] The hydrogen generation from steam reforming accounts for 0.5 Gt·year^{-1} CO_2 emissions and overall 1.6 tons of CO_2 are released per ton NH_3 produced, with an annual production of approximately 182 Mt, highlighting the enormous carbon footprint of this industrial reaction.[40,103] Nevertheless, ammonia plants are relatively energy efficient (70%), due to their large scale and synergistic effects when coupled on-site with steam-reforming.[103,104]

Ammonia formation beyond the Haber-Bosch process with alternative hydrogen sources would offer several advantages: 1) Water splitting as the hydrogen source avoids greenhouse gas emissions if powered by renewable energies, but is significantly more energy demanding (613.4 kJ·mol^{-1}) than using natural gas.[4] 2) The large scale centralized ammonia production favors ammonia plant locations with good infrastructure and easy access to starting materials, however this does not necessarily correlate with the location where ammonia and follow-up products like fertilizers are needed. Decoupling of steam-reforming and Haber-Bosch process could enable affordable, more decentralized ammonia production in areas of food shortage.[4] 3) Ammonia production is the starting point for most nitrogenous chemicals and optimizations would directly benefit the footprint of all other nitrogenous chemicals as well, as substantial part of the energy consumption and green-house gas emissions originate in the need for hydrogen gas as reductant.

The inherent inertness of dinitrogen is well-reflected in the need of high reactant pressures (150 – 250 bar) and high temperatures (400 – 500 °C) to obtain ammonia *via* the Haber-Bosch process.[104] Dinitrogen and hydrogen are fully cleaved on the catalyst surface ($Fe/Al_2O_3/K$) to form adsorbed hydrogen- and nitrogen atoms. The adsorption of N_2 is the rate-determining step with formation of nitrides being one of the main driving forces ($\Delta H^0 = -17$ kJ·mol^{-1}). Elucidation of the relevant surface processes was awarded with the Nobel Prize for *Gerhard Ertl* in 2007.[105] The energetically favorable formation of nitrides has stimulated intensive research not only towards homogeneous catalysis involving nitrides, but also for catalytic ammonia formation mediated by well-defined metal complexes.

For dinitrogen splitting into two terminal nitrides a stronger activation than in terminal N_2 complexes is necessary, which can be achieved upon dinuclear N_2 coordination. Three dinuclear coordination modes have to be distinguished: The dinuclear end-on (μ-η^1:η^1-N_2), dinuclear side-on (μ-η^2:η^2-N_2) and the hybrid dinuclear side-on-end-on (μ-η^2:η^1-N_2), which exhibit significant differences with regard to their activation properties. Since the two latter side-on coordination modes are predominantly found within early transition metal / lanthanide complexes and not occurring within the for this thesis relevant group 7 and group 8 metal complexes, they will not be discussed in more detail. However, their chemistry is intriguing and allows for some unprecedented functionalizations.[39] The metals in the μ-η^1:η^1-N_2 coordination mode are able to stabilize the bridging N_2 ligand in a series of oxidation states from neutral N_2, to highly reduced N_2^{4-} (hydrazido ligand). Activation of the N_2 bridge correlates with the charge transfer of the coordinating metals into N-N antibonding orbitals. This results in a higher degree of covalent metal-ligand interaction and delocalized bonding, which is reminiscent of the bonding situation in metal nitrosyl complexes. Consequently, *Wieghardt* proposed the introduction of a nomenclature for transition metal nitride complexes, reminiscent of the Enemark-Feltham notation for M-NO complexes.[106,107]

The first example of a μ-η^1:η^1-N_2 dinuclear complex was reported by *Taube* and coworkers and crystallographically characterized by the group of *Gray* in 1969 with the isolation of $[(NH_3)_5Ru(\mu\text{-}N_2)Ru(NH_3)_5]^{4+}$.[108,109] In the same publication they analyzed the bonding interactions in dinuclear, linearly-bridged N_2 TM complexes and correlated the N_2 activation degree with occupation of molecular orbitals in the M-N-N-M core. A similar description was published by *Chatt* and coworkers for the heteronuclear complex $[(PMe_2Ph)_4ClRe(\mu\text{-}N_2)CrCl_3(thf)_2]$ and adopted to threefold symmetry by *Bercaw* and *Cummins*.[110–112] The

simplified frontier MO schemes for N_2-bridged dinuclear complexes in two idealized symmetries are shown in Figure 1.3.[113]

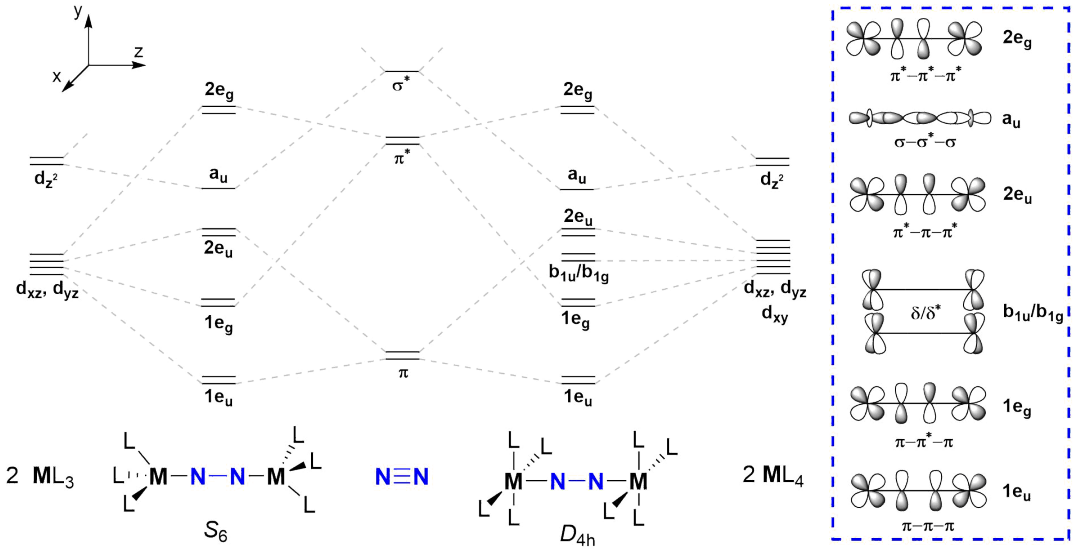

Figure 1.3: FMO schemes of dinuclear dinitrogen-bridged complexes of idealized S_6 (left) and D_{4h} (right) symmetry.

Combination of the N_2 and metal orbitals of π-symmetry forms four sets of doubly degenerate MO's ($1e_u$, $1e_g$, $2e_u$, $2e_g$), with increasing number of nodal planes. The nitrogen p_z orbitals are further overlapping with the metal d_z^2 orbitals, forming a relatively high-lying σ-orbital (a_u). Of the remaining metal orbitals, the d_{xy} orbital is in D_{4h} symmetry orthogonal to the ligand orbitals, but non-bonding with respect to the N_2 ligand. The corresponding metal-centered MO's (b_{1u}/b_{1g}) are therefore available for occupation, however, it should not influence the nitrogen bonding situation significantly. Of the mentioned orbitals, the $1e_g$ set ($\pi-\pi^*-\pi$) is bonding with respect to M-N and N-N antibonding, which is an important component of the overall dinitrogen activation. The antibonding $2e_u$ set ($\pi^*-\pi-\pi^*$) is basically the opposite with M-N antibonding and N-N bonding contributions, which destabilize the dinuclear arrangement. Full N-N bond cleavage requires population of the a_u MO ($\sigma-\sigma^*-\sigma$) with N-N antibonding character.

Structural (d_{NN}) and spectroscopic (ν_{NN}) descriptors, which are approximately inversely proportional,[36,114,115] are used to gauge the degree of dinitrogen activation. The groups of *Evans* and *Cummins* reported dinuclear N_2-bridged complexes of S_6 symmetry, which are in good agreement with the predicted N_2 activation based on the mentioned MO considerations (Table 1.1).[112,116–118] The group of *Evans* reported a linearly N_2-bridged discandium complex with a formal π^6 (= six electrons in the orbitals of π–symmetry: $1e_u$, $1e_g$, $2e_u$, $2e_g$) electron configuration of the ScNNSc core. The N-N IR stretch (ν_{NN} = 1644 cm^{-1}) and N-N bond length

(d_{NN} = 1.221(3) Å) indicate weak N_2 activation in comparison to molecular N_2 (ν_{NN} = 2331cm^{-1}, d_{NN} = 1.10 Å)[113], in compliance with only partial occupation of the N-N antibonding $1e_g$ orbitals. Similar observations were reported from *Liddle* and coworkers with a dinuclear dititanium complex, which showed significantly increased N_2 activation upon reduction from the neutral π^6 (d_{NN} = 1.121(6) Å, ν_{NN} = 1701 cm^{-1}) to dianionic π^8 (d_{NN} = 1.315(3) Å, ν_{NN} = 1201 cm^{-1}), which led to the formulation as a N_2^{4-} ligand coordinated by two Ti^{IV} centers in the latter case.[119,120] Furthermore, the authors found a strong influence of potassium ions coordinating to the N_2 bridge on the N-N bond parameters. As expected, a high degree of dinitrogen activation was observed in a dimolybdenum N_2-bridged complex with formal π^8 (d_{NN} = 1.265(5) Å, ν_{NN} = 1349 cm^{-1}) configuration and reduction of the dinuclear complex to π^9 (d_{NN} = 1.239(4) Å, ν_{NN} = 1503 cm^{-1}) and π^{10} (d_{NN} = 1.212(2) Å, ν_{NN} = 1630 cm^{-1}) configuration decreased the dinitrogen activation upon population of the N-N bonding $2e_u$ MO's.

Table 1.1: Comparison of structural and spectroscopic parameters of selected dinuclear dinitrogen-bridged complexes. (DMP = 3,5-dimethylphenyl).

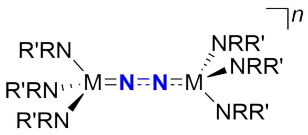

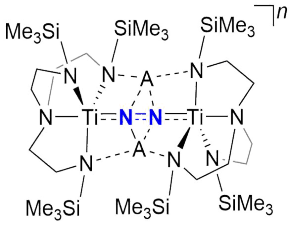

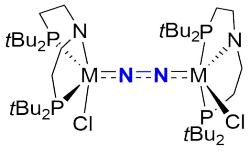

M	Sc	Mo	Mo	Mo	Ti	Ti	Mo	W	Re
R	TMS	DMP	DMP	DMP	–	–	–	–	–
R'	TMS	*t*Bu	*t*Bu	*t*Bu	–	–	–	–	–
A	–	–	–	–	–	K	–	–	–
n	2–	2+	1+	0	0	0	–	–	–
π / δ	π^6	π^8	π^9	π^{10}	π^6	π^8	$\pi^8\delta^4$	$\pi^8\delta^4$	$\pi^{10}\delta^4$
d_{NN} [Å]	1.221(3)	1.265(5)	1.239(4)	1.212(2)	1.121(6)	1.315(3)	1.258(9)	1.27(8)	1.202(10)
ν_{NN} [cm^{-1}]	1644	1349	1503	1630	1701	1201	1343	1392	1771

Dinuclear N_2 bridged complexes of idealized D_{4h} symmetry (e.g. octahedral or square pyramidal) show comparable degrees of activation up to a π^8 configuration, however, further increase of the electron count occupies the nonbonding b_{1u}/b_{1g} MO's and the metals need to formally provide more than four electrons each for occupation of the $2e_u$ orbital set. *Schneider* and coworkers reported various group 6 and 7 PNP pincer complexes, which are in good agreement with the MO considerations (Table 1.1). The dinuclear molybdenum N_2-bridged

complex [(($^{t\text{Bu}}$PNP)ClMo)$_2$(μ-N$_2$)] ($\pi^8\delta^4$, δ = electron count in the non-bonding b_{1u}/b_{1g} orbital set) exhibits strong activation of the N$_2$-bridge (d_{NN} = 1.258(9) Å, ν_{NN} = 1343 cm^{-1}), similar to its isoelectronic tungsten congener (d_{NN} = 1.27(8) Å, ν_{NN} = 1392 cm^{-1}).[121,122] In the corresponding dirhenium complex ($\pi^{10}\delta^4$) partial occupation of the N-N bonding $2e_u$ MO's significantly reduces the dinitrogen activation (d_{NN} = 1.202(10) Å, ν_{NN} = 1771 cm^{-1}).[123,124] Similarly, the initially described dinuclear N$_2$-bridged complex [(NH$_3$)$_5$Ru(μ-N$_2$)Ru(NH$_3$)$_5$]$^{4+}$ ($\pi^{12}\delta^4$) shows barely any dinitrogen activation (d_{NN} = 1.12 Å, ν_{NN} = 2100 cm^{-1}).[108]

All previously discussed examples exhibit strongly interacting ligands like amide π-donors, which might influence the relative ordering of the molecular orbitals or (de)stabilize potential nitride splitting products.[125,126] Calculations for the divanadium dinitrogen-bridged redox series [((Mes)$_3$V)$_2$(μ-N$_2$)]$^{0/-1/-2}$ with a truncated molecular model predicted the metal-centered δ/δ*-MO's to be LUMO and LUMO+1, presumably due to the absence of π-donating ligands.[127–129] Consequently, reduction leads to successive occupation of metal-centered, non-bonding orbitals and the N-N bond metrics are barely changed ($\pi^8\delta^1$: d_{NN} = 1.222(4) Å, $\pi^8\delta^2$: d_{NN} = 1.225(7) Å), in a similar situation to the previously discussed D_{4h} symmetric complexes. Protonation of the basic amide donor in the Mo and W PNP pincer derivatives by *Schneider* and coworkers caused a change of the spin multiplicity to a quintet ground-state ($1e_u^4 1e_g^4 b_{1u}^1 b_{1g}^1 2e_u^2$).[121,122] Computational analysis suggested a significantly decreased energy level of the $2e_u$ orbital set due to the weaker amine donor (compared to the amide donor prior to protonation).

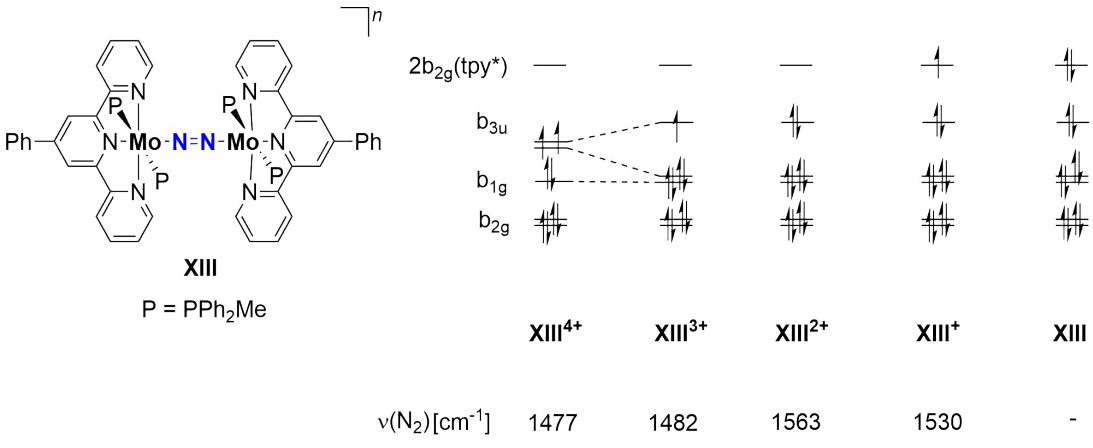

Figure 1.4: Simplified FMO scheme of a dinuclear dimolybdenum N$_2$ bridging complex **XIII** in different oxidation states.

Redox-active ligands are also capable of influencing the degree of dinitrogen activation, as demonstrated by *Chirik* and coworkers.[130,131] The octahedral dimolybdenum complexes were

isolated in five redox states (Figure 1.4) and the bond metrics of the dication are consistent with a $\pi^{10}\delta^4$ configuration and a $\{Mo^{II}_2(\mu\text{-}N_2^{2-})\}$ core. The first oxidation is consistent with reducing the occupation of the N-N bonding $2e_u$ orbitals and increasing the N_2 activation ($\pi^9\delta^4$). The second oxidation is accompanied by a ground-state multiplicity change to a triplet and removal of an electron of the non-bonding b_{1g} orbital ($\pi^9\delta^3$), with little impact on the N-N bond stretch. On the contrary, reduction of the dication is ligand centered, retains the $\pi^{10}\delta^4$ configuration and has little influence on the degree of N_2 activation.

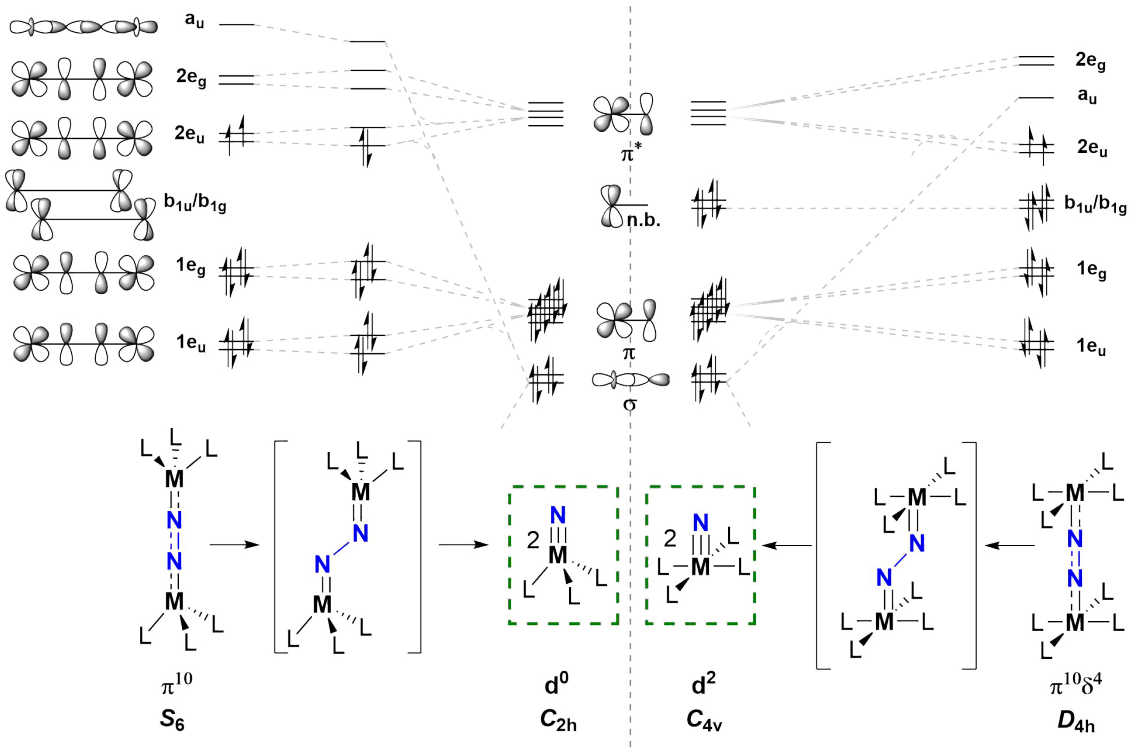

Figure 1.5: Simplified FMO schemes for the dinitrogen splitting from dinuclear dinitrogen-bridged complexes of idealized S_6 (left) and D_{4h} (right) symmetry.

The first example of dinitrogen splitting into well-defined terminal nitride complexes was reported by *Cummins* and coworkers in 1995.[112,132] Formation of the dinuclear dinitrogen-bridged molybdenum complex upon reaction of [Mo(NRAr)$_3$] (R = *t*Bu, Ar = 3,5-$C_6H_3Me_2$) with N_2 is only observed at low temperatures and subsequent warming of the dinuclear complex to room temperature led to dinitrogen splitting into the terminal nitride complex [Mo(N)(NRAr)$_3$] following first-order kinetics.[133] The dinuclear N_2 bridged complex has a π^{10} configuration, with reduced N_2 activation compared to the (di)cationic $\pi^{8/9}$ complexes (see above).

Full splitting of the dinitrogen ligand demands four electrons per formed nitride molecule for population of the bonding π-orbitals (Figure 1.5). Upon elongation of the N-N bond along the splitting reaction coordinate the symmetry is reduced and degeneracy of the π-symmetric orbitals is lifted, which results in a triplet-singlet spin-state change. Furthermore, the antibonding, rotationsymmetric a_u orbital drops significantly in energy, comcomitant with transfer of two electrons from the $2e_u$ level to the bonding σ-orbital of the nitride. This σ/π-transfer is possible along a distorted *zig-zag* transition state structure, which is in agreement with calculations on the truncated model compound $[((NH_2)_3Mo)_2(\mu\text{-}N_2)]$[134] or full system[135]. These considerations correlate the dinitrogen splitting to efficient σ/π-mixing and impose that (de)stabilizing the antibonding a_u orbital should in fact facilitate or inhibit σ/π-mixing in the *zig-zag* transition state. For example, ligands in *trans*-position to the dinitrogen bridge destabilize the a_u molecular orbital.[125,136] *Cummins* and coworkers demonstrated another example of the π^{10} configuration for dinitrogen splitting with the synthesis of stable dinuclear N_2-bridged $[((ArRN)_3Nb)_2(\mu\text{-}N_2)]$ (π^9, R = neopentyl, Ar = 3,5-$C_6H_3Me_2$), which reacted upon reduction to the neutral Mo^{VI} and anionic Nb^V nitride complexes, respectively.[117,137] *Copéret* and coworkers furthermore reported rapid thermal dinitrogen splitting from dinuclear dinitrogen-bridged Mo^{III} *tris(*tert-butoxy)silanolate complexes in five-coordinate geometry.[126]

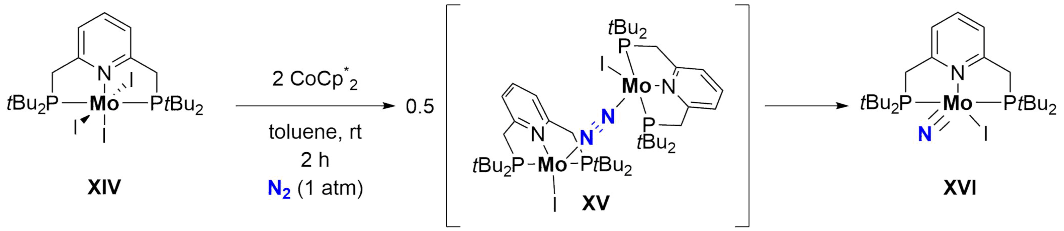

Scheme 1.4: Dinitrogen splitting upon reduction of Mo^{III} precursor **XIV** along proposed dinuclear intermediate **XV** ($\pi^{10}\delta^4$) to form terminal nitride complex **XVI**.

Thermal dinitrogen splitting from dinuclear complexes was also reported for complexes in idealized D_{4h} symmetry, which enables coordination geometries with more ligands. *Nishibayashi* and coworkers reported catalytic dinitrogen splitting and ammonia formation in the coordination sphere of a molybdenum PNP pincer complex **XIV**.[138,139] The authors proposed a five-coordinate, dinuclear N_2-bridged Mo complex **XV** ($\pi^{10}\delta^4$) as transient intermediate (Scheme 1.4), which was substantiated in a successive *in situ* EXAFS study. Pincer ligands are in general priviledged structures to study small molecule activation, due to their sterically and electronically modular modification potential of pincer backbone and phosphine substituents. Thus, it is not surprising that several molybdenum based platforms were found to

undergo dinitrogen splitting, ligated by pyrrole- (PNP),[140] phenyl- (PCP)[141] or phosphine-based (PPP)[142] pincer ligands. Notably, the latter example proved capable of synthesizing stoichiometric amounts of silylamine from N_2 and a disilane.

Recent developments shift the focus towards group 7 and later elements, as the nitrides, which are obtained from dinitrogen splitting, promise more versatile functionalization opportunities (see chapter 2.1). Dinitrogen activation in the coordination sphere of a PNP Technetium pincer complex was just recently described,[143] however, no dinitrogen splitting reported. Overreduction resulted in the formation of a Tc^{I}/Tc^{I} dinuclear N_2-bridged complex ($\pi^{12}\delta^{4}$) which showed little N_2 activation (ν_{NN} = 1974 cm^{-1},d_{NN} = 1.108(3) Å). This resembles the isoelectronic, heavier Rhenium congener reported by *Nishibayashi* and coworkers ($\pi^{12}\delta^{4}$,ν_{NN} = 1890 cm^{-1}, d_{NN} = 1.152(19) Å), which showed high activity in catalytic ammonia formation, likely *via* reactivity of the terminally coordinated N_2 ligands.[144]

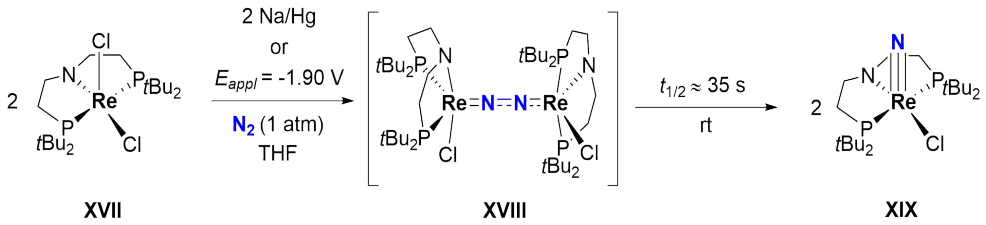

Scheme 1.5: (Electro)chemical dinitrogen splitting upon reduction of Re^{III} pincer complex **XVII** with formation of the dinuclear intermediate **XVIII** and the Re^{V} nitride product **XIX**.

In 2014, *Schneider* and coworkers reported the first example of full dinitrogen cleavage in the coordination sphere of a rhenium pincer complex (Scheme 1.5).[123] One electron reduction of the five-coordinate Re^{III} complex [($^{t\mathrm{Bu}}$PNP)$ReCl_2$] ($^{t\mathrm{Bu}}$PNP = $N(CH_2CH_2P t\mathrm{Bu}_2)_2$) under dinitrogen atmosphere furnished the corresponding nitride complex and computations supported a *zig-zag* transition state upon elongation of the N-N bond of the μ-N_2 ligand in the N_2-bridged intermediate. In a follow-up study the authors elucidated the complex mechanism for the formation of the dinuclear intermediate with the aid of electrochemical methods and were able to crystallographically characterize the thermally labile intermediate (d_{NN} = 1.202(10) Å, $\pi^{10}\delta^{4}$).[124] Furthermore, homogeneous electrochemical splitting in moderate yields (up to 60%) was demonstrated and the nitride product was implemented into a synthetic cycle, furnishing nitriles from N_2 and organic triflates.[145–147] Electrochemical dinitrogen splitting was further reported by *Masuda* and coworkers, who utilized a diphosphine

ligated Mo^0 terminal dinitrogen complex for oxidative electrochemical splitting *via* a dinuclear intermediate into the corresponding Mo nitride complex.[148]

Thermally inaccessible (endothermic) N_2 splitting was in certain cases realized upon photochemical excitation. This is especially attractive since the photochemically derived nitride complexes are expected to be more reactive than nitrides derived from thermal N_2 splitting, which are often relatively inert due to overstabilization. Unfortunately, photochemical dinitrogen splitting is still comparably rare.[149] *Floriani* and coworkers reported the thermally stable dinuclear complex $[((Mes)_3Mo)_2(\mu\text{-}N_2)]$ (π^{10}), which splits dinitrogen upon irradiation (λ = 365 nm) and forms a dinuclear bridging nitride complex. The diverging reactivity compared to the isoelectronic example initially reported by *Cummins* $[((NRAr)_3Mo)_2(\mu\text{-}N_2)]$ is attributed to a lack of π-donor ligands like amides.[150] The "*Cummins* complex" also showed photolytic cleavage of the N_2 bridge at low temperature.[118] Investigation of the photochemical process with transient spectroscopy revealed excitation from the $e_g^4e_u^2$ ground state to an $e_g^3e_u^3$ excited state, followed by internal conversion.[151] Dinitrogen splitting is finally induced by a bending motion of the Mo-N-N-Mo core from an activated vibrational mode.

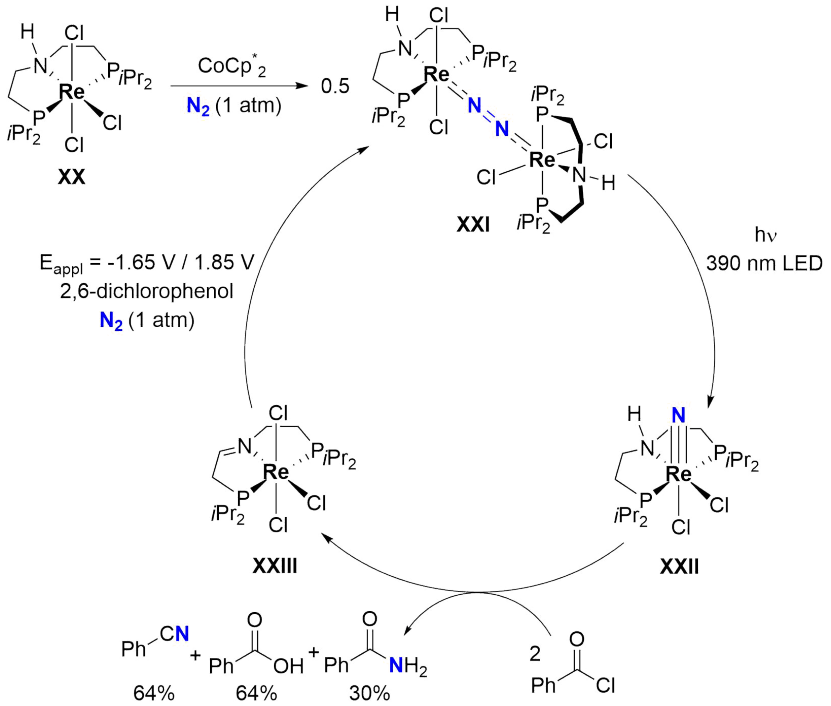

Scheme 1.6: (Electro)chemical three-step cycle for the synthesis of benzonitrile, benzoic acid and benzamide from N_2 and benzoyl chloride.

Schneider, Krewald and coworkers reported an interesting combination of metal-ligand cooperativity and photolytical dinitrogen splitting (Scheme 1.6).[152] PNP pincer Re^{III} complex **XX** formed upon reduction under N_2 a dark-blue, thermally stable $\pi^{10}\delta^4$ dinuclear Re^{II}/Re^{II} complex **XXI**, which reacted by cleavage of the N_2 ligand upon irradiation with UV light (λ = 390 nm). The product, Re^{V} nitride **XXII**, subsequently showed reactivity with benzoyl chloride in a metal-ligand cooperative fashion to form Re^{III} imine complex **XXIII** with an oxidized pincer backbone and benzonitrile, benzamide and benzoic acid. The dinuclear complex **XXI** could be regenerated (electro)chemically to close a synthetic cycle. The thermal stability of **XXI** was attributed to the presence of a ligand *trans* to the N_2 bridge, which rises the $\sigma-\sigma^*-\sigma$ MO in energy. This resembles the situation of a related photolytic dinitrogen splitting from an octahedral Re^{II} dinuclear dinitrogen complex reported by *Miller* and coworkers.[153] The only example of splitting of a dinitrogen ligand in the coordination sphere of Osmium was reported by *Kunkely* and *Vogler* with the splitting of $[(NH_3)_5Os(\mu\text{-}N_2)Os(NH_3)_5]^{5+}$ ($\pi^{11}\delta^4$) upon irradiation (λ = 250 – 390 nm).[154,155] Computations suggest that N_2 cleavage results from population of the $\sigma-\sigma^*-\sigma$ orbital, which decreases in energy along the reaction coordinate. Follow-up chemistry suggested the formation of a nitrosyl ligand upon oxidation with ClO_2, however, no isotopic labeling experiments were conducted.[156,157]

1.3 Motivation and Scope

In this part the dinitrogen activation and splitting in the coordination spheres of Re and Os PNP pincer complexes is examined. Initial results towards unprecedented splitting of gaseous dinitrogen with well-defined Os complexes will focus on the synthesis and spectroscopic characterization of dinuclear dinitrogen-bridged Os pincer complexes. The second part revolves around (electro)chemical dinitrogen splitting on a chemically robust pincer complex.

The aliphatic ligand backbone of *cis*-[($^{i\text{Pr}}$PNP)Re(N)Cl_2] (**XXII**) was shown to participate in proton coupled electron transfer reactions in which it was acting as a proton and electron reservoir.[152] While this ligand-centered reactivity was exploited productively in the synthesis of benzamide, it can cause detrimental side reactions with respect to nitride functionalization. Especially under oxidative conditions, the aliphatic pincer backbone may not be compatible with reactive reagents. In preliminary oxidation and functionalization attempts on the corresponding Re^{VI} nitride complex of **XXII** this was identified as a key problem.[158]

A plausible mitigation strategy involves the usage of a more robust divinylamide pincer ligand. However, (electro)chemical dinitrogen splitting of divinylamide pincer Rhenium complexes proceeds in significantly lower yields[159] and the backbone remains susceptible to electrophilic addition (e.g. protonation with HOTf)[146]. In an attempt to balance a high dinitrogen splitting yield with chemical stability we resorted to the diarylamide PNP pincer ligand ($^{\text{Ph}}$PNP = N(C_6H_3(4-Me)P*i*Pr_2)$_2$), which was introduced and commonly adopted by the groups of *Ozerov* and *Mindiola*.[160–167]

Ison and coworkers reported the synthesis of [($^{\text{Ph}}$PNP)Re(N)Cl], albeit not from N_2 splitting.[168] Moreover, the authors showed follow-up N-C bond formation by reaction with CO to form organic isocyanates. Synthetic access towards [($^{\text{Ph}}$PNP)Re(N)Cl] upon N_2 cleavage therefore **would enable the synthesis of organic isocyanates from N_2 and CO**, which is still a rare process. Furthermore, successful dinitrogen splitting would **establish a chemically robust nitride pincer platform** as starting point for **new oxidative functionalization of dinitrogen-derived nitride complexes**.

1.4 Formation and Oxidation of an Os^{II}/Os^{II} Dinuclear Dinitrogen-Bridged Complex

1.4.1 Synthesis and Spectroscopic Characterization of $[(({}^{Py}PNP)OsCl_2)_2(\mu\text{-}N_2)]$

Initial attempts for the formation of a dinuclear dinitrogen-bridged Osmium complex using the ${}^{iPr}P^{H}NP$ ((*i*Pr$_2$PCH$_2$CH$_2$)$_2$NH) ligand showed (see Chapter 3.3.2) that the aliphatic pincer backbone is susceptible to side reactions leading to mixtures of compounds and complicated selectivity control of the reaction outcome. Furthermore, only mononuclear terminal N_2 complexes were obtained, indicating that other factors like dispersion interactions might influence the equilibrium of terminal vs. bridging N_2 coordination.[169] As a consequence, the ligand system was changed to more sterically demanding and chemically robust pincer ligands. The ${}^{Ph}P^{H}NP$ ligand (bis(2-(diisopropylphosphaneyl)-4-methylphenyl)amine) and its derivatives are commonly used in transition metal chemistry.[160,170–174] Especially its chemical stability e.g. in vanadium alkylidene chemistry and the isolation of stable dinitrogen-bridged complexes[163,175] marked the formation of a ${}^{Ph}PNP$ Osmium complex as a synthetic target.

Stirring a suspension of $OsCl_3 \cdot 3\ H_2O$ in toluene with the ${}^{Ph}P^{H}NP$ ligand at 120 °C resulted in a gradual color change to intensely green over the course of several days. From the resulting mixture the Os^{IV} complex $[({}^{Ph}PNP)OsCl_3]$ (**1**) was isolated in moderate yield (40%) and characterized by X-ray crystallography, multinuclear NMR spectroscopy, mass spectrometry and elemental analysis. In the solid-state structure (isomorphous and isostructural to the related Re^{IV} trichloride complex $[({}^{Ph}PNP)ReCl_3]$, see chapter 1.5.2) the loss of the nitrogen-bound hydrogen atom is evident from the sum of the bond angles around the nitrogen atom ($\Sigma = 360°$) and its ideal planarity. The loss of the hydrogen atom could be explained by the release of H_2 (as for the formation of the related $[({}^{Ph}PNP)ReCl_3]$ complex, see chapter 1.5.2) or, based on the relatively low yield, by the formation of another product as acceptor of H-atom equivalents. In the $^{31}P\{^1H\}$ NMR spectrum **1** exhibits a resonance at $\delta_{31P} = -125.1$ ppm, which is characteristically high-field shifted analogous to other octahedral Re^{III}, Os^{IV} and the isolobal square planar Os^{II} complexes due to the influence of temperature independent paramagnetism (TIP).[176,177] This is generally explained as a consequence of mixing of higher spin states with the thermally well-separated closed shell ground state (second order Zeeman effect). This effect is also visible in the ^1H NMR spectrum of **1** (Figure 1.5), where some resonances appear shifted

(e.g. the benzylic CH_3 groups show a singlet at $\delta_H = 5.03$ ppm, whereas in most other complexes with the ^{Ph}PNP ligand the signal can be found around 2 ppm).

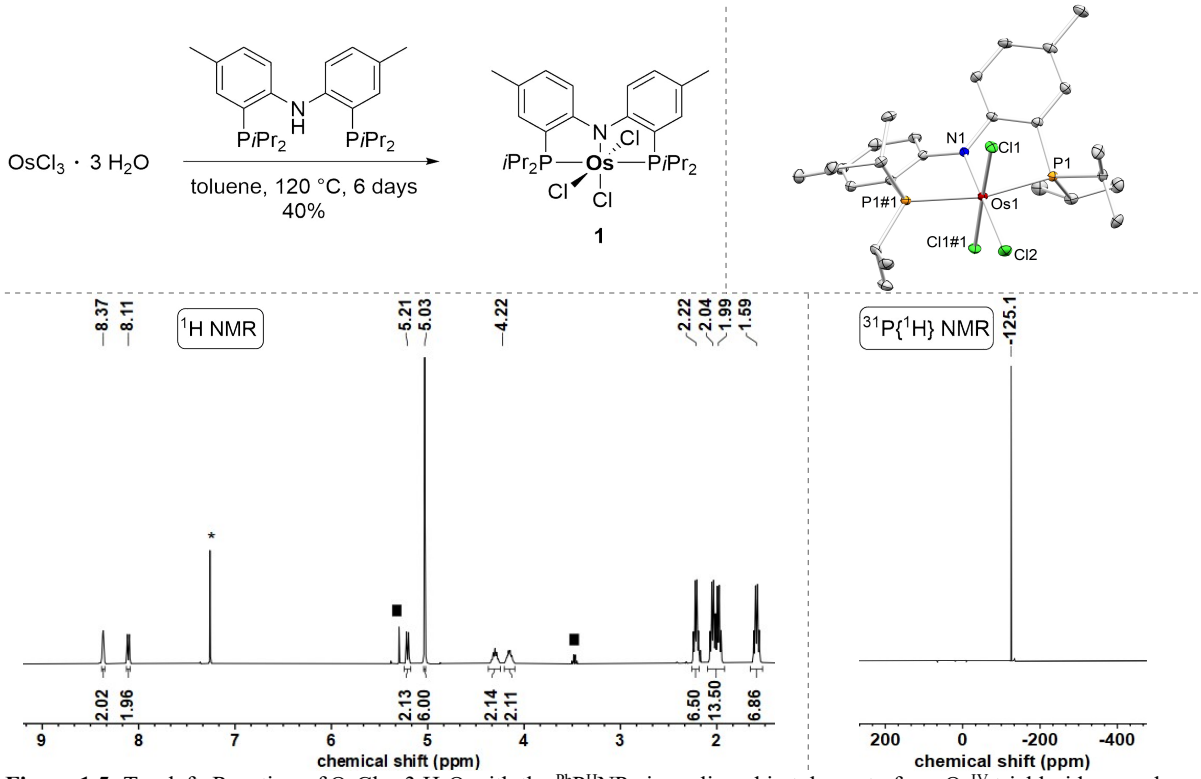

Figure 1.5: Top left: Reaction of $OsCl_3 \cdot 3\ H_2O$ with the $^{Ph}P^{H}NP$ pincer ligand in toluene to form Os^{IV} trichloride complex [(^{Ph}PNP)$OsCl_3$] (**1**) in 40% yield over the course of six days at 120 °C. Top right: Molecular structure of complex **1** from single-crystal X-ray diffraction (thermal ellipsoids drawn at the 50% probability level); hydrogen atoms are omitted for clarity. Selected bond lengths [Å] and angles [°]: Os1-N1 1.945(2), Os1-Cl1 2.3529(5), Os1-Cl2 2.3900(7), Os1-P1 2.3780(5), P1-Os1-P1#1 163.15(2), Cl1-Os1-Cl1#1 177.19(3). Bottom left: ^{1}H NMR spectrum of crystalline **1** dissolved in $CDCl_3$. Solvent signal is marked with an asterisk and residual solvent impurities (CH_2Cl_2 / Et_2O) are marked with black rectangles. Bottom right: $^{31}P\{^1H\}$ NMR spectrum of crystalline **1** dissolved in $CDCl_3$.

Electrochemical examination of **1** by cyclic voltammetry revealed a reversible reduction at $E_{1/2} = -0.87$ V (vs. $Fc^{+/0}$, 100 – 1000 mV/s), indicating that chloride loss is slow on the CV timescale. Preliminary attempts of reduction under N_2 atmosphere or reaction with azide to form an Osmium nitride were not successful. Further investigations on this platform conducted by *Martijn Tepaske* and *Marc Neben* revealed that chloride loss is difficult, leading to the formation of an anionic Osmate complex upon reduction.

The neutral, pyridine based pincer ligand ^{Py}PNP has been used in literature for the synthesis of dinitrogen-bridged dinuclear complexes. Two notable examples are the Molybdenum based [((^{Py}PNP)$Mo(N_2)_2)_2(\mu\text{-}N_2)$][178] or the more recent dinuclear Rhenium complex [((^{Py}PNP)$ReCl(N_2))_2(\mu\text{-}N_2)$][144], which both showed good activity in ammonia formation upon addition of electron and proton equivalents. The isoelectronic Os^{II}/Os^{II} dinuclear complex was

not reported, however, given that the synthesis of the Os^{III} complex [(^{Py}PNP)$OsCl_3$] (**2**) was described by *Goldman* and coworkers, facile access upon reduction under N_2 was envisioned.[179] After adapting the reported literature procedure from $Na_2[OsCl_6] \cdot 6\ H_2O$ to $(NH_4)_2[OsCl_6]$ to account for the different solubility of the Osmium precursor, reaction of the ^{Py}PNP ligand with $(NH_4)_2[OsCl_6]$ in 2-methoxyethanol at 120 °C for 24 hours furnished 85% of orange, paramagnetic [(^{Py}PNP)$OsCl_3$] (**2**) after workup.

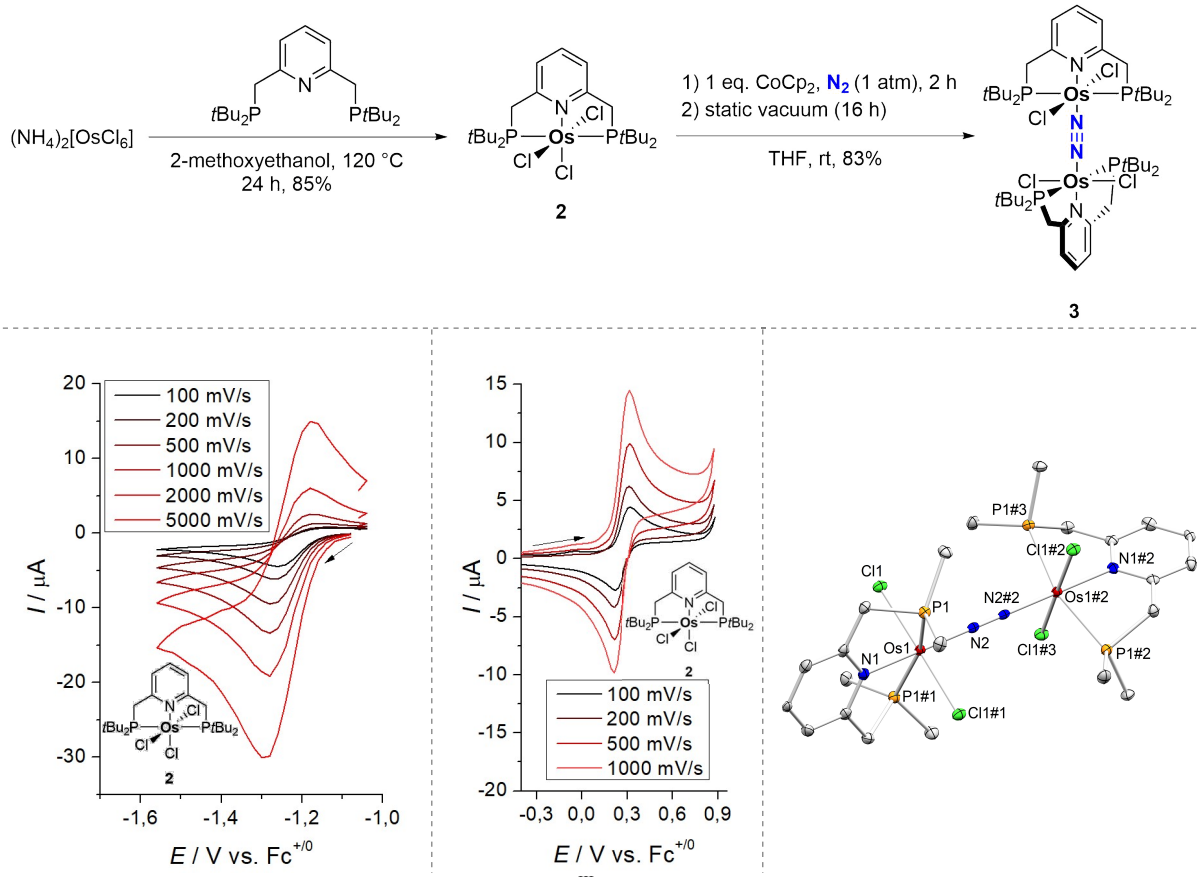

Figure 1.6: Top: Adapted, literature-known synthesis of Os^{III} complex **2** starting from $(NH_4)_2[OsCl_6]$ and formation of the dinuclear dinitrogen-bridged Os^{II}/Os^{II} complex [((^{Py}PNP)$OsCl_2$)$_2$(μ-N_2)] (**3**) upon initial reduction under N_2 and stirring under static vacuum. Bottom left: CV of Os^{III} complex **2** at different scan rates (1 mM **2**, THF, Ar, 0.2 M nBu$_4$NPF$_6$). Bottom right: Molecular structure of complex **2** from single-crystal X-ray diffraction (thermal ellipsoids drawn at the 50% probability level); Hydrogen atoms and one pentane solvent molecule are omitted for clarity. Furthermore, only the central carbon atoms of the tert-butyl substituents are shown. Selected bond lengths [Å] and angles [°]: Os1-N2 1.947(4), Os1-N1 2.065(4), Os1-P1 2.4105(9), N2-N2#2 1.120(7), N2-Os1-N1 180.0, N1-Os1-Cl1 89.558(19), N1-Os1-P1 80.64(2).

The CV of **2** revealed a quasi-irreversible reduction at $E_{pc} = -1.26$ V and a reversible oxidation at $E_{1/2} = +0.27$ V (Figure 1.6). The mild reduction potential of the $Os^{III/II}$ couple and its (quasi-)irreversibility are indicative of a chemical follow-up step after reduction (presumably chloride loss). Addition of one equivalent of $CoCp_2$ to a solution of **2** in THF under N_2 atmosphere led to a rapid color change to blood red. Single-crystals suitable for X-ray crystallography were grown from THF/pentane under argon atmosphere over the course of several days at room temperature. The solid-state structure suggested the formation of the

dinuclear dinitrogen-bridged $Os^{II/II}$ complex $[(({}^{Py}PNP)OsCl_2)_2(\mu\text{-}N_2)]$ (**3**, Figure 1.6). **3** crystallizes in the tetragonal space group $I4_1/a$ and both pincer subunits are twisted by 90° with respect to each other (*trans*,*trans*-isomer). The central N_{py}-Os-N-N-Os-N_{py} atoms lie on a crystallographically imposed symmetry axis, resulting in idealized 180° bond angles along this axis. The N-N bond length is d_{NN} = 1.120(7) Å, which is only slightly longer than the N-N bond in molecular N_2 (d_{NN} = 1.10 Å), suggestive of a low degree of activation and a mostly retained triple bond character of the N_2 ligand, as expected for the $\pi^{12}\delta^4$ electronic configuration. The N-N bond length in **3** is, furthermore, slightly shorter than the bond of the N_2 ligand in the isoelectronic complexes $[(({}^{Py}PNP)Mo(N_2)_2)_2(\mu\text{-}N_2)]$ (d_{NN} = 1.146(4) Å)[178] and $[(({}^{Py}PNP)ReCl(N_2))_2(\mu\text{-}N_2)]$ (d_{NN} = 1.152(19) Å)[144]. As an octahedral d^6 complex, **3** exhibits a diamagnetic ground state as evident from the sharp resonance in the $^{31}P\{^1H\}$ NMR (δ_{31P} = 26.6 ppm) and mostly sharp and *J*-resolved signals in the ^1H NMR. No IR stretch for the N_2 ligand was detected from solid, crystalline **3**, in agreement with the highly symmetric nature of the molecule in the solid-state.

Following the reduction of **2** under N_2 atmosphere *via* $^{31}P\{^1H\}$ NMR revealed that initially a mixture of compounds is formed (Figure 1.7). The main product besides **3** after 30 minutes under N_2 atmosphere exhibits a chemical shift of δ_{31P} = 31.1 ppm. Surprisingly, when the N_2 atmosphere was removed and the *J*-Young NMR tube inverted under static vacuum over night, the ratio of the signal at δ_{31P} = 31.1 ppm to **3** was significantly shifted towards **3**, suggesting that additional **3** was formed from the species at δ_{31P} = 31.1 ppm under static vacuum. Based on this observation the initial formation of a terminal N_2 complex $[({}^{Py}PNP)OsCl_2(N_2)]$ (**4**) upon reduction is proposed (Figure 1.7). This is further corroborated by IR measurements, in which a broadened band at ν = 2081 cm^{-1} (solid, ATR IR) was observed after 30 minutes under N_2 atmosphere, characteristic for a terminally coordinated and weakly activated N_2 ligand. After removal of the N_2 atmosphere and inverting the NMR tube under static vacuum the IR stretch at ν = 2081 cm^{-1} had almost disappeared, indicating the conversion of the proposed terminal N_2 complex into an IR silent species (with regard to the region of terminal N_2 ligands between 2100 and 1600 cm^{-1}). Furthermore, the IR shift is very similar to other octahedrally coordinated, terminal Os^{II} N_2 complexes (e.g. ν_{NN}(*trans*-$[({}^{iPr}P^{H}NP)OsCl_2(N_2)]$) = 2066 cm^{-1}, see chapter 3.3.2) and is in very good agreement with the DFT calculated value for a *trans*-$[({}^{Py}PNP)OsCl_2(N_2)]$ complex ($\nu_{NN,DFT}$(**4**) = 2095 cm^{-1}, BP86/def2-QZVP(Os,Cl,P,N);def2-SVP).

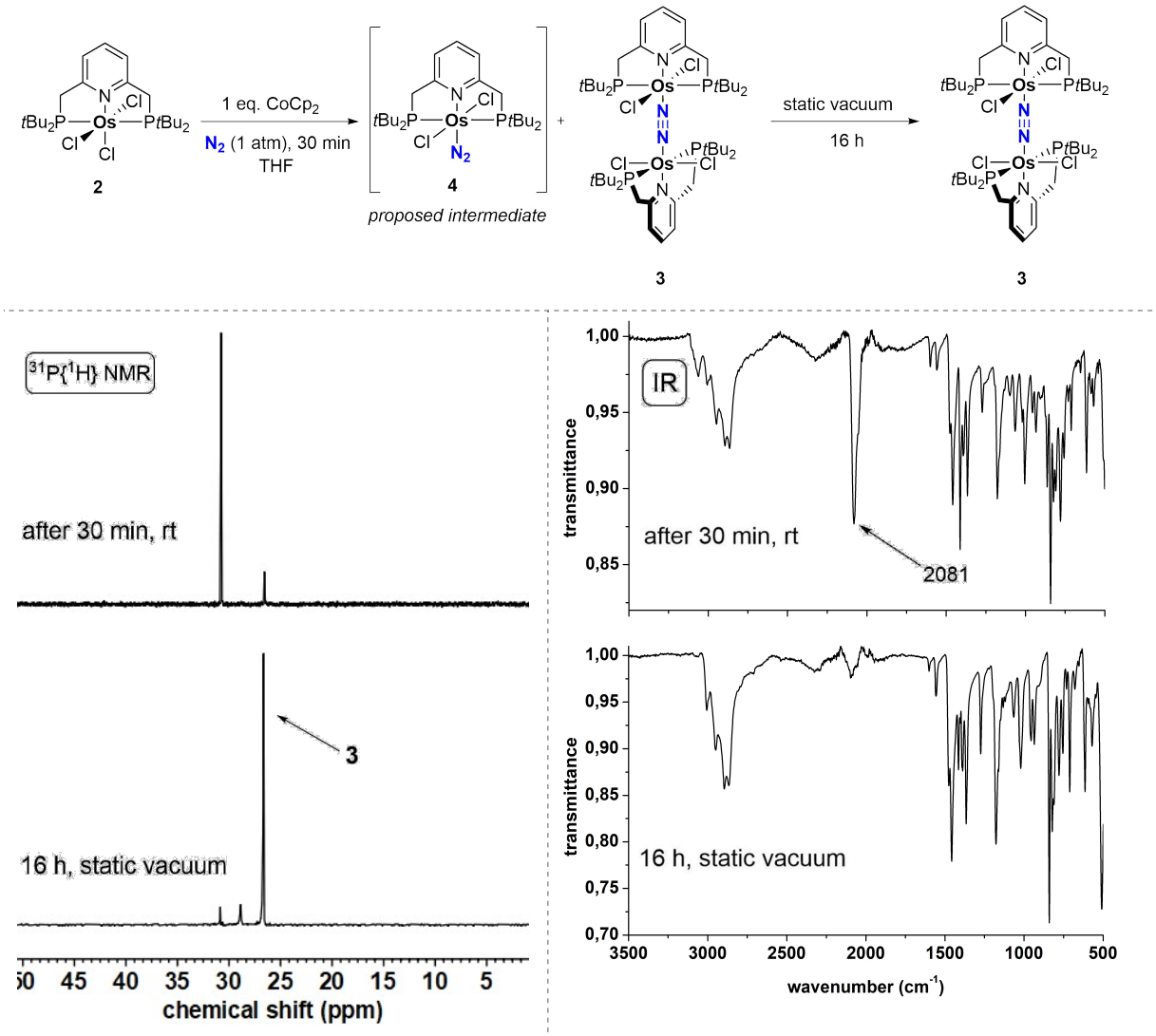

Figure 1.7: Top: Formation of the dinuclear dinitrogen-bridged Os^{II}/Os^{II} complex **3** upon application of static vacuum to the proposed Os^{II} terminal N_2 complex intermediate **4**. Bottom left: $^{31}P\{^1H\}$ NMR spectra after 30 min under N_2 atmosphere (top spectrum) and after 16 hours under static vacuum (bottom spectrum). Bottom right: IR (ATR, solid) spectra after 30 minutes under N_2 atmosphere and after 16 hours under static vacuum.

In a recent publication, *Holland*, *Miller*, *Goldman* and coworkers examined computationally the equilibrium of mononuclear terminal vs. dinuclear dinitrogen-bridged N_2 coordination to unveil underlying trends within series of isoelectronic metal complexes of different PNP pincer ligands.[169] They correlated the change in π-bond order from two terminal N_2 complexes to a dinuclear dinitrogen-bridged complex and one free N_2 molecule with the calculated free energy of this reaction. The formation of a μ-N_2 complex from two terminal d^6 N_2 complexes was calculated to be slightly energetically disfavored compared with the terminal N_2 complexes, however, the authors found that outer-sphere dispersion interactions between the pincer ligands can be capable of mitigating this energetic penalty, leading to admixtures of terminal and dinitrogen-bridged complexes. The initial formation of a mixture of terminal (**4**) and dinitrogen-

bridged complexes (**3**) is in agreement with these computational results and suggests the terminal N_2 complex **4** to be of similar energy compared to **3**. Application of a static vacuum subsequently shifts the equilibrium to the side of the dinitrogen-bridged complex **3** by "removing" one of the products (the free N_2) from the equilibrium. The formation of a μ-N_2 complex with the sterically demanding ^{Py}PNP ligand – in contrast to unsuccessful attempts on the less bulky $^{iPr}P^{H}$NP and ^{Ph}PNP ligands – could furthermore suggest beneficial contribution of the aforementioned dispersion interactions. In future experiments it would be interesting to systematically vary the steric demand of the ^{Py}PNP ligand by changing the organic substituents on the phosphorus atoms, as well as modifying the pincer backbone (e.g. using the oxygen-bridged "PONOP" ligand) and examine the influence on the equilibrium of terminal vs. bridging N_2 coordination.

The spectroscopic properties of **3** were investigated in more detail. In the resonance Raman spectrum (633 nm laser) of **3** in frozen THF-d_8 a sharp band at $\nu = 2056$ cm^{-1} was observed (Figure 1.8) in agreement with a bridging N_2 ligand, which was confirmed by measurement of the $^{15}N_2$-isotopologue **$^{15}N_2$-3** that showed a stretch at $\nu = 1991$ cm^{-1} for the $^{15}N_2$ ligand. The difference of the N_2 stretch for both isotopologues matches well with the expected value from the harmonic oscillator approximation ($\Delta\nu = 68$ cm^{-1}). The Raman band is significantly shifted to higher wavenumbers compared to the related d^6-d^6 dinuclear N_2-bridging complexes $[(^{Py}PNP)Mo(N_2)_2)_2(\mu\text{-}N_2)]$[178] and $[(^{Py}PNP)ReCl(N_2))_2(\mu\text{-}N_2)]$[144] (both ν = 1890 cm^{-1}, $\lambda_{exc.}$ = 514.4 nm). Furthermore, in both **3** and **$^{15}N_2$-3** isotopologues a similarly intense stretch at $\nu = 1601$ cm^{-1} can be assigned to the C=N bond(s) in the pyridine pincer backbone. In the UV/Vis spectrum two broad absorptions at λ = 418 and 517 nm were observed, which explains the blood-red color of **3**. Interestingly, in the ^{1}H NMR of **3** severe broadening of the hydrogen atoms of the tert-butyl groups was observed, indicating dynamic behaviour in solution on the NMR timescale that could not be resolved even by cooling down to –60 °C. From the ^{1}H-DOSY NMR (see appendix) a diffusion constant of $D = 5.5{\cdot}10^{-6}$ $cm^2{\cdot}s^{-1}$ was derived, verifying the presence of a dinuclear species in solution based on the calculated molecular weight (1590 $g \cdot mol^{-1}$).

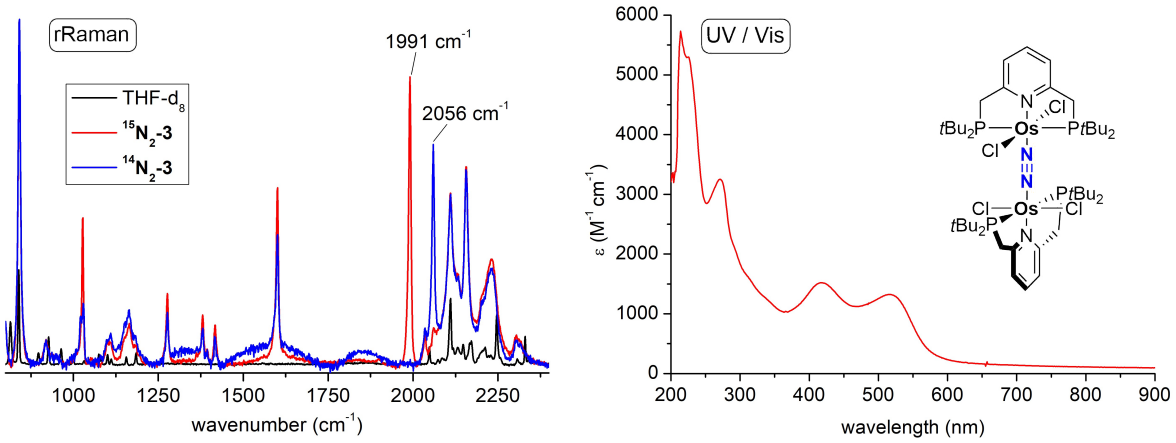

Figure 1.8: Left: Resonance Raman ($\lambda_{exc.}$ = 633 nm) of natural abundance **3** and **$^{15}N_2$-3** in frozen THF-d_8. Right: UV/Vis spectrum of **3** in THF solution (0.099 mM).

Based on the absorptions in the UV/Vis spectrum of **3** irradiation for potential photolytical dinitrogen cleavage was subsequently attempted. Irradiation of a solution of **3** in THF with a LED at λ_{max} = 467 nm resulted in the slow conversion (ca. 30% conversion after 15 hours irradiation) of **3** to the species in $^{31}P\{^1H\}$ NMR, which was assigned as the terminal N_2 complex **4** (see appendix), indicating metal-nitrogen bond cleavage at this wavelength. **3** can be stored for a long time in the solid state under argon atmosphere at ambient light conditions (no decomposition or formation of **4** was observed over the course of 1.5 years). Slow conversion of **3** to **4** was observed upon irradiation with higher energy wavelengths at λ_{max} = 456 and 427 nm. Interestingly, irradiation at λ_{max} = 390 nm did not form – according to the $^{31}P\{^1H\}$NMR – **4**, but rather unselectively several new resonances with one main, unidentified resonance at δ_{31P} = 39.0 ppm appeared. Although no photolytic splitting or selective functionalization was observed from **3** it would be interesting to examine its potential for ammonia formation upon addition of proton and electron equivalents in future experiments, in vein of the related molybdenum and rhenium dinuclear complexes reported by *Nishibayashi* and coworkers.

1.4.2 Reactivity of the Mixed-Valence $[(({}^{Py}PNP)OsCl_2)_2(\mu\text{-}N_2)]^+$ Complex

Based on the molecular orbital picture of the central M-N-N-M subunit for dinuclear dinitrogen-bridged complexes[152,169,180,181] the fully occupied HOMO in **3** is of M-N antibonding and N-N bonding character, partially explaining the strong N-N bond in **3** and the absence of dinitrogen splitting into nitrides from d^6 dinuclear dinitrogen-bridged complexes. The only example of

nitride formation upon dinitrogen splitting with Osmium complexes utilizes a mixed-valent Os^{II}/Os^{III} complex[182] ($\pi^{11}\delta^4$) while other examples of photolytic[152] or thermal[123,148,183,184] dinitrogen cleavage split from a $\pi^{10}(\delta^4)$ configuration. Accordingly, the oxidation of formally $\pi^{12}\delta^4$ complex **3** was investigated. The CV in THF (see appendix) revealed two reversible oxidations at $E_{1/2}$ = –0.42 V and +0.33 V (vs. $Fc^{+/0}$), respectively, in compliance with the proposed Os^{II}/Os^{II} to Os^{II}/Os^{III} and Os^{II}/Os^{III} to Os^{III}/Os^{III} oxidations.

Oxidation of **3** with one equivalent of ferrocenium salts (Fc[X], X = OTf, $[BF_4]$, $[Al(OC(CF_3)_3)_4]$ and $BArF_{24}$) in the dark resulted in a rapid color change to yellowgreen. In the $^{31}P\{^1H\}$ NMR no resonance was observed, in agreement with the formation of a paramagnetic species. Furthermore, in the ^1H NMR broadened resonances with no resolved *J*-coupling were observed and measurement of the magnetic moment in solution (μ_{eff} = 1.57 μ_B ± 0.1) suggested a S = ½ ground state based on the formation of a mixed-valent Os^{II}/Os^{III} dinuclear complex $\mathbf{5}^+$ (Figure 1.9).

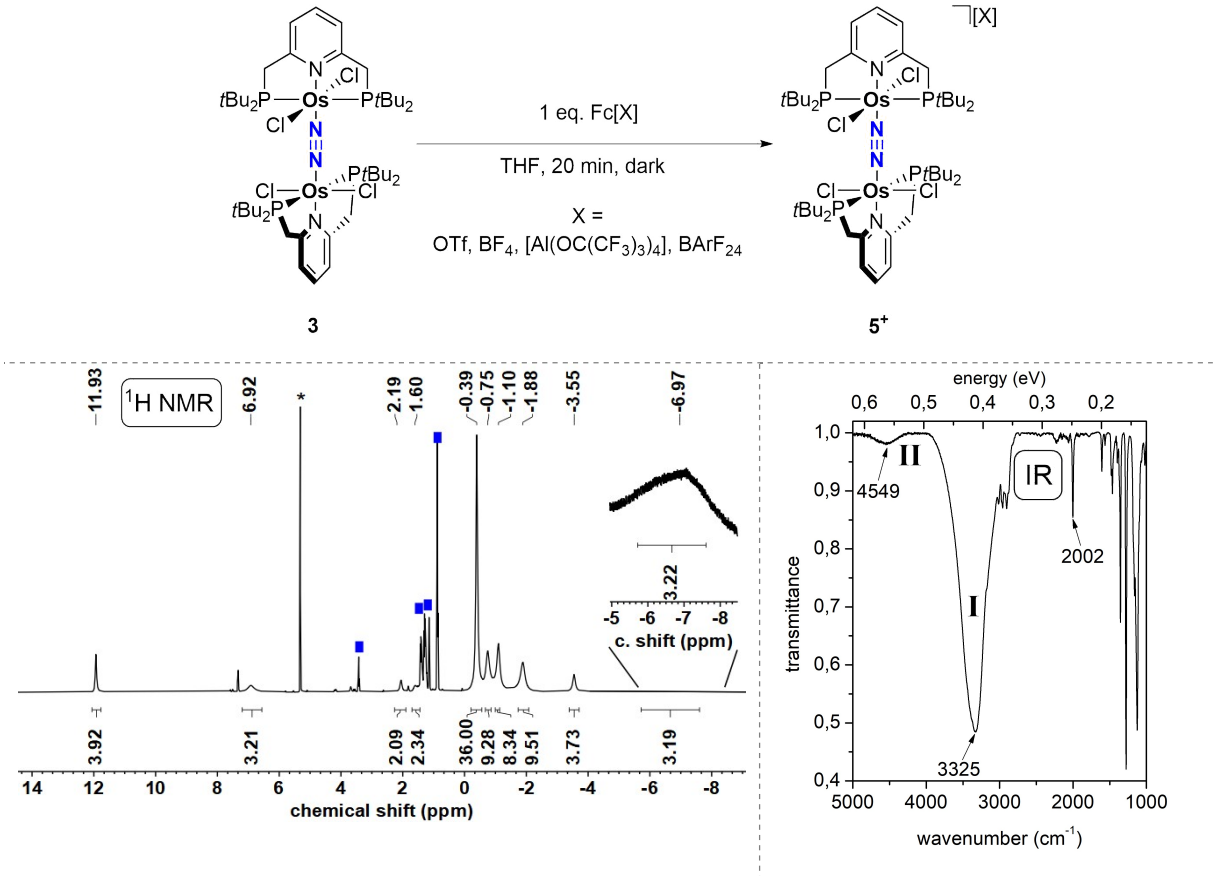

Figure 1.9: Top: Oxidation of **3** with one equivalent of ferrocenium salts to form the cationic mixed-valence Os^{II}/Os^{III} complex $\mathbf{5}^+$. Bottom left: ^1H NMR spectrum of crystalline $\mathbf{5}^{OTf}$ in CD_2Cl_2. Blue rectangles indicate pentane and diethylether impurities and the asterisk marks the residual solvent signal. Bottom right: IR (ATR, solid) of crystalline $\mathbf{5}^{BArF}$.

Spectroscopically, $\mathbf{5}^+$ is an extraordinarily interesting complex as Os^{II}/Os^{III} mixed-valent complexes like $\mathbf{5}^+$ were previously examined thoroughly, resulting in the well-known categorization into a localized to delocalized mixed-valence transition expressed in the Robin-Day classes I, II and III.[185–188] Consequently, the electronic absorption of $\mathbf{5}^+$ in different spectral areas was examined to gain information about the degree of delocalization. In the IR (ATR, solid) of $\mathbf{5}^+$ a very intense and broad absorption at $\nu = 3325$ cm^{-1} was observed, in addition to a weaker, broad absorption at 4549 cm^{-1}. A rather sharp, but weak band at $\nu = 2002$ cm^{-1} can be ascribed to the bridging N_2 ligand, based on very similar stretches for related Os^{II}-N_2-Os^{III} complexes (e.g. *trans*-,*trans*-$[((tpy)Cl_2Os)_2(\mu\text{-}N_2)]^+$, $\nu_{NN} = 2007$ cm^{-1}).[187] The appearance of a N_2 band in $\mathbf{5}^+$ can be an indication of electronic asymmetry on the timescale of the IR experiment, however, in contrast to other Os^{II}-N_2-Os^{III} complexes the intensity of the N_2 stretch in $\mathbf{5}^+$ is rather low. The two broad absorptions at $\nu = 3325$ cm^{-1} (band **I**) and $\nu = 4549$ cm^{-1} (band **II**), respectively, can be assigned as interconfigurational (IC) bands originating from transitions between the Kramer's doublets of the different orbital configurations of the $d\pi^5$ Os^{III} core.[186,187] Especially, the band shape and the relative intensity of the two transitions in $\mathbf{5}^+$ is strikingly similar to related Os^{II}-N_2-Os^{III} complexes, like $[((tpm)Cl_2Os)_2(\mu\text{-}N_2)]^+$ or $[((Tp)Cl_2Os)_2(\mu\text{-}N_2)]^-$.[187]

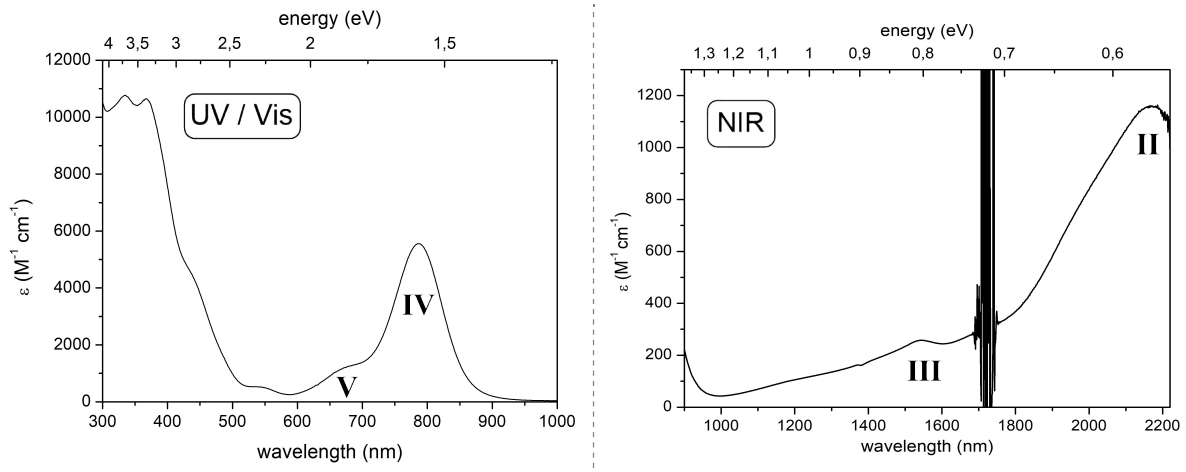

Figure 1.10: Left: UV/Vis spectrum of $\mathbf{5}^{\mathbf{BArF}}$ in THF. Right: Near IR spectrum of $\mathbf{5}^{\mathbf{BArF}}$ in THF. The region around 1730 nm shows artifacts produced by the spectrometer.

In the near IR spectrum of $\mathbf{5}^{\mathbf{BArF}}$ (Figure 1.10, right) the band at $\lambda = 2171$ nm ($\nu = 4606$ cm^{-1}, $\varepsilon = 1159$ M^{-1}cm^{-1}) could correspond to the relatively weak IC band in the solid IR spectrum (band **II**) at $\nu = 4543$ cm^{-1} (Figure 1.9), but for a reliable comparison the IR has to be recorded in solution, especially to compare the extinction coefficients. Three intervalence (IT) bands from the $d\pi$ orbitals on the Os^{II} core to the Os^{III} hole were assigned: The weak band at 1541 nm

(band **III**, ν = 6489 cm^{-1}, ε = 257 $M^{-1}cm^{-1}$) in the NIR spectrum, the intense absorption in the UV/Vis at 788 nm (band **IV**, ν = 12691 cm^{-1}, ε = 5570 $M^{-1}cm^{-1}$), as well as the "shoulder" type of absorption at 669 nm (band **V**, ν = 14948 cm^{-1}, ε = 1155 $M^{-1}cm^{-1}$) are in good agreement with the assigned bands for $[((tpm)Cl_2Os)_2(\mu\text{-}N_2)]^+$ and $[((Tp)Cl_2Os)_2(\mu\text{-}N_2)]^-$ (Table 1.2).[187]

Table 1.2: Comparison of characteristic interconfigurational (IC) and intervalence (IT) bands in dinitrogen-bridged diosmium complexes.[186,187]

complex	E_a [cm^{-1}] (ε [$M^{-1}cm^{-1}$]) $\Delta\nu_{1/2}$ [cm^{-1}]				
	band **I**	band **II**	band **III**	band **IV**	band **V**
$[((tpm)Cl_2Os)_2(\mu\text{-}N_2)]^+$ in DMSO	3460 (1500) 770	5200 (230) 1100	7000 (100) 1200	11400 (2100) 1300	12800 (750) 2200
$[((Tp)Cl_2Os)_2(\mu\text{-}N_2)]^-$ in CH_3CN	3580 (3730) 600	5240 (930) 1100	7070(320) 1300	11700 (5100) 1400	13100 (1500) 2200
$\mathbf{5}^+$ in THF	3325 (-) 362[a]	4606 (1159) 320[b]	6489 (257) 297	12691 (5570) 1469	14948 (1155) 1184[b]

[a] derived from solid-state ATR-IR. [b] very hard to determine, due to skewed baseline.

As pointed out by *Meyer* and coworkers, the presence of these bands alone is not sufficient to rule out electronic localization, but in combination with the presence of a weak N_2 stretch in the IR spectrum it can be inferred that electron transfer is rather slow on the timescale of the IR experiment. The relative sharpness of the IT bands, on the other hand, was interpreted as indication for a class II-III compound, as defined by *Meyer* and coworkers.[187] Unfortunately, no solid-state structure which could give additional structural information about localized oxidation states was obtained, since $\mathbf{5}^+$ crystallized with the weakly coordinating counterions $BArF_{24}^-$ and $[Al(OC(CF_3)_3)_4]^-$ only as very thin, poorly diffracting plates. Overall, the existence of the five characteristic absorptions in the IR/NIR and UV/Vis and their similar band shape and intensity is a strong indication that $\mathbf{5}^+$ can be assigned to the class II-III, like other related dinitrogen-bridged Osmium complexes.

Subsequently, the reactivity of $\mathbf{5}^+$ with focus on dinitrogen splitting was examined. Especially the example of *Kunkely* and *Vogler*,[154] the photolytic cleavage of dinitrogen from a $\pi^{11}\delta^4$ Os^{II}-N_2-Os^{III} complex, prompted irradiation experiments with $\mathbf{5}^+$. Irradiation of $\mathbf{5^{OTf}}$ with an LED at λ_{max} = 370 nm (close to one of the absorption maxima of $\mathbf{5}^+$) led to a colorchange from dark greenbrown to bright orange over the course of 4.5 hours at room temperature. In the ^1H NMR the disappearance of the signals for $\mathbf{5}^+$ is accompanied by the formation of a very broad signal around δ_H = –7 ppm and further broad, intense signals at δ_H = 18.14 and 12.42 ppm, respectively. These signals are reminiscent of the resonances from $[(^{Py}PNP)OsCl_3]$ (**2**) and

while they are not necessarily a sign for its formation, they might indicate more generally the formation of an Os^{III} species. In agreement with this assumption, single-crystals could be obtained from the reaction mixture and the solid state structure from X-ray diffraction suggested the formation of [(^{Py}PNP)OsCl$_2$(OTf)] (**6**) (Figure 1.11).

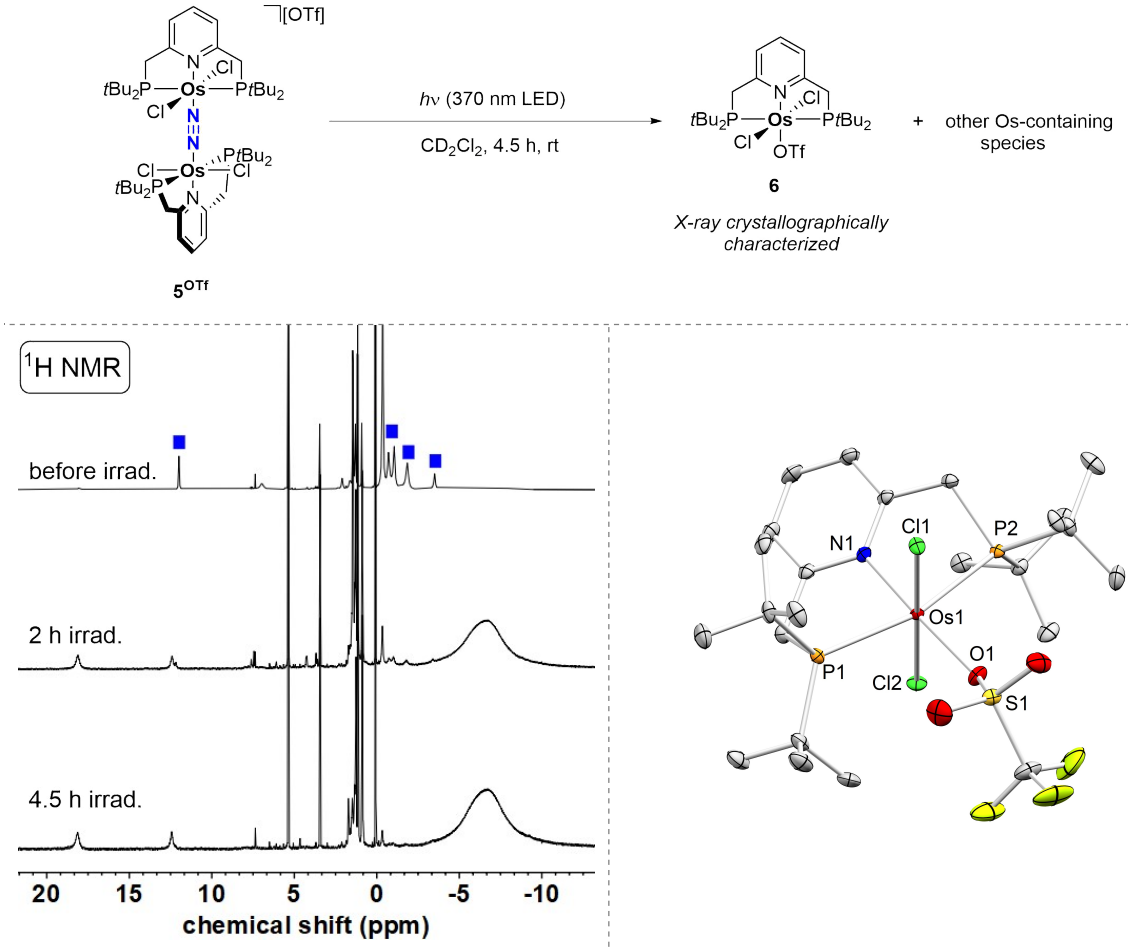

Figure 1.11: Top: Irradiation of mixed-valence complex $\mathbf{5}^{OTf}$ with a λ = 370 nm LED in CD_2Cl_2 to furnish a product mixture from which the Os^{III} complex [(^{Py}PNP)OsCl$_2$OTf] could be crystallographically characterized. Bottom left: ^{1}H NMR spectra from the irradiation experiment before the irradiation, after 2 hours and after 4.5 hours of irradiation. The starting material signals are marked with blue rectangles and the residual sharp signals in the spectrum before irradiation can be assigned as solvent impurities, including the residual solvent proton signal. Bottom right: Molecular structure of complex **6** from single-crystal X-ray diffraction (thermal ellipsoids drawn at the 50% probability level); Hydrogen atoms and two benzene solvent molecules are omitted for clarity. Selected bond lengths [Å] and angles [°]: Os1-N1 2.041(3), Os1-Cl1 2.3433(7), Os1-Cl2 2.3444(7), Os1-P1 2.4446(8), Os1-P2 2.4272(8), Os1-O1 2.120(2), Cl1-Os1-Cl2 179.11(3), N1-Os1-O1 174.82(9), P1-Os1-P2 163.15(3), Os1-O1-S1 138.82(14).

The bond metrics and especially the Os-Cl bonds of **6** are well comparable to the literature reported values for [(^{Py}PNP)OsCl$_3$].[179] Interestingly, no signal in the ^{31}P{^{1}H} NMR was observed in a range of δ_{31P} = +300 to −500 ppm, which is surprising, as it would be expected that Os^{II} complex(es) are formed upon Os-N bond cleavage as well. Furthermore, no nitride formation was detected according to mass spectrometry or NMR spectroscopy. The same

product **6** – judged by ^{1}H NMR – was obtained upon irradiation of $\mathbf{5^{OTf}}$ with an LED at λ_{max} = 440 nm with full conversion of the starting material already after 40 minutes. Only very slow conversion to the Os^{III} species was observed, when a sample was irradiated with a xenon lamp at λ_{max} = 280 nm (however, it has to be noted that the intensity of the xenon lamp is significantly lower). In future experiments it would be interesting to use rather weakly coordinating counterions for the irradiation experiment and compare the results with the irradiation of $\mathbf{5^{OTf}}$.

Preliminary attempts were made towards the synthesis of a dicationic, Os^{III}/Os^{III} complex upon two electron oxidation from neutral **3** ($E_{1/2}$ = +0.30 V) or one electron oxidation from cationic $\mathbf{5^{+}}$. In both cases a new, deeply green species was formed upon oxidation with silver oxidants or thianthrenium tetrafluoroborate (E°'(MeCN) = +0.86 V), which exhibits a broad $^{31}P\{^{1}H\}$ NMR resonance at δ_{31P} = –710 ppm. Unfortunately, upon workup the species seemingly decomposed (color change to bright orange) and could not be isolated and further characterized properly. Moreover, in the ^{1}H NMR broad signals in the region around δ_{1H} = –5 ppm appeared and could once again be an indication for the formation of an Os^{III} species. The $^{31}P\{^{1}H\}$ NMR shift for such a tentative Os^{III}/Os^{III} dinuclear N_2-bridging complex is quite unusual, as these strongly high-field shifted signals usually are observed for octahedral Re^{III}, Os^{IV} and isolobal square-planar Os^{II} complexes and are an expression of the influence of temperature independent paramagnetism. Magnetic measurements of this species in addition to further attempts towards isolation and photolytic or thermal dinitrogen splitting should be conducted in the future.

Finally, attempts to independently synthesize an Os^{VI} $[(^{Py}PNP)Os(N)Cl_2]^{+}$ nitride complex to obtain its spectroscopic signature were undertaken. Initially, an oxidation-azide sequence was tested, starting from Os^{III} complex $[(^{Py}PNP)OsCl_3]$ (**2**). In the CV **2** showed a reversible oxidation at $E_{1/2}$ = +0.27 V (Figure 1.6) and consequently reaction of **2** with thianthrenium tetrafluoroborate in CH_2Cl_2 furnished green Os^{IV} complex $[(^{Py}PNP)OsCl_3][BF_4]$ ($\mathbf{7^{BF4}}$). $\mathbf{7^{BF4}}$ exhibits a broadened $^{31}P\{^{1}H\}$ resonance at δ_{31P} = –462.4 ppm, characteristic for octahedral Os^{IV} complexes. Single-crystals of $\mathbf{7^{BF4}}$ could be obtained and the basic structure, as well as the BF_4 counterion were resolved, however, severe disorder of the entire pincer ligand prevented a satisfactory refinement of the data. Addition of $PPNN_3$ to $\mathbf{7^{BF4}}$ resulted in regeneration of Os^{III} complex **2**, with the azide apparently operating as a reductant. In a final approach, an Os^{VI} precursor, $[n Bu_4N][Os(N)Cl_4]$, was synthesized from $K_2[OsO_2(OH)_4]$, HCl, NaN_3 and $n Bu_4NNO_3$ in a modified literature procedure.[189] Subsequently, the ^{Py}PNP pincer ligand and $NaBArF_{24}$ as chloride abstracting agent were added in THF at 65 °C. The resulting brown

reaction mixture was layered with pentane and single-crystals were obtained. The solid-state structure suggested the formation of [(^{Py}PNP=N)OsCl$_3$] (**8**), effectively an NNP pincer ligand upon insertion of the nitride into an Os-P bond or direct reaction of the pincer ligand phosphorus atom with the nitride moiety of the precursor complex (Figure 1.12).

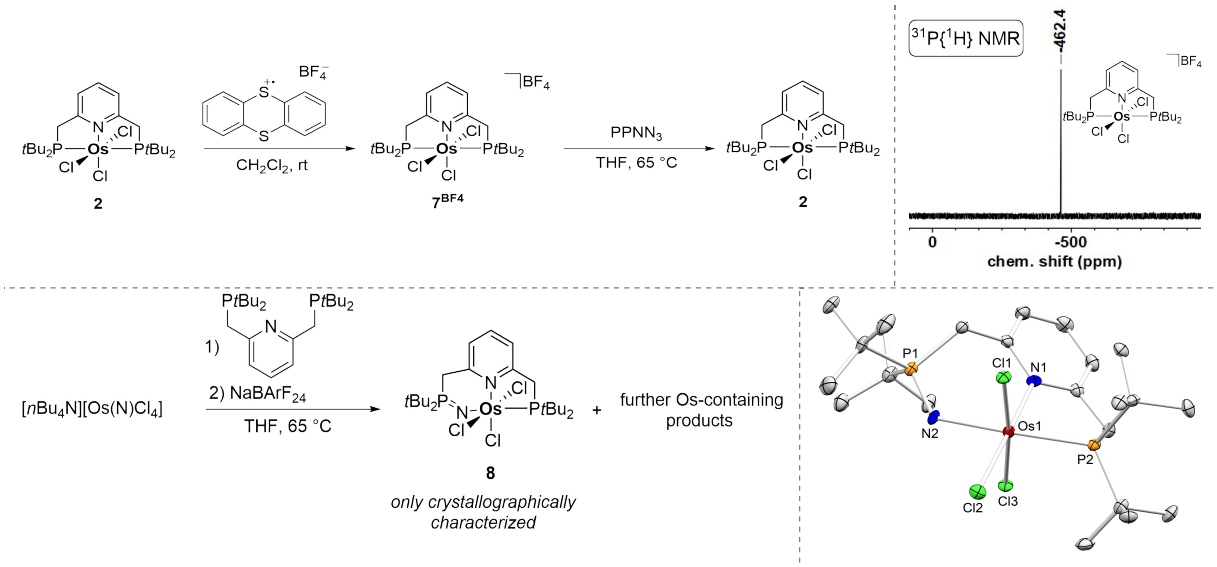

Figure 1.12: Attempts to synthesize a PNP Os^{VI} nitride complex. Top left: Oxidation of Os^{III} complex **2** with thianthrenium tetrafluoroborate to obtain Os^{IV} complex **7**. Subsequent reaction with $PPNN_3$, however, regenerated Os^{III} complex **2**. Top right: $^{31}P\{^1H\}$ NMR spectrum of **7** in CD_2Cl_2. Bottom left: Reaction of the Os^{VI} precursor [nBu$_4$N][Os(N)Cl$_4$] with the ^{Py}PNP pincer ligand and chloride abstracting agent NaBArF$_{24}$ to obtain a reaction mixture from which complex **8** was isolated, in which the nitride moiety inserted into the Os-P bond, forming an iminophosphorane. Bottom right: Molecular structure of complex **8** from single-crystal X-ray diffraction (thermal ellipsoids drawn at the 50% probability level). Hydrogen atoms are omitted for clarity. Selected bond lengths [Å] and angles [°]: Os1-N1 2.099(4), Os1-N2 2.128(4), Os1-Cl1 2.3489(11), Os1-Cl2 2.3824(12), Os1-Cl3 2.3855(11), P1-N2 1.599(4), Os1-P2 2.3507(13), N2-Os1-P2 172.95(12), P1-N2-Os1 126.8(2), N1-Os1-Cl2 176.08(11), Cl1-Os1-Cl3 174.15(4), N2-Os1-P2 172.95(12).

No N-H was found on the difference electron density map, which, however, does not necessarily exclude its presence, since no further analytical data for this compound were collected. Moreover, the structural parameters, especially the P-N-, as well as the adjacent N-Os bonds are very similar to an iminophosphorane from nitride insertion into an Os-P bond reported by *Florian Wätjen*,[190] which could be an indication for the presence of the same structural motif. The P-N bond in **8** is short (d_{PN} = 1.599(4) Å) and the adjacent Os-N bond long (d_{OsN} = 2.128(4) Å), considerably longer than literature known examples of Osmium imido complexes (e.g. d_{OsN} = 1.75 Å for [(Tp)Os(=NH)Cl$_2$]). [191,192] From these comparisons it appears reasonable to assume the presence of an iminophosphorane moiety, with a P=N double bond coordinating *via* the nitrogen atom to the Osmium with a single bond. No information were gained whether this complex is the main product of the reaction. Yet it still indicates that a potentially formed Os^{VI} nitride upon dinitrogen splitting from the dinuclear dinitrogen-bridged complexes would be electrophilic and can react with the phosphines of the pincer

ligand. Therefore, in future splitting attempts, **8** could be the final product and should be further characterized to identify it readily, when it is formed upon dinitrogen cleavage.

Attempts to activate and split dinitrogen on the pyridine pincer platform resulted in the following conclusions:

1. Under reductive conditions, Os^{III} trichloride complex [(^{Py}PNP)$OsCl_3$] (**2**) binds N_2 and the equilibrium between an Os^{II} terminal N_2 complex and the dinuclear dinitrogen-bridged Os^{II}/Os^{II} complex [((^{Py}PNP)$OsCl_2)_2(\mu\text{-}N_2)$] (**3**) could be shifted to **3** upon application of static vacuum over night.
2. **3** is a highly symmetric, diamagnetic $\pi^{12}\delta^4$ complex, showing as expected no IR stretch for the N_2 ligand, but a clearly defined Raman band was identified upon ^{15}N-labeling. Two reversible oxidations at $E_{1/2}$ = –0.42 and +0.33 V, respectively, indicated the potential isolation of mono- and dicationic $\pi^{11}\delta^4$ and $\pi^{10}\delta^4$ complexes, which can be especially interesting with regard to dinitrogen splitting.
3. One electron oxidation of **3** resulted in the formation of cationic mixed-valent complex $\mathbf{5}^+$, which showed similar spectroscopic parameters in IR, NIR and UV/Vis as previously reported Os^{II}-N_2-Os^{III} complexes. Two electron oxidation to a tentative Os^{III}-N_2-Os^{III} dinuclear complex showed a resonance in the $^{31}P\{^1H\}$ NMR at δ_{31P} = –710 ppm, however, in preliminary tests no complex could be isolated.
4. Irradiation experiments with the cationic $\mathbf{5}^+$ at λ_{max} = 370 and 440 nm resulted in metal-nitrogen bond cleavage and in the presence of the triflate counterion the Os^{III} complex [(^{Py}PNP)$OsCl_2$OTf] could be crystallographically characterized. No further products were isolated and no evidence for dinitrogen splitting was observed.

1.5 (Electro)chemical Dinitrogen Splitting with Re^{IV} Trihalide Pincer Complexes

Parts of the research presented in this chapter have been published in: "Rhenium-mediated Conversion of Dinitrogen and Nitric Oxide to Nitrous Oxide", L. Alig, K. A. Eisenlohr, Y. Zelenkova, S. Rosendahl, R. Herbst-Irmer, S. Demeshko, M. C. Holthausen, S. Schneider, *Angew. Chem. Int. Ed.* **2022**, *61*, e202112597.

1.5.1 Synthesis and Characterization of [(^{Ph}PNP)$ReCl_3$]

In analogy to the synthesis of [($^{iPr}P^{H}$NP)$ReCl_3$], the Re^{III} precursor [$ReCl_3(PPh_3)_2(MeCN)$] was reacted with the $^{Ph}P^{H}$NP ligand in benzene at 80 °C. The yellow-orange suspension darkened significantly over the course of 30 minutes and after workup an intensely purple solid was obtained, which was poorly soluble in most organic solvents, yet showed good solubility in chlorinated solvents like dichloromethane. With the aid of X-ray crystallography, the main product of the complexation reaction was identified as Re^{IV} complex [(^{Ph}PNP)$ReCl_3$] (**9**), which was further substantiated by mass spectrometry and elemental analysis. **9** exhibits sharp, paramagnetically shifted signals with no resolved *J*-coupling in the ^{1}H NMR spectrum (Figure 1.13) and the relative integrals are in agreement with C_2 symmetry in solution.

In the solid-state structure the comparatively short Re-N- and Re-Cl bonds are indicative of a high-valent Rhenium complex with substantial π-bonding.[145] Furthermore, the sum of bond angles around the nitrogen atom in **9** is equal to 360°, which is consistent with a planar geometry and loss of the ligand NH proton during complexation and is also supported by the absence of an N-H stretch in the IR spectrum (see Figure 1.14).

The magnetic susceptibility in solution (Evans' method, $\mu_{eff} = 1.63 \pm 0.1\ \mu_B$) is in agreement with an $S = ½$ ground state. In the X-band EPR spectrum of **9** no signal was resolved at 298 K (CH_2Cl_2) and at 5 K (CH_2Cl_2/MeCN) a signal barely started to emerge from the baseline. This might be due to a combination of poor solubility of **9** in anything but pure CH_2Cl_2, non-ideal glassing properties of the used solvent mixture and the time-scale of spin relaxation, as indicated by the relatively sharp signals in the ^{1}H NMR spectrum.

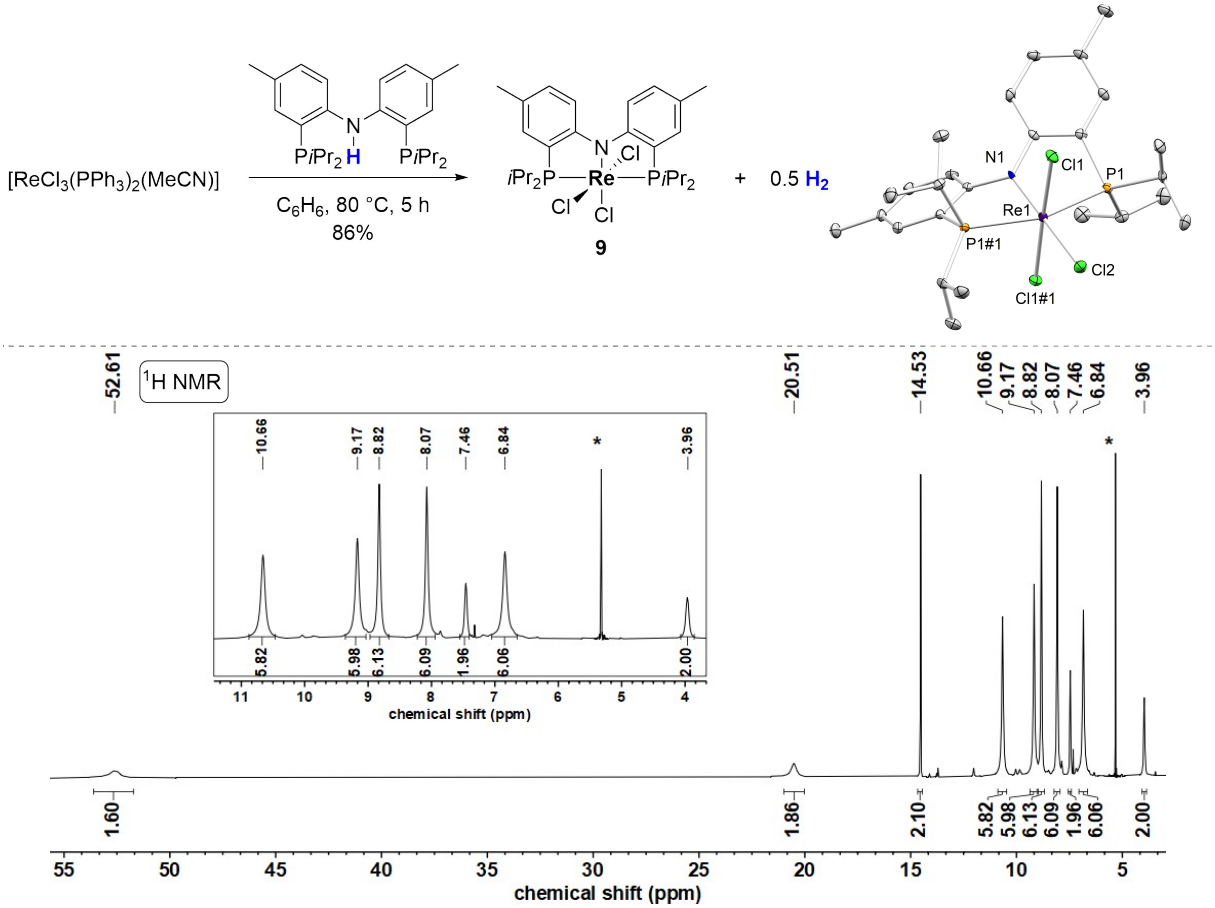

Figure 1.13: Top left: Reaction of $[ReCl_3(PPh_3)_2(MeCN)]$ with $^{Ph}P^{H}NP$ to obtain Re^{IV} complex **9**. Top right: Molecular structure of complex **9** from single-crystal X-ray diffraction (thermal ellipsoids drawn at the 50% probability level); hydrogen atoms are omitted for clarity. Selected bond lengths [Å] and angles [°]: Re1-N1 1.994(3), Re1-P1 2.4428(7), Re1-Cl1 2.3458(7), Re1-Cl2 2.3916(10); N1-Re1-Cl1 91.437(19), N1-Re1-Cl2 180.0, P1-Re1-P1#1 159.25(4), Cl1-Re1-Cl1#1 177.13(4), Cl1-Re1-Cl2 88.563(19). Bottom: ^{1}H NMR spectrum of **9** in CD_2Cl_2. The solvent signal is marked with an asterisk.

In the infrared spectrum, **9** exhibits a broad absorption of low intensity at ν = 3773 cm^{-1} and two broad absorptions of higher intensity at ν = 2238 and 2113 cm^{-1}, respectively. These absorptions were previously assigned to be of electronic origin and are often encountered for Re^{III} and Re^{IV} complexes.[190] The very intense purple color of **9** can be attributed to the broad absorption at λ = 566 nm (ε = 5312 $M^{-1}cm^{-1}$) and the "shoulder" area up to 450 nm (λ_{max} = 374 nm, ε = 7501 $M^{-1}cm^{-1}$) in the UV/Vis spectrum in dichloromethane solution (Figure 1.14), presumably due to LMCT transitions.

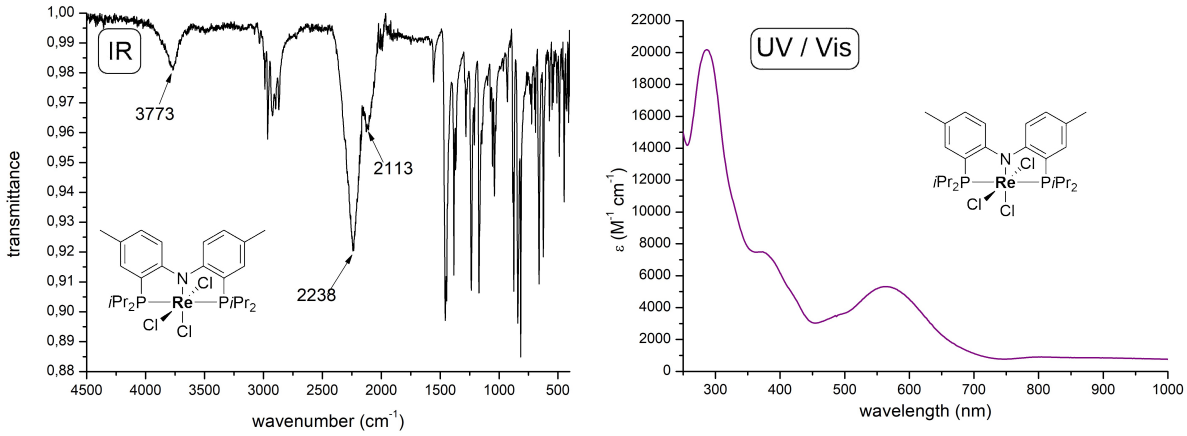

Figure 1.14: Left: ATR-IR spectrum of a microcrystalline sample of **9**. Right: UV/Vis spectrum of **9** in dichloromethane.

The formation of **9** from the reaction of ligand $^{Ph}P^{H}NP$ with $[ReCl_3(PPh_3)_2(MeCN)]$ implies the oxidation of the Rhenium center in the process of complexation. Additionally, the loss of the N-H hydrogen atom of the pincer ligand without addition of an external base hints at a more complex reaction. Similar pincer ligands with a central N-H moiety were shown to potentially act as an electron and proton reservoir and thus effectively function as an hydrogen atom transfer (HAT) reagent due to their significantly decreased $BDFE_{NH}$ upon metal coordination.[193,194] In agreement with that, dihydrogen could be detected *via* headspace analysis of the reaction of $^{Ph}P^{H}NP$ with $[ReCl_3(PPh_3)_2(MeCN)]$ (61%). Furthermore, the $BDFE_{NH}$ of a tentative $[(^{Ph}P^{H}NP)ReCl_3]$ intermediate was predicted by DFT (PBE0/def2-TZVP) to be low ($BDFE_{NH}$ = 38.1 kcal·mol^{-1}), which is consistent with the experimentally observed H_2 release.

In the $^{31}P\{^1H\}$ NMR spectrum of a complexation reaction after eight hours at 75 °C the release of triphenylphosphine (δ_{31P} = –5.4 ppm) alongside a small amount of unreacted ligand (δ_{31P} = –11.3 ppm), as well as several low intensity resonances was observed. In the ^1H NMR spectrum a low-intensity signal at δ_{1H} = 4.47 ppm matches the expected chemical shift of hydrogen in C_6D_6,[195] however, its very low intensity, as well as the presence of many other low-intensity signals of similar chemical shift render hydrogen as the origin of that particular signal unlikely. When the reaction was conducted in THF at 65 °C, the formation of new low intensity signals in the $^{31}P\{^1H\}$ NMR spectrum was observed. Two doublets at δ_{31P} = –449.4 and –463.4 ppm (J = 273 Hz), as well as a broadened resonance at δ_{31P} = –638.8 ppm are indicative of octahedral Re^{III} species, whose ^{31}P chemical shifts are high-field shifted due to temperature independent paramagnetism. Upon reduction of **9** with $CoCp_2$ in CD_3CN the same high-field shifted signals were obtained (yet both signals are low-field shifted by approximately 12 ppm) and mass

spectrometry (ESI) substantiated the tentative assignment of one of the species as [(^{Ph}PNP)ReCl$_2$(MeCN)] (Figure 1.15). However, despite numerous efforts, the complex could not be isolated. Interestingly, no Re^{III} species was observed when [ReCl$_3$(PPh$_3$)$_2$(MeCN)] was reacted with the lithiated ligand $^{Ph}P^{Li}NP$ in C_6D_6 but instead, a very unselective reaction judging by ^{1}H NMR spectroscopy.

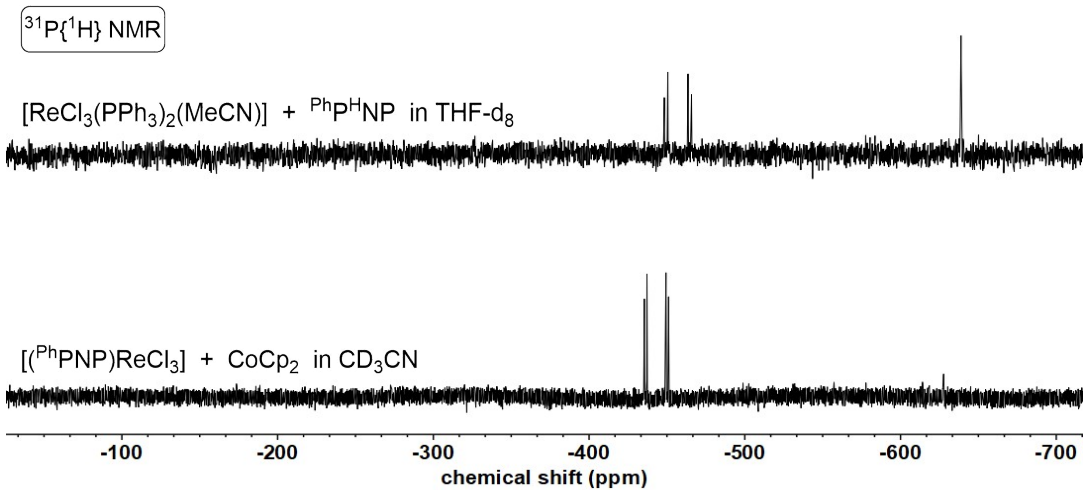

Figure 1.15: High-field section of the $^{31}P\{^1H\}$ NMR spectra of the reaction of [ReCl$_3$(PPh$_3$)$_2$(MeCN)] with $^{Ph}P^{H}NP$ ligand in THF-d$_8$ (top) and $^{31}P\{^1H\}$ NMR spectrum of the reduction of **9** with CoCp$_2$ in CD$_3$CN (bottom).

1.5.2 Reactivity of [(^{Ph}PNP)ReCl$_3$]

Electrochemical examination of [(^{Ph}PNP)ReCl$_3$] (**9**) by cyclic voltammetry revealed reductive features at E = –0.95, –2.40 and –2.96 V (Figure 1.16) and an oxidative feature at +0.11 V. The reversibility of the reduction at $E_{1/2}$ = –0.95 V and the oxidation at +0.11 V, respectively, were verified by separate scan-rate dependent measurements of these features and comparing the ratio of their cathodic and anodic peak currents (Figure 1.16, top right and bottom right).

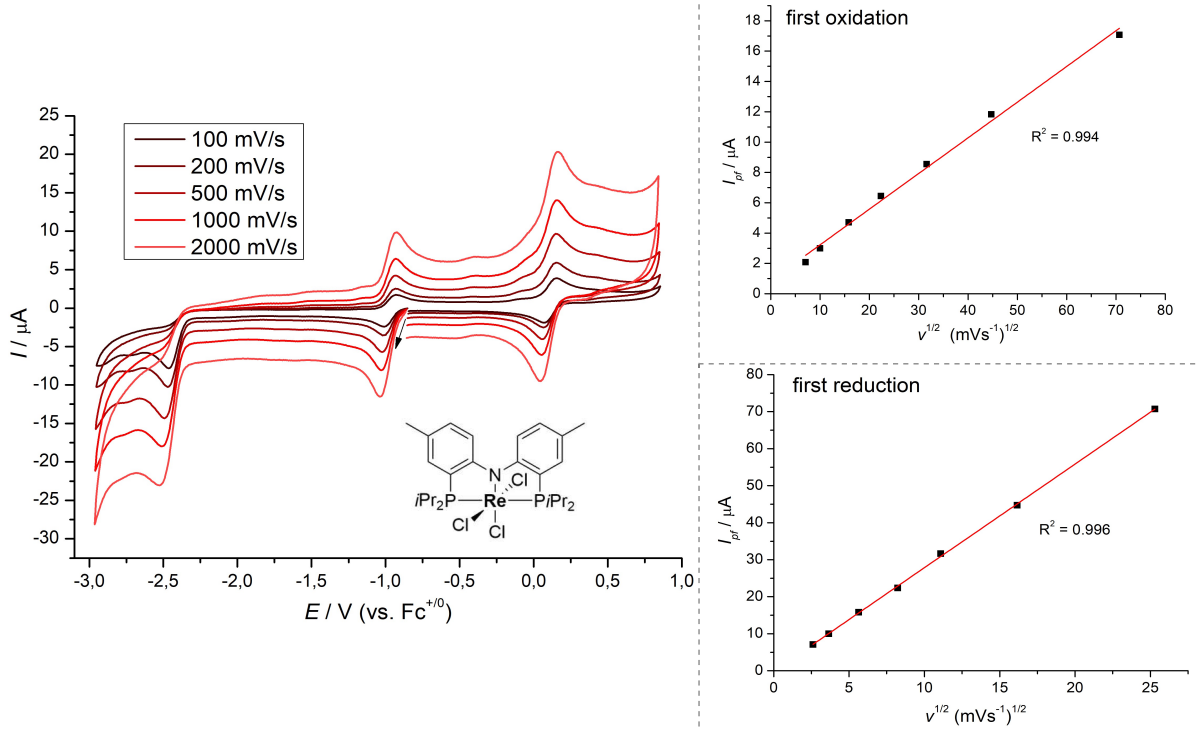

Figure 1.16: Left: Cyclic voltammogram of **9** in THF (0.1 mM **9**, Ar, 0.1 M nBu$_4$NPF$_6$). Top right: Randles-Sevcik plot of forward peak current against the square-root of the scan-rate for the first oxidation of **9** at $E_{1/2}$ = +0.11 V. Bottom right: Randles-Sevcik plot of forward peak current against the square-root of the scan-rate for the first reduction of **9** at $E_{1/2}$ = –0.95 V.

The reversible oxidation at $E_{1/2}$ = +0.11 V prompted attempts towards the accessibility of a cationic Re^{V} complex. Addition of one equivalent [AcFc][Al(OC(CF$_3$)$_3$)$_4$] to a suspension of **9** in 2-MeTHF/MeCN (1:1) led to a rapid color change to cherry red and crystallization of the [BF$_4$]-salt revealed the formation of [(^{Ph}PNP)ReCl$_3$]$^+$ (**10**$^+$) by single-crystal X-ray crystallography (Figure 1.17 top left). The axial Re-Cl bonds (with respect to the pincer plane), as well as the Re-N bond in **10**$^+$ are on average 0.025 Å shorter than their respective counterparts in **9**, whereas the equatorial Re-Cl bond is significantly shortened upon oxidation (Δ_d = 0.074 Å).

In the ^{1}H NMR spectrum of **10**^{BF4} (Figure 1.17, bottom) a mixture of paramagnetically shifted, very sharp and broad signals was observed over a range of approximately 200 ppm (δ_H = +131.86 to –64.57 ppm), with J-coupling partially resolved for some of the signals. The relative integrals suggest C_2 symmetry in solution and no ^{31}P resonance could be detected from δ_{31P} = +1000 to –2000 ppm. The magnetic susceptibility in CD_2Cl_2 solution (Evans' method) of μ_{eff} = 2.19 ± 0.1 μ_B and the shifted signals in the ^{1}H NMR spectrum, as well as the absence of a ^{31}P NMR signal are indicative of a non-diamagnetic ground-state. In fact, SQUID magnetometry of a crystalline sample of **10**$^{Al(OC(CF3)3)4}$ revealed a triplet ground state

configuration at 295 K (μ_{eff} = 2.37 ± 0.1 μ_B), but the sample was contaminated with an S = ½ impurity, which could not be separated despite numerous attempts. Furthermore, DFT calculations (PBE/def2-TZVP) predicted, in compliance with the spectroscopic evidence, the triplet spin state of **10**$^+$ to be 9.5 kcal·mol^{-1} lower in energy, with respect to the singlet state. The literature regarding Re^V complexes is dominated by nitride- and oxo complexes, which have in general diamagnetic ground states due to their strong-field nitrogen and oxygen ligands. Magnetic measurements on the prototypical Re^V compound $ReCl_5$, showed a magnetic moment of μ_{eff} = 2.21,[196] which is in good agreement with the magnetic moment of **10**$^+$.

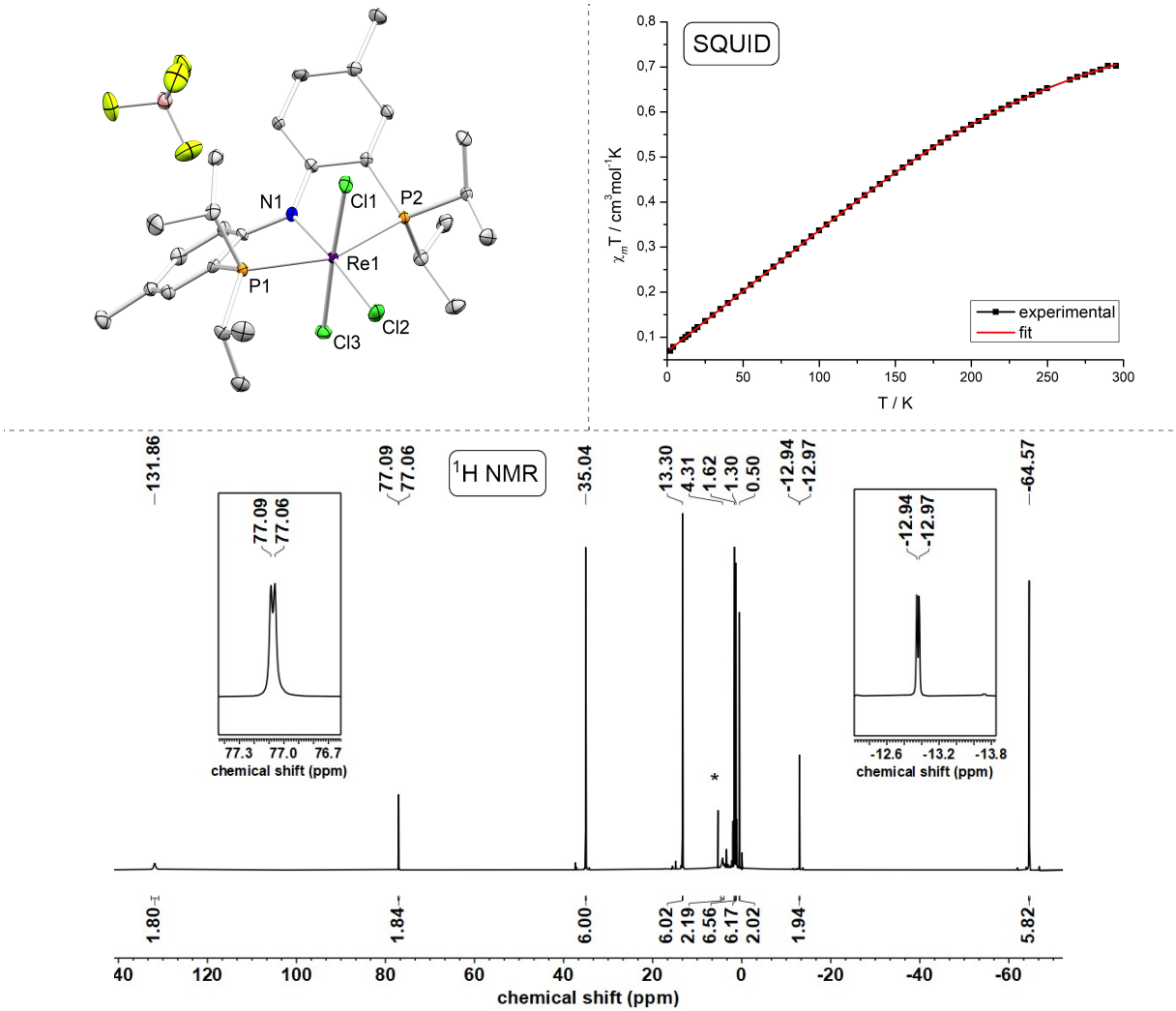

Figure 1.17: Top left: Molecular structure of **10**^{BF4} from single-crystal X-ray diffraction (thermal ellipsoids drawn at the 50% probability level); hydrogen atoms are omitted for clarity. Selected bond lengths [Å] and angles [°]: Re1-N1 1.977(4), Re1-Cl1 2.3111(11), Re1-Cl2 2.3172(11), Re1-Cl3 2.3200(11), Re1-P1 2.4720(11), Re1-P2 2.4892(11), N1-Re1-Cl1 94.54(11), N1-Re1-Cl2 175.70(11), Cl1-Re1-Cl2 88.76(4). Top right: SQUID data of **10**$^{Al(OC(CF3)3)4}$ g_1 = 2.004, D_1 = 424.973, TIP = 178.9 · 10^{-6} cm^{3}mol^{-1}. Bottom: ^{1}H NMR spectrum of **10**^{BF4} in CD_2Cl_2. The solvent signal is marked with an asterisk.

To examine potential reductive dinitrogen splitting on this Rhenium pincer platform, the reductive branch of the CV of neutral complex **9** was investigated in more detail. The reversible

reduction (Figure 1.16) of **9** at $E_{1/2}$ = –0.95 V stays reversible even at slow scan rates (25 mV/s), which hints at slow chloride loss on the CV time scale. While the electrochemical data suggest $CoCp_2$ to be a sufficiently strong electron donor to reduce **9**, numerous attempts to isolate a Re^{III} complex like $[(^{Ph}PNP)ReCl_3]^-$ or five-coordinate $[(^{Ph}PNP)ReCl_2]$ from **9** and $CoCp_2$ were unsuccessful and led to an inseparable, and partially THF-insoluble mixtures of compounds. The redbrown precipitate can be tentatively ascribed to the formation of $[CoCp_2][(^{Ph}PNP)ReCl_3]$, that slowly loses chloride, which was previously assumed for the related aliphatic Re^{III} complex $[(^{iPr}P^{H}NP)ReCl_3]$,[190] as well as crystallographically and spectroscopically verified for the isolable $Re^{III/II}$ complex couple $[(PONOP)ReCl_3]$ and $[CoCp_2][(PONOP)ReCl_2]$.[153,197] In these cases further driving force for chloride dissociation was induced with NaHg (for $[(^{iPr}P^{H}NP)ReCl_3]$) or $LiBEt_3H$ (for $[(PONOP)ReCl_3]$) in non-coordinating toluene solvent.

The differences in chloride dissociation kinetics were previously correlated to the electron-richness of the metal complex, e.g. $[(^{iPr}P^{H}NP)ReCl_3]$ is reduced at a 0.6 V more cathodic potential in comparison to $[(PONOP)ReCl_3]$ and the chloride dissociation is significantly faster.[197] The comparison of these complexes with **9**, however, is complicated, as ^{Ph}PNP is a monoanionic ligand and no uncharged $Re^{III}Cl_3$ complex is accessible. The second reduction potential of **9**, consequently does not represent a $Re^{III}Cl_3/[Re^{II}Cl_3]^-$ couple. Based on the electrochemical reversibility of the first reduction at $E_{1/2}$ = –0.95 V and the relatively negative potential at E_{pc} = –2.40 V the second reduction could potentially be attributed to a $[Re^{III}Cl_3]^-/[Re^{II}Cl_3]^{2-}$ reduction, followed by rapid chloride loss.

Sodium amalgam (E^0 = –2.36 V)[198] is, according to the cyclic voltammogram of **9**, not suitable as a selective one-electron reductant, as its potential is very close to the irreversible second reduction. To add driving force for chloride abstraction $CoCp_2$ and $NaBArF_{24}$ were jointly used. Addition of $CoCp_2$ to a suspension of **9** in benzene resulted in the above mentioned red suspension and interestingly the color change was not significantly slower compared to the reduction in THF. After stirring for several minutes, one equivalent $NaBArF_{24}$ was added upon which the solution slowly turned brown. Interestingly, the resulting ^1H NMR spectrum was blank and in the $^{31}P\{^1H\}$ NMR spectrum one broad resonance at δ_{31P} = –49.7 ppm could be observed, which was tentatively assigned to $[(^{Ph}PNP)ReCl_2]$ (**11**) based on follow-up reactivity. Addition of several drops of THF-d_8 to that sample, or reaction of **9** with $CoCp_2$ and $NaBArF_{24}$ in THF-d_8 (Figure 1.18, right) led to a fast color change to red and a new sharp peak in the

$^{31}P\{^{1}H\}$ NMR spectrum at δ_{31P} = –434.8 ppm appeared. The signals in the ^{1}H NMR were also clearly resolved in comparison to **11** and assignable to one species of C_2 symmetry in solution with strongly high-field shifted signals, which is characteristic for Re^{III} complexes.

complex	^{31}P NMR shift (ppm)
[(^{Ph}PNP)ReCl$_2$] (**11**)	–49.7
[(^{Ph}PNP)ReCl$_2$(thf)] (**12**)	–434.8
[($^{i Pr}$PNP)ReCl$_2$]	+10.0[190]
[($^{i Pr}$PNP)ReCl$_2$(thf)]	–14.5[190]
[($^{t Bu}$PNP)ReCl$_2$]	–51.5[123]
[(^{Ad}PNP)ReCl$_2$]	–90.2
[($^{t Bu}$P=N=P)ReCl$_2$]	–275.6[146]
[(^{Ad}P=N=P)ReCl$_2$]	–412.5
[($^{i Pr}$P^{H}NP)ReCl$_3$]	–1526[152]
[(^{Py}PNP)ReCl$_3$]	–1587[144]

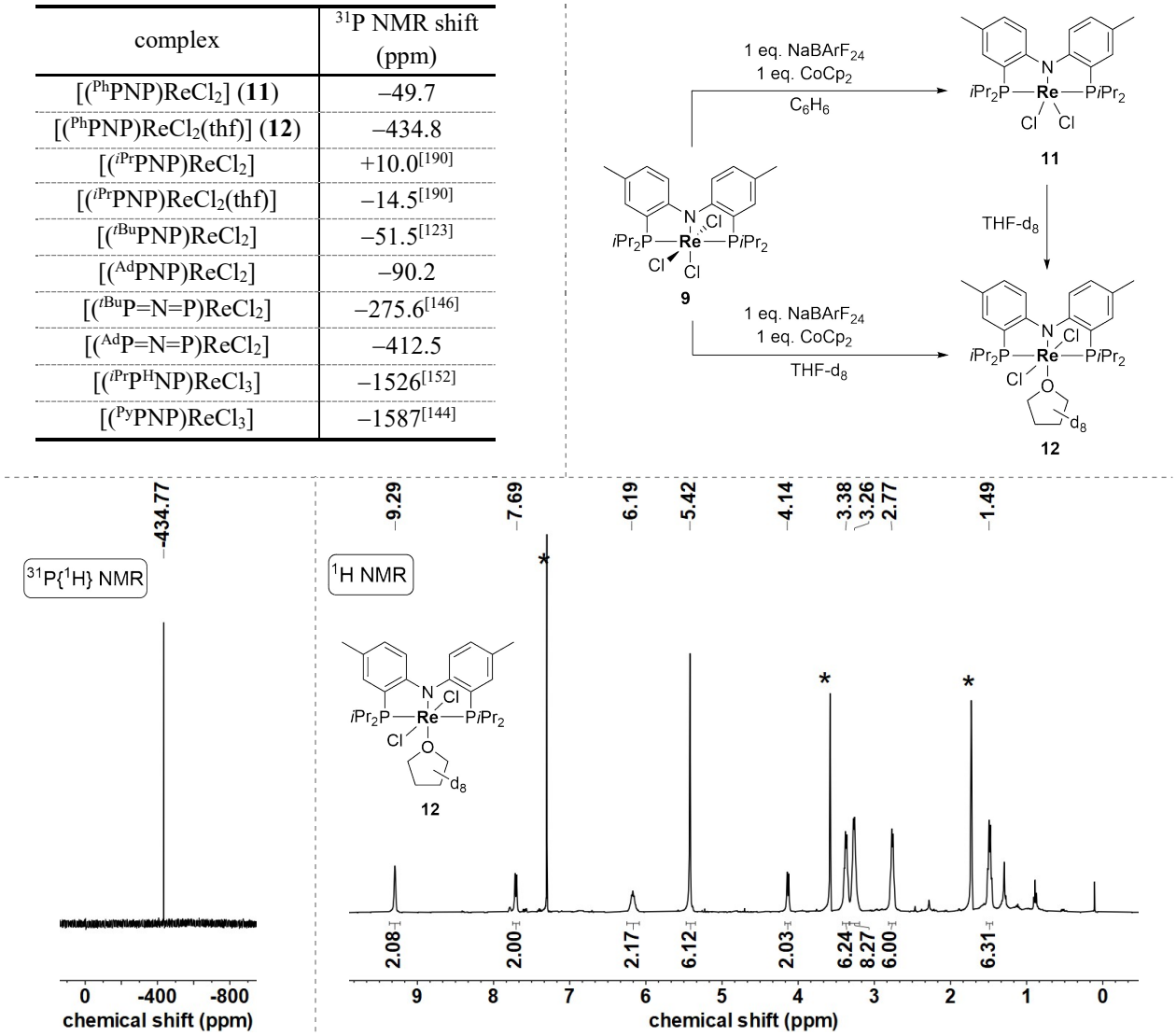

Figure 1.18: Top left: Table of $^{31}P\{^{1}H\}$ NMR shifts of selected five- and six-coordinate Re^{III} PNP pincer complexes. Top right: Solvent-dependent reactions of [(^{Ph}PNP)ReCl$_3$] with $CoCp_2$ and $NaBArF_{24}$ for the tentatively assigned formation of [(^{Ph}PNP)ReCl$_2$] (**11**) and [(^{Ph}PNP)ReCl$_2$(thf)] (**12**). Both species decompose in solution and were therefore not isolated. Bottom left: $^{31}P\{^{1}H\}$ NMR spectrum of d$_8$-**12** in THF-d$_8$. Bottom right: ^{1}H NMR spectrum of d$_8$-**12** in THF-d$_8$. Solvent signals, as well as a benzene impurity (δ_{1H} = 7.16 ppm) are marked with asterisks.

This clear transformation indicates the formation of [(^{Ph}PNP)ReCl$_2$(thf)] (**12**) upon addition of THF. However, **11** as well as **12** are quite sensitive compounds and decomposed within hours in solution, which precluded isolation and full characterization of these compounds. This is in line with the results derived on the [($^{i Pr}$PNP)ReCl$_2$] platform by *Maximilian Fritz* where the isolation of the analogous unsaturated [($^{i Pr}$P=N=P)ReCl$_2$] complex was unsuccessful due to highly unselective reactions.

The $^{31}P\{^{1}H\}$ NMR shift of **11** is in a similar range of five-coordinate Re^{III} pincer complexes (Figure 1.18, left) with aliphatic backbone ([(^{tBu}PNP)ReCl$_2$]: δ_{31P} = –51.5 ppm, [(^{Ad}PNP)ReCl$_2$]: δ_{31P} = –90.2 ppm), but quite different to the more closely-related unsaturated backbone pincer complexes ([(^{tBu}P=N=P)ReCl$_2$]: δ_{31P} = –275.6 ppm and [(^{Ad}P=N=P)ReCl$_2$]: δ_{31P} = –412.5 ppm). Furthermore, the $^{31}P\{^{1}H\}$ NMR signal of **12** is high-field shifted to a significantly higher degree upon THF coordination compared to the analogous [(^{iPr}PNP)ReCl$_2$]/[(^{iPr}PNP)ReCl$_2$(thf)] couple ($\Delta(\delta_{31P})$ = 385.1 ppm vs. $\Delta(\delta_{31P})$ = 24.5 ppm). These comparisons highlight the complex and non-trivial relationship between structural features and magnetic properties in Re^{III} complexes.

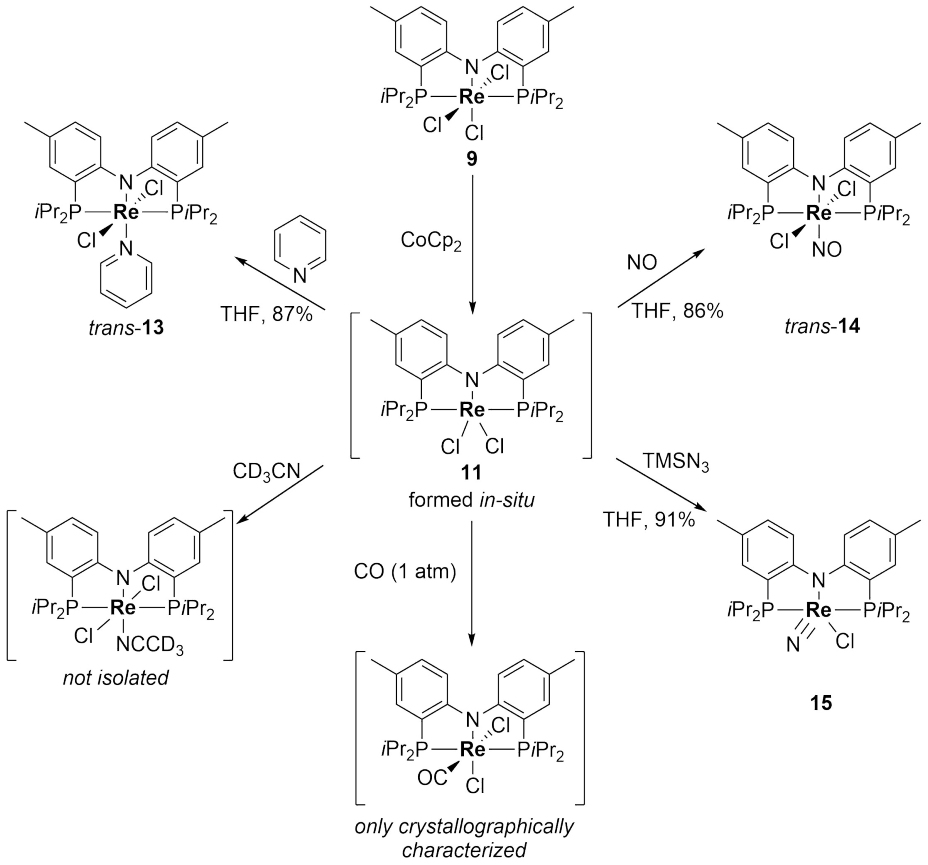

Scheme 1.7: Overview of the *in-situ* reduction of [(^{Ph}PNP)ReCl$_3$] (**9**) and follow-up reactivity of the Re^{III} platform for the formation and isolation of Re^{III} pyridine complex **13** (top left), nitrosyl complex *trans*-**14** (top right), Re^{V} nitride **15** (bottom right), Re^{III} carbonyl complex *cis*-[(^{Ph}PNP)Re(CO)Cl$_2$] (bottom) and formation of non-isolated [(^{Ph}PNP)ReCl$_2$(CD$_3$CN)] (bottom left).

The *in-situ* reduction of **9** with CoCp$_2$ proved to be a valuable platform for the formation of different rhenium complexes (Scheme 1.7) and, judging by the products, the intermediate reacted like a "[(^{Ph}PNP)ReCl$_2$] synthon". For example, reduction of **9** with CoCp$_2$ and subsequent addition of nitric oxide led to the formation of nitrosyl complex *trans*-**14**, which

will be further discussed in the context of nitride functionalization in part II. Furthermore, Re^{V} nitride complex **15** was obtained in high yield upon a reduction-azide sequence, which will be further discussed in the light of dinitrogen activation in chapter 1.5.3. Finally, addition of carbon monoxide to a suspension of [(^{Ph}PNP)$ReCl_2$] resulted in a color change from red-brown to green and then gradually to purple. Single-crystals suitable for X-ray crystallography were grown and revealed the formation of *cis*-[(^{Ph}PNP)Re(CO)Cl_2].

Reduction of **9** with $CoCp_2$ in pyridine/tetrahydrofuran yielded red crystals of the Re^{III} pyridine complex [(^{Ph}PNP)$ReCl_2(NC_5H_5)$] (**13**) in 87% yield. The complex features the characteristic NMR signature of a high-field shifted ^{31}P resonance (δ_{31P} = –619.9 ppm, $\Delta\nu_{1/2}$ = 112 Hz) and paramagnetically shifted, yet sharp ^{1}H NMR signals. In the infrared spectrum (ATR, crystalline sample), **13** exhibits a remarkably broad band with a pronounced plateau from $\nu = 3742$ to 3634 cm^{-1} (see Figure 1.19). This band is reminiscent of the broad O-H stretch of water, however, the IR stretch of water has a maximum transmittance at around $\nu_{OH} = 3300$ cm^{-1} and in the NMR spectrum of the same crystalline batch of **13** no trace of water could be detected. Previously, a very similar, broad absorption of [($^{i\text{Pr}}$P^{H}NP)$ReCl_3$] at $\nu = 3506$ cm^{-1} was attributed to an electronic absorption by NEVPT2/CASSCF/QDPT calculations and confirmed to be of electronic origin by variable-field magnetic IR measurements.[190] Therefore, higher-level computations and further experimental analysis are required to shed light on the origin of this remarkable band in the IR of **13**.

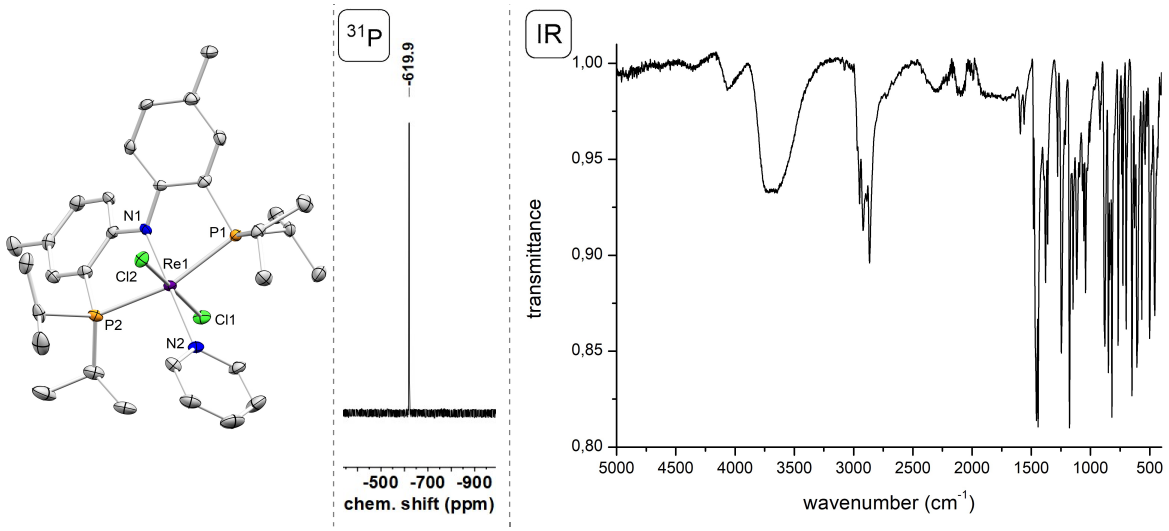

Figure 1.19: Left Molecular structure of **13** from single-crystal X-ray diffraction (thermal ellipsoids drawn at the 50% probability level); hydrogen atoms and a diethylether solvent molecule are omitted for clarity. Selected bond lengths [Å] and angles [°]: Re1-N1 1.980(3), Re1-N2 2.201(3), Re1-Cl1 2.4067(11), Re1-Cl2 2.4017(11), Re1-P1 2.4168(13), Re1-P2 2.4178(14), N1-Re1-N2 177.55(13), Cl1-Re1-Cl2 175.12(4), P1-Re1-P2 162.83(4). Mid: ^{31}P{^{1}H} NMR spectrum of **13** in C_6D_6. Right: ATR-IR spectrum of a crystalline sample of **13**.

In general, there is a pronounced tendency in favor of octahedral coordination for Rhenium complexes of iso-propyl pincer based platforms as opposed to tert-butyl pincer complexes (e.g. [($^{i\text{Pr}}$PNP)$ReCl_2$(thf)] is known,[190] but [($^{t\text{Bu}}$PNP)$ReCl_2$] does not coordinate THF). This can partially explain slow chloride loss from an anionic chloride complex upon reduction of **9** and the low stability of **11**. Moreover, it can potentially inhibit subsequent dinitrogen activation, as dinitrogen has to compete with solvent molecules like THF for the free coordination site.

Several attempts for dinitrogen activation and/or binding at Re^{III} were unsuccessful:

1) Addition of N_2 to *in situ* prepared **11** in non-coordinating solvents or **12** in THF led to a color change to intensely green, yet in the ^{31}P NMR no signal and in the ^{1}H NMR only a multitude of broad resonances was observed at −60 °C and no species could be isolated from the reaction mixtures. 2) Reduction of pyridine complex **13** with one equivalent of sodium amalgam under a dinitrogen atmosphere proved to be highly unselective and no traceable amount of a nitride complex could be observed. 3) Initial reaction of pyridine complex **13** with BPh_3 and subsequent addition of dinitrogen at −40 °C, adapted from a similar procedure reported by *Holland* and coworkers,[38] resulted in the formation of dark green crystals over night. The crystals, however, were not single-crystalline and the green mother liquor rapidly changed color to brown upon even slight warming, e.g. taking it out of the freezer for several seconds.

While these observations indicate N_2 reactivity, they also represent the labile binding of dinitrogen on the Re^{III} oxidation state. In this context the report of *Holland* and coworkers has to be mentioned,[38] where the authors isolated a dinuclear dinitrogen-bridging Re^{III}/Re^{III} complex, which was only stable at temperatures below −10 °C. Similar to the $^{\text{Ph}}$PNP platform, neither the five-coordinate Re^{III} complex of the pyrrole-based pincer [($^{\text{Pyrr}}$PNP)$ReCl_2$], nor a terminal N_2 complex could be observed. Exclusive dinuclear N_2 binding was attributed to computational predictions of terminal binding of N_2 to [($^{\text{Pyrr}}$PNP)$ReCl_2$] to be slightly endergonic. While the observations on the [($^{\text{Ph}}$PNP)$ReCl_2$] platform appear to be similar, no N_2-binding complex could be isolated and further attempts might be necessary to elucidate possible dinitrogen activation on the Re^{III} oxidation state.

The following information were gathered from the synthesis and the subsequent reactivity studies of trichloride complex [($^{\text{Ph}}$PNP)$ReCl_3$] (**9**):

1. Re^{IV} complex **9** was isolated as extremely intense purple crystals upon reaction of Re^{III} precursor [$ReCl_3(PPh_3)_2$(MeCN)] with the $^{\text{Ph}}$P$^{\text{H}}$NP ligand. From the solid-state structure

the loss of the amine hydrogen atom is evident and dihydrogen release was detected by headspace analysis.

2. **9** can be oxidized with outer-sphere oxidants to form paramagnetic Re^{V} complex $[(^{Ph}PNP)ReCl_3]^+$ (**10**$^+$). **10**$^+$ exhibits a triplet ground state in solution and is a rare example of a non-diamagnetic Re^{V} complex, highlighting the weak donor properties of the amide pincer ligand.
3. The reduction of **9** is reversible on the CV timescale, in agreement with the inability to isolate dichloride $[(^{Ph}PNP)ReCl_2]$ (**11**) upon chemical reduction. Solutions of **9** and cobaltocene reductant, however, acted as a "$[(^{Ph}PNP)ReCl_2]$" synthon and enabled the isolation of several octahedral $[(^{Ph}PNP)Re^{III}Cl_2(L)]$ adduct complexes (L = pyridine, CO, NO).

1.5.3 Dinitrogen Splitting with $[(^{Ph}PNP)ReCl_3]$

Since dinitrogen activation starting from the Re^{III} platform was hampered by the low stability of five-coordinate $[(^{Ph}PNP)ReCl_2]$ (**11**) and competitive N_2 coordination with solvent molecules, Re^{IV} complex $[(^{Ph}PNP)ReCl_3]$ (**9**) was tested as precursor for N_2 activation. As described in chapter 1.5.2, **9** features a fully reversible one-electron reduction at $E_{1/2}$ = –0.95 V indicating slow chloride loss on the CV time scale. To obtain the $\pi^{10}(\delta^4)$ electron configuration for a hypothetical dinuclear dinitrogen-bridged complex, **9** would have to be reduced by two electrons per rhenium center. The second, irreversible reduction of **9** at E_{pc} = –2.40 V thus might form a species capable of binding and splitting N_2 under dinitrogen atmosphere.

Sodium amalgam was chosen as reductant, as it is on the one hand a sufficiently strong electron donor (E^0 = –2.36 V in nonaqueous solvents)[198] and on the other hand it can add driving force to facilitate chloride loss by precipitation of NaCl. Consequently, **9** was reacted with 2.5 equivalents of NaHg in THF under an atmosphere of dinitrogen (Figure 1.20, top left).

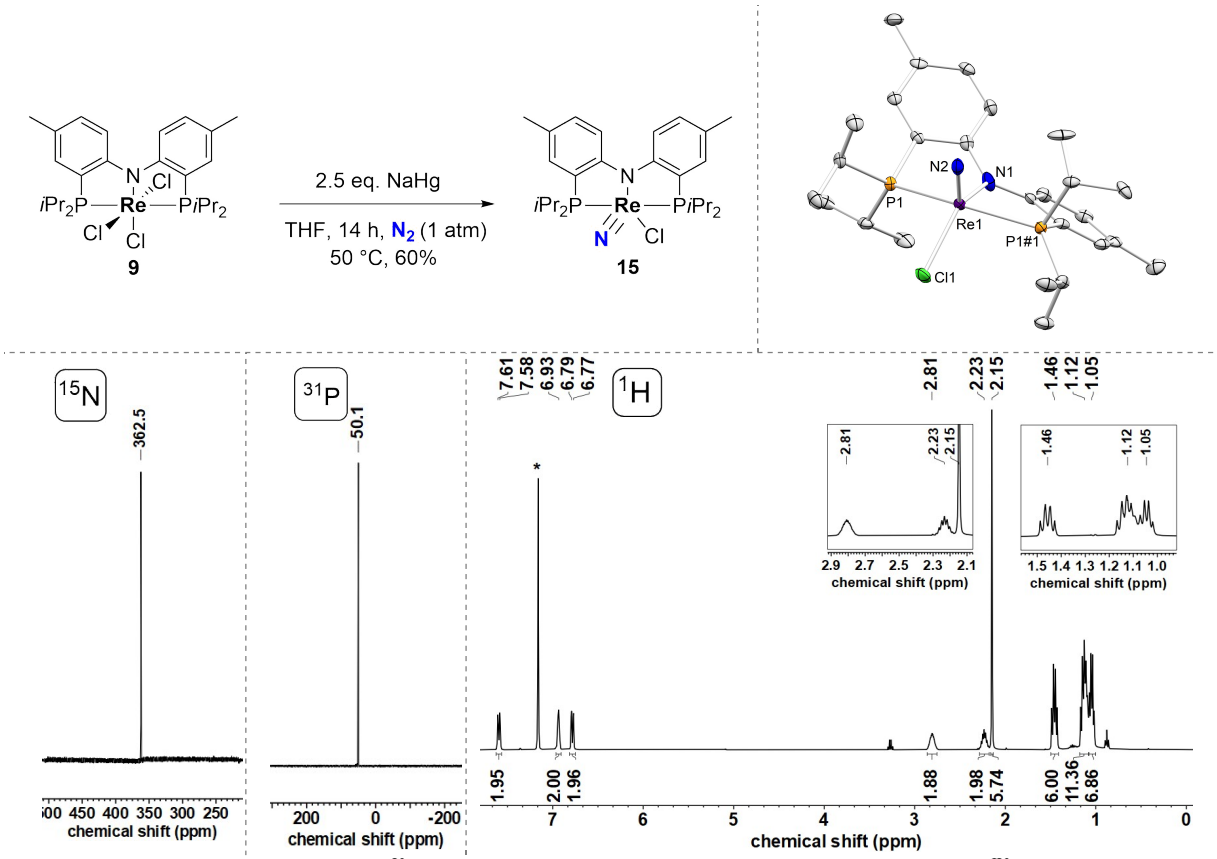

Figure 1.20: Top left: Formation of Re^{V} nitride complex **15** upon dinitrogen splitting mediated by Re^{IV} trichloride complex **9**. Top right: Molecular structure of **15** from single-crystal X-ray diffraction (thermal ellipsoids drawn at the 50% probability level); hydrogen atoms and a toluene solvent molecule are omitted for clarity. Selected bond lengths [Å] and angles [°]: Re1-N2 1.645(6), Re1-N1 2.071(4), Re1-Cl1 2.3987(17), Re1-P1 2.4152(11), Re1-P1#1 2.4121(11), N1-Re1-N2 116.7(2), N1-Re1-Cl1 132.10(6), P1-Re1-P1#1 153.74(4), N2-Re1-Cl1 111.1(2); $\tau^5 = 0.36$. Bottom left: $^{15}N\{^1H\}$ NMR of **^{15}N-15** in C_6D_6 from reduction of **9** with NaHg under an atmosphere of $^{15}N_2$. Bottom mid: $^{31}P\{^1H\}$ NMR spectrum of **15** in C_6D_6. Bottom right: ^1H NMR spectrum of **15** in C_6D_6. Solvent signal is marked with an asterisk.

The initially dark purple solution quickly turned red and subsequently green upon shaking at room temperature for several minutes, after which the solution was stirred for an additional 14 hours at 50 °C. $^{31}P\{^1H\}$ and ^1H NMR spectroscopy of the resultant orange-brown mixture indicated formation of the previously described[199] Re^{V} nitride complex **15** as the main species alongside a small amount of unidentified side-products. After workup **15** was obtained in 60% isolated yield as an orange solid. In contrast to the report by *Ison* and coworkers,[199] a solid-state structure from single-crystal X-ray crystallography of **15** was obtained by layering a saturated toluene solution with pentane at –80 °C. In the solid-state structure (Figure 1.20, top right), **15** adopts a significantly more distorted square-pyramidal coordination geometry ($\tau^5 = 0.36$), compared to other Re^{V} nitride complexes (Table 1.3), presumably owing to the constrained ligand geometry. On the other hand, the Rhenium nitride bond length of $d_{ReN} = 1.645(6)$ Å is in very good agreement with the respective bond in other Re^{V} nitride complexes[146,200,201] and the bond metrics, as well as the spin state are in general well-

reproduced by DFT calculations (PBE/def2-TZVP: $\tau^5_{calc.} = 0.30$; ^{1}**15**: ±0.0 kcal·mol^{-1}, ^{3}**15**: +42.1 kcal·mol^{-1}).

Table 1.3: Comparison of structural and spectroscopic parameters of Re^V nitride complexes.

complex	Re≡N bond length (Å)	τ^5 parameter	Re≡^{14}N (Re≡^{15}N) IR band (cm^{-1})	^{15}N NMR shift (ppm)
[(^{Ph}PNP)Re(N)Cl] (**15**)	1.645(6)	0.36	1080 (1047)	362.5
[($^{t Bu}$PNP)Re(N)Cl][202]	1.643(6)	0.14	1056 (1037)	371
[($^{t Bu}$P=N=P)Re(N)Cl][146]	1.647(18)	0.15	-	-
[($^{t Bu}$P^{O}NP)Re(N)Cl][mCBA][202]	1.638(7)	-	1078 (1042)	393
[($^{t Bu}$P^{H}NP)Re(N)Cl][202,203]	1.642	0.06	1108 (1075)	387
cis-[($^{i Pr}$P^{H}NP)Re(N)Cl$_2$][190]	1.669(2)	-	-	383.3

^{15}N-15 was obtained in 42% isolated yield by performing the reduction of **9** with 2.5 eq. NaHg under an atmosphere of $^{15}N_2$, indicating that dinitrogen splitting is the origin of the nitride nitrogen atom. In the ^{15}N NMR spectrum **^{15}N-15** exhibits a singlet signal at δ_{15N} = 362.5 ppm (Figure 1.20 bottom left, vs. CH_3NO_2), which is on the high-field end of previously reported chemical shifts of Re^V nitride complexes (Table 1.3).

The dinitrogen splitting reaction suffered from several low-quantity side-products of similar solubility and a very high sensitivity towards small changes in the reaction parameters. For example, performing the reaction at room temperature instead of 50 °C resulted in no observable nitride complex, even at prolonged reaction times, presumably due to an inherent kinetic barrier of one of the reaction steps. Therefore, a more convenient and reliable alternative synthetic access to **15** was required for large scale functionalization attempts starting from **15**.

In-situ reduction of [(^{Ph}PNP)ReCl$_3$] (**9**) and subsequent addition of an excess of trimethylsilyl azide yielded very clean **15** in high isolated yield (91%) and short reaction times. Other azide sources (e.g. PPNN$_3$, PPN$^+$ = $Ph_3P{=}N{=}PPh_3^+$) can be used as well, however, heating the reaction solution is mandatory owing to their limited solubility in THF solution. For example, the Re≡N band in the IR spectrum ($\nu_{Re\equiv N}$ = 1080 cm^{-1}) of **15** was unambiguously assigned by comparison with an IR spectrum of the **^{15}N-15** isotopologue (Table 1.3, Figure 1.21).

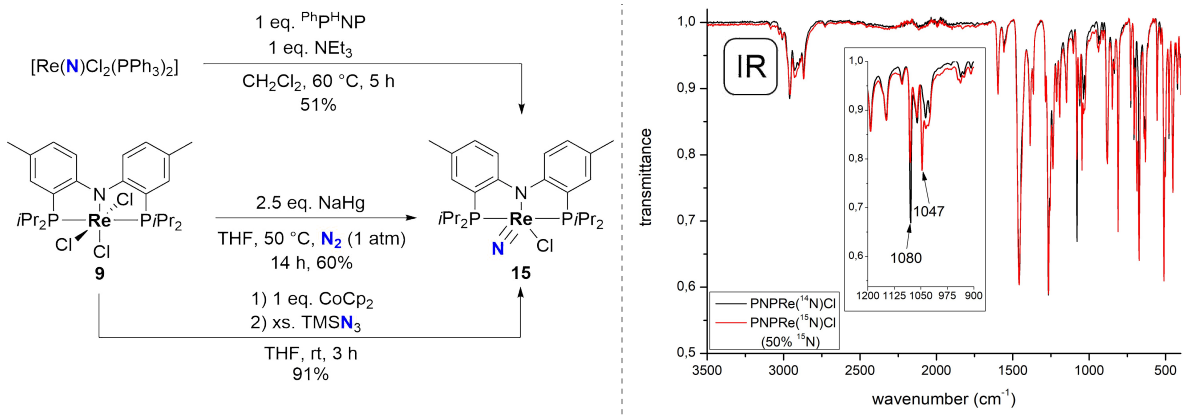

Figure 1.21: Left: Synthetic routes towards nitride complex **15**. The top reaction was reported previously by *Ison* and coworkers,[199] yet neither yield nor purity of the nitride could be reproduced and the reaction features harsh conditions (DCM at 60 °C). The middle reaction is the dinitrogen splitting from **9** described above. The bottom reaction describes the reduction-azide sequence leading to a highly pure nitride complex **15** in high yield. Right: Infrared spectra (ATR, solid) of **^{14}N-15** and **^{15}N-15** (50% ^{15}N, synthesized *via* reduction-azide sequence *vide infra*). The inset shows the region between 1200 and 900 cm^{-1}, where an assignment for the Re≡N band can be made based on comparison of the labeled sample with the natural abundance sample.

Ison and coworkers previously reported the synthesis of **15** starting from Re^{V} nitride precursor $[Re(N)Cl_2(PPh_3)_2]$,[199] however, **15** could be obtained by this route in only lower-than-reported yield and the purity was unsatisfying, since several involved species in that reaction show similar solubility (e.g. the $^{Ph}P^{H}NP$ ligand and PPh_3) and could not be removed entirely. Due to these complications follow-up experiments were in general performed using **15** derived by the reduction-azide sequence.

In summary, reduction of **9** with the strong reductant and chloride abstracting agent NaHg under an atmosphere of N_2 led to formation of Re^{V} nitride complex **15** by dinitrogen splitting. This still represents one of only a handful of examples of dinitrogen splitting with Rhenium pincer complexes into well-defined nitride complexes and enables nitride functionalization with a more chemically robust und geometrically constrained pincer backbone, potentially enabling new, unprecedented nitride reactivity.

1.5.4 (Electro)chemical Dinitrogen Splitting on the $[(^{Ph}PNP)ReX_3]$ Platform (X = Br,I)

The reduction of **9** by two electrons (E_{pc} = –2.40 V) requires a relatively harsh potential compared to other $Re^{III/II}$ redox couples (e.g. $[(^{tBu}PNP)ReCl_2]$: E_{pc} = –1.96 V)[204]. A significant anodic shift can be induced upon halide exchange towards better leaving groups like bromide

and iodide,[205] leading to milder potentials and allowing for the use of less hazardous reductants than NaHg. Therefore the halide exchange starting from **9** was examined in more detail.

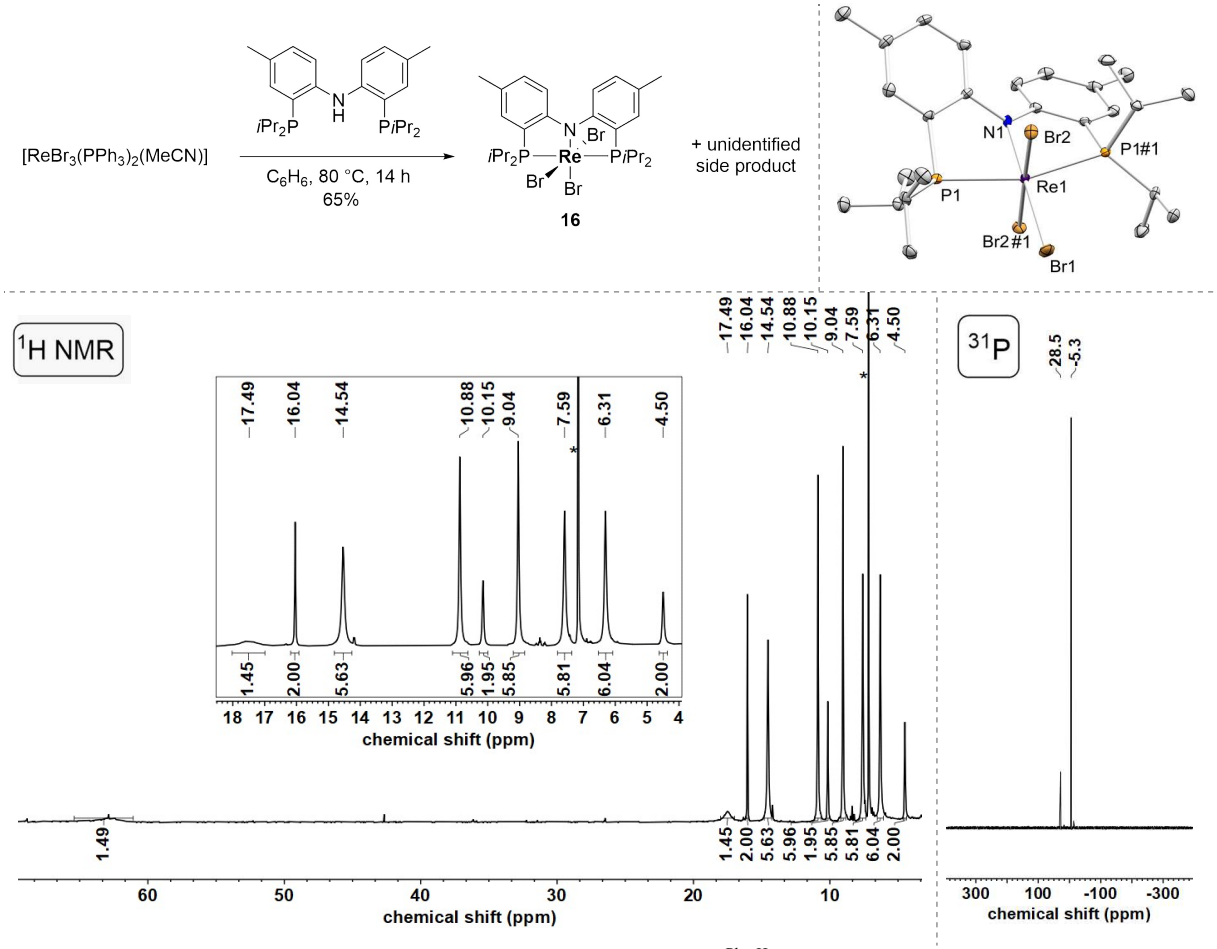

Figure 1.22: Top left: Reaction of $[ReBr_3(PPh_3)_2(MeCN)]$ with ligand $^{Ph}P^{H}NP$ to form **16** as the main species and one unidentified side product. Top right: Molecular structure of **16** from single-crystal X-ray diffraction (thermal ellipsoids drawn at the 50% probability level); hydrogen atoms are omitted for clarity. Selected bond lengths [Å] and angles [°]: Re1-N1 1.982(4), Re1-Br1 2.5240(5), Re1-Br2 2.4933(3), Re1-P1 2.4424(9), N1-Re1-Br1 180.0, N1-Re1-Br2 91.281(10), P1-Re1-P1#1 159.29(4). Bottom left: ^{1}H NMR spectrum after workup of a reaction mixture of $[ReBr_3(PPh_3)_2(MeCN)]$ with $^{Ph}P^{H}NP$. Solvent signal is marked with an asterisk. Bottom right: Crude $^{31}P\{^1H\}$ NMR of a reaction mixture of $[ReBr_3(PPh_3)_2(MeCN)]$ with $^{Ph}P^{H}NP$ after 14 h at 80 °C.

Chloride-to-bromide exchange on the related $[(^{t\text{Bu}}PNP)ReCl_2]$ platform by simple salt metathesis of the chloride precursor with sodium bromide resulted in incomplete exchange,[159] which is why such a reaction was not attempted starting from **9**. Instead, ligand $^{Ph}P^{H}NP$ was reacted with $[ReBr_3(PPh_3)_2(MeCN)]$ (Figure 1.22) in analogy to the chloride counterpart. The initial orange benzene suspension turned dark green upon heating for 14 hours at 80 °C and in the ^{31}P NMR spectrum formation of a Rhenium pincer complex was indicated by the release of triphenylphosphine, as well as the formation of another species with a ^{31}P NMR shift of $\delta_{31P} = 28.5$ ppm. In the ^{1}H NMR spectrum of a reaction mixture in C_6D_6, the main species exhibits paramagnetically shifted sharp signals of C_2 symmetry with no resolved *J*-coupling,

reminiscent of the signals of **9**. After workup to remove the triphenylphosphine, single crystals suitable for X-ray crystallography were grown by diffusion of pentane into a saturated benzene solution. The solid-state structure confirmed the formation of [(^{Ph}PNP)ReBr$_3$] (**16**), the bromide analog to **9** (Figure 1.22).

Unfortunately, all attempts to separate the side product from **16** by extraction, chromatography or crystallization were not successful, as the impurity shows similar properties to **16**. Furthermore, upon measuring $^{31}P\{^1H\}$ and ^1H spectra over the course of several days, it was observed that **16** decomposed in C_6D_6 solution and the intensity of the diamagnetic signals attributed to the impurity increased simultaneously in the ^1H NMR. Moreover, attempts to promote the selective formation of **16** by reacting ligand $^{Ph}P^{H}NP$ with [ReBr$_3$(PPh$_3$)$_2$(MeCN)] in the presence of varying amounts of oxidant and bromide transfer reagent *N*-bromosuccinimide (NBS), did not lead to improved selectivity.

16 could not be isolated in analytical purity, however, dinitrogen splitting was still attempted. Reaction of **16** with a small excess of sodium amalgam under dinitrogen atmosphere in THF led to a gradual color change from dark-green to red to forrest-green to brown-orange over the course of 14 hours at room temperature. $^{31}P\{^1H\}$ NMR spectroscopy of a reaction mixture indicated the formation of a main diamagnetic species at δ_{31P} = 49.4 ppm, with some minor side products visible. The spectroscopic yield was determined with the aid of an internal standard to be 64%. The identity of nitride bromide complex [(^{Ph}PNP)Re(N)Br] **17** was further verified by mass spectrometry and the NMR spectroscopic data were compared to an independently synthesized sample of **17**. In analogy to the reduction-azide sequence towards the synthesis of [(^{Ph}PNP)Re(N)Cl] (**15**), **16** was reduced with one equivalent CoCp$_2$ and subsequently treated with an excess of trimethyl silyl azide to obtain **17** in high yield (81%) and purity (Scheme 1.8). **17** features unsurprisingly very similar spectroscopic characteristics compared to **15**, which is most obvious in the similar $^{31}P\{^1H\}$ NMR chemical shift (**15**: δ_{31P} = 50.1 ppm, **17**: δ_{31P} = 49.4 ppm). Although single-crystals suitable for X-ray crystallography were obtained and the basic atomic connectivity was evident from the solid-state structure, no satisfying refinement was possible, precluding any structural comparison with other Re^{V} nitride complexes. **17** was furthermore characterized by mass spectrometry and elemental analysis.

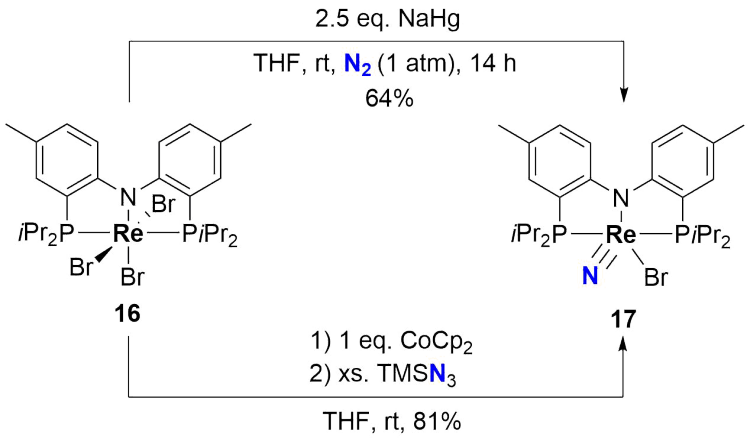

Scheme 1.8: Synthetic access to Re^{V} bromide complex **17**. Top reaction: Dinitrogen Splitting from Re^{IV} tribromide complex **16** with sodium amalgam. Bottom reaction: Reduction-azide sequence with $CoCp_2$ and $TMSN_3$ to obtain **17** in high yield.

Exchange of chloride with iodide showed the highest anodic shift within the Re^{III} halide series of the [(^{tBu}PNP)ReX$_2$] (X = Cl,Br,I) platform[159] compared to the chloride derivative and therefore the synthesis of the iodide derivative of [(^{Ph}PNP)ReCl$_3$] (**9**) was subsequently targeted. Two synthetic strategies were successful: First, halide exchange by salt metathesis with an excess of sodium iodide led to the selective formation of iodide complex [(^{Ph}PNP)ReI$_3$] (**18**). Second, initial preparation of [ReI$_3$(PPh$_3$)$_2$(MeCN)] by salt metathesis (not entirely characterized, but non-satisfactory solid-state structure of wine-red single crystals suggested the formation of this species) and subsequent reaction with ligand ^{Ph}P^{H}NP resulted in the formation of **18** as well. However, the second synthetic route releases several lipophilic byproducts (e.g. PPh$_3$), which exhibit a similar solubility in comparison with **18**. Thus, **18** was prepared in all succeeding reactions from the salt metathesis with sodium iodide and **9**. Ink-blue single crystals of **18** were obtained upon layering a saturated toluene solution with pentane at –80 °C and the solid state structure (Figure 1.23), as well as mass spectrometry and elemental analysis confirmed the exchange of three chloride- for iodide ligands.

Interestingly, similarly to chloride analog **9**, **18** exhibits several broad absorptions (see Figure 1.23, bottom right) in the infrared spectrum (e.g. at ν = 3813 cm^{-1} and 2327 cm^{-1}), which were – as stated above – ascribed to electronic absorptions in the related [(^{iPr}P^{H}NP)ReCl$_3$] complex and are frequently observed for Re^{III} and Re^{IV} complexes (c.f. Figure 1.19 for [(^{Ph}PNP)Re^{III}Cl$_2$(py)]). Moreover, in the ^{1}H NMR spectrum of **18** in C_6D_6 the broadened low-field shifted signals suggest C_2 symmetry in solution, however, two signals with an anticipated integral of two could not be observed (up to +200 ppm). It is important to note, that in the spectra of the chloride- and bromide analogues, **9** and **16**, respectively, two distinctly broadened

signals were observed at the relative low-field end compared to the other signals. Thus, the lack of two signals in **18** can be attributed to either severe broadening below the detection threshold or an even further low-field shift of these signals.

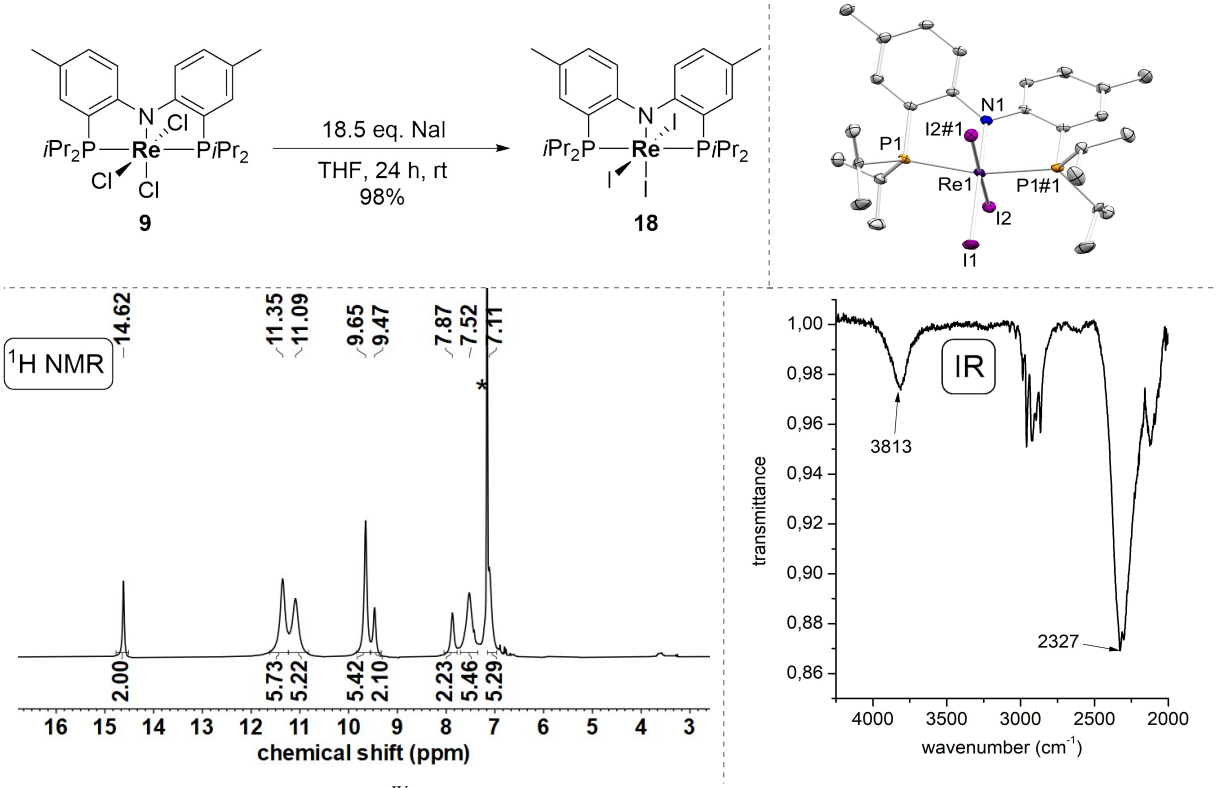

Figure 1.23: Top left: Synthesis of Re^{IV} triiodide complex **18** by salt metathesis with sodium iodide. Top right: Molecular structure of **18** from single-crystal X-ray diffraction (thermal ellipsoids drawn at the 50% probability level); hydrogen atoms are omitted for clarity. Selected bond lengths [Å] and angles [°]: Re1-N1 1.972(4), Re1-P1 2.4505(9), Re1-I1 2.7066(4), Re1-I2 2.7163(3), N1-Re1-I1 180.0, N1-Re1-P1 81.79(2), P1-Re1-P1#1 163.58(4), N1-Re1-I2 88.680(6), I2-Re1-I2#1 91.321(6). Bottom left: ^{1}H NMR spectrum of **18** in C_6D_6. Solvent signal is marked with an asterisk. For an assumed C_2 symmetry in solution there are two signals with an integral of two missing. In analogy to the spectra of the chloride- (**9**) and bromide analog (**16**), two very broad, low-field shifted signals were expected. However, despite scanning up to δ_{IH} = +200 ppm, no additional signals were found. Presumably these signals are even further shifted or broadened to a degree that is not visible anymore. Bottom right: Branch of the IR (ATR, solid) spectrum of **18**.

With the synthesis of **18** in hand, the attention was turned to dinitrogen activation, as **18** should have more favorable halide dissociation kinetics, as well as milder reduction potentials compared to chloride complex **9**. Electrochemical examination *via* cyclic voltammetry confirmed both of these implications. In the CV (Figure 1.24, left) under argon, two reductive features are well-resolved. The first reduction at E_{pc} = –0.79 V, as well as the second reduction at E_{pc} = –1.69 V are fully irreversible, even at high scan rates (up to 1000 mV/s). This implies, that iodide dissociation from **18** is significantly faster (at least on the CV timescale) compared to chloride complex **9**. Moreover, this can potentially indicate more facile access to the Re^{III} dihalide species, since the transiently formed triiodide rhenate complex rapidly loses iodide. Unfortunately, preliminary attempts to isolate the diiodide complex [(^{Ph}PNP)ReI_2] by reduction

in (non)coordinating solvents were unsuccessful. The potential of the second reduction at E_{pc} = –1.69 V displays an anodic shift upon chloride-to-iodide substitution of Δ_E = 0.71 V and if this reduction is tentatively assigned to the $Re^{III/II}$ couple it allows for the use of the considerably milder reductant decamethylcobaltocene ($CoCp^*_2$) for (potential) dinitrogen activation on the Re^{II} oxidation state. The anodic shift for the first reduction is not as significant (Δ_E = 0.16 V), but also reflects the better leaving group character of iodide.

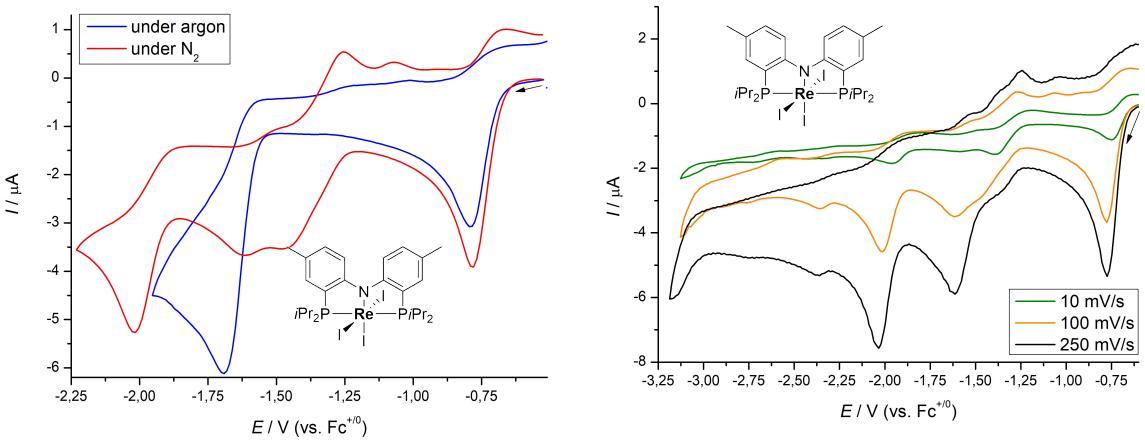

Figure 1.24: Left: Cyclic voltammogram of **18** under argon and dinitrogen (1 mM **18**, 100 mV/s, THF, 0.2 M nBu$_4$NPF$_6$). Right: Cyclic voltammogram of **18** under dinitrogen atmosphere at 10 mV/s and 100 mV/s scan rates (1 mM **18**, N_2, THF, 0.2 M nBu$_4$NPF$_6$). The N_2-based data were measured by *Yaroslava Zelenkova*.

Under dinitrogen atmosphere (Figure 1.24, left, red trace) the potential of the first reduction is barely changed, however, the second reduction is split into several new features over a broad range of several hundred millivolts. Upon examination at different scan rates (Figure 1.24, right), the reduction at E_{pc} = –1.69 V is significantly diminished in current and a new, seemingly irreversible feature appeared at E_{pc} = –1.38 V. This feature is more pronounced at low scan rates and might therefore be dependent on a previous rate-determining chemical step, e.g. iodide dissociation. As it is only present under N_2 atmosphere, it could potentially be assigned to dinitrogen binding at the Re^{III} stage after halide dissociation. At low scan-rates enough "[(^{Ph}PNP)$Re^{III}I_2$]" after halide dissociation is accumulated, which slowly binds N_2 to form [(^{Ph}PNP)$Re^{III}I_2(N_2)$] that is tentatively reduced at E_{pc} = –1.38 V. The ability to bind dinitrogen at the Re^{III} oxidation state was previously linked to the inverse degree of π-donation of the pincer ligand as a consequence of Lewis-acidity of the resulting five-coordinate complex,[38] however, preliminary results from infrared spectroelectrochemical examination, conducted by *Yaroslava Zelenkova*, indicate that N_2 binding occurs on the Re^{II} oxidation state after the second reduction. Moreover, a new clearly resolved reduction at E_{pc} = –2.02 V appears exclusively

under dinitrogen atmosphere corroborating the assumption of N_2-involving follow-up chemistry.

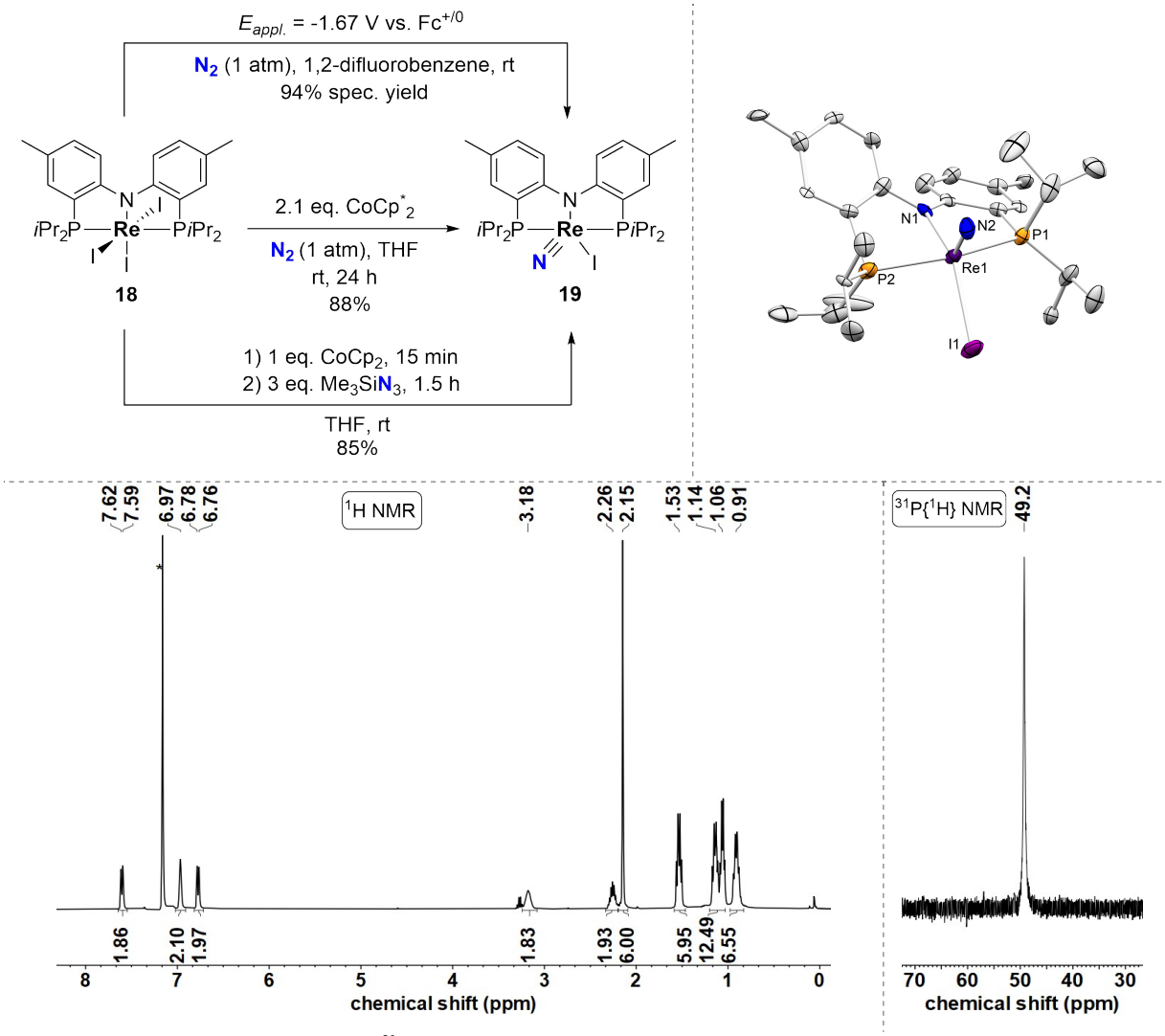

Figure 1.25: Top left: Synthesis of Re^V iodide nitride complex **19**. Top reaction: Electrochemical dinitrogen splitting by controlled potential electrolysis with an applied potential of $E_{appl.}$ = –1.75 V under dinitrogen atmosphere. Mid reaction: Chemical dinitrogen splitting upon reduction of **18** with 2.1 eq. $CoCp^*_2$ in THF under N_2. Bottom reaction: Reduction-azide sequence upon reduction with $CoCp_2$ and treatment with excess trimethylsilyl azide in THF. Top right: Molecular structure of **19** from single-crystal X-ray diffraction (thermal ellipsoids drawn at the 50% probability level); hydrogen atoms are omitted for clarity. Selected bond lengths [Å] and angles [°]: Re1-N2 1.667(13), Re1-N1 2.057(6), Re1-P1 2.380(3), Re1-P2 2.476(4), Re1-I1 2.707(2), N1-Re1-I1 139.7(4), P1-Re1-P2 152.37(13), N2-Re1-I1 104.0(6), N1-Re1-N2 115.6(7), τ^5 = 0.18. Bottom left: ^{1}H NMR spectrum of **19** after isolation in C_6D_6. Solvent signal is marked with an asterisk. Bottom right: ^{31}P{^{1}H} NMR spectrum of **19** after isolation.

Encouraged by the electrochemical examination, chemical dinitrogen splitting was attempted. Reaction of 2.1 equivalents of $CoCp^*_2$ with **18** under an atmosphere of dinitrogen in THF resulted in a distinct, rapid color change from ink-blue to red to green and then more slowly to orange-brown, concomitant with the precipitation of a yellow solid. The reaction was stirred for 24 hours at room temperature and ^{31}P{^{1}H} NMR, as well as ^{1}H NMR spectroscopy indicated

the formation of one main, diamagnetic species with C_2 symmetry in solution. The similar spectroscopic data in comparison to nitride chloride complex **15** suggested the formation of the Re^{V} nitride iodide complex [(^{Ph}PNP)Re(N)I] (**19**), confirmed by further characterization (elemental analysis and mass spectrometry). After workup, **19** was obtained in very high yield (88%) as an orange solid (Figure 1.25). Orange single-crystals suitable for X-ray crystallography were obtained from toluene / pentane at room temperature and the solid-state structure confirmed the formation of **19** ($\tau^5 = 0.18$).

The origin of the nitride nitrogen atom was confirmed with the aid of $^{15}N\{^1H\}$ NMR spectroscopy by performing the reduction of triiodide **18** under an atmosphere of $^{15}N_2$ (δ_{15N} = 365.1 ppm). Similarly to the chloride- and bromide nitride syntheses, a reduction-azide sequence was tested for the synthesis of **19** as well. **19** could be obtained on this route in comparable yield (85%), however, reaction times, scalability and workup proved to be more convenient than *via* the dinitrogen splitting route.

The milder reaction conditions of the dinitrogen splitting starting from the triiodide complex **18** compared to its chloride analogue are remarkable, as they not only allow for dinitrogen splitting at room temperature compared to heating to 50 °C for **9**, but also the nitride yield is significantly higher, resulting in a more facile workup of the product. This can be partially ascribed to the more favorable halide dissociation kinetics of the iodide derivative, but also the milder reduction potentials are leading to potentially less pronounced side reactions. With this relatively mild chemical dinitrogen splitting at room temperature in hand and several recent examples of electrochemical dinitrogen splitting in mind,[124,146,148] controlled potential electrolysis (CPE) of triiodide complex **18** was conducted. Based on the peak current of the broadened second reduction under N_2 atmosphere (c.f. Figure 1.24), a potential of $E_{appl.} = -1.75$ V was applied to provide a sufficient driving force for electrolysis, but potentially applying an overpotential.

Over the course of 90 minutes ($E_{appl.} = -1.75$ V) the CPE solution of **18** in THF under an atmosphere of dinitrogen changed the color from ink-blue to red to green to orange, similarly to the color change during the chemical dinitrogen splitting. In total 1.88 e^-·mol^{-1} were transferred, implying almost complete conversion of the starting material. Measuring CV's in increasing time intervals (Figure 1.26) revealed the slow decay of the features assigned to starting material **18** and concommitant appearance and rise of the features belonging to nitride

complex **19** (Figure 1.26, bottom right, e.g. the reduction at E_{pc} = –2.8 V). With the aid of an internal standard, the spectroscopic yield of **19** was determined to 73% (Faradaic efficiency, FE = 78%). The identity of **19** was further verified by NMR spectroscopic comparison with an independently synthesized sample and by mass spectrometry. The non-quantitative yield of **19** upon electrochemical N_2 splitting can be attributed to the potentially high Lewis-acidity of coordinatively unsaturated intermediates (e.g. five-coordinate [(^{Ph}PNP)$Re^{III}I_2$] upon one-electron reduction). Especially, THF as a Lewis-basic solvent could inhibit N_2 coordination by occupying the free coordination site at the Rhenium metal. Consequently, this hypothesis was probed by performing the CPE in a polar, non-coordinating solvent.

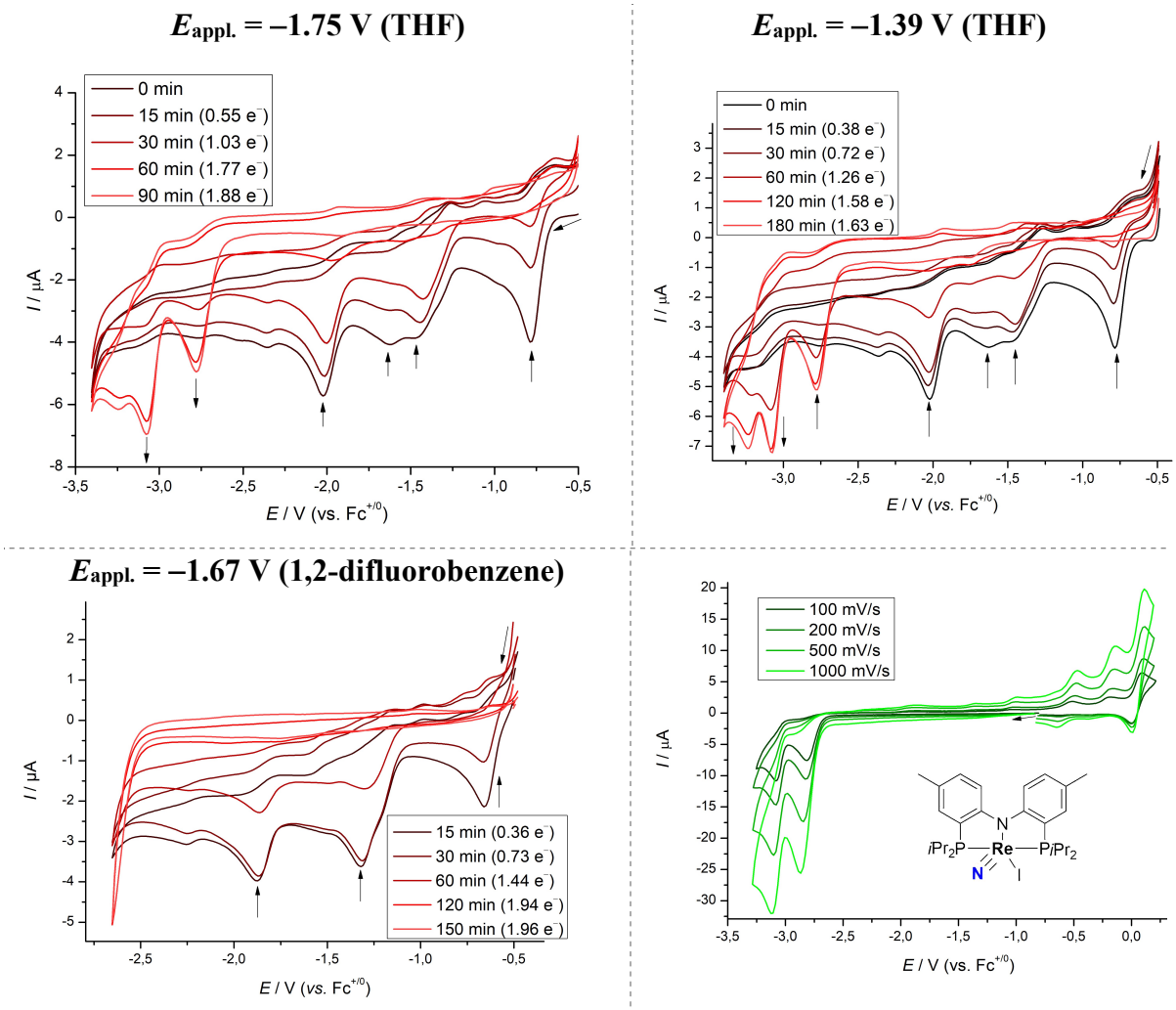

Figure 1.26: Top left: Cyclic voltammograms of the controlled potential electrolysis of **18** under N_2 atmosphere (E_{appl} = –1.75 V, 100 mV/s, 1 mM **18**, 0.2 M nBu$_4$NPF$_6$, THF). Top right: Cyclic voltammograms of the controlled potential electrolysis of **18** under N_2 atmosphere ($E_{appl.}$ = –1.39 V, 100 mV/s, 1 mM **18**, 0.2 M nBu$_4$NPF$_6$, THF) performed by *Yaroslava Zelenkova*. Bottom left: Cyclic voltammograms of the CPE of **18** under N_2 atmosphere ($E_{appl.}$ = –1.67 V, 1 mM **18**, 0.2 M nBu$_4$NPF$_6$, 1,2-difluorobenzene). Bottom right: Cyclic voltammogram of **19** (2 mM **19**, Ar, 0.2 M nBu$_4$NPF$_6$).

In fact, CPE of **18** in 1,2-difluorobenzene at $E_{appl.} = -1.67$ V furnished 94% of **19** (spectroscopic yield). During the CPE 1.96 e^{-}·mol^{-1} were transferred, resulting in a Faradaic efficiency of overall 98%. This represents the by far highest and essentially quantitative yield for homogeneous, electrochemical N_2 splitting reported to date. A high dinitrogen splitting yield is pivotal for any system that is envisioned to catalytically form bonds with a dinitrogen-derived nitride nitrogen and was realized with the [(^{Ph}PNP)ReI_3] system for the first time.

The reductive feature at $E_{pc} = -1.38$ V that exclusively appeared at low scan-rates under N_2 atmosphere (Figure 1.24, right) was further investigated. CPE at $E_{appl.} = -1.39$ V in THF performed in collaboration with *Yaroslava Zelenkova* resulted in very similar observations compared to the CPE at $E_{appl.} = -1.75$ V. The current of the features of **18** gradually decayed and features assignable to nitride **19** appeared over the course of three hours at room temperature. The spectroscopic yield of **19** determined with an internal standard was 46%, which can, in combination with the lower-than-expected amount of transferred electrons (Figure 1.26, top right) be explained with lower selectivity. Based on the potential of the feature at $E_{pc} = -1.38$ V and its irreversibility, chemical reduction with the milder reductant cobaltocene ($E = -1.33$ V in CH_2Cl_2)[198] was subsequently attempted. In agreement with the electrochemical splitting, addition of 2.0 eq. $CoCp_2$ to **18** in THF resulted in formation of nitride **19** within one hour at room temperature (82% isolated yield). Apparently, the thermodynamic sink that is $[CoCp_2][I]$ precipitation is sufficient to drive the irreversible reduction to completion.

In conclusion, halide exchange from chloride to iodide induced a significant anodic potential shift for the $Re^{IV/III}$ and the $Re^{III/II}$ irreversible reductions. More precisely, the anodic shift for the second reduction under argon equals to $\Delta E = 0.71$ V, which is attributed to the formation of a Re^{II} species that potentially binds and activates dinitrogen. Furthermore, under N_2 atmosphere a new reductive feature appeared, which could be utilized for CPE at $E_{appl.} = -1.39$ V, resulting in an overall anodic shift of $\Delta E = 0.99$ V, which is remarkably high and has in combination with the better leaving group characteristics of iodide compared to chloride the following implications on dinitrogen splitting:

1. The distinctly milder reduction potential of [(^{Ph}PNP)ReI_3] (**18**) at $E_{pc} = -1.69$ V under argon allows for the use of $CoCp^*_2$ as reductant and a new feature at low scan rates under N_2 at $E_{pc} = -1.38$ V hinted at possibly even milder conditions, which was

confirmed with rapid dinitrogen splitting using $CoCp_2$, as well as CPE at $E_{appl.} = -1.39$ V in moderate to good yields.

2. The milder conditions and faster halide dissociation in general appear to contribute to significantly increased chemical dinitrogen splitting yields on the iodide complex platform (**9**: 60%, **18**: 88%) and enabled room temperature controlled potential electrolysis in 73% spectroscopic yield with 78% Faradaic efficiency in THF.
3. The yield of electrochemical N_2 splitting could be even further increased by performing the CPE in a non-coordinating solvent (1,2-difluorobenzene), resulting in 94% spectroscopic and 98% Faradaic efficiency in nitride **19**. This is the first time that homogeneous, electrochemical dinitrogen splitting resulted in near quantitative nitride yields.
4. The comparatively faster halide dissociation provides a free coordination site on the Re^{III} stage, which is potentially accessible for dinitrogen binding, as was tentatively assigned at slow scan rates in the CV of **18** under dinitrogen. Preliminary IR-SEC experiments, however, indicate that N_2 binding happens after the second reduction at the Re^{II} oxidation state.

1.6 Conclusion

This chapter was divided in two sections: **A)** Dinitrogen activation by (dinuclear) Osmium dinitrogen complexes and **B)** (Electro)chemical dinitrogen splitting with Re^{IV} complexes ligated by a chemically robust pincer ligand.

Synthesis of the stable Os^{II}/Os^{II} dinuclear dinitrogen-bridged complex ($\pi^{12}\delta^4$) [((^{Py}PNP)$OsCl_2$)$_2$(μ-N_2)] (**3**) was achieved upon reduction of an Osmium trichloride precursor complex. Spectroscopic evidence suggested initial formation of a mononuclear terminal dinitrogen complex, which could be converted to **3** by stirring under static vacuum (Scheme 1.9). The dinitrogen ligand in **3** is weakly activated, as expected for N_2-bridged complexes of similar electronic configuration. Oxidation of **3** furnished the cationic, mixed-valent complex [((^{Py}PNP)$OsCl_2$)$_2$(μ-N_2)]$^+$ (**5**$^+$, $\pi^{11}\delta^4$), concomitant with a slightly higher degree of N_2 activation. Preliminary functionalization and photolytic N_2 cleavage attempts from **3** and **5**$^+$ were not successful, but electrochemical examination by cyclic voltammetry suggested the accessibility of a dicationic $\pi^{10}\delta^4$ complex.

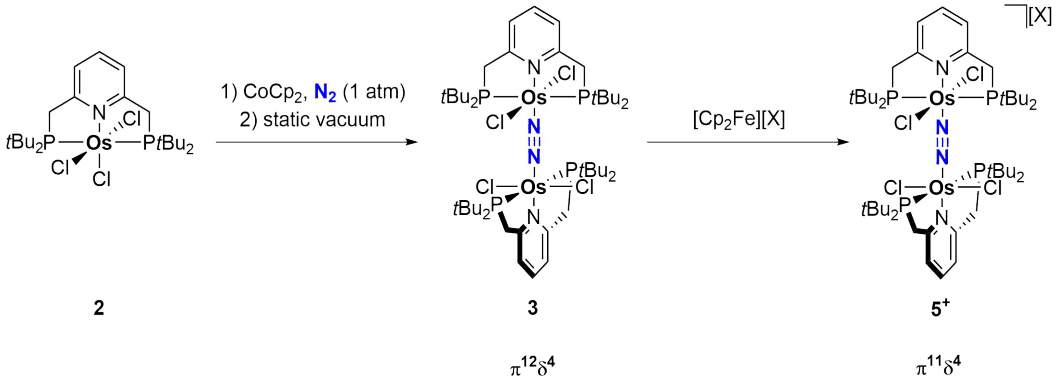

Scheme 1.9: Synthesis of $\pi^{12}\delta^4$ and $\pi^{11}\delta^4$ dinuclear, N_2-bridged Osmium pincer complexes.

The Re^{IV} complex [(^{Ph}PNP)$ReCl_3$] (**9**) was isolated upon reaction of the $^{Ph}P^{H}NP$ ligand with a Re^{III} precursor without additional base. Metal oxidation in this case is attributed to comcomitant H_2 evolution from weakening of the ligand N-H upon bonding to the metal. **9** exhibits a reversible ($E_{1/2}$ = –0.95 V) and a second irreversible (E_{pc} = –2.40 V, both vs. $Fc^{+/0}$) reduction in the CV under N_2. Reduction of **9** with Na/Hg under N_2 atmosphere resulted in the isolation of Re^{V} nitride [(^{Ph}PNP)Re(N)Cl] (**15**) upon dinitrogen splitting in 60% isolated yield. Electrochemical dinitrogen splitting *via* controlled potential electrolysis (CPE) with **9** was

unsuccessful, which was attributed to slow chloride dissociation kinetics of the first reduction, as evident from the reversible reduction in the CV.

Implementation of a better leaving group was realized upon salt metathesis with NaI to form Re^{IV} complex [(^{Ph}PNP)ReI$_3$] (**18**). As expected, both reductions in the CV of **18** are irreversible, indicating facile iodide loss. Moreover, the second reduction is significantly shifted to a milder reduction potential (E_{pc} = –1.69 V). Consequently, the mild reducing agent cobaltocene was sufficient to achieve dinitrogen splitting in 82% isolated yield (Figure 1.27). Electrochemical dinitrogen splitting *via* CPE ($E_{appl.}$ = –1.75 V) in THF yielded 73% [(^{Ph}PNP)Re(N)I] (**19**) with a Faradaic efficiency of 78% upon transfer of 1.88 e^-·mol^{-1} over the course of 90 minutes at room temperature.

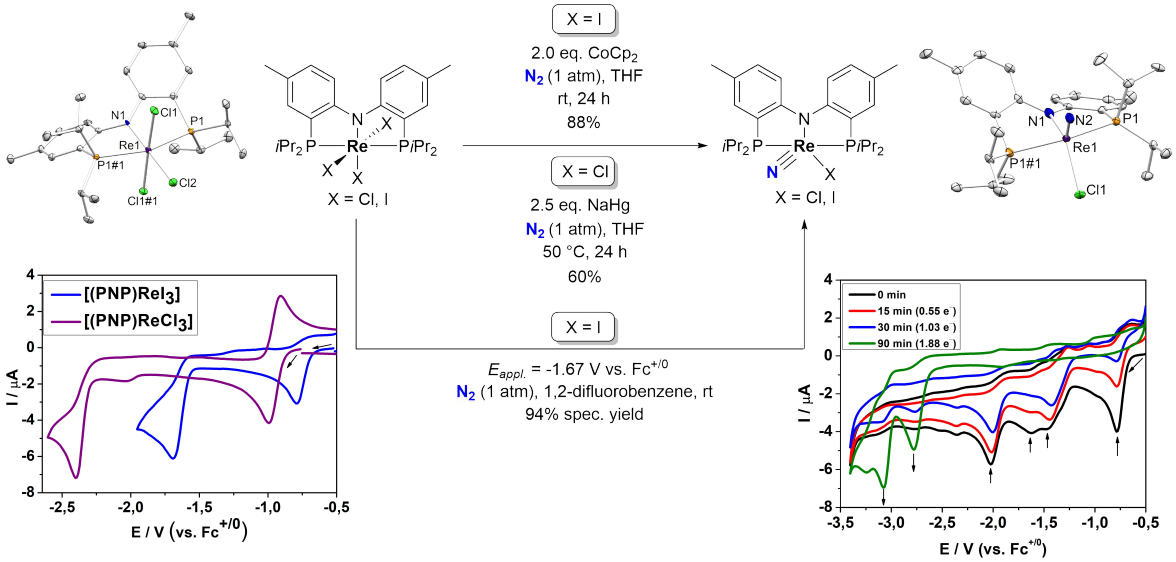

Figure 1.27: Summary of the (electro)chemical dinitrogen splitting mediated by Re^{IV} PNP pincer complexes.

This high electrochemical dinitrogen splitting yield could be further improved by conducting CPE in a non-coordinating solvent. In fact, performing CPE ($E_{appl.}$ = –1.67 V) in 1,2-difluorobenzene resulted in unprecedented, essentially quantitative (94%) formation of nitride **19** with very high Faradaic efficiency (98%).

Part II: Transfer of (Electro)chemically Dinitrogen-Derived Nitride to Nitric Oxide

2.1 General Reactivity of Rhenium- and Osmium Nitride Complexes

Formation of terminal transition metal nitride complexes *via* dinitrogen splitting has gained considerable attention in recent years, as this methodology circumvents the initial energy-demanding overreduction of N_2 to ammonia and subsequent NH_3 oxidation processes at high temperatures.[40,181,206,207] This shortcut is particularly desirable, because the nitride complexes allow for selective reactivity with reagents of interest to synthesize a vast range of different nitrogenous bulk and fine chemicals. Rhenium- and Osmium nitride complexes are especially intriguing compounds, since they show – despite their adjacency in the periodic table in the middle of the transition-metal block – distinctly different reactivity patterns. In the following paragraphs, the main properties of the metal-nitride manifold with respect to the bonding situation and electronic structure, as well as various factors influencing the nitride complex philicity and selected examples of their reactivity are shown and will be discussed.

The terminal nitride ligand refers to a closed-shell, formal trianionic nitrogen atom that forms a triple-bond when bonded to a metal center.[208] To predict and modify the reactivity of transition metal nitrides, it is essential to understand the electronic structure of the metal-nitride moiety. *Gray* and *Ballhausen* developed a molecular orbital description for multiply-bonded ligands to metals,[209] which initially was used for the description of the octahedral vanadyl ion $[VO(H_2O)_5]^{2+}$, but was soon expanded to other metal-ligand combinations and complex symmetries as well.[210] Applying this concept to octahedral metal-nitride complexes of idealized C_{4v} symmetry results in the MO scheme shown in Figure 2.1 on the left. The bonding σ- and antibonding σ^*-MO evolve from interaction of the empty d_z^2 metal orbital and the filled p_z nitrogen orbital. The doubly degenerate π- and the antibonding π^*-MO's are composed of the interaction of filled p_x and p_y nitrogen orbitals with d_{xz} and d_{yz} metal orbitals, resulting in an overall formal bond order of three.[208,211,212] In d^0 nitride complexes the π-MO constitutes the HOMO of such a complex, whereas up to a d^2 electronic configuration the higher, nonbonding d_{xy} orbital is filled. From these considerations the upper limit for octahedral nitride d-electron count is evident, as the antibonding π^*-orbitals have to be populated if the d-electron

count exceeds two.[212] This electronic limitation is reflected for example in the very low reduction potentials of Re d^2 nitrides and the instability of Fe^V (d^3) nitride complexes.[159,213] The scarcity of octahedral late transition metal nitrides past Osmium is connected to the needed low d-electron count.

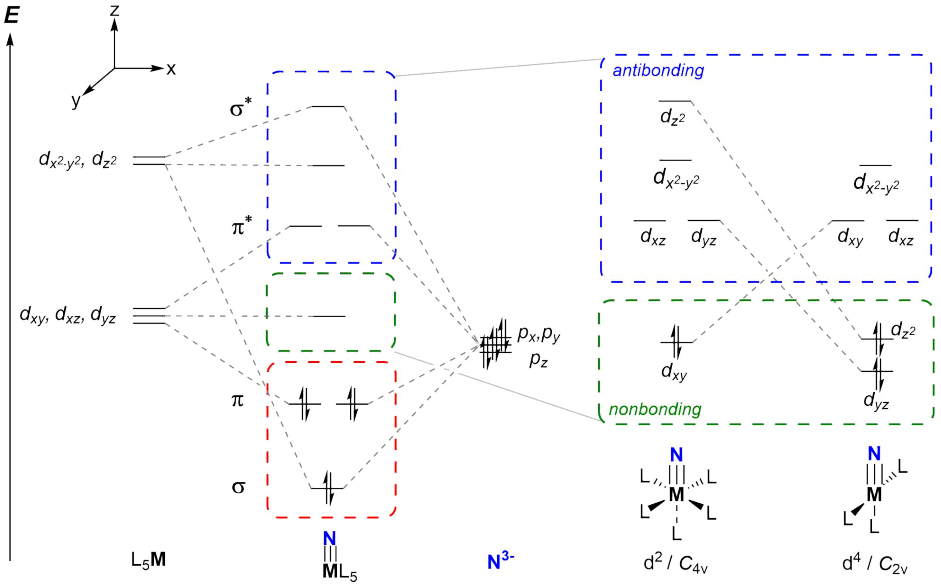

Figure 2.1: Left: Orbital interaction scheme of filled nitrogen p-orbitals with empty metal d-orbitals to construct a d^0 metal nitride. Right: Frontier MO scheme of a d^2 metal nitride of idealized C_{4v} symmetry and transformation to isolobal d^4 metal nitride of C_{2v} symmetry.

Higher d-electron counts can be achieved by symmetry reduction, e.g. from an idealized C_{4v} to a C_{2v} symmetry associated with reduction of the coordination number to four in square planar nitride complexes, which share an isolobal relationship with octahedral nitride complexes (Figure 2.1, right).[210] The d_{yz} and d_z^2 orbitals in square planar nitrides are significantly reduced in energy, essentially becoming nonbonding. Consequently, up to four d-electrons can occupy these metal-centered, nonbonding orbitals. Notable examples include the d^4 complexes [(^{Si}PNP)Ru(N)] (^{Si}PNP = [(SiMe$_2$CH$_2$P*t*Bu$_2$)$_2$N]$^-$) from the *Caulton* group,[214] as well as [($^{t\text{Bu}}$P=N=P)Ir(N)]$^+$ and [($^{t\text{Bu}}$P=N=P)Os(N)] from *Schneider* and coworkers.[215,216] Within this coordination geometry it was even possible to stabilize the open-shell d^5 complex [($^{t\text{Bu}}$P=N=P)Ir(N)] and the diamagnetic d^6 [(PDI)Ir(N)] (PDI = pyridinediimino) nitride.[215,217]

From the mentioned MO considerations the expected reactivity of the metal-nitride moiety can be established. Three main factors determine the nitride reactivity: The metal of the nitride complex, the oxidation state and the ancillary ligand set.[208,211,218] Essentially, these variations are influencing the relative contributions of metal and nitrogen to the frontier molecular orbitals. The metal variation explains the overarching reactivity trend among the transition-metal block.

Depending on the metal, the energetic level of the empty d-orbitals is higher, similar to or lower than the filled nitrogen p-orbitals, as the d-orbital energies decrease from the early to the late transition metals (Figure 2.2).[218,219] Hence, the relative metal orbital coefficient of the π^*-LUMO is highest for early transition metals and decreases along the d-series, while the nitrogen orbital coefficient in turn increases.[220] The inverse relation is found for the occupied π–MO, which shows the highest nitrogen contribution for early transition metals and small contribution for late metals.

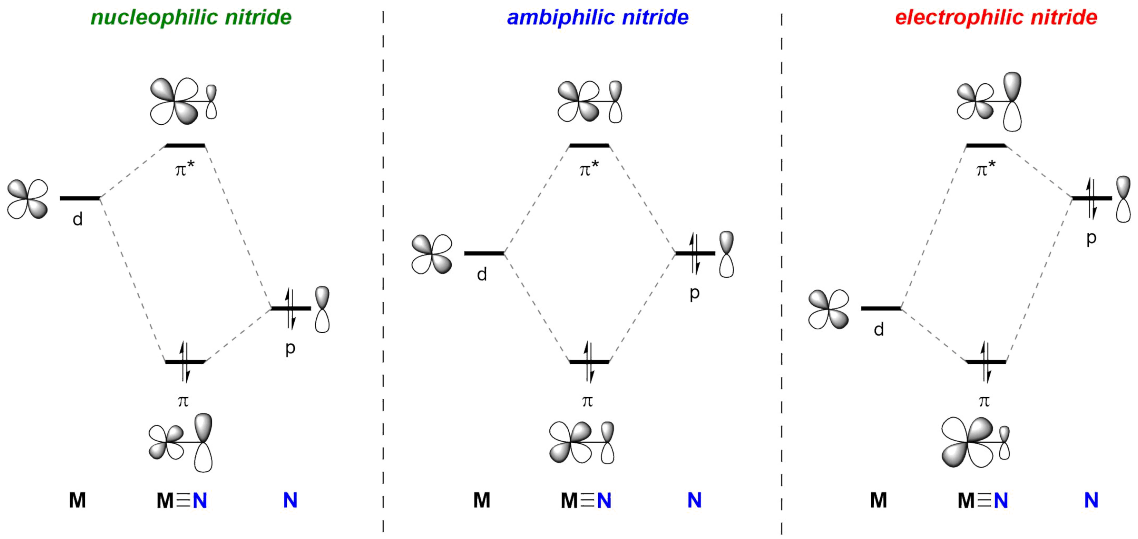

Figure 2.2: Simplified MO scheme of the π-interaction between filled p-orbitals of nitrogen and empty metal d-orbitals of suitable symmetry to form the two π-bonds contributing to the M≡N bond. Depending on the energetic level of the metal d-orbitals, the relative contributions of M and N to the π- and π*-bonds result in a nucleophilic (left), ambiphilic (mid), or electrophilic nitride (right).

Based on this, nucleophilic reactivity is expected for early metal nitrides with high nitrogen π–MO character and electrophilic reactivity for complexes of late transition metals with a low-lying π^*–LUMO of high nitrogen character.[208,211,212] The intermediate case, where d- and p-orbitals occupy similar energetic levels, corresponds to ambiphilic nitrides that are expected to be found mainly at the center of the transition metal block. As a consequence, Rhenium and Osmium are situated in a special location of the periodic table with respect to the philicity of their nitride complexes. Re^{V} nitride complexes are generally considered as nucleophilic and Os^{VI} nitrides mainly as electrophilic, but depending on the ligand set the philicity can be influenced. Coupling of dinitrogen splitting and nitride functionalization in the coordination sphere of Rhenium and Osmium therefore holds the prospect of ambiphilic reactivity and compatibility with a wide range of reagents.

The Rhenium d^2 nitride complexes of the generalized formula $[Re^{V}(N)Cl_2(PR_3)_2]$ and related complexes derived by phosphine substitution were investigated thoroughly with regard to their nitride reactivity.[208] For example, reaction of $[Re(N)(N(SPPh_2)_2)_2]$ with the electrophiles BCl_3,[221] $(CF_3CO)_2O$, CH_3COCl and $[Ph_3C]BF_4$[222] resulted in selective nitride functionalization and the formation of N-B- and N-C bonds. Interestingly, hydrolysis of the formed acylimido complexes with electron withdrawing substituents ($L_5Re{=}N{-}COCX_3$; X = F, Cl) furnished the parent N-H imido complex, while less withdrawing substituents formed the octahedral terminal oxo complexes.[222] In general, reactivity of Rhenium nitrides is observed towards BCl_3/BBr_3,[221,223–225] (electron-poor) organoboranes,[223,226–230] $GaCl_3$,[223,226] CPh_3^+,[231,232] benzyl chloride,[232] acid chlorides or anhydrides,[152,222] MeOTf / EtOTf[123,183,232] and S_2Cl_2[226,233,234] with predominantly adduct formation and only minor decrease of the Re-N bond order, apparent from the minor elongation of the Re-N bond length (Scheme 2.1). The main exception of the listed examples is the formation of a thionitrosyl ligand upon addition of S_2Cl_2, where significant bond reorganization takes place. These reactions are mostly seen in terms of Lewis acid – Lewis base adduct formation, implying an inherent nucleophilic character of the Rhenium nitride moiety.

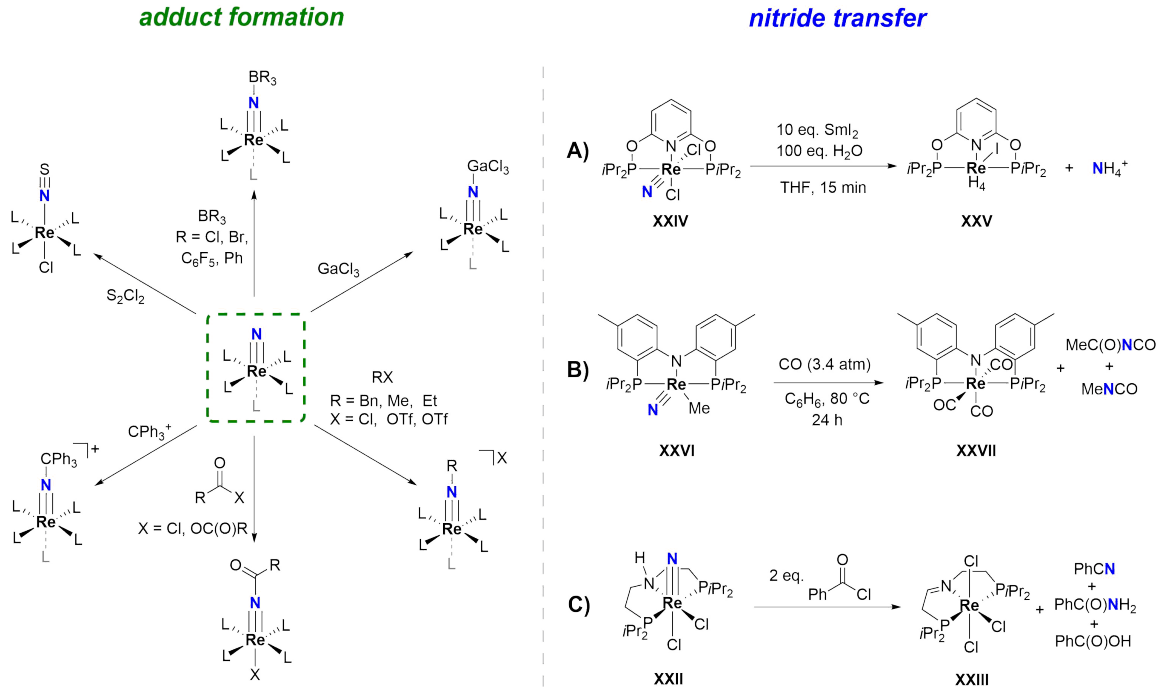

Scheme 2.1: Left: Adduct formation upon reaction of Re^{V} nitrides with electrophiles. The references for each reaction can be found in the text. Right: Examples of nitride transfer from Re^{V} nitride complexes. **A)** Nitride hydrogenation of **XXIV** with excess $Sm^{II}I_2$ and H_2O to form ammonia (detected as ammonium) and a Rhenium hydride complex **XXV**.[201] **B)** Nitride carbonylation of **XXVI** with high pressure carbon monoxide to form organic isocyanates and a Rhenium tricarbonyl complex **XXVII**.[168] **C)** Metal-ligand cooperative nitride transfer upon reaction of **XXII** with benzoyl chloride and formation of benzonitrile, benzamide and benzoic acid, as well as an imine Re^{III} trichloride pincer complex **XXIII**.[152]

In addition to adduct formation, several nitride transfer reactions with Re^{V} nitride complexes were reported. *Miller* and coworkers showed the hydrogenation of octahedral *cis*-[(PONOP)Re(N)Cl_2] (**XXIV**) with the reagent combination of SmI_2 and H_2O to form ammonia (detected as ammonium) as the main nitrogen-containing product (Scheme 2.1, right, A).[201] *Ison* and coworkers investigated the remarkable reaction of [(^{Ph}PNP)Re(N)Me] (**XXVI**) with high pressures of CO (Scheme 2.1, right, B).[168] Organic isocyanates were formed through initial coordination of CO, followed by insertion of CO into the Re-C bond and reaction of additional CO with the nitride. Furthermore, *Schneider* and coworkers reported the metal-ligand cooperative functionalization of Re^{V} pincer nitride complex **XXII** with benzoyl chloride.[152] Ligand oxidation provides two protons and two electrons for the functionalization to finally form benzonitrile, benzamide and benzoic acid (Scheme 2.1, right, C). These nitride transfer reactions can be implemented into synthetic cycles, if the Rhenium containing product can be used to regenerate the Rhenium nitride (e.g. by dinitrogen splitting).

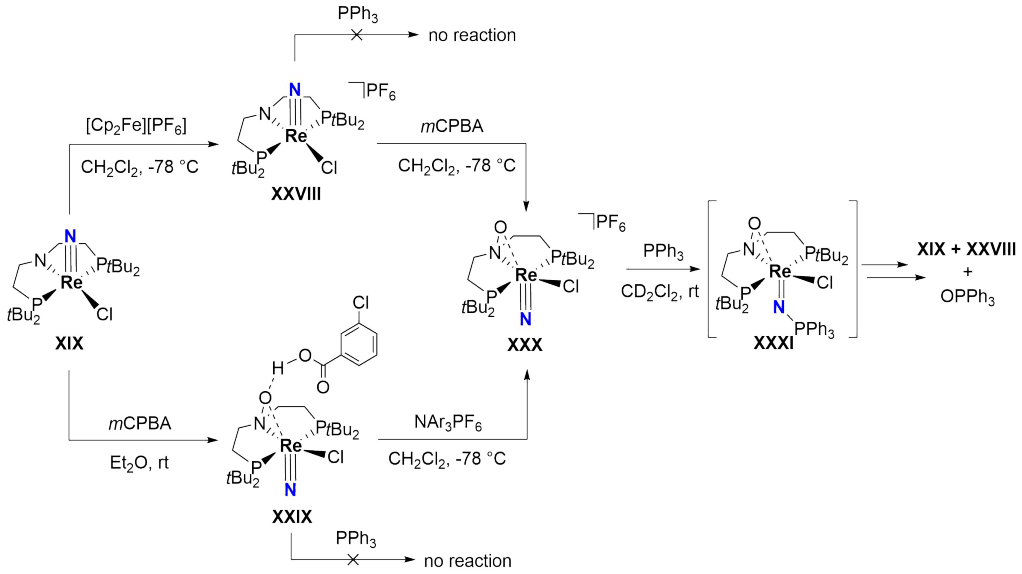

Scheme 2.2: Formal *umpolung* of a nucleophilic, dinitrogen-derived Re^{V} nitride **XIX** upon sequential oxidation and pincer oxygenation. The Re^{VI} $P^{O}NP$ pincer nitride complex **XXX** reacts with triphenylphosphine to form an unstable iminophosphorane **XXXI** upon N-P bond formation.

Exceptions to the predominantly nucleophilic reactivity of Re^{V} nitride complexes apart from the reaction with CO are rare. One report by *Martell* and coworkers described the formation of [Re($NPPh_3$)(atp)$_2$] (atp = 2-aminothiophenolate) upon reaction of [Re(N)Cl_2(PPh_3)$_2$] with 2-aminothiophenol and base.[235] Unfortunately, no further analysis of the origin of this unusual reactivity was reported. Moreover, *Hanack*, *Sundermeyer* and coworkers reported the loss of the nitride ligand in a phthalocyaninato ligated rhenium nitride complex upon heating with

excess PPh_3 to 220 °C for 30 minutes under reduced pressure.[236] Based on the formed dinuclear bridging oxo complex, they suggested initial reaction of nitride and phosphine and release of parent iminophosphorane upon hydrolysis. No further spectroscopic evidence was provided.

As mentioned above, the nitride reactivity can be influenced – in addition to the participating metal – by the oxidation state and the ancillary ligand set. This is especially relevant for Rhenium and Osmium nitride complexes as they lie in the transition region between nucleophilic and ambiphilic/electrophilic reactivity and vice versa. Moreover, dinitrogen-derived Re^V nitrides are often overstabilized as part of the thermodynamic driving force of N_2-splitting and require specialized ligand sets to increase nitride reactivity. *Mayer, Holland* and coworkers examined modifications on the nucleophilic, dinitrogen-derived Re^V nitride [($^{t\text{Bu}}$PNP)Re(N)Cl] (**XIX**) to enable coupling of N_2 splitting and nitride functionalization with nucleophiles.[202,237] This attempted *umpolung* of the nitride reactivity included two approaches: Oxidation from Re^V to Re^{VI} (**XXVIII**) was supposed to reduce electron density and therefore increase electrophilicity of the Re-N manifold. Furthermore, oxygenation of the pincer ligand resulted in a P^ONP nitroxide pincer ligand (**XXIX**), with the oxygen atom in *trans*-position to the nitride ligand. Introduction of a ligand in *trans*-position was demonstrated to increase reactivity significantly in case of Ru^{VI} salen complexes.[238] Both modifications had to be applied simultaneously to achieve substantially altered nitride reactivity: The Re^{VI} complex [($^{t\text{Bu}}P^ONP$)Re(N)Cl]$^+$ (**XXX**) was reported to react with triarylphosphines to form unstable phosphinimide complexes (**XXXI**) upon N-P bond formation, which decomposed to the non-oxygenated Re^V and Re^{VI} nitride complexes [($^{t\text{Bu}}$PNP)Re(N)Cl]$^{0/+}$ and the corresponding phosphine oxides.

Reactivity of Os^{VI} nitrides was investigated mainly by the groups of *Mayer* and *Meyer*. No efficient dinitrogen splitting route towards stable Os^{VI} nitride complexes is reported to date, in contrast to their isoelectronic Re^V counterparts. Only one paper by *Kunkely* and *Vogler* reports photolytic dinitrogen splitting of a mixed-valence Os^{II}/Os^{III} dinuclear complex, however, the bridging N_2 unit is derived from hydrazine oxidation and not from gaseous dinitrogen.[182] The reactivity of Os^{VI} nitrides is considerably more varied compared to Re^V nitrides.[208] On the one hand, reactivity towards boranes (adduct formation),[239] CPh_3^+,[240] and MeOTf / MeI[239,241,242] was observed. On the other hand, nitride reactivity towards boranes (insertion into B-C bond),[242,243] carbenes,[244] Grignard reagents,[242,245] cyclohexadiene (4+1 cycloaddition),[246] C-C double bonds,[247,248] cyanide,[249–251] CS_2 and N_3^-,[252] N_3^-,[252–254] amines,[255,256] NO,[257]

phosphanes,[258–263] $SPPh_3$,[264] Me_3NO[262,265] and S_8 / Se[262] was reported. Generally, Os^{VI} complexes show nucleophilic and electrophilic reactivity, with significantly more examples reported of reactions in which the nitride acts as an electrophile (Scheme 2.3).

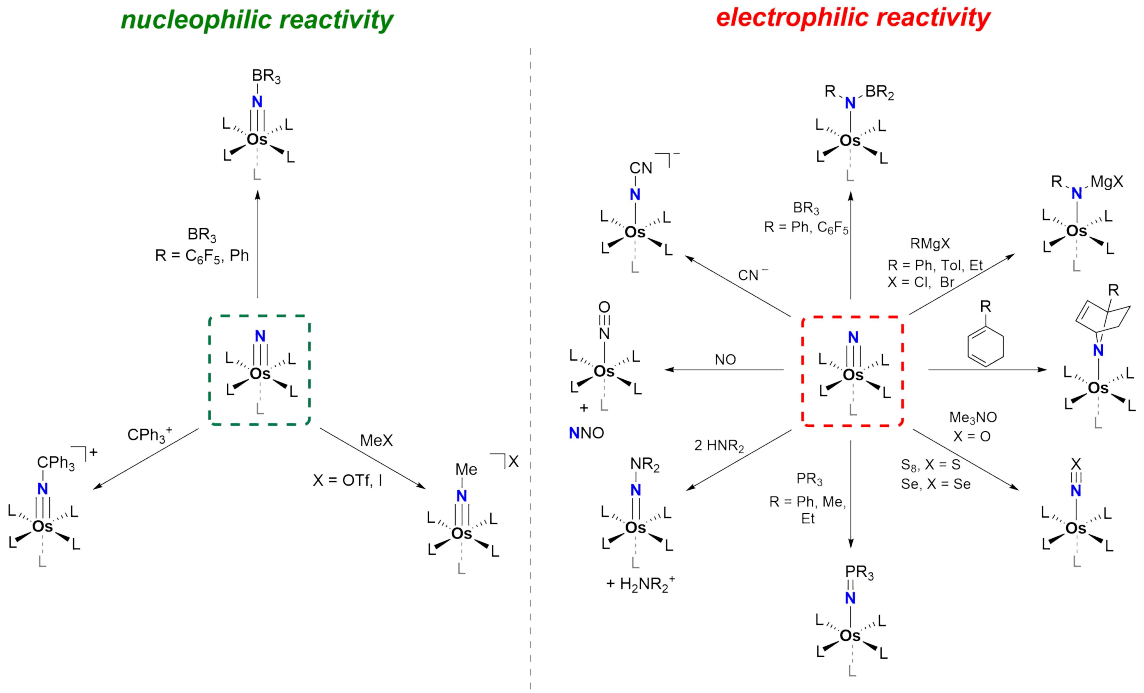

Scheme 2.3: Summary of Os^{VI} nitride reactivity. Citations can be found in the text. Left: Nucleophilic reactivity of Os^{VI} nitride complexes. Right: Selected examples of electrophilic reactivity of Os^{VI} nitride complexes. Particularly for the reaction with NO the classification as electrophilic reactivity is not precise. Furthermore, phosphines can, in addition to their nucleophilic reactivity, also react as electrophiles.[216]

The nitride reactivity of Os^{VI} nitrides can be controlled depending on the ancillary ligand set, resulting in some remarkable examples where minor ligand substitution reactions drastically changed the effective nitride philicity. Arguably the most thoroughly investigated complex in that regard is the octahedral $[TpOs(N)Cl_2]$ (**XXXII**, Tp = hydro*tris*(1-pyrazolyl)borate),[245] first reported by *Mayer* and coworkers. Numerous studies examined its reactivity, concluding that the Os-N moiety is strongly electrophilic with accessible, low-lying π^*-orbitals of high nitrogen character.[245,266] This is reflected in the reactivity towards Grignard reagents to form an N-C bond and rapid reactivity towards phosphanes to form iminophosphoranes (Scheme 2.4). Moreover, no reactivity was observed towards MeOTf or $BF_3 \cdot Et_2O$, consistent with the electrophilic description of the nitride. Interestingly, reaction with electron-poor organoboranes like $B(C_6F_5)_3$ resulted in nitride insertion into one of the three B-C bonds. Substitution of the chloride- for phenyl ligands furnished $[TpOs(N)Ph_2]$ (**XXXIII**), which showed significantly altered reactivity.[242] For example, adduct formation was observed for the reaction of $[TpOs(N)Ph_2]$ with $B(C_6F_5)_3$ and only very slow reactivity towards PPh_3, which led

to the conclusion that [TpOs(N)Ph$_2$] is significantly less electrophilic compared to its chloride analogue and was rather comparable to nucleophilic manganese nitrides.[257]

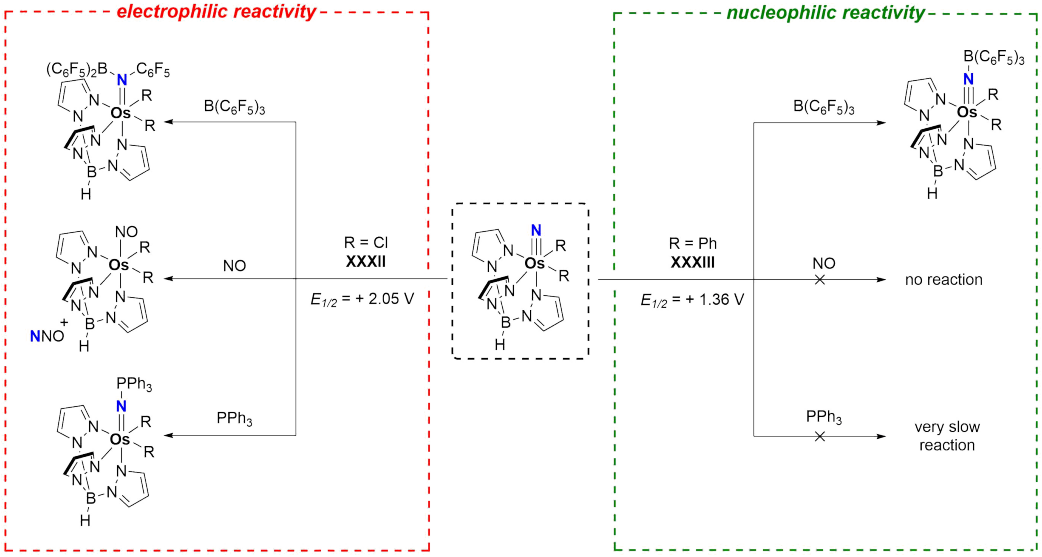

Scheme 2.4: Change in nitride reactivity of Os^{VI} nitride complexes induced upon chloride (electrophilic) to phenyl (nucleophilic) exchange.

Mayer and coworkers examined the electrochemical properties of Os^{VI} nitride and related complexes to observe trends among a series of isoelectronic metal complexes and different ligand substitution patterns.[213] They correlated the d^2/d^1 redox couple with the general electron richness of the metal complex, as oxidation should remove an electron from the metal-centered non-bonding d_{xy} orbital in octahedral d^2 nitrides. For [TpOs(N)Cl$_2$] (**XXXII**) they found a very anodic half-wave potential of $E_{1/2}$ = +2.05 V (lower limit), which was significantly reduced to $E_{1/2}$ = +1.36 V for the phenyl derivative **XXXIII** (potentials vs. Fc$^{+/0}$ in MeCN). The more facile oxidation of **XXXIII** compared to **XXXII** might therefore indicate a more electron-rich complex and explain its nucleophilic reactivity. Furthermore, the authors stated that the Os$^{VII/VI}$ redox-couple is drastically more oxidizing compared to the isoelectronic Re$^{VI/V}$ couple, exemplifying the inherent electrophilic character of most Os^{VI} nitrides. Consequently, this limits the use of the mostly reversible d^2/d^1 redox couple as an "universal", metal-independent electrophilicity scale for nitride reactivity.

2.2 Relevance and Reactivity of Lower Nitrogen Oxides

"How much carbon does it take to make nitric acid?" is an interesting question that framed a summarizing review article regarding nitrogen transformations beyond fossil fuels by several groups working in the field of nitrogen fixation and functionalization.[4] The answer at the beginning of the third decade of the twenty-first century still has to be *a large amount*, which is especially concerning as the product does not contain a single carbon atom. The industrial synthesis of oxidized nitrogen products generally requires two energy-demanding processes. Initial splitting of the strong, inert dinitrogen triple-bond *via* the Haber-Bosch process provides reduced nitrogen in the form of ammonia. Subsequently, the ammonia is fed into the Ostwald process, as an umbrella term for heterogeneous, catalytic ammonia oxidation. Both processes demand, despite being highly optimized, harsh reaction conditions and/or chemicals that were synthesized from fossil sources (e.g. hydrogen from methane by steam reforming). The synthesis of nitric acid from the Haber-Bosch – Ostwald process sequence with hydrogen gas derived from steam reforming is particularly wasteful, yet most of the 55 Mt/year HNO_3 are manufactured this way, mainly due to the lack of viable alternatives.[4,267]

Direct dinitrogen oxidation is largely unknown, yet it could reduce the agricultural carbon footprint significantly, as 80% of the produced HNO_3 is used for fertilizers.[267] However, the lack of biological examples and the evolution of a complex interplay between dinitrogen reducing- and ammonia oxidizing bacteria instead, indicate fundamental chemical obstacles.[4] Direct formation of *N*-oxides from N_2 and O_2 is only known under especially harsh conditions (e.g. N_2 fixation by lightning[1,268] or in thermal plasmas[269]), owing to the symmetry-forbidden bimolecular reaction between both gases. One possibility to circumvent this reaction is electrochemical coupling of cathodic N_2 reduction / splitting with anodic N_2 oxidation / nitride functionalization for which suitable catalysts still have to be developed.[207]

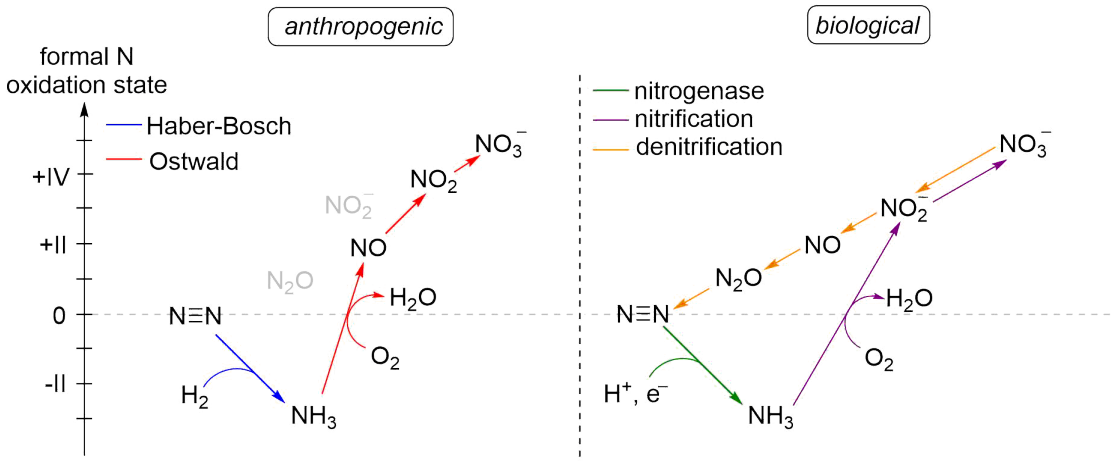

Figure 2.3: Comparison of simplified anthropogenic and biological nitrogen fixation and oxidation pathways.

Nitrogen oxides are also relevant as hazardous pollutants, take part in biological processes and are produced by different bacteria in a similar sequence to the anthropogenic nitrogen oxide synthesis upon reduction of dinitrogen to ammonia[23] and subsequent oxidation up to nitrate. Dinitrogen reduction is carried out by nitrogenase containing microbes, which provide ammonia that is oxidized with O_2 by nitrifying bacteria and archaea to nitrite or, under low O_2 conditions, to nitrous oxide (Figure 2.3).[1,270] Nitrite can be further oxidized to nitrate, or nitrate is synthesized directly from a recently discovered, restricted group of proteobacteria from ammonia.[271,272] On the other hand, complete denitrification – or reduction – of nitrate to gaseous dinitrogen can be carried out by many microbes, which contain the necessary reductase enzymes.[273] These denitrification processes constitute a major loss of bioavailable nitrogen in the forms of N_2O or N_2 and are used for example as detoxification mechanism of hazardous *N*-oxides like NO.[1]

From the comparison of anthropogenic *N*-oxide synthesis with the biological N-cycle, it is evident that synthesis of *N*-oxides proceeds in both cases in only one direction: Reduction of dinitrogen, oxidation of ammonia and then – in case of the biological N-cycle – successive reduction back to dinitrogen. Reversal of the N-cycle, the synthesis of *N*-oxides directly from dinitrogen would circumvent the energy-demanding ammonia formation by steam reformed hydrogen gas or *via* the nitrogenase enzyme and improve atom-economy significantly. Synthesis of NO from dinitrogen is particularly desirable, as it is the initial product of the Ostwald process and the further oxidation up to nitric acid for fertilizers is an already established process. Thus, it is worthwhile to examine the chemistry of the lower *N*-oxides in more detail.

Nitric oxide or nitrogen monoxide is the most simple, stable radical at room temperature and attracted scientists of various disciplines because of its complex reactivity pattern and widespread application potential. However, it took until 1998's Nobel prize for medicine and physiology awarded "*for their discoveries concerning nitric oxide as a signaling molecule in the cardiovascular system*" to R. F. Furchgott, L. J. Ignarro and F. Murad to raise attention for the inorganic radical to a broader audience. This bilateral character of NO, being a highly reactive radical gas on one hand, yet selective secondary messenger molecule under physiological conditions in the complex and essential cardiovascular system on the other hand, adequately frames the motivation behind nitric oxide based research.

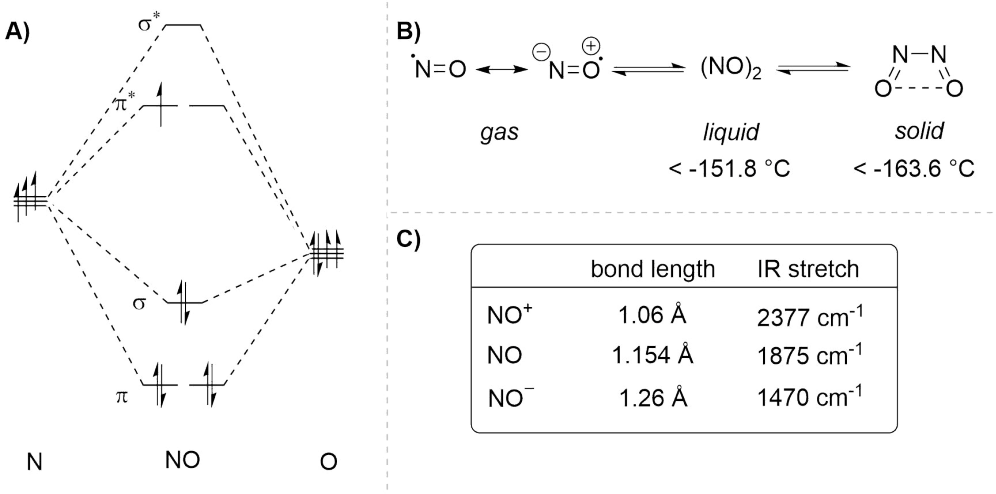

Figure 2.4: Frontier MO scheme (**A**) and properties (**B**) of nitric oxide, nitrosonium cation and nitroxyl anion (**C**).[274–278]

NO exhibits remarkable properties: At standard conditions it is a paramagnetic, monomeric gas, which gradually dimerizes upon temperature reduction to ultimately form *Z*-configured $(NO)_2$ dimers in the solid state below −163.6 °C (Figure 2.4B).[279,280] The reactivity of the $(NO)_2$ dimer in comparison to the parent monomer is dramatically changed, as it can act as an oxygen atom donor driven by the formation of the N-N double bond in N_2O, which itself can act as a potent OAT reagent.[281] This reactivity mode is also partially occurring in the nitric oxide reductase (NOR) enzymes, where dinuclear binding and dimerization of NO is assumed to be triggered by reduction, resulting in the formation of a hyponitrite ($N_2O_2^{2-}$) or ($N_2O_2^{\bullet-}$) intermediate.[282,283] Protonation by glutamic acid residues in proximity to the active center, and release of N_2O, as well as H_2O was concluded based on the X-ray crystallographic characterization of the NOR.[284] The overall reduction of nitric oxide to nitrous oxide proceeds

in biological systems as part of prokaryotic denitrification or as a detoxification mechanism.[5,285]

From simple molecular orbital considerations, the bond order between nitrogen and oxygen is 2.5, which correlates with its bond length (d_{NO} = 1.154 Å)[274] between N_2 and O_2.[286] The reactivity of NO is dominated by its π^*-SOMO, with spin density polarized towards the nitrogen atom (ca. 65%).[275,287] The π^*-orbital polarization is opposite to the π-orbital polarization, resulting in a rather unpolar molecule with a low intensity IR stretch (ν_{NO} = 1875 cm^{-1}).[286] Owing to the π^*-radical character, bonds with NO are formed from and to the nitrogen terminus and radical coupling is one of the main reaction motifs.[275]

The electronic structure of nitrosyl transition metal complexes is infamous for its complexity due to the redox-noninnocent character of nitric oxide as ligand. The NO ligand bonding interactions are in general described within the framework of a Dewar-Chatt-Duncanson bonding model,[288,289] which was initially used as description of metal-alkene complexes, but soon extended to other ligands exhibiting frontier orbitals of π-symmetry. Based on this, the interaction with the NO ligand is decomposed into two parts: A classical σ-bond from the NO to the metal and π-backdonation of filled d-orbitals into the π^*-orbitals of NO. Depending on the metal oxidation state and electron richness, the contribution of the π-interaction might vary. In general, NO is considered an exceptionally good π-acceptor ligand due to its capability of excessive π-backbonding and stabilization of low oxidation states. Increase of π-backbonding is accompanied by reduction of the N-O bond order from 3 in linearly coordinated NO, to 2 in bent NO (∢(M-N-O) = 120°), as consequence of electron density donation into the N-O π^*-orbitals.[286] The ambiguity of the NO coordination mode (NO^+, $NO^\bullet$ or NO^-) led to the introduction of the Enemark-Feltham nomenclature that is independent of oxidation states and emphasizes the amount of electrons in orbitals of π-symmetry within the MNO fragment.[107]

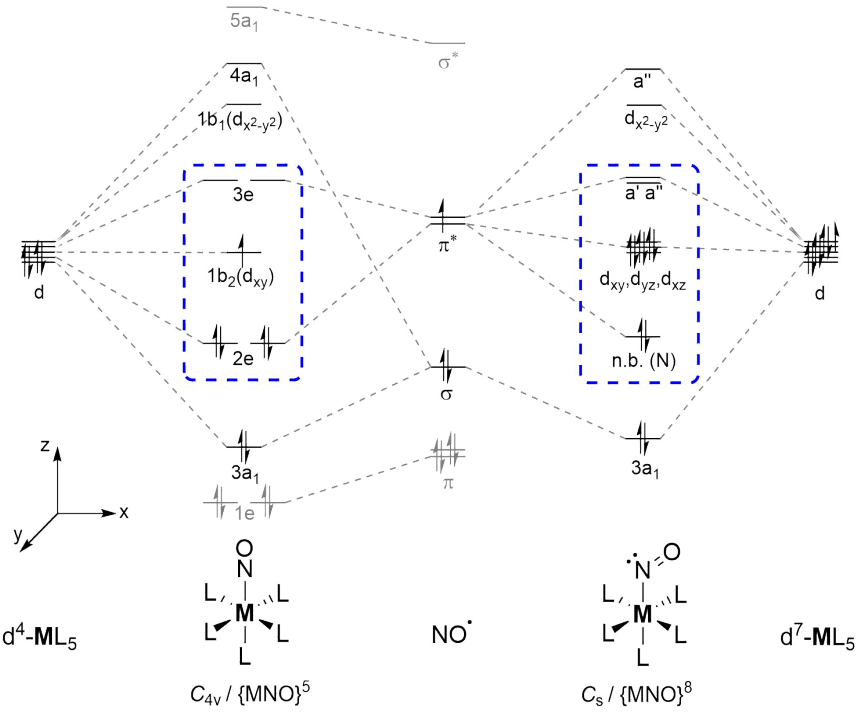

Figure 2.5: Simplified MO scheme for nitrosyl transition metal complexes of idealized C_{4v} (linear NO, left) and C_s (bent NO, right) symmetry according to *Enemark* and *Feltham*.[107,274] The FMO sets relevant for the Enemark-Feltham nomenclature $\{MNO\}^n$ are highlighted in blue boxes.

Enemark and *Feltham* collected valuable MO considerations with their seminal publication, to analyze the electronic structures of nitrosyl complexes of various geometries and electron counts.[107] For octahedral NO complexes of idealized C_{4v} symmetry the simplified MO scheme is shown in Figure 2.5, left.[107] The $3a_1$ orbital represents the σ-bond interaction and is mainly localized on nitrogen. The degenerate 2e orbitals evolve from the interaction of the NO π^*-orbitals and d-orbitals of matching symmetry (d_{xz},d_{yz}) and are M-N bonding and N-O antibonding in character (corresponds to π-backbonding, if the orbitals are filled). Changing the metal and/or the ancillary ligands can significantly change the electron distribution between M and NO in the 2e orbitals, as the π^*-NO orbitals are close in energy compared to the metal d-orbitals. Consequently, the π-backbonding interaction and the bond order of the nitrosyl ligand are especially sensitive to changes at the metal complex (c.f. $[Fe(CN)_5(NO)]^{2-}$, ν_{NO} = 1939 cm^{-1} vs. $[Mn(CN)_5(NO)]^{3-}$, ν_{NO} = 1700 cm^{-1})[107].

The $1b_2$ orbital is non-bonding (d_{xy}) and metal-centered, therefore its occupation should not significantly influence the MNO unit. The 3e orbitals are anti-bonding with respect to M-N and N-O and the $1b_1$ orbital is high in energy, yet non-bonding and metal-centered (d_x^2-$_y^2$). Important conclusions can be drawn from these MO considerations: The occupation (n = x + y + z) of the orbital set $(2e)^x(1b_2)^y(3e)^z$ states the amount of electrons in orbitals of π-

symmetry and allows for comparison of octahedral nitrosyl complexes in the Enemark-Feltham nomenclature $\{MNO\}^n$, independent of the charge on NO. Moreover, an upper limit (n = 6, filling the non-bonding $1b_2/d_{xy}$-orbital) without occupation of M-N antibonding orbitals (3e) is conceivable. Increasing the electron count beyond n = 6 would occupy the antibonding 3e orbitals in linear nitrosyl complexes. This unfavorable state is avoided by bending of the NO, which reduces the highest possible symmetry of octahedral nitrosyl complexes to C_s. Additionally, a non-bonding, nitrogen-centered orbital will be occupied by two electrons, resulting in a d^6 metal configuration for $\{MNO\}^8$ complexes, in which the NO can be seen as an NO^- ligand (Figure 2.5, right).[107]

An interesting example is the reaction of $[Mn(CO)_5]^-$ with NO^+, which yields the five-coordinate $[Mn(CO)_4(NO)]$. This can be explained with a six-coordinate intermediate, in which the energetic level of the $1b_1$ ($d_{x^2-y^2}$) is lower than the 3e orbitals and occupation of $1b_1$ ultimately leads to ligand labilization and substitution. One possibility to sustain a high electron count and a linear NO ligand is symmetry reduction (e.g. in C_{3v} symmetry (d_{xy}, $d_{x^2-y^2}$) or C_{2v} (d_{xy}, d_{z^2}) two metal-centered orbitals are of similar energy and consequently up to 8 electrons can occupy (non)bonding orbitals of the relevant orbital set).[107]

Not only the electronic structure of nitrosyl complexes is interesting, but also reactions of coordinated NO in transition metal complexes or free NO with TM complexes. The oxygen atom terminus in nitrosyl complexes is Lewis basic and can form adducts with suitable Lewis acids,[290–293] especially with electron-poor boranes. Borane adduct formation reduces electron density in the N-O unit and consequently increased π-backbonding, decreased IR stretch wavenumbers and bent nitrosyl bridges.[294–298] *Berke* and coworkers utilized the NO bending upon silylium cation coordination to improve catalyst efficiency in catalytic hydrosilylation and alkene hydrogenation.[298–300] Formation of an isonitrosyl ligand upon oxidation of $[HRe(NO)_2(PiPr_3)_2]$ with 0.5 equivalents of trityl cation was observed, in which the cationic "$[Re(NO)_2(PiPr_3)_2]$" fragment coordinates *via* the metal on the terminal oxygen atom.[301] Moreover, terminal and unusual side-on coordination at nitrosyl ligands has been crystallographically observed for sodium cations[302] and formation of a methoxyimido ligand upon methylation with a trimethyloxonium salt.[303] Interestingly, protonation was not only observed at the terminal oxygen atom, but also at the nitrogen, resulting in a formal "HNO" ligand (Scheme 2.5).[304]

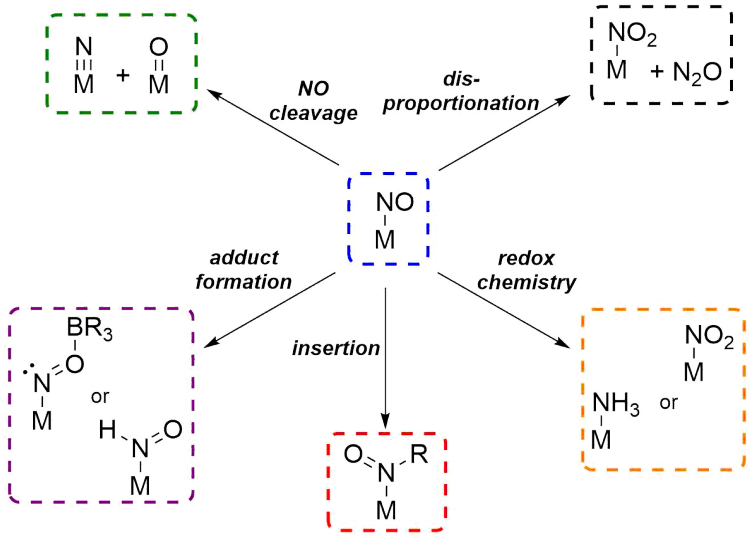

Scheme 2.5: Summary of reaction types of transition metal nitrosyl complexes.

Additionally, examples of nitrosyl ligand cleavage were reported. *Cummins* and coworkers reported the splitting of chromium nitrosyl complexes with the oxophilic reagent [V(Mes)$_3$(THF)] to generate nitride and oxo complexes, respectively.[305] Further examples of complete cleavage of the N-O bond involving Mo and W complexes have been reported.[306,307] *Sellmann* and coworkers reported on the reduction of a nitrosyl ligand to hydroxylamine at a Mo complex, which they were able to implement into a synthetic cycle.[308] Relatively few reports can be found for the insertion of NO into other bonds.[309] Reported are the migratory insertion of NO into the cobalt-carbon bond of [CpCo(NO)Me][310–314] and the chromium-carbon bond of [CpCr(NO)$_2$Me][315], leading in both cases to organic nitroxyl compounds reminiscent of ketones. Furthermore, insertion of NO into a coordinated allyl ligand[316] and intricate reactivity of an alkylidene with coordinated NO at a Rhenium complex center was described by *Berke* and coworkers.[317]

The nitrosyl ligand can be reduced or oxidized, which was used synthetically for its removal or substitution.[318] For example, electrochemical reduction of the cationic Osmium nitrosyl complex *cis*-[(tpy)OsCl$_2$(NO)]$^+$ in acidic media results in formation of the corresponding ammine complex.[265] Oxidation of the nitrosyl to nitro or nitrate ligands has been studied more comprehensively,[319–324] yet the prerequisites for an oxidizable nitrosyl ligand are not well-understood. Finally, NO disproportionation to N_2O and NO_2 is commonly observed for copper complexes, which mimic the presumed reaction mechanism at the active center of the nitric oxide reductase.[5,325,326] Recent reports described the release of N_2O from NO upon deoxygenative coupling at dinitrosyl iron complexes with oxophilic rare-earth metal

complexes[327] and polarization of a cobalt porphyrin nitrosyl complex dimer by hydrogen bonding.[328]

In contrast to the vast variety of coordination chemistry of nitric oxide, is the chemistry of nitrous oxide rather underdeveloped. Nitrous oxide is the nitrogen oxide with formally the lowest oxidation state and an intermediate in the denitrification process, as well as a product of several biological processes, like detoxification *via* the nitric oxide reductase enzyme family or imcomplete nitrification under low O_2 conditions.[5] Consequently, natural sources contribute significantly to overall N_2O emissions, which are concerning as N_2O has approximately 300 times the global warming potential of CO_2.[329] Furthermore, it could be shown that terrestrial N_2O emissions have almost doubled from preindustrial levels until 2010 (from ca. 7 Tg N yr^{-1} to ca. 13 Tg N yr^{-1}), with anthropogenic fertilizer usage and livestock production as main driving forces.[330] Industrial production of N_2O gas involves the controlled decomposition of NH_4NO_3, which requires initial nitrate synthesis.[331] The chemistry of nitrous oxide is dominated by its ability to act as an oxygen atom donor, driven by the thermodynamically favorable formation of the strong triple bond in dinitrogen.[332] This reactivity is especially pronounced for early-transition metal complexes which concomitantly form especially stable oxo complexes.[163,333–335] Less pronounced is the tendency of N_2O to react upon N-N bond cleavage.[336,337] Interestingly, *Severin* and coworkers have shown that N_2O can form covalent bonds with organic carbenes, resulting in the synthesis of solid, isolable compounds, which itself can act as oxygen atom donors.[338,339]

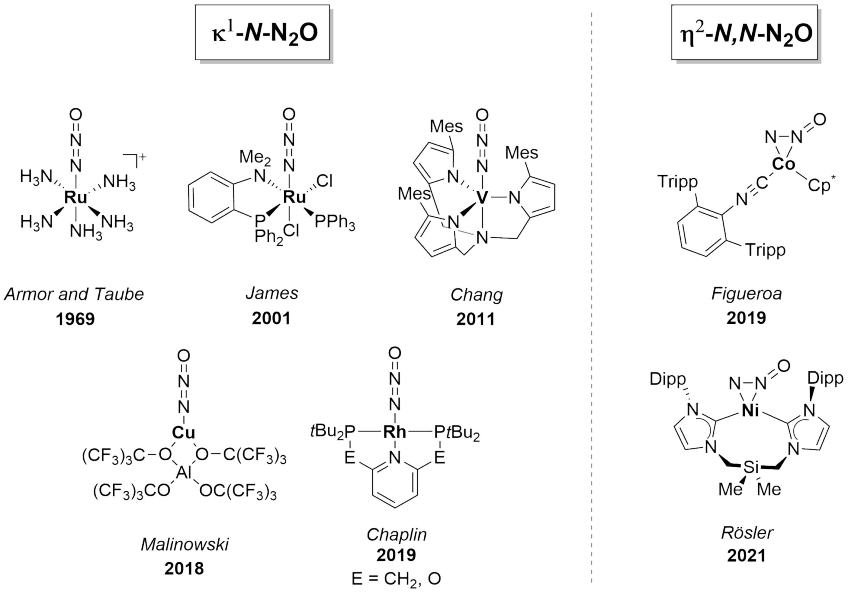

Figure 2.6: Summary of reported N_2O transition metal complexes.

Capture and selective decomposition of N_2O or usage as oxidant are highly desirable, given its detrimental effects on climate and global fixed nitrogen budgets.[1] Biological decomposition of N_2O happens with the aid of the nitrous oxide reductase (N_2OR) enzyme, which deoxygenates N_2O upon release of N_2 and leads to formation of dinuclear copper oxo bridges.[340] Two main obstacles prevent the development of efficient N_2O decomposition. On the one hand, decomposition into N_2 and O_2 has a high activation barrier (ca. 59 kcal·mol^{-1})[341] and on the other hand, N_2O is a very poor σ-donor and π-acceptor, complicating its binding to transition metals to study and develop efficient small molecule activation.[342] Consequently, transition metal N_2O complexes are rare. The first example was reported by *Armor* and *Taube* (Figure 2.6), with the thermally unstable $[Ru(NH_3)_5(N_2O)]^+$ complex, which could not be isolated. However, the κ^1-*N* coordination mode of N_2O was implied from spectroscopic measurements and computations.[343,344] Since then, N_2O complexes exhibiting the same κ^1-*N* coordination mode have been isolated and characterized for V,[345] Ru[346], Rh[347] and Cu[348]. Recently, *Figueroa* and coworkers extended the coordination modes for nitrous oxide with the isolation and characterization of a side-on η^2-*N*,*N*-N_2O cobalt complex.[341] Furthermore, *Rösler* and coworkers reported a nickel complex based on this coordination mode of N_2O.[349] Nevertheless, all these complexes are relatively labile, highlighting the weak binding of a neutral N_2O ligand.

Reactivity of nitric oxide and nitrous oxide with transition metal nitrides is connecting the two *N*-oxides with (potential) dinitrogen splitting. The electrophilic Os nitride complex **XXXII** showed facile nitride transfer to NO, resulting in the formation of nitrous oxide and an Osmium nitrosyl complex (c.f. Scheme 2.4).[257] Substitution of chloride to phenyl in **XXXIII** on the other hand resulted in no appreciable reactivity towards NO, indicating that the electrophilic and oxidizing character of **XXXII** is relevant for nitride transfer reactivity. *Caulton* and coworkers reported comparable nitride transfer reactivity of a square-planar d^4 Ruthenium nitride complex (**XXXIV**) and the concomitant formation of nitrous oxide.[350] Curiously, **XXXIV** also reacted with N_2O upon oxygen atom transfer to form the corresponding nitrosyl complex. For both reactions a mechanism that includes initial ligand binding and then intramolecular oxygen transfer (for the N_2O reaction) or attack of a second NO equivalent to the nitride (for the NO reaction) was predicted by DFT calculations, forming the same Ruthenium nitrosyl complex (Scheme 2.6). Notably, *Cummins* and coworkers reported a

remarkable example of the selective N-N bond cleavage of N_2O to molybdenum nitride and nitrosyl complexes,[336] which formally is the microscopic reverse reaction of the nitride transfer to NO.

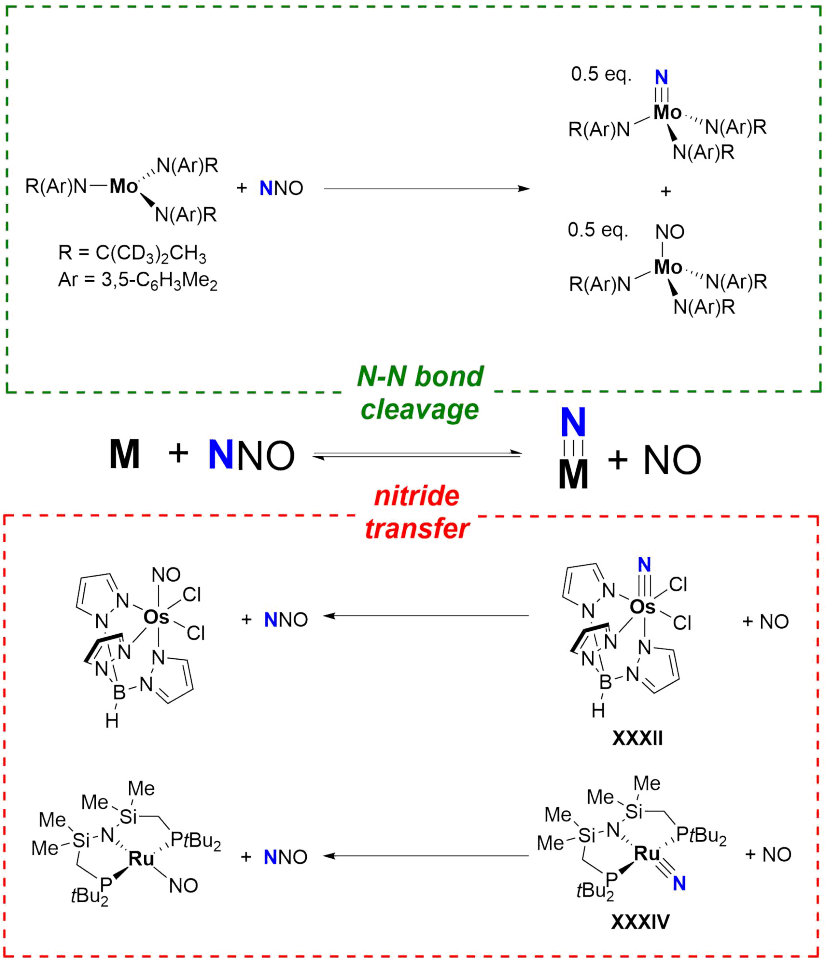

Scheme 2.6: N-N bond cleavage of N_2O and nitride transfer to NO as mutual microscopic reverse reactions, as well as selected literature examples of both reaction types.

The facile formation of a nucleophilic nitride could indicate that metal complexes which form stable, nucleophilic nitrides rather react with N_2O (under consideration of possible side reactions like oxygen atom transfer), whereas reactive, electrophilic nitride complexes rather react upon nitride transfer to NO. *Mayer* and coworkers rationalized this reversal of reactivity as a consequence of the relative thermodynamic stability of the metal-nitride bonds.[257] The estimated upper limit of the Os≡N bond strength in $[TpOs(N)Cl_2]$, derived from a thermochemical cycle, is < 135 kcal·mol^{-1}, which is substantially lower than the Mo≡N bond obtained upon N_2O activation (155.3 ± 3.3 kcal·mol^{-1}). This appears to be part of the reason, why the equilibrium of the main reaction in Scheme 2.6 lies on the side of the starting materials for electrophilic osmium nitrides and on the product side for nucleophilic molybdenum nitrides.

2.3 Motivation and Scope

In this part, the reactivity of the dinitrogen-derived Re^{V} nitride complex [(^{Ph}PNP)Re(N)Cl] will be examined extensively. Particular focus will be layed on the extension of the common reactivity of nucleophilic Re^{V} nitride complexes towards new reagents and modification of the system to influence its reactivity.

Formation of nitrogenous products as a result of homogeneous dinitrogen splitting is often hampered by overstabilization of the nitride reaction products as part of the required driving force to split dinitrogen. The examples of successful dinitrogen-derived nitride functionalization rely predominantly on early-to-mid transition metal complexes. The resulting nitride complexes are nucleophilic and consequently dinitrogen-derived nitride functionalization is restricted to reactions with electrophiles of early-to-mid main group elements (e.g. adduct formation with electron-poor boranes). Reactions of nucleophilic Mo or Re nitrides with main-group element reagents beyond group 14 are exceedingly rare (nitride coupling to dinitrogen is a notable exception) and demand "umpolung" strategies to enhance the reactivity / electrophilicity of the nitride moiety, due to the high reactivity and lack of stable group 15 or 16 electrophiles.

Ultimately, syntheses of *N*-oxides like NO_3^- from dinitrogen-derived nitrides would circumvent the energy-demanding initial Haber-Bosch process and the need for dihydrogen gas, which is wastefully lost as H_2O in the subsequent Ostwald process. Unfortunately, oxygenation of dinitrogen-derived Mo or Re nitrides has not been reported yet, due to the lack of a sufficiently reactive nitride complex of suitable philicity for common oxygen atom transfer (OAT) reagents.

In the previous part, the synthesis of Re^{V} nitride [(^{Ph}PNP)Re(N)X] (X = Cl, I) upon (electro)chemical dinitrogen splitting in high yields was reported. In the following part, the **philicity of the nitride will be examined** upon reactions with various reagents. The **chemical robustness** of the pincer ligand backbone will be demonstrated **with selective reactions towards highly reactive group 16 electrophiles**. Moreover, the **accessibility of nitrogen oxides** will be probed by **reaction with OAT reagents**, culminating in extensive experimental and computational investigations regarding the **nitride transfer to nitric oxide**, which is a reaction type that was exclusively observed for electrophilic Ru and Os nitride complexes not derived from N_2 splitting.

2.4 Reactivity of Re^{V} and Re^{VI} Nitride Complexes [(^{Ph}PNP)Re(N)Cl]$^{0/+}$

Parts of the research presented in this chapter have been published in: "Rhenium-mediated Conversion of Dinitrogen and Nitric Oxide to Nitrous Oxide", L. Alig, K. A. Eisenlohr, Y. Zelenkova, S. Rosendahl, R. Herbst-Irmer, S. Demeshko, M. C. Holthausen, S. Schneider, *Angew. Chem. Int. Ed.* **2022**, *61*, e202112597.

2.4.1 Properties and Oxidation of [(^{Ph}PNP)Re(N)Cl]

The synthesis of [(^{Ph}PNP)Re(N)Cl] (**15**) by dinitrogen splitting with sodium amalgam and, alternatively, by a reduction-azide sequence was described in chapter 1.5.3. **15** exhibits typical spectroscopic characteristics of Re^{V} nitride pincer complexes, e.g. it is a diamagnetic complex of d^2 electronic configuration with a large calculated singlet-triplet gap (42.1 kcal·mol^{-1}, PBE/def2-TZVP). *Mayer* and coworkers correlated electrochemical properties of isoelectronic Re^{V}- and Os^{VI} with the electron-richness of the complex of interest.[213] Particularly the d^2/d^1 redox couple potentials showed a good correlation with Hammett parameters, albeit only three data points were collected. In the CV (Figure 2.7), **15** features a fully reversible oxidation at the mild potential of $E_{1/2}$ = +0.03 V, as well as an irreversible second oxidation at E_{pc} = +0.81 V (both potentials vs. $Fc^{+/0}$). Furthermore, an irreversible reduction at the very negative potential of E_{pc} = –3.12 V was observed.

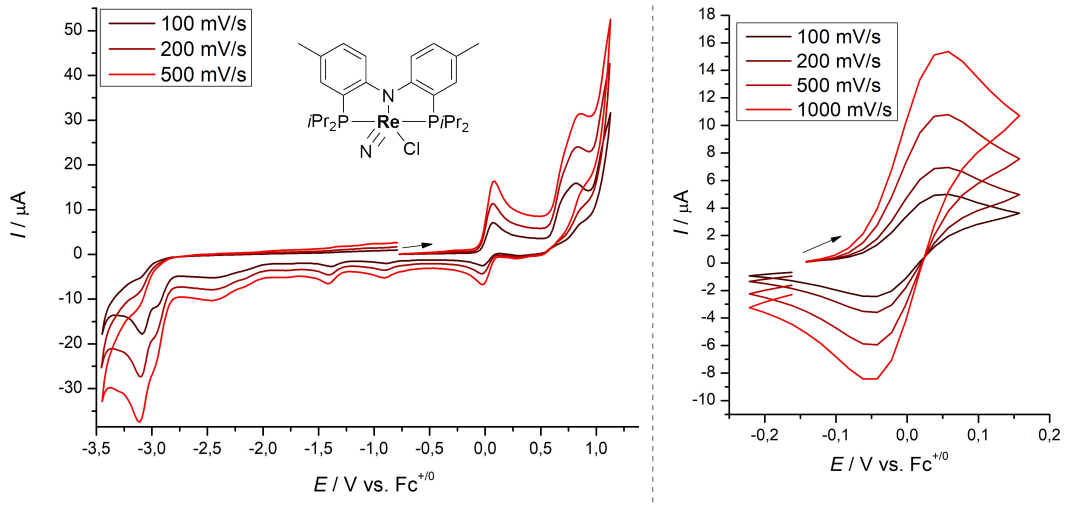

Figure 2.7: Left: Cyclic voltammogram of **15** (2 mM **15**, THF, Ar, 0.2 M nBu$_4$NPF$_6$). Right: Scan-rate dependent measurement of the oxidative wave at $E_{1/2}$ = +0.03 V.

Reactivity of the nitride moiety with nucleophiles is mainly influenced by the energetic location and character of the π^*-orbitals of the Re≡N triple bond. The electrochemical data suggest that

15 is relatively electron-rich and hence nucleophilic reactivity with suitable electrophiles is expected. The reversible oxidation in the CV of **15** indicates, that a Re^{VI} complex is accessible with one-electron outer-sphere oxidants. As expected, addition of 1.0 eq. [AcFc][X] ([X] = [BF_4], [$Al(OC(CF_3)_3)_4$]) to a solution of **15** in CH_2Cl_2 at –40 °C led to a rapid color change from bright orange to intense cherry-red. Investigation of the resultant reaction mixture by ^{1}H NMR spectroscopy revealed that the starting material resonances had vanished and no new signals were formed. Single-crystals suitable for X-ray crystallography were grown from dichloromethane/pentane by gas-phase diffusion and confirmed the oxidation of **15** to [(^{Ph}PNP)Re(N)Cl][BF_4] (**20^{BF4}**, Figure 2.8).

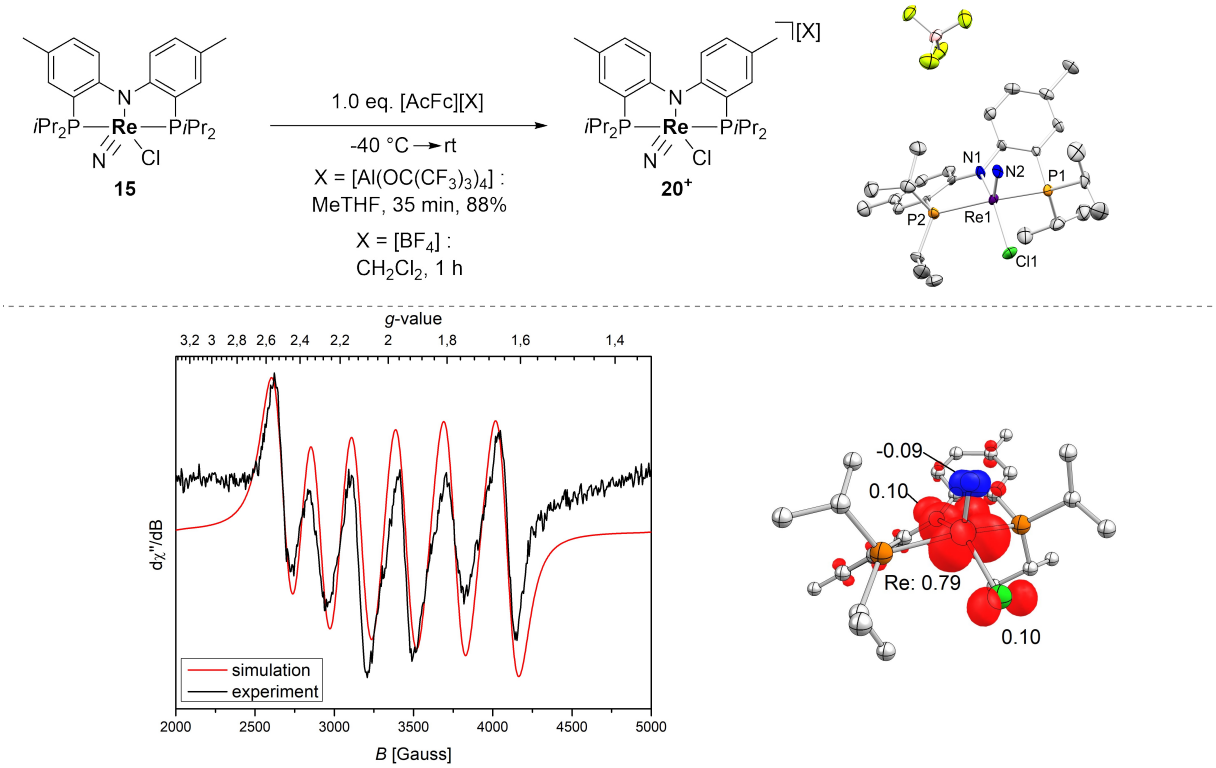

Figure 2.8: Top left: Oxidation of Re^{V} nitride **15** with outer-sphere oxidant [AcFc][X] (X = BF_4, [$Al(OC(CF_3)_3)_4$]) to form Re^{VI} complex **20**$^+$. Top right: Molecular structure of **20^{BF4}** from single-crystal X-ray diffraction (thermal ellipsoids drawn at the 50% probability level); Hydrogen atoms are omitted for clarity. Selected bond lengths [Å] and angles [°]: Re1-N2 1.648(8), Re1-N1 2.016(7), Re1-P1 2.478(2), Re1-P2 2.465(2), Re1-Cl1 2.332(2), P2-Re1-P1 149.97(7), Cl1-Re1-N1 145.4(2), N2-Re1-N1 106.9(4), N2-Re1-Cl1 107.3(3); τ^5 = 0.08. Bottom left: X-band EPR spectrum (black trace) and simulation (red trace) of crystalline **20^{BF4}** in CH_2Cl_2 at room temperature. The initial simulation was performed by *Prof. Dr. Joshua Telser*, which was afterwards slightly modified and resimulated. Final simulation and technical parameters: g_{iso} = 1.97, A_{iso}(Re) = 780 MHz, Gaussian broadening: 95 MHz, Lorentzian broadening: 95 MHz, microwave frequency: 9.413 GHz, microwave power: 9.882 mW, modulation frequency: 100 kHz, modulation amplitude: 4.00 G, conversion time: 327.68 ms, time constant: 81.92 ms. Bottom right: Spin density plot of **20**$^+$. The red isosurface indicates excess α spin density and the blue isosurface indicates excess β spin density.

In the solid-state structure **20**$^+$ adopts a slightly distorted square-pyramidal coordination geometry with a Re≡N bond length of d_{ReN} = 1.648(8) Å and no close contacts between the BF_4 counterion and hydrogen atoms of the pincer ligand were observed (Figure 2.8). Interestingly,

the Re≡N bond is barely affected by oxidation, but the coordination geometry is quite significantly changed towards a square-pyramid (τ^5(**15**) = 0.36 / τ^5(**20**$^+$) = 0.08). The X-band EPR spectrum of crystalline **20**$^{\mathbf{BF4}}$ dissolved in CH_2Cl_2 at room temperature (Figure 2.8, bottom left) shows a distinct six-line pattern, typical for EPR spectra of Rhenium compounds (I($^{185/187}$Re) = 5/2). The isotropic signal (g_{iso} = 1.97) exhibits a hyperfine interaction of A_{Re} = 780 MHz, which indicates a large contribution of metal-centered spin density. In agreement with that, DFT calculations (PBE0/SARC-Zora-TZVP;def2-SVP) also predict a major contribution of Rhenium-centered α spin density (77%), with a minor contribution from the pincer ligand nitrogen atom (11%) and excess β spin density (9%) due to spin polarization on the nitride nitrogen atom. This can be rationalized with the MO considerations for TM nitrides (c.f. Figure 2.1), which support the SOMO of d^1 nitrides to be the metal-centered, non-bonding d_{xy} orbital, orthogonal to the Re≡N bond.

Encouraged by the facile synthetic access to the Re^{VI} nitride complex [(^{Ph}PNP)Re(N)Cl]$^+$ (**20**$^+$) and literature precedent of ambiphilic reactivity of a Re^{VI} P^{O}NP pincer complex[202], the functionalization and particularly the oxygenation of **20**$^+$ to a nitrosyl/nitro/nitrate complex would represent the entry into oxidative dinitrogen functionalization.[207] Problematic for the functionalization of **20**$^+$ is its susceptibility to reduction. This is particularly an obstacle when reactivity with nucleophiles, which intrinsically are electron-rich and potential reductants, was examined. Evidently, reduction is one of the main problems for the functionalization of the related Re^{VI} nitride *cis*-[($^{i\text{Pr}}$P^{H}NP)Re(N)Cl$_2$][BF$_4$][158] which exhibits a very similar $Re^{VI/V}$ redox couple potential ($E_{1/2}$ = +0.07 V) compared to **15**/**20**$^+$ ($E_{1/2}$ = +0.03 V). However, unlike *cis*-[($^{i\text{Pr}}$P^{H}NP)Re(N)Cl$_2$][BF$_4$], **20**$^+$ is not susceptible to pincer deprotonation and should, in combination with the chemically more robust pincer backbone, lead to more selective transformations.

20$^+$ was reacted with common nucleophiles like morpholine, PhMgBr, diphenylamine and IMes-N_2O, but these reactions resulted in mixtures of compounds, with the Re^{V} nitride **15** as the main product. This resembles the susceptibility to reduction observed in the case of Re^{VI} nitride *cis*-[($^{i\text{Pr}}$P^{H}NP)Re(N)Cl$_2$][BF$_4$]. Furthermore, reactivity towards oxygen atom transfer reagents like Me_3NO, *m*CPBA, pyridine-*N*-oxide, TEMPO or Ag_2O was examined. In none of the investigated reactions an IR stretch in the characteristic region for nitrosyl bands was observed, but rather unselective decomposition to many products, as judged by $^{31}P\{^1H\}$ NMR spectroscopy. Finally, the reactivity of **20**$^+$ towards strong-field ligands was tested by *Leonard*

Hartung (Master thesis, University of Göttingen).[351] The reaction with PMe_3 was unselective according to $^{31}P\{^{1}H\}$ NMR spectroscopy, resulting in numerous resonances. The reactions of **20**$^{+}$ with CO (ν = 2020 cm^{-1}) and *t*BuNC (ν = 2200 cm^{-1}) showed characteristic stretches in the IR spectra, suggesting the formation of simple coordination adducts with **20**$^{+}$.

The results of the electronic structure examination by EPR spectroscopy and DFT calculations, as well as reactivity studies, revealed the following information of the reactivity of Re^{VI} nitride **20**$^{+}$:

1. The spin density is, according to the EPR parameters and MO considerations, mainly located in the Re centered d_{xy} orbital.

2. No selective reactivity of [(^{Ph}PNP)Re(N)Cl]$^{+}$ (**20**$^{+}$) towards various reagents like CO, amines and Me_3NO or other oxygen atom donors was observed. Instead, reduction to Re^{V} nitride [(^{Ph}PNP)Re(N)Cl] (**15**) was frequently encountered.

In the following chapters, functionalization attempts starting from the parent Re^{V} nitride **15** will be discussed in more detail.

2.4.2 Reactivity of [(^{Ph}PNP)Re(N)Cl] towards H-, B- and C-Electrophiles

The synthesis (chapter 1.5.3) and oxidation (chapter 2.4.1) of Re^{V} nitride complex [(^{Ph}PNP)Re(N)Cl] (**15**) were described previously. Ammonia formation, which recently was reported from the Re^{V} nitride complex *cis*-[(PONOP)Re(N)Cl_2],[201] as well as a Re^{I}/Re^{I} dinuclear dinitrogen-bridging complex[144] with PCET reagents was examined for the [(^{Ph}PNP)Re(N)Cl] (**15**) system. Addition of 10 eq. SmI_2 and 100 eq. H_2O to a solution of **15** in THF furnished ammonium after acidic workup. NMR spectroscopic quantification with an internal standard resulted in 13.5% ammonium yield. This yield is considerably lower compared to the *cis*-[(PONOP)Re(N)Cl_2] complex (74%) and the dinuclear Re^{I}/Re^{I} complex (catalytic, 8.4 eq. NH_3, $HPCy_3[BArF_{24}]$). However, it has to be noted that the SmI_2/H_2O reaction with **15** was only conducted once and PCET reactions are highly sensitive to the nature of the proton source and reductant. The ammonium yield with other reagent combinations might therefore be higher.

Similar to other nucleophilic Re^{V} nitride complexes, **15** can bind Lewis acids *via* the nitride nitrogen atom. Addition of the electron-poor borane $B(C_6H_3(CF_3)_2)_3$ ($BArF_{18}$) to a solution of **15** in C_6D_6 caused only an insignificant color change and $^{31}P\{^{1}H\}$ NMR spectroscopy revealed a spectrum of higher order, with two doublets representing the major species (Figure 2.9), presumably due to conformational isomerism. Magnetically inequivalent ^{31}P nuclei of complexes with the ^{Ph}PNP ligand were observed by *Ozerov* and coworkers for the Re^{V} oxo complex *cis*-[(^{Ph}PNP)Re(O)Cl_2],[352] resulting in two broadened doublets as well. Single-crystals suitable for X-ray crystallography were grown from fluorobenzene / pentane at –40 °C over night. In agreement with the assumption of a Lewis-basic, nucleophilic nitride nitrogen atom, **21** exhibits an N-B bond (d_{NB} = 1.593(8) Å) to $BArF_{18}$ and the coordination geometry is slightly more pyramidalized compared to **15** (τ^5(**21**) = 0.27, c.f. τ^5(**15**) = 0.36). The Re-$N_{nitride}$ bond length is furthermore slightly prolonged upon borane coordination (d_{ReN}(**21**) = 1.680 Å vs. 1.645 Å in **15**).

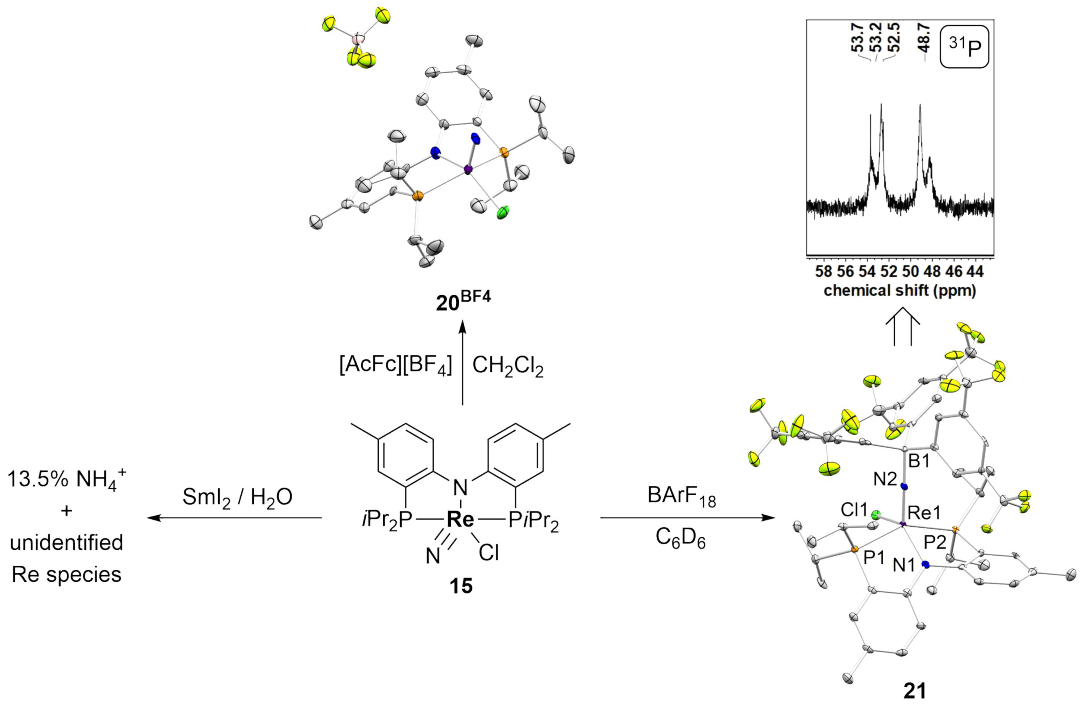

Figure 2.9: Summary of the reactivity of Re^{V} nitride **15** upon oxidation (top), N-H- (left) and N-B bond (right) formation. Molecular structure of **21** from single-crystal X-ray diffraction (thermal ellipsoids drawn at the 50% probability level); hydrogen atoms are omitted for clarity. Selected bond lengths [Å] and angles [°]: Re1-N1 2.024(4), Re1-N2 1.680(5), N2-B1 1.593(8), Re1-Cl1 2.3619(14), N1-Re1-Cl1 134.79(13), P1-Re1-P2 150.90(5), N1-Re1-N2 118.45(19), Re1-N2-B1 175.1(4); τ^5 = 0.27.

No reactivity was observed upon addition of diphenyl ammonium triflate to **15**. Hence, the stronger acid $[H(OEt_2)_2][BArF_{24}]$ was tested. Vacuum transfer of CD_2Cl_2 to the solid starting materials and subsequent thawing to –60 °C resulted in a cherry-red homogeneous solution.

NMR spectra recorded at −60 °C indicated the vanishing of the ^{31}P resonance of **15** and the appearance of several broad signals. In the ^{1}H NMR spectrum, very broad signals among the relatively sharp resonances for the $BArF_{24}$ anion and diethylether were observed. Unfortunately, warming to room temperature led to quick decomposition and appearance of numerous resonances in the ^{31}P spectrum. Thus, it remains unclear, whether or not this temperature-sensitive species might be a parent imido complex or originated from protonation of the pincer ligand nitrogen atom.

Organic triflates were previously shown to be sufficiently electrophilic to overcome the inherent stability of nitride complexes.[145,146] Reactivity of **15** with EtOTf in C_6D_6 was observed upon prolonged heating. A species with two inequivalent phosphorus atoms (as judged by ^{31}P{^{1}H} NMR) was obtained, which – according to mass spectrometry – is the addition of an ethyl-fragment to **15** (see experimental appendix). Unfortunately, despite numerous attempts, no species could be isolated from the reaction mixtures. **15** furthermore reacted with CO (reaction first conducted by *Leonard Hartung*)[351] to form a terminally coordinated, diamagnetic carbonyl complex, as evident from ^{31}P{^{1}H} NMR (δ_{31P} = 48.5 ppm) and IR (ATR, ν = 2016 cm^{-1}) spectroscopies. This complex, which presumably is [(^{Ph}PNP)Re(N)(CO)Cl], appeared to be stable even upon prolonged heating and no isocyanate formation was observed. No further structural information could be obtained (More detailed spectroscopic information on the reactions of **15** with EtOTf and CO can be found in the experimental appendix).

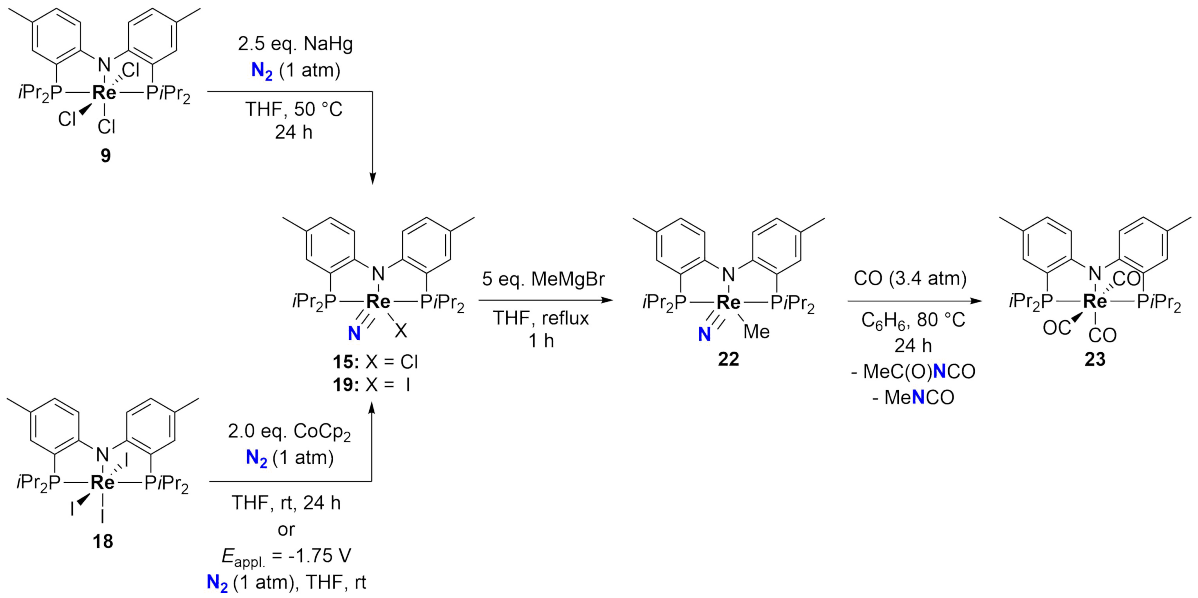

Scheme 2.7: Sequence of (electro)chemical dinitrogen splitting to form Re^{V} nitride complexes **15** and **19** and subsequent halide-to-methyl exchange and N-C bond formation to obtain Re^{I} tricarbonyl complex **23** and organic isocyanates as byproducts. The reactions from **15** to **22** and from **22** to **23** were previously reported by *Ison* and coworkers.[199]

Additionally, *Ison* and coworkers reported N-C bond formation starting from chloride-to-methyl exchange with methylmagnesium bromide and subsequent addition of carbon monoxide.[199] The reaction with CO proceeded upon elimination of acetyl isocyanate or methyl isocyanate (Scheme 2.7). Hence, it is possible to synthesize organic isocyanates from N_2, CO and Grignard reagent based on the results described in chapter 1.5.3 and chapter 1.5.4. The main problem of this synthetic pathway is that three carbonyl ligands are introduced in the product complex [(^{Ph}PNP)Re(CO)$_3$] (**23**) as a consequence of the high CO pressure required. This results in significant stabilization of the complex as a thermodynamic sink (also reflected in the DFT calculations by *Ison* and coworkers)[168] which is atom ineconomic and inhibits closure of a chemical cycle.

In a similar example on the "[($^{t Bu}$PNP)W]" complex platform, carbonyl ligands were introduced for photolytic N_2 cleavage and more CO was required to form an isocyanate ligand from the dinitrogen-derived nitride.[353] Substitution of the NCO and CO ligands for chloride was the synthetic bottleneck (30% yield) and complicated the overall synthetic cycle significantly (7 steps). It would therefore be highly desirable to simplify the synthetic cycle of cyanate formation from N_2 by using a CO transfer reagent that is capable of transferring selectively one equivalent of CO to prevent occupation of free coordination sites.

Acid chlorides like benzoyl chloride were shown to react with nucleophilic rhenium nitrides upon N-C bond formation.[200] Addition of one equivalent of benzoyl chloride to nitride **15** in C_6D_6, however, resulted in no appreciable change in the $^{31}P\{^1H\}$ and ^1H NMR spectra, even upon heating to 80 °C for prolonged periods (<5% conversion). To promote reactivity, more electrophilic acid chlorides were subsequently envisioned to react with **15**. The more reactive oxalyl chloride is mostly used in Swern oxidations, where it is electrophilic enough to react with weakly nucleophilic DMSO to form a sulfonium ion intermediate.[354] More recently it has gained considerable attention as selective carbon monoxide synthon and source.[355,356] In fact, addition of 0.5 equivalents of oxalyl chloride to a stirring solution of nitride **15** in toluene at −80 °C resulted in a slow but significant darkening of the solution. After stirring the solution for additional 2 hours at room temperature and workup, dark violet crystals suitable for X-ray crystallography were obtained from slow diffusion of pentane into a saturated benzene solution. The solid state structure (Figure 2.10) revealed the formation of Re^{IV} isocyanate complex *cis*-[(^{Ph}PNP)Re(NCO)Cl$_2$] (*cis*-**24**), with an essentially linear NCO moiety (176.2°).

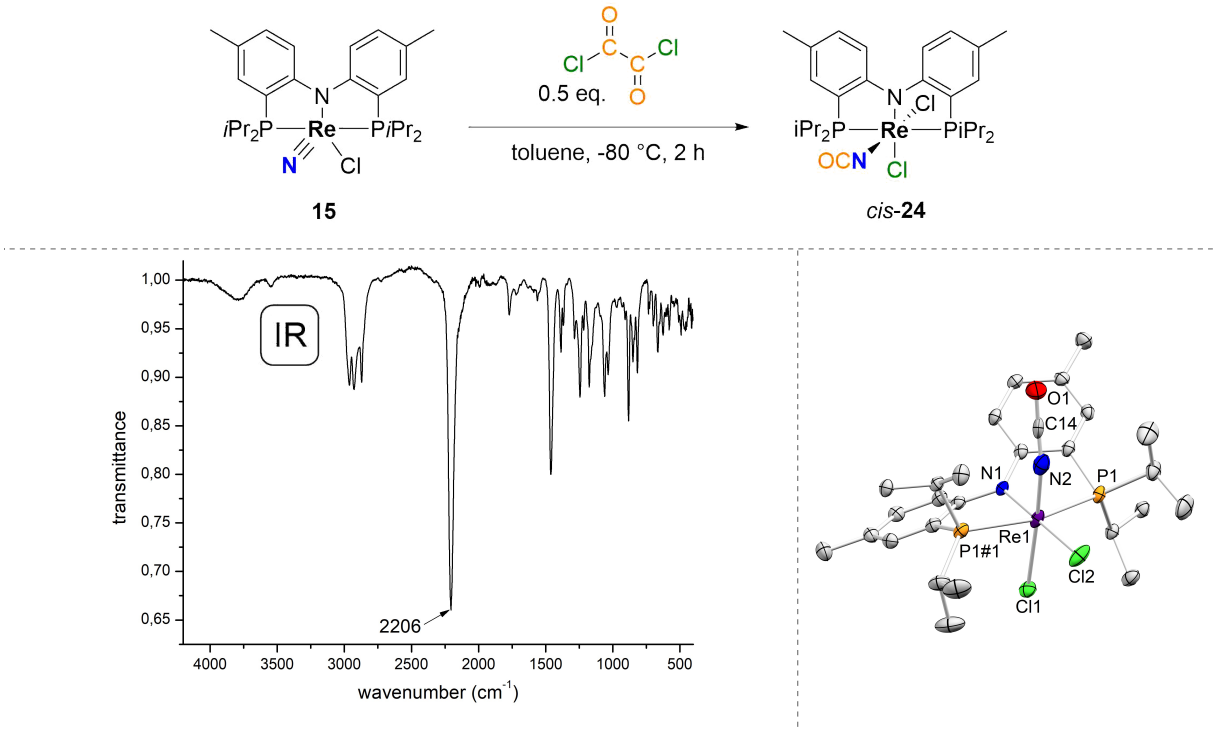

Figure 2.10: Top: Reaction of dinitrogen-derived nitride complex **15** with 0.5 eq. of oxalyl chloride to form the Re^{IV} isocyanate complex *cis*-**24**. Bottom left: ATR-IR of crystalline *cis*-**24**. Bottom right: Molecular structure of *cis*-**24** from single-crystal X-ray diffraction (thermal ellipsoids drawn at the 50% probability level); Hydrogen atoms are omitted for clarity. Selected bond lengths [Å] and angles [°]: Re1-N2 1.891(9), Re1-N1 1.981(3), Re1-Cl1 2.4353(2), Re1-Cl2: 2.3941(11), N2-C14: 1.162(11), C14-O1: 1.228(11), Re1-N2-C14: 166.4(12), N2-C14-O1: 176.2(13), N2-Re1-Cl1 89.6(4).

In this context it has to be mentioned that solely based on the crystal structure no distinction between an isocyanate or a cyanate complex can be made. However, preliminary DFT calculations (PBE0/def2-TZVP;SVP) predict a much narrower Re-O-C (for the cyanate ligand) angle ($\sphericalangle_{DFT}$ = 140.1°), than the Re-N-C angle (for *cis*-**24**, $\sphericalangle_{DFT}$ = 170.4°), which is significantly closer to the experimentally derived angle ($\sphericalangle_{exp.}$ = 166.4°). Therefore *cis*-**24** is described hereafter as an isocyanate complex.

cis-**24** shows similar NMR spectroscopic properties compared to trichloride [(^{Ph}PNP)$ReCl_3$] (**9**), for example, broadened, yet relatively sharp signals with no resolved *J*-coupling are observed. The very intense IR stretch at ν = 2206 cm^{-1} is characteristic for the formation of an isocyanate ligand and was reasonably well reproduced by DFT ($\nu_{NCO,DFT}$(*cis*-**24**) = 2245 cm^{-1}, BP86/def2-QZVP;SVP).

The formation of *cis*-**24** is interesting for several reasons: 1) Formation of isocyanates from dinitrogen-derived nitrides is still a rare reaction,[353] yet isocyanates are industrially relevant products. 2) Oxalyl chloride does not only act as a carbon monoxide synthon, but also provides a chlorine atom equivalent, resulting in an atom economic transformation. 3) Formation of

coordinatively saturated *cis*-**24** prevents carbon monoxide binding, which greatly facilitates any potential synthetic cycle involving this reaction. 4) Isocyanate is considered a pseudohalide, therefore *cis*-**24** is not only similar to the starting complex for dinitrogen splitting $[(^{Ph}PNP)ReCl_3]$ (**9**) in terms of oxidation state, but also similar reactivity (for example facile (pseudo)halide substitution) is expected from both complexes. This would reduce the chemical cycle for dinitrogen to (iso)cyanate formation to 2-3 steps (depending on whether isocyanate to chloride exchange is necessary or if dinitrogen splitting is possible from *cis*-**24** as well).

Some valuable, general information for functionalization of the nitride **15** could be derived from the reaction with oxalyl chloride. Apparently it is necessary or at least beneficial to provide a sixth ligand that coordinatively stabilizes a five-coordinate intermediate in the process of nitride functionalization. In the reaction with oxalyl chloride, these are chlorine atoms and in the case of the reported reaction by *Ison* and coworkers to organic isocyanates, carbon monoxide is employed to coordinatively saturate and therefore stabilize the reaction product.[199] Furthermore, it could be shown by independent reaction of nitride **15** with CO, which did not result in formation of the NCO ligand, that the barrier for direct CO addition to the nitride is too high. Initial nucleophilic attack of the nitride at one of the electrophilic carbon atoms in oxalyl chloride is presumably the first step, followed by chlorine atom transfer. The concept of enabling or facilitating reactivity by substituting the actual reagent with a synthon that exhibits enhanced reactivity might be utilized in future nitride functionalizations to transfer other groups to the relatively inert nitrides.

As mentioned, the formation of Re^{IV} complex *cis*-**24** upon functionalization of Re^{V} nitride **15** is the precursor to closing a chemical cycle including dinitrogen splitting and functionalization with oxalyl chloride (Figure 2.11, left). Either direct splitting of dinitrogen from *cis*-**24** or exchange of isocyanate with chloride could theoretically regenerate trichloride **9**.

Electrochemical examination of *cis*-**24** by cyclic voltammetry under argon atmosphere revealed a reversible first reduction at $E_{1/2}$ = –0.87 V and an irreversible second reduction at E_{pc} = –2.35 V (Figure 2.11, right), which is 80 mV and 50 mV anodically shifted compared to trichloride **9** ($E_{1/2}$ = –0.95 V and E_{pc} = –2.40 V). Consequently, dinitrogen splitting using sodium amalgam as reductant was tested starting from *cis*-**24**. Addition of 2.2 equivalents of sodium amalgam to a solution of *cis*-**24** in THF at room temperature under N_2 resulted in a gradual color change from deep purple to red to green, after which – in analogy to dinitrogen

splitting with **9** – the solution was stirred for 10 hours at 50 °C. In the $^{31}P\{^{1}H\}$ NMR and mass spectrum of the reaction solution, however, no appreciable amount of nitride complexes could be found.

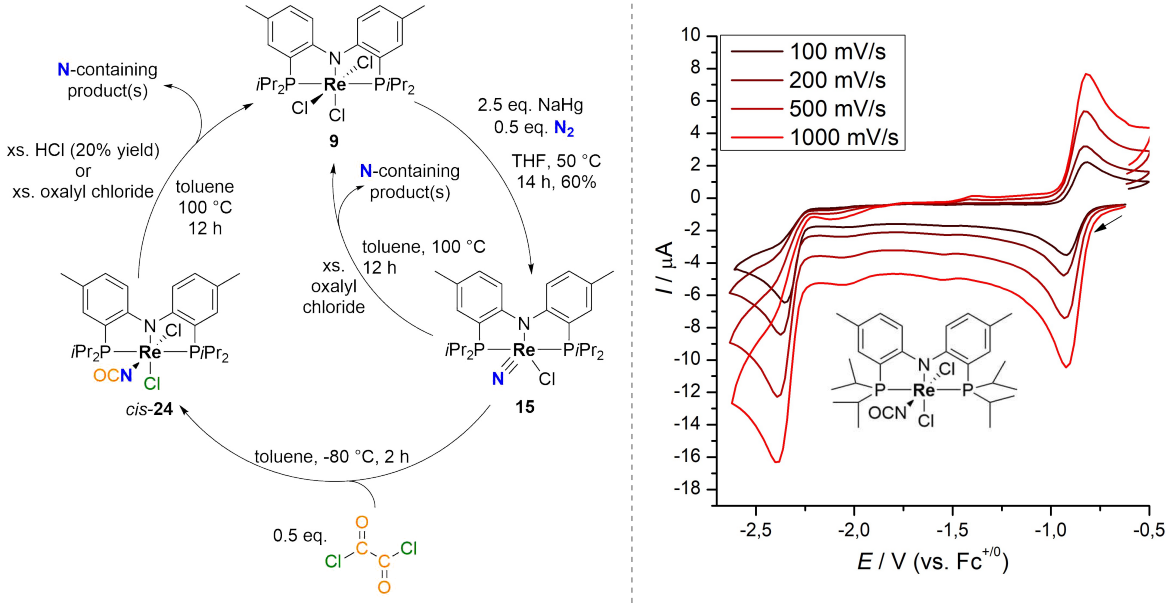

Figure 2.11: Left: Three- (outer cycle) or two-step (inner cycle) chemical cycle from the combination of dinitrogen splitting, nitride functionalization with oxalyl chloride and starting material regeneration with excess HCl or oxalyl chloride. The green chlorine atom in *cis*-**24** indicates that a chlorine atom equivalent is transfered. Right: Cyclic voltammogram of *cis*-**24** in THF under argon (1mM *cis*-**24**, Ar, 0.2 M nBu$_4$NPF$_6$).

Preliminary attempts to regenerate trichloride complex **9** from *cis*-**24** upon NCO to Cl ligand substitution were conducted. No reaction was observed using stoichiometric or excess amounts of TMSCl with *cis*-**24**. Interestingly, heating *cis*-**24** with an excess of hydrochloric acid in toluene for 12 hours resulted in the regeneration of **9** in moderate, unoptimized yields (19%). Finally, trichloride **9** could also be regenerated starting from nitride **15** by either reacting sequentially with 0.5 eq. oxalyl chloride and excess HCl (without isolation of *cis*-**24**, 20% recovered **9**) or directly with an excess of oxalyl chloride, as evident from ^{1}H NMR and IR spectroscopy and mass spectrometry. The nitride transfer product could not be identified in initial ^{15}N-labeling studies, but this and mechanistic information will be examined in the near future.

In conclusion, the reactivity of Re^{V} nitride [(^{Ph}PNP)Re(N)Cl] (**15**) towards H-, B- and C-electrophiles was examined with the following results:

1. **15** is an electron-rich nitride complex, as reflected in its mild, reversible oxidation potential $E_{1/2}(Re^{VI/V})$ = +0.03 V. Consequently, oxidation with adequate outer-sphere oxidants achieved the formation of paramagnetic Re^{VI} complex [(^{Ph}PNP)Re(N)Cl]$^{+}$.

2. Protonation of **15** with strong acids resulted in a distinct color change at low temperature, but unselective decomposition at room temperature. Addition of the PCET reagent system SmI_2/H_2O resulted in formation of 13.5% NH_4^+ after acidic workup.
3. The Lewis-basic nitride moiety can bind electron-deficient boranes, as demonstrated in the X-ray crystallographically characterized [(^{Ph}PNP)Re(NBArF$_{18}$)Cl] complex. Strong carbon electrophiles like EtOTf react with **15** according to spectroscopic evidence, however, no product could be isolated.
4. Reactivity upon initial halide-to-methyl exchange and subsequent reaction with CO was previously reported by *Ison* and coworkers to yield organic isocyanates.[199] Direct reaction of **15** with CO, however, forms presumably a terminal carbonyl complex with no N-C bond formation according to spectroscopic measurements.
5. Reaction of **15** with 0.5 equivalents of oxalyl chloride forms the Re^{IV} isocyanate complex *cis*-[(^{Ph}PNP)Re(NCO)Cl_2] (*cis*-**24**) upon N-C bond formation. Furthermore, initial studies indicate that trichloride [(^{Ph}PNP)$ReCl_3$] (**9**) can be regenerated by reacting *cis*-**24** with excess HCl (20% recovered **9**, *cis*-**24** not isolated, but formed *in situ*) or oxalyl chloride, closing a three- or two-membered chemical cycle (depending on whether *cis*-**24** is isolated or formed *in situ*).

2.4.3 Nitride Functionalization with Chalcogen Atom Donors

Reactivity of **15** towards oxygen atom transfer (OAT) reagents was tested, similarly to the attempts on the Re^{VI} complex **20**$^+$ (see chapter 2.4.1). No reactivity was observed towards TEMPO, pyridine-*N*-oxide, KO_2/18-crown-6 and Na_2O/15-crown-5. Addition of *m*CPBA, *t*BuOOH or NaOCl · 5 H_2O to a solution of **15** in benzene (*m*CPBA), fluorobenzene (*t*BuOOH) or DCM / H_2O (NaOCl · 5 H_2O) resulted in a rapid color change to intense green. Analysis of the reaction products after solvent evaporation by infrared spectroscopy, however, showed no clearly recognizable IR stretch in the region between 2000 and 1600 cm^{-1}, which would indicate formation of a terminal nitrosyl complex. While mass spectrometry indicated addition of one oxygen-atom equivalent, no single species could be isolated from the reaction mixtures. Addition of a stock solution of Me_3NO to a stirring solution of **15** in MeCN / toluene at –40 °C led to a slow initial color change to green and upon warming to room temperature the color

gradually changed to blue. In the $^{31}P\{^{1}H\}$ NMR of the reaction mixture several low intensity signals were observed, with one of them (δ_{31P} = 57 ppm) in a similar range to the product of stirring the $^{Ph}P^{H}NP$ ligand under air (δ_{31P} = 58 ppm), suggesting ligand oxygenation by Me_3NO. The intense blue color prompted the question, whether a paramagnetic species was formed during the reaction (Figure 2.12).

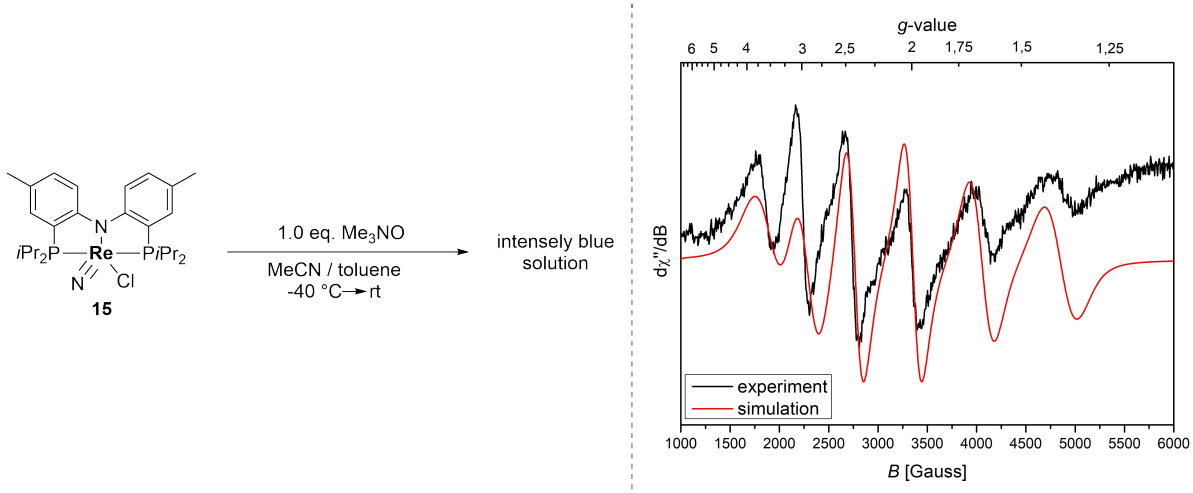

Figure 2.12: Left: Reaction of Re^{V} nitride complex **15** with one equivalent of Me_3NO at low temperature to obtain an intensely blue solution upon warming to room temperature. Right: X-band EPR spectrum (black trace) and simulation (red trace) at room temperature in THF of the reaction of **15** with 1.0 eq. Me_3NO in MeCN/toluene. Simulation and technical parameters: g_{iso} = 1.92, A_{iso}(Re) = 1575 MHz, Gaussian broadening: 50 MHz, Lorentzian broadening: 150 MHz, *A*-strain: 300 MHz, microwave frequency: 9.417 GHz, microwave power: 7.837 mW, modulation frequency: 100 kHz, modulation amplitude: 4.00 G, conversion time: 163.84 ms, time constant: 20.48 ms.

In the X-band EPR spectrum at room temperature, a severely broadened six-line pattern from 1500 to 4700 Gauss was observed. Simulation of the spectrum revealed an isotropic *g*-value of 1.92 and an extremely large Re HFI of A_{iso}(Re) = 1575 MHz. The substantial deviation from g_e indicates a large contribution of metal-centered spin density. The isotropic hyperfine interaction is one of the largest yet reported for Rhenium complexes and implies a spin density of 4.4% in a ^{187}Re 6s orbital according to the atomic parameters of *Morton* and *Preston*.[357] The formation of a $S \neq 0$ species upon addition of Me_3NO, however, indicates the occurrence of a redox process to presumably Re^{IV} or Re^{VI}. In the infrared spectrum of the product mixture, a low intensity IR stretch at ν = 1648 cm^{-1} was found, indicating the formation of a nitrosyl complex, but in comparison to the typical region of C-H stretching vibrations it is evident that it rather belongs to a minor product. The intense IR stretch at ν = 900 cm^{-1} could be an indication of a Re=O structural motif, as in *cis*-[(^{Ph}PNP)Re(O)Cl$_2$] (ν = 940 cm^{-1}) reported by *Ozerov* and coworkers.[352] Unfortunately, no species could be isolated from this mixture.

Finally, reactivity of **15** towards other chalcogen donor reagents was tested. The more electrophilic Iridium and Osmium nitride complexes were shown to react with elemental sulfur (S_8) and propylene sulfide, respectively.[262,358] However, for the nucleophilic Rhenium nitride **15** it was envisioned that in particular the stable and relatively inert S_8 molecule might not be electrophilic enough to react with the nucleophilic nitride moiety, as reported in the literature for other Rhenium nitride complexes as well.[359] Thus, the more reactive, electrophilic S^{I} reagent S_2Cl_2 was chosen, which can also transfer a chlorine atom for stabilization of coordinatively unsaturated intermediates (c.f. reactivity with oxalyl chloride, chapter 2.4.2).

Slow addition of a stock solution of 0.5 eq. S_2Cl_2 in DCM to a stirring solution of **15** in dichloromethane at –90 °C resulted in a gradual color change from bright orange to brown to green over the course of two hours. Only very broad resonances were observed in the ^{1}H NMR spectrum after the reaction, indicating the formation of a paramagnetic species. Recrystallization from the ternary system of benzene / cyclopentane and pentane yielded dark green crystals suitable for X-ray crystallography. From the solid state structure the formation of the thionitrosyl complex *cis*-[(^{Ph}PNP)Re(NS)Cl$_2$] (*cis*-**25**) could be confirmed. This formally constitutes the first nitrogen-chalcogen bond formation from a dinitrogen-derived Rhenium nitride, extending nitride functionalization for the first time into group 16. Furthermore, a chlorine atom was transferred, resulting in formation of an octahedral, coordinatively saturated complex.

The Re-N_{NS} bond (d_{ReN} = 1.810(8) Å) in the solid-state structure of *cis*-**25** is only slightly longer than the related bond in *cis*-[(^{Ph}PNP)Re(NO)Cl$_2$] (d_{ReN}) = 1.797(7) Å, see chapter 2.5.3), but the N-S bond is significantly longer than the corresponding N-O bond (d_{NS} = 1.553(8) Å / d_{NO} = 1.184(7) Å). This large difference in bond lengths of the nitrosyl and thionitrosyl ligands within the otherwise same coordination geometry was also observed in Iridium, Ruthenium and Osmium (thio)nitrosyl complexes. This was, in combination with the IR frequencies (*vide infra*), attributed to weaker nitrogen-chalcogen bonding in thionitrosyl complexes compared to nitrosyl complexes.[262,358,360] The Re-N-S bond angle in *cis*-**25** is slightly more bent (∢(Re-N-S) = 170.0(5)°), than the Re-N-O angle in *cis*-[(^{Ph}PNP)Re(NO)Cl$_2$] (∢(Re-N-O) = 178.2(8)°) and in the [(^{tBu}P=N=P)Ir(NE)] (E = O, S, Se) series (∢(Ir-N-E) = 177.4 – 179.5°),[358] which could be an indication of increased π-backbonding (Figure 2.13).

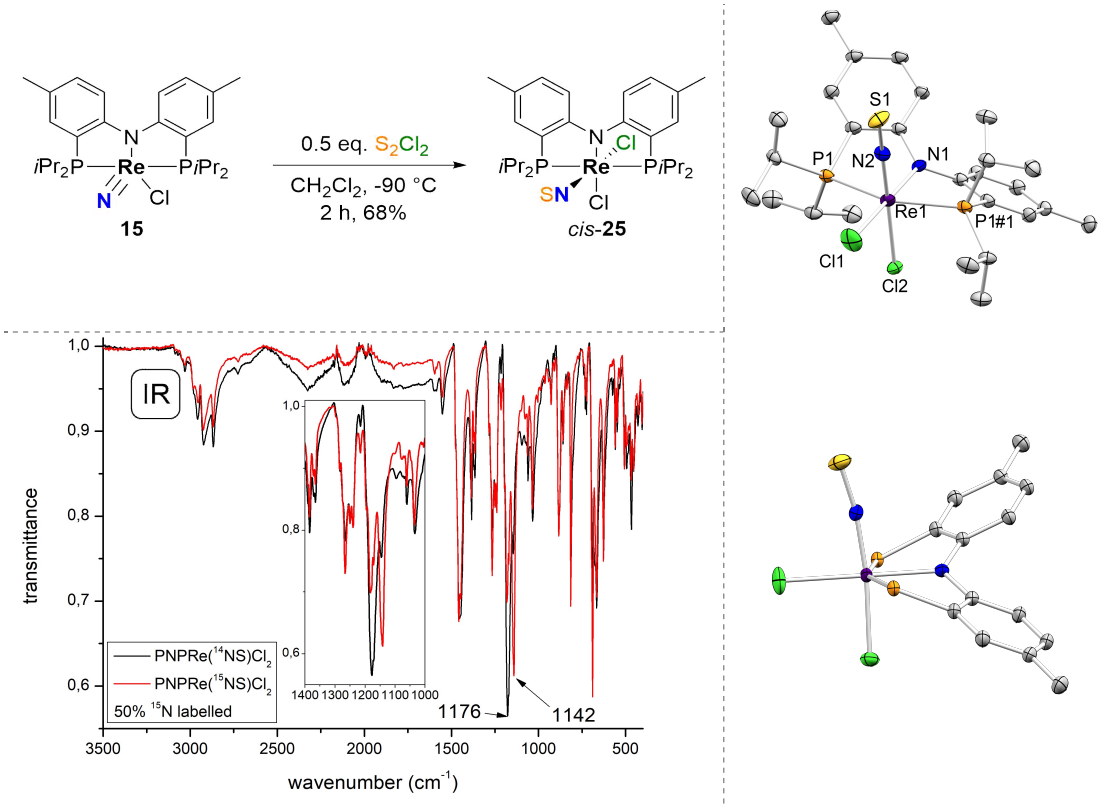

Figure 2.13: Top left: Reaction of nitride **15** with 0.5 eq. S_2Cl_2 in DCM at –90 °C to form thionitrosyl complex *cis*-**25** upon sulfur atom transfer. Bottom left: IR (ATR, solid) spectrum comparison of natural abundance *cis*-**25** (black trace) and ^{15}N-labeled **25** (red trace, 50% ^{14}N/^{15}N). Top right: Disordered molecular structure of *cis*-**25** from single-crystal X-ray diffraction (thermal ellipsoids drawn at the 50% probability level); Hydrogen atoms and a benzene solvent molecule are omitted for clarity. Selected bond lengths [Å] and angles [°]: Re1-N2 1.810(8), N2-S1 1.553(8), Re1-P1 2.4615(10), Re1-N1 2.055(4), Re1-Cl1 2.3858(14), Re1-Cl2 2.374(2), Re1-N2-S1 170.0(5), P1-Re1-P1#1 155.65(4), Cl1-Re1-N1 180.0. Bottom right: Side view of the molecular structure of *cis*-**25**. Hydrogen atoms, a benzene solvent molecule and the isopropyl groups are omitted for clarity.

The formation of the thionitrosyl complex was also confirmed by LIFDI mass spectrometry, not only with the natural abundance nitride complex, but also with the ^{15}N-labeled isotopomer (50% ^{14}N/^{15}N). In the infrared spectrum of a crystalline sample of *cis*-**25** (Figure 2.13) an intense stretch at ν = 1176 cm^{-1} was observed. IR of the ^{15}N-*cis*-**25** isotopomer (50% ^{14}N/^{15}N) revealed a new band at ν = 1142 cm^{-1}, which matches precisely the calculated isotopic ^{14}N/^{15}N shift ($\Delta\nu$ = 34 cm^{-1}) and hence was attributed to the N-S stretch of the thionitrosyl moiety ($\nu_{NS,DFT}$(BP86/def2-QZVP;SVP) = 1227 cm^{-1}). The IR stretch at 1176 cm^{-1} is within, yet at the lower end of the typical range of rhenium thionitrosyl complexes (ν_{NS} = 1160 – 1230 cm^{-1}).[234]

The high NO/NS IR frequency ratio (ν_{NO}/ν_{NS} = 1.45, upon comparison with *cis*-[(^{Ph}PNP)Re(NO)Cl$_2$], ν(NO) = 1702 cm^{-1}) was previously correlated to a comparably weaker N-S bond in the square-planar Iridium complexes [($^{t Bu}$P=N=P)Ir(NE)], E = O, S)[358] and octahedral Osmium NO- and NS complexes [TpOs(NE)Cl$_2$] (E = O, S).[262] *Vyboishchikov* and

Frenking investigated computationally the bonding interaction between a truncated Rhenium nitride ($Cl_2(PH_3)_3Re(N)$) and different groups.[361] They found a strong decrease of bond strength towards the heavier chalcogens, with the largest relative difference between O and S. Hence, they described the bonding interaction in the Re-N-S, -N-Se and -N-Te scaffolds as donor-acceptor interaction of a Re≡N moiety with a singlet chalcogen atom. The Rhenium nitrosyl bonding situation was, in this context, described as Re=N=O. The bonding parameters and vibrational spectroscopy of *cis*-**25** are in good agreement with such a description and suggest a rather weak nitrogen-sulfur bond.[358]

In solution *cis*-**25** exhibits a magnetic moment ($\mu_{eff} = 1.66 \pm 0.1 \mu_B$) close to the spin-only value of a $S = ½$ ground state. In the X-band EPR spectrum of **25** in toluene (Figure 2.14) the broad, characteristic six-line pattern of the Rhenium hyperfine interaction (HFI) was observed. Simulation of this spectrum derived an isotropic *g*-value of $g_{iso} = 1.98$ and an isotropic Re HFI of $A_{iso}(Re) = 819$ MHz, which corresponds to spin density of 2.3% in the Re 6s orbital.[357] The large metal contribution to the spin density was well reproduced by DFT (PBE0/SARC-Zora-TZVP(Re);def2-TZVP), which found the spin density to be predominantly located at the Re metal center (>99%) in the d_{xy} and d_{xz} orbitals (Figure 2.14), resembling the basic MO considerations for the related nitrosyl complexes.

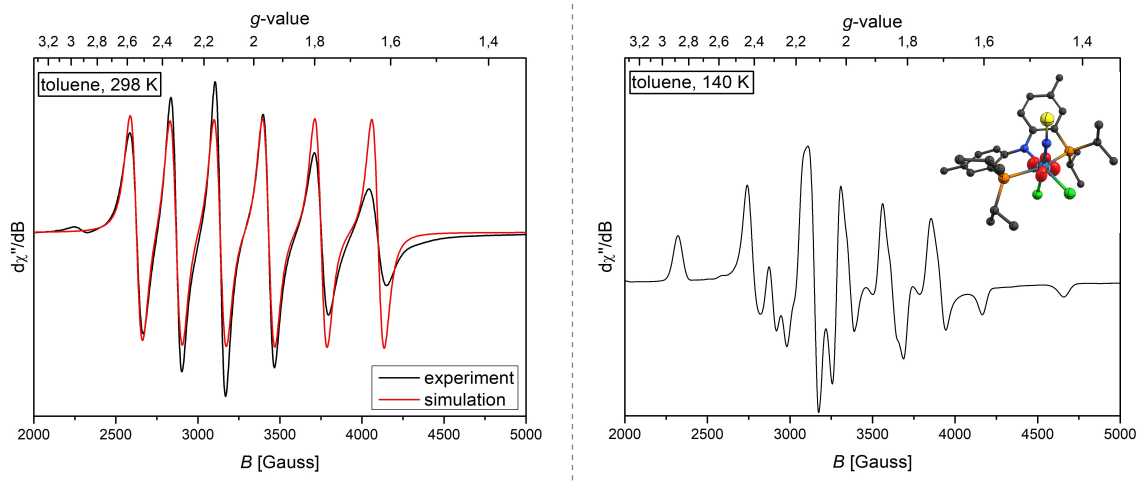

Figure 2.14: Left: X-band EPR spectrum of *cis*-**25**. Simulation and technical parameters: $g_{iso} = 1.98$, $A_{iso}(Re) = 819$ MHz, Gaussian broadening: 40.2 MHz, Lorentzian broadening: 53.2 MHz, microwave frequency: 9.422 GHz, microwave power: 4.953 mW, modulation frequency: 100 kHz, modulation amplitude: 4.00 G, conversion time: 81.92 ms, time constant: 20.48 ms. Right: X-band EPR spectrum of *cis*-**25** in frozen toluene glass at 140 K. Technical parameters: microwave frequency: 9.425 GHz, microwave power: 9.867 mW, modulation frequency: 100 kHz, modulation amplitude: 4.00 G, conversion time: 167.77 ms, time constant: 40.92 ms. Inset: Spin density plot of *cis*-**25** (PBE0/SARC-Zora-TZVP(Re);def2-TZVP). The red isosurface represents excess α spin density.

The EPR spectrum of *cis*-**25** in frozen toluene proved to be significantly more complex, so that no satisfying simulation could be obtained. However, from the general shape of the spectrum a

relatively large *g*-anisotropy, characteristic for metal-centered spin density, can be assumed (especially from the signals at ca. 2300 and 4700 Gauss, respectively). Furthermore, it appears that the HFI of Rhenium, and potentially, of phosphorus or nitrogen is only resolved for one or two of the three *g*-values. For a more thorough analysis of the HFI in the low temperature EPR spectrum an additional EPR experiment at Q-band frequency or 2D EPR techniques might prove useful to deconvolute the HFI contributions and g-anisotropy.

The reactivity of Re^{V} nitride towards chalcogen atom donors was investigated with the following results:

1. Selective oxygenation of the nitride moiety was not observed under the investigated conditions. In the case of *m*CPBA, *t*BuOOH and NaOCl · 5 H_2O a rapid color change to intensely green was observed, albeit with no evidence for the formation of an N-O bond. Addition of Me_3NO to **15** resulted in a color change to blue and a resonance in the X-band EPR was observed, but no significant nitrosyl IR stretch could be detected.
2. Reaction of **15** with 0.5 equivalents of S_2Cl_2 resulted in the formation of {ReNS}^{5} thionitrosyl complex *cis*-[(^{Ph}PNP)Re(NS)Cl_2] (*cis*-**25**) upon sulfur- and chlorine atom transfer, which is the first reported nitrogen-chalcogen bond formation with a dinitrogen-derived nitride complex.

2.5 Dinitrogen-Derived Nitride Transfer to Nitric Oxide

Parts of the research presented in this chapter have been published in: "Rhenium-mediated Conversion of Dinitrogen and Nitric Oxide to Nitrous Oxide", L. Alig, K. A. Eisenlohr, Y. Zelenkova, S. Rosendahl, R. Herbst-Irmer, S. Demeshko, M. C. Holthausen, S. Schneider, *Angew. Chem. Int. Ed.* **2022**, *61*, e202112597.

2.5.1 Synthesis and Characterization of [(^{Ph}PNP)Re(NO)$_2$Cl] upon Nitride Transfer

The Re^{V} nitride [(^{Ph}PNP)Re(N)Cl] (**15**) was shown to react with hydrogen- and boron electrophiles, sufficiently strong carbon electrophiles and carbon monoxide (chapter 2.4.2). Nitrogen- and oxygen electrophiles required for the formation of N-N- or N-O bonds, on the other hand, are highly reactive (e.g. NCl_3 or peroxides are potentially explosive), which poses a selectivity problem in presence of other nucleophilic moieties like phosphine donor atoms. Nitric oxide was shown to react with rather electrophilic Os^{VI} nitrides and ambiphilic Ru^{IV} nitrides upon formation of nitrous oxide.[257,350] However, based on EPR studies, spin density of NO is mainly located at the nitrogen atom (ca. 65%), which coincides with the most electrophilic atom in nitric oxide.[275,287] Consequently, reactivity with nucleophilic nitrides should be feasible, especially considering that the potentially formed N-N bond in nitrous oxide is relatively strong and elimination of gaseous nitrous oxide could serve as a sufficiently strong driving force.

Addition of one atmosphere of nitric oxide to **15** in C_6D_6 resulted in gradual darkening of the solution over the course of 30 minutes. The absence of a signal in the $^{31}P\{^1H\}$ NMR and concomitant appearance of very broad signals in the ^1H NMR indicated the formation of a paramagnetic species (Figure 2.15, bottom left). Crystals suitable for X-ray crystallography were obtained by slow gas-phase diffusion of pentane into a saturated solution in benzene. In the solid state structure the formation of [(^{Ph}PNP)Re(NO)$_2$Cl] (**26**, formally $\{Re(NO)_2\}^7$) and disorder of the nitrosyl and chloride ligand(s) over all three non-pincer ligated positions was observed. From this solid-state structure it was therefore not possible to unequivocally determine the isomeric configuration of the complex. The crystal structure disorder is dictated by the crystallographically imposed two-fold axis through N1-Re1-N3-O2 (spacegroup $P2_n$). Solving and refining the structure in a lower symmetry space group (P_n) revealed that the crystal structure actually consists of two separate molecules (c.f. crystallographic appendix). The

predominant species is *cis*-**26**, cocrystallized with a significantly smaller amount of the mononitrosyl complex *cis*-[(PNP)Re(NO)Cl_2] (*cis*-**14**, see chapter 2.5.3). In this crystallographic solution, no evidence for the formation of *trans*-[(PNP)Re(NO)$_2$Cl] could be found.

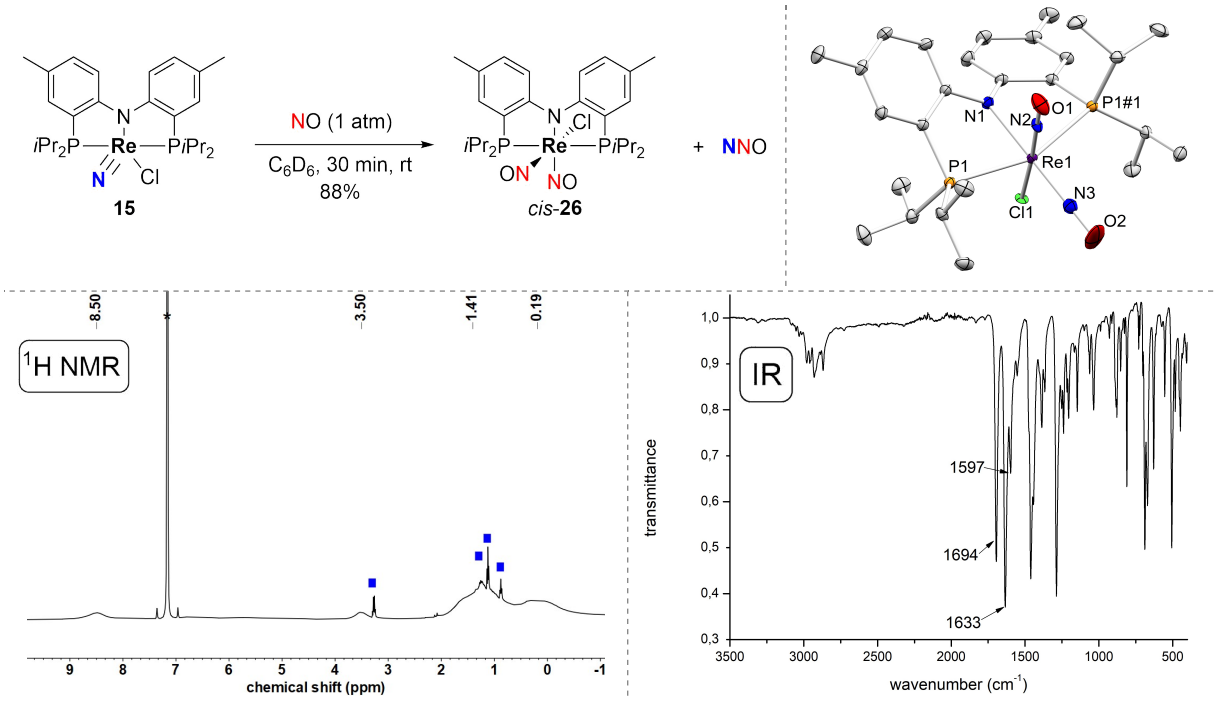

Figure 2.15: Top left: Reaction of Re^V nitride **15** with one atmosphere of nitric oxide to form [(^{Ph}PNP)Re(NO)$_2$Cl] (**26**) and nitrous oxide. Top right: Disordered molecular structure of **26** from single-crystal X-ray diffraction (thermal ellipsoids drawn at the 50% probability level); hydrogen atoms and the co-crystallized *cis*-[(^{Ph}PNP)Re(NO)Cl_2] are omitted for clarity. Selected bond lengths [Å] and angles [°]: Re1-N1 2.098(2), Re1-N2 1.880(5), N2-O1 1.119(6), Re1-Cl1 2.364(2), Re1-N3 1.819(6), N3-O2 1.161(7), Re1-P1 2.4402(6), N1-Re1-N3 180.0, P1-Re1-P1#1 155.49(2), Re1-N2-O1 177.6(6), Cl1-Re1-N2 177.3(6), Re1-N3-O2 180.0. Bottom left: ^{1}H NMR spectrum of **26** in C_6D_6 after workup. Solvent signal is marked with an asterisk and residual diethylether and pentane are marked with blue rectangles. Bottom right: ATR-IR of crystalline and analytically pure **26**.

Most dinitrosyl complexes exhibit *cis*-coordination as a result of population of non-bonding orbitals with n > 4 in $\{M(NO)_2\}^n$ manifolds. In fact, only one *trans*-coordinating dinitrosyl complex is reported, where the geometry is enforced with a tetradentate ligand in the equatorial plane.[362] The nitrosyl ligands in **26** are essentially linear (∢(Re-N-O_{ax}) = 177.6°, ∢(Re-N-O_{eq}) = 180.0° (on the crystallographic axis [b]), and their bond lengths (d_{NOax}= 1.119 Å, d_{NOeq} = 1.161 Å) are in good agreement with previously reported [$ReBr_2(NO)_2(PPh_3)_2$] (∢(Re-N-O) = 178.3° / 180°; d_{NO} = 1.166 Å / 1.09 Å)[363] and [$Re(CO)Cl_2(NO)(PPh_3)_2$] (∢(Re-N-O) = 180°; d_{NO} = 1.157 Å)[364]. Furthermore, the axial Re-Cl bond is shorter than the equatorial

[b] The metrics of the equatorial NO are not reliable due to the crystallographic axis.

Re-Cl bond (d_{ReClax}: 2.364 Å; d_{ReCleq}: 2.393 Å), which can be interpreted in terms of an inverse structural *trans*-effect imposed by the strong π-acceptor NO.[362]

In the IR (ATR-IR) of a crystalline and analytically pure sample of **26** three sharp and intense bands in the characteristic region for $\{Re(NO)_2\}^7$ complexes (ν_{NO} = 1600 – 1750 cm^{-1})[362] at ν = 1694 cm^{-1}, 1633 cm^{-1} and 1597 cm^{-1}, respectively, were observed. The intensity ratio would be in agreement with a mixture of *cis*- and *trans*-**26**, since the symmetric stretch for *trans*-**26** is expected to cause only a small change in the dipolar momentum, compared to the asymmetric stretch and the two stretches for *cis*-**26**. No difference in intensity or number of IR stretches was observed between solid-state and liquid IR (toluene), suggesting a high isomerization barrier at room temperature. DFT calculations on the BP86/def2-QZVP;SVP level of theory reproduced the expected intensity ratio for a mixture of the two isomers (Figure 2.16). Furthermore, the calculated wavenumbers for the stretches are in good agreement with the experimentally determined values ($\Delta\nu$ = 20 – 40 cm^{-1}) and were significantly better reproduced on GGA functionals like PBE and especially BP86, rather than with the hybrid functional PBE0 (further information on the benchmarking can be found in the computational section). The BP86 functional was previously shown to deliver good structural and vibrational agreement between calculated transition-metal nitrosyl complexes and experimentally determined properties.[365] The low intensity IR stretch of *trans*-**26** at $\nu_{NO,DFT}$ = 1723 cm^{-1} is superimposed with one of the stretches of *cis*-**26** at $\nu_{NO,DFT}$ = 1719 cm^{-1}, resulting in overall three intense IR stretches predicted by DFT for a mixture of both compounds (Figure 2.16).

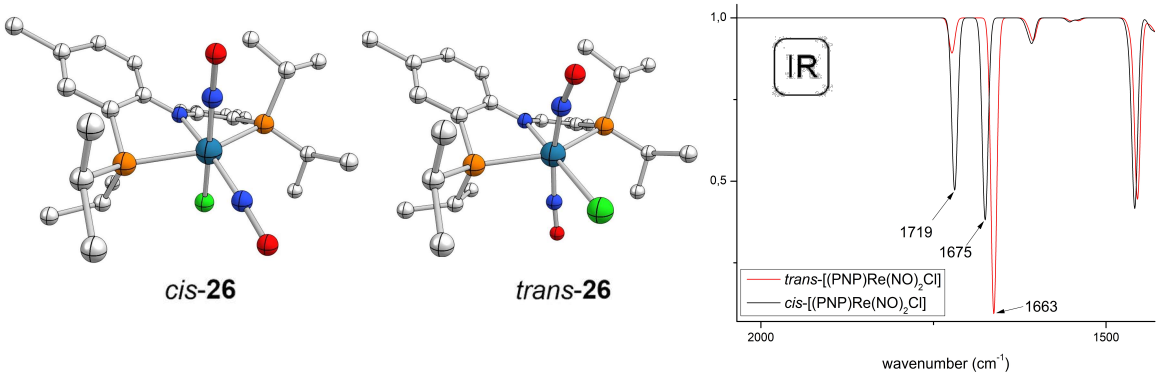

Figure 2.16: Left: DFT-optimized (BP86/def2-QZVP;SVP) structures of *cis*-**26** (top) and *trans*-**26** (bottom). Right: Calculated infrared spectrum of *cis*-**26** (black trace) and *trans*-**26** (red trace).

DFT calculations reproduced the solid-state structure of *cis*-**26** reasonably well, however, significant bending of the nitrosyl ligands in *trans*-**26** (Figure 2.16) was observed. Additionally, *trans*-**26** was calculated to be 17.3 kcal·mol^{-1} higher in energy than the *cis*-**26** isomer, which

would render formation of *trans*-**26** energetically unfavorable. Since this barrier was neither determined experimentally, nor predicted computationally it is not possible to exclude the formation of *trans*-**26**, which still might be formed as a minor, kinetic product.

One possibility to elucidate the origin of the observed IR stretches in the region of interest is isotopic labeling. The reduction of higher *N*-oxides to nitric oxide is a well-known detection method for nitrates. Upon reduction with Fe^{II} ions, nitric oxide is formed, which coordinates in aqueous, acidic solution to the iron forming $[Fe(H_2O)_5(NO)]^+$, the so-called "brown-ring" chromophore. This elusive species, known since the 19th century, was just recently crystallographically characterized[366] and prompted the formation of isotopically labeled nitric oxide in a modified procedure. $Na^{15}NO_2$ (98% ^{15}N-labeled) was chosen as the precursor and reacted with $FeSO_4 \cdot 7\ H_2O$ and concentrated H_2SO_4 (further details can be found in the experimental appendix).

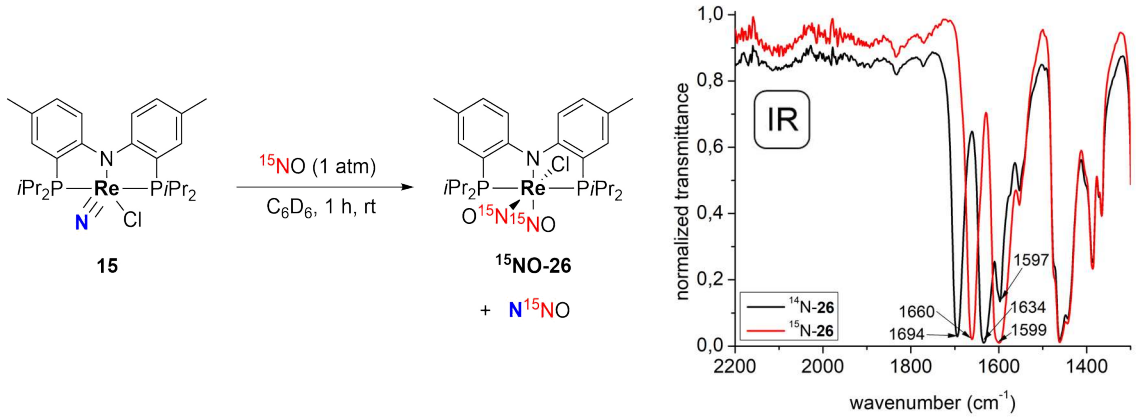

Figure 2.17: Left: Reaction of Re^V nitride **15** with ^{15}NO, produced upon reduction of $Na^{15}NO_2$ with $FeSO_4 \cdot 7\ H_2O$ and H_2SO_4, to form isotopically labeled **^{15}NO-26** and $^{14}N^{15}NO$ (not detected). Right: Branch of the normalized transmittance IR (ATR, solid) of natural abundance **26** (black trace) and **^{15}NO-26** (red trace).

The produced ^{15}NO gas was purified by low-temperature (–110 °C) gas distillation and finally vacuum transferred to a solution of **15** in benzene. After workup, infrared spectroscopy confirmed the exclusive formation of **^{15}NO-26** (Figure 2.17). The concomitantly formed $^{14}N^{15}NO$ was not examined, because of experimental limitations (from condensation of a large amount of gas into a *J*-Young NMR tube was refrained for safety reasons), but could potentially be separated and analyzed (e.g. via liquid IR) from the product reaction mixture in a future experiment. Upon comparison of the IR spectra of natural abundance **26** and **^{15}NO-26**, an isotopic shift to lower wavenumbers ($\Delta\nu$ = 34 and 35 cm^{-1}, respectively) was observed for the ^{15}N-labeled isotopologue (Figure 2.17) and is in excellent agreement with the calculated value ($\Delta\nu_{calc}$ = 33.9 cm^{-1}) derived from the harmonic oscillator approximation. Furthermore, the

exclusive formation of **^{15}NO-26** was verified by high-resolution mass spectrometry, with no formation of significant amounts of **^{14}NO-26**.

From the three relatively intense IR stretches in natural abundance **26** at ν = 1694, 1634 and 1597 cm $^{-1}$, only the bands at ν = 1694 and 1634 cm^{-1} are shifted to ν = 1660 and 1599 cm^{-1}, respectively. The band at ν = 1597 cm^{-1} is not shifted in the isotopologue **^{15}NO-26** and is superimposed with the broad stretch at ν = 1599 cm^{-1}, verifying that this band does not belong to a nitrosyl ligand, but could rather be an aromatic C=C double bond stretch. From the relative intensities of the stretches at ν = 1694 and 1634 cm^{-1}, as well as ν = 1660 and 1599 cm^{-1}, respectively, it can be derived, that the main species formed upon reaction with NO is *cis*-**26**. The formation of a minor amount of *trans*-**26**, however, can not be excluded, as the IR region between ν = 1700 and 1550 cm^{-1} is crowded with broad signals and thus a low intensity stretch of minor amounts of *trans*-**26** could potentially be superimposed with other bands. Nevertheless, from the combination of solid-state structural information, DFT calculations and ^{15}N-labeling experiments, it can be derived that the predominant isomer is *cis*-**26**.

In benzene solution, **26** exhibits a magnetic moment (μ_{eff} = 1.69 ± 0.1 μ_B) close to the spin-only value for a S = ½ ground state and consistently, only very broad signals in the ^{1}H NMR spectrum were observed (Figure 2.15). The room temperature X-band EPR spectrum of crystalline **26** dissolved in dichloromethane is dominated by one multiline signal (Figure 2.18). Simulation of the major isotropic signal revealed a g-value (g_{iso} = 2.009), close to the g_e = 2.0023 value and a relatively small, Re hyperfine coupling constant (A_{iso}(Re) = 140 MHz), which correlates to a spin density of 0.4% in a Re 6s orbital.[357] The g-value and small Re HFI indicate little metal contribution to the spin density, which was observed for the related [(^{Ph}PNP)Re(CO)$_3$]$^+$ (g_{iso} = 2.013, a_{iso} = 6.01(5) mT).[367] DFT calculations (PBE0/SARC-Zora-TZVP;def2-SVP) for the *cis*-**26** isomer predicted excess α spin density predominantly on the nitrosyl ligands (99%) and excess β spin density on the rhenium metal center, presumably from spin polarization (Figure 2.18, top right). Spin density distribution for hypothetical *trans*-**26** is predicted to be comparable, yet this structure exhibits unlike *cis*-**26** (<S^2> = 0.84) significant multiconfigurational character as indicated by spin contamination (<S^2>(*trans*-**26**) = 1.13).

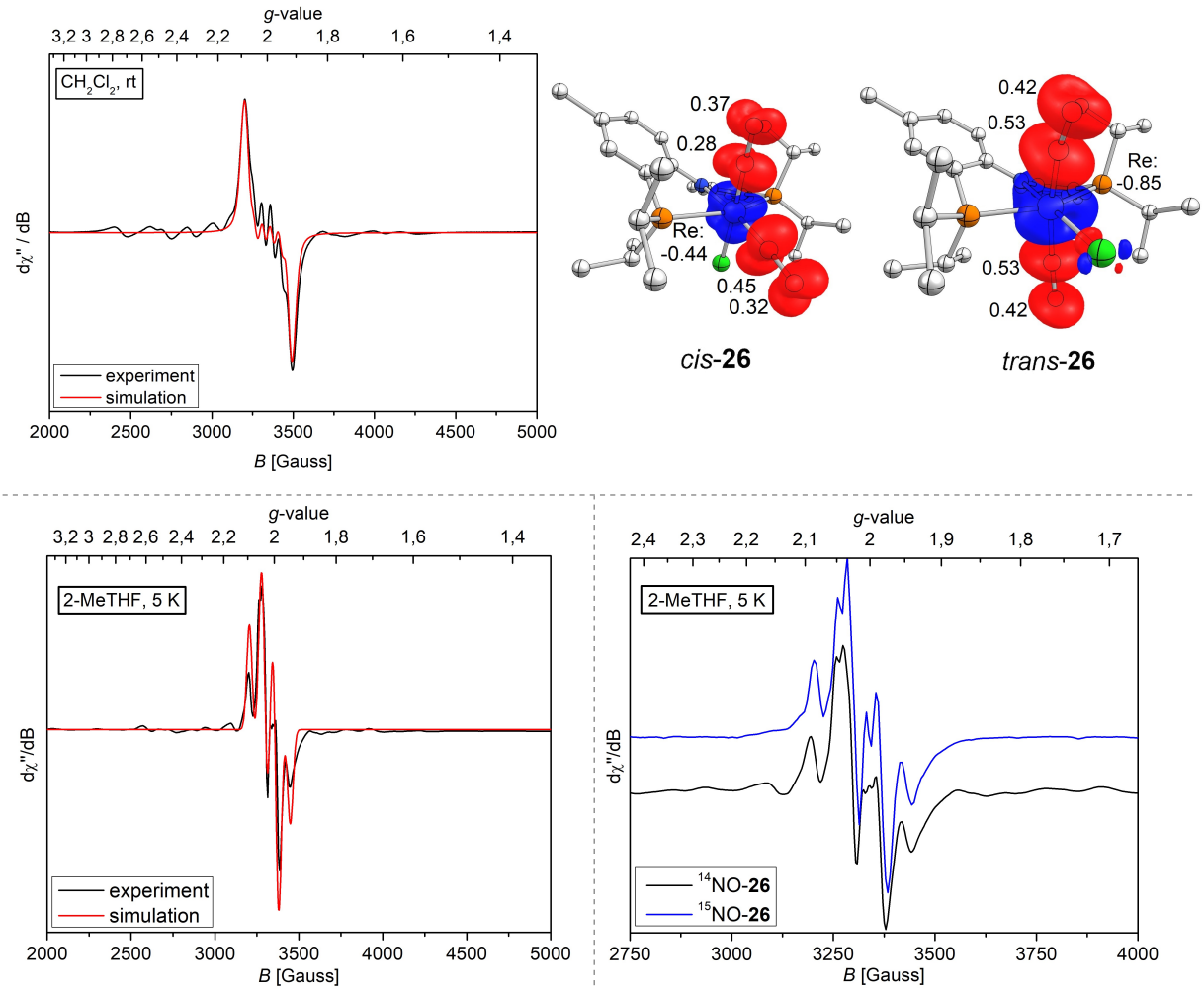

Figure 2.18: Top left: X-band EPR spectrum (black trace) of crystalline **26** in dichloromethane solution at room temperature and simulation (red trace). Simulation and technical parameters: g_{iso} = 2.009, A_{iso}(Re) = 140 MHz, Gaussian broadening: 43 MHz, Lorentzian broadening 20 MHz, microwave frequency: 9.411 GHz, microwave power: 9.874 mW, modulation frequency: 100 kHz, modulation amplitude: 4.00 G, conversion time: 81.92 ms, time constant: 20.48 ms. Top right: Spin density plot of *cis*-**26** and *trans*-**26** (PBE0/SARC-Zora-TZVP(Re);def2-TZVP). The red isosurface represents excess α spin density and the blue isosurface excess β spin density. Small numbers indicate excess α (positive sign) and β spin (negative sign). Bottom left: X-band EPR spectrum of **26** (black trace) in frozen 2-methyltetrahydrofuran at 5 K and simulation (red trace). Simulation and technical parameters: g_{iso} = 2.023, A_{Re} = 48 MHz, A_{31P} = 200 MHz, A_{31P} = 200 MHz, microwave frequency: 9.381 GHz, microwave power: 2.482 mW, modulation frequency: 100 kHz, modulation amplitude: 4.00 G, conversion time: 81.92 ms, time constant: 20.48 ms. Bottom right: X-band EPR spectrum of **^{14}NO-26** (black trace) and **^{15}NO-26** (blue trace) in frozen 2-methyltetrahydrofuran at 5 K.

Kaim and coworkers reported several related examples of ligand-centered Re bipyridyl radicals, which exhibit similarly to **26** a small Re HFI, but no resolved nitrogen or carbon hyperfine interaction, which was attributed to significant line broadening in these cases.[368,369] Furthermore, DFT calculations of the EPR parameters for *cis*-**26** reproduced the simulated *g*-value ($g_{iso,DFT}$ = 2.025) and Re HFI ($A_{iso,DFT}$(Re) = 191 MHz) reasonably well. The experimentally not observed ^{14}N HFI of the nitrosyl ligands were predicted ($A_{iso,DFT}(^{14}N_{NO})$ = 28 and 25 MHz) to be almost one order of magnitude smaller than the Re

HFI, which could explain its absence in the EPR spectrum at room temperature. In agreement to this, simulation attempts whilst taking the ^{14}N HFI of the DFT calculated magnitude into account, did not change the signal shape.

In the X-band EPR of **26** in a 2-methyltetrahydrofuran glass at 5 K no *g*-tensor anisotropy, but one main signal with a *g*-value of $g = 2.023$ was resolved (Figure 2.18, bottom left). The signal was simulated with small HFI contributions from Re ($A_{Re} = 48$ MHz) and two ^{31}P nuclei ($A_{31P} = 200$ MHz). Furthermore, a not completely resolved part of the signal at 3350 Gauss is reminiscent of a three-line pattern and could originate from a ^{14}N HFI. It remains unclear, why no *g*-anisotropy was resolved at low temperature, but other simulation parameters including different *g*-tensor values and nuclei, did not lead to an improved simulation. To verify a possible nitrogen contribution to the hyperfine interaction, an EPR spectrum of a sample of [(^{Ph}PNP)Re(^{15}NO)$_2$Cl] (**^{15}NO-26**) was recorded (Figure 2.18, bottom right) and compared to the measurement of the natural abundance sample. Interestingly, the part of the signal at 3350 Gauss in **^{15}NO-26** is split into two peaks, which indicates contribution of ^{15}N ($I = ½$) to the HFI in and would accordingly corroborate the ligand-centered spin density derived from DFT calculations. However, further EPR measurements for example at higher frequency (Q-/W-band) or pulsed EPR (ENDOR, HYSCORE) are necessary to deconvolute the hyperfine interactions and identify the elemental contributions.

The electronic structure of *cis*-**26** is intriguing, as according to the MO considerations for nitrosyl complexes (c.f. Scheme 2.5) an $\{MNO\}^7$ complex is expected to be intermediate between linear $\{MNO\}^6$ and bent $\{MNO\}^8$. However, the introduction of a second nitrosyl ligand in $\{M(NO)_2\}^7$ reduces the symmetry to an idealized C_{2v} symmetry with lifting of the orbital degeneracies.[107] The electronic structure of *cis*-**26** might be comparable to octahedral $\{Mo(NO)_2\}^6$ complex *cis*-[$MoCl_2(NO)_2(PPh_3)_2$],[370] for which slight bending was rationalized by mixing of energetically low-lying, unoccupied π^*_{b1}(NO-centered) with the filled orbitals. In $\{Re(NO)_2\}^7$ complex *cis*-**26** this NO antibonding orbital could be partially filled, giving rise to NO centered spin density. This is in agreement with DFT calculations of *Machura* and coworkers for the $\{Re(NO)_2\}^7$ complex *cis*-[$ReBr_2(NO)_2(PPh_3)_2$], which predicted the SOMO to be of π^*_{NO} character as well.[363]

Finally, the destination of the nitride nitrogen atom of **15** in the reaction product(s) was tracked with the aid of ^{15}N-labeling experiments. The formation of the nitrosyl rhenium complex [(^{Ph}PNP)Re(NO)$_2$Cl] (**26**) from nitride **15** and NO can proceed within two mechanistic

scenarios: 1) Nitride **15** could be oxygenated from NO or its dimer $(NO)_2$, resulting in a nitrosyl complex with no additional products. 2) Nitride transfer from **15** to nitric oxide would result in formation of nitrous oxide, while the coordinatively unsaturated rhenium complex could bind further nitric oxide equivalents to form the dinitrosyl complex. Both pathways can be distinguished by ^{15}N-labeling of the nitride, as the oxygenation pathway would lead to a ^{15}NO labeled Rhenium complex, whereas the nitride transfer would form ^{15}N-labeled nitrous oxide and a natural abundance nitrosyl complex.

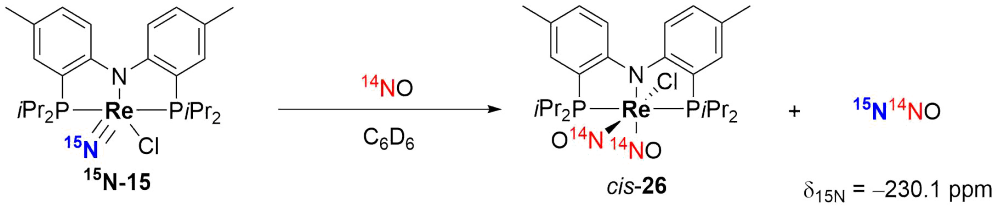

Scheme 2.8: Reaction of ^{15}N-labeled **^{15}N-15** (50% terminally labeled) with natural abundance NO (here simplified as ^{14}NO) and formation of natural abundance nitrosyl complex *cis*-**26** and the exclusive isotopomer and isotopologue $^{15}N^{14}NO$, as evident from its characteristic ^{15}N NMR resonance.

Reaction of **^{15}N-15** (50% $^{15}N/^{14}N$) with natural abundance nitric oxide (Scheme 2.8) resulted in the formation of *cis*-[(^{Ph}PNP)Re$(NO)_2$Cl] (*cis*-**26**), with no incorporation of any appreciable amount of the ^{15}N label in the final Rhenium complex, as judged by IR spectroscopy and mass spectrometry. Performing the reaction of **^{15}N-15** with nitric oxide in a *J*-Young NMR tube and examination of the reaction solution by ^{15}N NMR spectroscopy revealed the formation of a 1:1:1 triplet at δ_{15N} = –230.1 ppm (J_{15N14N} = 6.1 Hz). In analogy to the reactivity of the more electro- or ambiphilic osmium and ruthenium nitrides,[257,350] the signal at δ_{15N} = –230.1 ppm was identified as terminally ^{15}N-labeled $^{15}N^{14}NO$, as the exclusive isotopomer and isotopologue formed in this reaction. This confirmed nitride transfer as the prevalent reaction mechanism over nitride oxygenation. Nitrous oxide was furthermore detected and quantified by calibrated liquid infrared measurements (93.8 ± 4.3%). The high yield in N_2O is in good agreement with the yield of the Rhenium complex product **26** (88%). Further spectroscopic data of nitrous oxide detection and substrate scope of the nitride transfer are discussed in chapter 2.5.6.

Concluding, reactivity of Re^{V} nitride [(^{Ph}PNP)Re(N)Cl] (**15**) with nitric oxide was investigated, with the following information gained:

1. The rhenium-containing product of the reaction of **15** with NO is the paramagnetic dinitrosyl complex [(^{Ph}PNP)Re$(NO)_2$Cl] (**26**), as evident by the solid-state structure. However, initial ambiguity of the configuration of both nitrosyl ligands (*cis*- or *trans*-

position) in the solid-state structure motivated further attempts to distinguish both isomers spectroscopically.

2. With the aid of ^{15}N-labeling upon reaction with ^{15}NO two IR stretches of similar oscillator strength could be assigned to the main product, implying that the predominant isomer formed during the reaction with NO is *cis*-[(^{Ph}PNP)Re(NO)$_2$Cl]. The formation of small amounts of *trans*-[(^{Ph}PNP)Re(NO)$_2$Cl] could not be excluded based on the measurements, yet is energetically unfavorable according to DFT calculations.
3. EPR measurements of the natural abundance **26** and its ^{15}N-isotopologue revealed a relatively small metal contribution to the spin density (reproduced by DFT) and no ^{14}N HFI was resolved, despite significant spin density on the NO ligands.
4. Upon reacting **^{15}N-15** with natural abundance NO only ^{14}NO was incorporated into **26** and concomitant terminally labeled ^{15}N^{14}NO was detected via ^{15}N-NMR and liquid IR spectroscopies, indicating that nitride transfer to nitric oxide occurred.

2.5.2 Redox Reactivity of [(^{Ph}PNP)Re(NO)$_2$Cl]

In the following chapter the redox reactivity of [(^{Ph}PNP)Re(NO)$_2$Cl] (*cis*-**26**) is presented, since mechanistic experiments (chapter 2.5.4) indicated the formation of a Re-NO containing byproduct of the nitride transfer reaction. In the cyclic voltammogram of *cis*-**26** a fully reversible oxidation at $E_{1/2}$ = –0.21 V was accompanied by a second oxidation at $E_{1/2}$ = +0.50 V (Figure 2.19). Furthermore, an irreversible reduction at E_{pc} = –1.63 V, as well as a reductive feature at $E_{1/2}$ = –2.87 V were observed.

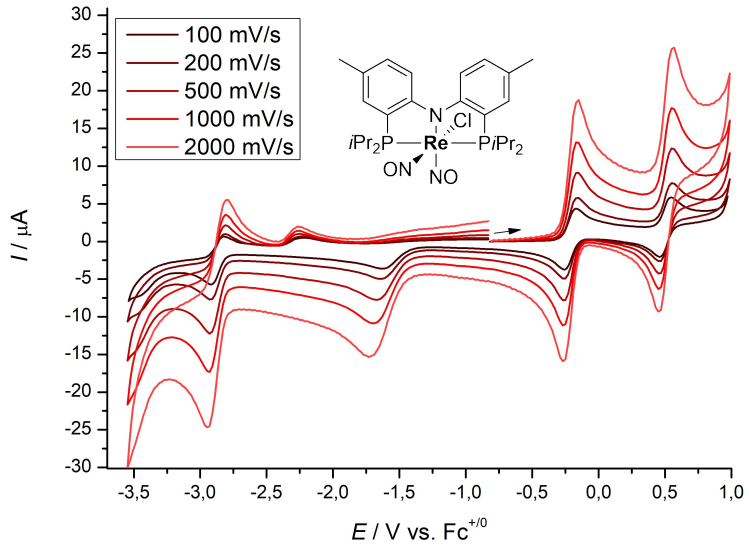

Figure 2.19: Scan-rate dependent cyclic voltammograms of *cis*-**26** (1 mM *cis*-**26**, Ar, THF, 0.2 M nBu$_4$NPF$_6$) at room temperature.

Reaction of one equivalent of outer-sphere oxidant [AcFc][Al(OC(CF$_3$)$_3$)$_4$] (E°' = +0.27 V in CH$_2$Cl$_2$)[198] with **26** in acetonitrile resulted in a dark brown solution. After workup, crystals suitable for X-ray crystallography were obtained upon layering a saturated diethylether solution with pentane at –80 °C. As anticipated, the cationic dinitrosyl complex *cis*-[(^{Ph}PNP)Re(NO)$_2$Cl][Al(OC(CF$_3$)$_3$)$_4$] (*cis*-**27**$^{\mathbf{Al(OC(CF3)3)4}}$) was obtained, judging by the solid-state structure (Figure 2.20).

Upon oxidation, the bond lengths and bond angles of the nitrosyl ligands are barely affected. In contrast, the IR (Figure 2.20, mid left, ATR, solid) of crystalline *cis*-**27**$^{\mathbf{Al(OC(CF3)3)4}}$ shows two broadened bands at ν = 1834 and 1757 cm^{-1}, which represents an oxidation-induced hypsochromic shift of 140 and 124 cm^{-1}, respectively. Previously, IR shifts of on average 125 cm^{-1} in a {FeNO}$^{6-9}$ complex series were observed by *Neese* and coworkers and attributed to metal-centered oxidation, whereas nitrosyl IR shifts of 50 – 80 cm^{-1} in redox series of ruthenium and osmium catecholate complexes were attributed to remote oxidations on the redox-active organic ligand.[371,372]

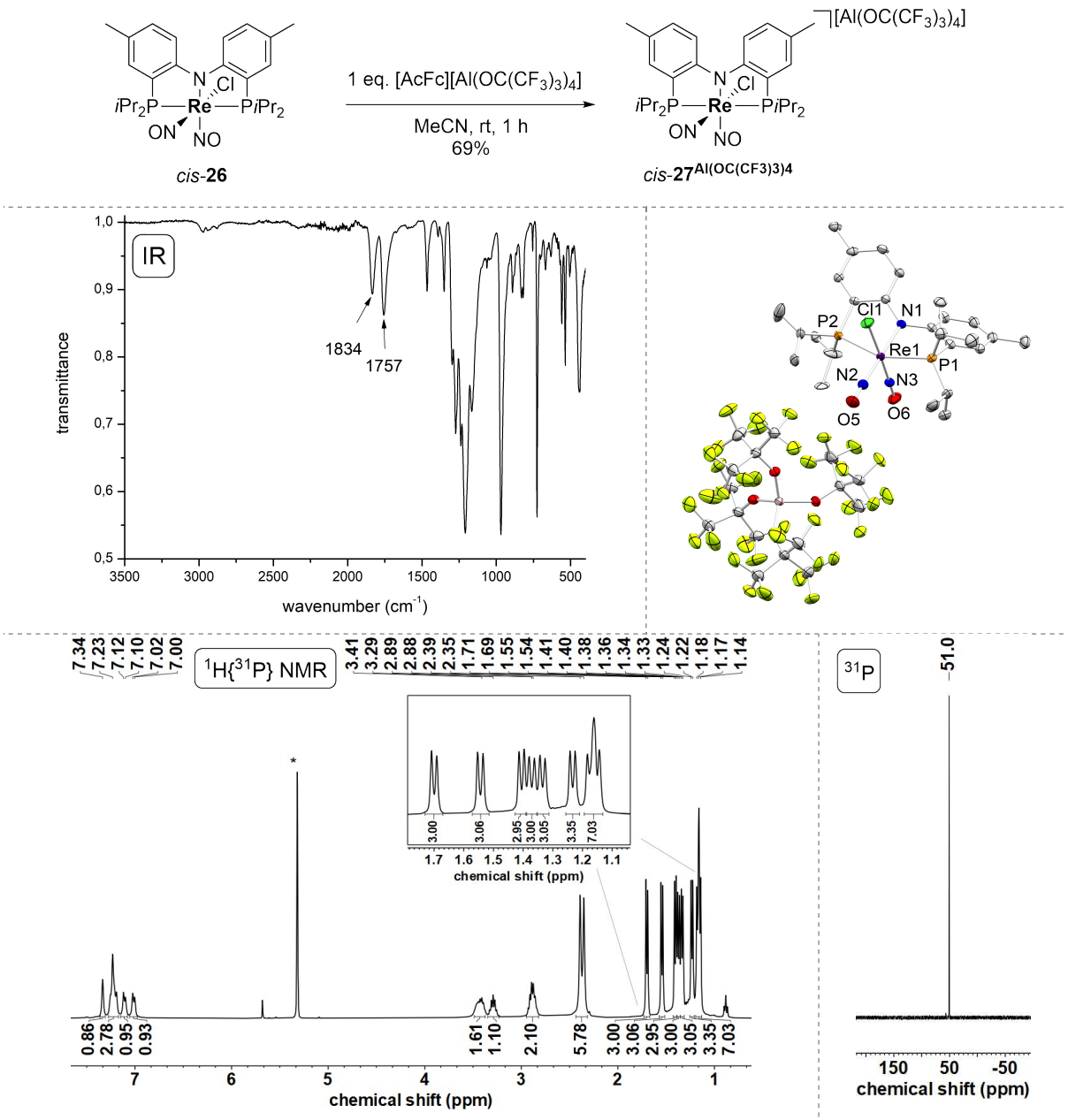

Figure 2.20: Top: Oxidation of cis-**26** to obtain *cis*-[(^{Ph}PNP)Re(NO)$_2$Cl][Al(OC(CF$_3$)$_3$)$_4$] (*cis*-**27**$^{Al(OC(CF3)3)4}$). Mid left: ATR-IR of crystalline *cis*-**27**$^{Al(OC(CF3)3)4}$. Mid right: Molecular structure of *cis*-**27**$^{Al(OC(CF3)3)4}$ from single-crystal X-ray diffraction (thermal ellipsoids drawn at the 50% probability level); hydrogen atoms are omitted for clarity. Selected bond lengths [Å] and angles [°]: Re1-N1 2.061(3), Re1-N2 1.847(4), N2-O5 1.156(5), Re1-N3 1.813(4), N3-O6 1.147(5), Re1-Cl1 2.3801(12), Re1-P1 2.4615(11), Re1-P2 2.4705(12), Re1-N2-O5 177.3(4), Re1-N3-O6 178.2(4), P1-Re1-P2 155.60(4), N1-Re1-N2 176.60(17), Cl1-Re1-N3 178.03(12). Bottom left: ^{1}H{^{31}P} NMR spectrum of *cis*-**27**$^{Al(OC(CF3)3)4}$ in CD_2Cl_2 at room temperature. Solvent signal is marked with an asterisk. Bottom right: ^{31}P{^{1}H} NMR spectrum of *cis*-**27**$^{Al(OC(CF3)3)4}$ in CD_2Cl_2 at room temperature.

Well-resolved, sharp signals in the ^{1}H NMR spectrum of *cis*-**27**$^{Al(OC(CF3)3)4}$ in CD_2Cl_2, as well as a sharp singlet in the ^{31}P{^{1}H} NMR spectrum at δ_{31P} = 51.0 ppm (Figure 2.20) indicate a diamagnetic ground-state for *cis*-**27**$^+$. Interestingly, in solution *cis*-**27**$^+$ exhibits only C_1 symmetry, evident from two separate signals for the benzylic CH_3 groups of the pincer and eight magnetically inequivalent CH_3 groups of the iso-propyl substituents. Notably, only the

cis-**27**$^{+}$ isomer is formed upon oxidation according to the solid-state structure and IR information and no isomerization on the NMR timescale was observed at room temperature. Hence, these results might add to previously discussed spectroscopic evidence that the starting material **26** consists predominantly or even exclusively of the *cis*-isomer.

Another interesting detail from the CV of *cis*-**26** is the second oxidation at $E_{1/2}$ = +0.50 V (Figure 2.19), which suggests relatively mild, synthetic accessibility of a dicationic $[(^{Ph}PNP)Re(NO)_2Cl]^{2+}$ complex. The mild oxidation potential(s) is / are indicative of high electron density and the low oxidation state of *cis*-**26** and especially the assumed dicationic $[(^{Ph}PNP)Re(NO)_2Cl]^{2+}$ is expected to exhibit substantially weakened Re-N_{NO} bonds. This could be relevant for photolytic removal of the NO ligand(s) to regenerate a high-valent Rhenium halide complex for N_2 activation.

The reduction of *cis*-$[(^{Ph}PNP)Re(NO)_2Cl]$ (*cis*-**26**) in the CV at E_{pc} = −1.63 V (Figure 2.19) is irreversible, indicating a coupled chemical follow-up process after reduction (EC mechanism). Reduction of **26** with one equivalent of $CoCp^*_2$ resulted in chloride loss and formation of five-coordinate $\{Re(NO)_2\}^8$ complex $[(^{Ph}PNP)Re(NO)_2]$ (**28**) in good yields (Figure 2.21). Orange single-crystals suitable for X-ray crystallography were obtained by layering a saturated toluene solution of **28** with pentane at –40 °C.

The solid-state structure (Figure 2.21) of **28** is intermediate between square-pyramidal and trigonal-bipyramidal (τ^5 = 0.52) and exhibits a comparably long Re-N_{pincer} bond (d_{ReN} = 2.157(5) Å), representative of the low oxidation state in **28**. Upon reduction, the nitrosyl bond angle decreased (from ∢(Re-N-O) = 177.3°/180.0° (*cis*-**26**) to 170.6° (**28**)) and the N-O bond length increased from d_{NO} = 1.119 Å / 1.161 Å (*cis*-**26**) to 1.203 Å (**28**), consistent with reduction of the N-O bond order as a result of stronger π-backbonding. In THF-d_8 solution **28** exhibits C_{2v} symmetry, evident from one signal for the four central CH resonances of the *iso*-propyl groups in the ^{1}H NMR spectrum (Figure 2.21). In the $^{31}P\{^1H\}$ NMR spectrum one sharp singlet at δ_{31P} = 49.0 ppm is observed, highlighting the remarkably narrow chemical shift range of these complexes (compare δ_{31P}(*cis*-**27**$^{+}$) = 51.0 ppm, which is formally two oxidation states higher).

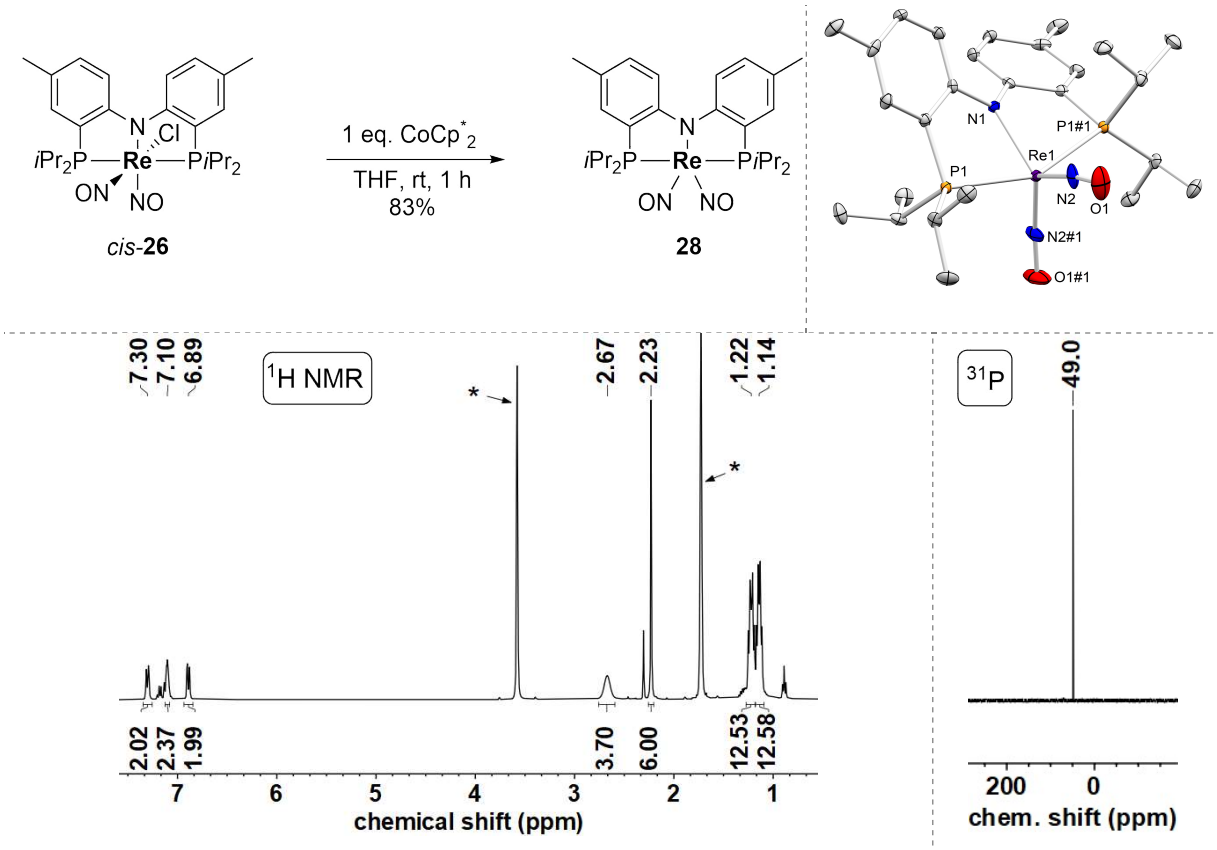

Figure 2.21: Top left: Reduction of **26** to obtain five-coordinate dinitrosyl complex **28**. Top right: Molecular structure of **28** from single-crystal X-ray diffraction (thermal ellipsoids drawn at the 50% probability level); hydrogen atoms are omitted for clarity. Selected bond lengths [Å] and angles [°]: Re1-N1 2.157(5), Re1-N2 1.766(3), N2-O1 1.203(4), Re1-P1 2.4129(11), Re1-N2-O1 170.6(4), N1-Re1-N2 121.10(13), N2-Re1-N2#1 117.8(3), P1-Re1-P1#1 152.35(5), P1-Re1-N2 100.13(11); $\tau^5 = 0.52$. Bottom left: ^{1}H NMR spectrum of **28** in THF-d_8 at room temperature. Solvent signals are marked with asterisks. Bottom right: ^{31}P{^{1}H} NMR spectrum of **28** in THF-d_8 at room temperature.

Similarly to [(^{Ph}PNP)Re(NO)$_2$Cl] (**26**), three intense IR bands in the region between 1700 – 1500 cm^{-1} at ν = 1615, 1594 and 1566 cm^{-1} were observed (Figure 2.22, black trace). To assign the nitrosyl IR stretches, the ^{15}N-labeled isotopologue **^{15}NO-28** was prepared by reduction of [(^{Ph}PNP)Re(^{15}NO)$_2$Cl] with CoCp*$_2$. While **^{15}NO-28** showed an identical spectroscopic signature in the ^{1}H- and ^{31}P{^{1}H} NMR spectra compared to the natural abundance compound, a distinct difference in the IR spectrum was observed. **^{15}NO-28** exhibits two intense stretches at 1574 and 1534 cm^{-1} and one low intensity signal at 1594 cm^{-1}. The experimentally observed shifts upon isotopic labeling ($\Delta\nu$ = 41 and 28 cm^{-1} respectively) are only in moderate agreement with the calculated shift ($\Delta\nu_{calc.}$ = 34 cm^{-1}) for isotopic substitution of the Re-$^{14/15}$N-O fragment. Furthermore, the third IR band in **^{14}NO-28** at 1594 cm^{-1} is significantly less intense in **^{15}NO-28**, yet appears not to be shifted. Neither originating in a nitrosyl ligand, nor being a stretch of **28**, the band at 1594 cm^{-1} therefore was assigned to an IR active, possibly aromatic impurity. Labeling of **^{15}NO-28** was additionally verified by a ^{15}N{^{1}H} NMR spectrum (Figure

2.22, right), showing one well-resolved triplet resonance at δ_{15N} = 65.5 ppm ($^{2}J_{15N\text{-}31P}$ = 3.5 Hz), which indicates coupling of ^{15}N with two magnetically equivalent phosphorus atoms. A similar spectroscopic signature was reported for labeled Re^{I} complex [(PCy$_3$)$_2$ReI$_2$(η^1-H$_2$)(^{15}NO)] (δ_{15N} = –49.4 ppm, $^{2}J_{15N\text{-}31P}$ = 5 Hz), albeit with a different chemical shift.[299]

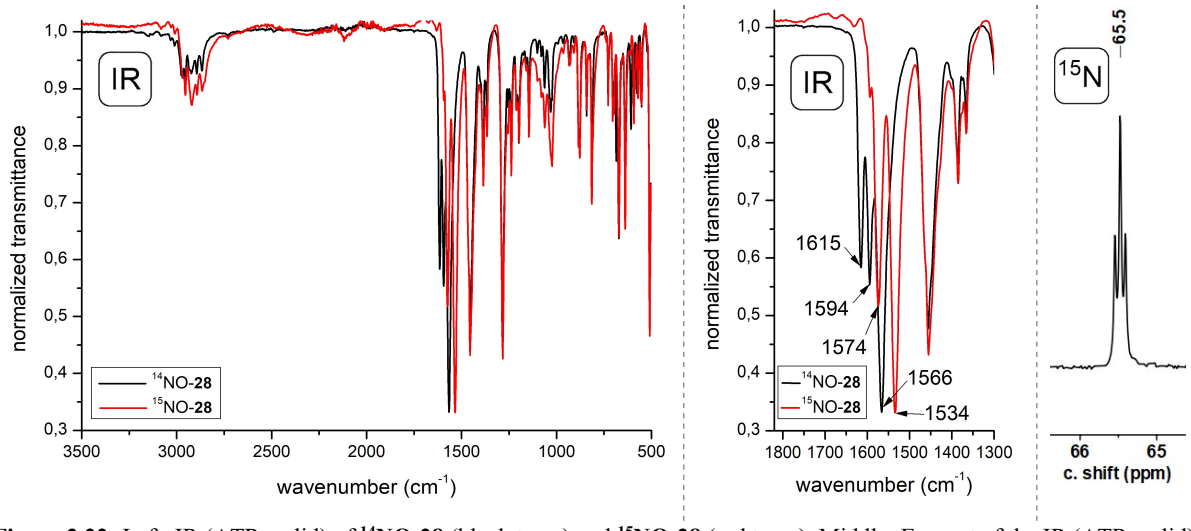

Figure 2.22: Left: IR (ATR, solid) of **^{14}NO-28** (black trace) and **^{15}NO-28** (red trace). Middle: Excerpt of the IR (ATR, solid) of **^{14}NO-28** (black trace) and **^{15}NO-28** (red trace). Right: ^{15}N{^{1}H} NMR spectrum of **^{15}NO-28** in C_6D_6 at room temperature.

The formal oxidation state of **28** can either be viewed as d^8 Re$^{–I}$ or d^6 Re^{I}, depending on the electronic formulation of the nitrosyl ligands (e.g. the comparable complexes [(PR$_3$)$_2$Re(NO)$_2$]$^+$ (R = *i*Pr, Cy) were assigned as Re$^{–I}$ complexes)[373]. The formulation as [(^{Ph}PNP)Re^{-I}(NO)$_2$] would – in a very simplified picture – obey the 18 valence electrons rule. The bond lengths and angles of the nitrosyl ligands in **28** from the solid-state structure and the IR stretches indicate significant N-O bond weakening compared to free NO (ν_{NO} = 1875 cm^{-1}) and are closer to NO$^–$ (ν_{NO} = 1470 cm^{-1}).[275] The nitrosyl bond angle in **28** with ∢(Re-N-O) = 170.6° on the other hand is much closer to linear NO$^{+/0}$, than to bent NO$^–$ (∢(NO) = 120°), which was termed as one of the main criterions for determining the electronic character of nitrosyl ligands. However there is in general no clear correlation between the IR stretch and the M-N-O bond angle of nitrosyl ligands.[300,362] Based on simple molecular orbital considerations bending of the NO ligand for a {MNO}^{8} complex is often encountered,[274,362] but not experimentally observed in **28**. This can potentially be ascribed to lower symmetry in **28** and consequentially lifted orbital degeneracies, so that more electrons can be "stored" in non-bonding orbitals, instead of population of N-O antibonding, ligand centered orbitals.

Complex **28** was observed as an intermediate / byproduct in several mechanistic experiments (see chapter 2.5.4), which motivated the investigation of follow-up chemistry. Five-coordinate

28 is, in contrast to dichloride complex [(^{Ph}PNP)ReCl$_2$] (**11**), considerably less Lewis-acidic, and for example does not bind THF, which is in line with the presence of two strong π-acceptor ligands. Addition of one atmosphere of NO to **28** resulted in a slow color change from orange to yellow, vanishing of the ^{31}P NMR resonance and formation of several new broad signals in the ^{1}H NMR. Yellow crystals could be obtained from this reaction mixture, however, they diffracted very poorly and were not suitable for an X-ray crystallographic measurement. In the ATR-IR of these crystals two intense stretches at ν = 1701 and 1641 cm^{-1}, as well as a weaker band at 1598 cm^{-1} were observed (see appendix). This is comparable to the number and relative intensities of the IR stretches that were observed for the related [(^{Ph}PNP)Re(CO)$_3$] by *Ozerov* and coworkers.[367] In combination with the lack of sharp resonances in the ^{1}H NMR, the formation of a trinitrosyl {Re(NO)$_3$}^{9} complex [(^{Ph}PNP)Re(NO)$_3$] from this reaction could be an explanation and can potentially explain the disappearance of [(^{Ph}PNP)Re(NO)$_2$] in the low temperature *in situ* IR and VT NMR experiments under NO atmosphere (see chapter 2.5.4). However, another possibility is the reoxidation of **28** to **26**, based on the very similar IR stretches to **26**. In addition to reactivity with NO, **28** can – in a similar manner to a report of *Berke* and coworkers – react with the Lewis acidic borane B(C$_6$F$_5$)$_3$, which binds to the oxygen terminus of one of the NO ligands, resulting in significant ligand bending (∢(Re-N-O): 133.4°, see appendix).

In conclusion, the redox chemistry of [(^{Ph}PNP)Re(NO)$_2$Cl] (**26**) was investigated, with the following findings:

1. **26** can be oxidized with outer-sphere oxidants to form the diamagnetic, cationic {Re(NO)$_2$}^{6} complex *cis*-[(^{Ph}PNP)Re(NO)$_2$Cl]$^+$ (*cis*-**27**$^+$). The oxidation selectively forms the *cis*-isomer with no structural ambiguity, which can be an indication that the starting material also consists only of the *cis*-**26** isomer.
2. In the CV another oxidation at more anodic potential was observed, suggesting that a {Re(NO)$_2$}^{5} complex is synthetically accessible. Such a complex would be expected to exhibit significantly weakened binding to NO and could be relevant in terms of photolytic NO release.
3. Irreversible reduction of **26** leads to chloride loss and formation of a rare example of a {Re(NO)$_2$}^{8} complex, [(^{Ph}PNP)Re(NO)$_2$] (**28**). The diamagnetic complex was encountered as a byproduct of mechanistic experiments regarding the nitride transfer (chapter 2.5.4) and therefore has a certain relevance to the reaction mechanism.

2.5.3 Experimental Evaluation of the Nitride Transfer Reaction

In this chapter, several additional experiments are compiled to gain information about the reaction mechanism of the nitride transfer reaction. From the reaction products it can be derived that the mechanism consists of several steps and intermediates can potentially be synthetically accessed or spectroscopically observed.

Mayer and coworkers reported that CCl_4 can prevent the formation of an Osmium nitrosyl complex from nitric oxide coordination by chlorine atom transfer, resulting in the exclusive formation of [$TpOsCl_3$].[257] This requires and therefore implies a Lewis-acidic, five-coordinate intermediate, that formally abstracts a chlorine atom from CCl_4. It was envisioned that low-valent intermediates of the nitride transfer from [(^{Ph}PNP)Re(N)Cl] (**15**) to nitric oxide could be trapped by CCl_4 and indirectly unveil information about the reaction mechanism.

The reaction of **15** with one atmosphere of nitric oxide in CD_2Cl_2/CCl_4 (4:1) resulted in a rapid color change within seconds to intense forest green (Figure 2.23). Appearance of very broad signals in the ^{1}H NMR spectrum and vanishing of the ^{31}P{^{1}H} NMR resonance of **15** indicated the formation of a paramagnetic species. Single crystals suitable for X-ray crystallography were grown over the course of several days from CH_2Cl_2/Et_2O at –40 °C. The solid-state structure indicated the formation of {ReNO}^{5} complex *cis*-[(^{Ph}PNP)Re(NO)Cl_2] (*cis*-**14**), which was isolated as the reaction product after workup in 84% yield as a green solid. The formation of *cis*-**14** as the exclusive product of the reaction in presence of CCl_4 indicates the intermediacy of the five-coordinate intermediate [(^{Ph}PNP)Re(NO)Cl], which abstracts a chlorine atom from CCl_4 or in absence thereof reacts with NO to [(^{Ph}PNP)Re$(NO)_2$Cl]. Although complexes of the ^{Ph}PNP ligand appear to favor octahedral over five-fold coordination, the few examples of five-coordinate ^{Ph}PNP complexes are stabilized by strong π-donor and/or π-acceptor ligands (e.g. [(^{Ph}PNP)Re(N)Cl], [(^{Ph}PNP)Re$(CO)_2$][374] or [(^{Ph}PNP)Re$(NO)_2$]). Accordingly, [(^{Ph}PNP)Re(NO)Cl] might be stable or even isolable.

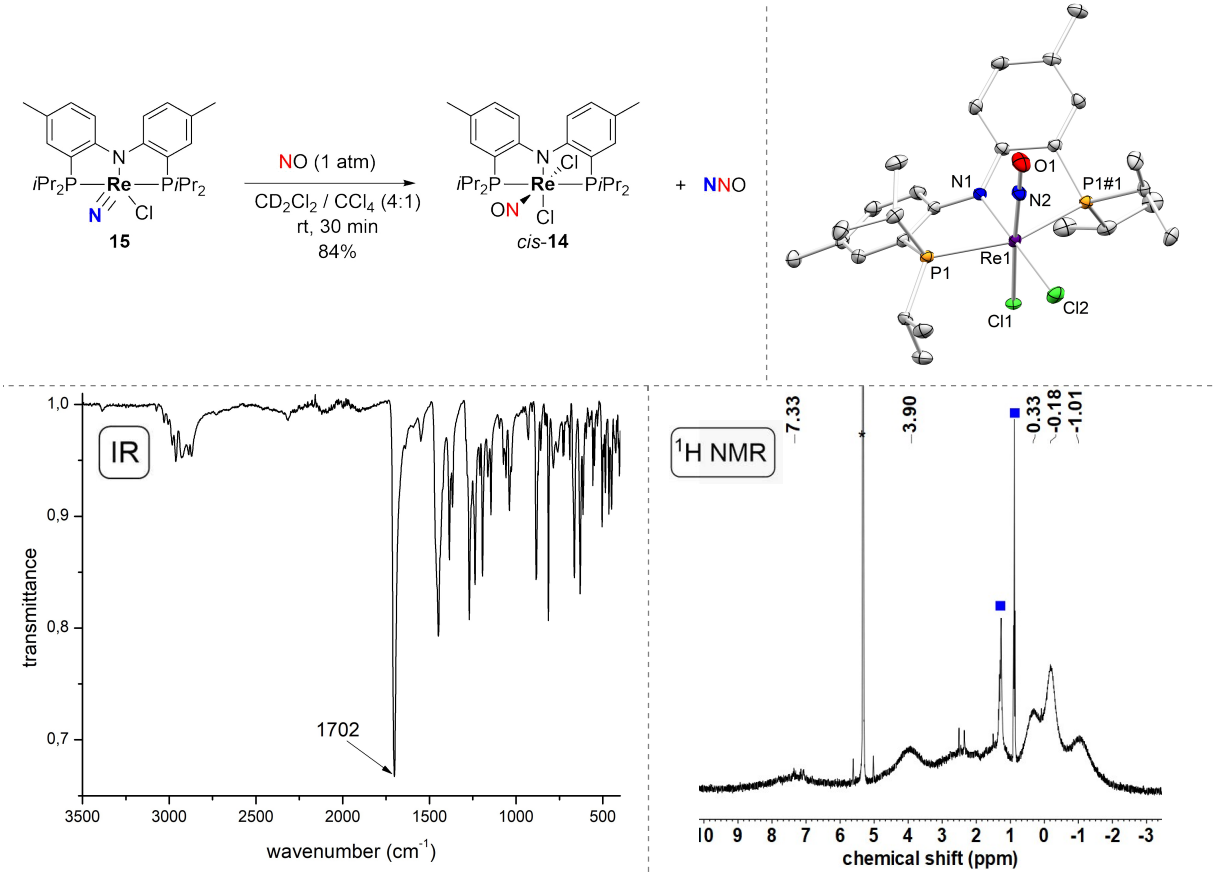

Figure 2.23: Top left: Reaction of Re^{V} nitride **15** with nitric oxide in CD_2Cl_2/CCl_4 to yield $\{ReNO\}^5$ complex *cis*-**14**, as well as nitrous oxide. Top right: Molecular structure of *cis*-**14** from single-crystal X-ray diffraction (thermal ellipsoids drawn at the 50% probability level); hydrogen atoms are omitted for clarity. Selected bond lengths [Å] and angles [°]: Re1-N2 1.797(7), N2-O1 1.184(7), Re1-Cl1 2.354(2), Re1-Cl2 2.3941(8), Re1-N1 2.050(3), Re1-P1 2.4495(6), Re1-N2-O1 178.2(8), N1-Re1-Cl2 90.76(5), P1-Re1-P1#1 157.17(3), Cl1-Re1-N2 177.2(3). Bottom left: Infrared (ATR, solid) spectrum of crystalline *cis*-**14**. Bottom right: ^{1}H NMR spectrum of a saturated solution of *cis*-**14** in CD_2Cl_2. The solvent signal is marked with an asterisk and residual pentane is marked with a blue rectangle.

The N-O bond length (d_{NO} = 1.184 Å) in the solid-state structure of *cis*-**14**, as well as the essentially linear coordination geometry of the nitrosyl ligand (∢(Re-N-O): 178.2°) are in the common range of other $\{ReNO\}^5$ complexes (d_{NO}: 1.12–1.26 Å, ∢(Re-N-O): 171.9–180°).[362] One very intense stretch in the IR (ATR) of crystalline *cis*-**14** at ν_{NO} = 1702 cm^{-1} ($\nu_{NO,DFT}$ = 1731 cm^{-1}) was observed, indicating weak backbonding into the nitrosyl π^*-orbitals, which again is in good agreement with the IR band of previously reported $\{ReNO\}^5$ complexes (ν_{NO} = 1660 – 1770 cm^{-1}) and confirms the presence of only one nitrosyl ligand.[362] The synthesis of *cis*-**14** was further verified by elemental analysis and LIFDI mass spectrometry. The concurrent formation of nitrous oxide upon nitride transfer was verified *via* ^{15}N NMR spectroscopy (see chapter 2.5.6).

In solution, *cis*-**14** exhibits a magnetic moment of μ_{eff} = 1.69 ± 0.1 μ_B, which is indicative of a S = ½ ground state and explains the severely broadened signals in the ^{1}H NMR spectrum. The

magnetic properties were further investigated in the solid-state by SQUID magnetometry (Figure 2.24), which showed constant susceptibility over a wide temperature range (μ_{eff} = 1.85 μ_B at 295 K) and a strong decrease at low temperature. In the X-band EPR spectrum at room temperature in dichloromethane solution, a six-line pattern was observed and could be simulated with Re HFI (g_{iso} = 1.996, A_{iso}(Re) = 782 MHz, Figure 2.24). Due to the large linewidth no further HFI was resolved and DFT calculations predicted similar EPR parameters (g_{DFT} = 1.999, A_{DFT} = 626 MHz).

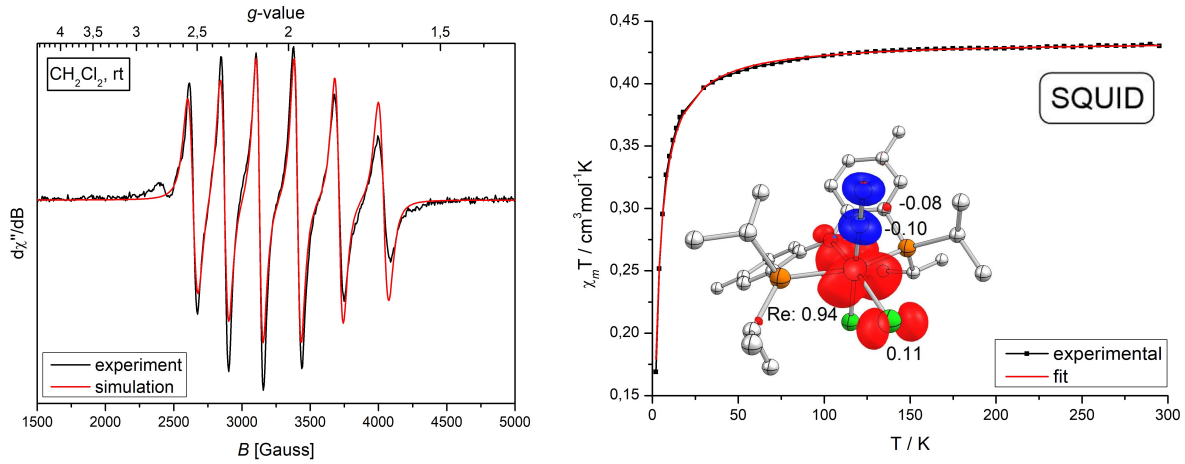

Figure 2.24: Left: X-band EPR of *cis*-**14** (black trace) at room temperature in CH_2Cl_2 and simulation (red trace). Simulation and technical parameters: g_{iso} = 1.996, A_{Re} = 782 MHz, Gaussian broadening: 9.9 MHz, Lorentzian broadening: 50.6 MHz, microwave frequency: 9.410 GHz, microwave power: 1.564 mW, modulation frequency: 100 kHz, modulation amplitude: 4.00 G, conversion time: 81.92 ms, time constant: 20.48 ms. Right: $\chi_M T$ vs. T plot of *cis*-**14**. Fitting parameters: g = 2.153, D = 0, TIP = 10.4·10^6 cm^3·mol^{-1}. Inset: Spin density plot (PBE0/SARC-Zora-TZVP;def2-TZVP) of *cis*-**14**. The red isosurface represents excess α spin (positive sign) and the blue isosurface represents excess β spin density (negative sign).

The experimentally observed Re HFI corresponds to a spin density of 2.2% in a Re 6s orbital and the predominant metal contribution is well reproduced by spin density analysis (PBE0/SARC-Zora-TZVP(Re);def2-TZVP), placing 94% spin density in Rhenium centered orbitals orthogonal to the NO bond axis and minor spin polarization on the NO ligand (Figure 2.24).[357] The electronic structure description derived from SQUID, EPR and DFT is in good agreement with the simplified MO considerations for linear nitrosyl complexes, which also predict the SOMO to be the metal-centered d_{xy} orbital (c.f. Figure 2.5).[107] Unfortunately, in the X-band EPR spectrum of *cis*-**14** in frozen CH_2Cl_2, a signal was barely resolved and the poor solubility of *cis*-**14** in any non-chlorinated solvents or glassing agents prevented satisfying low temperature EPR spectroscopy and resolution of potential *g*-anisotropy and smaller HFI contributions.

The formation of the mononitrosyl complex could not be prevented by performing the reaction in neat CCl_4 or CH_2Cl_2 or in presence of NCS, indicating that binding of one NO occurs on an earlier stage of the reaction mechanism compared to abstraction of a chloride from CCl_4. The exclusive formation of *cis*-**14** in presence of CCl_4 furthermore implies that chlorine atom abstraction of [(^{Ph}PNP)Re(NO)Cl] is preferred over reaction with another nitric oxide equivalent.

cis-**14** was envisioned as a platform to explore nitrosyl dissociation or functionalization with the aim to regenerate a Re^{IV} or Re^{III} species like [(^{Ph}PNP)$ReCl_2(NO_2)$] or even [(^{Ph}PNP)$ReCl_3$] for closing a synthetic cycle and probing the potential for catalytic nitride transfer to nitric oxide. Unfortunately, no reactivity of *cis*-**14** towards air, excess Me_3NO (for nitrosyl oxygenation) or $TMSN_3$ (formation of a nitride) was observed. Unselective decomposition was detected by irradiation in the presence of *N*-chlorosuccinimide in CD_2Cl_2/CCl_4 at λ_{max} = 305 nm for several hours and by reaction with *m*CPBA, with no evidence for the formation of [(^{Ph}PNP)$ReCl_3$]. Furthermore, no product could be isolated from the reactions of *cis*-**14** with *n*Bu_4NOH or KOH/18-crown-6, rather indicating chloride to hydroxide exchange according to mass spectrometry.

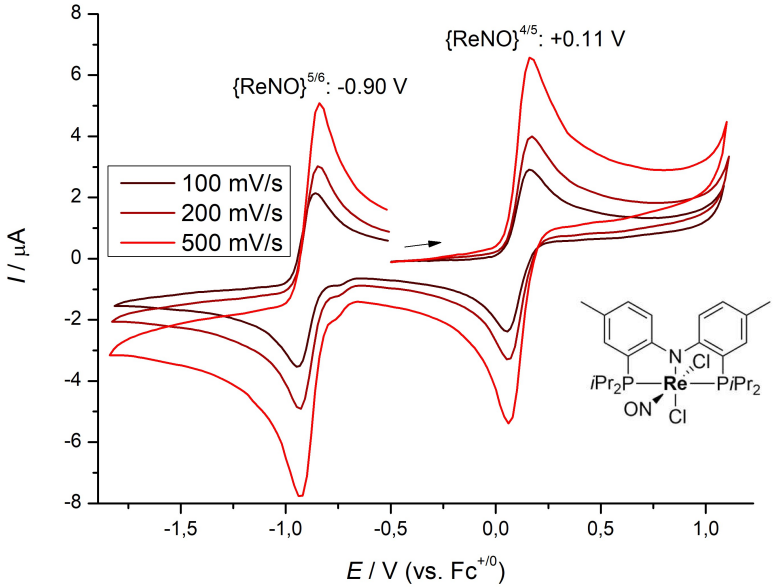

Figure 2.25: Left: Scan-rate dependent cyclic voltammograms of *cis*-**14** in THF (1 mM *cis*-**14**, Ar, 0.2 M *n*Bu_4NPF_6).

According to the infrared spectrum, reduced π-backbonding to the nitrosyl ligand in *cis*-**14** should result in a weakened Re-NO bond (compare $\nu(NO_{gas})$ = 1875 cm^{-1}). As the π-backbonding correlates with electron density on the metal, oxidation leads to less tightly bound nitrosyl ligands (and higher wavenumbers) and could be used to release NO from the

rhenium complex. This is reflected in literature, where most transition metal complexes that exhibit (photo)dissociation of NO show IR stretches above ν = 1720 cm^{-1}.[365,375,376] However, the electronic structure of metal-nitrosyl complexes and its implications on bond strength are complex and can not be simplified to one parameter. For example, the {MnNO}^{6} complex [Mn(PaPy$_3$)(NO)]$^+$ (PaPy$_3^-$ = *N*,*N*-bis(2-pyridylmethyl)amine-*N*-ethyl-2-pyridine-2-carboxamide) exhibits an intense IR stretch at ν = 1733 cm^{-1} and releases NO at low-energy visible light (λ = 500–600 nm), whereas complexes with higher wavenumber IR stretches do not show photorelease of NO.[365]

In the cyclic voltammogram of *cis*-**14** (Figure 2.25) in THF a reversible oxidation at $E_{1/2}$ = +0.11 V and a reversible reduction at $E_{1/2}$ = –0.90 V were observed. The mild potentials prompted the exploration of the cationic and anionic mononitrosyl complexes. Reaction of *cis*-**14** with one-electron oxidants like [AcFc][X] (X = BF_4, OTf, [Al(OC(CF$_3$)$_3$)$_4$]) or Ag^I salts resulted in an immediate color change to the extraordinarily intensely purple colored {ReNO}^{4} complex [(^{Ph}PNP)Re(NO)Cl$_2$][OTf] (*cis*-**29^{OTf}**) (very similar to permanganate in color and intensity), according to the solid-state structure (Figure 2.26). Following the reaction *via* UV-Vis spectroelectrochemistry showed a clean conversion from *cis*-**14** to *cis*-**29$^+$**, evident from three isosbestic points. In the IR spectrum, oxidation is accompanied by a relatively small hypsochromic shift of the NO stretch of 44 cm^{-1} (to ν_{NO} = 1746 cm^{-1}). Interestingly, an EPR signal was obtained from analytically pure material, which significantly differs in its simulated parameters (g_{iso} = 1.999, A_{iso}(Re) = 430 MHz) from the starting material *cis*-**14**. On several occasions, however, sharp, *J*-resolved ^{31}P{^{1}H}-, as well as ^{1}H NMR spectra were obtained. It therefore remains questionable, whether the same species was present in these measurements. Moreover, *cis*-**29$^+$** showed decay, as solutions of *cis*-**29$^+$** in apparently pure solvent (e.g. THF) turned gradually green upon standing for several hours, which could either indicate re-reduction to *cis*-**14** or another reactivity like hydrogen atom transfer.

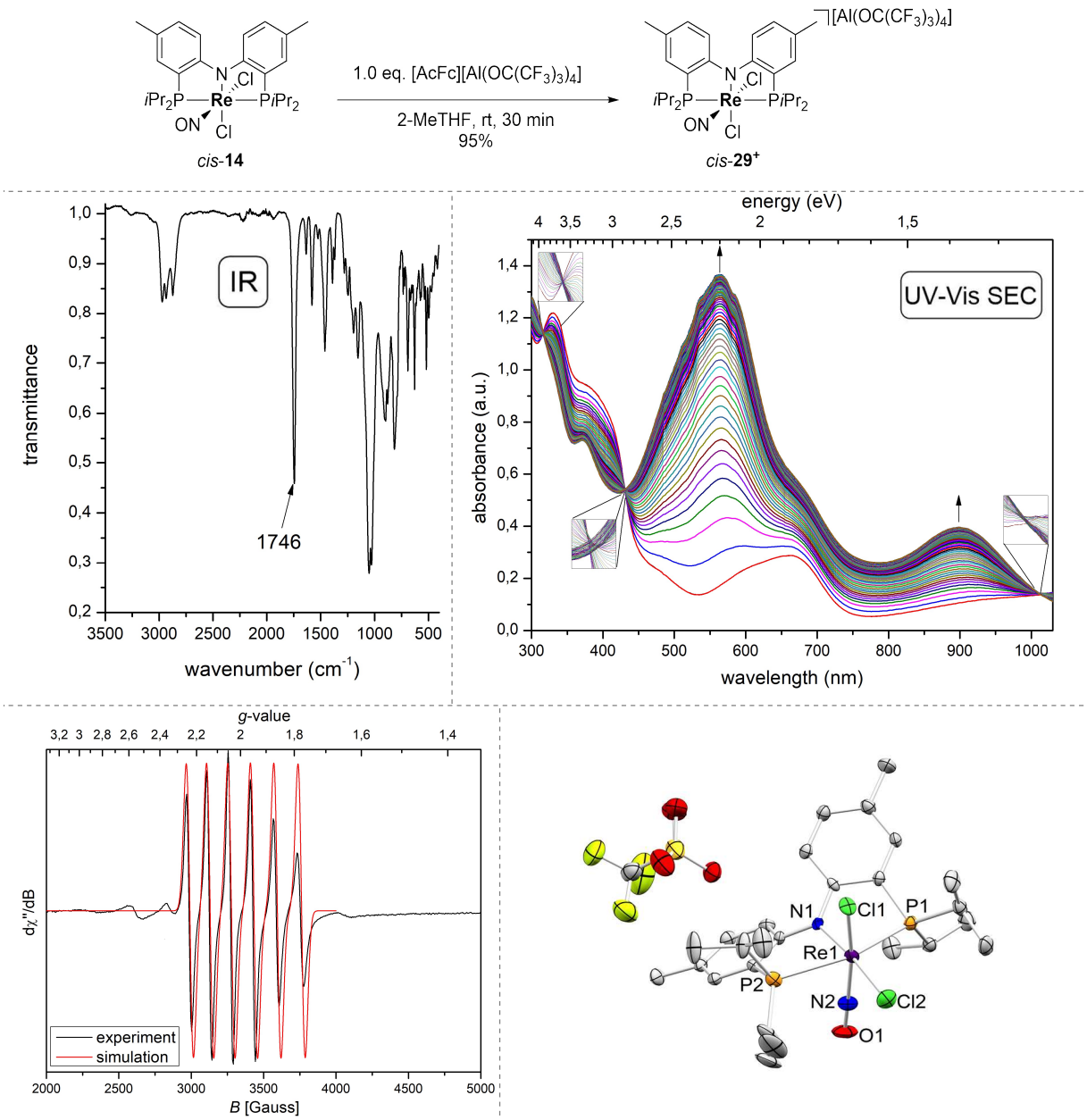

Figure 2.26: Top: Oxidation of *cis*-**14** in 2-MeTHF to form the cationic $\{ReNO\}^4$ complex [(^{Ph}PNP)Re(NO)Cl$_2$][Al(OC(CF$_3$)$_3$)$_4$] (*cis*-**29**$^{Al(OC(CF3)3)4}$). Mid left: ATR-IR (solid) of crystalline *cis*-**29**^{OTf}. Mid right: UV-Vis spectroelectrochemistry of the oxidation of *cis*-**14** to *cis*-**29**$^+$ in THF under argon atmosphere. The red line is recorded at t = 0 s and the interval between the traces is 10 seconds. Bottom left: X-band EPR spectrum (black trace) and simulation (red trace) of the product of the oxidation of *cis*-**14** with [AcFc][Al(OC(CF$_3$)$_3$)$_4$] in 2-MeTHF at room temperature. Simulation and technical parameters: g_{iso} = 1.999, A_{iso}(Re) = 430 MHz, microwave frequency: 9.4150 GHz, microwave power: 9.872 mW, modulation frequency: 100 kHz, modulation amplitude: 4.00 G, conversion time: 81.92 ms, time constant: 20.48 ms. Bottom right Molecular structure of *cis*-**29**^{OTf} from single-crystal X-ray diffraction (thermal ellipsoids drawn at the 50% probability level); hydrogen atoms are omitted for clarity. Selected bond lengths [Å] and angles [°]: Re1-N1 2.028(8), N2-O1 1.218(18), Re1-Cl2 2.357(6), Re1-Cl1 2.368(10), P1-Re1-P2 157.0(3), Cl1-Re1-N2 178.6(10), Cl2-Re1-N1 171.6(4).

Attempts, to selectively eliminate the nitrosyl ligand from *cis*-**29**$^+$ were unsuccessful. Irradiation of *cis*-**29**$^+$ in CD_2Cl_2/CCl_4 with a Xenon lamp and a band pass filter at $\lambda = 337$ nm did not result in any observable change. Irradiation with a cut-off filter at $\lambda > 305$ nm, however, led to unselective decomposition, as judged by ^{1}H NMR and IR spectroscopy. Thermal extrusion of NO was attempted in a solution of *cis*-**29**$^+$ in CD_3CN/CCl_4 at 80 °C over night under static vacuum. Again, unselective decomposition was observed according to the ^{1}H NMR spectrum, but in the IR spectrum, a weak, broadened band at $\nu = 1711$ cm^{-1} indicated formation of a new, nitrosyl containing species (c.f. ν_{NO}(*trans*-**14**): 1710 cm^{-1}). No appreciable amounts of [(^{Ph}PNP)ReCl$_3$] could be detected. Finally, the stability of [(^{Ph}PNP)ReCl$_3$] (**9**) under an atmosphere of nitric oxide was tested to investigate, whether a chemical cycle involving the regeneration of [(^{Ph}PNP)ReCl$_3$] from an nitrosyl complex, can be closed. Upon addition of NO, the color rapidly changed to brown and ^{1}H NMR spectroscopy indicated unselective formation of numerous products. The IR spectrum suggested the formation of *trans*-**14** as the predominant species, which highlights, that reactions with NO can involve complex redox processes. This result shows, that a chemical cycle can not be closed under an atmosphere of nitric oxide, as the starting trichloride complex [(^{Ph}PNP)ReCl$_3$] would directly react unselectively with NO. Other approaches to prevent the formation of an NO complex in the first place would be necessary to obtain a closed chemical cycle.

Mayer and coworkers used [TpOsCl$_2$OTf]$^-$ as a surrogate to probe their hypothesis of the intermediacy of "[TpOsCl$_2$]" in the nitride transfer to nitric oxide.[257] It was therefore of interest, whether [(^{Ph}PNP)ReCl$_2$] (**11**) would be an intermediate in the reaction of [(^{Ph}PNP)Re(N)Cl] (**15**) with nitric oxide in CH_2Cl_2/CCl_4 for the formation of *cis*-**14**. It was reported in chapter 1.5.2, that the evidently Lewis-acidic **11** could not be isolated, but rather was prepared *in situ* by reduction of [(^{Ph}PNP)ReCl$_3$] with CoCp$_2$. If addition of nitric oxide to **11** would result in the formation of *cis*-**14**, it could be concluded, that **11** is an intermediate of the reaction. Consequently, [(^{Ph}PNP)ReCl$_3$] (**9**) was reduced with one equivalent of CoCp$_2$ and after the characteristic red-brown color, which was tentatively assigned to **11**, had developed, nitric oxide was added to the suspension in fluorobenzene. After stirring for 15 minutes at room temperature the color had changed to deep green and NMR spectroscopy of the crude reaction mixture indicated the formation of a paramagnetic species, which did not match with the signals observed from *cis*-**14**.

In the solid state structure, obtained from X-ray crystallography, the formation of *trans*-**14** was evident (Figure 2.27). In the solid state structure, the pincer nitrogen- and rhenium atoms, as well as the nitrosyl ligand lie on a crystallographic two-fold axis of the orthorhombic Fdd2 space group, resulting in a perfectly linear (∢(Re-N-O) = 180.0°) coordination geometry. The N-O bond length is equal (d_{NO} = 1.184 Å) to the respective bond length of the nitrosyl ligand in *cis*-**14** and the Re-N_{pincer} bond in *trans*-**14** is noticeably longer (Δd = 0.057 Å) than in *cis*-**14**. In the infrared spectrum (Figure 2.27, ATR, solid), *trans*-**14** exhibits one intense stretch at ν_{NO} = 1710 cm^{-1}, which is a hypsochromic shift of 8 cm^{-1} compared to *cis*-**14**.

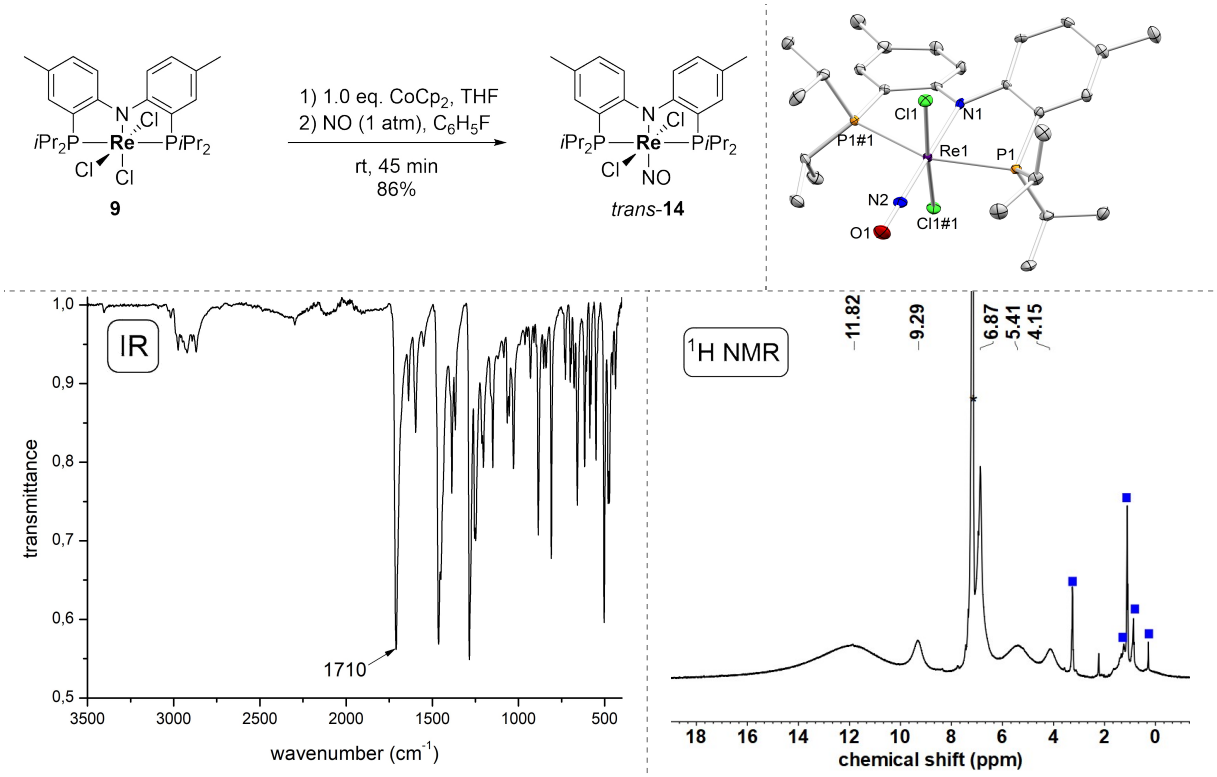

Figure 2.27: Top left: Reaction of Re^{IV} trichloride complex **9** with cobaltocene and nitric oxide to form $\{ReNO\}^5$ complex *trans*-**14** in 86% isolated yield. Top right: Molecular structure of *trans*-**14** from single-crystal X-ray diffraction (thermal ellipsoids drawn at the 50% probability level); hydrogen atoms are omitted for clarity. Selected bond lengths [Å] and angles [°]: Re1-N2 1.777(8), N2-O1 1.184(9), Re1-N1 2.107(9), Re1-Cl1 2.3647(8), Re1-P1 2.4799(10), Re-N2-O1 180.0, N1-Re1-N2 180.0, P1-Re1-P1#1 157.07(5), Cl1-Re1-Cl1#1 174.29(6). Bottom left: Infrared spectrum (ATR, IR) of crystalline *trans*-**14**. Bottom right: ^{1}H NMR spectrum of *trans*-**14** in C_6D_6 at room temperature. Solvent signal is marked with an asterisk and residual pentane, Et_2O and silicon grease are marked with blue boxes.

The magnetic moment in solution (μ_{eff} = 1.69 ± 0.1 μ_B) and the characteristic, broad six line pattern caused by Re HFI (g_{iso} = 2.049, A_{iso}(Re) = 967 MHz, 2.7% spin density in Re 6s orbital)[357] in the X-band EPR spectrum of *trans*-**14** are in agreement with a S = ½ ground state (Figure 2.28). These isotropic EPR parameters indicate predominant metal contribution to the spin density, which was also predicted by DFT calculations (PBE0/SARC-Zora-TZVP(Re);def2-TZVP, >99% spin density on Re) and MO considerations.[107] The low

temperature EPR spectrum in 2-MeTHF glass at 141 K was significantly more complex than the room temperature spectrum. No satisfactory simulation could be obtained, however, a global best-fit was obtained, matching the shape of the main signals (Figure 2.28, right). This fit exhibits moderate g-anisotropy (g_x = 1.994, g_y = 1.996, g_z = 1.91) and significant, approximately axial anisotropy of the Re HFI (A_x = 1414 MHz, A_y = 250 MHz, A_z = 1450 MHz). Contribution of other nuclei to the HFI could not be simulated properly and overall led to worse match with the experimental data. However, especially in the region between 3100 and 4000 Gauss, contribution of ^{31}P nuclei could potentially explain the unresolved splitting pattern.

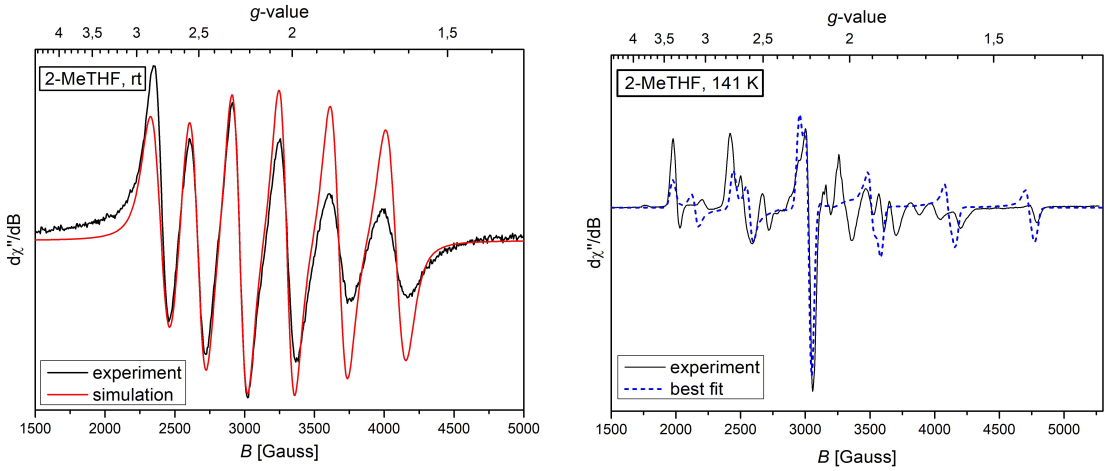

Figure 2.28: Left: X-band EPR spectrum of *trans*-**14** (black trace) in 2-MeTHF at room temperature and simulation (red trace). Simulation and technical parameters: g_{iso} = 2.049, A_{iso}(Re) = 967 MHz, Gaussian broadening: 61.6 MHz, Lorentzian broadening: 79.4 MHz, microwave frequency: 9.415 GHz, microwave power: 9.882 mW, modulation frequency: 100 kHz, modulation amplitude: 4.00 G, conversion time: 163.84 ms, time constant: 40.96 ms. Right: X-band EPR spectrum of *trans*-**14** in 2-MeTHF glass at 141 K (black trace) and global best-fit (dotted blue trace). Fit and technical parameters: g_x = 1.994, g_y = 1.996, g_z = 1.91, A_x = 1414 MHz, A_y = 250 MHz, A_z = 1450 MHz, Gaussian broadening: 40 MHz, microwave frequency: 9.428 GHz, microwave power: 9.870 mW, modulation frequency: 100 kHz, modulation amplitude: 4.00 G, conversion time: 163.84 ms, time constant: 40.96 ms.

The exclusive formation of *trans*-**14** from "[(^{Ph}PNP)ReCl$_2$]" and NO and the formation of *cis*-**14** from [(^{Ph}PNP)Re(N)Cl] and NO in presence of CCl_4 raised the question, whether one of the two isomers is the thermodynamic product and if isomerization is thermally or photochemically accessible. DFT calculations (PBE0/SARC-Zora-TZVP(Re);def2-TZVP) placed the *cis*-isomer 2.3 kcal·mol^{-1} lower in energy. Isomerization of *trans*-**14** into *cis*-**14** was not observed upon heating of *trans*-**14** in THF to 65 °C for one day. However, irradiation of a THF solution of *trans*-**14** with an LED lamp at λ_{max} = 427 nm resulted in the precipitation of crystalline, barely THF-soluble *cis*-**14** in essentially quantitative yield (95% yield). This is in agreement with *cis*-**14** being the thermodynamic product and indicates an isomerization barrier, which is not thermally accessible (at least under the conditions that were tested) but can be overcome by irradiation. Overall, the intermediacy of the [(^{Ph}PNP)ReCl$_2$] complex **11** in the

nitride transfer reaction can be excluded based on the fact, that *trans*-**14** instead of *cis*-**14** was formed upon addition of NO.

Synthetic access to the presumed intermediate of the nitride transfer [(^{Ph}PNP)Re(NO)Cl] could enable direct reaction with NO and CCl_4 to further verify its intermediacy. A chlorine atom abstraction - reduction sequence starting from one of the two mononitrosyl isomers **14** was envisioned to form [(^{Ph}PNP)Re(NO)Cl]. Addition of $TlPF_6$ to *trans*-**14**, however, did not result in any appreciable change in the NMR. In the CV's of *cis*-**14** (cf. chapter 2.5.3) and *trans*-**14** (Figure 2.29) reversible $\{ReNO\}^{5/4}$ reductions at $E_{1/2}$ = –0.90 and –0.83 V, respectively, were observed. Addition of the strong reductant $CoCp^*_2$ to a green, stirring solution of *trans*-**14** or *cis*-**14** resulted in a rapid color change to pale orange. Slow diffusion of pentane into a saturated THF solution resulted in the formation of pale needles over night. In compliance with the reversibility of the reduction in the CV, the solid-state structure confirmed the formation of the anionic $\{ReNO\}^6$ complex [$CoCp^*_2$][*cis*-{(^{Ph}PNP)Re(NO)Cl_2}] (*cis*-**30**$^-$). Furthermore, the *cis*-isomer configuration was confirmed, indicating a reduction-induced isomerization starting from *trans*-**14**. Unfortunately, while the connectivity of atoms was derived from the solid-state structure, no satisfying refinement could be obtained, which prevents discussion of bond lengths and angles.

cis-**30**$^-$ exhibits sharp signals with resolved *J*-coupling in the ^{1}H NMR spectrum and a singlet in the ^{31}P NMR spectrum (δ_{31P} = 25.6 ppm). In the IR spectrum an intense stretch at ν = 1632 cm^{-1} was observed, which corresponds to a bathochromic shift of 70 cm^{-1} upon reduction from *cis*-**14** and 78 cm^{-1} from *trans*-**14**. This is at the lower end of the typical range for $\{ReNO\}^6$ complexes, which are typically found between ν_{NO} = 1640 and 1760 cm^{-1}.[362] Unfortunately, addition of one equivalent of $TlPF_6$ to *cis*-**30**$^-$ resulted in the formation of several peaks in the ^{31}P{^{1}H} NMR, indicative of an unselective reaction. Scanning of different reaction conditions (dilution, temperature, solvent) did not improve the selectivity as judged by ^{31}P{^{1}H} NMR and, furthermore, no species could be isolated from the reaction mixture.

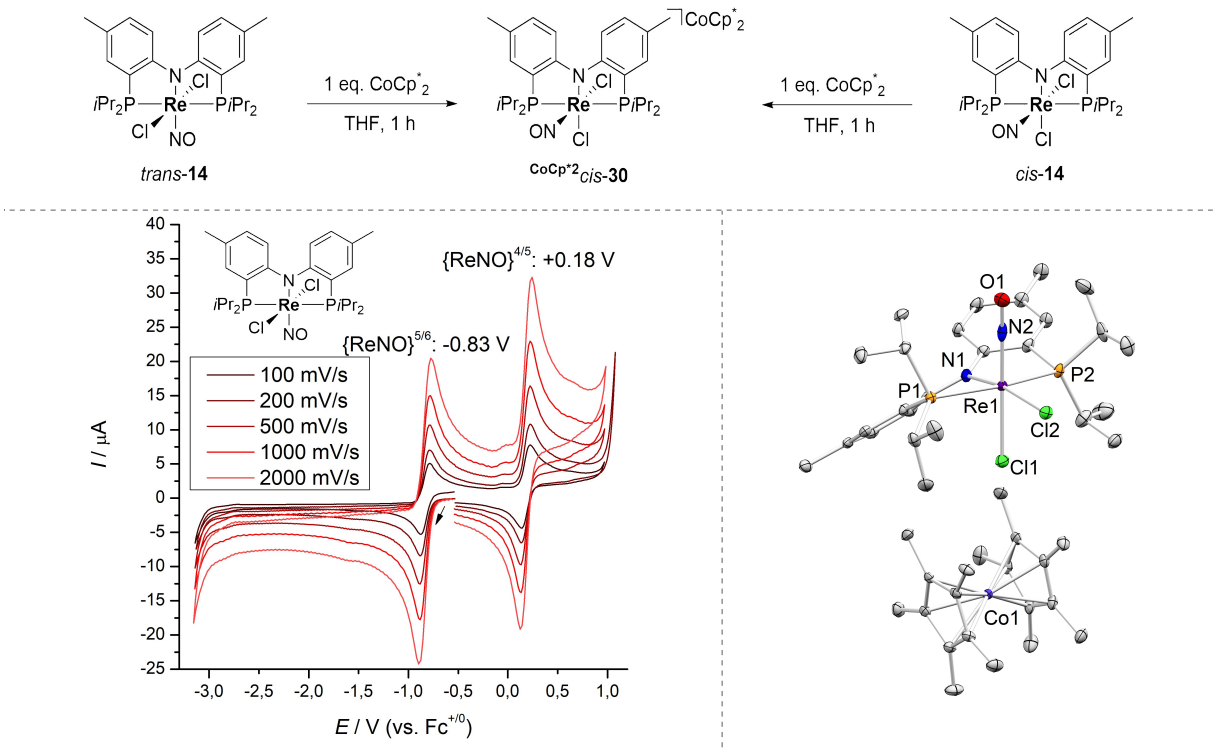

Figure 2.29: Top: Reaction of $\{ReNO\}^5$ complex *trans*-**14** with $CoCp^*_2$ to form the $\{ReNO\}^6$ complex *cis*-**30**$^-$ upon reduction-induced isomerization. Bottom left: Cyclic voltammogram of *trans*-**14** in THF under argon atmosphere (1 mM *trans*-**14**, Ar, 0.2 M nBu$_4$NPF$_6$). Bottom right: Molecular structure of *cis*-**30**$^-$ from single-crystal X-ray diffraction (thermal ellipsoids drawn at the 50% probability level). No satisfying refinement was possible.

Experiments to verify and/or trap intermediates of the proposed reaction mechanism of the nitride transfer reaction revealed the following information:

1. Performing the reaction of nitride **15** with NO in presence of CCl_4 led to the exclusive formation of *cis*-[(^{Ph}PNP)Re(NO)Cl$_2$] (*cis*-**14**). From this result it was rationalized that the five-coordinate [(^{Ph}PNP)Re(NO)Cl] is an intermediate, which reacts with NO (to **26**) or CCl_4 (to *cis*-**14**) depending on the reaction conditions.
2. No selective functionalization and/or NO-elimination of *cis*-**14** or its oxidation product *cis*-**29**$^+$ complex could be achieved, which would have enabled a chemical cycle. In fact, the regeneration of the [(^{Ph}PNP)ReCl$_3$] (**9**) starting complex of dinitrogen splitting was shown to be not possible under these reaction conditions (1 atm of nitric oxide), as **9** reacts unselectively with NO to form numerous nitrosyl complexes.
3. Reduction of [(^{Ph}PNP)ReCl$_3$] (**9**) with cobaltocene to form the [(^{Ph}PNP)ReCl$_2$] intermediate and subsequent addition of NO resulted in the exclusive formation of *trans*-[(^{Ph}PNP)Re(NO)Cl$_2$] (*trans*-**14**), which in turn excludes the intermediacy of [(^{Ph}PNP)ReCl$_2$] in the reaction of **15** with NO in presence of CCl_4, as the only isomer formed under these conditions is *cis*-**14**.

4. *trans*-**14** can be reduced to the anionic, diamagnetic $\{ReNO\}^6$ complex *cis*-$[(^{Ph}PNP)Re(NO)Cl_2]^-$ upon isomerization, which was subjected to subsequent chloride abstraction. Unfortunately the attempted reactions towards five-coordinate $[(^{Ph}PNP)Re(NO)Cl]$, which could be a central intermediate in the reaction mechanism, were very unselective, which could be an indication that the complex is not stable.

2.5.4 Spectroscopic Examination of the Nitride Transfer

To observe intermediates, which could give valuable information regarding the mechanism, the reaction was followed with spectroscopic methods. The reaction of **15** with nitric oxide was monitored *via* variable temperature ^1H and $^{31}P\{^1H\}$ NMR with PPh_3O and 1,3,5-trimethoxybenzene as internal standards (Figure 2.30). In the $^{31}P\{^1H\}$ NMR spectra the decay of the resonance (δ_{31P} = 50.2 ppm) of **15** over the course of approximately 196 minutes was recognizable. Furthermore, the formation of two low intensity signals around δ_{31P} = 51.5 ppm and an additional signal at δ_{31P} = 49.2 ppm already 6 minutes after addition of NO was observed. The signal at δ_{31P} = 49.2 ppm can be assigned to the dinitrosyl complex $[(^{Ph}PNP)Re(NO)_2]$ (**28**), which was observed in other mechanistic experiments as well (*vide infra*). The two resonances at δ_{31P} = 51.5 ppm remained until the end of the reaction and can therefore be assigned as minor side products. The $[(^{Ph}PNP)Re(NO)_2]$ resonance vanished with the nitride signal and could also be an intermediate (which will be discussed in the context of stoichiometric NO addition experiments, *vide infra*).

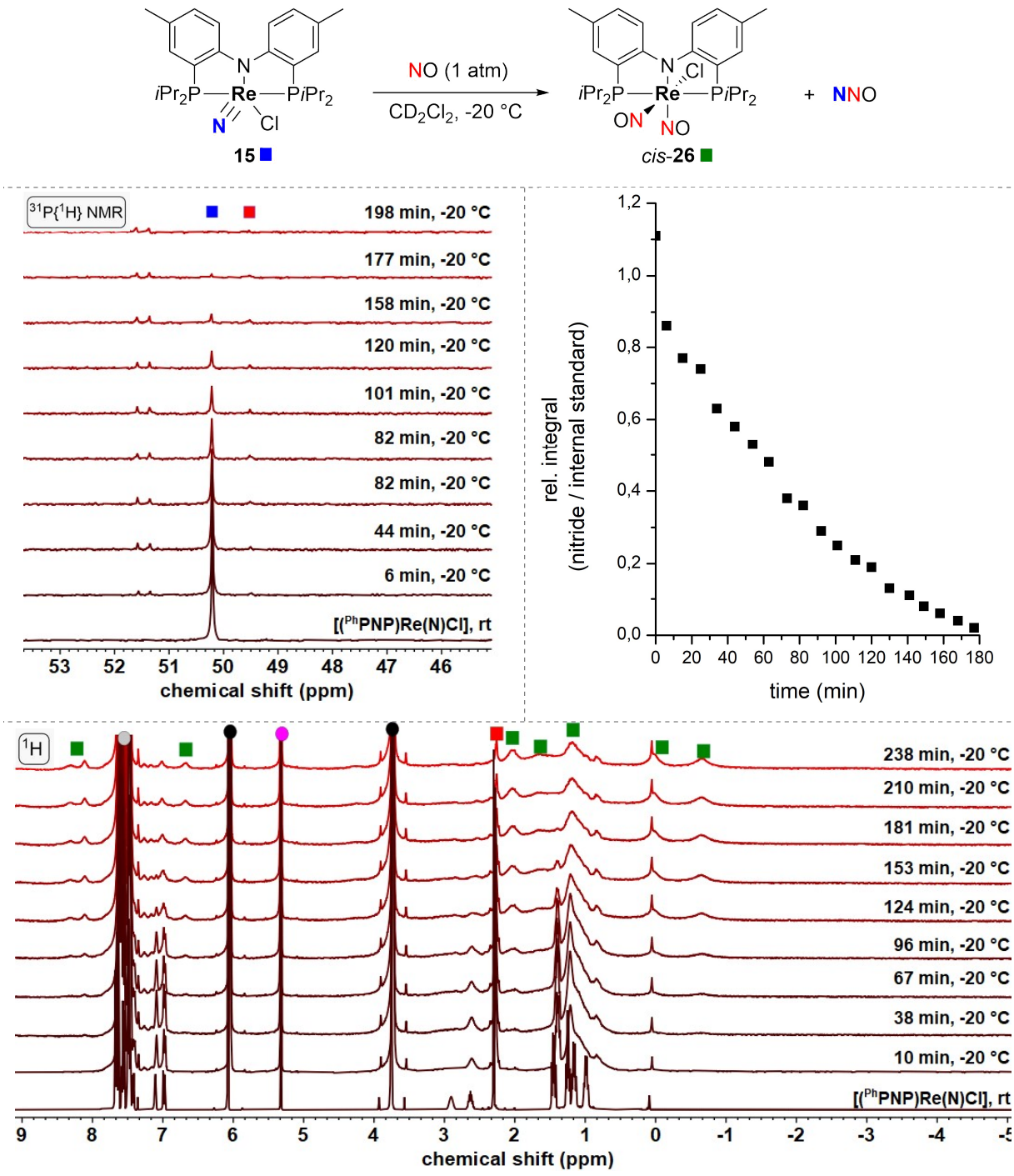

Figure 2.30: Top: Reaction of nitride **15** with NO (1 atm) in CD_2Cl_2. Mid left: Sequence of $^{31}P\{^1H\}$ NMR spectra of the reaction of **15** with NO (1 atm) in CD_2Cl_2. The signals marked with the blue rectangle correspond to the nitride complex **15** and the red rectangle marks the signal, which corresponds to the dinitrosyl complex [(^{Ph}PNP)Re(NO)$_2$] (**28**). Mid right: Plot of the relative integral ($^{31}P\{^1H\}$ NMR) of nitride **15** starting material (δ_{31P} = 50.2 ppm) vs. internal standard (PPh_3O, δ_{31P} = 27.1 ppm) against time (min). The first data point at t = 0 min was measured at room temperature and after application of NO, the *J*-Young NMR tube was inevitably warmed up for a short period of time for the transfer to the NMR spectrometer. Bottom: ^1H NMR spectra of the reaction of **15** with NO (1 atm) in CD_2Cl_2. Green rectangle: [(^{Ph}PNP)Re(NO)$_2$Cl] (**26**), red rectangle: [(^{Ph}PNP)Re(NO)$_2$] (**28**) , grey circle: PPh_3O internal standard, black circles: 1,3,5-trimethoxybenzene internal standard, violet circle: solvent signal.

The decrease of the starting material signal was – after a strong decrease from 0 to 6 minutes – approximately linear over the period of 196 minutes. Interestingly, one of the four signals of the isopropyl methyl groups at δ_{1H} = 1.4 ppm remained sharp with resolved *J*-coupling even at –20 °C after 96 minutes (Figure 2.30). The decrease of the starting material can be monitored by this resonance or the intense singlet of the benzylic CH_3 groups of the pincer ligand backbone at δ_{1H} = 2.18 ppm. The time-resolved change of the resonances in the ^{1}H NMR overall matches the observed decrease in the starting material in the ^{31}P{^{1}H} NMR spectra. Additionally, the formation of the broad resonances of the paramagnetic reaction product [(^{Ph}PNP)Re(NO)$_2$Cl] (**26**) is visible in the ^{1}H NMR spectra, with no intermediates detected.

The reaction of **15** with NO was subsequently followed at variable NO pressure to possibly gain kinetic information about the initial reaction of NO with **15**. For this, the decay of the ^{31}P{^{1}H} NMR resonance of **15** relative to an internal standard (PPh_3O) depending on the applied NO pressure (0.2, 0.4 and 0.6 atm) was monitored (Figure 2.31).

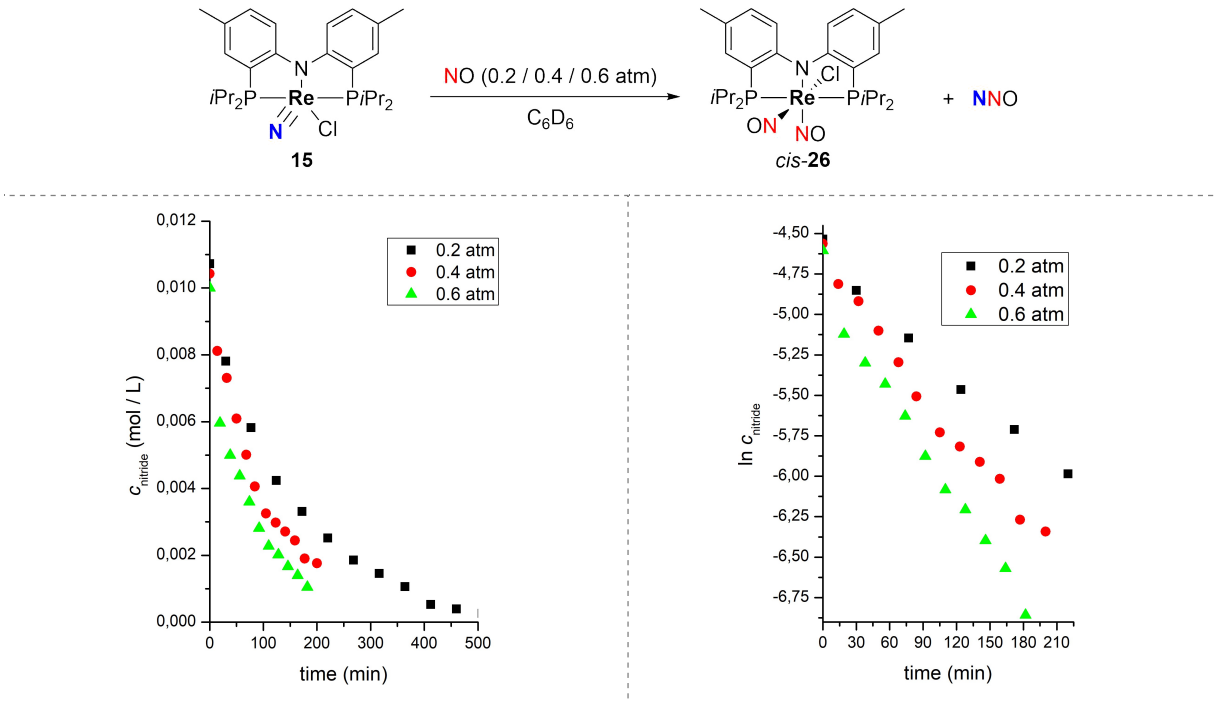

Figure 2.31: Top: NO pressure-dependent reaction of **15** with nitric oxide. Bottom left: Plot of the decay of the nitride concentration (determined by ^{31}P{^{1}H} NMR spectroscopy) vs. time. Bottom right: Plot of the natural logarithm of nitride concentration vs. time.

As expected, the rate of starting material decay increased with nitric oxide pressure (Figure 2.31). The reaction with 0.2 atm NO took 8 hours to full conversion of **15**, whereas the reaction with 0.6 bar nitric oxide was close to completion after approximately 3 hours. All three reactions showed a strong decay of starting material within the first two data points and a

reduced reaction rate afterwards (most apparent in the 0.6 atm reaction, green triangles). This could be indicative of a fast reaction of **15** with dissolved NO and, after the entire NO in the solution is depleted, the reaction rate would be limited by the rate of nitric oxide mass transport from the gas phase to the solvent. The solubility of NO in C_6H_6 is extrapolated in the literature from vapor pressure measurements as 13 mmol·L^{-1}.[275,377]

According to Henry's law, the equilibrium concentration of gas in a solution is linearly dependent on the partial gas pressure. Hence, a concentration of 2.6 mmol·L^{-1} nitric oxide at a pressure of 0.2 atm in benzene can be assumed, which is only a fraction of the starting concentration of nitride (approx. 10 mmol·L^{-1}). Accordingly, the requirements for pseudo-first order conditions are only met at NO pressures of higher than approximately 8 atm. In the example shown above it is more reasonable to assume that the dissolved NO reacts rapidly with the nitride and the reaction is subsequently limited by the rate of dissolving further NO in benzene. Additional factors for the slow reaction are 1) the small cross-section of gas and liquid in a *J*-Young NMR tube, limiting the dissolution rate further and 2) no stirring, shaking or rotating of the solution was performed, which could also explain the slower reaction compared to a stirring solution in a Schlenk flask.

Low temperature *in situ* IR spectroscopy can be a powerful tool to observe transient nitrosyl complex intermediates. Unfortunately, the employed *ReactIR* diamond probehead showed poor sensitivity in the region of interest, so that a very high nitride concentration (95.4 mmol·L^{-1}) was necessary (Figure 2.32).

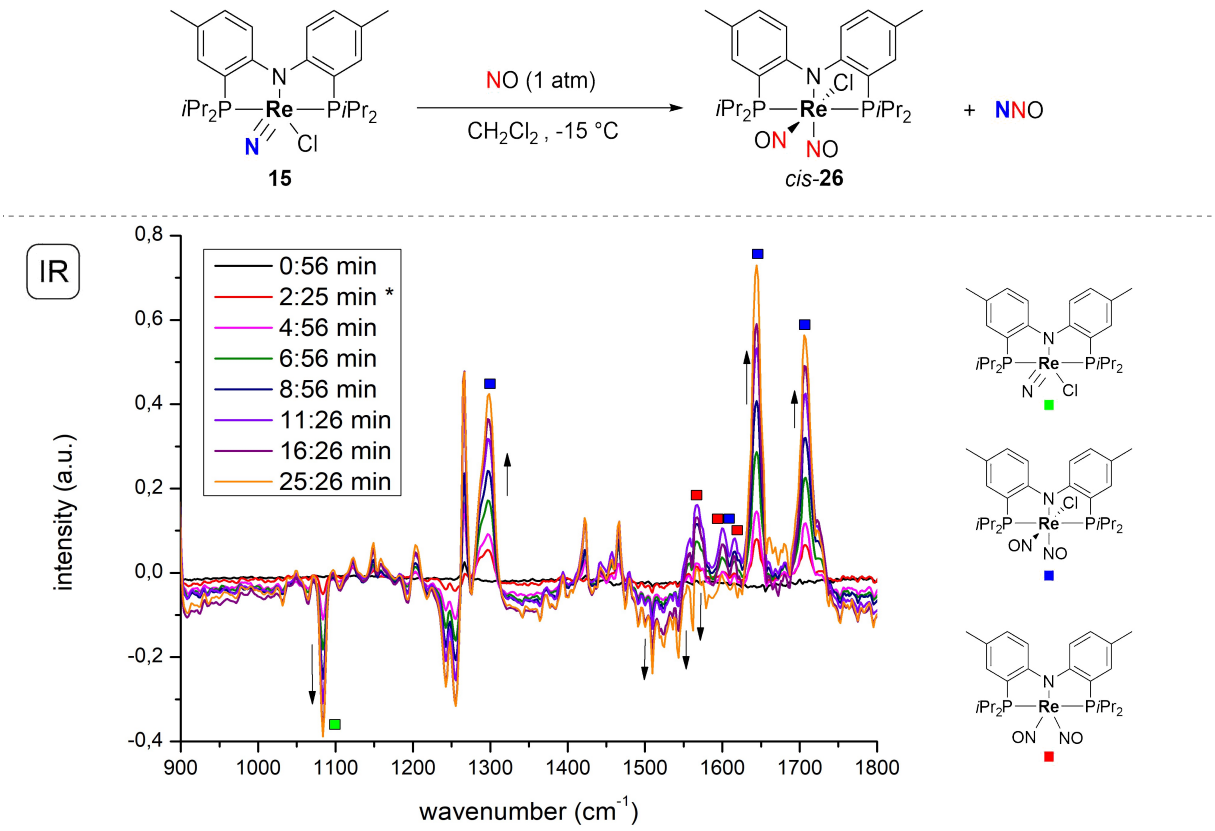

Figure 2.32: *In situ* liquid IR of the reaction of **15** with nitric oxide (1 atm) in dichloromethane at −15 °C with constant, vigorous stirring. The first recorded spectrum is a spectrum of **15** in dichloromethane before addition of nitric oxide. Every spectrum recorded afterwards is a difference spectrum with respect to the first spectrum, to show the change over time. The first spectrum after addition of NO is marked with an asterisk.

Performing the reaction of **15** with nitric oxide (1 atm) in dichloromethane at −15 °C with vigorous stirring revealed the formation of two intense bands at ν = 1644 and 1703 cm^{-1} over the course of 59 minutes, which can be attributed to **26** (from independent liquid IR measurements of **26**, a hypsochromic shift of 10 cm^{-1} with regard to the solid-state IR was confirmed). A faster reaction at slightly elevated temperature and with stirring was observed in the IR spectroscopic experiment, compared to slow, diffusion controlled reactivity in the NMR tube. Interestingly, three lower intensity bands (red rectangles, Figure 2.32) were observed to increase in intensity up to 13 minutes and decrease afterwards until the end of the experiment. These stretches can be assigned to the dinitrosyl complex [(^{Ph}PNP)Re(NO)$_2$] (**28**), which is consistent with its observation in the low temperature NMR experiment (Figure 2.30). No further stretches were observed in the range of 1500 - 2000 cm^{-1}. However, it has to be pointed out that the signal-to-noise ratio of the *in situ* IR experiment is poor, despite the high concentration, which could prevent observation of low-intensity intermediates.

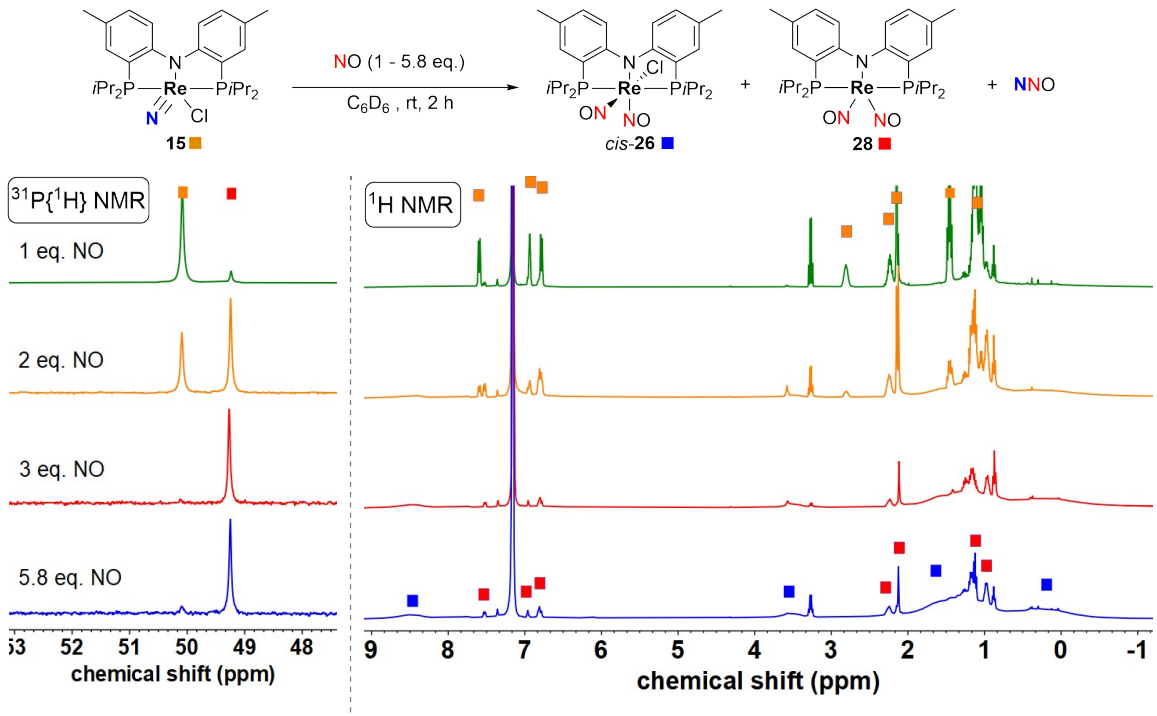

Figure 2.33: Left: $^{31}P\{^{1}H\}$ NMR spectra after reaction of **15** with the noted equivalents of nitric oxide for two hours. Right: ^{1}H NMR spectra after reaction of **15** with the noted equivalents of nitric oxide for two hours. Further sharp resonances originate from traces of diethylether and *n*-pentane upon storage of the deuterated solvent in a glovebox.

Finally, addition of stoichiometric amounts of nitric oxide to **15** and spectroscopic evaluation of the resulting products was conducted. With a gas-tight microsyringe a defined amount of nitric oxide gas was added to a stirring solution of **15** in benzene under argon. Under the assumption of nitric oxide being an ideal gas, the volumes for 1, 2, 3 and 5.8 eq. were added in independent reactions. After stirring the solutions for two hours at room temperature, the volatiles were removed under reduced pressure and the residue taken up in C_6D_6 for NMR spectroscopic examination (Figure 2.33). In the $^{31}P\{^{1}H\}$ NMR spectrum after the addition of one equivalent of NO the main resonance was still originating from the starting material **15** and a second, less intense resonance appeared at δ_{31P} = 49.2 ppm, which can be attributed to the dinitrosyl complex [(^{Ph}PNP)Re(NO)$_2$] (**28**). Interestingly, when the same reaction was conducted in presence of CCl_4 with one equivalent of NO, no other species apart from starting material **15** and product complex *cis*-[(^{Ph}PNP)Re(NO)Cl$_2$] was detected. This observation indicates that chlorine atom abstraction inhibits the side reaction to form **28**, either because it reacts earlier in the mechanism with CCl_4, or the same intermediate reacts preferably / faster with CCl_4.

Addition of two equivalents of NO to **15** in C_6H_6 led to formation of more **28**, which became the main resonance in the $^{31}P\{^{1}H\}$ NMR spectrum. In an independent quantification experiment

with an internal standard, it was derived that after addition of two equivalents of NO 16% nitride remained unconverted and 22% of **28** were formed (relative to starting material). After addition of three and 5.8 equivalents NO, no nitride starting material was left and only the resonance for **28** could be observed in the $^{31}P\{^{1}H\}$ NMR spectrum. These qualitative observations were also well reproduced by the corresponding ^{1}H NMR spectra, which showed the formation of the sharp, diamagnetic signals of **28** and additionally the extremely broad resonances of the main paramagnetic reaction product [(^{Ph}PNP)Re(NO)$_2$Cl] (**26**), with no other species present.

The complete vanishing of the nitride resonance in the $^{31}P\{^{1}H\}$ NMR upon addition of three equivalents of NO is in agreement with the proposed need of three equivalents to form the reaction products (two NO in the final rhenium complex and one equivalent is coupled with the nitride to form N_2O). The origin of the formation of **28**, however, is unclear. Experimental indications hint at a correlation between a low concentration of dissolved NO and formation of **28**, as it appeared predominantly in the stoichiometric addition of NO (Figure 2.33). For these experiments it is important to know that the NO was added to the gas space above the reaction solution and consequently reactivity with NO in C_6H_6 can be limited by mass transport into the solution, which is highly dependent on the experimental conditions (temperature, stirring). For example, **28** was observed in small percentage in the low temperature NMR reaction of **15** with NO at −20 °C in CD_2Cl_2 and in this reaction a strong decay of starting material in the time between the first two data points was observed as well, with essentially linear decay afterwards. This could be an indication that the formation of **28** is correlated to a relative shortage of NO in solution (in comparison to the gas phase) due to low solubility and a small liquid-gas phase cross-section in the NMR tube. Possibilities to avoid low relative concentration of NO with respect to rhenium complex concentration would be a more dilute rhenium concentration in a larger diameter reaction vessel with vigorous stirring and sufficient NO pressure. Accordingly, when the reaction of **15** and 1 atm NO was conducted in a Schlenk flask on a more preparative scale with high dilution, no **28** was observed.

The mechanistic aspects of the formation of **28** are intriguing. The lack of a chloride ligand in **28** suggests that an intermediate loses chloride (for example upon reduction) or that a chloride ligand is substituted by a nitric oxide molecule, which was demonstrated by the reactivity of [(^{Ph}PNP)ReCl$_3$] (**9**) with nitric oxide and the formation of *trans*-[(^{Ph}PNP)Re(NO)Cl$_2$] (*trans*-**14**) as the main product. Disproportionation of the main reaction product *cis*-[(^{Ph}PNP)Re(NO)$_2$Cl] (*cis*-**26**) into [(^{Ph}PNP)Re(NO)$_2$] (**28**) and *cis*-[(^{Ph}PNP)Re(NO)$_2$Cl]$^+$ (*cis*-**27**$^+$) can be excluded,

as no *cis*-**27**$^{+}$ was detected by NMR or IR spectroscopies. A possible hypothesis involves the initial formation of the proposed five-coordinate intermediate [(^{Ph}PNP)Re(NO)Cl], which – depending on the conditions – reacts with NO (to *cis*-**26**) or CCl_4 (to *cis*-**14**). If neither NO, nor CCl_4 is present, [(^{Ph}PNP)Re(NO)Cl] could abstract a chlorine atom from product **26**, which would result in formation of **28** (observed spectroscopically) and *cis*-**14** (co-crystallized in the solid-state structure of **26**). However, this proposed, correlated formation has to be examined in more detail to draw conclusions for the actual reaction mechanism.

Spectroscopic examination of the reaction of **15** with NO revealed the following information:

1. NMR spectroscopic investigation of the reaction at variable temperature and NO pressures revealed direct formation of the product **26** without any observed intermediates (at –20 °C).
2. The conversion of **15** with reduced pressure of NO showed, independent of the pressure, a strong decrease within the first measurement interval and afterwards a linear decay. This was attributed to low solubility of NO in organic solvents, which precludes kinetic analysis *via* NMR spectroscopy, as no pseudo-first order conditions can be reached below approximately 8 atm NO.
3. In the VT-IR experiment, as well as in stoichiometric additions of nitric oxide to **15**, the formation of another low-quantity species, independently identified as [(^{Ph}PNP)Re(NO)$_2$] (**28**), was observed and correlated to low NO concentrations in solution. Interestingly, no side product was detected if one equivalent NO was added to **15** in presence of CCl_4, indicating that chlorine atom abstraction is preferred or occurs earlier in the mechanism over the side reaction pathway forming **28**.

2.5.5 Computational Investigation of the Nitride Transfer

Scheme 2.9 summarizes a plausible minimum reaction pathway based on the experimentally and spectroscopically obtained information, which was the foundation for computational investigations. Reactivity of dimerized NO, four-coordinate intermediates and other coordination modes of N_2O or NO are not considered to simplify the reaction pathway.

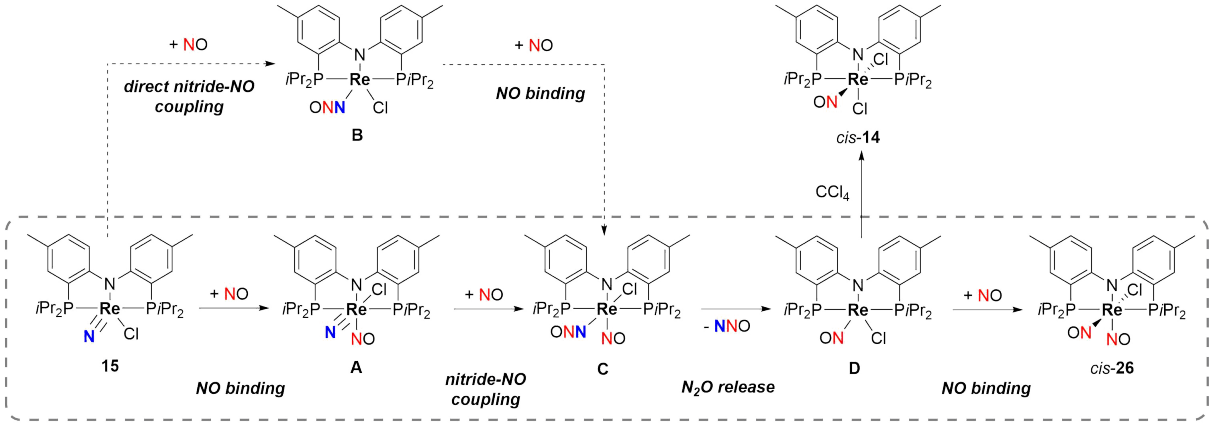

Scheme 2.9: Plausible mechanism and intermediates of the nitride transfer of Re^{V} nitride complex **15** to nitric oxide.

Starting from Re^{V} nitride **15** two possible pathways for a reaction with NO are conceivable (Scheme 2.9): On the one hand, binding of NO to the free coordination site would result in six-coordinate, formal Re^{IV} nitride nitrosyl intermediate **A**. On the other hand, direct attack of an external nitric oxide molecule at the nitride nitrogen atom forms five-coordinate nitrous oxide intermediate **B**. The coordination of NO to form intermediate **A** appears to be more likely, since an octahedral complex is formed (in contrast to five-coordinate intermediate **B**). Additionally, experimental indications (IR, mass spectrometry) from the reaction of **15** with the related ligand CO (similarly to NO a strong π-acceptor) suggest, that carbon monoxide is binding to the free coordination site of **15**, as well. The nitrous oxide ligand in intermediate **B** would be expected to be labile, possibly forming a highly Lewis-acidic four-coordinate [(^{Ph}PNP)ReCl] complex upon rapid dissociation. The observed high selectivity throughout the reaction is a clear counterindication to the formation of such a reactive intermediate.

Intermediate **A** could react with an external nitric oxide molecule at the nitride nitrogen atom, forming a nitrous oxide ligand in intermediate **C**, which alternatively can be formed upon coordination of NO to the free coordination site in intermediate **B**. The coordination of a strong π-acceptor like NO to a five-coordinate nitride in **A** should in principle deplete electron density and lower the π*-orbitals of the nucleophilic Re-nitride moiety and could lead to a rather

ambiphilic or even electrophilic reactivity of open-shell intermediate **A** with another nitric oxide molecule. Nitrous oxide release – which is, based on the lability of known N_2O complexes, expected to be facile – from **C** gives the five-coordinate intermediate [(^{Ph}PNP)Re(NO)Cl] **D**, which was deduced to be an intermediate from the formation of *cis*-[(^{Ph}PNP)Re(NO)Cl_2] (*cis*-**14**) in presence of CCl_4 (chapter 2.5.3).

The proposed minimal reaction pathway (scheme 2.9) was evaluated with the aid of DFT computations to examine the interaction between nitride complex **15** and NO. These preliminary computations on the PBE/def2-TZVP level of theory (see computational appendix) were considerably extended by *Kim Eisenlohr* from the research group of *Prof. Dr. Max Holthausen*. The range-separated hybrid functional ωB97X-D and the def2-TZVPP basis-set were employed after careful benchmarking against the explicitly correlated CCSD(T*)-F12b/cc-pVTZ-PP coupled-cluster method. The obtained results are (with permission of *Kim Eisenlohr*) displayed and discussed in this chapter.

Direct nitride-NO coupling from ^{1}**15** to a five-coordinate Rhenium N_2O complex (^{2}**B**) was found to have a high barrier of 30.2 kcal·mol^{-1} (^{D}**TS4**, Figure 2.34). In this transition state, the nitride interacts with the SOMO π* orbital of NO as evident from the angle of the interaction. The direct N-N bond formation product ^{2}**B** is 24.5 kcal·mol^{-1} higher in energy than the starting materials, rendering the direct nitride-NO coupling from ^{1}**15** highly endergonic. This is in line with the experimental observation that low-valent five-coordinate complexes of the ^{Ph}PNP ligand require π-acceptor ligands to stabilize the formally low oxidation state. Interestingly, the N_2O ligand in ^{2}**B** is significantly bent, indicating a low N-N bond order. The Wiberg bond indices, derived from natural population analysis, however, indicate a rather equal bond order distribution in the N_2O manifold (Re-N: 1.60, N-N: 1.41, N-O: 1.56). The high barrier and endergonic N-N bond formation, in contrast to experimental observations, render the direct nitride-NO coupling energetically highly unfavorable (Figure 2.34).

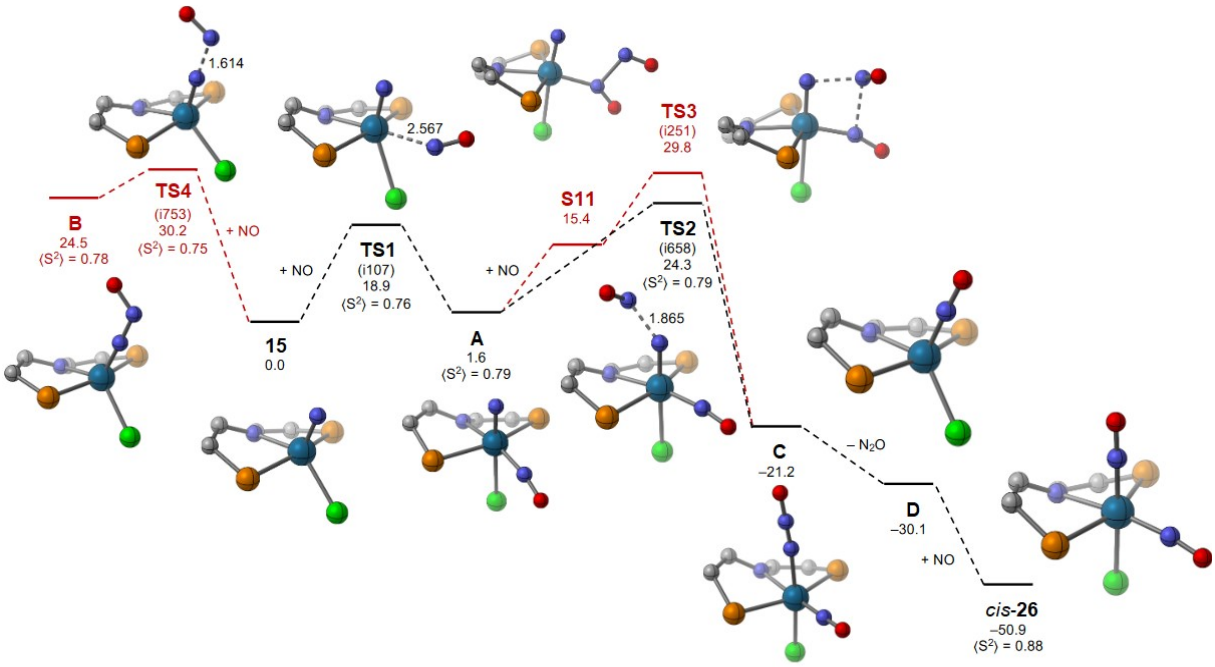

Figure 2.34: Calculated free energies (in kcal·mol^{-1}) for the reaction of Re^{V} nitride **15** with NO (ωB97X-D/def2-TZVPP//ωB97X-D/def2-SVP). The full model with aromatic backbone and phosphorus substituents was employed, but only the first coordination sphere is displayed to improve visibility. Small numbers at the structures indicate distances in Å.

On the other hand, binding of nitric oxide to the free coordination site of ^{1}**15** was found to have a room temperature accessible barrier of 18.9 kcal·mol^{-1} (^{2}**TS1**) and is almost thermoneutral (+1.6 kcal·mol^{-1}), forming the doublet ground state intermediate ^{2}**A**. Two pathways for reactivity with a second NO equivalent starting from ^{2}**A** were found. One pathway involves structures where the nitrosyl ligand acts as a relay for the second NO equivalent by developing a close contact interaction between the bound and incoming NO in an intermediate structure (**S11**, +15.4 kcal·mol^{-1}). The associated transition state (^{1}**TS3**, +29.8 kcal·mol^{-1}) is similarly high as the direct nitride-NO coupling (^{2}**TS4**, +30.2 kcal·mol^{-1}) and involves an interaction between the nitride nitrogen atom, the free NO nitrogen- and the bound nitrosyl nitrogen atoms. An alternative pathway shows direct interaction of the second NO equivalent with the nitride (^{BS}**TS2**, BS = broken symmetry solution, +24.3 kcal·mol^{-1}, $d_{N\text{-}NO}$ = 1.865 Å) in the transition state. While both pathways lead to highly exergonic (–21.2 kcal·mol^{-1}) formation of nitrosyl-N_2O complex **C**, the comparatively lower barrier of ^{BS}**TS2** is accessible at room temperature and consequently more in line with the experimental observations. However, the preferred pathway of NO coordination and reaction of a second NO with the nitride nitrogen does not explain why intermediate **A** could not be observed or isolated at low temperature. At low temperature the $\Delta\Delta G$ of ^{2}**TS1** and ^{BS}**TS2** is expected to be sufficiently large to at least detect appreciable amounts of ^{2}**A** by means of spectroscopic methods.

Subsequent nitrous oxide loss from **[1]C** was computed to be barrierless and exergonic, furnishing the five-coordinate intermediate **[1]D**, which can form the dinitrosyl complex **[2]26** upon NO addition, as well as the mononitrosyl complex *cis*-**[2]14** in presence of CCl_4. Consequently, nitric oxide binding to the free coordination site was calculated to be significantly exergonic for the formation of *cis*-**[2]26** (–50.9 kcal·mol^{-1}) and substantially less exergonic for *trans*-**[2]26** (–32.6 kcal·mol^{-1}), effectively reproducing the energetic difference between the two dinitrosyl isomers obtained on the BP86/def2-QZVP;SVP level of theory (c.f. chapter 2.5.1).

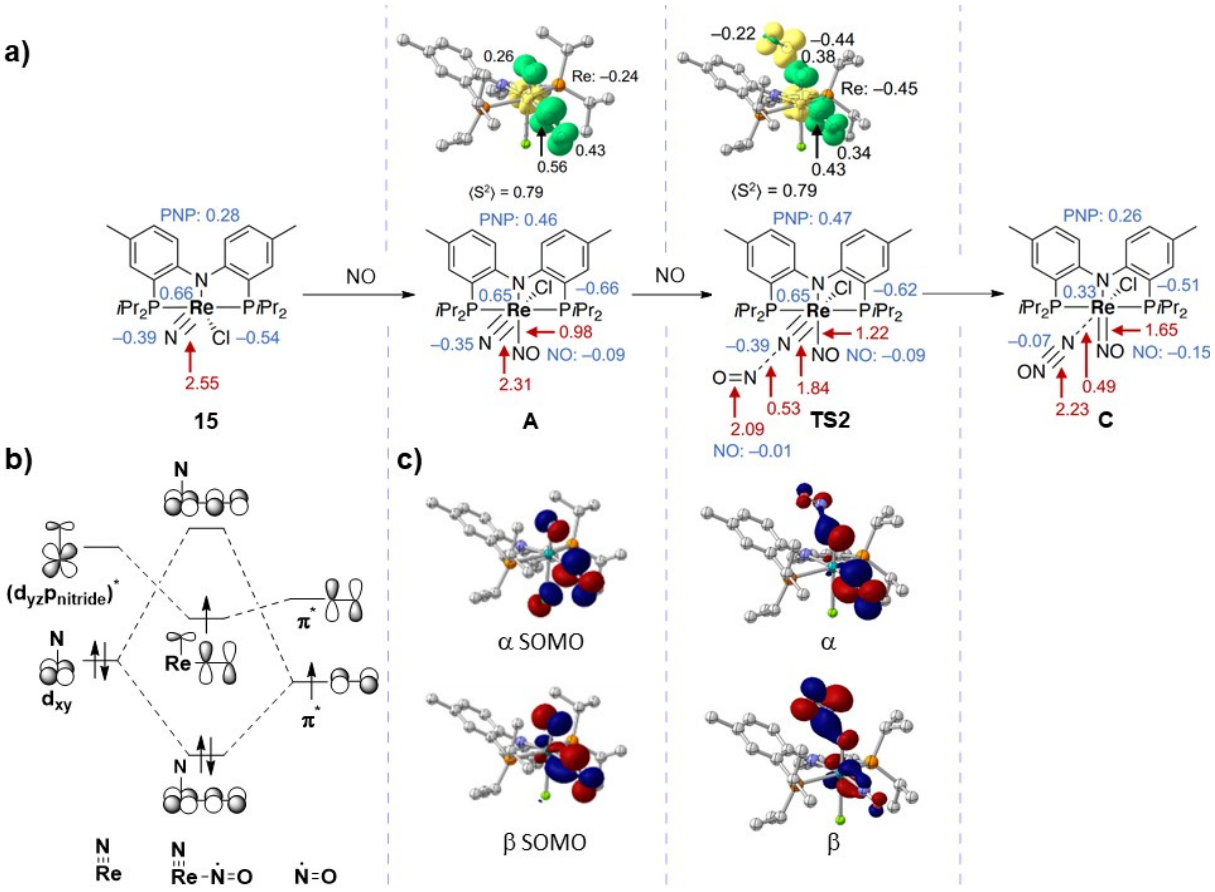

Figure 2.35: a) Spin density (top, positive numbers indicate excess α spin and negative numbers indicate excess β spin) and NBO (mid) analysis of the initial NO coordination and subsequent nitride-NO coupling. Blue numbers indicate natural population analysis charges and red numbers indicate Wiberg bond indices (WBI). **b)** Qualitative MO diagram of mixing of the nitride and NO frontier orbitals. **c)** α- and β-SOMO of intermediate **[2]A** (left) and α- and β-UCO (right, unrestricted corresponding orbitals) of the broken-symmetry solution of **[BS]TS2** (right).

Analysis of the spin density distribution in intermediate **[2]A** revealed significant spin polarization between the nitride nitrogen atom (0.26α spin) and the rhenium metal (0.24β spin). Furthermore, the spectator nitrosyl ligand acts as a spin- or electron reservoir (0.99α spin). This spin segregation in **[2]A** (Figure 2.35a) is accompanied by weakening of the Re≡N triple bond, evident from reduction of the Wiberg bond indices (WBI) from 2.55 (**[1]15**) to 2.31 (**[2]A**), as

derived by natural bond orbital (NBO) analysis. Mixing of the non-bonding d_{xy} and Re≡N LUMO with the NO π^*-orbitals results in the SOMO of ^{2}**A** (Figure 2.35b and c), which exhibits significant nitride nitrogen-, as well as NO contribution. Consequently, another nitric oxide molecule can react upon radical N-N coupling with the nitride *via* a significantly reduced barrier as compared to direct nitride-nitric oxide coupling at closed-shell ^{1}**15**.

Initially, a covalent N-N σ-bond is formed upon spin pairing (β-orbital in ^{BS}**TS2**, Figure 2.35c) of the incoming NO π^*-SOMO with the non-bonding SOMO of ^{2}**A** (Figure 2.35b). Transfer of spin density to the nitride (0.38α spin on the nitride), reduced spin density on the bound nitrosyl ligand (0.77α spin) and further weakening of the Re≡N triple bond (WBI(Re≡N) = 1.84) in ^{BS}**TS2** are evident from spin density and NBO analysis, respectively (Figure 2.35a). Notably, the WBI of the Re-N_{NO} bond increases from ^{2}**A** (0.98) to ^{BS}**TS2** (1.22), indicating stabilization of the spin polarization in ^{BS}**TS2** upon increased π-backbonding to the nitrosyl ligand. This electronic reorganization along the reaction coordinate towards the nitride facilitates N-N coupling and results in the formation of closed-shell intermediate **C**. Concomitant formal reduction of the metal is stabilized by π-backbonding to the nitrosyl ligand, as expressed in the increased WBI of the Re-N_{NO} bond in **C** (1.65). According to NBO analysis, a N≡N triple bond is formed (WBI_{NN} = 2.23) and the nitrous oxide ligand is very weakly bound to the metal center ($WBI_{Re\text{-}N2O}$ = 0.49). Overall, the initial NO coordination facilitates and mediates the electronic reorganization within the triple bond metathesis from Re≡N to N≡NO.

The induction of spin density on the nitride by NO coordination, which can be viewed as nitridyl character is the focal point of the nitride transfer reaction. Similar examples are reported for the reduction of closed-shell Os^{VI} to Os^{V} nitrides, which are susceptible to nitride N-N coupling with subsequent formation of stable Os^{II} dinuclear dinitrogen-bridged complexes.[185,378,379] Furthermore, certain Os^{VI} nitrides with carefully tailored ligands were shown to abstract hydrogen atoms after photoexcitation with visible light.[380] The proposed mechanism also includes initial reduction to Os^{V} followed by proton transfer to the nitride.[c] In the herein reported Re^{V} example the excess electron is provided by the nitric oxide ligand (reductive nitrosylation) in intermediate ^{2}**A**, which can be seen as a Re^{IV} nitride (isoelectronic to Os^{V}).

[c] Notably, *Taube* and coworkers reported N_2 release from Os^{VI} nitride *trans*-$[Os(N)Cl_3(py)_2]$ upon heating in pyridine without additional reductant.[523]

The spin density on the nitride appears to be sufficiently reduced by the strong π-accepting NO ligand to prevent nitride coupling, in a remarkable balance between reactivity and selectivity.

In conclusion, the computational examination of the nitride transfer reaction pathway revealed the following information:

1. Nitride transfer to nitric oxide upon initial NO coordination proceeds *via* a significantly reduced barrier, compared to direct nitride-NO coupling.
2. Initial NO coordination activates the Re≡N bond upon spin polarization and significant spin density is "stored" on the nitrosyl ligand. Radical N-N coupling is simultaneously facilitated along the reaction coordinate by weakening of the Re≡N bond upon increasing spin polarization and transfer of substantial spin density to the nitride nitrogen atom.
3. The electronic reorganization from a Re≡N to a N≡NO triple bond is mediated by the spectator NO ligand, which stabilizes the formal metal reduction by significant π-backbonding.

2.5.6 Nitrous Oxide Determination and Prerequisites for the Nitride Transfer from Five- and Six-Coordinate Re^{V} Nitride Complexes

The rhenium-containing product of the reaction of [(^{Ph}PNP)Re(N)Cl] (**15**) with nitric oxide was characterized in chapter 2.5.1 and nitrous oxide formation upon nitride transfer was verified upon liquid IR and ^{15}N-labeling experiments. In this chapter, the spectroscopic evidence for nitrous oxide formation and the substrate scope with respect to various five- and six-coordinate nitride complexes for the nitride transfer to NO will be discussed.

Nitrous oxide formation was observed by ^{15}N-labeling in the reaction of **15** in CD_2Cl_2/CCl_4 with NO or $NOBF_4$ and of the iodo nitride complex [(^{Ph}PNP)Re(N)I] (**19**) with NO, indicating that nitride transfer as outlined above is the prevalent reaction mechanism in these three reactions (see chapter 2.5.3). Interestingly, analysis of the IR spectrum (Figure 2.36) after the reaction of **15** with 1 eq. of $NOBF_4$ in CD_2Cl_2/CCl_4 revealed the formation of [(^{Ph}PNP)Re(NO)Cl_2]$^+$ (*cis*-**29**$^+$), with no other intense stretches in the characteristic region for nitrosyl ligands. This could be an indication, that **15** is in a first step oxidized by $NOBF_4$ to Re^{VI}

nitride **20**$^{+}$ and subsequently reacts with the released NO (the stoichiometry would impose an incomplete conversion of the starting material). In future studies, independent investigation of the reactivity of Re^{VI} nitride **20**$^{+}$ towards NO could yield valuable information about the nature of the nitride-NO interaction.

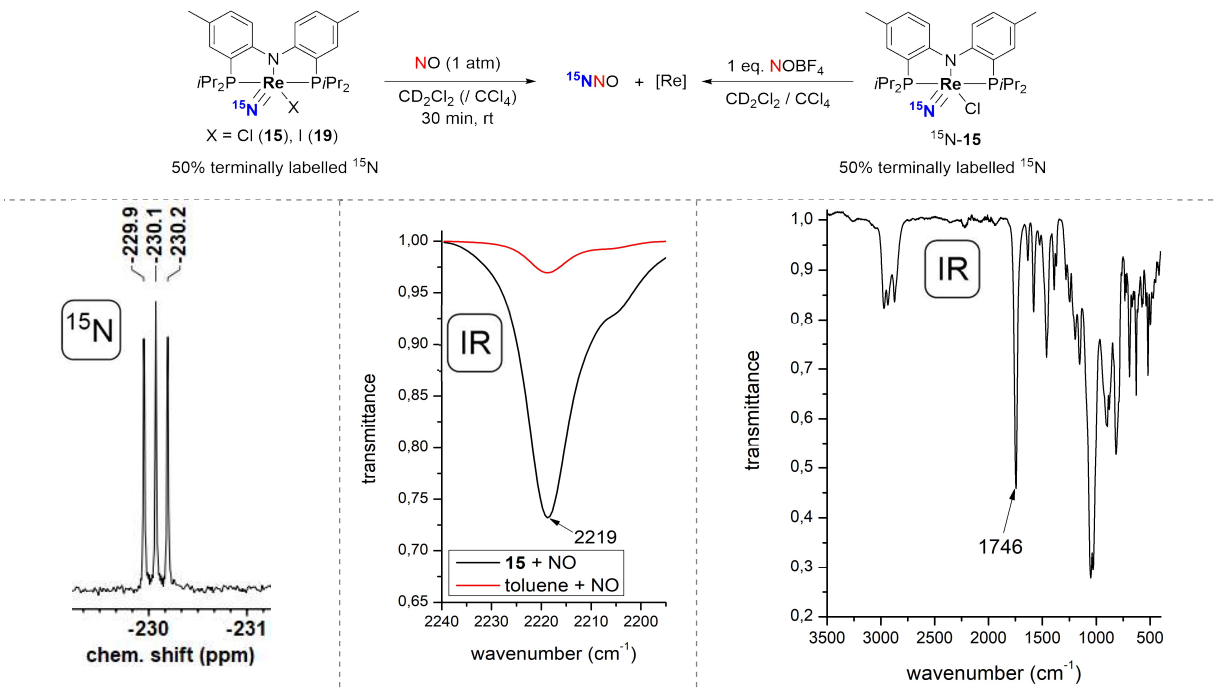

Figure 2.36: Top: Reaction of **^{15}N-15** with 1 eq. of $NOBF_4$ and reaction of **15** and **19** with natural abundance nitric oxide. Bottom left: $^{15}N\{^1H\}$ NMR spectrum of the reaction of **^{15}N-15** with 1 eq. of $NOBF_4$ in CD_2Cl_2. Bottom mid: Part of the liquid FT-IR spectrum of a reaction mixture of natural abundance **15** with NO. Depicted is the stretch of N_2O at 2219 cm^{-1},[257] which was also used for quantification. Bottom right: IR (ATR, solid) of the reaction mixture of **^{15}N-15** with 1 eq. $NOBF_4$ in CD_2Cl_2 / CCl_4 after evaporation to dryness.

To test the assumption that a free coordination site is needed for nitride transfer reactivity of Re^{V} nitrides, the octahedral nitride complex complex *cis*-[($^{i\text{Pr}}$P^{H}NP)Re(N)Cl$_2$] (*cis*-**31**) was reacted with NO. After heating a dichloromethane solution of *cis*-**31** under 1 atmosphere of NO to 40 °C for 8 hours, no change in the ^{1}H and $^{31}P\{^1H\}$ NMR spectra was observed. However, when the chloride abstracting agent $NaBArF_{24}$ ($BArF_{24}$ = $B(C_6H_3(CF_3)_2)_4$) was allowed to react with *cis*-**31** for 15 minutes prior to nitric oxide addition, rapid color change to violet was observed (Scheme 2.10). Terminally labeled $^{15}N^{14}NO$ was detected upon reaction of **^{15}N-31** with NO (performed by *Sven Rosendahl*). This suggests that nitride transfer reactivity is linked to a free coordination site in Re^{V} nitride complexes and corroborates the computationally found activation of nitride **15** upon initial NO coordination. The diethylether-soluble product exhibited only one, broadened band in the IR at ν = 1770 cm^{-1}, which is in the characteristic range for $\{ReNO\}^4$ or $\{ReNO\}^5$ complexes.[362] Further studies have to be carried out to clarify

the identity of the Re product complex. In comparison, the five- coordinate Re^{V} nitride [($^{t\text{Bu}}$PNP)Re(N)Cl] (**32**) reacted directly with NO upon heating to 80 °C to form the crystallographically observed {Re(NO)$_2$}^{7} complex [($^{t\text{Bu}}$PNP)Re(NO)$_2$]Cl.

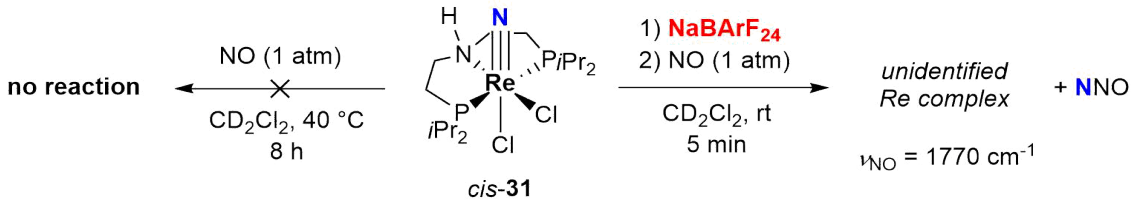

Scheme 2.10: Reactivity of *cis*-**31** towards NO depending on the presence of a free coordination site.

Nitride complex [($^{\text{Ph}}$PNP)Re(N)I] (**19**) was obtained by (electro)chemical dinitrogen splitting starting from triiodide complex [($^{\text{Ph}}$PNP)ReI$_3$] (**18**) in very high yields (up to 94% electrochemically, chapter 1.5.4). The reaction of **19** with one atmosphere of nitric oxide resulted in darkening of the solution over the course of one hour at room temperature. In the ^{1}H NMR, the sharp signals of diamagnetic starting material **19** vanished and many broad signals appeared. Concurrently, the singlet of **19** in the ^{31}P{^{1}H} NMR disappeared and two low intensity resonances were formed. Two intense stretches at 1704 and 1640 cm^{-1} in the infrared spectrum (Figure 2.37, ATR, solid) of that reaction mixture were observed after evaporation of the volatiles. This resembles the two intense stretches of *cis*-[($^{\text{Ph}}$PNP)Re(NO)$_2$Cl] (*cis*-**26**) obtained from reaction of **15** with NO and indicates the exclusive formation of *cis*-[($^{\text{Ph}}$PNP)Re(NO)$_2$I] (*cis*-**33**). Furthermore, the shift of 7–10 cm^{-1} is in good agreement with previously reported correlation of chloride-to-iodide exchange and wavenumber shift in {Re(NO)$_2$}^{7} complexes.[362]

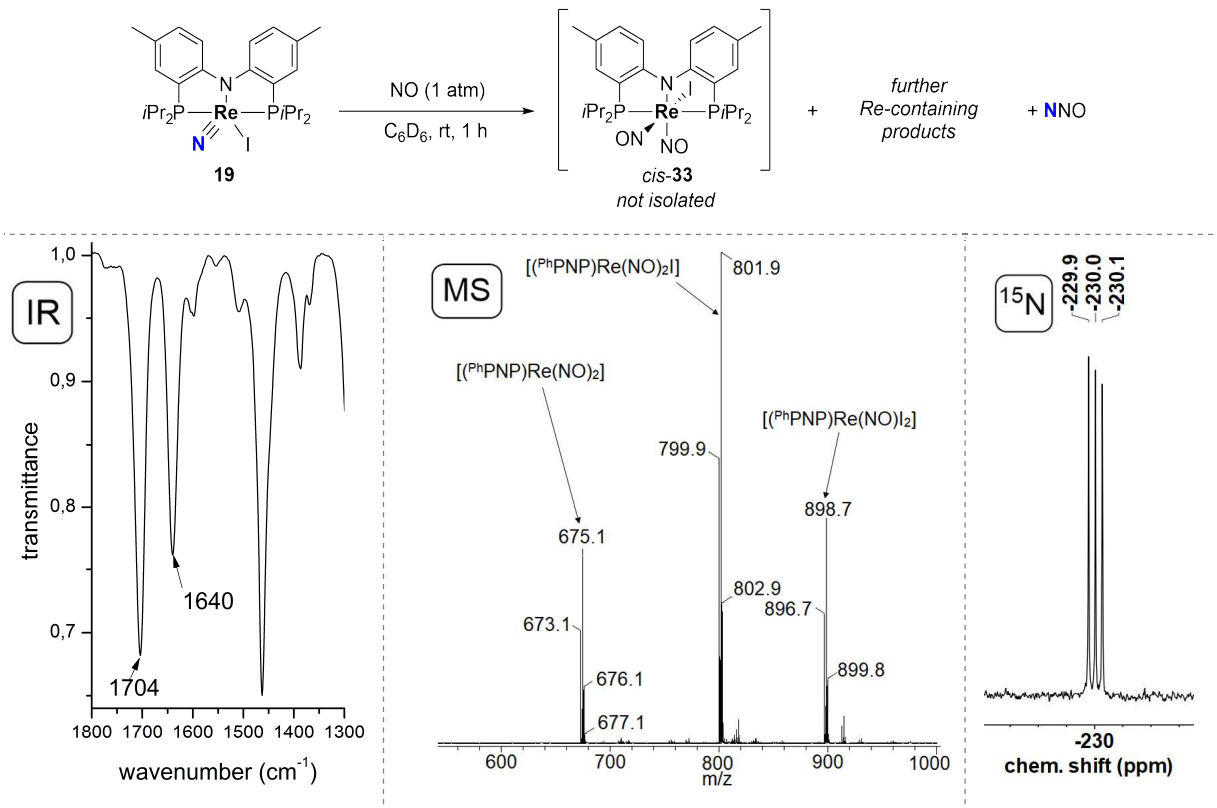

Figure 2.37: Top: Reaction of Re^{V} nitride complex **19** with one atmosphere of nitric oxide to form Re nitrosyl complexes, as well as nitrous oxide. Bottom left: IR spectrum (ATR, solid) of the reaction mixture after evaporation of the volatiles. Bottom mid: LIFDI mass spectrum of the reaction mixture in toluene. Bottom right: Excerpt of the $^{15}N\{^{1}H\}$ NMR spectrum of the reaction mixture of [(^{Ph}PNP)Re(^{15}N)I] (**^{15}N-19**, 50% ^{15}N-labeled) with nitric oxide in C_6D_6. Depicted is the 1:1:1 triplet of terminally labeled ^{15}NNO.

A contradicting result was obtained from LIFDI mass spectrometry. The mass spectrum (Figure 2.37) shows three mass peaks at *m/z* = 675.1 ([(^{Ph}PNP)Re(NO)$_2$] (**28**): M_{calc} = 674.8), *m/z* = 801.9 ([(^{Ph}PNP)Re(NO)$_2$I] (*cis*-**33**): M_{calc} = 801.7) and *m/z* = 898.7 ([(^{Ph}PNP)Re(NO)I$_2$]: M_{calc} = 898.6) and the isotopic patterns of each peak are consistent with the assigned species. The peak at *m/z* = 675.1 can be a product of method-induced fragmentation of an iodide from the species at *m/z* = 801.9, although this is rather rarely observed in LIFDI as it is considered a soft ionization technique. The peak at *m/z* = 898.7, however, corresponds to a diiodide complex, which must be a product of a chemical process and indicates possible disproportionation, as the starting complex only has one iodide ligand. Unfortunately, no compound could be isolated from the reaction mixture and further investigations are necessary to clearly identify the rhenium-containing products of this reaction. Formation of nitrous oxide upon nitride transfer to nitric oxide was verified by reaction of ^{15}N-labeled [(^{Ph}PNP)Re(^{15}N)I] (**^{15}N-19**, 50% ^{15}N-labeled) with nitric oxide and subsequent ^{15}N NMR spectroscopy of the reaction solution. In the $^{15}N\{^{1}H\}$ NMR spectrum, a 1:1:1 triplet centered at δ_{15N} = –230.0 ppm was observed, characteristic for dissolved, terminally ^{15}N-labeled nitrous oxide (Figure 2.37).

2.6 Conclusion

This part focused mainly on the reactivity of the Re^{V} nitride complex [(^{Ph}PNP)Re(N)Cl]. The general philicity of the complex was determined and several unprecedented reactivities were found in the process.

[(^{Ph}PNP)Re(N)Cl] (**15**) can be described as a relatively electron-rich nitride complex with a mild oxidation potential. The corresponding Re^{VI} nitride was isolated upon oxidation, however, no selective functionalization with various reagents was observed.

15 showed ammonia formation (13.5%) upon reaction with excess SmI_2 and H_2O. Furthermore, the adduct complex of **15** and an electron-poor organoborane was characterized crystallographically. Unselective reactions were observed towards strong acids and while reactivity towards EtOTf was observed, no product could be isolated. Interestingly, no isocyanate formation was observed upon reaction with carbon monoxide. However, formation of the Re^{IV} isocyanate complex *cis*-[(^{Ph}PNP)Re(NCO)Cl_2] from **15** was realized upon addition of oxalyl chloride (0.5 eq.) in an atom-economic reaction, avoiding the usage of toxic CO gas. Furthermore, trichloride complex [(^{Ph}PNP)$ReCl_3$] (**9**) could be regenerated in moderate yield (up to 20%) upon reacting *in situ* generated *cis*-[(^{Ph}PNP)Re(NCO)Cl_2] with excess HCl or oxalyl chloride, closing a two- or three-membered synthetic cycle consisting of dinitrogen splitting from **9** to **15** and nitride functionalization with (excess) oxalyl chloride and HCl.

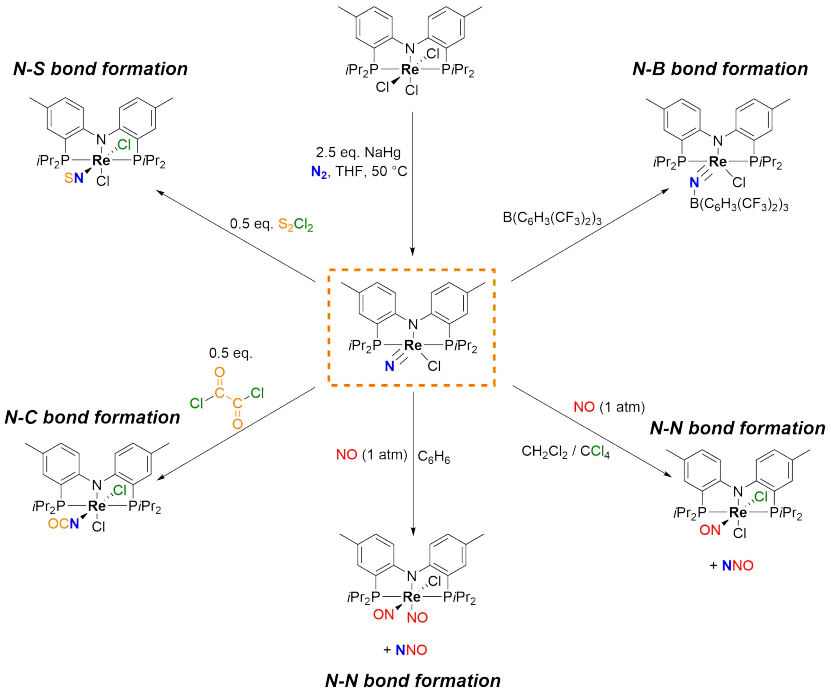

Figure 2.38: Summary of nitride-element bond formation reactions reported in this chapter.

Based on these reactions, **15** is considered as a relatively inert nucleophilic nitride, with similar reactivity compared to other (dinitrogen-derived) Re^{V} nitride complexes. Reactivity towards oxygen atom transfer reagents like *m*CPBA, pyridine-*N*-oxide, Me_3NO or *t*BuOOH was observed, however, the reactions were unselective and no spectroscopic evidence of N-O bond formation was found. Contrary, **15** reacted selectively with S_2Cl_2 to form the first dinitrogen-derived nitride-chalcogen bond in the thionitrosyl complex *cis*-[(^{Ph}PNP)Re(NS)Cl_2].

Finally, reactivity towards the stable radical nitric oxide was examined. Addition of NO to **15** furnished the dinitrosyl complex [(^{Ph}PNP)Re(NO)$_2$Cl] (**26**) and N_2O upon nitride transfer to nitric oxide in essentially quantitative yield (93.8 ± 4.3%). Upon reaction with ^{15}NO and with the aid of DFT calculations the main product **26** was determined as the *cis*-isomer. Moreover, ^{15}N-labeling studies of the nitride complex confirmed nitride transfer as the prevalent reaction mechanism over nitride oxygenation. Further mechanistic studies implied the intermediacy of a five-coordinate [(^{Ph}PNP)Re(NO)Cl] complex, based on the formation of *cis*-[(^{Ph}PNP)Re(NO)Cl_2] upon reaction of **15** with NO in presence of Cl atom donor CCl_4. No intermediates could be observed with several spectroscopic methods at low temperature.

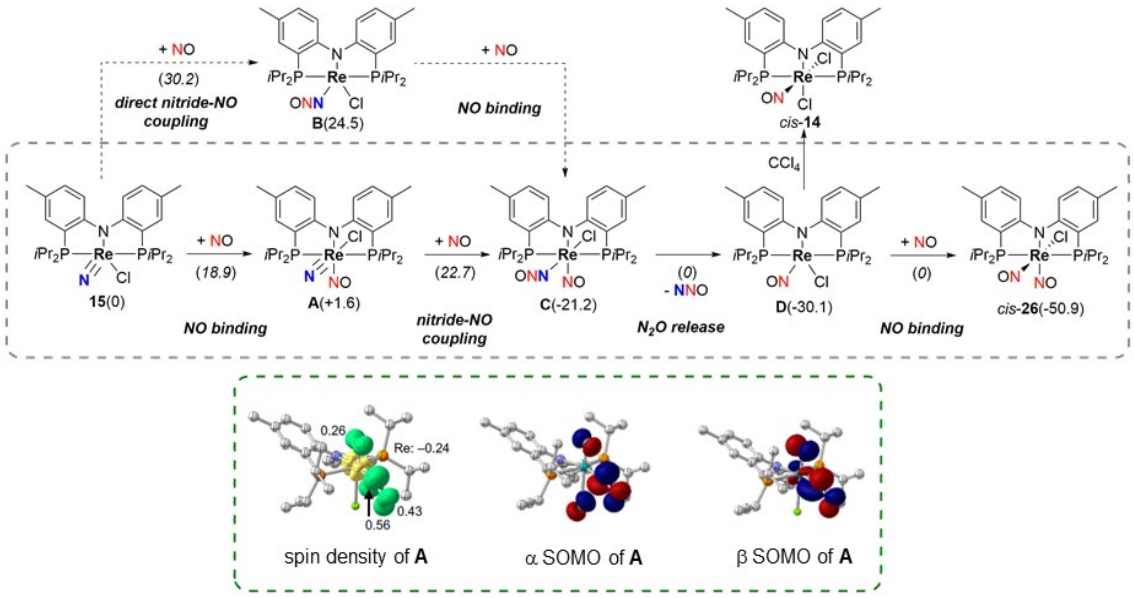

Figure 2.39: Mechanistic proposal for the nitride transfer reaction of **15** to nitric oxide based on experimental observations and DFT calculations (computed reaction barriers in italics and free energies relative to nitride **15** in kcal·mol^{-1}), as well as spin density distribution (excess α spin in green, excess β spin in yellow) and α and β-SOMO of intermediate **A**.

Computational studies support a mechanism of initial NO coordination to five-coordinate **15**, followed by nitride-NO coupling of a second, external NO equivalent. In agreement with that, related, six-coordinate *cis*-[($^{iPr}P^{H}$NP)Re(N)Cl_2] shows nitride transfer reactivity only after

chloride abstraction. Initial formation of a nitrosyl nitride complex **A** reduces the barrier for nitride-NO coupling compared to direct nitride-NO coupling at **15**. This was rationalized by induction of significant spin polarization and weakening of the Re≡N bond upon initial NO binding. Along the reaction coordinate, substantial spin density is transferred to the nitride nitrogen atom and spin polarization along Re≡N increases, facilitating radical N-N coupling. The electron reorganization and formal reduction of the metal is additionally stabilized by backbonding to the strong π-accepting NO ligand.

Conclusively, the first example of a nucleophilic, dinitrogen-derived nitride that undergoes facile nitride transfer to nitric oxide was reported. In combination with (electro)chemical dinitrogen splitting this reaction allows for the unprecedented comproportionation of N_2 and NO mediated by Rhenium complexes to form nitrous oxide. This represents the first formation of an *N*-oxide from a well-defined dinitrogen-derived nitride complex, which circumvents the initial energy demanding formation of ammonia for the synthesis of N_2O.

Part III: Metal-Ligand Cooperative Azide Hydrogenation at Osmium Pincer Complexes

3.1 Functional Pincer Ligands in Hydrogenation Catalysis

The term "pincer" ligand was introduced by *Shaw* in 1976 and was initially referring to monoanionic, tridentate ligands with a central phenyl moiety (σ-donor) and two amino- or phosphinomethyl groups in ortho-position, as defined by *van Koten* and *Albrecht*.[381,382] Since then, this rather specific definition has been considerably extended and nowadays pincer ligands generally describe tridentate, meridionally coordinating ligands, which consist of two coordinating peripheral pincer "arms" and a linking "backbone" with a central donor group. This structure allows for modular tailoring of the pincer properties and a vast array of pincers with various donor groups, structural motifs and electronic properties are described in literature.[383] In general, pincer complexes exhibit high thermal stability and allow for well-defined reactivity on the three remaining coordination sites, which makes them priviledged structures for the study of small molecule activation and catalysis.[130,384–391] In addition to their function as simple spectator ligands, which improve solubility and thermal stability, pincer ligands can also participate (reversibly) in chemical transformations, for which the term functional pincer ligand was introduced.[130]

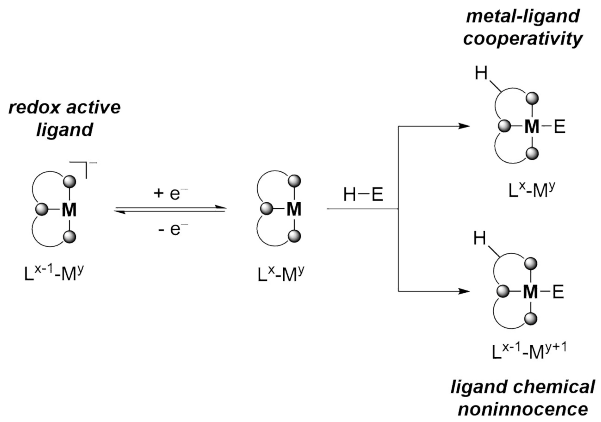

Scheme 3.1: Schematic description of redox activity (left), metal-ligand cooperativity (top right) and ligand chemical noninnocence (bottom right).[130,392]

Functional pincer ligands engage in a reaction mechanism mostly *via* two main concepts: As redox active ligands or upon metal-ligand cooperativity (MLC). Both concepts are exploited in

various chemical transformations, however, their occurrence in hydrogenation (catalysis) is the most prominent and thoroughly investigated.[130,384,390] The different concepts are summarized in Scheme 3.1. Redox active pincer complexes provide low-lying, ligand-centered HOMO or LUMO orbitals, which often are of similar energy compared to the metal-based frontier orbitals and complicate the assignment of a formal oxidation state of the metal.[393–396] The ligand therefore can act as a highly reducible electron reservoir and enable unprecedented reactivity. One particularly popular redox active ligand platform is the PDI (pyridinediimine) pincer ligand, for which many complexes could be isolated and their electronic structure was examined in detail.[397–404] PDI complexes can "store" up to three electrons in low-lying ligand based orbitals, stabilizing electron rich species relevant for catalysis.[405,406] Furthermore, modular changes at the PDI ligand can significantly influence the ligand acceptor orbital as expressed in the reduction potential.[400,407]

One illustrative example is the PDI iron complex **XXXV** (Scheme 3.2A), which is generally formulated as a catalytically inactive [(PDI^0)Fe^{II}Cl$_2$] complex.[398] Two electron reduction is ligand-centered and upon chloride loss complex **XXXVI** is obtained and described as closed-shell, ligand diradical [(PDI^{2-})Fe^{II}(N$_2$)$_2$] or zerovalent [(PDI^0)Fe^0(N$_2$)$_2$] with substrate accessible, vacant metal-centered orbitals. Consequently, **XXXVI** was found to mediate cyclization reactions and act as a very active catalyst in the hydrogenation of olefins.[408] Redox active ligands often exhibit good activity and selectivity in hydrogenation catalysis of unpolar substrates like olefins.

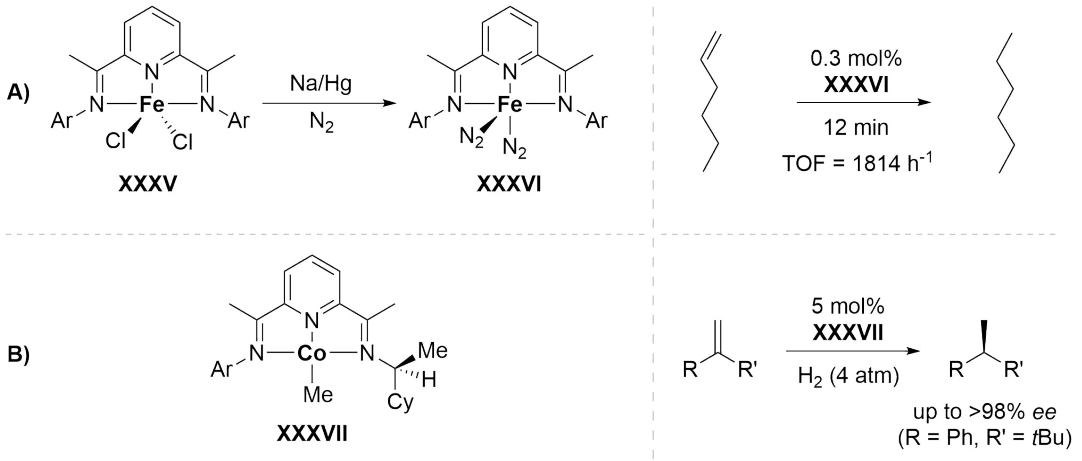

Scheme 3.2: Examples of redox-active PDI ligands in (asymmetric) catalysis of olefins. (Ar = 2,6-diisopropylphenyl).

For example *Chirik* and coworkers reported on the asymmetric hydrogenation of prochiral olefins employing a chiral PDI cobalt catalyst **XXXVII** (Scheme 3.2B).[409] With 5 mol% catalyst loading, an enantiomeric excess of up to 98% was achieved for a broad range of

substrates. In addition to PDI ligands, terpyridine (terpy)[410,411] and pyridine *bis*oxazoline (pybox)[407,412,413] are commonly employed, potentially redox active pincer ligands.

In general, metal-ligand cooperative (MLC) reactions involve the following three criteria: 1. Metal and ligand participate in bond formation or cleavage. 2. Metal and ligand undergo (reversible) chemical modifications during bond activation. 3. In the first coordination sphere the coordination mode of the cooperative ligand is significantly changed upon bond activation.[130,384] The success of metal-ligand cooperativity was significantly stimulated by the seminal work of *Noyori* and coworkers employing and examining diphosphine ruthenium catalysts with bidentate amine ligands (**XXXVIII**) for catalytic hydrogenation of polar double bonds.[414–416] They found the N-H groups of the amine ligands to be pivotal for high catalytic activity, which was attributed to metal-ligand cooperative H_2 cleavage. Initially, concerted transfer of hydride and proton to the substrate without precoordination was proposed as the reason for the high catalytic activity. Another influential discovery regarding MLC was the so called *Shvo's* catalyst **XXXIX**, a dinuclear ruthenium complex with a sterically-demanding, proton-responsive cyclopentadienone ligand.[417,418] In a similar principle to *Noyori* type catalysts, dihydrogen is cooperatively split between the cyclopentadienone moiety and the metal center, resulting in a very active (de)hydrogenation catalyst for polar double bonds.[419]

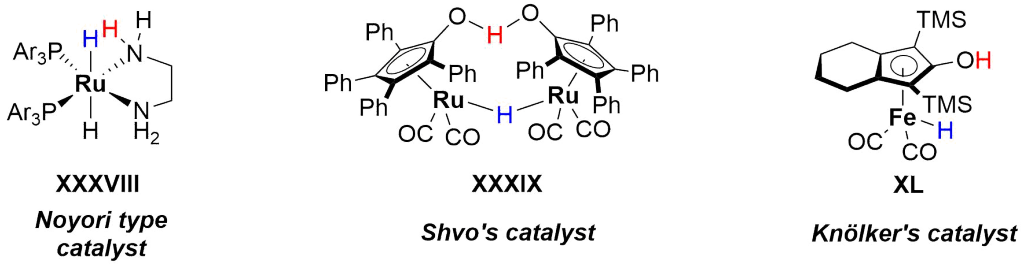

Figure 3.1: Structures of important MLC complexes for catalytic hydrogenation of polar double bonds.

Interestingly, the direct iron analogue to **XXXIX** showed little to no catalytic activity. *Knölker* and coworkers, however, described the synthesis of a related mononuclear Fe catalyst **XL**, which showed high catalytic activity in the hydrogenation of polar double bonds, for example aldehydes and ketones.[420,421] This and the PDI related work, mainly of *Chirik* and coworkers, initiated a paradigm shift away from noble metal catalysis towards the usage of base metal complexes.

The implementation of MLC base metal hydrogenation catalysis using functional pincer complexes was reported by *Langer* et al. in 2011 with the catalytic hydrogenation of ketones

using the PNP pincer Fe^{II} complex **XLI** as (pre)catalyst in presence of a base. With a catalyst loading as low as 0.05 mol% they achieved good catalyst robustness (TON = 1880) and activity (TOF = 430 h^{-1}).[422] For this type of pyridine-based pincer complexes an "aromatization-dearomatization" concept was assumed to be prevalent upon deprotonation of the benzylic methylene linkers.[384,423] The "dearomatized" amido resonance structure is structurally evident from a shortened C-C bond in the backbone and various metal complexes have been isolated with a dearomatized pincer ligand.[424–431] Furthermore, a low-spin d^6 configuration of the 3d metal, necessary for H_2 binding, is enforced by strong π-acceptor ligands like CO.[130] For the reaction of ketone hydrogenation with **XLI** as catalyst an inner-sphere MLC mechanism was proposed, based on stoichiometric control experiments (Scheme 3.3)[422]: Deprotonation forms dearomatized **XLII**, which binds the substrate (**XLIII**), followed by migratory insertion (**XLIV**), MLC H_2 heterolysis (**XLV**) and product elimination to regenerate **XLII**. However, this inner-sphere mechanism was later disputed by *Yang*, who proposed an outer-sphere hydride transfer from an iron dihydride species based on DFT calculations.[432]

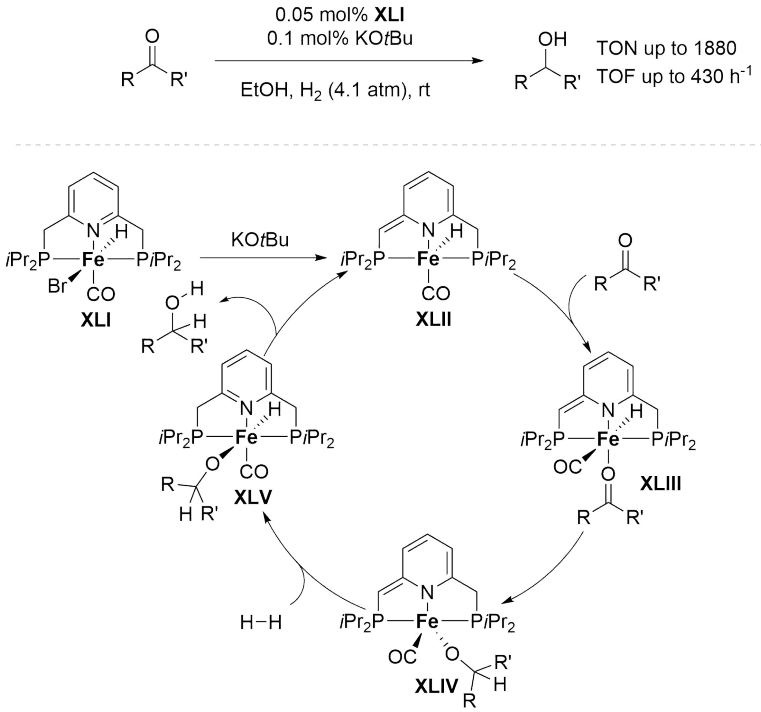

Scheme 3.3: Top: Catalytic hydrogenation of ketones with Fe^{II} catalyst **XLI**. Bottom: Initially proposed reaction mechanism.

Since then, several MLC catalyst variations with similar activity were reported. For example, *Kirchner* and coworkers described pincer ligands with amine linkers,[433] as well as borane ligands,[434] which remove the need for base-mediated activation and examples of isoelectronic Mn pincer complexes[435–437]. Interestingly, an example of a Co^{II} (pre)catalyst without strong

field ligands was reported by *Kempe* and coworkers.[438] The catalytic hydrogenation of polar double bonds with pyridine-based pincer ligands was further extended to aldehydes,[433,438–440] amides,[441] nitriles,[442] esters[443,444] and CO_2[445,446].

A second popular pincer structural motif employed in MLC catalysis with 3d metals are the aliphatic diphosphinoamines of the type **XLVI** (Scheme 3.4), which were significantly influenced by high activity of related tetradentate complexes from *Morris* and coworkers.[130,447–449] In contrast to the pyridine-based pincer they act *via* the amine-amide couple, which is more acidic than the CH_2 linker of, for example, **XLI**. Additionally, the aliphatic pincer backbone allows for conformational flexibility and the pincer complexes often contain strong-field ligands like CO, to enforce the low-spin configuration of the base-metal. Interestingly, the first reports of catalytic ketone hydrogenation employed a square-planar low-spin Co^{II} complex without CO ligands by *Hanson* and coworkers.[450,451] The relevance of MLC for the catalytic mechanism was demonstrated by the catalytic inactivity of the backbone N-methylated Co complex. In 2014 the groups of *Jones* and *Schneider* reported catalytic activity of the five-coordinate Fe^{II} pincer complex **XLVI** in ketone hydrogenation.[452] In the proposed mechanism, the pincer backbone acts reversibly as a proton reservoir, which is transferred to the substrate together with the iron hydride. The catalytic hydrogenation of ketones,[453–457] aldehydes,[454] amides,[458,459] nitriles,[460,461] esters[458,462,463] and CO_2[445,446,464,465] with similar aliphatic diphosphinoamine pincer complexes of Fe, Mn and Co was reported. Notably, the groups of *Hazari* and *Schneider* reported an extremely active Fe^{II} pincer catalyst for the dehydrogenation of formic acid to CO_2 (0.0001 mol% cat., TON up to 983642, TOF up to 196728 h^{-1}).[466]

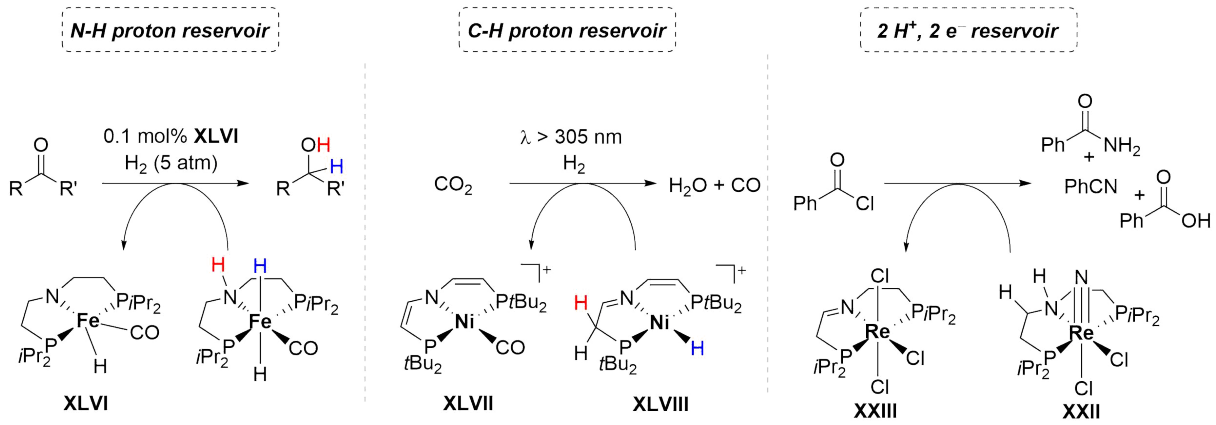

Scheme 3.4: Simplified schematic functions of aliphatic diphosphino amine/amide pincer complexes, as well as an example for a divinylamide pincer complex system.

The facile, catalytic (de)hydrogenation with base metal pincer complexes allowed for their implementation into larger scale "borrowing hydrogen" reaction schemes.[130,467–472] In these reactions (de)hydrogenation is often followed by a condensation reaction and (re)hydrogenation, leading to the build-up of more complex molecules like *N*-heterocycles. *Schneider* and coworkers demonstrated a two-step, stoichiometric, reverse water-gas shift reaction with a divinylamide Ni^{II} pincer complex **XLVII** upon irradiation. In this case, the ligand accepts a proton not *via* the amide/amine couple, but rather one of the C=C double bonds is reversibly protonated in **XLVIII**.[473–475] Furthermore, *Schneider* and coworkers reported the metal-ligand cooperative synthesis of benzamide, benzonitrile and benzoic acid upon nitride transfer from **XXII** to benzoyl chloride.[200] In this example the aliphatic pincer ligand acted as a two proton and two electron reservoir, resulting in the formation of the oxidized imine ligand in **XXIII**. This report highlights the potential of aliphatic diphosphinoamine pincer ligands in metal-ligand cooperative transformations. However, given that the corresponding divinylamide pincer complexes are often isolable, the question arises, whether even more than two protons and two electrons might be transferred from the pincer backbone to suitable substrates.

3.2 Motivation and Scope

This chapter is divided into two subunits. In a first step, the potential of aliphatic Osmium pincer complexes with regard to the formation of dinuclear dinitrogen-bridged complexes and splitting thereof will be evaluated. In a second step, metal-ligand cooperative transformations with the aliphatic pincer backbone will be investigated, based on results that were obtained in the first part of this chapter.

The groups of *Holland*, *Miller* and *Goldman* systematically investigated the formation of dinuclear dinitrogen-bridged complexes with pincer ligands binding to different metals by DFT calculations.[169] They found a correlation of the stability of the dinuclear complexes compared to mononuclear terminal N_2 with the amount of formed π-bonds in the dinuclear product and free N_2. Furthermore, they particularly pointed out the influence of dispersion forces on the formation of dinuclear dinitrogen-bridged complexes. This is especially important for d^6/d^6 ($\pi^{12}\delta^4$) dinuclear complexes, as they are expected to exhibit only weak dinitrogen activation and weak metal-N_2 bonding due to occupation of antibonding orbitals. Additionally, formation of $\pi^{12}\delta^4$ dinuclear complexes from terminal N_2 complexes of different ligands and metals were calculated to be isoenergetic or slightly endergonic, which would result in no reaction or unselective formation.

Motivated by the facile formation of the thermally stable, dinuclear dinitrogen-bridged complex $[((^{i\text{Pr}}P^{H}NP)ReCl_2)_2(\mu\text{-}N_2)]$,[152] the question was raised, whether an isoelectronic Osmium analogue would be accessible. For this, the **synthesis of a dinuclear dinitrogen-bridged Osmium pincer complex based on the $^{i\text{Pr}}P^{H}NP$ ligand was attempted**. Starting from common Osmium precursor complexes, the synthesis of N_2 complexes was investigated. Furthermore, based on the literature report of MLC with the Rhenium complex of the $^{i\text{Pr}}P^{H}NP$ ligand, the potential for **new, unprecedented metal-ligand cooperative reaction types with the aliphatic pincer backbone was examined.**

3.3 Synthesis and Properties of Aliphatic Osmium Pincer Complexes

3.3.1 Os^{II} Complexes on the *iso*-Propyl Based Pincer Platform

Osmium nitrides in the formal oxidation states +IV and +VI are interesting synthetic targets for nitride functionalization, as they exhibit ambiphilic and electrophilic reactivity, respectively. However, their synthesis upon dinitrogen splitting from coordinated N_2 is still extremely rare, although it could enable functionalization of these electrophilic nitrides with ubiquitous nucleophiles like H_2O. The factors which control for example terminal N_2 coordination over formation of a N_2-bridging dinuclear complex are not well understood yet, but a recent computational investigation highlighted the at first counterintuitive influence of outer-sphere dispersive interactions on the terminal-N_2 / bridging-N_2 equilibrium.[169]

Previous work on Osmium complexes with the sterically demanding $^{t\mathrm{Bu}}P^{H}NP$ platform neither led to the isolation of dinitrogen (bridging) complexes, nor were any indications of dinitrogen splitting on this platform found.[190,216] Instead, the synthesis of a terminal Os^{IV} nitride complex from an azide source was shown and its ambiphilic reactivity was demonstrated. As an extension to this work, the impact of reducing the steric bulk on dinitrogen chemistry was investigated in more detail by utilizing the $^{i\mathrm{Pr}}P^{H}NP$ platform and will be discussed in this chapter.

Reaction of the $^{i\mathrm{Pr}}P^{H}NP$ ligand with the green Os^{II} precursor $[OsCl_2(PPh_3)_3]$ in THF resulted in an orange solution after stirring for one hour at room temperature. $^{31}P\{^{1}H\}$ NMR spectroscopy of the resulting solution indicated full conversion of the starting materials and appearance of two new resonances at $\delta_{31P} = -3.0$ (d) and -25.9 (t) ppm, respectively. The doublet and triplet multiplicity and the 2:1 integral ratio in combination with equal coupling constants ($J = 12.9$ Hz) implied the scalar coupling of one phosphorus (from triphenylphosphine) to two chemically equivalent phosphorus atoms (from the pincer ligand). Large red-orange single crystals suitable for X-ray crystallography were obtained from THF / pentane at room temperature and confirmed the proposed binding motif with the formation of the product Os^{II} complex *trans*-$[(^{i\mathrm{Pr}}P^{H}NP)OsCl_2(PPh_3)]$ (*trans*-**34**).

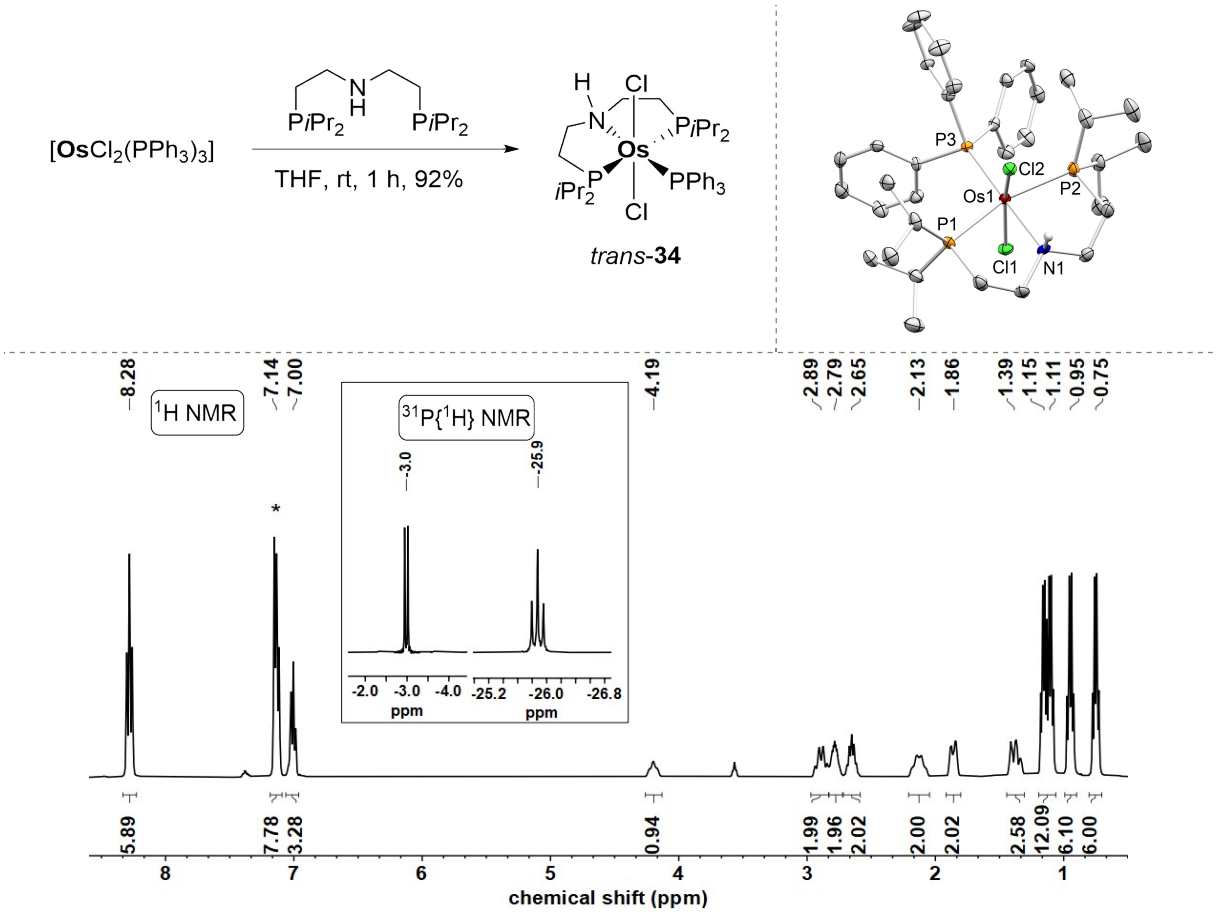

Figure 3.2: Top left: Reaction of Os^{II} precursor $[OsCl_2(PPh_3)_3]$ with the $^{iPr}P^{H}NP$ ligand to form *trans*-[($^{iPr}P^{H}NP$)$OsCl_2(PPh_3)$] (*trans*-**34**). Top right: Molecular structure of *trans*-**34** from single-crystal X-ray diffraction (thermal ellipsoids drawn at the 50% probability level); hydrogen atoms except for nitrogen-bound ones, one THF and one pentane solvent molecule are omitted for clarity. Selected bond lengths [Å] and angles [°]: Os1-N1 2.212(4), Os1-P3 2.3068(14), Os1-P1 2.3836(15), Os1-P2 2.3828(16), Os1-Cl1 2.4379(15), Os1-Cl2 2.4560(14), N1-Os1-P3 177.07(13), P1-Os1-P2 161.63(5), Cl1-Os1-Cl2 164.84(5). Bottom: ^{1}H NMR spectrum of *trans*-**34** in C_6D_6. Solvent signal is marked with an asterisk and superimposed with signals from the PPh_3 moiety. Inlet: Sections of the $^{31}P\{^{1}H\}$ NMR spectrum of *trans*-**34** in C_6D_6.

The sum of angles around the pincer nitrogen atom and the significant pyramidalization confirmed the presence of an amine moiety in the pincer backbone (Figure 3.2). Interestingly, both chloride ligands are significantly bent towards the pincer ligand (∢(Cl1-Os1-Cl2): 164.84°), most likely due to the steric bulk of the triphenylphosphine ligand causing the distortion of the octahedral coordination geometry. *trans*-**34** is a prototypical, diamagnetic 18 valence electron d^6 complex, as represented by sharp signals in the NMR spectrum with well resolved *J*-coupling.

The more bulky $^{tBu}P^{H}NP$ pincer ligand reacted with the $[OsCl_2(PPh_3)_3]$ to form the Os^{IV} complex *cis*-[(^{tBu}PNP)$Os(H)Cl_2$] presumably after oxidative addition of an Os^{II} intermediate into the pincer ligand N-H bond.[216] The striking difference in reactivity might be explained with the larger steric demand of the tert-butyl substituted pincer ligand, which prevents PPh_3

coordination and instead indirectly enables oxidative addition. In contrast, the PPh_3 coordination in *trans*-**34** "traps" the five-coordinate intermediate and prevents any further oxidative addition reactivity. This motivated attempts to eliminate the triphenylphosphine ligand in *trans*-**34**, to either promote oxidative addition to Os^{IV} or coordinate for example dinitrogen, for further studies on N_2 splitting and functionalization.

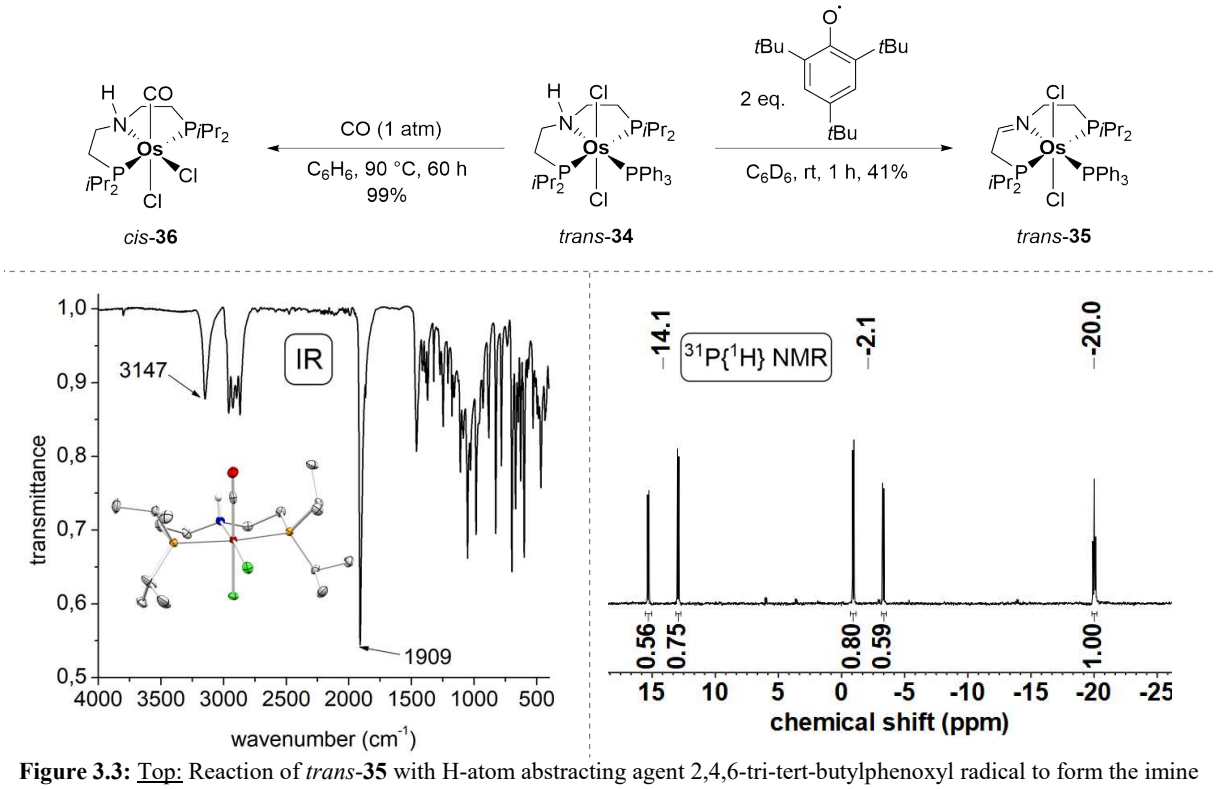

Figure 3.3: Top: Reaction of *trans*-**35** with H-atom abstracting agent 2,4,6-tri-tert-butylphenoxyl radical to form the imine complex *trans*-[(^{Imine}PNP)$OsCl_2(PPh_3)$] (*trans*-**35**, right) or reaction over a prolonged period with CO to form the terminal carbonyl complex *cis*-[($^{iPr}P^{H}$NP)$OsCl_2(CO)$] (*cis*-**36**, left). Bottom left: ATR-IR of crystalline *cis*-**36**. Inset: Solid-state structure of *cis*-**36** obtained from X-ray crystallography. Bottom right: $^{31}P\{^1H\}$ NMR of *trans*-**35** in C_6D_6 at room temperature.

In fact, addition of one equivalent *N*-chlorosuccinimid (NCS) as two-electron oxidant and chlorine atom donor to *trans*-**34** in benzene and heating to 80 °C for 12 hours resulted in incomplete conversion to a new species with reduced symmetry in solution, as evident from the increased multiplicity of the newly formed resonances in the ^1H and $^{31}P\{^1H\}$ NMR spectra. The same species was selectively formed upon addition of two equivalents of the hydrogen atom acceptor 2,4,6-tri-tert-butylphenoxyl radical at room temperature and was identified as the backbone-oxidized imine complex *trans*-[(^{Imine}PNP)$OsCl_2(PPh_3)$] (*trans*-**35**). The formation of *trans*-**35**, which was further verified by mass spectrometry, indicates that NCS only oxidized the pincer backbone and not the metal center and that the PPh_3 ligand was still bound to the metal. The X-ray diffraction solid-state structure of *trans*-**35** confirmed the basic connectivity

of atoms, however, because of its poor overall quality it is not suitable for any further discussion of bond lengths or angles.

Elimination of triphenylphosphine from *trans*-**34** was further probed by addition of the oxygen atom transfer reagent IMesN_2O (IMes = *bis*(2,4,6-trimethylphenyl)imidazole-2-ylidene) and with CS_2, but no reactivity with *trans*-**34** was observed in both cases, despite prolonged heating. Further attempts towards a free coordination site upon chloride abstraction from *trans*-**34** or *trans*-**35** with reagents like KO*t*Bu, NaHMDS, $NaBArF_{24}$ or NaHg showed unselective reactions with numerous products, judged by $^{31}P\{^{1}H\}$ spectroscopy. The only and surprisingly selective way of removing the PPh_3 ligand in *trans*-**34**, was substitution with carbon monoxide. Reacting *trans*-**34** with one atmosphere of CO in benzene at 90 °C for 60 hours resulted in the precipitation of colorless crystals in the reaction flask. After workup *cis*-[($^{i\text{Pr}}P^{H}$NP)Os(CO)Cl_2] (*cis*-**36**) was identified by mass spectrometry, X-ray crystallography and IR spectroscopy (ν_{CO} = 1909 cm^{-1}, ν_{NH} = 3147 cm^{-1}) as the main reaction product (Figure 3.3). X-ray diffraction of single crystals of *cis*-**36** confirmed the formation of the *cis*-isomer upon isomerization during the reaction.

In conclusion, the coordination chemistry of the *iso*-propyl based pincer ligand was found to be distinctly different compared to its tert-butyl substituted derivative. Reaction of Os^{II} precursor [$OsCl_2(PPh_3)_3$] with the $^{i\text{Pr}}P^{H}$NP ligand resulted in the formation of Os^{II} complex *trans*-[($^{i\text{Pr}}P^{H}$NP)$OsCl_2(PPh_3)$] (*trans*-**34**), whereas in case of the $^{t\text{Bu}}P^{H}$NP ligand the Os^{IV} complex *cis*-[($^{t\text{Bu}}$PNP)Os(H)Cl_2] was obtained upon oxidative addition by *Florian Wätjen*.[216] This divergent reactivity was mainly attributed to differences in the steric bulk, but prevented further attempts towards N_2 fixation in the case of the iso-propyl based complex. As a consequence, other Osmium precursors were tested and will be discussed in the next chapter.

3.3.2 Dinitrogen Activation Attempts with Os^{III} Pincer Complexes

The previously mentioned complexes were formed starting from Os^{II} precursor [$OsCl_2(PPh_3)_3$]. Os^{II} precursor enable facile access to the Os^{III} oxidation state at which dinitrogen activation is expected in analogy to isoelectronic Re^{II} compounds and due to their inherent stability many Os^{II} precursors are known. However, surprisingly reactions of the $^{i\text{Pr}}P^{H}$NP ligand with other Os^{II} complexes than [$OsCl_2(PPh_3)_3$], for example with [Os(H)Cl(CO)$(PPh_3)_2$],

$[OsCl_2(CO)(PPh_3)_2]$ and $[OsCl_2(p\text{-cymene})]_2$ were very unselective, judging by the respective $^{31}P\{^1H\}$ NMR spectra. Other precursor like $[OsCl_2(PMe_3)_4]$ were inert towards ligand exchange and showed no reactivity with the pincer ligand after heating for prolonged periods. Another common entry into Osmium coordination chemistry starts with the Os^{IV} precursor salt $(NH_4)_2[OsCl_6]$. Unfortunately, heating the $^{i\text{Pr}}P^{H}NP$ ligand with $(NH_4)_2[OsCl_6]$ in DCM / EtOH at 60 °C or in chlorobenzene at 130 °C resulted in brown solutions and no species could be isolated from the product mixture.

Lastly, Os^{III} precursors were considered, especially in the form of the commercially available chloride complex $OsCl_3 \cdot 3\ H_2O$. The black solid is barely soluble in common organic solvents and therefore surface controlled reactivity at elevated temperatures was expected. In fact, heating a suspension of $OsCl_3 \cdot 3\ H_2O$ with the $^{i\text{Pr}}P^{H}NP$ ligand in toluene to 115 °C for three days resulted in a gradual color change from black to orange-brown with significant precipitation. After workup, the poorly soluble solid was taken up in $CDCl_3$ and in the ^1H NMR spectrum broad resonances in the region from $\delta_{1H} = -5$ to -14 ppm were observed (Figure 3.4). Brown single crystals suitable for X-ray crystallography were obtained from dichloromethane / diethylether at room temperature and confirmed the formation of Os^{III} complex $[(^{i\text{Pr}}P^{H}NP)OsCl_3]$ (**37**).

Follow-up chemistry (*vide infra*), as well as mass spectrometry implied the presence of a second species as product, which was identified as the corresponding imine complex $[(^{\text{Imine}}PNP)OsCl_3]$ (**38**). The N-H hydrogen atom in the molecular structure of **37** (Figure 3.4) was found on the residual density map and the pyramidalization of the nitrogen coordination geometry indicated the presence of the amine moiety. On the other hand, one of the two N-C bond lengths is significantly shorter (d_{NC} = 1.379 Å), than the other N-C bond in the structure (d_{NC} = 1.468 Å), which could be an indication of co-crystallization of the imine complex **38**. This is especially relevant as **38** crystallizes (see chapter 3.4.2) in the same orthorhombic space group ($P2_12_12_1$) as **37** with similar unit cell dimensions. Hence, a certain amount of co-crystallized imine complex can not be excluded based on the solid-state structure due to their isomorphous unit-cells and appear realistic based on the distinctly different C-N bond lengths.

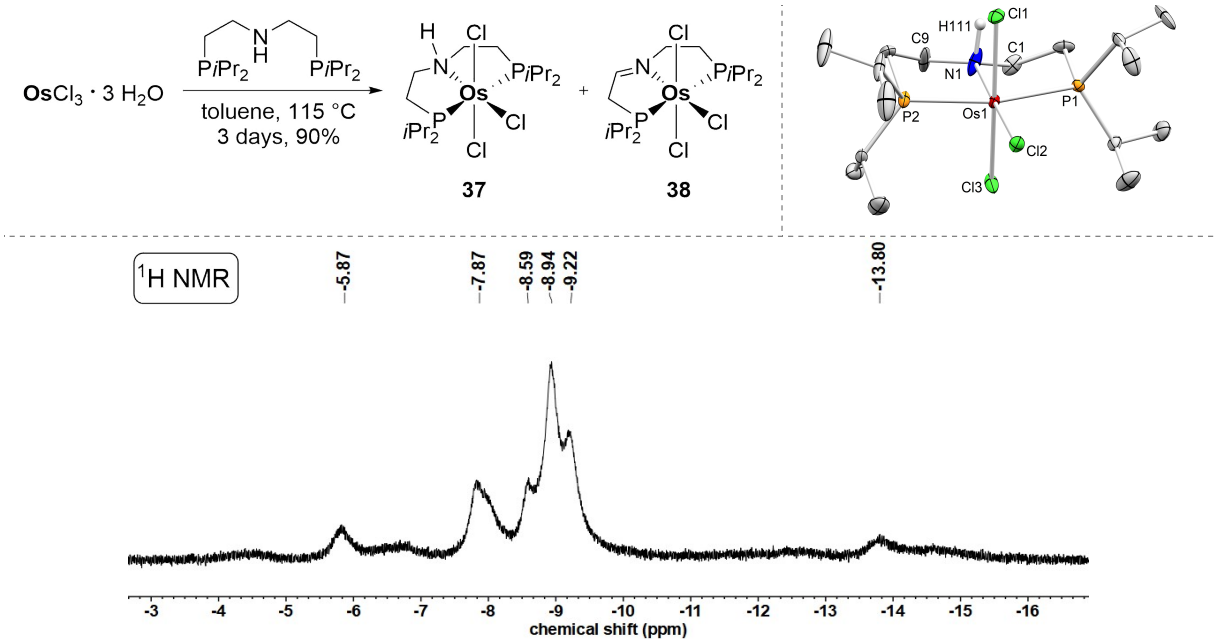

Figure 3.4: Top left: Reaction of Osmium chloride trihydrate with the $^{i\text{Pr}}\text{P}^{\text{H}}\text{NP}$ ligand to form a mixture of the Os^{III} complexes [($^{i\text{Pr}}\text{P}^{\text{H}}\text{NP}$)$\text{OsCl}_3$] (**37**) and [($^{\text{Imine}}\text{PNP}$)$\text{OsCl}_3$] (**38**). Top right: Molecular structure of **37** from single-crystal X-ray diffraction (thermal ellipsoids drawn at the 50% probability level); Hydrogen atoms except for nitrogen-bound ones are omitted for clarity. Selected bond lengths [Å] and angles [°]: Os1-N1 2.098(5), Os1-P1 2.3832(15), Os1-P2 2.3846(15), Os1-Cl1 2.3692(15), Os1-Cl2 2.3925(14), Os1-Cl3 2.3632(15), N1-C1 1.468(8), N1-C9 1.379(8), Cl1-Os1-Cl3 176.24(6), Cl2-Os1-N1 178.43(18), P1-Os1-P2 163.54(5), Os1-N1-C9 119.(4), C9-N1-C1 115.6(5), Os1-N1-C1 116.3(4). Bottom left: ^{1}H NMR spectrum branch of the reaction of Osmium chloride trihydrate with the $^{i\text{Pr}}\text{P}^{\text{H}}\text{NP}$ ligand.

Numerous attempts to separate these two complexes with various types of extraction methods, chromatography column materials and crystallization attempts were not successful and the amine **37** and imine **38** were in all cases obtained as a mixture. Even variation of reaction conditions or applying dihydrogen to a product mixture did not lead to a selective conversion towards **37** and thus all following reactions from this material were carried out from such a mixture. Further complications were induced by the very similar NMR signature of the two paramagnetic Os^{III} complexes, which precluded direct quantification of the amine/imine ratio by NMR. Ultimately, the concomitant formation of the amine and imine complex can be interpreted as consequence of weak C-H- and N-H bonds in **37**, foreshadowing the reactivity observed with azide sources (see chapter 3.4.1).

With the Os^{III} complexes in hand, attention was turned towards dinitrogen activation. Three approaches towards Os^{III} N_2 complexes from the trichlorides **37** and **38** are conceivable: First, chloride abstraction would lead to a cationic complex, which could bind and activate dinitrogen. Second, reduction of **37**/**38** under N_2 would presumably lead to Os^{II}-N_2 complexes, which then could be re-oxidized to obtain the Os^{III}-N_2 synthesis target. Third, reaction of **37**/**38** with an

adequate base could lead to dehydrohalogenation and consequently a free coordination site, which could be accessible for dinitrogen coordination.

No reaction was observed by ^{1}H NMR spectroscopy for the addition of NaOTf to **37**/**38** in THF under N_2 atmosphere. Addition of the stronger chloride abstracting agent $TlPF_6$ to **37**/**38** also resulted in no noticeable change in the NMR, however, after workup a solid-state structure was obtained from X-ray crystallography, indicating that the Lewis-acidic Thallium cation was tetrahedrally coordinated by two Cl ligands of **37**, as well as two fluorine atoms of the PF_6 anion. However, the structure was of poor quality, precluding discussion on anything exceeding the basic connectivity of atoms. Nevertheless, the results of the NaOTf and $TlPF_6$ addition to **37**/**38** demonstrate that the chloride ligands in these Os^{III} complexes are strongly bound and can not be abstracted easily.

As a consequence, reduction of **37**/**38** under dinitrogen atmosphere was probed. Addition of one equivalent of sodium amalgam to a solution of **37**/**38** in THF under dinitrogen atmosphere led to a gradual brightening of the reaction solution from brown-orange to yellow. ^{31}P{^{1}H} NMR spectroscopy indicated the formation of two main species with a multiplicity of two doublets (δ_{31P} = 25.5 ppm, J = 303 Hz) and a singlet (δ_{31P} = 17.7 ppm), respectively, (one signal of the doublet multiplicity is superimposed with the singlet at δ_{31P} = 16.7 ppm, Figure 3.5). X-ray crystallography revealed the formation of the two terminal dinitrogen complexes *trans*-[(^{iPr}P^{H}NP)OsCl$_2$(N$_2$)] (*trans*-**39**) and *trans*-[(^{Imine}PNP)OsCl$_2$(N$_2$)] (*trans*-**40**), which were found to cocrystallize. The two N-C bonds in the pincer backbone of the imine complex *trans*-**40** ($d_{N4\text{-}C17}$ = 1.281(11) Å and $d_{N4\text{-}C25}$ = 1.483(10) Å) are significantly more unequal in comparison to the corresponding bonds in amine complex *trans*-**39** ($d_{N1\text{-}C1}$ = 1.474(9) Å and $d_{N1\text{-}C9}$ = 1.436(10) Å). The presence of the imine structural motif was further verified by the almost perfect planar geometry at N4, expressed in the sum of the three bond angles around N4 very close to 360° in *trans*-**40** (Σ = 359.6°). The bond lengths in the dinitrogen ligands are similar (*trans*-**39**: d_{NN} = 1.097(8) Å, *trans*-**40**: d_{NN} = 1.102(8) Å) and the small difference could be an effect of the mildly stronger donor character of the imine backbone and consequently enhanced π-backbonding to the N_2-ligand.

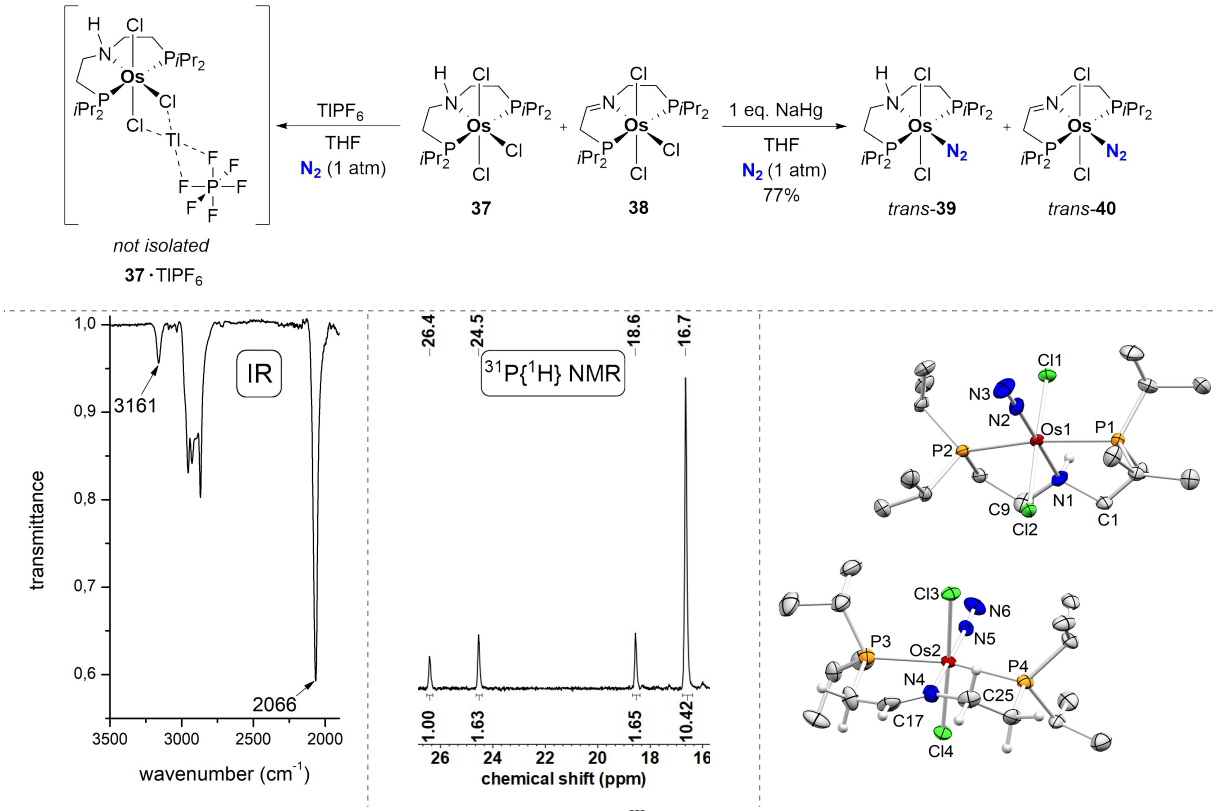

Figure 3.5: Top: Attempts for dinitrogen binding from the Os^{III} starting complexes **37** and **38**. Left: Attempted chloride abstraction with $TlPF_6$. Right: Reduction of the **37**/**38** mixture under dinitrogen atmosphere to obtain the terminal N_2 complexes *trans*-[($^{iPr}P^{H}NP$)$OsCl_2(N_2)$] (*trans*-**39**) and *trans*-[(^{Imine}PNP)$OsCl_2(N_2)$] (*trans*-**40**). Bottom left: Part of the IR spectrum (ATR, solid) of the mixture of *trans*-**39** and *trans*-**40**. Bottom mid: $^{31}P\{^1H\}$ NMR spectrum of *trans*-**39** and *trans*-**40** in C_6D_6 solution. Bottom right: Cocrystallized molecular structures of *trans*-**39** and *trans*-**40** from single-crystal X-ray diffraction (thermal ellipsoids drawn at the 50% probability level); Hydrogen atoms except for selected ones are omitted for clarity. Selected bond lengths [Å] and angles [°]: Os1-N1 2.117(6), Os1-N2 1.914(6), N2-N3 1.097(8), Os1-Cl1 2.4231, Os1-Cl2 2.4224(18), N1-C9 1.436(10), N1-C1 1.474(9), Os2-N5 1.921(7), Os2-N4 2.065(7), N5-N6 1.102(8), Os2-Cl3 2.4263(18), Os2-Cl4 2.4189(19), N4-C17 1.281(11), N4-C25 1.483(10), Os1-N2-N3 177.9(7), N1-Os1-N2 179.4(3), Cl1-Os1-Cl2 173.48(7), C9-N1-C1 115.5(6), C9-N1-Os1 116.1(5), C1-N1-Os1 115.2(5), Os2-N5-N6 175.0(6), N4-Os2-N5 175.8(3), Cl3-Os2-Cl4 174.88(7), C17-N4-Os2 123.0(6), C17-N4-C25 119.5(7), Os2-N4-C25 117.1(5).

The formation of the two species *trans*-**39** and *trans*-**40** is in agreement with the $^{31}P\{^1H\}$ NMR spectrum and its relative multiplicities, as well as the fact that the starting material consisted out of the amine/imine complex mixture of **37** and **38**. Under the assumption that the relative ratio of amine to imine complex is unchanged upon reduction, the ratio of starting material **37**/**38** can be indirectly determined with the aid of quantitative $^{31}P\{^1H\}$ NMR spectroscopy from the ratio of *trans*-**39** to *trans*-**40** (64% / 36%). Interestingly, in the IR spectrum of solid *trans*-**39**/*trans*-**40** only one intense stretch for the N_2 ligand(s) was observed (ν_{NN} = 2066 cm^{-1}), indicative of weak π-backbonding from the metal to the N_2 ligand. As the absorption is relatively broad (FWHM = 37 cm^{-1}) it is reasonable to assume that the expected second band is superimposed, which is also in agreement with DFT calculations (BP86/def2-QZVP;SVP) predicting similar IR stretches for the N_2 ligands in *trans*-**39** ($\nu_{N2,DFT}$ = 2081 cm^{-1}) and

trans-**40** ($\nu_{N2,DFT}$ = 2100 cm^{-1}). The bond metrics indicate very weak dinitrogen activation, as expected for d^6 terminal N_2 complexes.

The formation of terminal N_2 complexes on the Os^{II} oxidation state is in line with the recent computational analysis of the terminal-N_2 / bridging-N_2 equilibrium, which obtained a slightly uphill energy for formation of a dinitrogen-bridging dinuclear complex from two terminal N_2 d^6 complexes, especially for pincer ligands with relatively small substituents on the phosphorus atoms.[169] In future studies the formation of a dinitrogen-bridging dinuclear complex could be promoted by applying static vacuum for prolonged time, as it was shown to potentially shift the equilibrium from terminal (η^1-N_2) to bridging (μ-η^1:η^1-N_2) coordination mode (see chapter 1.2).

Electrochemical examination of the *trans*-**39**/*trans*-**40** mixture by cyclic voltammetry (Figure 3.6) revealed a reversible oxidative feature under N_2 atmosphere at $E_{1/2}$ = +0.02 V (vs. $Fc^{+/0}$). Vacuum transfer of THF-d_8 to a solid mixture of *trans*-**39**/*trans*-**40** and one equivalent of [AcFc][$Al(OC(CF_3)_3)_4$] under N_2 atmosphere resulted in a deeply red solution. After inverting the *J*-Young NMR tube for three hours at room temperature a $^{31}P\{^1H\}$ NMR spectrum was recorded. In the spectrum the resonance of the starting material at δ_{31P} = 17.0 ppm is considerably broadened and new peaks appeared at δ_{31P} = −16.3, −17.7 and −36.8 ppm, respectively. The resonance at δ_{31P} = −36.8 ppm was later identified as Os^{IV} amide complex [($^{i\text{Pr}}$PNP)$OsCl_3$], while the identity of the other signals remains unresolved.

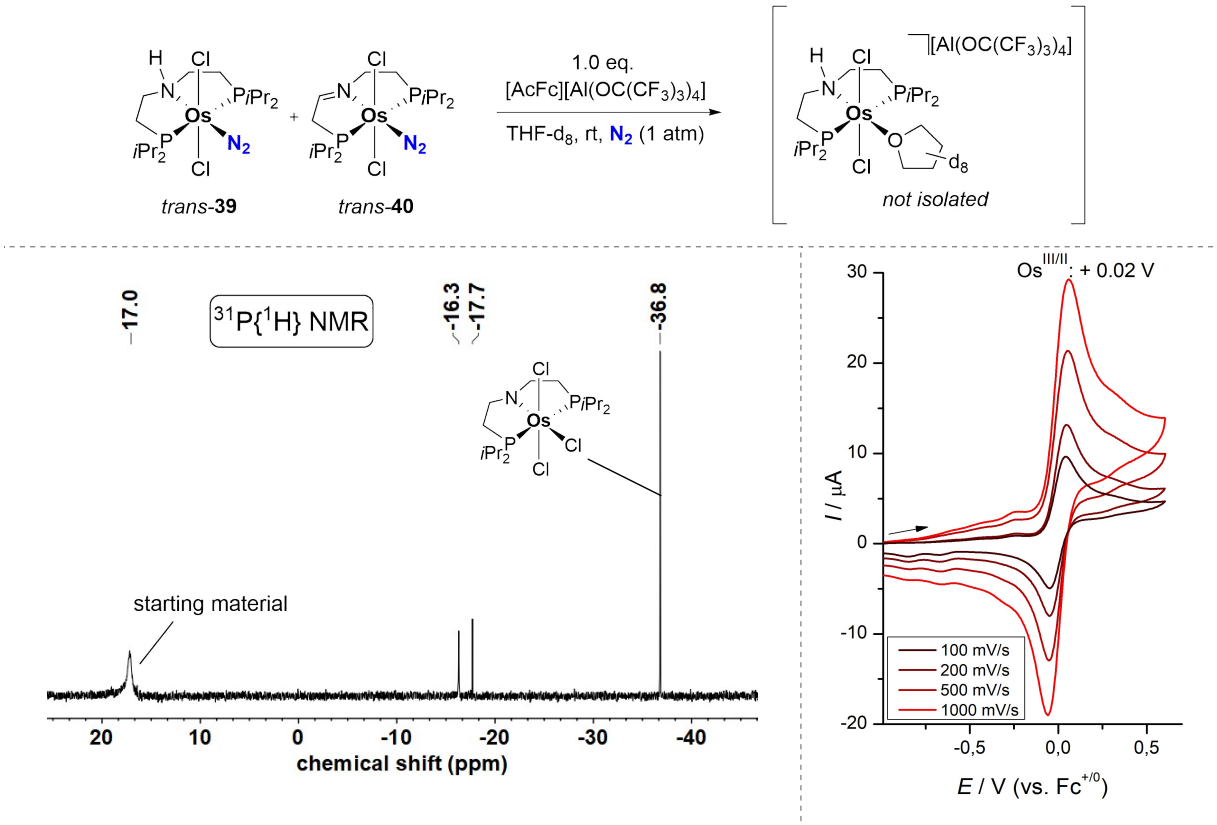

Figure 3.6: Top: Oxidation of the terminal Os^{II} N_2 complexes *trans*-**39** and *trans*-**40**. The drawn product was obtained from a solid-state structure of single crystals with poor quality. Bottom left: $^{31}P\{^1H\}$ NMR spectrum of the reaction mixture after three hours at room temperature. Bottom right: Cyclic voltammograms at different scan rates of the *trans*-**39**/*trans*-**40** mixture under N_2 atmosphere (THF, 1 mM *trans*-**39**/*trans*-**40**, N_2 (1 atm), 0.2 M nBu$_4$NPF$_6$).

The diamagnetic products in the $^{31}P\{^1H\}$ NMR spectrum indicate a more complex reaction than an one electron oxidation, possibly suggesting disproportionation or potential inversion of the $Os^{IV/III}$ couple, as the Os^{IV} complex [($^{i\text{Pr}}$PNP)OsCl$_3$] was formed and the unidentified diamagnetic products must either be Os^{II} or Os^{IV} species. From the reaction mixture low-quality single crystals were obtained and investigated by X-ray crystallography. The electron density suggested the formation of [($^{i\text{Pr}}$P$^{\text{H}}$NP)OsCl$_2$(thf)][Al(OC(CF$_3$)$_3$)$_4$], however, the heavy disorder in the aluminate counterion precluded a satisfying refinement of the data. Nevertheless, coordination of solvent THF indicated that N_2 is weakly bound and substituted on the Os^{III} oxidation state and in future studies the reaction could be repeated in a non-coordinating solvent like 1,2-difluorobenzene.

Reactions of **37**/**38** with bases like KO*t*Bu and a phosphazene base (Verkade's base) under dinitrogen atmosphere resulted unexpectedly in the formation of various signals in the $^{31}P\{^1H\}$ NMR spectrum and one of them matches the chemical shift of the Os^{II} terminal N_2 complex *trans*-**39**, indicating redox chemistry. However, based on the generally exceedingly unselective reactions the reactions with base were not further pursued.

In conclusion, the attempts towards N_2 activation from Os^{III} complexes revealed the following information:

1. Reactions of the $^{i\text{Pr}}P^{H}NP$ ligand with Os^{II} precursors apart from $[OsCl_2(PPh_3)_3]$ and with $(NH_4)_2[OsCl_6]$ were unselective. $OsCl_3 \cdot 3\ H_2O$ reacted with the $^{i\text{Pr}}P^{H}NP$ ligand upon formation of the product mixture $[(^{i\text{Pr}}P^{H}NP)OsCl_3]$ (**37**) and $[(^{\text{Imine}}PNP)OsCl_3]$ (**38**).
2. Chloride abstraction from these Os^{III} complexes was not successful and in the case of $TlPF_6$ structural evidence even showed coordination of Tl^+ by two chloride ligands of **37**, indicating that the chloride ligands in **37** and **38** are strongly bound to the Osmium center.
3. Reduction of **37**/**38** under N_2 atmosphere furnished the Os^{II} terminal N_2 complexes *trans*-$[(^{i\text{Pr}}P^{H}NP)OsCl_2(N_2)]$ (*trans*-**39**) and *trans*-$[(^{\text{Imine}}PNP)OsCl_2(N_2)]$ (*trans*-**40**) complexes. Unfortunately, oxidation of these complexes resulted in mixtures of compounds, which indicated disproportionation or replacement of the N_2 ligand for solvent THF.

3.4 Metal-Ligand Cooperative Azide Hydrogenation with a Functional Pincer Ligand

3.4.1 Metal-Ligand Cooperative Azide Hydrogenation to Ammonia

In the course of the examination of dinitrogen activation starting from the Os^{III} complexes [($^{i\mathrm{Pr}}P^{H}NP$)$OsCl_3$] (**37**) and [($^{\mathrm{Imine}}$PNP)$OsCl_3$] (**38**), the independent synthesis of the proposed dinitrogen splitting product, Os^{VI} nitride complex [($^{i\mathrm{Pr}}P^{H}NP$)Os(N)Cl_2] was attempted. One common route towards terminal nitride complexes utilizes an azide source for halide-azide exchange and subsequent thermal or irradiative decomposition of the metal-azide complex, driven by the formation of the strong metal-nitrogen triple bond, as well as release of dinitrogen. One chloride ligand of the starting metal complex is usually precipitated with the cation provided by the starting material azide salt to add further driving force:

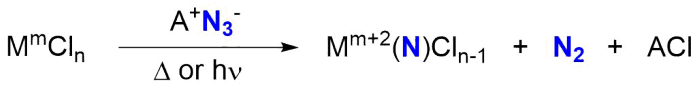

Scheme 3.5: Generalized equation for the formation of transition metal (M) nitride complexes upon azide decomposition.

Based on this equation, the metal nitride complexes are expected to be two formal oxidation states higher than the metal chloride precursors. Hence, reaction of the Os^{III} precursor complexes **37** and **38** with a suitable azide source should result in the formation of Os^{V} nitride complexes, which are generally known to be unstable and either disproportionate, decompose unselectively or react upon nitride coupling and formation of bridging dinitrogen dinuclear complexes. This would also be a viable access into dinitrogen activation chemistry and based on these considerations, the **37**/**38** mixture was reacted with azide.

In fact, addition of one equivalent of $PPNN_3$ (PPN = $Ph_3P{=}N{=}PPh_3^+$) to a suspension of **37**/**38** in THF resulted in no appreciable color change at room temperature over the course of one hour, most likely because of the poor solubility of metal complex and azide source in THF. Heating the solution to 65 °C, however, resulted in a gradual, yet relatively fast color change from brown to emerald green and precipitation of a white solid. The solution was heated for additional 12 hours and afterwards large green crystals had formed above the solvent surface. X-ray crystallography of these crystals revealed the formation of anionic, formal Os^{III} complex [PPN][($^{i\mathrm{Pr}}$P=N=P)$OsCl_3$] ($^{\mathrm{PPN}}$**41**) as the main product (48% isolated yield after workup, Figure 3.7).

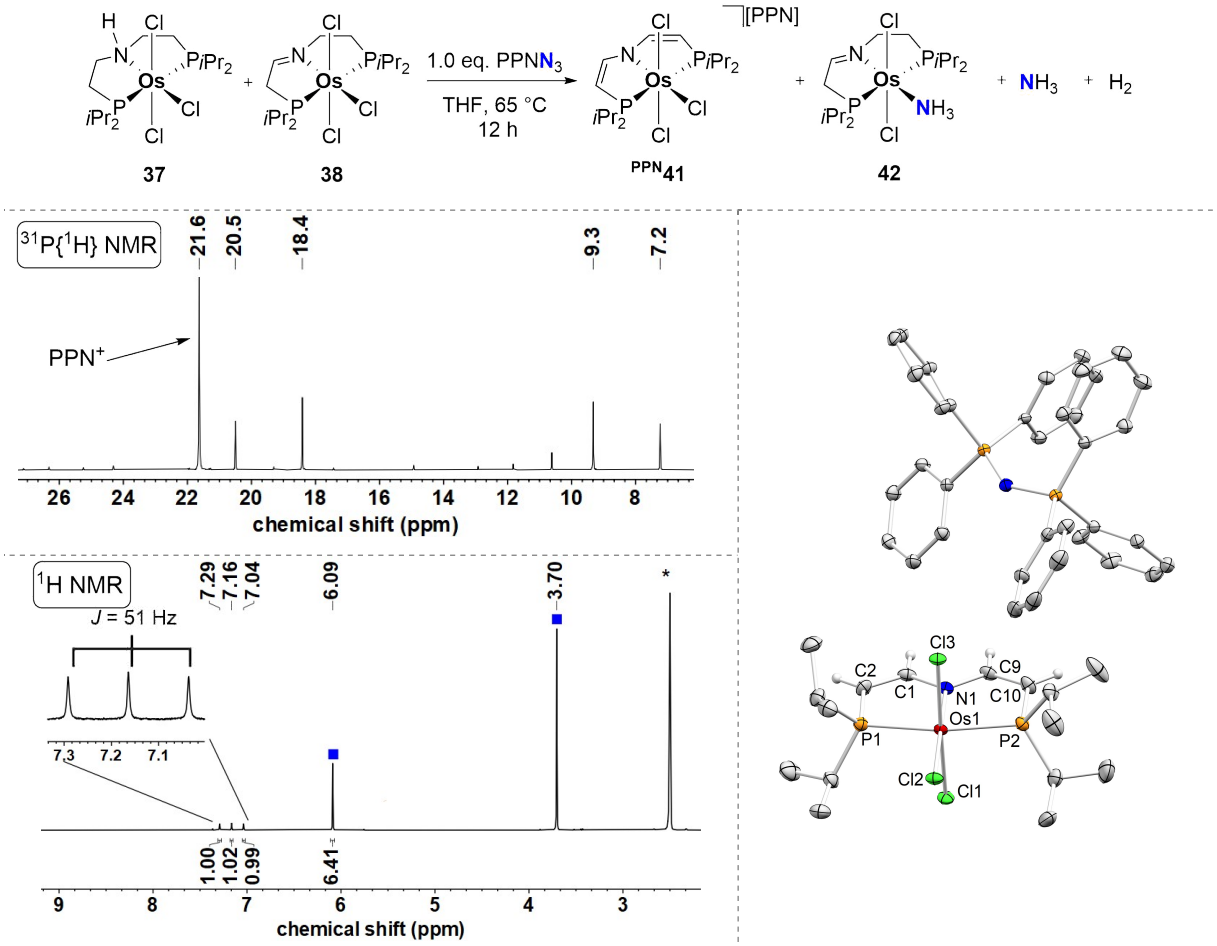

Figure 3.7: Top: Reaction of the Os^{III} complex mixture **37**/**38** with $PPNN_3$ to form unsaturated, anionic Os^{III} complex $[PPN][(^{iPr}P{=}N{=}P)OsCl_3]$, Os^{II} ammine complex $[(^{Imine}PNP)OsCl_2(NH_3)]$, as well as ammonia and dihydrogen. Mid left: $^{31}P\{^1H\}$ NMR spectrum of the reaction mixture of **37**/**38** with $PPNN_3$ in THF-d_8 at room temperature. Bottom left: ^1H NMR spectrum in DMSO-d_6 of the reaction volatiles after acidic workup to protonate the ammonia. Internal standard signals (1,3,5-trimethoxybenzene) are marked with a blue rectangle and the solvent signal is marked with an asterisk. Bottom right: Molecular structures of ^{PPN}**41** from single-crystal X-ray diffraction (thermal ellipsoids drawn at the 50% probability level); Hydrogen atoms except for selected ones on the pincer backbone and one THF solvent molecule are omitted for clarity. Selected bond lengths [Å] and angles [°]: Os1-N1 2.016(2), Os1-Cl1 2.3900(7), Os1-Cl2 2.4190(7), Os1-Cl3 2.3962(7), N1-C1 1.372(4), N1-C9 1.374(4), C1-C2 1.352(4), C9-C10 1.341(4), Cl1-Os1-Cl3 177.04(3), P1-Os1-P2 164.86(3), Cl2-Os1-N1 179.16(7), C1-N1-C9 119.3(2), C1-N1-Os1 120.4(2), Os1-N1-C9 120.4(2), N1-C1-C2 122.8(3).

Interestingly, the pincer backbone in ^{PPN}**41** is dehydrogenated / oxidized and two C-C double bonds are formed upon loss of formally five hydrogen atoms from **37** and three hydrogen atoms with respect to **38**. As a consequence, the pincer backbone is planarized, expressed in the sum of the three bond angles around the backbone nitrogen atom ($\Sigma = 360°$) and the bond lengths in the pincer backbone, which are in the typical range for C-C double bonds ($d_{C1\text{-}C2} = 1.352(4)$ Å, $d_{C9\text{-}C10} = 1.341(4)$ Å). The paramagnetic, anionic Os^{III} complex **41**$^-$ exhibits two broad signals (FWHM = 110 and 179 Hz) in the ^1H NMR spectrum at $\delta_{1H} = -3.59$ and -5.77 ppm, respectively and no further signals were observed. The identity of **41**$^-$ as an anionic trichloride

complex was further verified by negative-mode HRMS ESI spectrometry (found: m/z = 597.0661, calcd.: 597.0668, Δ = 1.1 ppm).

Examination of the reaction solution by $^{31}P\{^{1}H\}$ NMR spectroscopy revealed the additional formation of a diamagnetic species with two chemically inequivalent phosphorus nuclei (Figure 3.7), evident from the two doublets at δ_{31P} = 19.5 and 8.3 ppm (J = 338 Hz), respectively, in addition to a signal from the partially dissolved PPN^+ cation (δ_{31P} = 21.6 ppm). This species was identified upon mass spectrometry as the imine Os^{II} complex [(^{Imine}PNP)$OsCl_2(NH_3)$] (**42**) and isolated from the reaction mixture in 22% yield. The presence of an ammonia ligand prompted the question for its origin and whether free ammonia is formed in the reaction as well. Thus, the reaction volatiles were condensed onto HCl in dioxane (4 M) and after stirring for 30 minutes and thorough evaporation of the solvents the residue was taken up in DMSO-d_6. In the ^{1}H NMR (Figure 3.7) the characteristic 1:1:1 triplet ($^{2}J_{NH}$ = 51 Hz) of natural abundance ammonium ($I(^{14}N)$ = 1) was observed and with the aid of an internal standard (1,3,5-trimethoxybenzene) it was possible to determine the yield of ammonia in the reaction volatiles to 23% (relative to the Osmium complex concentration). Moreover, when ammonia was determined directly from the reaction mixture (not from the volatiles but rather upon direct addition of acid to the reaction mixture) the overall yield was 93% relative to Os starting material concentration, indicating an essentially quantitative formation of ammonia. Additionally, dihydrogen was detected *via* gas phase chromatographic examination of the reaction headspace. Upon calibration, the amount of dihydrogen produced in the reaction was determined to 1.61 equivalents with respect to the Osmium complex concentration. However, it has to be noted that agreement of the linear fit and the measured data was non-ideal (R^2 = 0.959) and therefore the amount of dihydrogen is presumably overestimated.

Isotopically labeled $PPNN_3$ (50% terminally labeled ^{15}N) was utilized to verify the azide as the origin of the free, as well as coordinated ammonia, excluding potential decomposition of the pincer ligand or PPN^+ cation under the given reaction conditions. After acidic workup of the reaction mixture as described above, the ^{1}H NMR showed the formation of a new doublet signal at δ_{31P} = 7.13 ppm ($^{2}J_{15NH}$ = 72 Hz), indicative of $^{15}NH_4^+$ formation ($I(^{15}N)$ = ½) in addition to the 1:1:1 triplet of $^{14}NH_4^+$. Their relative integrals (1.03:1.00) were basically equal, corroborating the assumption of the 50% terminally labeled $PPN^{15}N_3$ as the origin. Further evidence was obtained with the $^{1}H\{^{15}N\}$ NMR spectrum from the same sample in which only a singlet for $^{15}NH_4^+$ was observed (Figure 3.8). Finally, ^{15}N NMR spectroscopy utilizing the

INEPT (insensitive nuclei enhanced by polarization transfer) pulse sequence ($\delta_{15N}(^{15}NH_4^+) = -357$ ppm), as well as a ^{1}H-^{15}N-HSQC spectrum indirectly confirmed the formation of free $^{15}NH_3$ during the reaction. While these spectra were collected from the vacuum-transferred reaction volatiles, the solid, Osmium-containing residue was examined for ^{15}N-labeled ammonia coordination complexes. In the INEPT-^{15}N spectrum only one resonance at $\delta_{15N} = -442.2$ ppm was observed, which was assigned to the labeled imine complex [(^{Imine}PNP)OsCl$_2$($^{15}NH_3$)] (**^{15}NH$_3$-42**).

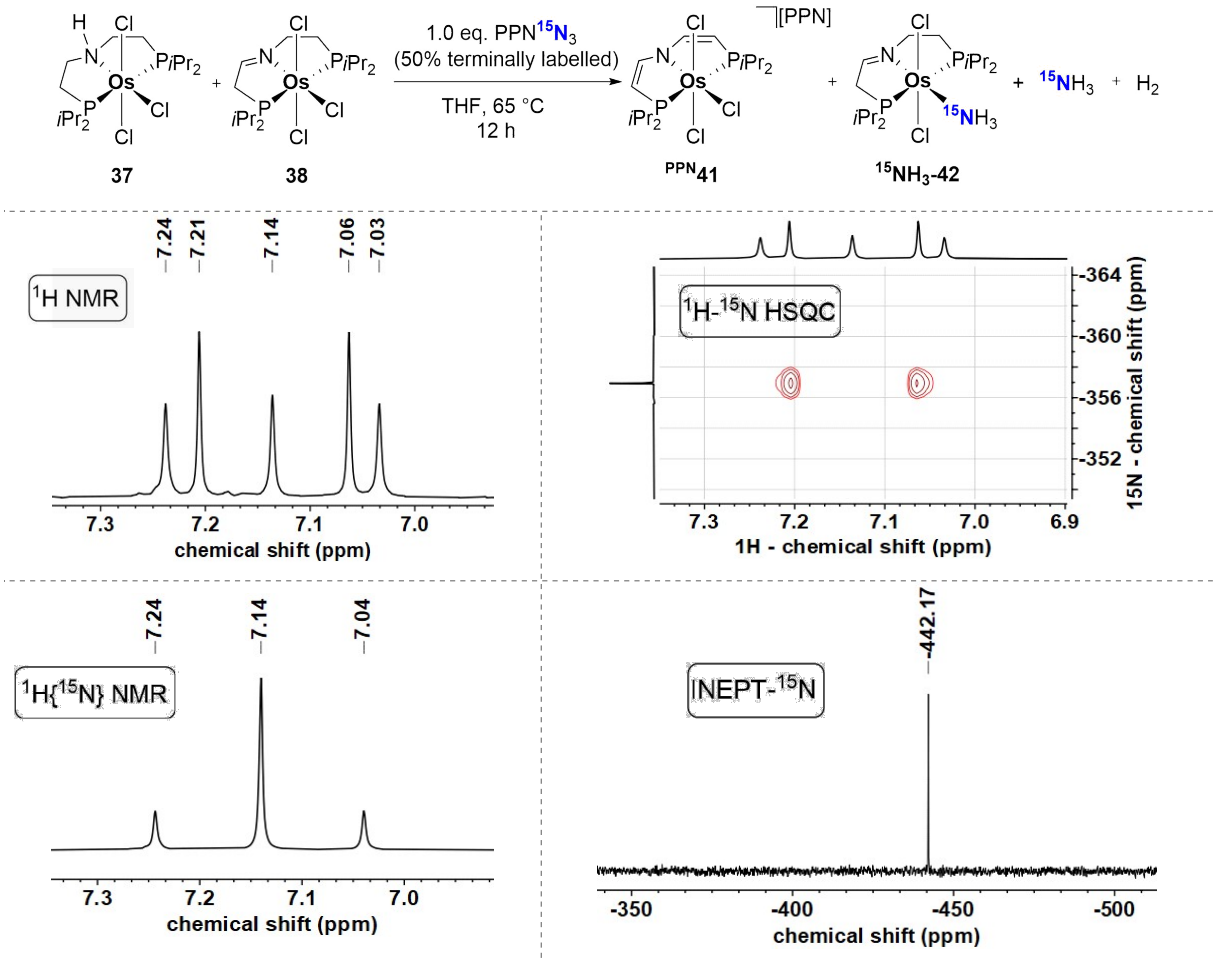

Figure 3.8: Top: Reaction of **37/38** with ^{15}N-labeled PPNN$_3$ (50% terminally labeled azide). Mid left: ^{1}H NMR spectrum in DMSO-d$_6$ of the reaction volatiles after acidic workup. Depicted is the 1:1:1 triplet of $^{14}NH_4^+$ ($^2J_{NH}$ = 51 Hz), as well as the doublet $^{15}NH_4^+$ ($^2J_{NH}$ = 72 Hz). Mid right: ^{1}H-^{15}N-HSQC spectrum in DMSO-d$_6$ of the reaction volatiles after acidic workup. Depicted are the crosspeaks between the ^{15}N signal of $^{15}NH_4^+$ ($\delta_{15N} = -357$ ppm) and the ^{1}H doublet (δ_H = 7.14 ppm, $^2J_{NH}$ = 72 Hz). Bottom left: ^{1}H{^{15}N} NMR spectrum in DMSO-d$_6$ of the reaction volatiles after acidic workup. In this spectrum, the singlet for the $^{15}NH_4^+$ coincides with the central signal for the 1:1:1 triplet of $^{14}NH_4^+$. Bottom right: INEPT-^{15}N spectrum of the solid residue of the reaction with labeled azide. The peak at $\delta_{15N} = -442.17$ ppm was assigned to complex **^{15}NH$_3$-42**.

These NMR spectroscopic results indicate in combination with the formation of the dehydrogenated pincer complex **41**$^-$ that hydrogen atoms are transferred from the pincer backbone to the azide. This could be explained with initial formation of a highly reactive Os^V

nitride complex that abstracts hydrogen atoms in an intra- or intermolecular fashion, which represents a metal-ligand cooperative azide hydrogenation harnessing the functional $^{i\text{Pr}}\text{P}^{\text{H}}\text{NP}$ ligand in an unprecedented way as a five proton, four electron reservoir (starting from **37**). Previous metal-ligand cooperative approaches utilized these aliphatic amine PNP pincer ligands either as a proton relay or as a source of two protons and two electrons.[130,200,384] This azide hydrogenation highlights the full potential of this ligand class for "storing" proton and electron equivalents in the pincer backbone.

Variation of the reaction conditions was subsequently probed and the results are summarized in Table 3.1. Performing the reaction with $n\text{Bu}_4\text{NN}_3$ (entry 2) resulted in 40% NH_3 yield from the volatiles and 97% from the reaction mixture. Interestingly, reaction with $TMSN_3$ or AdN_3 (entries 3 and 4) as azide sources did not result in formation of any appreciable amount of ammonia. The reaction with $TMSN_3$ was slow and unselective, while no reaction could be observed with AdN_3 according to NMR spectroscopy. Apparently, the N-Si bond in $TMSN_3$ and the N-C bond in AdN_3 are too strong and inhibit salt metathesis, as initiation of the reaction. Performing the reaction with $PPNN_3$ at room temperature for 2 days resulted in the formation of only 15% NH_3 (entry 5). Using C_6D_6 or $CDCl_3$ as solvents (entries 6 and 7) furnished no detectable amount of ammonia. In the case of C_6D_6 this might be ascribed to low solubility of the reactants in benzene, whereas in $CDCl_3$ the reaction was unselective, presumably due to reaction of the solvent with a reactive intermediate. Using an excess of $PPNN_3$ (entry 8) yielded 75% NH_3 from the volatiles, which is a significant increase from using one equivalent. Excess of sodium azide (entry 9) in ethanol furnished no appreciable amount of ammonia. Finally, additives were examined. Addition of 5 equivalents of H-atom donor TEMPO-H (entry 10) resulted in practically unchanged yield of 25% NH_3. Presence of NaN_3 in combination with $PPNN_3$ (entry 11) did not significantly change the ammonia yield as well. Performing the reaction under H_2 (1.2 atm) interestingly did decrease the ammonia yield notably (entry 12, 6% NH_3). No apparent difference was found when the reaction was performed under argon (entry 1) or nitrogen atmosphere (entry 13).

Table 3.1: Summary of reaction conditions for the reaction of **37/38** with azide sources.

entry	azide source	reaction conditions	NH_3 yield (%)[a]
1	$PPNN_3$ (1 eq.)	THF, 65 °C, 12 h	23% (volat.) / 93% (full)
2	nBu_4NN_3 (1 eq.)	THF, 65 °C, 12 h	40% (volat.) / 97% (full)
3	$TMSN_3$ (1 eq.)	THF, 65 °C	-
4	AdN_3 (1 eq.)	THF, 65 °C	-
5	$PPNN_3$ (1 eq.)	THF, rt, 2 days	15% (volat.)
6	$PPNN_3$ (1 eq.)	C_6D_6, 65 °C, 3 days	-
7	$PPNN_3$ (1 eq.)	$CDCl_3$, 65 °C, 2 days	-
8	$PPNN_3$ (xs.)	THF, 65 °C, 2 days	75% (volat.)
9	NaN_3 (xs.)	EtOH, 65 °C, 22 h	-
10	$PPNN_3$ (1 eq.)	THF, 5 eq. TEMPO-H, 18 h, 65 °C	25% (volat.)
11	$PPNN_3$ (1 eq.)	THF, 10 eq. NaN_3, 65 °C, 12 h	21% (volat.)
12	$PPNN_3$ (1 eq.)	THF, H_2 (1.2 atm), 65 °C, 12 h	6% (volat.)
13	$PPNN_3$ (1 eq.)	THF, N_2 (1.0 atm), 65 °C, 12 h	27% (volat.)

[a] determined as NH_4^+.

Overall the reaction conditions appear to be quite sensitive to changes, especially of the azide source, where solubility and dissociation of the azide salt strongly influence the ammonia yield. Furthermore, the solvent also plays a crucial role, not only in terms of solubilizing the reactants, but it can also react with intermediates as assumed for $CDCl_3$. External sources of additional hydrogen atoms like TEMPO-H and hydrogen gas did not increase the ammonia yield, but rather had no appreciable influence (TEMPO-H) or were even detrimental for the yield (hydrogen). These experimental findings suggest that the dehydrogenated product of the reaction, **41**$^-$, can not simply be re-saturated with TEMPO-H and that hydrogen gas presumably leads to side reactions (for example formation of osmium hydride complexes), decreasing the overall ammonia yield. Accordingly, independent attempts to react **41**$^-$ with hydrogen or H-atom donors resulted only in unselective reactions with no appreciable amount of backbone-hydrogenated Osmium complexes, precluding catalytic applications with this complex.

Finally, the reaction progress from **37/38** to **41**$^-$ and **42** was followed *via* variable temperature NMR spectroscopy at 60 °C in THF-d_8 (Figure 3.9) to search for possible intermediates, which could give valuable insight into the reaction mechanism. For this, the reactants were mixed in a *J*-Young NMR tube, inserted into the NMR spectrometer and subsequently heated to 60 °C under constant rotation to facilitate admixture of the components. In the $^{31}P\{^1H\}$ NMR spectrum the gradual increase of the two doublets of imine complex **42** was observed in addition to the initially present resonance for the PPN cation. Furthermore, despite non-ideal conditions with regard to mixing of the reactants in the NMR tube, it appears from the NMR that the

reaction is complete after 119 minutes, as the relative ratio of the PPN signal and the resonances for **42** did not change significantly afterwards anymore. In the ^{1}H NMR spectra the gradual appearance and increase of the two broad signals originating in the Osmate complex **41**$^{-}$ was observed. In agreement with the observations from the ^{31}P{^{1}H} NMR spectra no further Osmate complex was formed after 123 minutes. Additionally, the sharp *J*-resolved signals of the imine complex **42** were detected (green rectangles). Unfortunately, no intermediates were observed in both temperature rows, indicating that possible intermediates are transient and react on a faster time scale than the NMR experiment.

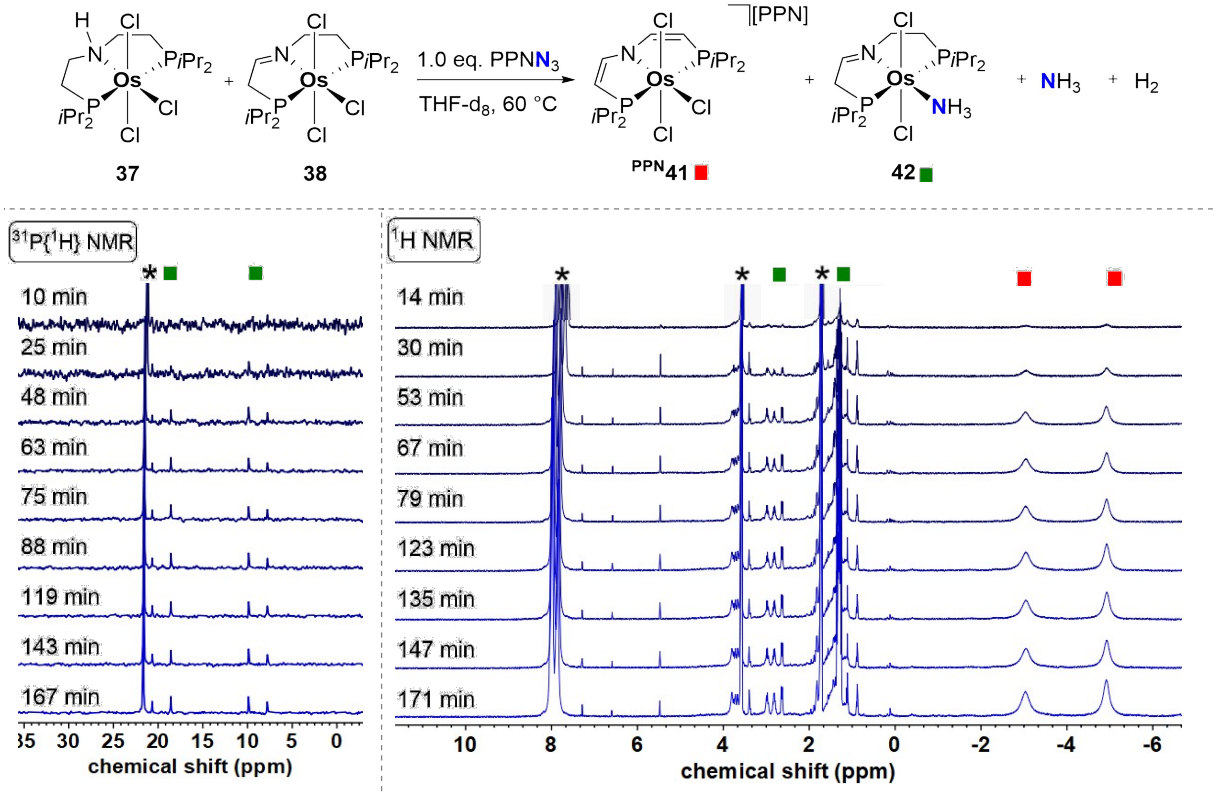

Figure 3.9: Top: Reaction conditions of the VT-NMR experiment at 60 °C in THF-d$_8$. Bottom left: ^{31}P{^{1}H} NMR spectra of the above depicted reaction at 60 °C after indicated time intervals. The resonance belonging to the PPN cation (δ_{31P} = 21.6 ppm) is marked with an asterisk. The green rectangles mark the signals (two doublets) originating in the formation of imine complex **42**. Bottom right: ^{1}H NMR spectra of the above depicted reaction at 60 °C after indicated time intervals. Asterisks mark the signals for the PPN cation (around δ_{1H} = 8 ppm), as well as the solvent residual signals. The red rectangles indicate the broad signals which can be ascribed to the formation of anionic Os^{III} complex **41**$^{-}$. The green rectangles indicate sharp, *J*-coupling resolved signals of the diamagnetic Os^{II} complex **42**.

In general, the reaction stoichiometry is complicated due to the starting material product mixture, as well as the product mixture, consisting not only out of the two main products **41**$^{-}$ and **42** (Σ(yield) = 70%), but also some further, unidentified Osmium complexes. Under the assumption that **37** provides five H^{+} and four e^{-} and that imine complex **38** is reduced by one electron, as well as the transformation of azide to ammonia which is a three proton two electron

process the formation of approximately one equivalent of dihydrogen is expected (Scheme 3.6). Upon headspace analysis the amount was determined as 1.61 eq. H_2 relative to Osmium complex concentration, however, as mentioned above, the value is presumably overestimated. Furthermore, as 30% unidentified products are formed it is reasonable to assume that additional dihydrogen can originate from these side products as well.

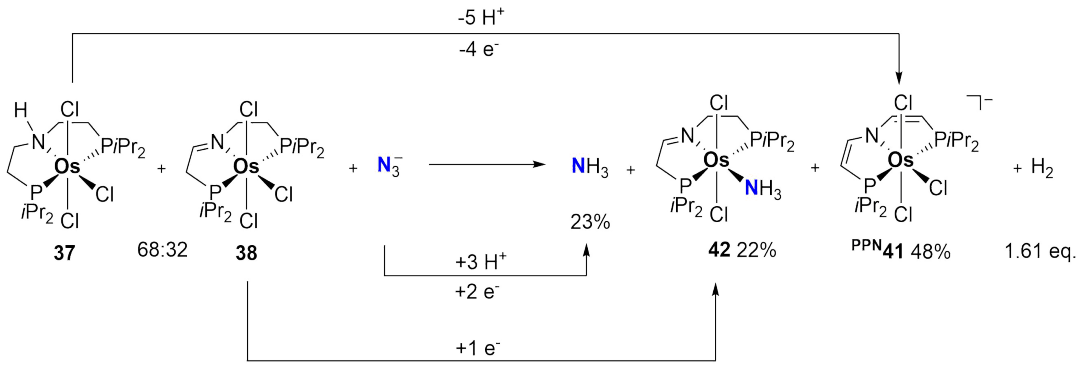

Scheme 3.6: Formal balance of proton and electron transfer between starting materials and reaction products. Yields for **42** and **41**$^-$ are isolated yields and the ratio of the starting materials **37** and **38** was indirectly determined upon reduction under N_2 and $^{31}P\{^1H\}$ NMR integration of the resulting diamagnetic N_2 complexes. The amount of H_2 was determined *via* headspace analysis of the reaction mixture with GC.

The assumption that **37** reacts exclusively towards **41**$^-$ and that **38** is reduced to Os^{II} complex **42** is arbitrary, but circumvents the problem, how ammonia is formed at the Osmium center, released and subsequently chloride is bound again to form osmate complex **41**$^-$. In the attempts towards dinitrogen activation at the Osmium trichloride complexes it was shown that chloride abstraction is difficult and removal of one chloride ligand was only possible upon reduction. Unfortunately, no information about the reaction mechanism could be obtained, neither by varying the reaction conditions, nor by following the reaction progress *via* VT-NMR. From related Osmium chemistry of the groups of *Meyer* and *Mayer* it appears reasonable to postulate a reactive Osmium nitride complex as intermediate that intra- or intermolecularly abstracts hydrogen atoms from the pincer backbone. This would imply either initial chloride to azide exchange or reduction of the Os^{III} starting material(s) to Os^{II} complexes (azide could potentially act as a reductant) and removal of one chloride ligand, which opens a free coordination site. This postulation stimulated further attempts to characterize the complexes with different degree of backbone unsaturation as discussed in the next chapter.

In conclusion, the following information could be obtained from the above described experiments:

1. Reaction of the **37**/**38** mixture with inorganic azide sources did not, as expected, lead to the formation of an Osmium nitride complex, but free ammonia (up to 97%) and dihydrogen were formed in conjunction with the backbone dehydrogenated complex [PPN][($^{i\text{Pr}}$P=N=P)OsCl$_3$] (**41**$^-$) and Os^{II} ammine complex [($^{\text{Imine}}$PNP)OsCl$_2$(NH$_3$)] (**42**).
2. The origin of the free ammonia, as well as the coordinated ammonia in **42** from the azide was verified with terminally labeled PPN^{15}N$_3$ (50% labeled ^{15}N/^{14}N) and the obtained ^{15}NH$_3$ was observed by several different NMR spectroscopic experiments.
3. Unfortunately, no further mechanistic information could be obtained, as in VT-NMR direct formation of the products without any appreciable amount of intermediates was observed.

3.4.2 The *iso*-Propyl Based Pincer Ligand as 5H$^+$ / 4e$^-$ Reservoir

The observed dehydrogenated product **41**$^-$ of the azide hydrogenation sparked interest in the series of complexes that have gradually less hydrogen atoms in the pincer backbone. Thus, starting from the **37**/**38** mixture stepwise abstraction of hydrogen atoms was attempted and will be discussed in this chapter.

Addition of 0.5 equivalents of 1,4-benzoquinone to the **37**/**38** mixture resulted in no apparent change in color, however in the ^{31}P{^{1}H} NMR spectrum the formation of an intense resonance at δ_{31P} = –39.8 ppm indicated the formation of a diamagnetic species with a high field shift presumably due to the influence of temperature independent paramagnetism (TIP). Slow gas phase diffusion of pentane into a saturated THF solution furnished brown crystals, which were suitable for X-ray crystallography. The solid-state structure (Figure 3.10) confirmed the formation of the Os^{IV} complex [($^{i\text{Pr}}$PNP)OsCl$_3$] (**43**) upon H-atom abstraction from amine complex **37**. The sum of angles around the pincer nitrogen atom is close to 360° (Σ = 359.4°), verifying the loss of the amine N-H hydrogen atom. The two bonds to carbon atoms from the nitrogen atom are distinctly uneven in their length indicating that a species with an imine moiety in the pincer backbone might be cocrystallized. This is reasonable given that the unit cells of

42 ($P2_12_12_1$, a = 7.3334(7) Å, b = 12.6637(11) Å, c = 24.004(2) Å, $\alpha = \beta = \gamma = 90°$) and of imine complex **38** (see below, $P2_12_12_1$, a = 7.2705 Å, b = 12.4671(8) Å, c = 24.2081(15) Å, $\alpha = \beta = \gamma = 90°$) can be considered isomorphous. Additionally, in the ^{1}H NMR of crystalline material the characteristic broad signals of the Os^{III} complex **38** were observed, suggesting that **38** from the starting material is still present and not converted into another species.

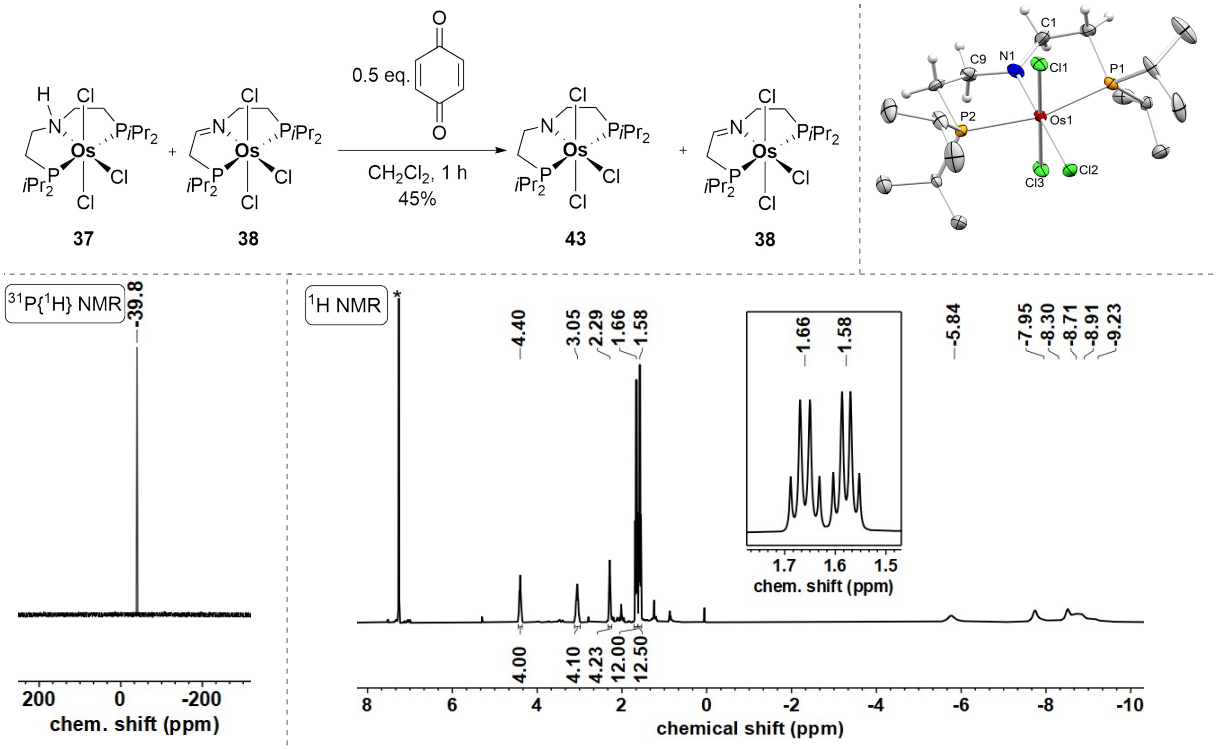

Figure 3.10: Top left: Reaction of the **37**/**38** Os^{III} complex mixture with 0.5 equivalents of benzoquinone to form a mixture of the Os^{IV} complex [($^{i\text{Pr}}$PNP)$OsCl_3$] (**43**) and the imine complex **38**. Top right: Molecular structures of **43** from single-crystal X-ray diffraction (thermal ellipsoids drawn at the 50% probability level); Hydrogen atoms except for selected ones on the pincer backbone are omitted for clarity. Selected bond lengths [Å] and angles [°]: Os1-N1 1.966(5), Os1-Cl1 2.3751(16), Os1-Cl2 2.4034(15), Os1-Cl3 2.3739(16), Os1-P1 2.3855(16), Os1-P2 2.3852(17), N1-C1 1.394(8), N1-C9 1.467(8), C1-N1-C9 114.9(5), C1-N1-Os1 124.3(5), C9-N1-Os1 120.2(4), Cl1-Os1-Cl3 178.91(6), P1-Os1-P2 164.60(6). Bottom left: ^{31}P{^{1}H} NMR spectrum of **43**/**38** in $CDCl_3$. Bottom right: ^{1}H NMR spectrum of crystalline **43**/**38** in $CDCl_3$. Solvent signal is marked with an asterisk.

43 exhibits sharp *J*-resolved signals in the ^{1}H NMR spectrum of C_2 symmetry and the high field shift in the ^{31}P{^{1}H} NMR presumably due to the influence of TIP is expected for Os^{IV} complexes.[476] The BDFE of the N-H bond in **37** was calculated by DFT (PBE0/def2-TZVP;SMD(THF)) to 67.4 kcal·mol^{-1} in THF. The employed H-atom abstracting agent benzoquinone has two BDFE's (65.2 and 80.0 kcal·mol^{-1}, but in DMSO)[477] for the first and second H-atom abstraction, respectively. From this it can be derived that the first BDFE of benzoquinone is in the range of the N-H BDFE for **37**, enabling the H-atom abstraction and oxidation to Os^{IV}. In this context, the next BDFE of the adjacent C-H was calculated as well. Surprisingly, the C-H BDFE of the transformation from amide complex **43** to imine complex

38 was calculated (PBE0/def2-TZVP;SMD(THF)) to be 46.5 kcal·mol^{-1}, which indicates a relatively weak C-H bond and could for example explain the formation of dihydrogen in the azide hydrogenation or even the partial formation of **38** from $OsCl_3 \cdot 3\ H_2O$ and the $^{i\mathrm{Pr}}P^{\mathrm{H}}NP$ ligand. In a future experiment it would be interesting to examine the reaction solution for the formation of the **37**/**38** mixture for dihydrogen. The low second BDFE is also a plausible explanation why no formation of amide **43** was observed in this case, but rather direct, partial formation of imine **38**.

In analogy to dinitrogen splitting starting from isoelectronic Re^{III} complexes, addition of reductant under N_2 atmosphere was examined with **43**. Reaction of the **43**/**38** mixture with one equivalent of $CoCp_2$ under N_2 resulted in the formation of several dia- and paramagnetic products as judged by ^1H and $^{31}P\{^1H\}$ NMR. Interestingly, among the paramagnetic products two resonances in the ^1H NMR spectrum matched the signals for anionic Os^{III} complex **41**$^-$, the main product of the metal-ligand cooperative azide hydrogenation to ammonia. Motivated by this and in knowledge of the partially low BDFE's of the pincer backbone the reaction solution was tested for ammonia. A low quantity of ammonium was detected after acidic workup (below 10%), however, under $^{15}N_2$ atmosphere only $^{14}NH_4^+$ was detected, indicating that a nitrogen-containing impurity (presumably even ammonium salt) was the origin of the detected ammonium.

The low calculated $BDFE_{CH}$ sparked interest whether the pure imine complex **38** was synthetically accessible from Os^{IV} amide **43**, which was contaminated with **38** and could not be separated from the imine complex despite numerous attempts. One equivalent of TEMPO (BDFE = 66.5 kcal·mol^{-1} in MeCN)[477] was added to the **43**/**38** mixture and the solution stirred for 27 hours at room temperature. ^1H and $^{31}P\{^1H\}$ NMR spectroscopy indicated the lack of signals of Os^{IV} complex **43** and instead only signals of the imine complex **38** were observed. After workup and recrystallization single crystals of **38** were obtained from CH_2Cl_2/pentane and examined by X-ray crystallography (Figure 3.11). In the solid-state structure the planar coordination geometry around the pincer nitrogen atom is evident by the sum of angles ($\Sigma = 360°$), as well as the distinctly shorter C-N bond of the imine moiety ($d_{N1\text{-}C9} = 1.304$ Å) compared to the N-CH_2 bond ($d_{N1\text{-}C1} = 1.445$ Å).

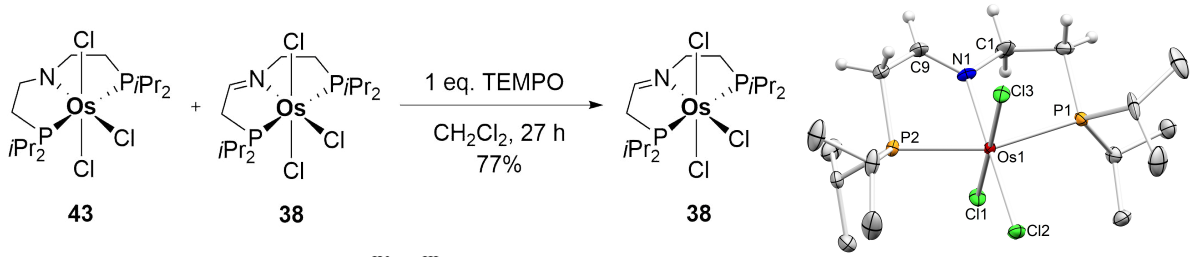

Figure 3.11: Left: Reaction of the Os^{IV}/Os^{III} complex mixture **43**/**38** with one equivalent of TEMPO to obtain pure imine complex **38**. Right: Molecular structures of **38** from single-crystal X-ray diffraction (thermal ellipsoids drawn at the 50% probability level); Hydrogen atoms except for selected ones on the pincer backbone are omitted for clarity. Selected bond lengths [Å] and angles [°]: Os1-N1 2.056(4), Os1-Cl1 2.3718(10), Os1-P1 2.3788(11), Os1-P2 2.3752(10), Os1-Cl2 2.3839(10), Os1-Cl3 2.3767(10), N1-C1 1.445(6), N1-C9 1.304(6), Os1-N1-C1 118.7(3), Os1-N1-C9 121.7(3), C1-N1-C9 119.6(4), Cl1-Os1-Cl3 177.09(4), P1-Os1-P2 162.67(4).

The facile and clean synthesis of pure **38** from **43**/**38** with TEMPO not only shows that the C-H bond adjacent to the nitrogen atom in **43** has a relatively low BDFE (in agreement to the DFT calculations), amenable to the comparatively weak H-atom abstracting agent TEMPO, but also that the next BDFE towards dehydrogenation of the pincer backbone must be considerably higher. That is, because relative to **43** an excess of TEMPO was used and could potentially abstract an H-atom from **38** if the remaining C-H BDFE's would be low enough. In the IR spectrum of **38** (see appendix) no N-H (from amine complex **37**) or O-H (from TEMPO-H) stretches were observed, but a separated band of medium intensity at ν = 1611 cm^{-1} was assigned to the C=N double bond stretch, based on DFT calculations ($\nu_{CN,DFT}$ = 1706 cm^{-1}, PBE0/def2-TZVP). Determination of the magnetic moment in solution (Evans' method) revealed a magnetic moment of μ_{eff} = 1.77 ± 0.1 μ_B, in compliance with an S = ½ low spin ground state.

The BDFE for abstracting an H-atom from **38** for the formation of a vinylamide complex was computed (PBE0/def2-TZVP) to be comparatively high ($BDFE_{CH}$ = 72.9 kcal·mol^{-1}), which is in agreement with the observation that no H-atom is abstracted from **38** with TEMPO. Interestingly, the two BDFE's towards the divinylamide complex [($^{i\mathrm{Pr}}$P=N=P)$OsCl_3$] (**44**) are lower (BDFE(vinylamide-enimide) = 49.5 kcal·mol^{-1}, BDFE(enimide-divinylamide) = 69.4 kcal·mol^{-1}) so that selective formation of one of these intermediates might not be possible. Accordingly, addition of one equivalent of the strong H-atom abstractor 2,4,6-tri-tert-butylphenoxyl radical (BDFE = 77.1 kcal·mol^{-1} in MeCN)[477] did result in mixtures of compounds according to ^{1}H and ^{31}P{^{1}H} NMR spectroscopy. Addition of 5 equivalents of 2,4,6-tri-tert-butylphenoxyl radical to the **37**/**38** mixture resulted in the appearance of three distinct species in the ^{31}P{^{1}H} NMR spectrum at δ_{31P} = –39.9 (s), –110.1 (2 x d) and –274.7 (s) ppm, respectively (Figure 3.12). The species at δ_{31P} = –39.9 ppm was attributed to

Os^{IV} complex [($^{i\mathrm{Pr}}$PNP)$OsCl_3$] (**43**), but the other two resonances remained unknown. From the signal multiplicity and the increasing TIP influence the two doublets at $\delta_{31P} = -110.1$ ppm were assigned to vinylamide Os^{IV} complex [($^{i\mathrm{Pr}}$P=NP)$OsCl_3$] (**45**) and the signal at $\delta_{31P} = -274.7$ ppm to the divinylamide Os^{IV} complex [($^{i\mathrm{Pr}}$P=N=P)$OsCl_3$] (**44**). Furthermore, in the ^{1}H NMR the characteristic signals for the imine complex **38** were detected. For full conversion towards divinylamide complex **44** an excess of 2,4,6-tri-tert-butylphenoxyl radical (10 equivalents) and heating (65 °C) was necessary, but furnished deeply green **44** in 92% isolated yield.

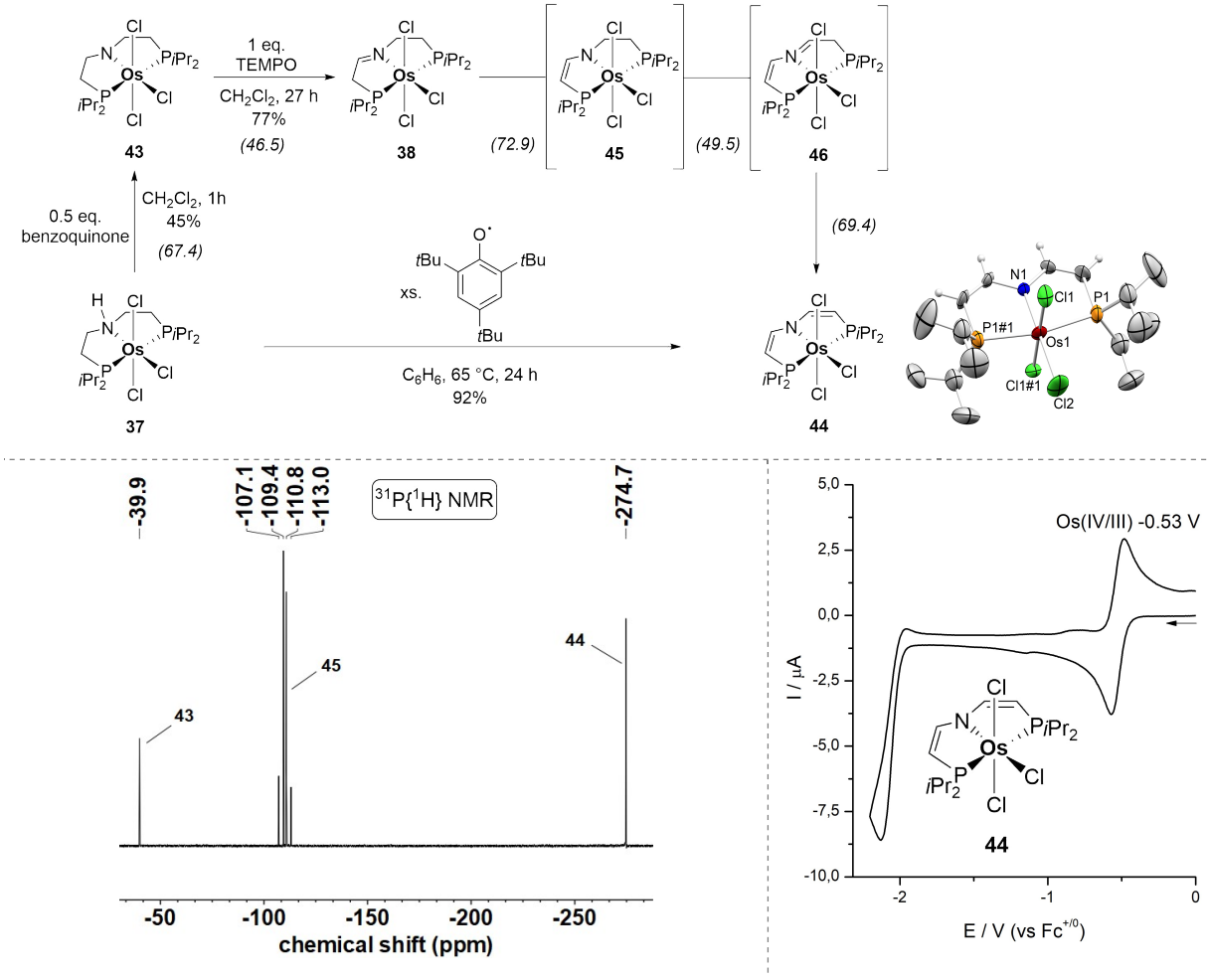

Figure 3.12: Top left: Summary of H-atom abstractions starting from amine complex **37**. Complexes **37** and **43** were obtained as mixtures with **38**, but to aid visibility only the main species is depicted. Complex **45** was not isolated, but observed in $^{31}P\{^1H\}$ NMR and the intermediacy of **46** is implied by the reaction product. Computed BDFE's (PBE0/def2-TZVP) are denoted in italic numbers below the reaction arrows (in kcal·mol^{-1}). Top right: Molecular structures of **44** from single-crystal X-ray diffraction (thermal ellipsoids drawn at the 50% probability level); Hydrogen atoms except for selected ones on the pincer backbone are omitted for clarity. Selected bond lengths [Å] and angles [°]: Os1-N1 1.958(12), Os1-Cl1 2.341(6), Os1-Cl2 2.377(4), Os1-P1 2.383(4), N1-Os1-Cl2 180.0, P1-Os1-P1#1 166.9(3). Bottom left: $^{31}P\{^1H\}$ NMR spectrum of the imcomplete reaction of **37**/**38** with 5 equivalents of 2,4,6-tri-tert-butylphenoxyl radical at room temperature. The spectrum indicated incomplete H-atom abstraction from the pincer backbone implied by the presence of intermediates **45** and **43**. Bottom right: Reductive branch of the CV of **44** (100 mV/s, 1 mM **44**, THF, Ar, 0.1 M nBu$_4$NPF$_6$).

The isolated complex **44** exhibits, as assigned above, a signal at δ_{31P} = –280.6 ppm in the $^{31}P\{^{1}H\}$ NMR spectrum, indicative of TIP influence on the chemical shift, characteristic for octahedral Os^{IV} complexes. The solid-state structure of **44** (Figure 3.12) obtained from single crystal X-ray crystallography verified the dehydrogenated backbone with the perfectly planar and symmetric pincer backbone, also reflected in the highly symmetric tetragonal space group P-42$_1$m. Electrochemical examination of **44** *via* cyclic voltammetry revealed a mild, reversible reduction at $E_{1/2}$ = –0.53 V, which is in agreement with previous evidence, that anionic, Os^{III} trichloride complex $[(^{iPr}P{=}N{=}P)OsCl_3]^-$ (**41**$^-$) is a stable complex that does not lose chloride. Indeed, addition of mild, one electron reductants like $CrCp_2$ or $CoCp_2$ to **44** formed the osmate complex **41**$^-$, as judged by NMR spectroscopy and mass spectrometry. The second reduction in the CV of **44** at E_{pc} = –2.13 V is irreversible and attempts to reduce with two equivalents of sodium amalgam under N_2 formed a new main species in the $^{31}P\{^{1}H\}$ NMR spectrum with two doublets at δ_{31P} = 26.2 and 20.6 ppm, respectively. However, despite numerous attempts the identity of the species could not be resolved. The chemical shift indicates an octahedral / five-coordinate Os^{II} complex (no TIP influence) and the signal multiplicity suggests either the formation of a dinuclear complex or cyclometallation. In a future experiment it would be interesting to distinguish between these two possibilities, for example with a DOSY NMR experiment.

In conclusion, the Os^{III} pincer complexes $[(^{iPr}P^{H}NP)OsCl_3]$ (**37**) and $[(^{Imine}PNP)OsCl_3]$ (**38**) were examined with regard to the susceptibility of the pincer backbone towards H-atom abstraction. Abstraction of one H-atom with 0.5 equivalents benzoquinone from the **37**/**38** mixture furnished Os^{IV} complex **43**, with **38** as a contaminant. Further H-atom abstraction to pure **38** was achieved with TEMPO. The DFT calculations predict the first $BDFE_{NH}$ to be significantly higher (67.4 kcal·mol^{-1}), than the second $BDFE_{CH}$ (46.5 kcal·mol^{-1}). Interestingly, the BDFE for the next H-atom abstraction towards the formal vinylamide Os^{IV} complex $[(^{iPr}P{=}NP)OsCl_3]$ (**45**) was calculated to be significantly higher (72.9 kcal·mol^{-1}), which could explain, why in the first place a mixture of **37**/**38** is formed and no further dehydrogenated complexes are formed. **45** is observed in $^{31}P\{^{1}H\}$ NMR as an intermediate but it was not possible to isolate this species. The divinylamide Os^{IV} complex $[(^{iPr}P{=}N{=}P)OsCl_3]$ (**44**) is obtained upon heating any of the intermediates and/or **37** with an excess of the strong H-atom abstracting agent 2,4,6-tri-tert-butylphenoxyl radical. **44** can be reduced by one electron, furnishing the anionic Os^{III} complex **41**$^-$, which is the main product of the metal-ligand cooperative azide hydrogenation reaction, highlighting that pincer complex **37** can act as a 5 proton 4 electron donor.

3.5 Conclusion

This part consisted of two different subunits. In the first part, the accessibility of dinuclear dinitrogen-bridged Osmium complexes was investigated. In the second part, new, unprecedented metal-ligand cooperative reactivity with the aliphatic pincer backbone was examined.

Using Os^{III} chloride hydrate as precursor yielded an intractable mixture of the paramagnetic Os^{III} complexes [($^{i\text{Pr}}$P$^{\text{H}}$NP)OsCl$_3$] (**37**) and [($^{\text{Imine}}$PNP)OsCl$_3$] (**38**). No chloride abstraction and N_2 binding was observed with reagents like $TlPF_6$ under N_2 atmosphere. Reduction of the **37**/**38** mixture under N_2 furnished the terminal Os^{II} N_2 complexes *trans*-[($^{i\text{Pr}}$P$^{\text{H}}$NP)OsCl$_2$(N$_2$)] (*trans*-**39**) and *trans*-[($^{\text{Imine}}$PNP)OsCl$_2$(N$_2$)] (*trans*-**40**), however no formation of a dinuclear complex or even dinitrogen splitting was observed upon oxidation.

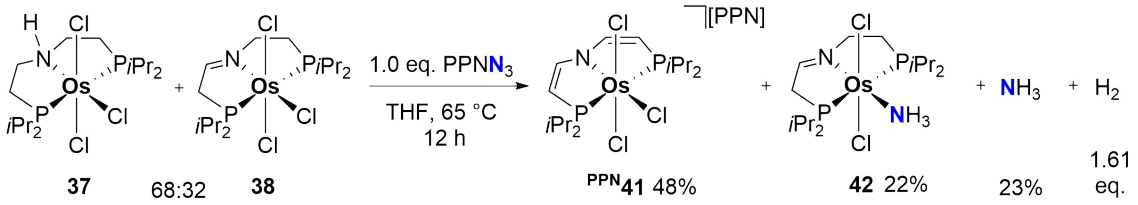

Scheme 3.7: Metal-ligand cooperative azide hydrogenation in the coordination sphere of Os^{III} pincer complexes. The ratio of the **37**/**38** mixture is determined indirectly, while the product yields are isolated yields. H_2 was determined *via* GC.

Reaction of the **37**/**38** mixture with inorganic azide sources did not, as anticipated, result in the formation of an Osmium nitride complex, but formed ammonia (up to 97%), dihydrogen, as well as the fully backbone dehydrogenated complex [($^{i\text{Pr}}$P=N=P)OsCl$_3$] (**41**$^-$) and an Os^{II} ammine complex **42**. The azide was verified as the source of the ammonia nitrogen atom upon ^{15}N-labeling experiments, which in combination with the dehydrogenated backbone indicate a metal-ligand cooperative azide hydrogenation, in which the ligand acts as a 5 proton 4 electron reservoir. However, the reaction stoichiometry remains ill-defined due to the starting material mixture of paramagnetic compounds.

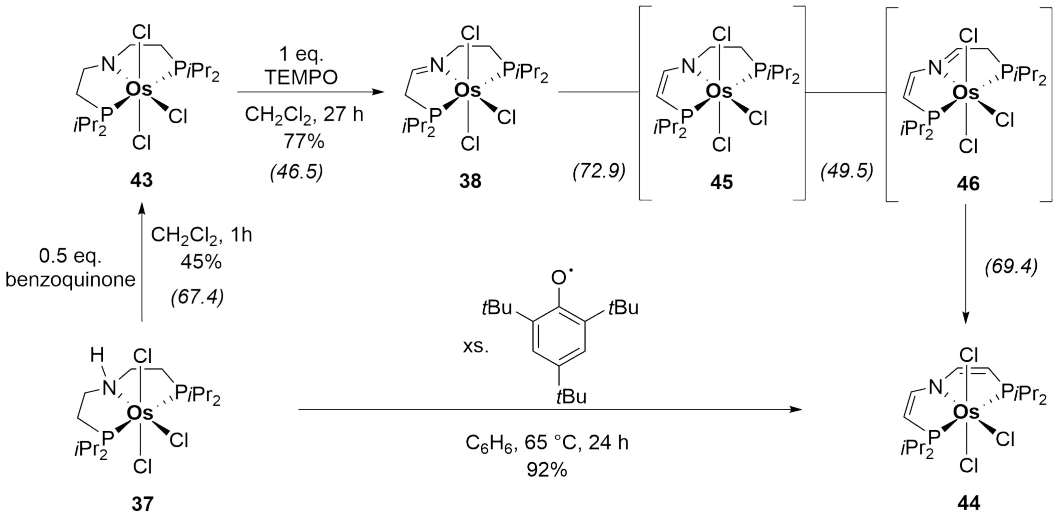

Scheme 3.8: Summary of H-atom abstraction steps starting from amine complex **37**. Complexes **37** and **43** were obtained as a mixture with **38**, but to aid visibility only the main species is depicted. Computed BDFE's (PBE0/def2-TZVP) are denoted in italic numbers below the reaction arrows (in kcal·mol^{-1}).

Finally, the relevant Osmium pincer complexes with varying degree of backbone dehydrogenation were isolated and their C-H or N-H BDFE's determined with the aid of DFT calculations. Interestingly, the second and fourth BDFE's are significantly lower than the first, third and fifth (Scheme 3.8). For example, the energy for Os^{III} amine to Os^{IV} amide ($BDFE_{NH}$ = 67.4 kcal·mol^{-1}) is considerably higher than for Os^{IV} amide to Os^{III} imine ($BDFE_{CH}$ = 46.5 kcal·mol^{-1}). A similar trend is obtained for the Os^{III} imine to Os^{IV} vinylamide ($BDFE_{CH}$ = 72.9 kcal·mol^{-1}) and Os^{IV} vinylamide to Os^{III} vinylimine ($BDFE_{CH}$ = 49.5 kcal·mol^{-1}). This could be an explanation for the experimentally observed dihydrogen formation.

Part IV: Outlook

Major advancements in the understanding and control of dinitrogen activation and nitride reactivity were achieved with the experimental and computational work described in this thesis. In several areas the results represent a cornerstone for future investigations to find new systems for the combination of dinitrogen splitting with (oxidative) functionalization schemes for unprecedented, dinitrogen-derived nitrogenous products.

The synthesis of two stable, dinuclear dinitrogen-bridged Osmium complexes based on a pyridine pincer $[(({}^{Py}PNP)OsCl_2)_2(\mu\text{-}N_2)_2]^{0/+}$ was described. They exhibit $\pi^{12}\delta^4$ and $\pi^{11}\delta^4$ electronic configurations, respectively, and preliminary experimental and electrochemical investigations indicated that a dicationic $\pi^{10}\delta^4$ complex might be accessible. As a consequence, this is expected to reduce the N-N bonding interaction present in $\pi > 8$ electronic configurations due to occupation of the $2e_u$ orbital set. From the activated, dicationic platform the cleavage of the bridging dinitrogen ligand could be induced thermally or photochemically and investigated in detail (Scheme 4.1). The produced Os^{VI} nitride complex is expected to exhibit electrophilic reactivity, allowing for coupling of dinitrogen splitting with oxidative or oxygenative functionalization.

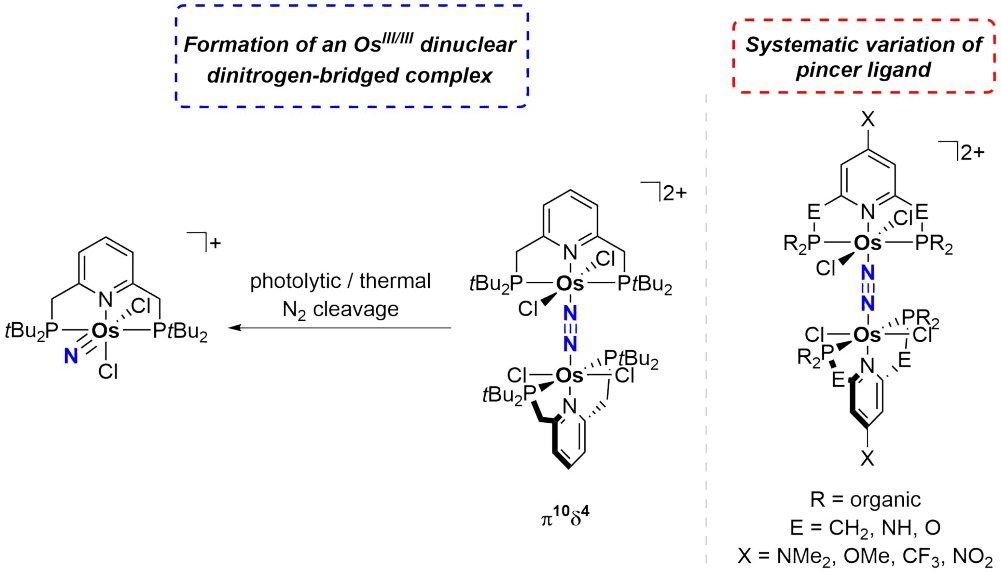

Scheme 4.1: Possible strategies towards dinitrogen cleavage in the coordination sphere of Osmium: Synthesis of an $Os^{III/III}$ dinuclear dinitrogen-bridged complex and photolytic or thermal N_2 cleavage to cationic Os^{VI} complexes (left). Systematic variation of donor groups, linkers and pincer backbone to study their influence on dinitrogen splitting (right).

One main advantage of pincer ligands is their modularity and flexible tailorability towards the problem at hand. In case of well-defined dinitrogen splitting in the coordination sphere of Osmium, the formation of dinitrogen-bridged dinuclear Osmium complexes, as well as the subsequent N_2 cleavage could be investigated. This should be accompanied by systematic variation of the organic substituents on the phosphorus atoms, the linkers and the pincer backbone. A deeper understanding of the underlying influence of donor properties on the energetic ordering and levels of the relevant molecular orbitals could be achieved this way. The experimental study could be accompanied or preceded by an extensive computational study, which could identify priviledged structures for Osmium-mediated dinitrogen splitting.

Electrochemical dinitrogen splitting with Rhenium pincer complexes was advanced in this thesis to reach essentially quantitative nitride yield and Faradaic efficiency. Furthermore, the use of relatively mild potentials for chemical reduction of [(^{Ph}PNP)ReI$_3$] could enable compatibility with functionalization reagents. For example, preliminary experimental results from *Yaroslava Zelenkova* indicate that $Sm^{II}I_2$, a mild reductant, is sufficient to achieve high yield dinitrogen splitting mediated by [(^{Ph}PNP)ReI$_3$]. This could be combined with PCET upon addition of water or alcohols, so that overall potential, electrocatalytic ammonia formation from N_2, H_2O and [(^{Ph}PNP)ReI$_3$] would be realized (Scheme 4.2). The high electrochemical dinitrogen splitting yields reported in this thesis suggest that [(^{Ph}PNP)ReI$_3$] could be a priviledged platform for the study of such reactions. Additionally, the exclusive use of iodide ligands in reductant and rhenium complex could facilitate the regeneration of the starting complex. Further studies of the dinitrogen cleavage with [(^{Ph}PNP)ReI$_3$] and the origin of the high splitting yields might influence future synthetic guidelines for high yield or even catalytic dinitrogen cleavage.

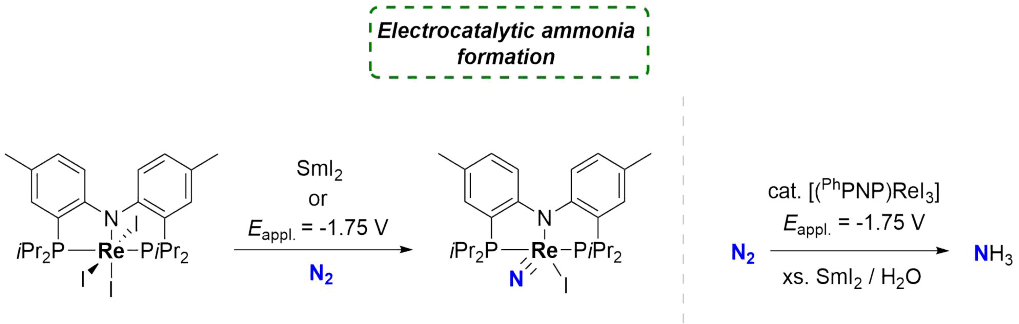

Scheme 4.2: Potential electrocatalytic ammonia formation mediated by (pre)catalyst [(^{Ph}PNP)ReI$_3$].

Nitride reactivity was explored extensively throughout the reported experimental and computational work. One major observation regarding nitride functionalization was the beneficial effect of a stabilizing sixth ligand for complexes of the ^{Ph}PNP ligand. For example, both the formation of a thionitrosyl dichloride complex, as well as an isocyanate dichloride complex from nitride and oxalyl chloride introduced a chloride ligand to stabilize the coordinatively unsaturated product as an octahedral complex. These findings could facilitate future functionalization approaches on this system, by choosing reagents that comcomitantly introduce stabilizing spectator ligands.

Other approaches for altering the nitride philicity might include different variations of the pincer complex, e.g. substituents on the aromatic rings of the pincer backbone or at the phosphorus donors. Furthermore, introduction of a ligand in *trans*-position to the nitride could enhance its inherent reactivity. The reported nitride transfer reactivity to NO and the experimental and computational examination gave valuable insight into possible, unprecedented reactivity of a dinitrogen-derived nitride complex. Experimental observation of intermediates was not possible, however, with very fast techniques like stopped-flow IR intermediates of the nitride transfer could be detected in future experiments.

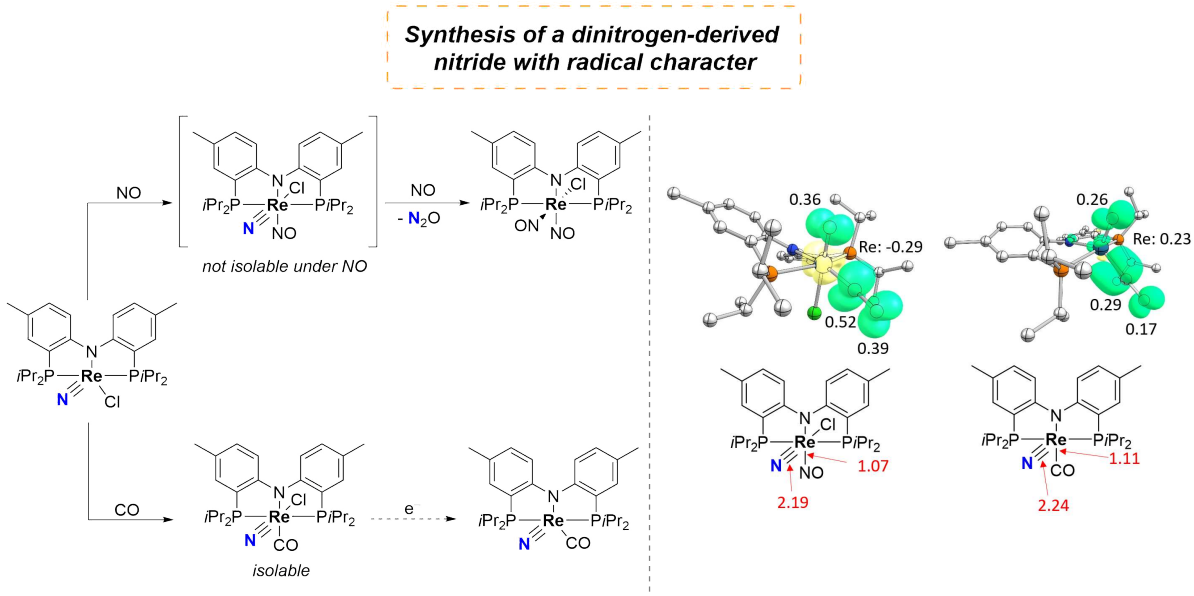

Scheme 4.3: Left: Formation of intermediate [(^{Ph}PNP)Re(N)(NO)Cl] and synthesis of a related Re^{IV} carbonyl complex. Right: Spin density distribution and Wiberg bond indices (WBI) of selected bonds in [(^{Ph}PNP)Re(N)(NO)Cl] (left) and [(^{Ph}PNP)Re(N)(CO)Cl] (right, both PBE0/def2-TZVP;def2-SVP).

DFT calculations supported initial NO coordination that weakens the Re≡N upon spin polarization and induces spin density on the nitride. Formally, the nitride character was shifted from nucleophilic to radical upon NO coordination. Unfortunately, the initially formed nitride

NO complex could not be isolated, preventing examination of other radical coupling reactions. A related model complex could be accessible with a carbonyl ligand. Addition of CO to [(^{Ph}PNP)Re(N)Cl] furnished, according to spectroscopic evidence, the terminal carbonyl complex [(^{Ph}PNP)Re(N)(CO)Cl]. Subsequent reduction (and presumably chloride loss) could yield five-coordinate [(^{Ph}PNP)Re(N)(CO)], which is formally Re^{IV}, like [(^{Ph}PNP)Re(N)(NO)Cl] and could potentially exhibit comparable nitride reactivity.

Preliminary DFT calculations (PBE0/def2-TZVP;SVP) support this assumption. Spin density analysis of [(^{Ph}PNP)Re(N)(CO)] places 0.26α spin on the nitride nitrogen atom ([(^{Ph}PNP)Re(N)(NO)Cl] = 0.36α spin). Furthermore, CO acts as an electron reservoir (0.46α spin), but to a substantially smaller degree than NO (0.91α spin). Interestingly, only minor spin polarization at Re is predicted for [(^{Ph}PNP)Re(N)(CO)]. NBO analysis indicates a weakened triple bond in [(^{Ph}PNP)Re(N)(CO)] ($WBI_{Re\equiv N}$ = 2.24) with respect to Re^{V} nitride [(^{Ph}PNP)Re(N)Cl] ($WBI_{Re\equiv N}$ = 2.50), again similar to [(^{Ph}PNP)Re(N)(NO)Cl] ($WBI_{Re\equiv N}$ = 2.19). These computational findings predict a similar nitride character of [(^{Ph}PNP)Re(N)(CO)] compared to [(^{Ph}PNP)Re(N)(NO)Cl], which makes it an interesting and potentially isolable synthetic target to study radical nitride reactivity towards nitric oxide and other radical reagents, like TEMPO, oxygen or organic radicals. This could extend the scope of nitrogenous products obtained from dinitrogen-derived nitrides significantly. A conceivable approach to independently synthesize [(^{Ph}PNP)Re(N)(NO)Cl] could be the reaction of *trans*-[(^{Ph}PNP)Re(NO)Cl_2] with an azide source. This could potentially allow for detailed nitride reactivity studies of this formal Re^{IV} complex beyond nitric oxide reactivity.

Conclusively, the advancements in the area of (electro)chemical dinitrogen splitting and (control of) dinitrogen-derived Rhenium nitride reactivity are the foundation for future, unprecedented transformations of dinitrogen. Especially the gained understanding of the influence of ligands and spin density on nitride reactivity holds the prospect for groundbreaking, new functionalization schemes.

Part V: Appendix

5.1 Synthetic and Analytic Methods

5.1.1 Synthetic Methods and Materials

All synthetic procedures were performed under inert gas atmosphere of Ar or N_2 gas (5.0, derived from *Linde*), with standard Schlenk and glovebox techniques, unless otherwise noted. All glassware was cleaned in KOH/*i*PrOH baths and HCl baths and rinsed with deionized water, before drying at 130 °C. All Schlenk line techniques involved additional heating of the vessels under applied vacuum. Small scale reactions were performed either in *J-Young* NMR tubes or in glass vials in the glovebox under inert gas conditions.

CO gas (*Air Liquide*, ≥99.997%) was purified by storing it in a cooled (ca. −78 °C) metal tube for at least one hour prior to use. H_2 gas (≥99.9999%, *Linde*) was purified by a high capacity moisture filter (*Pure Gas Products*) prior to use. NO gas (>99.5%, *Linde*), was purified by storing it in a cooled (ca. −100 °C) metal tube for at least one hour prior to use. N_2O gas (>99.9%, *Linde*) and $^{15}N_2$ (98% labelled, *Sigma Aldrich*) were used without further purification.

Cyclopentane, H_2O, 2-methoxyethanol, ethanol, pyridine and CCl_4 were degassed by two successive freeze-pump-thaw cycles and stored under argon. Fluorobenzene, 1,2-difluorobenzene, and chlorobenzene were dried over CaH_2 for at least one week and distilled by trap-to-trap transfer *in vacuo* and degassed *via* three freeze-pump-thaw cycles prior to use. Pentane, diethylether, toluene, benzene, acetonitrile, THF and dichloromethane were purchased in HPLC quality (*Sigma Aldrich*) and dried using a MBraun Solvent Purification System. Such pre-dried THF, toluene, diethylether and benzene, as well as 2-MeTHF were further dried for at least one week over Na/K alloy, distilled by trap-to-trap transfer *in vacuo* and degassed *via* three freeze-pump-thaw cycles, before storing in an inert gas glovebox. Deuterated solvents were obtained from Euriso-Top GmbH, dried over Na/K alloy (THF-d_8, C_6D_6, toluene-d_8), CaH_2 ($CDCl_3$, CD_2Cl_2, CD_3CN) or molecular sieves (3 Å, DMSO-d_6). THF-d_8, C_6D_6, toluene-d_8, CD_2Cl_2, CD_3CN were further transferred by trap-to-trap transfer *in vacuo* and degassed *via* three freeze-pump-thaw cycles.

$OsCl_3 \cdot 3\ H_2O$ (99.99%, *Alfa Aesar*), $(NH_4)_2[OsCl_6]$ (*Heraeus*), ^{Py}PNP (*Sigma Aldrich*), $CoCp_2$ (Sigma Aldrich), $TMSN_3$ (*Sigma Aldrich*), BPh_3 (*Sigma Aldrich*), NEt_3 (*Sigma Aldrich*), PPh_3 (*Sigma Aldrich*), $CoCp^*_2$ (*Sigma Aldrich*), $^{Ad}P^HNP$, PhMgBr in THF (*Sigma Aldrich*), Ag_2O (*abcr*), mCPBA (*abcr*), Me_3NO (*Sigma Aldrich*), pyridine-*N*-oxide (*TCI*), PMe_3 in THF (*Sigma Aldrich*), SmI_2 in THF (0.1M, *abcr*), oxalyl chloride (*Sigma Aldrich*), 15-crown-5 (*Sigma Aldrich*), 18-crown-6 (*Sigma Aldrich*), KO_2 (*abcr*), Na_2O (*Alfa Aesar*), *t*BuOOH in H_2O (*Alfa Aesar*), S_2Cl_2 (*Sigma Aldrich*), $NOBF_4$ (*Sigma Aldrich*), KO*t*Bu (*Sigma Aldrich*), NaHMDS (*Sigma Aldrich*), $TlPF_6$ (*abcr*), HCl in dioxane (4M), 1,3,5-trimethoxybenzene (*Sigma Aldrich*), PPh_3O (*Sigma Aldrich*), AdN_3 (*Sigma Aldrich*), nBu$_4$NN_3 (*Sigma Aldrich*), NaN_3 (*Sigma Aldrich*), benzoquinone (*TCI*), $Na^{15}NO_2$ (98% labelled, *Sigma Aldrich*), $FeSO_4 \cdot 7\ H_2O$, H_2SO_4 (98%) and HOTf were used as purchased. Sodium iodide was dried under high vacuum (10^{-5} mbar) at 100 °C for two days and stored in an argon glovebox prior to use. TEMPO was sublimed and EtOTf distilled, before storing in an argon glovebox at –35 °C in the dark. $FeCp_2$ and $FeCp^*_2$ were sublimed and nBu$_4$NPF_6 was dried overnight (80 °C, $<10^{-3}$ mbar) before use. Silica gel 60 silanized (*Merck KGaA*) was heated to 120 °C *in vacuo* for 5 days prior to use.

$[ReCl_3(PPh_3)_2(MeCN)]$,[476] $[ReBr_3(PPh_3)_2(MeCN)]$,[476] ^{Ph}PNP,[160,173] $^{tBu}P^HNP$,[478] $^{iPr}P^HNP$,[478] thianthrenium BF_4,[479] $NaBArF_{24}$,[480] $PPNN_3$,[481] $PPN^{15}NN_2$,[202] IMes-N_2O,[338] 2,4,6-tri-*tert*-butylphenoxyl,[482] $[H(OEt_2)_2][BArF_{24}]$[483], [nBu$_4$N][Os(N)Cl_4],[189] $[OsCl_2(PPh_3)_3]$[484] and TEMPO-H[485] were synthesized according to the reported literature procedures. Ferrocenium and acetylferrocenium salts were synthesized according to modified procedures for the synthesis of $[AcFc][BF_4]$ (with different silver precursors).[198] Na/Hg was prepared upon dissolving sodium in mercury.

5.1.2 Analytical Methods

Nuclear Magnetic Resonance (NMR)

NMR spectra were recorded on Bruker Avance III HD 300, Bruker Avance III 400, Bruker Avance III HD 400, Bruker Avance Neo 400, Bruker Avance III HD 500 and Bruker Avance Neo 600 spectrometers and calibrated to the residual solvent resonances (THF-d_8: δ_H = 3.58 ppm; C_6D_6: δ_H = 7.16 ppm, δ_C = 128.4 ppm; toluene-d_8: δ_H = 2.08 ppm; $CDCl_3$ δ_H = 7.26 ppm;

CD_2Cl_2, δ_H = 5.32 ppm, δ_C = 53.84 ppm, DMSO-d_6: δ_H = 2.50 ppm, CD_3CN: δ_H = 1.94 ppm) relative to Me_4Si.[195] ^{15}N and ^{31}P NMR chemical shifts are referenced to external nitromethane and phosphoric acid standards, respectively. Signal multiplicities are abbreviated as: s (singlet), d (doublet), t (triplet), vt (virtual triplet), sept (septet), m (multiplet), br (broad). Solution magnetic moments were determined at room temperature by Evans' method, modified by *Sur* with correction for the diamagnetic contribution.[486]

Vibrational Spectroscopy (IR and rRaman)

Solid IR spectra were recorded with a Bruker ALPHA FT-IR spectrometer with a Platinum ATR module inside an argon glovebox. Significant bands are denoted with: vs (very strong), s (strong), m (medium), w (weak), br (broad). Liquid IR spectra were recorded with a Thermo Scientific Nicolet iZ10 FT-IR spectrometer. The liquid IR cell with KBr windows was purged with argon gas and the inlet and outlet ports sealed with rubber septums. The solutions of interest were injected through the rubber septum *via* syringe prior to placing the cell in the spectrometer holder. For the N_2O quantification experiments, defined volumes of N_2O were allowed to dissolve in 1 mL toluene for 15 minutes before injecting the solution into the liquid IR cell. The obtained calibration curve was taken to quantify the amount of N_2O formed in the reaction of [(^{Ph}PNP)Re(N)Cl] with NO in 1 mL toluene.

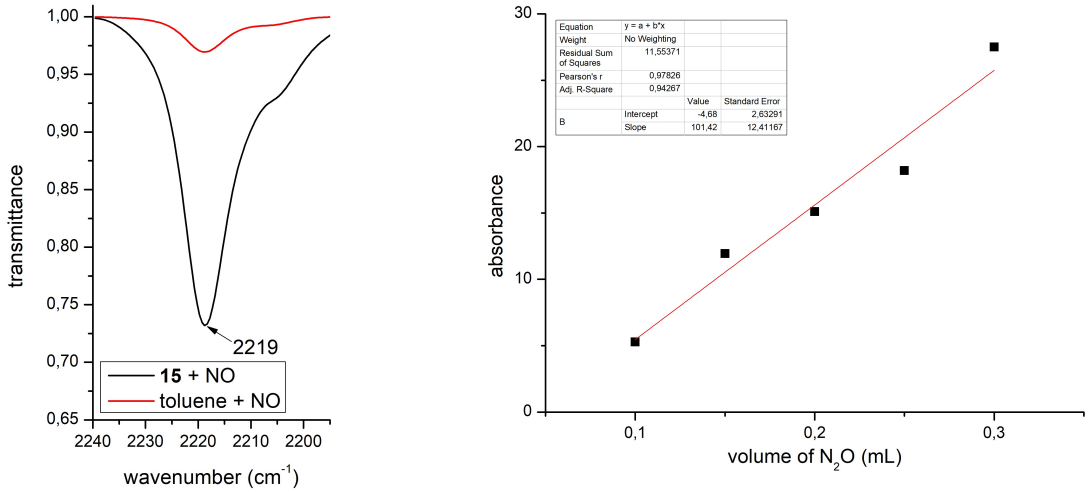

Figure 5.1: Left: Liquid IR measurement of NO-saturated toluene (red trace) and the reaction mixture of [(^{Ph}PNP)Re(N)Cl] + NO in toluene. Depicted is the band of N_2O (2219 cm^{-1}). Right: Calibration curve for measured absorbance depending on added volume of N_2O in toluene.

In situ liquid IR spectra were recorded with a Mettler Toledo ReactIR iC10 (MCT detector) with an AgX FiberConduit and a 9.5 mm DiComp probe. The probehead was fitted to the reaction flask with a rubber septum. For the *in situ* IR measurement of the reaction of [(^{Ph}PNP)Re(N)Cl] with NO, the reaction flask was evacuated and flushed with argon three times before backfilling the atmosphere with nitric oxide at −15 °C. One background spectrum of [(^{Ph}PNP)Re(N)Cl] under static vacuum in CH_2Cl_2 was recorded (t = 0 min). Afterwards, IR spectra were recorded every 30 seconds.

Resonance Raman spectra were recorded with a Horiba Scientific LabRAM HR 800 spectrometer, with open-electrode CCD detector and a free space optical microscope and a HeNe-laser (632.8 nm).

Mass Spectrometry, Elemental Analysis and Gas Chromatography

Mass spectra were obtained either via the FD ionization method (LIFDI-MS) on a JEOL accuTOF JMS-T100GCV or via electrospray ionization (ESI-MS) on Bruker microTOF and maXis by the “Zentrale Massenabteilung” at the Georg-August Universität Göttingen.

Elemental analyses were obtained from the analytical laboratories at the Georg-August Universität Göttingen on an Elementar Vario EL 3 instrument. Headspace analysis via gas chromatography was carried out with a Shimadzu GC-2014, equipped with a TCD detector.

SQUID magnetometry

Temperature-dependent magnetic susceptibility measurements were carried out with a *Quantum Design* MPMS3 SQUID magnetometer equipped with a 7 Tesla magnet in the range from 295 to 2.0 K at a magnetic field of 0.5 T. The solid, powdered sample was contained in a polycarbonate capsule and fixed in a non-magnetic sample holder. The raw data were corrected for diamagnetic contributions of the sample holder using the mpView.1.4.1 program[487]. The molar susceptibility was corrected for diamagnetic contribution using the Pascal constants and the increment method according to Haberditzl.[488] Experimental data were modelled with the *julX* program[489] using a fitting procedure to the spin Hamiltonian $\hat{H} = g\mu_B \vec{B} \cdot \vec{S}$.

Temperature-independent paramagnetism (*TIP*) was included according to $\chi_{calc} = \chi + TIP$. Intermolecular interactions were considered in a mean field approach by using a Weiss temperature Θ.[490] The Weiss temperature Θ (defined as $\Theta = zJ_{inter}S(S + 1)/3k$) relates to intermolecular interactions zJ_{inter}, where J_{inter} is the interaction parameter between two nearest neighbor magnetic centers, k is the Boltzmann constant (0.695 $cm^{-1}\cdot K^{-1}$) and z is the number of nearest neighbors.

UV-Vis and UV-Vis SEC

UV-Vis spectra were recoreded on an Agilent Cary 60 photospectrometer equipped with an Unisoku Cryostat and magnetic stirrer using quartz cuvettes and screw-cap with septum or *J-Young* cap. The UV-Vis samples were prepared in an argon filled glovebox with Na/K or CaH_2 dried solvents. UV-Vis spectroelectrochemistry (SEC) was recorded in a UV-Vis cell with a 1 mm thin-layer, a platinum mesh working electrode, a platinum disk (A = 0.071 cm^2) counter electrode and a silver wire reference electrode. UV-Vis data were recorded with a BWTEK ExemplarLS, via fiber optics.

Cyclic Voltammetry (CV) and Controlled Potential Electrolysis (CPE)

Cyclic voltammograms were recorded either with a *Metrohm* PGSTAT101 potentiostat and the Nova 2.1 software in an argon filled glovebox or with a *Gamry* 600 reference potentiostat using the Gamry software in an N_2 filled glovebox. The data were recorded in a three-neck flask equipped with a glassy carbon working electrode (1.6 mm diameter), platinum wire counter electrode and a silver wire pseudo-reference electrode internally referenced against the $FeCp_2^{+/0}$ couple. Controlled potential electrolyses were performed with a glassy carbon rod working electrode, a platinum wire counter electrode in a fritted compartment with $FeCp_2$ as sacrificial reductant and a silver wire as pseudo-reference electrode in a fritted sample holder with continuos stirring. All electrochemical experiments were conducted using a 0.2 M solution of nBu$_4$NPF$_6$ in THF or 1,2-difluorobenzene with appropriate internal resistance compensation.

For reversibility analysis of electrochemical features in the CV the peak currents i_p were analyzed according to the *Randles-Sevcik* equation:

$$i_p = 0.446\, nFAC^0 \left(\frac{nF\nu D_o}{RT}\right)^{1/2}$$

with n = number of transferred electrons, F = Faraday constant, A = electrode surface in cm^2, C^0 = analyte concentration in $mol \cdot cm^{-3}$, ν = scan rate in $V \cdot s^{-1}$ and D_o = diffusion coefficient of the oxidized species in $cm^2 \cdot s^{-1}$.[491] Thus, the peak currents and the square-root of the scan-rate linearly correlate for a perfectly reversible electron transfer process. Quasi-reversible electron-transfer processes are expected to deviate from this linear correlation.

Electron Paramagnetic Resonance (EPR)

X-band EPR spectra were recorded on a Bruker ELEXSYS-II E500 CW-EPR spectrometer equipped with a digital temperature control system (ER 4131VT) using liquid nitrogen as coolant. Liquid samples were prepared in an argon-filled glovebox and filled into air-tight, Teflon stoppered quartz glass *J-Young* EPR tubes. The recorded data were simulated using the EasySpin package for Matlab (v5.2.28).[492]

X-ray Crystallography

Suitable single crystals for X-ray structure determination were selected from the mother liquor under an inert gas atmosphere and transferred in protective perfluoro polyether oil on a microscope slide. The selected and mounted crystals were transferred to the cold gas stream on the diffractometer. The diffraction data were obtained at 100 K on a Bruker D8 three-circle diffractometer, equipped with a PHOTON 100 CMOS detector or PHOTON III detector and two INCOATEC microfocus sources with Quazar mirror optics (Mo-Kα radiation, λ = 0.71073 Å). The data obtained were integrated with SAINT, and a semiempirical absorption correction from equivalents with SADABS was applied. The structure was solved and refined using the Bruker SHELX 2014 software package.[493–497] All non-hydrogen atoms were refined with anisotropic displacement parameters. All C-H hydrogen atoms were refined isotropically on calculated positions by using a riding model with their U_{iso} values constrained to 1.5 U_{eq} of their pivot atoms for terminal sp_3 carbon atoms and 1.2 U_{eq} for all other carbon atoms.

5.2 Additional Experimental Results

5.2.1 DOSY NMR, CV and Irradiation Studies of [((^{Py}PNP)OsCl$_2$)$_2$(μ-N$_2$)]

In the ^{1}H NMR of [((^{Py}PNP)OsCl$_2$)$_2$(μ-N$_2$)] (Figure 5.2) broadened signals were observed, which raised the question for dynamic exchange in solution. The broadness could not be resolved upon cooling down to −60 °C. In the ^{31}P{^{1}H} NMR one sharp singlet was observed, independent of the temperature. Therefore, ^{1}H-DOSY NMR (Figure 5.3) was employed, to verify the presence of a dinuclear species in solution.

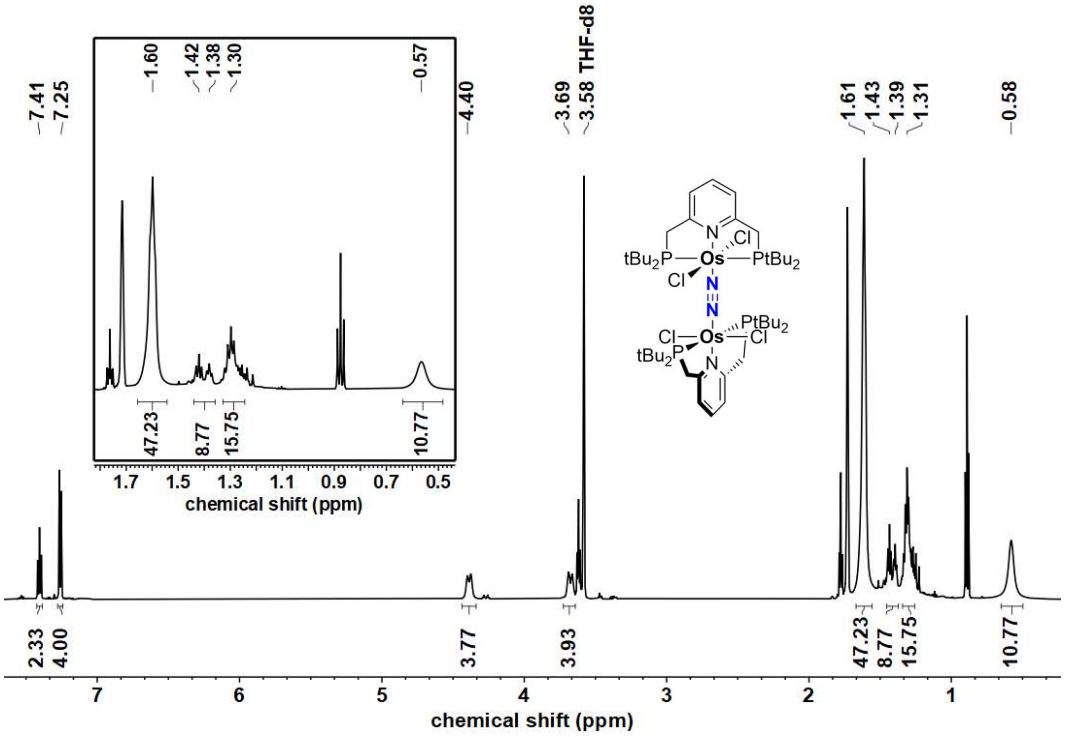

Figure 5.2: ^{1}H NMR spectrum of crystalline [((^{Py}PNP)OsCl$_2$)$_2$(μ-N$_2$)] in THF-d$_8$.

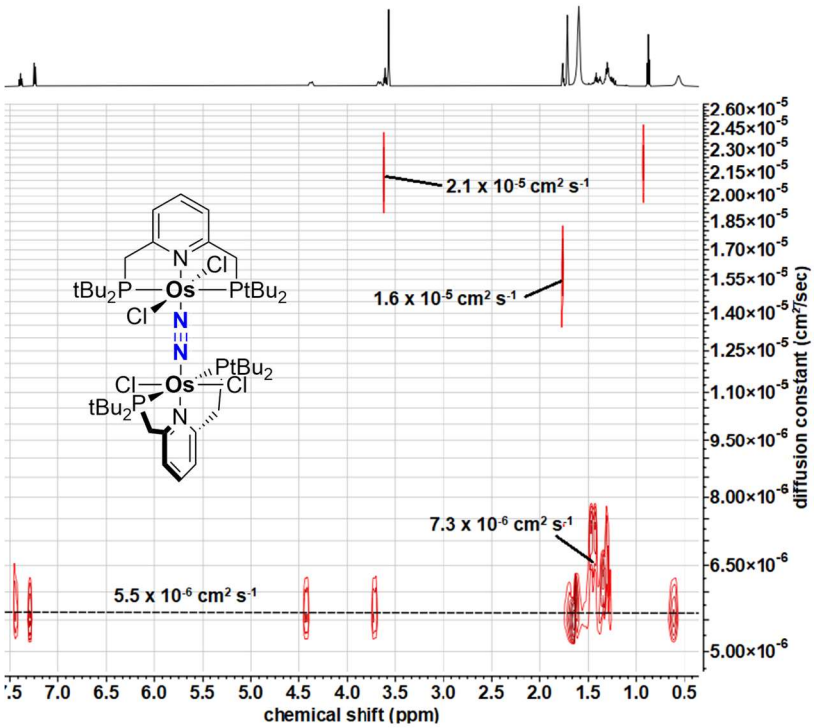

Figure 5.3: Transformed ^{1}H-DOSY NMR (298 K, 600 MHz, THF-d_8) of [((^{Py}PNP)$OsCl_2$)$_2$(μ-N_2)].

The diffusion constants derived from the ^{1}H-DOSY NMR can be correlated to the hydrodynamic radius of the respective species according to the *Stokes-Einstein* equation:

$$D = \frac{k_B T}{6\pi\eta R_0}$$

with D = diffusion coefficient, k_B = Boltzmann constant, T = temperature, η = solvent viscosity, R_0 = hydrodynamic radius of the species

The hydrodynamic radius can be – approximately – correlated to the molecular weight of the species of interest. This approximation implies an idealized spherical shape of the molecule, as well as its solvent shell, which obviously is not always the case and inevitably induces an error. The molecular weight therefore is only given as an estimate.

Table 5.1: Diffusion coefficients and estimated molecular weights derived from the ^{1}H-DOSY NMR experiment.

diffusion coefficient	estimated molecular weight
$2.1 \cdot 10^{-5}$ cm^{2}s^{-1}	98 g·mol^{-1}
$1.6 \cdot 10^{-5}$ cm^{2}s^{-1}	166 g·mol^{-1}
$7.3 \cdot 10^{-6}$ cm^{2}s^{-1}	850 g·mol^{-1}
$5.5 \cdot 10^{-6}$ cm^{2}s^{-1}	1590 g·mol^{-1}

From these molecular weight estimates for the species in solution it is evident, that a dinuclear species with a relatively high molecular weight is the main species. Its molecular weight is higher, than expected for [((^{Py}PNP)OsCl$_2$)$_2$(μ-N$_2$)] (M = 1356 g·mol^{-1}), which can be ascribed to the generally high error or additional solvent cage molecules. From comparison with the derived diffusion coefficient for the THF solvent molecule (2.1 ·10^{-5} cm^{2}s^{-1}) and its estimated molecular weight (98 g·mol^{-1}) it appears reasonable, that the molecular weight is systematically overestimated. Furthermore, the ^{1}H-DOSY NMR spectrum revealed the participation of another species of a molecular weight around 850 g·mol^{-1}. This could correspond to a mononuclear, terminal N$_2$ complex, which is in solution in an equilibrium with the dinuclear dinitrogen-bridged complex. However, this observation is in contrast to the ^{31}P{^{1}H} NMR, which shows no other species in solution. Further measurements, for example liquid IR, could help to distinguish between these two species.

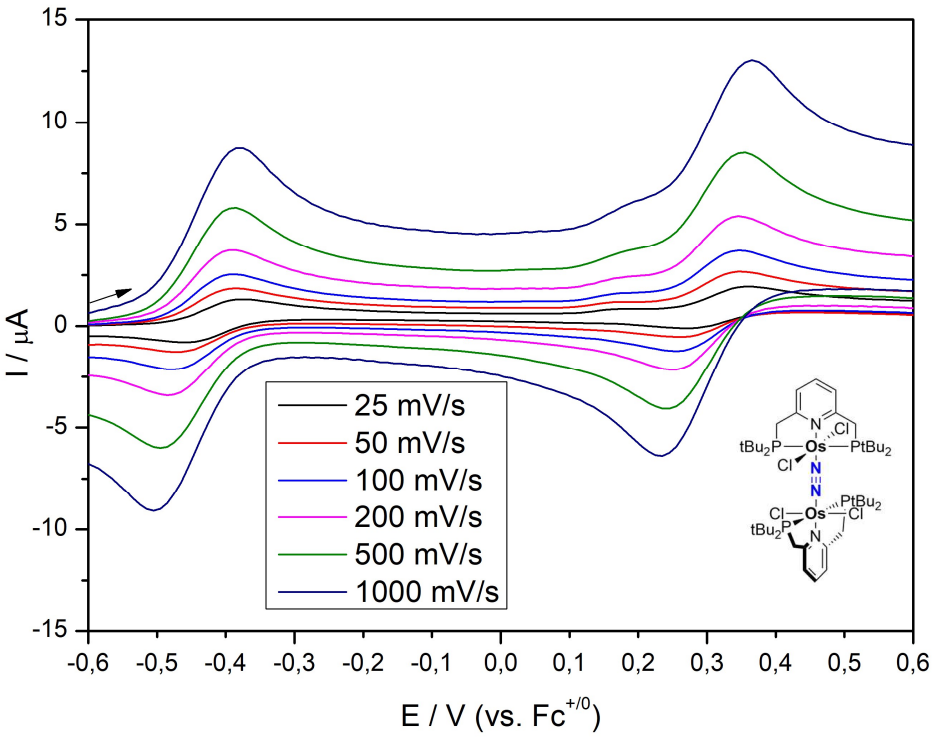

Figure 5.4: Cyclic voltammogram of [((^{Py}PNP)OsCl$_2$)$_2$(μ-N$_2$)] in THF under Argon (1 mM [((^{Py}PNP)OsCl$_2$)$_2$(μ-N$_2$)], Ar, 0.2 M nBu$_4$NPF$_6$).

Two distinct oxidations were observed in the cyclic voltammogram of [((^{Py}PNP)OsCl$_2$)$_2$(μ-N$_2$)] (Figure 5.4). The first, reversible feature at $E_{1/2}$ = –0.42 V is relatively mild and assigned to the $\pi^{12}\delta^4$ to $\pi^{11}\delta^4$ oxidation, which removes electrons from a metal-nitrogen antibonding and nitrogen-nitrogen bonding orbital. The second, reversible feature at $E_{1/2}$ = +0.33 V can be

assigned to the $\pi^{11}\delta^4$ to $\pi^{10}\delta^4$ oxidation. The wave shape of the backwave in Figure 5.4 is significantly influenced by features at higher voltage.

Irradiation of [((^{Py}PNP)OsCl$_2$)$_2$(μ-N$_2$)] was attempted with different wavelength LED lamps. Initially irradiation close to one of the absorption maxima with a lamp at λ_{max} = 467 nm was conducted (Figure 5.5, left). In this case the formation of a second peak at δ_{31P} = 31 ppm was observed and could indicate metal-nitrogen bond cleavage and formation of a terminal dinitrogen complex. This transformation was slow, yet relatively selective. Irradiation with higher energy wavelengths at λ_{max} = 390, 370 and 427 nm (Figure 5.5, right) did not form the presumed terminal dinitrogen complex, but very slowly several other species, of which the unidentified resonance at δ_{31P} = 39 ppm was the main species. No indication for dinitrogen splitting and nitride formation could be found by NMR spectroscopic and mass spectrometric examination of the reaction products.

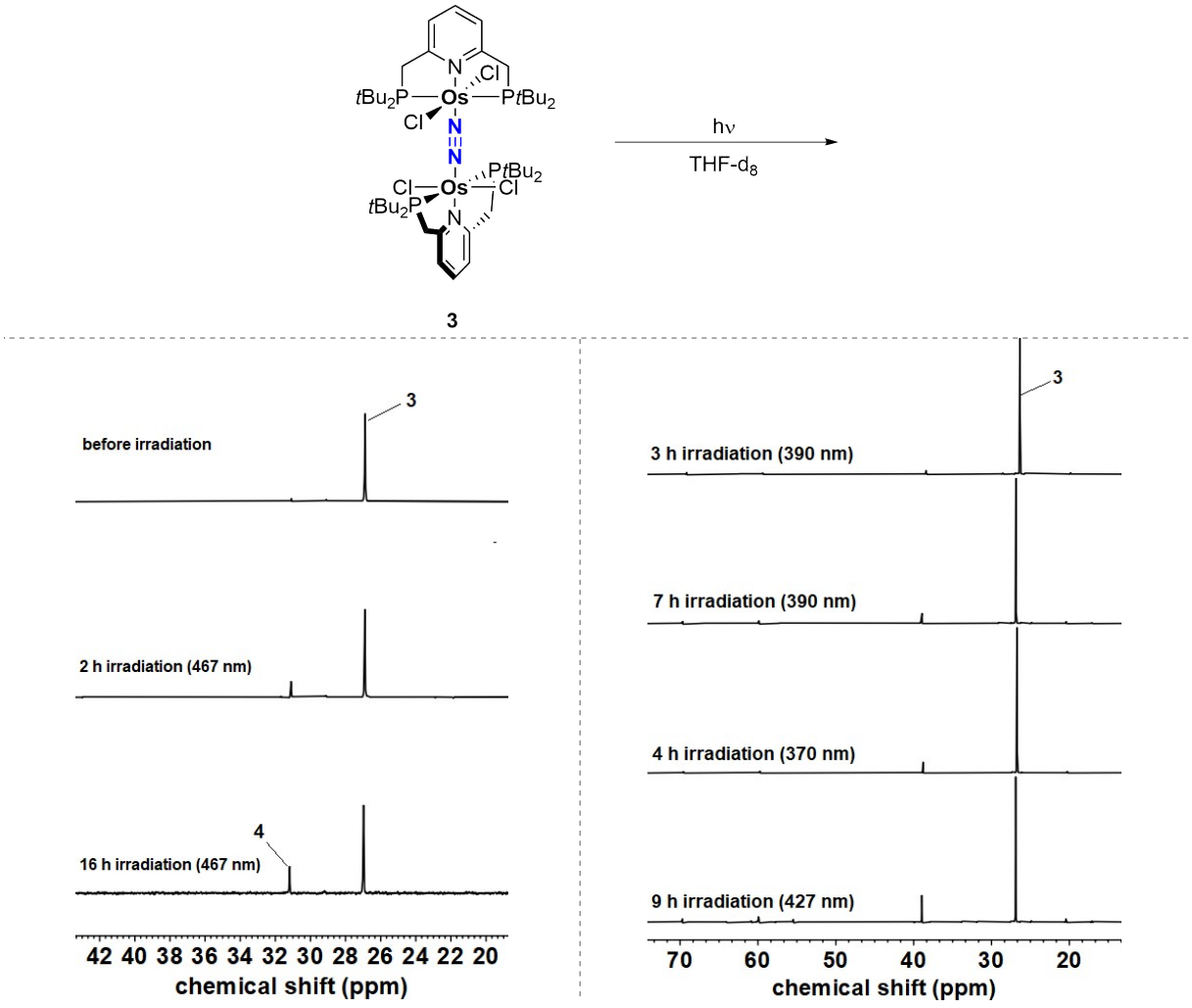

Figure 5.5: ^{31}P{^{1}H} NMR spectra of irradiation experiments of [((^{Py}PNP)OsCl$_2$)$_2$(μ-N$_2$)] with different wavelength LED lamps.

5.2.2 SQUID Magnetometry of $[((^{Py}PNP)OsCl_2)_2(\mu\text{-}N_2)]^+$

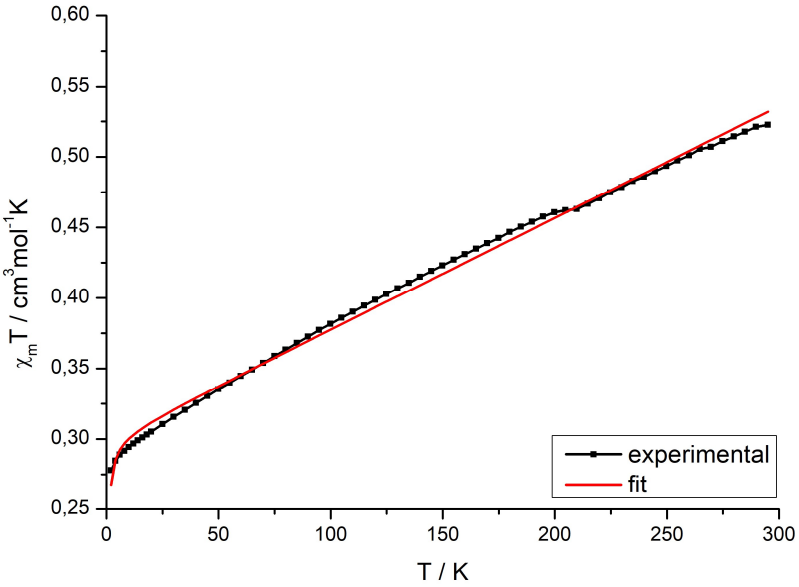

Figure 5.6: $\chi_m T$ vs. T plot for $[((^{Py}PNP)OsCl_2)(N_2)]^+$. Fitting parameters: $g = 1.786$, $D = 0$, $TIP = 788.9 \cdot 10^{-6}$ cm^3·mol^{-1}.

5.2.3 Additional Analytical Data of $[(^{Ph}PNP)ReCl_3]$

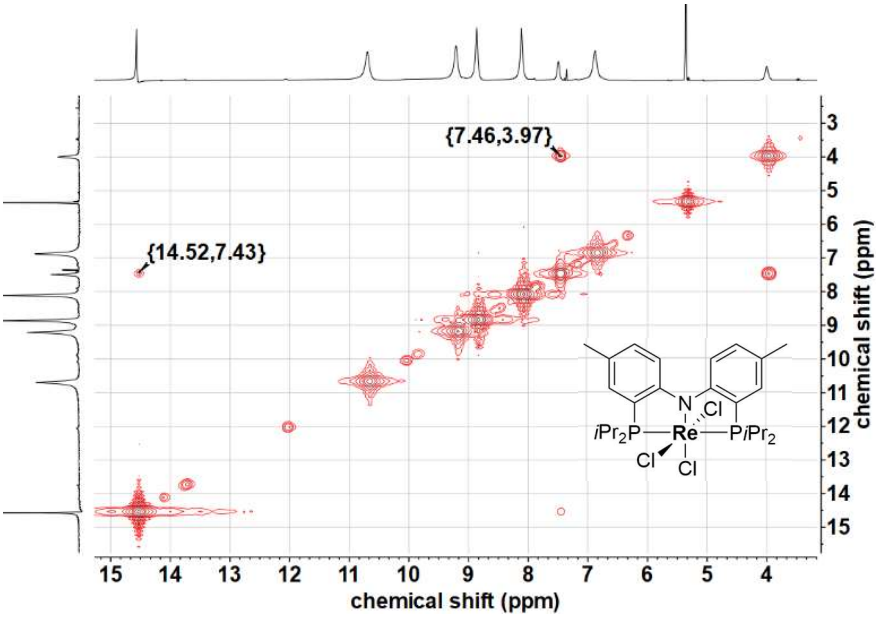

Figure 5.7: ^{1}H-^{1}H-COSY NMR of **9** in CD_2Cl_2.

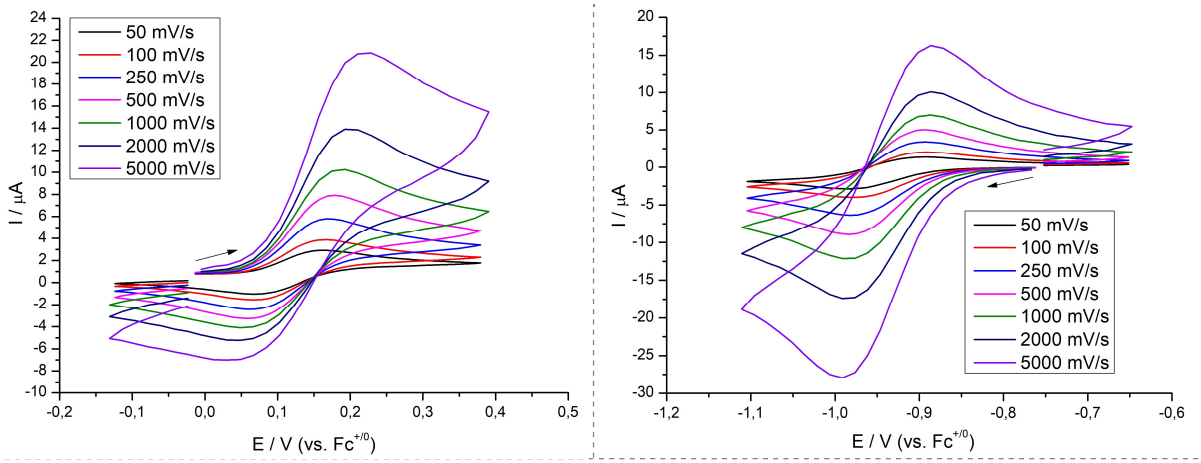

v / mVs^{-1}	$i_{p,f}$ / µA	$i_{p,r}$ / µA
50	2.086	2.483
100	2.990	3.256
250	4.711	4.749
500	6.449	6.260
1000	8.557	7.941
2000	11.834	10.532
5000	17.071	14.922

v / mVs^{-1}	$i_{p,f}$ / µA	$i_{p,r}$ / µA
50	2.609	2.489
100	3.649	3.590
250	5.640	5.803
500	8.233	8.529
1000	11.081	11.701
2000	16.153	17.009
5000	25.3	27.382

Figure 5.8: Left: Scan-rate dependent cyclic voltammogram of the first oxidation of [(^{Ph}PNP)ReCl$_3$] under argon atmosphere (1 mM [(^{Ph}PNP)ReCl$_3$], 0.2 M *n*Bu$_4$NPF$_6$) and Randles-Sevcik analysis of forward peak current vs. reverse peak current. Right: Scan-rate dependent cyclic voltammogram of the first oxidation of [(^{Ph}PNP)ReCl$_3$] under argon atmosphere (1 mM [(^{Ph}PNP)ReCl$_3$], 0.2 M *n*Bu$_4$NPF$_6$) and Randles-Sevcik analysis of forward current vs. reverse current. Data recorded by *Yaroslava Zelenkova*.

5.2.4 Spectroscopic Yield Determination of Electrochemical N_2 Splitting

[(^{Ph}PNP)ReI$_3$] was electrolyzed for 150 minutes at room temperature ($E_{appl.}$ = −1.67 V) in non-coordinating 1,2-difluorobenzene in a N_2 glovebox, during which the color changed from dark blue to red to green and finally to orange. After transfer of 1.96 e$^-$ per mol the CPE was stopped, the solvent removed under reduced pressure and the residue taken up in benzene and transferred to an argon-filled glovebox. Two-fold extraction with benzene over a short silanized silica column and removal of the solvent under reduced pressure furnished an orange powder, which was analyzed *via* ^{31}P{^{1}H} NMR spectroscopy and quantified with the aid of an internal standard (Figure 5.9). The chemical shift matched the shift of an independently synthesized sample of [(^{Ph}PNP)Re(N)I]. Furthermore, [(^{Ph}PNP)Re(N)I] as the main electrolysis product was verified upon high-resolution mass spectrometry (ESI).

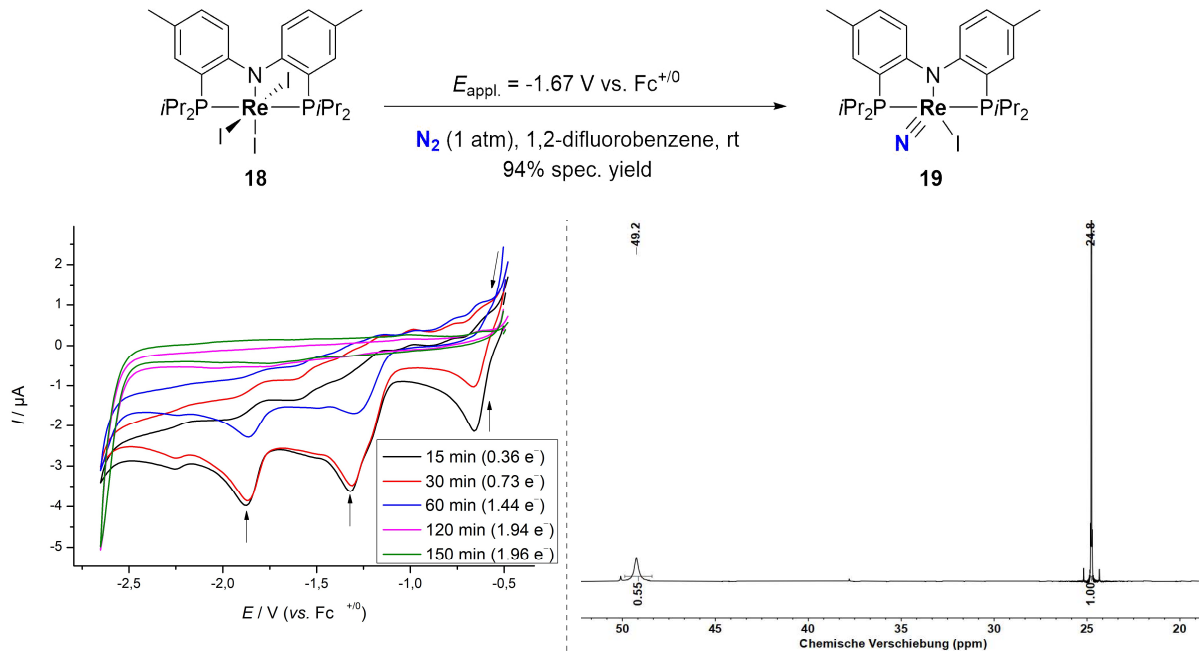

Figure 5.9: Left: Cyclic voltammograms of the CPE of **18** under N_2 atmosphere ($E_{appl.}$ = −1.67 V, 1 mM **18**, 0.2 M nBu$_4$NPF$_6$, 1,2-difluorobenzene). Right: $^{31}P\{^1H\}$ NMR spectrum in C_6D_6 after workup of the CPE of [(^{Ph}PNP)ReI$_3$] in 1,2-difluorobenzene under N_2 atmosphere. The peak at δ_{31P} = 49.2 ppm corresponds to nitride complex **19** and the peak at δ_{31P} = 24.8 ppm originates in PPh_3O as internal standard.

5.2.5 Reactivity of [(^{Ph}PNP)Re(N)Cl] towards EtOTf and CO

Addition of ethyl triflate to a solution of **15** in C_6D_6 led to no apparent change in color and of the resonances of the $^{31}P\{^1H\}$ and ^1H NMR spectra after three hours at room temperature. The sample was subsequently heated to 80 °C for 12 hours and ^{31}P NMR spectroscopy indicated the formation of two new diamagnetic species (δ_{31P} = 37.0 ppm, J = 212 Hz; δ_{31P} = 28.2 ppm, J = 225 Hz) with two doublet multiplicities (Figure 5.10). After additional 24 hours at 80 °C the starting material signal was completely consumed and the signal at δ_{31P} = 37.0 ppm was clearly recognizable as the major species. Mass spectrometry suggested the addition of an ethyl fragment to the complex, however, despite numerous attempts no species could be isolated from the resulting reaction mixture. Due to the lack of structural information it furthermore is not entirely clear, what the origin of the multiplicity in the $^{31}P\{^1H\}$ NMR spectrum is, but similarly to other reported complexes with the ^{Ph}PNP ligand, conformational isomerism is a reasonable explanation.[352]

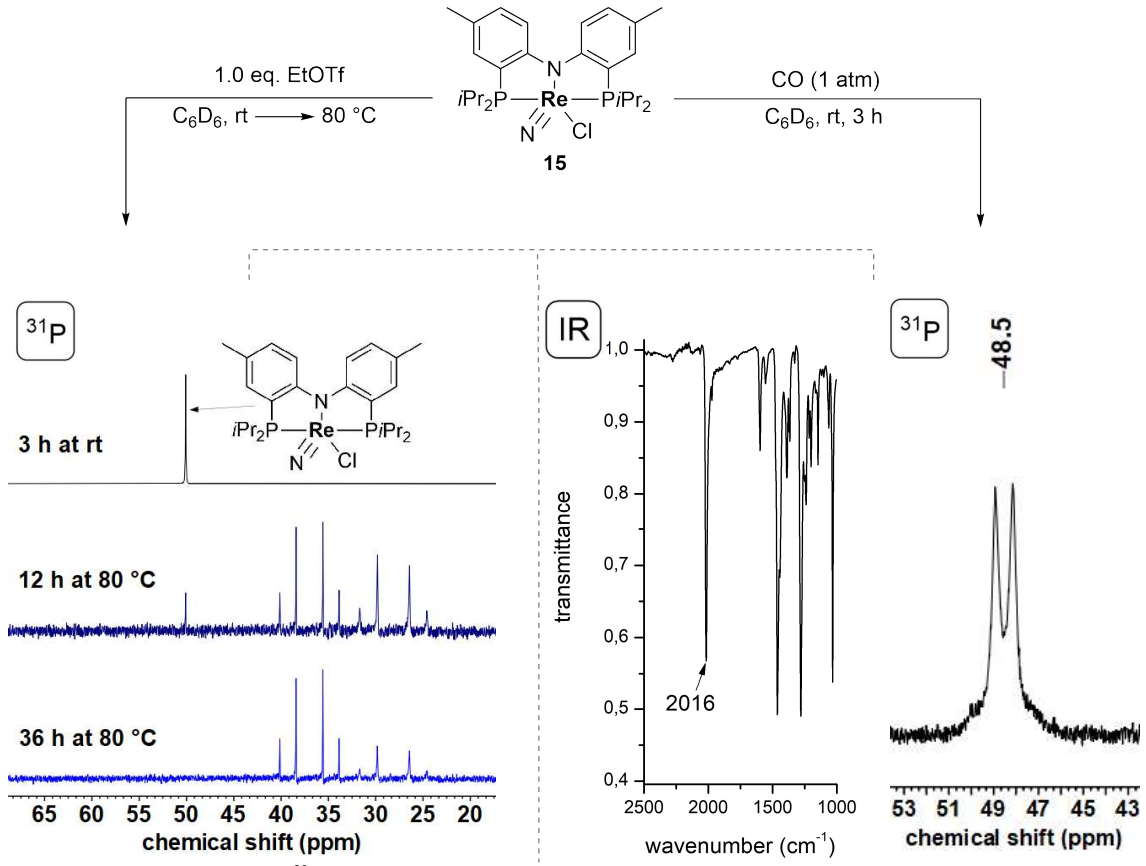

Figure 5.10: Top: Reaction of Re^{V} nitride **15** with EtOTf (left arrow) and CO (right arrow). The reaction products are not isolated and spectroscopic data are presented instead. Bottom left: $^{31}P\{^{1}H\}$ NMR spectra of the reaction of **15** with EtOTf in C_6D_6. The signal at $\delta_{31P} = 50.1$ ppm can be assigned to **15** and two new diamagnetic species are formed upon heating for prolonged periods. Bottom mid: ATR-IR (solid) of the reaction of **15** with carbon monoxide after removing of the CO gas and lyophilization of the residue. A sharp IR stretch at $\nu = 2016$ cm^{-1} is observed, which can be tentatively assigned to a Re carbonyl complex based on the typical wavenumber of terminal CO ligands. Bottom right: $^{31}P\{^{1}H\}$ NMR spectrum of the reaction mixture of **15** with carbon monoxide after 3 hours at room temperature. The reaction of **15** with CO was first performed and reported by *Leonard Hartung* in the course of his Master's thesis and reproduced here with similar results.[351]

Reactivity of **15** with carbon monoxide was initially examined by *Leonard Hartung* in the course of his Master's thesis[351] and reproduced with the aim of gaining more information on coordination of strong ligands on the Re^{V} nitride platform and to investigate whether formation of a Re^{III} isocyanate carbonyl complex is accessible. Addition of CO to a solution of **15** in C_6D_6 resulted in only a minor color change, however in the $^{31}P\{^{1}H\}$ NMR spectrum of the mixture under CO the formation of a broad signal of higher order was observed. From the peak shape it appears to consist out of two doublets with excessive roofing effect that leads to attenuation and broadening of the outer signals. Nevertheless, the signal multiplicity indicates two inequivalent phosphorus atoms of the pincer ligand, which for example could originate from hindered isomerization of the two backbone conformers on the NMR timescale at room temperature.

The almost unchanged chemical shift with respect to **15** contradicts the formation of a Re^{III} species which often show influence by temperature independent paramagnetism (however, in this context it has to be noted, that this effect is often quenched with strong-field ligands and such complexes exhibit ^{31}P shifts in the "common" range (e.g. [*cis*-($^{t\text{Bu}}$PNP)Re(CO)Cl_2)] δ_{31P} = 31 ppm).[498] Furthermore, in the IR (ATR, solid, Figure 5.10, bottom mid) a sharp and intense stretch at $\nu = 2016$ cm^{-1} was observed, which is rather indicative of a weakly activated Rhenium-bound carbonyl ligand than the formation of an isocyanate ligand ($\nu \geq 2200$ cm^{-1}). Mass spectrometry (ESI) furthermore verified the addition of only one CO equivalent to the complex and in combination with the spectroscopic evidence the formation of a [(^{Ph}PNP)Re(N)(CO)Cl] adduct complex appears reasonable. Even heating for 2 days under CO at 50 °C, performed by *Leonard Hartung*, resulted in the observation of the same spectroscopic evidence, which leads to the conclusion, that the barrier for isocyanate formation is too high at the given conditions. Despite several attempts no crystals suitable for X-ray crystallography could be obtained, which precluded further structural analysis.

5.2.6 Formation and Purification of ^{15}NO gas

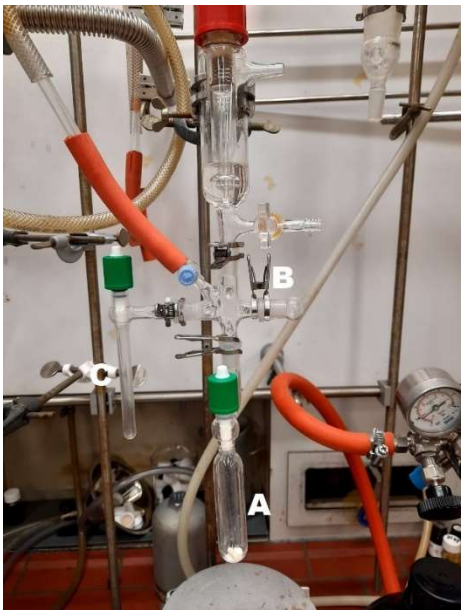

Figure 5.11: Reaction setup for the formation of ^{15}NO upon reduction of $Na^{15}NO_2$ with $FeSO_4$ and H_2SO_4. **A:** Reaction flask, **B:** Transfer line, **C:** Condensation flask.

Caution: The reaction scale was carefully adjusted to the volume of the flasks and transfer line. During the entire process (if not completely immersed in liquid nitrogen) the reaction flask,

transfer line and condensation flask were connected to an overpressure valve to prevent pressure build-up.

Under a nitrogen atmosphere, $Na^{15}NO_2$ (98% ^{15}N labelled, 255.0 mg, 3.64 mmol, 1.00 eq.) is dissolved in 1 mL degassed water and cooled to 2-3 °C using an ice bath. $FeSO_4 \cdot 7\ H_2O$ (1.02 g, 3.68 mmol, 1.01 eq.), dissolved in 4 mL degassed water is added to the $Na^{15}NO_2$ solution. The mixture is frozen (liq. N_2) and 1 mL conc. H_2SO_4 (95-97%) is added. Subsequently, vacuum is applied to the reaction flask (**A**), the reaction mixture warmed to room temperature and stirred until the brown color vanishes and no further gas evolution is observed. The reaction mixture is again frozen with liquid nitrogen to condense the gaseous nitric oxide. The reaction flask is closed and vacuum is applied to the transfer line (**B**) and the condensation flask (**C**). Afterwards, the condensation flask is closed, the reaction flask is opened and warmed to −110 °C. After 20 min the reaction flask (**A**) is closed, the condensation flask opened and cooled with liquid N_2 to condense ^{15}NO in **C**. After 20 min the condensation flask is closed and the reaction flask opened again, kept at −110 °C for 20 min and connected to the transfer line, before closing it again and condensing NO into **C** for another 20 min. **Note:** Direct trap-to-trap vacuum transfer from **A** to **C**, led to NO of lower purity, presumably from higher *N*-oxides, which was avoided by only condensing the ^{15}NO gas that was evolved into the transfer line (**B**).

5.2.7 Functionalization of [(^{Ph}PNP)Re(NO)$_2$]

Addition of one atmosphere of NO to **28** resulted in a slight color change from orange to yellow, vanishing of the ^{31}P NMR resonance and formation of several new broad signals in the ^{1}H NMR. Yellow crystals could be obtained from this reaction mixture, however, they were not suitable for an X-ray crystallographic measurement. In the ATR-IR of these crystals two intense stretches at ν = 1701 and 1641 cm^{-1}, as well as a weaker band at ν = 1598 cm^{-1} were observed (Figure 5.12, bottom left). This is comparable to the number and relative intensities of the IR stretches that were observed for the related [(^{Ph}PNP)Re(CO)$_3$] by *Ozerov* and coworkers.[367] In combination with the paramagnetic appearance of the NMR the formation of a trinitrosyl {Re(NO)$_3$}^{9} complex [(^{Ph}PNP)Re(NO)$_3$] from this reaction seems possible and can potentially explain the disappearance of [(^{Ph}PNP)Re(NO)$_2$] in the low temperature *in situ* IR and VT NMR experiments under NO atmosphere.

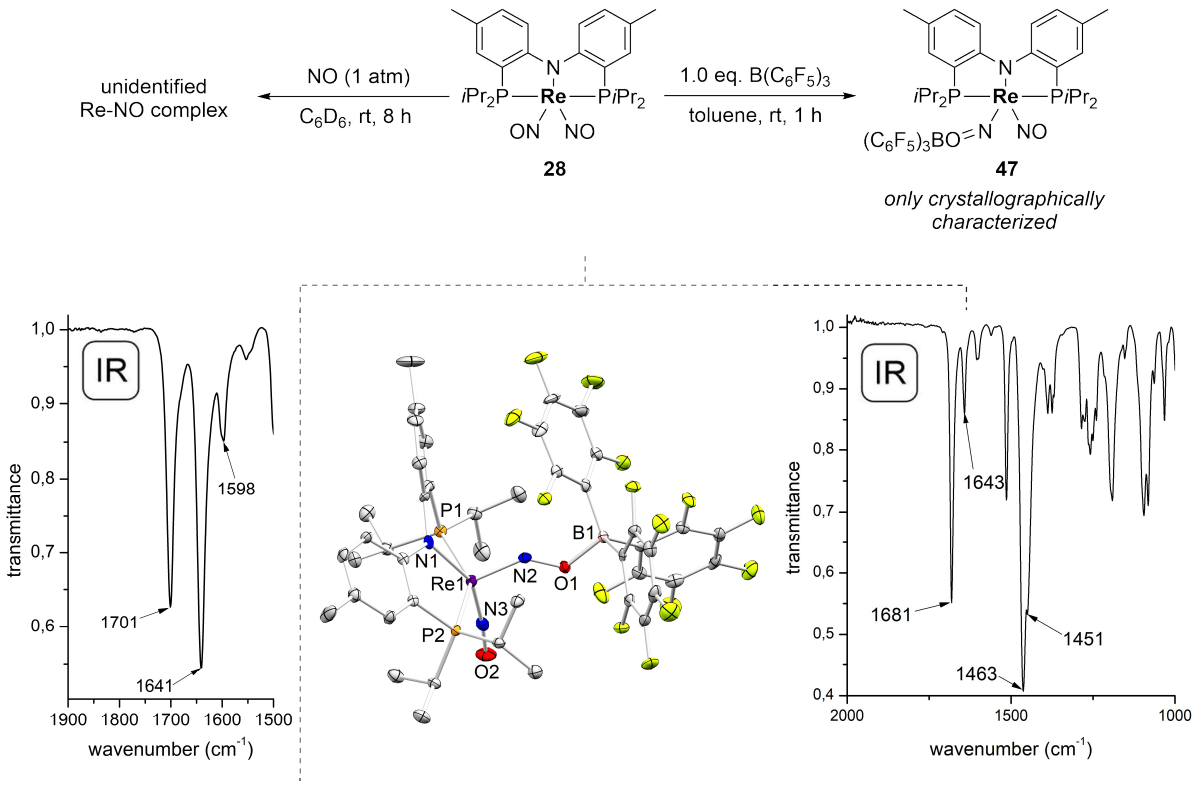

Figure 5.12: Top: Reactivity of **28** towards nitric oxide (left arrow) to form a paramagnetic NO containing compound, which is tentatively assigned to be trinitrosyl complex [(^{Ph}PNP)Re(NO)$_3$] or [(^{Ph}PNP)Re(NO)$_2$]$^+$ and reactivity towards Lewis-acidic borane B(C$_6$F$_5$)$_3$ (right arrow). Bottom left: ATR-IR (solid) of crystals obtained from the reaction of **28** with one atmosphere of nitric oxide gas. Bottom mid: Molecular structure of from single-crystal X-ray diffraction (thermal ellipsoids drawn at the 50% probability level); hydrogen atoms and a toluene solvent molecule are omitted for clarity. Selected bond lengths [Å] and angles [°]: Re1-N1 2.080(4), Re1-N2 1.785(4), N2-O1 1.315(5), O1-B1 1.548(6), Re1-N3 1.758(4), N3-O2 1.207(5), N1-Re1-N3 152.32(15), N1-Re1-N2 103.42(17), Re1-N3-O2 174.0(3), Re1-N2-O1 133.4(3), N2-O1-B1 118.3(3), P1-Re1-P2 145.97(4); τ^5 = 0.11. Bottom right: ATR-IR (solid) of crystalline [(^{Ph}PNP)Re(NO)(NOB(C$_6$F$_5$)$_3$)] (**47**).

Based on literature precedence the reactivity of the nitrosyl ligands was investigated. *Berke* and coworkers showed, that strong Lewis acids like B(C$_6$F$_5$)$_3$ are capable of binding to the oxygen terminus of electron-rich {Re(NO)$_2$}^{8} complexes, resulting in strongly bent NO ligands.[300] Addition of B(C$_6$F$_5$)$_3$ to a stirring solution of **28** in toluene at room temperature did not result in any recognizable color change. Crystals suitable for X-ray crystallography were obtained upon layering the reaction solution with pentane at −80 °C. As expected, in the solid-state structure (Figure 5.12, bottom right) the Lewis-acidic borane is coordinating to the oxygen atom of one nitrosyl ligand in [(^{Ph}PNP)Re(NO)(NOB(C$_6$F$_5$)$_3$))] (**47**), resulting in a strongly bent nitrosyl ligand ($\sphericalangle_{ReNO}$ = 133.4°) and significant increase in N-O bond length (**28**: d_{NO} = 1.203 Å, **47**: d_{NO} = 1.315 Å), while the second nitrosyl ligand remains almost linear ($\sphericalangle_{ReNO}$ = 174.0°, d_{NO} = 1.207 Å). These metrics are very similar compared to the {Re(NO)$_2$}^{8} adduct complex [(P*i*Pr$_3$)$_2$ReCl(NO)(NOB(C$_6$F$_5$)$_3$)] ((**47'**), $\sphericalangle_{ReNO}$ = 131.4°, d_{NO} = 1.301 Å).[300] In the IR of **47** intense stretches at ν = 1681 and 1463 cm^{-1}, as well as a weaker band at ν = 1643 cm^{-1} were observed. The band at ν = 1681 cm^{-1} can be ascribed to the linear NO (**47'**: ν_{NO} = 1712 cm^{-1}),

whereas the assignment for the bent NO ligand proves to be more difficult. The intense stretch at ν = 1463 cm^{-1} can either originate in the activated NO or in the numerous C-F bonds of the Lewis-acidic borane and is also present in **47'** (ν = 1461 cm^{-1}). However, the authors assigned a band of lower oscillator strength at ν = 1288 cm^{-1} as the activated NO ligand stretch, without any further information.[300] To conclusively assign the IR stretch for the bent NO ligand a ^{15}N-labelling experiment would be necessary.

5.2.8 IR Spectrum of [(^{Imine}PNP)OsCl$_3$]

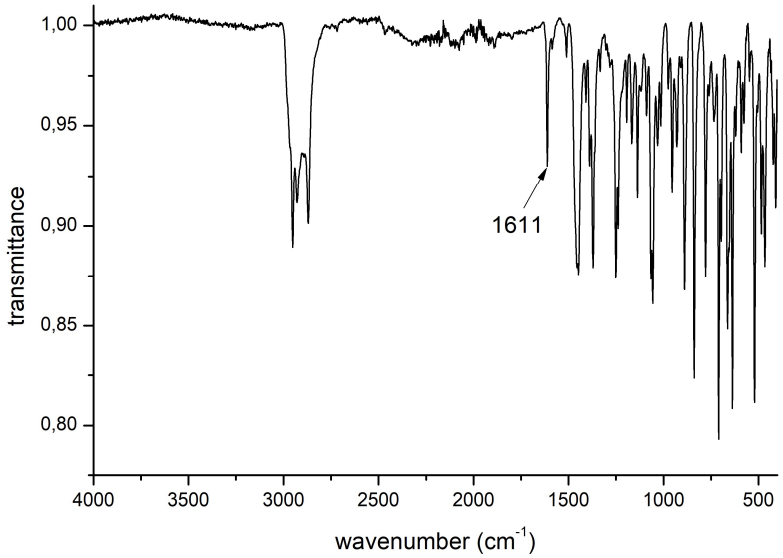

Figure 5.13: IR Spectrum (ATR, solid) of crystalline [(^{Imine}PNP)OsCl$_3$] (**38**). No clearly separated N-H stretch is observable. Furthermore, the sharp stretch at 1611 cm^{-1} is assigned to the C=N double bond, based on supporting DFT calculations.

5.2.9 NMR-Spectroscopic Quantification of Ammonia as Ammonium

In addition to the indophenolic titration, ammonia can be quantified as ammonium *via* NMR spectroscopy. For this, the analyte solution (either the entire reaction solution or the reaction volatiles after vacuum transfer to a separate flask) is frozen with liquid nitrogen and 2 mL HCl in dioxane (4 M) added onto the frozen solution under N_2 atmosphere. After application of vacuum, the flask is closed and allowed to warm to room temperature. The acidified analyte solution is stirred vigorously for 30 minutes, after which the solvent is removed under reduced pressure. Direct analysis of the solid residue requires thorough drying upon moderate heating under dynamic vacuum over night. In that case, the dry solid residue can afterwards be taken up in DMSO-d_6 and a defined amount of internal standard can be added for quantification purposes. The ammonia from the solid residue can also be released upon addition of aqueous

or ethanolic KOH solution and condensed into another flask. This can be used to separate the ammonia/ammonium from other reaction products, which could prevent NMR quantification by superimposition with the ammonium resonances.

5.3 Synthetic Procedures

5.3.1 Synthesis of [(^{Ph}PNP)OsCl$_3$] (**1**)

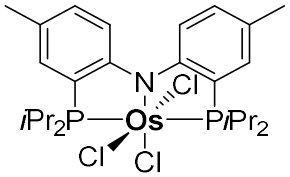

$OsCl_3 \cdot 3\ H_2O$ (30.0 mg, 85.6 µmol, 1.00 eq.) and $^{Ph}P^{H}NP$ (36.8 mg, 85.7 µmol, 1.00 eq.) are suspended in 5 mL toluene and heated to 120 °C for six days, while treating the suspension every day in an ultrasonic bath for at least 30 min. The solvent is removed under reduced pressure and the residue washed with pentane (3 x 2 mL), diethylether (3 x 2 mL) and benzene (1 x 1 mL) through a short Celite plug. Afterwards the residue is extracted with dichloromethane and the solvent removed to obtain [(^{Ph}PNP)OsCl$_3$] (25.1 mg, 34.6 µmol, 40%) as an intense green powder. Single crystals suitable for X-ray crystallography are obtained by slow diffusion of pentane into a saturated THF solution of [(^{Ph}PNP)OsCl$_3$].

EA: Calcd. for $C_{26}H_{40}Cl_3NOsP_2$ (725.14): C, 43.07; H, 5.56; N,1.93. Found: C, 42.79; H, 5.57; N, 1.90.

MS: LIFDI: *m/z* = 725.2 (100%), calcd. for $C_{26}H_{40}Cl_3N_1P_2Os$ (725.1).

1H NMR ($CDCl_3$, 400.24 MHz): δ = 8.37 (s, 2H, C_{Ar}-H), 8.11 (d, $^3J_{HH}$ = 8.5 Hz, 2H, C_{Ar}-H), 5.21 (d, $^3J_{HH}$ = 8.5 Hz, 2H, C_{Ar}-H), 5.03 (s, 6H, Ar(CH_3)$_2$), 4.22 (dsept, 4H, $^3J_{HH}$ = 7.0 Hz, $^2J_{HP}$ = 59.4 Hz, $(CH_3)_2CH$), 2.22 (dd, 6H, $^3J_{HH}$ = 7.0 Hz, $^3J_{HH}$ = 14.3 Hz, (CH_3)$_2$), 2.04 (dd, 6H, $^3J_{HH}$ = 7.0 Hz, $^3J_{HH}$ = 14.3 Hz, (CH_3)$_2$), 1.99 (dd, 6H, $^3J_{HH}$ = 7.0 Hz, $^3J_{HH}$ = 14.3 Hz, (CH_3)$_2$), 1.59 (dd, 6H, $^3J_{HH}$ = 7.0 Hz, $^3J_{HH}$ = 14.3 Hz, (CH_3)$_2$) ppm.

^{13}C{^{1}H} NMR ($CDCl_3$, 100.65 MHz): δ = 152.8 (t, 2C, *J* = 8.7 Hz, $C_{quart.}$), 152.1 (t, 2C, *J* = 16.7 Hz, $C_{quart.}$), 151.5 (m, 2C, $C_{quart.}$), 127.0 (s, 2C, C_{Ar}-H), 120.2 (s, 2C, C_{Ar}-H), 119.6 (s, 2C, C_{Ar}-H), 35.7 (t, 2C, *J* = 12.9 Hz, CH(*C*H$_3$)$_2$), 32.8 (t, *J* = 12.9 Hz, CH(*C*H$_3$)$_2$), 21.2 (s, *C*H(CH$_3$)$_2$), 19.7 (s, *C*H(CH$_3$)$_2$), 19.5 (s, *C*H(CH$_3$)$_2$), 18.2 (s, *C*H(CH$_3$)$_2$), 14.2 (s, 2C, 2 x Ar(*C*H$_3$)) ppm.

^{31}P{^{1}H} NMR ($CDCl_3$, 161.99 MHz): δ = –125.1 ppm.

5.3.2 Synthesis of [((^{Py}PNP)OsCl$_2$)$_2$(μ-N$_2$)] (**3**)

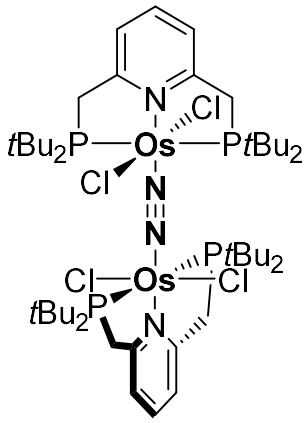

[(^{Py}PNP)OsCl$_3$] (64.2 mg, 92.8 μmol, 1.00 eq.) and CoCp$_2$ (17.5 mg, 92.5 μmol, 1.00 eq.) are stirred in 10 mL THF for two hours under N$_2$ atmosphere. Afterwards, the solution is degassed once *via* freeze-pump-thaw and stirred for additional 16 hours at room temperature. The solvent is removed under reduced pressure and the residue washed with 3 x 2 mL pentane and extracted with THF. [((^{Py}PNP)OsCl$_2$)$_2$(μ-N$_2$)] (51.8 mg, 38.6 μmol, 83%) is obtained as red crystals upon recrystallization from THF/pentane. Blood red single crystals suitable for X-ray crystallography are obtained by slow gas-phase diffusion of pentane into a saturated THF solution of [((^{Py}PNP)OsCl$_2$)$_2$(μ-N$_2$)].

EA: Anal. Calcd. for $C_{46}H_{86}Cl_4N_4Os_2P_4 \cdot C_5H_{12}$: C, 43.34; H, 6.99; N, 3.96. Found: C, 43.53; H, 6.92; N, 3.78.

MS: ESI (THF) 1342.37, calcd. for $C_{46}H_{86}Cl_4N_4Os_2P_4$ (1342.38).

CV: $E_{1/2}$ vs. Fc^+/Fc^0 (THF, V) = 0.33 ($Os^{III/III}$ / $Os^{III/II}$), –0.42 ($Os^{III/II}$ / $Os^{II/II}$), –2.93 (irrev.).

UV/Vis (THF, rt): λ / nm (ε / M^{-1} cm^{-1}) = 517 (1326), 418 (1520), 271 (3252).

rRaman (THF-d$_8$, cm^{-1}, 633 nm): 1991 (μ-^{15}N$_2$), 2056 (μ-^{14}N$_2$).

^{1}H NMR (THF-d$_8$, 600.25 MHz): δ = 7.41 (t, $^3J_{HH}$ = 7.9 Hz, 2H, para-C*H*-pyridine), 7.25 (d, $^3J_{HH}$ = 7.9 Hz, 4H, meta-C*H*-pyridine), 4.40 (br d, $^2J_{HH}$ = 14.0 Hz, 4H, PC*H*$_2$Py), 3.69 (br d, $^2J_{HH}$ = 14.0 Hz, 4H, PC*H*$_2$Py), 1.60 (br m, 48H, 16 x C*H*$_3$), 1.31 (m, 18H, 6 x C*H*$_3$), 0.58 (br s, 6H, 2 x C*H*$_3$) ppm.

^{13}C{^{1}H} NMR (THF-d$_8$, 100.65 MHz): δ = 169.3 (t, *J* = 3.0 Hz, ortho-*C*-pyridine), 136.2 (s, 2C, para-*C*H-pyridine), 120.5 (t, 4C, *J* = 4.1 Hz, meta-*C*H-pyridine), 39.4 (t, 4C, *J* = 8.6 Hz, 4 x *C*H$_2$P), 33.2 (br s, 16C, 16 x *C*H$_3$), 31.7 (m, 6C, 6 x *C*H$_3$), 31.0 (m, 2C, 2 x *C*H$_3$) ppm.

^{15}N{^{1}H} NMR (THF-d$_8$, 50.71 MHz): δ = –121.49 ppm.

^{31}P{^{1}H} NMR (CD_2Cl_2, 162.01 MHz): δ = 26.5 ppm.

5.3.3 Synthesis of $[(({}^{Py}PNP)OsCl_2)_2(\mu\text{-}N_2)][Al(OC(CF_3)_3)_4]$ ($\mathbf{5}^+$)

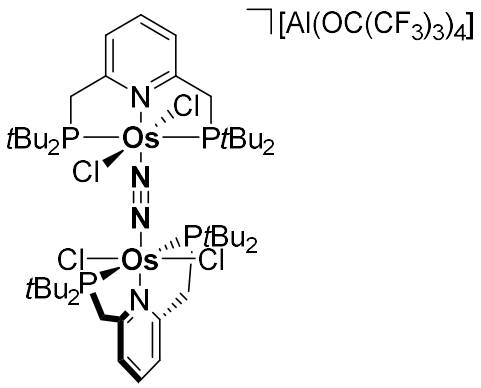

$[(({}^{Py}PNP)OsCl_2)_2(\mu\text{-}N_2)]$ (20.0 mg, 14.9 µmol, 1.00 eq.) is dissolved in 5 mL THF in the dark and $[Fe(C_5H_5)_2][Al(OC(CF_3)_3)_4]$ (16.8 mg, 14.9 µmol, 1.00 eq.) added in small portions to the stirred solution. The solution is stirred for additional 20 minutes in the dark after which the solvent is evaporated and the residue washed with pentane (5 x 2 mL). Upon extraction with diethylether and recrystallization from diethylether layered with pentane in the freezer at −40 °C $[(({}^{Py}PNP)OsCl_2)_2(\mu\text{-}N_2)][Al(OC(CF_3)_3)_4]$ is obtained as brown needles (28.6 mg, 12.4 µmol, 83%).

EA: Anal. Calcd. for $C_{62}H_{86}AlCl_4F_{36}N_4O_4Os_2P_4$: C, 32.26; H, 3.76; N, 2.43. Found: C, 31.80; H, 3.17; N, 2.27.

UVVis (THF, rt): λ / nm (ε / M^{-1} cm^{-1}) = 336 (10743), 370 (10672), 440 (shoulder, 4306), 669 (1155), 788 (5570).

NIR (THF, rt): λ / nm (ε / M^{-1} cm^{-1}) = 1541 (257), 2171 (1159).

IR: (ATR, cm^{-1}): 4549 (br), 3325 (br vs), 2002 (m, $\mu\text{-}N_2$).

MS: HRMS-ESI (THF) *m/z*: 1342.3721, calcd. for $C_{46}H_{86}Cl_4N_4Os_2P_4^+$ (1342.3731).

^{1}H NMR (CD_2Cl_2, 400.25 MHz): δ = 11.93 (br s, 4H, 4 x meta-C*H*-pyridine), 6.92 (br s, 3H, CH_3), 2.19 (br s, 2H, 2 x para-C*H*-pyridine), 1.60 (br s, 3H, CH_3), −0.39 (br s, 36H, 12 x CH_3), −0.75 (br s, 9H, 3 x CH_3), −1.10 (br s, 8H, 4 x CH_2), −1.88 (br s, 9H, 3 x CH_3), −3.55 (br s, 3 H, CH_3), −6.97 (br s, 3H, CH_3) ppm. Based on the integration, two CH_3 groups were not assigned and could not be found in the measured range between +200 and −100 ppm, probably due to severe broadening or shift outside of this range.

Magnetic susceptibility (rt, CD_2Cl_2): μ_{eff} = 1.57 ± 0.1 μ_B.

5.3.4 Synthesis of [(^{Ph}PNP)ReCl$_3$] (**9**)

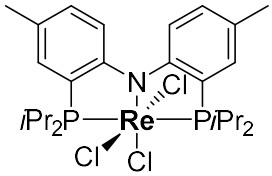

[ReCl$_3$(PPh$_3$)$_2$(MeCN)] (115.5 mg, 134.6 µmol, 1.00 eq.) and $^{Ph}P^{H}NP$ (57.8 mg, 134.5 µmol, 1.00 eq.) are suspended in 10 mL benzene and heated to 80 °C for 5 hours. The solvent is removed under reduced pressure and the dark residue washed with diethylether (5 x 3 mL) and benzene (2 x 5 mL) and extracted with dichloromethane. The solvent is evaporated to obtain [(^{Ph}PNP)ReCl$_3$] (83.6 mg, 115.9 µmol, 86%) as a dark violet solid, which can be recrystallized by gas-phase diffusion of diethylether into a saturated dichloromethane solution. Single crystals suitable for X-ray crystallography are obtained by slow diffusion of pentane into a saturated dichloromethane solution.

EA: calcd. for $C_{26}H_{40}Cl_3NP_2Re$: C, 43.31; H, 5.59; N, 1.94. Found: C, 43.44; H, 5.55; N, 1.96.

MS: LIFDI: *m/z* = 720.1 (100%), calcd. for $C_{26}H_{40}Cl_3NReP_2$ = 720.1.

UV/Vis: (THF, rt): λ / nm (ε / M^{-1} cm^{-1}) 288 (20178), 374 (7501), 566 (5312).

IR: (ATR, cm^{-1}): 3773 (br), 2238 (br).

CV: $E_{1/2}$ vs. Fc$^+$/Fc^0 (THF, V) = +0.11 (Re^{V}/Re^{IV}, rev.), –0.97 (Re^{IV}/Re^{III}, rev.), –2.46 (Re^{III}/Re^{II}, irrev.).

^{1}H NMR (CD_2Cl_2, 300.16 MHz): δ = 52.61 (2H, br s), 20.51 (2H, br s), 14.53 (2H, br s), 10.66 (6H, br s), 9.17 (6H, br s), 8.82 (6H, br s), 8.07 (6H, br s), 7.46 (2H, br s), 6.84 (6H, br s), 3.96 (2H, br s) ppm.

Magnetic susceptibility (r.t., CD_2Cl_2): μ_{eff} = 1.63 ± 0.1 μ_B.

5.3.5 Synthesis of [(^{Ph}PNP)ReCl$_3$][Al(OC(CF$_3$)$_3$)$_4$] (**10**$^+$)

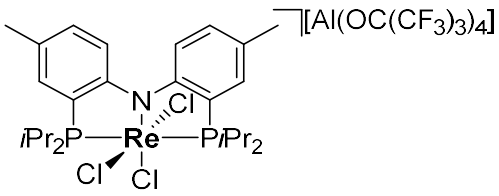

[(^{Ph}PNP)ReCl$_3$] (13.0 mg, 18.0 µmol, 1.00 eq.) and [AcFc][Al(OC(CF$_3$)$_3$)$_4$] (21.4 mg, 18.0 µmol, 1.00 eq.) are suspended in 5 mL 2-MeTHF/MeCN (1:1) and stirred for 30 minutes at room temperature. The solvent is removed under reduced pressure and 20 mL pentane added under vigorous stirring. After five minutes the solvent is decanted and the residue recrystallized from diethylether/pentane at −80 °C. [(^{Ph}PNP)ReCl$_3$][Al(OC(CF$_3$)$_3$)$_4$] (27.7 mg, 16.4 µmol, 91%) is obtained as violet crystals. Single crystals for X-ray crystallography are obtained as the [BF$_4$] salt upon slow diffusion of diethylether into a saturated acetonitrile solution of [(^{Ph}PNP)ReCl$_3$][BF$_4$] at room temperature.

EA: calcd. for C$_{42}$H$_{40}$AlCl$_3$F$_{36}$NO$_4$P$_2$Re: C, 29.88; H, 2.39; N, 0.83. Found: C, 29.35; H, 2.51; N, 0.79.

MS: LIFDI: *m/z* = 720.0 (100%), calcd. for C$_{26}$H$_{40}$Cl$_3$N$_1$P$_2$Re$_1$ = 720.1.

^{1}H-NMR (CD$_2$Cl$_2$, 300.16 MHz): δ = 131.86 (br s, 2 H), 77.08 (d, 2 H, *J* = 8.9 Hz), 35.04 (s, 6 H), 13.30 (s, 6 H), 4.31 (br s, 2 H), 1.62 (s, 6 H), 1.30 (s, 6 H), 0.50 (s, 2 H), −12.96 (d, 2 H, *J* = 8.9 Hz), −64.57 (s, 6 H).

Magnetic susceptibility (r.t., CD$_2$Cl$_2$): μ_{eff} = 2.19 ± 0.1 μ_B.

5.3.6 Synthesis of [(^{Ph}PNP)ReCl$_2$] (**11**)

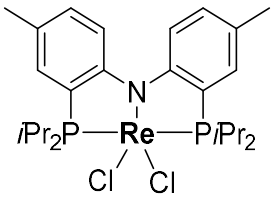

[(^{Ph}PNP)ReCl$_3$] (22.1 mg, 30.6 µmol, 1.00 eq.) and (27.2 mg, 30.6 µmol, 1.00 eq.) NaBArF$_{24}$ are dissolved in benzene and stirred for one hour at room temperature. Removal of the solvent under reduced pressure is followed by extraction of the residue with diethylether and recrystallization from diethylether / pentane at −80 °C over night. To 32.2 mg red crystalline material is added CoCp$_2$ (3.2 mg, 16.9 µmol, 0.55 eq.) in THF and the mixture stirred for one hour at room temperature. The solvent is removed under reduced pressure and the residue extracted with benzene and filtered over a short silica plug and the

benzene removed *via* lyophilization. [(^{Ph}PNP)ReCl$_2$] is obtained as a red solid, which showed only very broad resonances in the ^{1}H NMR in C_6D_6.

^{31}P{^{1}H} NMR (C_6D_6, 161.93 MHz): δ = –49.7 (br, s) ppm.

5.3.7 Synthesis of [(^{Ph}PNP)ReCl$_2$(thf)] (**12**)

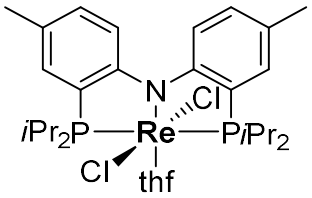

[(^{Ph}PNP)ReCl$_3$] (22.1 mg, 30.6 µmol, 1.00 eq.) and NaBArF$_{24}$ (27.2 mg, 30.6 µmol, 1.00 eq.) are dissolved in benzene and stirred for one hour at room temperature. Removal of the solvent under reduced pressure is followed by extraction of the residue with diethylether and recrystallization from diethylether / pentane at –80 °C over night. To 32.2 mg red crystalline material are added $CoCp_2$ (3.2 mg, 16.9 µmol, 0.55 eq.) in THF and the mixture stirred for one hour at room temperature. The solvent is removed under reduced pressure, the residue extracted with benzene and filtered over a short silica plug and the benzene removed *via* lyophilization. [(^{Ph}PNP)ReCl$_2$(thf)] was obtained upon dissolving the red solid in THF.

^{1}H NMR (THF-d$_8$, 400.13 MHz): δ = 9.29 (s, 2H, 2 x C$_{aryl}$-*H*), 7.69 (d, 2H, $^3J_{HH}$ = 8.2 Hz, 2 x C$_{aryl}$-*H*), 6.19 (sept, 2H, $^3J_{HH}$ = 6.8 Hz, 2 x C*H*(CH$_3$)$_2$), 5.42 (s, 6H, 2 x aryl-C*H*$_3$), 4.14 (d, 2H, $^3J_{HH}$ = 8.2 Hz, 2 x C$_{aryl}$-*H*), 3.38 (m, 6H, CH(C*H*$_3$)$_2$), 3.26 (m, 6H, CH(C*H*$_3$)$_2$), 2.77 (m, 6H, CH(C*H*$_3$)$_2$), 1.49 (m, 6H, CH(C*H*$_3$)$_2$) ppm. The signal for two central C-*H* atoms of two *iso*-propyl groups could not be found, but based on the integration it might be superimposed with the signal at 3.26 ppm.

^{31}P{^{1}H} NMR (C_6D_6, 161.91 MHz): δ = –434.8 (s) ppm.

5.3.8 Synthesis of *trans*-[(^{Ph}PNP)ReCl$_2$(py)] (*trans*-**13**)

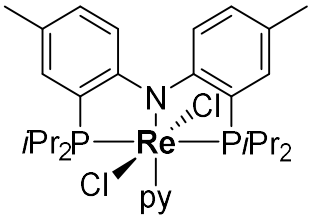

[(^{Ph}PNP)ReCl$_3$] (20.0 mg, 27.7 µmol, 1.00 eq.) is suspended in a mixture of THF/pyridine (ca. 10:1) and $CoCp_2$ (5.2 mg, 27.5 µmol, 0.99 eq.) are added. The mixture is stirred for 30 minutes at room temperature and the solvent removed under reduced pressure. The residue is extracted with diethylether and concentrated, so that the solution was still homogeneous, but saturated. [(^{Ph}PNP)ReCl$_2$(py)] (15.4 mg, 24.1 µmol, 87%) are obtained as red crystals suitable for X-ray crystallography upon storing the saturated diethylether solution for several days at –80 °C.

MS: LIFDI: *m/z* = 685.1 (100%), calcd. for $C_{26}H_{40}Cl_2NP_2Re$ = 685.2 ([M] - py).

IR (ATR, cm^{-1}): 4057 (w), 3742 – 3634 (br, m).

^{1}H NMR (C_6D_6, 400.25 MHz): δ = 9.75 (s, 2H, 2 x C_{aryl}-H), 8.40 (m, 2H, py-C_{ortho}-H), 8.23 (m, 2H, 2 x C_{aryl}-H), 7.71 (sept, 2H, $^3J_{HH}$ = 6.9 Hz, 2 x C*H*$(CH_3)_2$), 7.27 (m, 2H, py-C_{meta}*H*), 6.76 (s, 6H, 2 x aryl-C*H*$_3$), 4.98 (tm, 1H, $^3J_{HH}$ = 7.5 Hz, py-C_{para}-*H*), 4.61 (m, 6H, CH(C*H*$_3$)$_2$), 4.53 (m, 6H, CH(C*H*$_3$)$_2$), 3.64 (d, 2H, $^3J_{HH}$ = 8.3 Hz, 2 x C_{aryl}-H), 2.78 (m, 2H, 2 x C*H*$(CH_3)_2$), 2.70 (m, 6H, CH(C*H*$_3$)$_2$), 0.88 (m, 6H, CH(C*H*$_3$)$_2$) ppm.

^{13}C NMR (C_6H_6, 100.65 MHz): δ = 196.5 (s, py-*C$_{ortho}$*H), 186.2 (t, *J* = 18.1 Hz, *C$_{aryl,quart}$*), 149.7 (s, 2 x (CH_3)*C$_{aryl,quart}$*), 142.9 (s, py-*C$_{para}$*H), 142.5 (s, *C$_{aryl}$*-H), 125.0 (t, *J* = 8.5 Hz, *C$_{aryl,quart}$*), 119.2 (s, py-*C$_{meta}$*H), 112.8 (s, *C$_{aryl}$*-H), 106.2 (s, *C$_{aryl}$*-H), 99.0 (t, *J* = 11.1 Hz, *C*H$(CH_3)_2$), 59.2 (t, *J* = 11.7 Hz, *C*H$(CH_3)_2$), 21.7 (s, CH(*C*H$_3$)$_2$), 21.3 (s, CH(*C*H$_3$)$_2$), 19.5 (s, CH(*C*H$_3$)$_2$), 16.2 (s, CH(*C*H$_3$)$_2$), 15.6 (s, CH(*C*H$_3$)$_2$), 9.1 ((*C*H$_3$)C$_{aryl}$) ppm.

^{31}P{^{1}H} NMR (C_6D_6, 161.96 MHz): δ = –619.9 (s) ppm.

5.3.9 Synthesis of *cis*-[(^{Ph}PNP)ReCl$_2$(CO)]

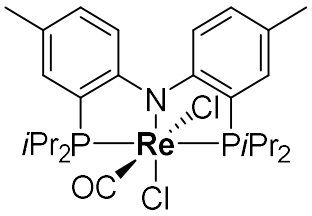

[(^{Ph}PNP)ReCl$_3$] (8.0 mg, 11.1 µmol, 1.00 eq.) and CoCp$_2$ (2.1 mg, 11.1 µmol, 1.00 eq.) are suspended in 0.6 mL THF in a J-Young NMR tube. The mixture is inverted for 30 minutes at room temperature before the suspension is degassed by two successive freeze-pump-thaw cycles and backfilled with one atmosphere of carbon monoxide. The mixture is inverted for additional 12 hours during which the color first changed from redbrown to forest green and after two hours under CO to intense purple. IR spectroscopy of the resultant solid after evaporation of the volatiles indicated the formation of a mixture of CO-containing complexes. Purple single crystals suitable for X-ray crystallography were obtained from toluene / pentane at −80 °C over the course of several days (see crystallographic section).

5.3.10 Synthesis of *cis*-[(^{Ph}PNP)Re(NO)Cl$_2$] (*cis*-**14**)

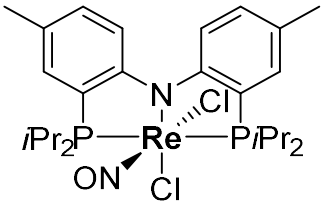

[(^{Ph}PNP)Re(N)Cl] (43.1 mg, 64.9 µmol, 1.00 eq.) is dissolved in 5 mL CH$_2$Cl$_2$/CCl$_4$ (4:1) and degassed *via* two successive freeze-pump-thaw cycles. Nitric oxide (1 atm) is applied at room temperature and a color change from orange to forrest green was observed. The reaction solution is stirred for 30 minutes at room temperature and the solvent removed under reduced pressure. The residue is washed with diethylether (3 x 2 mL) and benzene (3 x 2 mL) and extracted with dichloromethane. *cis*-[(^{Ph}PNP)Re(NO)Cl$_2$] (39.2 mg, 54.8 µmol, 84%) is obtained as green crystals upon layering a saturated dichloromethane solution with diethylether at –40 °C, which are suitable for X-ray crystallography. Analytically pure compound is obtained upon dissolving the crystals in dichloromethane and filtering over a short silica plug.

EA: Calcd. for $C_{26}H_{40}Cl_2N_2OP_2Re$: C, 43.64; H, 5.63; N, 3.91. Found: C, 43.99; H, 5.74; N, 3.68.

MS: LIFDI: *m/z* (100%) = 715.1, calcd. for $C_{26}H_{40}Cl_2N_2O_1P_2Re_1$ = 715.2.

^{1}H-NMR (CD_2Cl_2, 400.25 MHz): δ = 4.03 (br s), 0.33 (br s), –0.20 (br s), –1.03 (br s) ppm.

IR: (ATR, cm^{-1}): 1702 (vs).

CV: $E_{1/2}$ vs. Fc^+/Fc^0 (THF, V) = +0.11 (rev.), –0.90 (rev.).

Magnetic susceptibility (r.t., CD_2Cl_2): μ_{eff} = 1.69 ± 0.1 μ_B.

5.3.11 Synthesis of *trans*-[(^{Ph}PNP)Re(NO)Cl$_2$] (*trans*-**14**)

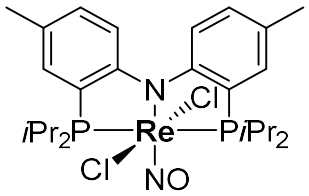

[(^{Ph}PNP)ReCl$_3$] (20.0 mg, 27.7 µmol, 1.00 eq.) and $CoCp_2$ (5.2 mg, 27.5 µmol, 0.99 eq.) are suspended in 5 mL THF and stirred for 30 min at room temperature. The solvent is removed under reduced pressure and the residue dissolved in 10 mL fluorobenzene. The reaction mixture is degassed *via* a freeze-pump-thaw cycle and nitric oxide (1 atm) applied upon thawing and rapid stirring. The solution is stirred for 15 min at room temperature and afterwards the solvent removed under reduced pressure. The residue is washed with pentane (5 x 2 mL) and diethylether (1 x 2 mL) and extracted with benzene. *trans*-[(^{Ph}PNP)Re(NO)Cl$_2$] (17.0 mg, 23.8 µmol, 86%) are obtained upon lyophilization as an intense green powder. Single crystals suitable for X-ray crystallography are obtained by slow diffusion of pentane into a saturated solution of *trans*-[(^{Ph}PNP)Re(NO)Cl$_2$] in benzene via the gas phase.

EA: calcd. for $C_{26}H_{40}Cl_2N_2OP_2Re$: C, 43.64; H, 5.63; N, 3.91. Found: C, 44.43; H, 5.66; N, 4.03.

MS: LIFDI: *m*/*z* = 715.0 (100%), calcd. for $C_{26}H_{40}Cl_2N_2OP_2Re$: 715.2.

IR (ATR, cm^{-1}): 1710 (vs).

^{1}H-NMR (C_6D_6, 400.24 MHz): δ = 11.83 (br s), 9.34 (br s), 6.88 (br s), 5.43 (br s), 4.15 (br s).

CV: $E_{1/2}$ vs. Fc^+/Fc^0 (THF, V) = +0.19 V (rev.), –0.83 (rev.).

Magnetic susceptibility (r.t., C_6D_6): μ_{eff} = 1.69 ± 0.1 μ_B.

5.3.12 Synthesis of [(^{Ph}PNP)Re(N)Cl] (**15**)

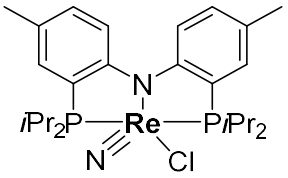

Via dinitrogen cleavage

To [(^{Ph}PNP)ReCl$_3$] (15.0 mg, 20.8 µmol, 1.00 eq.) and Na/Hg (700 mg, 1 M, 2.50 eq.) are added 10 mL THF under an N_2-atmosphere and stirred for 3 minutes at room temperature until the color had changed from dark violet to dark green. The solution is heated to 50 °C while stirring for 24 hours. The solvent is removed under reduced pressure and the residue extracted with pentane to obtain (8.2 mg, 12.4 µmol, 60%) [(^{Ph}PNP)Re(N)Cl] as an orange solid.

Via reduction-azide sequence

[(^{Ph}PNP)ReCl$_3$] (70.0 mg, 97.1 µmol, 1.00 eq.) and $CoCp_2$ (18.4 mg, 97.3 µmol, 1.00 eq.) in 10 mL THF are stirred for 30 min at room temperature. Afterwards Me_3SiN_3 (39.0 µL, 293.8 µmol, 3.02 eq.) is added and the suspension stirred for an additional three hours at room temperature. The solvent is removed under reduced pressure and the residue extracted with benzene. After removal of the solvent via lyophilization, [(^{Ph}PNP)Re(N)Cl] (58.8 mg, 88.5 µmol, 91%) is obtained as an orange powder. Single crystals suitable for X-ray crystallography were grown over the course of several days by layering an almost saturated solution of [(^{Ph}PNP)Re(N)Cl] in toluene with pentane at −80 °C.

Synthesis of [^{Ph}PNPRe(^{15}N)Cl] via dinitrogen splitting

In a *J*-Young NMR tube 0.5 mL THF-d_8 is vacuum-transferred to [(^{Ph}PNP)ReCl$_3$] (20.0 mg, 27.7 µmol, 1.00 eq.) and Na/Hg (933 mg, 1 M, 2.50 eq.) and $^{15}N_2$ applied upon thawing. The NMR tube is shaken for 3 minutes until the color has changed to deeply green. Afterwards the solution is heated to 50 °C for 16 hours. The solvent is removed under reduced pressure, the residue is extracted with benzene and filtered over a short silica plug. [(^{Ph}PNP)Re(^{15}N)Cl] (7.8 mg, 11.7 µmol, 42%) was obtained as a dark orange solid.

Synthesis of [^{Ph}PNPRe(^{15}N)Cl] via reduction-azide sequence (50% labelled ^{15}N)

[(^{Ph}PNP)ReCl$_3$] (30.7 mg, 42.6 µmol, 1.00 eq.) and $CoCp_2$ (8.1 mg, 42.8 µmol, 1.00 eq.) in 5 mL THF are stirred for 1 hour at room temperature and subsequently PPN^{15}NN$_2$ (24.7 mg, 42.5 µmol, 1.00 eq., 50% terminally labelled ^{15}N) added to the reaction mixture. The suspension is heated to 65 °C for 20 hours after which the solvent was removed under reduced pressure. The residue was extracted with

benzene and the solvent removed via lyophilization. [(^{Ph}PNP)Re(^{15}N)Cl] (26.7 mg, 40.1 µmol, 94%) was obtained as an orange solid.

EA: calcd. for $C_{26}H_{40}ClN_2P_2Re$: C, 47.02; H, 6.07; N, 4.22. Found: C, 47.21; H, 6.12; N, 4.21.

MS: LIFDI: *m*/*z* = 664.2 (100%), calcd. for $C_{26}H_{40}ClN_2P_2Re$ = 664.2.

IR: (ATR, cm^{-1}) = 1080 (Re≡^{14}N), 1047 (Re≡^{15}N).

^{1}H NMR (C_6D_6, 400.25 MHz): δ = 7.60 (d, 2H, $^3J_{HH}$ = 8.4 Hz, C_{aryl}-*H*), 6.93 (s, 2H, C_{aryl}-*H*), 6.78 (d, 2H, $^3J_{HH}$ = 8.4 Hz, C_{aryl}-*H*), 2.81 (m, 2H, C*H*(CH_3)$_2$), 2.23 (sept, 2H, $^3J_{HH}$ = 6.2 Hz, C*H*(CH_3)$_2$), 2.15 (s, 6H, (*H*$_3$C-aryl)), 1.46 (dd, 6H, $^3J_{HP}$ = 16.2 Hz, $^3J_{HH}$ = 8.2 Hz, CH(C*H*$_3$)$_2$), 1.12 (m, 12H, CH(C*H*$_3$)$_2$), 1.05 (dd, 6H, $^3J_{HP}$ = 16.2 Hz, $^3J_{HH}$ = 8.2 Hz, CH(C*H*$_3$)$_2$) ppm. To assign the ^{1}H shifts and J_{HP} coupling constants, additional spectra (^{1}H-^{1}H-COSY, ^{1}H{^{31}P} NMR) were measured.

^{13}C{^{1}H} NMR (C_6D_6, 100.65 MHz): δ = 166.7 (m, *C*$_{aryl}$-P), 132.2 (s, *C*$_{aryl}$-H), 132.1 (s, *C*$_{aryl}$-H), 122.3 (s, *C*$_{aryl}$), 117.7 (s, *C*$_{aryl}$-H), 23.6 (vt, $^1J_{CP}$ = 13.7 Hz, P*C*H(Me)$_2$), 20.3 (s, *C*H$_3$-Ar), 18.4 (s, CH(*C*H$_3$)$_2$), 17.9 (s, CH(*C*H$_3$)$_2$), 17.7 (s, CH(*C*H$_3$)$_2$), 16.8 (s, CH(*C*H$_3$)$_2$) ppm. For the assignment of the ^{13}C NMR shifts a combination of 1D (^{13}C{^{1}H}, ^{13}C-APT) and 2D (^{13}C-^{1}H-HSQC, ^{13}C-^{1}H-HMBC) spectra were measured.

^{15}N{^{1}H} NMR (C_6D_6, 50.73 MHz): δ = 362.5 ppm.

^{31}P{^{1}H} NMR (C_6D_6, 162.01 MHz): δ = 50.1 ppm.

CV: $E_{1/2}$ vs. Fc^+/Fc^0 (THF, V) = +0.84 (irrev.), +0.08 (Re^V/Re^{VI}), –3.1 (irrev.).

5.3.13 Synthesis of [(^{Ph}PNP)ReBr$_3$] (**16**)

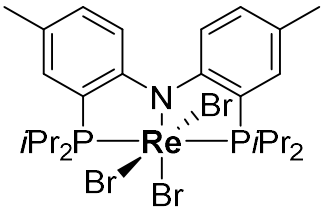

[ReBr$_3$(PPh$_3$)$_2$(MeCN)] (115.4 mg, 116.4 µmol, 1.00 eq.) and ^{Ph}PNPH (50.0 mg, 116.3 µmol, 1.00 eq.) are suspended in 20 mL benzene and heated to 80 °C for 7 hours. The solvent is removed under reduced pressure and the dark residue washed with pentane (5 x 5 mL) and extracted with a diethylether/benzene mixture (1:1). The solvent is removed under reduced pressure and the residue recrystallized from benzene / pentane. [(^{Ph}PNP)ReBr$_3$] (64.8 mg, 75.8 µmol, 65%) is obtained as a dark green powder.

Single crystals suitable for X-ray crystallography are obtained by slow diffusion of pentane into a saturated benzene solution of [(^{Ph}PNP)ReBr$_3$].

MS: LIFDI: *m/z* = 853.9 (100%), calcd. for $C_{26}H_{40}Br_3NP_2Re$ (854.0).

^{1}H NMR (C_6D_6, 300.16 MHz): δ = 62.43 (br s, 2H), 17.49 (br s, 2H), 16.04 (s, 2H), 14.54 (s, 6H), 10.88 (s, 6H), 10.15 (s, 2H), 9.04 (s, 6H), 7.59 (s, 6H), 6.31 (s, 6H), 4.50 (s, 2H) ppm.

5.3.14 Synthesis of [(^{Ph}PNP)Re(N)Br] (**17**)

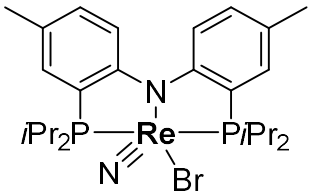

[(^{Ph}PNP)ReBr$_3$] (15.0 mg, 17.6 µmol, 1.00 eq.) and $CoCp_2$ (3.3 mg, 17.4 µmol, 0.99 eq.) are suspended in 5 mL THF and stirred for 30 min at room temperature. Afterwards, Me_3SiN_3 (7.0 µL, 52.7 µmol, 3.00 eq.) is added to the solution and the mixture stirred for three hours at room temperature. The solvent is removed under reduced pressure and the residue extracted with toluene. [(^{Ph}PNP)Re(N)Br] (10.0 mg, 14.1 µmol, 81%) is obtained as orange, analytically pure crystals upon layering a saturated toluene solution with pentane at −80 °C.

EA: Calcd. for $C_{26}H_{40}BrN_2P_2Re$: C, 44.07; H, 5.69; N, 3.95. Found: C, 44.61; H, 5.51; N, 3.68.

MS: LIFDI: *m/z* = 708.0 (100%), calcd. for $C_{26}H_{40}BrN_2P_2Re$ (708.1).

^{1}H NMR (C_6D_6, 400.25 MHz): δ = 7.59 (d, 2H, $^3J_{HH}$ = 8.6 Hz, C_{aryl}-*H*), 6.95 (s, 2H, C_{aryl}-*H*), 6.78 (d, 2H, $^3J_{HH}$ = 8.6 Hz, C_{aryl}-*H*), 2.95 (sept, 2H, $^3J_{HH}$ = 7.0 Hz, 2 x C*H*$(CH_3)_2$), 2.25 (sept, 2H, $^3J_{HH}$ = 6.9 Hz, 2 x C*H*$(CH_3)_2$), 2.15 (s, 6H, 2 x *H*$_3$C-aryl), 1.49 (dd, 6H, $^3J_{HP}$ = 17.0 Hz, $^3J_{HH}$ = 8.4 Hz, 2 x CH(C*H*$_3)_2$), 1.14 (dd, 6H, $^3J_{HP}$ = 17.0 Hz, $^3J_{HH}$ = 8.4 Hz, 2 x CH(C*H*$_3)_2$), 1.05 (m, 12H, 4 x 2 x CH(C*H*$_3)_2$) ppm.

^{31}P{^{1}H} NMR (C_6D_6, 162.02 MHz): δ = 49.5 ppm.

5.3.15 Synthesis of [(^{Ph}PNP)ReI$_3$] (**18**)

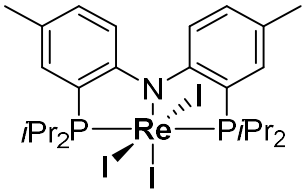

[(^{Ph}PNP)ReCl$_3$] (63.4 mg, 87.9 µmol, 1.00 eq.) and NaI (245 mg, 1.63 mmol, 18.5 eq.) are suspended in 10 mL THF and stirred at room temperature for 24 hours. The solvent is removed under reduced pressure, the residue suspended in pentane and filtered over a short silica plug. The crude product is extracted from the silica plug with benzene and the solvent removed *via* lyophilization. [(^{Ph}PNP)ReI$_3$] (84.9 mg, 85.2 µmol, 98%) is obtained as an ink-blue solid upon extraction with benzene and subsequent lyophilization. Upon slow evaporation of a saturated diethylether solution [(^{Ph}PNP)ReI$_3$] can be obtained as dark crystals which are suitable for X-ray crystallography. Analytically pure compound is obtained by dissolving the crystals in benzene and filtering it over a short silica plug.

EA: calcd. for $C_{26}H_{40}I_3N_1P_2Re_1$: C, 31.37; H, 4.05; N, 1.41. Found: C, 31.56; H, 4.18; N, 1.23.

MS: LIFDI: *m/z* = 995.8 (100%), calcd. for $C_{26}H_{40}I_3N_1P_2Re$: 995.9.

IR: (ATR, cm^{-1}) = 3813 (br), 2327 (br).

^{1}H NMR (C_6D_6, 400.24 MHz): δ = 14.62 (2H, br), 11.36 (6H, br), 11.11 (6H, br), 9.65 (6H, br), 9.48 (2H, br), 7.85 (2H, br), 7.51 (6H, br), 7.10 (partially superimposed with the solvent signal, 6H, br) ppm.

CV: $E_{1/2}$ vs. Fc^+/Fc^0 (THF, Ar, V) = +0.12 (Re^V/Re^{IV}, rev.), –0.79 (Re^{IV}/Re^{III}, irrev.), –1.69 (Re^{III}/Re^{II}, irrev.).

Magnetic susceptibility (r.t., C_6D_6): μ_{eff} = 1.62 ± 0.1 μ_B.

5.3.16 Synthesis of [(^{Ph}PNP)Re(N)I] (**19**)

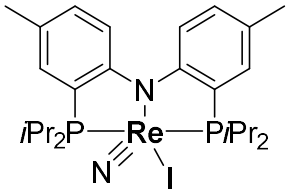

Via dinitrogen splitting

8 mL THF are added to [(^{Ph}PNP)ReI$_3$] (25.0 mg, 25.1 µmol, 1.00 eq.) and $CoCp^*_2$ (17.4 mg, 52.8 µmol, 2.10 eq.) under an N_2 atmosphere. The mixture is stirred for 24 hours at room temperature and subsequently the solvent is removed under reduced pressure. The residue is extracted with diethylether and the solvent removed under reduced pressure to obtain [(^{Ph}PNP)Re(N)I] (17.2 mg, 22.7 µmol, 90%) as an orange-brown solid. Further purification is realized upon washing the crude product with a very small amount of cold (−40 °C) acetonitrile, extraction with diethylether and removal of solvent under reduced pressure. The orange solid is then washed with a very small amount of cold (−80 °C) diethylether.

Via reduction-azide sequence

[(^{Ph}PNP)ReI$_3$] (10.0 mg, 10.0 µmol, 1.00 eq.) and $CoCp_2$ (1.9 mg, 10.0 µmol, 1.00 eq.) are dissolved in 4 mL THF and stirred for 15 minutes at room temperature until the color changed to red. The suspension is filtered into a stirring solution of Me_3SiN_3 (4 µL, 30.1 µmol, 3.01 eq.) in 5 mL of THF. The mixture is stirred for 1.5 hours at room temperature and the solvent removed under reduced pressure. The residue is extracted with diethylether, the solvent removed under reduced pressure and extracted with diethylether again to obtain [(^{Ph}PNP)Re(N)I] (6.4 mg, 8.5 µmol, 85%) as an orange solid after solvent evaporation.

EA: Calcd. for $C_{26}H_{40}INP_2Re$: C, 41.33; H, 5.34; N, 3.71. Found: C, 41.72; H, 5.47; N, 3.56.

MS: LIFDI: *m/z* = 756.1 (100%), calcd. for $C_{26}H_{40}I_1N_2ReP_2$ (756.1).

^{1}H NMR (C_6D_6, 400.24 MHz): δ = 7.60 (d, 2H, $^3J_{HH}$ = 8.3 Hz, C_{aryl}-*H*), 6.96 (s, 2H, C_{aryl}-H), 6.77 (d, 2H, $^3J_{HH}$ = 8.3 Hz, C_{aryl}-*H*), 3.18 (m, 2H, C*H*$(CH_3)_2$), 2.26 (sept, 2H, $^3J_{HH}$ = 6.4 Hz, C*H*$(CH_3)_2$), 2.15 (s, 6H, ((C*H*$_3$)-Ar)$_2$), 1.53 (dd, 6H, $^3J_{HP}$ = 16.1 Hz, $^3J_{HH}$ = 7.9 Hz, CH(C*H*$_3$)$_2$), 1.14 (dd, 6H, $^3J_{HP}$ = 16.1 Hz, $^3J_{HH}$ = 7.9 Hz, CH(C*H*$_3$)$_2$), 1.06 (dd, 6H, $^3J_{HP}$ = 13.3 Hz, $^3J_{HH}$ = 6.6 Hz, CH(C*H*$_3$)$_2$), 0.91 (dd, 6H, $^3J_{HP}$ = 17.1 Hz, $^3J_{HH}$ = 7.7 Hz, CH(C*H*$_3$)$_2$) ppm.

^{13}C{^{1}H} NMR (C_6D_6, 100.65 MHz): δ = 166.6 (m, C_{aryl}-P), 132.2 (s, C_{aryl}-H), 131.9 (s, C_{aryl}-H), 128.8 (s, $C_{aryl,quart.}$), 122.0 (s, $C_{aryl,quart.}$), 24.0 (vt, 4C, $^1J_{CP}$ = 14.3 Hz, P*C*H(Me)$_2$), 20.3 (s, 2C, *C*H$_3$-Ar), 18.9

(s, *C*H$_3$), 18.0 (s, *C*H$_3$), 17.9 (s, *C*H$_3$), 16.9 (s, *C*H$_3$) ppm. Assignments for carbon and hydrogen atoms and coupling constants were derived from a combination of additional 1D- (^{1}H{^{31}P}, ^{13}C{^{1}H}-APT) as well as 2D-NMR (HSQC, HMBC, COSY) experiments.

^{15}N{^{1}H} NMR (C$_6$D$_6$, 50.72 MHz): δ = 365.1 ppm (s).

^{31}P{^{1}H} NMR (C$_6$D$_6$, 162.01 MHz): δ = 49.3 ppm (s).

5.3.17 Synthesis of [(^{Ph}PNP)Re(N)Cl][Al(OC(CF$_3$)$_3$)$_4$] (**20**$^+$)

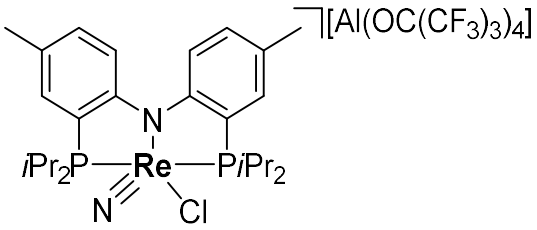

[(^{Ph}PNP)Re(N)Cl] (6.0 mg, 9.0 µmol, 1.00 eq.) and [AcFc][Al(OC(CF$_3$)$_3$)$_4$] (10.8 mg, 9.0 µmol, 1.00 eq.) are dissolved in 5 mL 2-MeTHF and stirred for 35 minutes at room temperature. The solvent is removed under reduced pressure and 20 mL pentane added under vigorous stirring. After five minutes the solvent is decanted and the residue recrystallized from diethylether/pentane at −80 °C to obtain [(^{Ph}PNP)Re(N)Cl][Al(OC(CF$_3$)$_3$)$_4$] (12.9 mg, 7.9 µmol, 88%) as dark violet needles, which are analytically pure. Single crystals of the BF$_4$ salt, which are suitable for X-ray crystallography, are obtained by slow exchange of a saturated dichloromethane solution with pentane upon gas-phase diffusion.

EA: Calcd. for C$_{42}$H$_{40}$AlClF$_{36}$N$_2$O$_4$P$_2$Re ([Al(OC(CF$_3$)$_3$)$_4$] anion): C, 30.92; H, 2.47; N, 1.72. Found: C, 30.88; H, 2.52; N, 1.73.

MS: LIFDI: *m/z* = 664.3 (100%), calcd. for C$_{26}$H$_{40}$ClN$_2$P$_2$Re = 664.2.

5.3.18 Synthesis of [(^{Ph}PNP)Re(NB($C_6H_3(CF_3)_2$))Cl] (**21**)

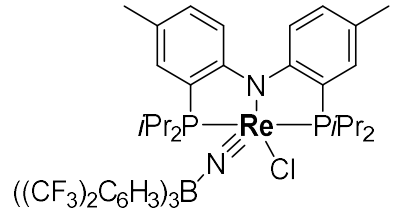

[(^{Ph}PNP)Re(N)Cl] (4.3 mg, 6.5 µmol, 1.00 eq.) and $B(C_6H_3(CF_3)_2)_3$ (4.3 mg, 6.5 µmol, 1.02 eq.) are dissolved in 0.5 mL C_6D_6 in a J-Young NMR tube and inverted for 15 minutes at room temperature. The residue is – after evaporation of the solvent under reduced pressure – taken up in a small amount of fluorobenzene and layered with pentane. Upon slow diffusion single crystals can be grown at –40 °C over the course of several days, which were suitable for X-ray crystallography (see crystallographic section).

^{31}P{^{1}H} NMR (C_6D_6, 162.01 MHz): δ = 53.2 (d, J = 146 Hz, 1P), 48.7 (d, J = 146 Hz, 1P) ppm.

5.3.19 Synthesis of *cis*-[(^{Ph}PNP)Re(NCO)Cl_2] (*cis*-**24**)

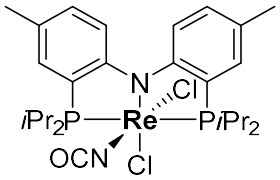

[(^{Ph}PNP)Re(N)Cl] (10.0 mg, 15.1 µmol, 1.0 eq.) is dissolved in 5 mL toluene and cooled to −80 °C. Subsequently, a stock solution of oxalyl chloride (0.65 µL, 7.6 µmol, 0.50 eq.) in toluene is added slowly to the stirring, cold solution of [(^{Ph}PNP)Re(N)Cl]. After complete addition the solution is stirred at low temperature for two hours during which the color gradually darkened. After stirring for two hours at room temperature the solution turns dark violet and the solvent is removed under reduced pressure. The residue is extracted with benzene and filtered over a short silica column. Removal of the benzene solvent upon lyophilization yields *cis*-[(^{Ph}PNP)Re(NCO)Cl_2] (8.7 mg, 12.0 µmol, 80%) as a dark violet solid. Single crystals suitable for X-ray crystallography are obtained from benzene / pentane at room temperature over night.

MS: LIFDI: *m*/*z* (%) = 727.0 (100), calcd. for $C_{27}H_{40}Cl_2N_2OP_2Re$ = 727.2.

IR: (ATR, cm^{-1}): 2206 (vs) cm^{-1}.

^{1}H NMR (C_6D_6, 300.16 MHz): δ = 16.45 (br s, 1H), 15.93 (br s, 1H), 15.78 (br s, 3H), 15.22 (br s, 3H), 11.22 (br s, 3H), 9.53 (br s, 1H), 9.03 (br s, 1H), 8.76 (br s, 6H), 8.03 (br s, 1H), 7.84 (br s, 3H), 7.65 (br s, 6H), 7.50 (br s, 3H), 5.40 (br s, 3H), 5.31 (br s, 3H) ppm.

CV: $E_{1/2}$ vs. Fc^+/Fc^0 (THF, V) = –0.87 (Re^{IV}/Re^{III}, rev.), –2.35 (Re^{III}/Re^{II}, irrev.).

5.3.20 Synthesis of *cis*-[(^{Ph}PNP)Re(NS)Cl$_2$] (*cis*-**25**)

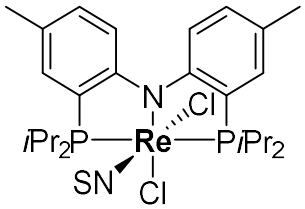

[(^{Ph}PNP)Re(N)Cl] (13.5 mg, 20.3 µmol, 1.00 eq.) are dissolved in 5 mL CH_2Cl_2 and cooled to –90 °C. A stock solution of S_2Cl_2 (0.6 mL, 0.5 eq., 12.5 mM in CH_2Cl_2) is added dropwise to the stirring solution. After 2 hours the reaction is warmed to room temperature and stirred for another hour. The solvent is removed under reduced pressure and the residue extracted with toluene. After recrystallization from toluene / pentane at –80 °C and filtering over a short silica column, *cis*-[(^{Ph}PNP)Re(NS)Cl$_2$] (10.1 mg, 13.8 µmol, 68%) is obtained as a green solid. Crystals suitable for X-ray crystallography are obtained from the ternary system benzene / cyclopentane and pentane over the course of several days.

MS: LIFDI: *m*/*z* (%) = 731.0 (100), calcd. for $C_{26}H_{40}ClN_2P_2ReS$ = 731.1; *m*/*z* (%) = 732.0 (100), calcd. for $C_{26}H_{40}Cl^{14}N_2{}^{15}NO_2P_2Re$ = 732.1.

IR: (ATR, cm^{-1}): 1176 (s, ^{14}NS), 1142 (s, ^{15}NS) cm^{-1}.

Magnetic susceptibility (r.t., CD_2Cl_2): μ_{eff} = 1.66 ± 0.1 μ_B.

5.3.21 Synthesis of *cis*-[(^{Ph}PNP)Re(NO)$_2$Cl] (*cis*-**26**)

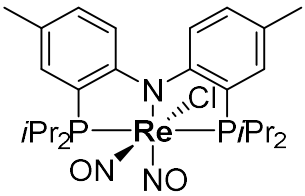

Synthesis of [(^{Ph}PNP)Re(^{14}NO)$_2$Cl]

[(^{Ph}PNP)Re(N)Cl] (30.0 mg, 45.2 µmol) is dissolved in 5 mL benzene and degassed *via* two successive freeze-pump-thaw cycles. Nitric oxide (1 atm) is applied at room temperature and the solution stirred for 12 hours. The solvent is removed *via* lyophilization and the residue washed with diethylether (3 x 2 mL) and extracted with benzene. [(^{Ph}PNP)Re(NO)$_2$Cl] (28.2 mg, 39.7 µmol, 88%) is obtained upon lyophilization. Analytically pure compound is obtained by filtering the benzene extract over a silica plug and recrystallization from toluene / pentane at −80 °C. Single crystals suitable for X-ray crystallography are obtained upon layering an almost saturated solution of [(^{Ph}PNP)Re(NO)$_2$Cl] in benzene with pentane.

Synthesis of [(^{Ph}PNP)Re(^{15}NO)$_2$Cl]

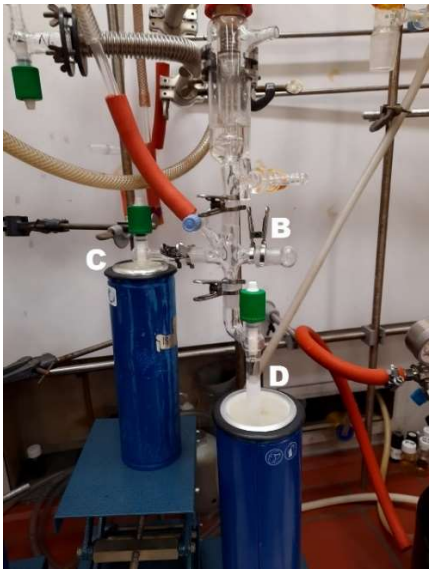

Figure 5.14: Reaction setup for the reaction of ^{15}NO with [(PNP)Re(N)Cl]; **B**: transfer line, **C**: condensation flask, **D**: and nitride flask.

A reaction flask with [(PNP)Re(N)Cl] (11.0 mg, 16.6 µmol) dissolved in 2 mL benzene is attached to the transfer line **B** (see preparation of ^{15}NO, chapter 5.2.6). The reaction flask is immersed in liquid nitrogen, the headspace evacuated and afterwards the flask is closed. Flask **C**, containing the purified and condensed ^{15}NO gas is carefully warmed to −110 °C (EtOH/liq. N_2 bath) while open to the transfer line **B**. The ^{15}NO gas in the transfer line is condensed into **D** with the aid of liquid nitrogen, after closing

the connection to **C**. After 30 min, the nitride flask is connected to an overpressure valve (while immersed in liquid nitrogen) and warmed to room temperature. The mixture is stirred for one hour at room temperature. The solvent is removed upon lyophilization and the crude product recrystallized from toluene/pentane at −80 °C to obtain [(PNP)Re(^{15}NO)$_2$Cl] (7.6 mg, 10.7 μmol, 65%) as green-brown crystals.

EA: calcd. for $C_{26}H_{40}ClN_3O_2P_2Re$: C, 43.97; H, 5.68; N, 5.92. Found: C, 44.20; H, 5.80; N, 5.82.

MS: LIFDI: *m/z* (%) = 710.0 (100), calcd. for $C_{26}H_{40}ClN_3O_2P_2Re$ = 710.18.

IR: (ATR, cm^{-1}): 1695 (^{14}NO, vs), 1634 (^{14}NO, vs); 1660 (^{15}NO), 1599 (^{15}NO).

CV: $E_{1/2}$ vs. Fc^+/Fc^0 (THF, V) = +0.60 (rev.), −0.13 (rev.), −1.55 (irrev.), −2.76 (rev.).

^{1}H NMR (C_6D_6, 400.24 MHz): δ = 8.50 (br s), 3.50 (br s), 1.41 (br s), 0.19 (br s).

Magnetic susceptibility (r.t., C_6D_6): μ_{eff} = 1.69 ± 0.1 μ_B.

5.3.22 Synthesis of *cis*-[(^{Ph}PNP)ReCl(NO)$_2$][Al(OC(CF$_3$)$_3$)$_4$] (*cis*-**27**$^+$)

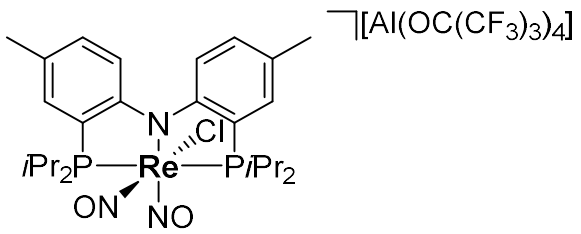

cis-[(^{Ph}PNP)ReCl(NO)$_2$] (8.6 mg, 12.0 μmol, 1.00 eq.) and [AcFc][Al(OC(CF$_3$)$_3$)$_4$] (14.4 mg, 12.0 μmol, 1.00 eq.) are suspended in 5 mL acetonitrile and stirred for one hour at room temperature. The solvent is removed under reduced pressure and 20 mL pentane added to the residue under vigorous stirring. The solution is decanted off after five minutes and the residue recrystallized from diethylether/pentane at −80 °C to obtain *cis*-[(^{Ph}PNP)ReCl(NO)$_2$][Al(OC(CF$_3$)$_3$)$_4$] (14.3 mg, 8.3 μmol, 69%) as brown crystals, which were also suitable for X-ray crystallography.

EA: calcd. for $C_{42}H_{40}AlClF_{36}N_3O_6P_2Re$: C, 30.08; H, 2.40; N, 2.51. Found: C, 30.29; H, 2.45; N, 2.13.

MS: LIFDI: *m/z* = 710.1 (100%), calcd. for $C_{26}H_{40}ClN_3O_2P_2Re$ = 710.2.

IR: (ATR, cm^{-1}): 1834 (br, m), 1757(br, m).

^{1}H NMR (CD_2Cl_2, 400.25 MHz): δ = 7.33 (s, 1H, C_{aryl}-*H*), 7.23 (m, 3H, C_{aryl}-*H*), 7.11 (d, 1H, $^3J_{HH}$ = 8.1 Hz, C_{aryl}-*H*), 7.01 (d, 1H, $^3J_{HH}$ = 8.1 Hz, C_{aryl}-*H*), 3.42 (sept, 1H, $^3J_{HH}$ = 6.9 Hz, C*H*(CH$_3$)$_2$), 3.30 (sept,

1H, $^{3}J_{HH}$ = 6.9 Hz, C*H*(CH$_3$)$_2$), 2.88 (m, 2H, 2 x C*H*(CH$_3$)$_2$), 2.39 (s, 3H, *H*$_3$C-aryl), 2.35 (s, 3H, *H*$_3$C-aryl), 1.70 (dd, 3H, $^{3}J_{HH}$ = 8.0 Hz, $^{3}J_{HP}$ = 17.1 Hz, HC(C*H*$_3$)), 1.55 (dd, 3H, $^{3}J_{HH}$ = 7.7 Hz, $^{3}J_{HP}$ = 17.1 Hz, HC(C*H*$_3$)), 1.37 (m, 9H, 3 x HC(C*H*$_3$)), 1.23 (dd, $^{3}J_{HH}$ = 7.7 Hz, $^{3}J_{HP}$ = 17.1 Hz, HC(C*H*$_3$)), 1.16 (m, 6H, 2 x HC(C*H*$_3$)). To assign the coupling constants and signal multiplicities additional spectra (^{1}H-^{1}H-COSY, ^{1}H{^{31}P} NMR) were measured.

^{13}C{^{1}H} NMR (CD_2Cl_2, 100.65 MHz): δ = 134.5 (s, 2 x C_{aryl}-H), 132.5 (s, C_{aryl}-H), 131.8 (s, C_{aryl}-H), 125.5 (s, 2 x $C_{quart.}$), 122.6 (s, 2 x $C_{quart.}$), 119.9 (s, C_{aryl}-H), 119.7 (s, C_{aryl}-H), 116.8 (s, 2 x $C_{quart.}$), 29.5 (m, *C*H(CH$_3$)$_2$), 24.9 (m, *C*H(CH$_3$)$_2$), 24.6 (m, *C*H(CH$_3$)$_2$), 24.1 (m, 2 x *C*H(CH$_3$)$_2$), 21.6 (s, CH(*C*H$_3$)$_2$), 20.4 (s, *C*H$_3$-Ar), 20.3 (s, *C*H$_3$-Ar), 19.4 (s, CH(*C*H$_3$)$_2$), 18.8 (s, CH(*C*H$_3$)$_2$), 18.7 (s, CH(*C*H$_3$)$_2$), 18.0 (s, CH(*C*H$_3$)$_2$), 17.8 (s, CH(*C*H$_3$)$_2$), 17.7 (s, CH(*C*H$_3$)$_2$), 16.4 (s, CH(*C*H$_3$)$_2$) ppm. For the assignment of the ^{13}C NMR shifts a combination of 1D (^{13}C{^{1}H}, ^{13}C-APT) and 2D (^{13}C-^{1}H-HSQC, ^{13}C-^{1}H-HMBC) spectra were measured.

^{19}F{^{1}H} NMR (CD_2Cl_2, 376.57 MHz): δ = –75.8 (s) ppm.

^{31}P{^{1}H} NMR (CD_2Cl_2, 162.02 MHz): δ = 51.0 (s) ppm.

5.3.23 Synthesis of [(^{Ph}PNP)Re(NO)$_2$] (**28**)

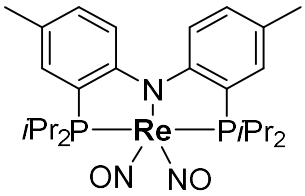

[(^{Ph}PNP)Re(NO)$_2$Cl] (8.0 mg, 11.3 µmol, 1.00 eq.) and $CoCp_2$ (3.7 mg, 11.2 µmol, 0.99 eq.) are dissolved in 5 mL THF and stirred for one hour at room temperature. The suspension is filtered and the solvent removed under reduced pressure. The residue is washed with pentane, extracted with benzene and filtered over a silica plug. [(^{Ph}PNP)Re(NO)$_2$] (6.3 mg, 9.3 µmol, 83%) is obtained as bright orange powder upon lyophilization. Analytically pure compound is obtained by recrystallization from toluene / pentane at –40 °C. Single crystals suitable for X-ray crystallography are obtained over the course of several days by layering a saturated toluene solution of [(^{Ph}PNP)Re(NO)$_2$] with pentane at –40 °C.

EA: calcd. for $C_{26}H_{40}N_3O_2P_2Re$: C, 46.28; H, 5.98; N, 6.23. Found: C, 46.64; H, 6.03; N, 5.95.

MS: ESI: *m/z* = 675.2150, calcd for $C_{26}H_{40}N_3O_2P_2Re$: 675.2149.

IR: (ATR, cm^{-1}) = 1615 (^{14}NO, s), 1594 (s), 1566 (^{14}NO, vs) ; 1574 (^{15}NO), 1534 (^{15}NO).

^{1}H NMR (THF-d_8, 400.24 MHz): δ = 7.30 (d, 2H, $^{3}J_{HH}$ = 8.5 Hz, C_{aryl}-*H*), 7.10 (s, 2H, C_{aryl}-*H*), 6.89 (d, 2H, $^{3}J_{HH}$ = 8.5 Hz, C_{aryl}-*H*), 2.67 (m, 4H, C*H*$(CH_3)_2$), 2.23 (s, 6H, 2 x *H*$_3$C-Ar), 1.22 (dd, 12H, $^{3}J_{HP}$ = 17.6 Hz, $^{3}J_{HH}$ = 6.9 Hz, CH(C*H*$_3)_2$), 1.14 (dd, 12H, $^{3}J_{HP}$ = 17.6 Hz, $^{3}J_{HH}$ = 6.9 Hz, CH(C*H*$_3)_2$) ppm. To assign the ^{1}H shifts and J_{HP} coupling constants, additional spectra (^{1}H-^{1}H-COSY, ^{1}H{^{31}P} NMR) were measured.

^{13}C{^{1}H} NMR (CD_2Cl_2, 100.65 MHz): δ = 162.7 (vt, $^{1}J_{CP}$ = 10.4 Hz, *C*$_{aryl}$), 132.8 (s, *C*$_{aryl}$-H), 132.5 (s, *C*$_{aryl}$-H), 127.7 (vt, J_{CP} = 4.0 Hz, *C*$_{aryl}$), 119.1 (vt, J_{CP} = 24.5 Hz, *C*$_{aryl}$), 117.3 (vt, J_{CP} = 4.7 Hz, *C*$_{aryl}$-H), 25.3 (br s, *C*H$(CH_3)_2$), 20.6 (s, *C*H$_3$-Ar), 18.3 (s, CH(*C*H$_3)_2$), 17.3 (s, CH(*C*H$_3)_2$) ppm. For the assignment of the ^{13}C NMR shifts a combination of 1D (^{13}C{^{1}H}, ^{13}C-APT) and 2D (^{13}C-^{1}H-HSQC, ^{13}C-^{1}H-HMBC) spectra were measured.

^{15}N{^{1}H} NMR (C_6D_6, 50.72 MHz): δ = 65.5 (t, $^{2}J_{31P\text{-}15N}$ = 3.5 Hz, ^{15}*N*O).

^{31}P{^{1}H} NMR (THF-d_8, 161.91 MHz): δ = 49.0 ppm.

5.3.24 Synthesis of *cis*-[(^{Ph}PNP)Re(NO)Cl$_2$][Al(OC(CF$_3$)$_3$)$_4$] (*cis*-**29**$^{+}$)

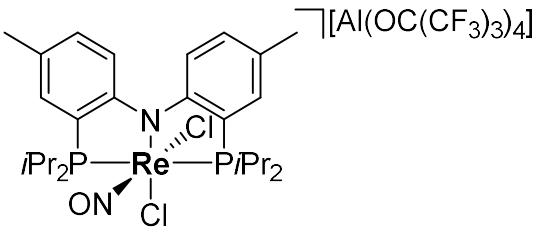

cis-[(^{Ph}PNP)ReCl$_2$(NO)] (6.9 mg, 9.6 µmol, 1.00 eq.) and [AcFc][Al(OC(CF$_3$)$_3$)$_4$] (11.5 mg, 9.6 µmol, 1.00 eq.) are suspended in 5 mL 2-MeTHF and stirred for 30 minutes at room temperature. The solvent is removed under reduced pressure and 20 mL pentane added under vigorous stirring. After five minutes the solution is decanted and the residue recrystallized from diethylether/pentane at −80 °C. *cis*-[(^{Ph}PNP)Re(NO)Cl$_2$][Al(OC(CF$_3$)$_3$)$_4$] (15.3 mg, 9.1 µmol, 95%) are obtained as dark violet, analytically pure crystals. Single crystals suitable for X-ray crystallography are obtained as the triflate salt by slow diffusion of pentane into a saturated solution in dichloromethane.

EA: calcd. for $C_{42}H_{40}AlCl_2F_{36}N_2O_5P_2Re$: C, 29.98; H, 2.40; N, 1.66. Found: C, 30.31; H, 2.43; N, 1.59.

MS: LIFDI: *m/z* (100%) = 715.1, calcd. for $C_{26}H_{40}Cl_2N_2O_1P_2Re_1$ = 715.2.

IR: (ATR, cm^{-1}): 1769 (vs).

^{1}H-NMR (CD_2Cl_2, 400.25 MHz): δ = 7.53 (m, 3H, C_{aryl}-*H*), 7.43 (m, 1H, C_{aryl}-*H*), 7.37 (m, 2H C_{aryl}-*H*), 3.84 (m, 1H, C*H*$(CH_3)_2$), 3.57 (m, 1H, C*H*$(CH_3)_2$), 2.66 (m, 2H, C*H*$(CH_3)_2$), 2.33 (s, 3H, C_{aryl}-C*H*$_3$),

2.32 (s, 3H, C_{aryl}-CH_3), 1.74 – 1.44 (m, 12H, 4 x CH(CH_3)$_2$), 1.24 (dd, 3H, $^3J_{HP}$ = 15.0 Hz, $^3J_{HH}$ = 7.2 Hz, CH(CH_3)$_2$), 1.02 – 0.86 (m, 9H, 3 x CH(CH_3)$_2$) ppm.

^{31}P{^{1}H}-NMR (CD_2Cl_2, 162.01 MHz): δ = 46.0 (d, $^2J_{PP}$ = 262 Hz), 37.8 (d, $^2J_{PP}$ = 262 Hz) ppm.

Magnetic susceptibility (r.t., CD_2Cl_2): μ_{eff} = 1.23 ± 0.1 μ_B.

5.3.25 Synthesis of [CoCp$_2$]*cis*-[(^{Ph}PNP)Re(NO)Cl$_2$] (**^{CoCp2}*cis*-30**)

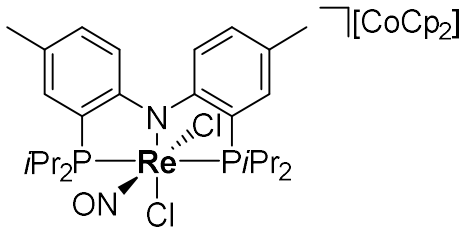

trans-[(^{Ph}PNP)Re(NO)Cl$_2$] (10.0 mg, 14.0 µmol, 1.00 eq.) and CoCp$_2$ (2.6 mg, 13.7 µmol, 0.98 eq.) are dissolved in 5 mL THF and stirred for 1.5 hours at room temperature. The solvent is removed under reduced pressure and the residue extracted with benzene/THF 1:1. [CoCp$_2$]*cis*-[(^{Ph}PNP)Re(NO)Cl$_2$] is obtained as an orange solid (8.3 mg, 9.2 µmol, 66%).

IR: (ATR, cm^{-1}): 1632 (s).

^{1}H NMR (CD_3CN, 400.25 MHz): δ = 7.25 (d, 2H, $^3J_{HH}$ = 8.3 Hz, C_{aryl}-*H*), 7.11 (s, 2H, C_{aryl}-*H*), 6.80 (d, 2H, $^3J_{HH}$ = 8.4 Hz, C_{aryl}-*H*), 5.67 (s, 10H, Co(C$_5H_5$)$_2$), 2.80 (m, 4H, 4 x C*H*(CH$_3$)$_2$), 2.23 (s, 6H, *H*$_3$C-Ar), 1.41 – 1.24 (m, 24H, 4 x CH(CH_3)$_2$) ppm.

^{31}P{^{1}H}-NMR (CD_2Cl_2, 162.02 MHz): δ = 25.6 ppm.

5.3.26 Addition of CO to [(^{Ph}PNP)Re(N)Cl]

[(^{Ph}PNP)Re(N)Cl] (5.0 mg, 7.5 µmol) are dissolved in 0.5 mL C_6D_6 in a J-Young NMR tube and the solution degassed by two successive freeze-pump-thaw cycles. The NMR tube is backfilled with one atmosphere of carbon monoxide and inverted for two hours at room temperature. ^{31}P{^{1}H} NMR spectroscopy indicated full conversion of starting material [(^{Ph}PNP)Re(N)Cl] to a new species. Mass spectrometry and IR spectroscopy indicated the formation of a terminal carbonyl complex.

MS: ESI: *m/z* = 657.2165, calcd for $C_{27}H_{40}N_2OP_2Re$: 675.2169 ([M] – Cl).

IR: (ATR, cm^{-1}): 2016 (s).

$^{31}P\{^{1}H\}$ NMR (C_6D_6, 161.98 MHz): δ = 48.5 (br) ppm.

5.3.27 Synthesis of *trans*-[($^{i\mathrm{Pr}}P^{\mathrm{H}}$NP)$OsCl_2(PPh_3)$] (*trans*-**34**)

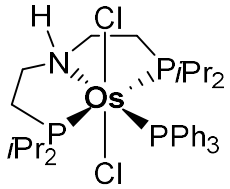

$[OsCl_2(PPh_3)_3]$ (498.0 mg, 475 µmol, 1.00 eq.) and $^{i\mathrm{Pr}}P^{\mathrm{H}}$NP (145.1 mg, 475 µmol, 1.00 eq.) are dissolved in 15 mL THF and stirred at room temperature for one hour. Afterwards the solvent is reduced to 2-3 mL and precipitation initiated upon addition of pentane. After filtration and washing with 3 x 5 mL pentane the complex is extracted with benzene and lyophilized to obtain *trans*-[($^{i\mathrm{Pr}}P^{\mathrm{H}}$NP)$OsCl_2(PPh_3)$] (363.9 mg, 437 µmol, 92%) as an orange solid. Single crystals suitable for X-ray crystallography can be obtained by slow diffusion of pentane into a saturated THF solution.

EA: Anal. Calcd. for $C_{34}H_{52}Cl_2NOsP_3 \cdot 0.5\ C_4H_8O \cdot 0.5\ C_5H_{12}$: C, 51.32; H, 6.94; N, 1.55. Found: C, 50.92; H, 6.68; N, 1.59.

MS: LIFDI: *m/z* = 829.2 (100%), calcd. for $C_{34}H_{52}Cl_2N_1OsP_3$ (829.2).

^{1}H NMR (C_6D_6, 400.25 MHz): δ = 8.28 (m, 6H, 6 x C_{aryl}-H (ortho)), 7.14 (m, 6H, C_{aryl}-H (meta)), 7.00 (m, 3H, C_{aryl}-H (para)), 4.19 (t, 1H, *J* = 11.6 Hz, N*H*), 2.89 (m, 2H, 2 x N-CH_2), 2.79 (sept, 2H, $^{3}J_{HH}$ = 7.4 Hz, 2 x C*H*$(CH_3)_2$), 2.65 (sept, 2H, $^{3}J_{HH}$ = 7.4 Hz, 2 x C*H*$(CH_3)_2$), 2.13 (m, 2H, 2 x P-CH_2), 1.87 (m, 2H, 2 x P-CH_2), 1.39 (m, 2H, 2 x N-CH_2), 1.15 (dd, 6H, $^{3}J_{HP}$ = 13.8 Hz, $^{3}J_{HH}$ = 7.3 Hz, CH(C$H_3)_2$), 1.11 (dd, 6H, $^{3}J_{HP}$ = 13.8 Hz, $^{3}J_{HH}$ = 7.4 Hz, CH(C$H_3)_2$), 0.95 (dd, 6H, $^{3}J_{HP}$ = 13.7 Hz, $^{3}J_{HH}$ = 7.4 Hz, CH(C$H_3)_2$), 0.75 (dd, $^{3}J_{HP}$ = 13.7 Hz, $^{3}J_{HH}$ = 7.4 Hz, CH(C$H_3)_2$) ppm.

$^{13}C\{^{1}H\}$ NMR (C_6D_6, 100.65 MHz): δ = 145.9 (s, C_{aryl}), 145.5 (s, C_{aryl}), 136.0 (d, *J* = 8.8 Hz, C_{aryl}), 128.7 (s, 2 x C_{aryl}), 126.9 (d, *J* = 8.8 Hz, C_{aryl}), 51.2 (s, *C*H_2), 24.4 (dt, *J* = 10.4, 2.0 Hz, *C*H_2), 23.5 (t, *J* = 11.5 Hz, *C*H$(CH_3)_2$), 21.6 (s, *C*H_2), 21.3 (t, *J* = 10.4 Hz, *C*H$(CH_3)_2$), 20.8 (s, CH(*C*$H_3)_2$), 20.7 (s, 2 x CH(*C*$H_3)_2$), 20.3 (s, CH(*C*$H_3)_2$) ppm.

$^{31}P\{^{1}H\}$ NMR (C_6D_6, 162.02 MHz): δ = –3.0 (d, 2P, $^{2}J_{PP}$ = 13.7 Hz, *i*$Pr_2P(CH_2)_2N$), –25.9 (t, 1P, $^{2}J_{PP}$ = 13.7 Hz, *P*Ph_3) ppm.

5.3.28 Synthesis of *trans*-[($^{\text{Imine}}$PNP)OsCl$_2$(PPh$_3$)] (*trans*-**35**)

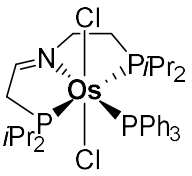

trans-[($^{i\text{Pr}}$P$^{\text{H}}$NP)OsCl$_2$(PPh$_3$)] (20.0 mg, 24.1 µmol, 1.00 eq.) and 2,4,6-tri-*tert*-butylphenoxyl radical (12.6 mg, 48.2 µmol, 2.00 eq.) are dissolved in 0.6 mL C_6D_6 in a *J*-Young NMR tube and inverted for one hour at room temperature during which the color gradually changed from bright orange to yellow. Subsequently, the solvent is removed upon lyophilization and the residue extracted with pentane. Yellow crystals of *trans*-[($^{\text{Imine}}$PNP)OsCl$_2$(PPh$_3$)] (8.3 mg, 10.0 µmol, 41%) are obtained upon cooling a saturated pentane solution to –40 °C over the course of several days.

MS: LIFDI: *m/z* = 827.2 (100%, [M$^+$]), calcd. for $C_{34}H_{50}Cl_2N_1OsP_3$ (827.2).

^{1}H NMR (C_6D_6, 300.13 MHz): δ = 8.22 (m, 6H, C_{aryl}-*H*), 7.49 (m, 1H, N=C-*H*), 7.15 (m, 6H, C_{aryl}-*H*), 7.03 (m, 3H, C_{aryl}-*H*), 3.63 (dt, 2H, $^3J_{HH}$ = 6.2 Hz, $^3J_{HP}$ = 19.8 Hz, PC*H*$_2$CH$_2$), 2.15 (sept, 2H, $^3J_{HH}$ = 7.3 Hz, C*H*(CH$_3$)$_2$), 2.64 (m, 2H, PC*H*$_2$C=N), 2.34 (sept, 2H, $^3J_{HH}$ = 7.3 Hz, C*H*(CH$_3$)$_2$), 1.73 (m, 2H, N-C*H*$_2$), 1.23 (m, 6H, CH(C*H*$_3$)$_2$), 1.17 (m, 6H, CH(C*H*$_3$)$_2$), 0.90 (m, 12H, 2 x CH(C*H*$_3$)$_2$) ppm.

^{31}P{^{1}H} NMR (C_6D_6, 121.49 MHz): δ = 14.1 (dd, 1P, $^2J_{PP}$ = 12.7 Hz, $^2J_{PP}$ = 288.1 Hz), P_{pincer}), –2.1 (dd, 1P, $^2J_{PP}$ = 12.7 Hz, $^2J_{PP}$ = 288.1 Hz, P_{pincer}), –20.0 (vt, *J* = 12.8 Hz, *P*Ph$_3$) ppm.

5.3.29 Synthesis of *cis*-[($^{i\text{Pr}}$P$^{\text{H}}$NP)Os(CO)Cl$_2$] (*cis*-**36**)

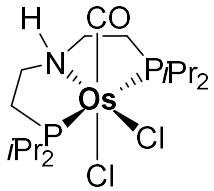

trans-[($^{i\text{Pr}}$P$^{\text{H}}$NP)OsCl$_2$(PPh$_3$)] (49.3 mg, 59.5 µmol) are dissolved in 1 mL benzene and degassed *via* a freeze-pump-thaw cycle. Subsequently, CO (1 atm) is applied and the solution stirred at 90 °C for 60 hours. The excess CO is removed *via* two freeze-pump-thaw cycles and the suspension filtered. Further extraction with benzene and lyophilization furnishes an off-white solid that is dissolved in 1 mL dichloromethane and precipitated upon addition of 10 mL pentane. The precipitate is filtered, washed with pentane (3 x 1 mL) and diethylether (3 x 1 mL) and extracted with dichloromethane. *cis*-

[($^{i\text{Pr}}$P$^{\text{H}}$NP)Os(CO)Cl$_2$] (26.3 mg, 44.2 µmol, 74%) is obtained as an off-white powder. Single crystals suitable for X-ray crystallography are obtained upon diffusion of pentane into dichloromethane.

MS: HRMS-ESI: *m/z* = 618.1216 ([M] + Na$^+$), calcd. for $C_{17}H_{37}Cl_2NNaOOsP_2$ (618.1215).

IR: (ATR, cm^{-1}) = 3147 (m, N*H*), 1909 (s, CO).

^{1}H NMR ($CDCl_3$, 300.13 MHz): δ = 3.88 (m, 1H, N*H*), 3.25 (sept, 2H, $^3J_{HH}$ = 7.2 Hz, C*H*(CH$_3$)$_2$), 3.14 (m, 2H, C*H*$_2$), 2.74 (m, 2H, C*H*$_2$), 2.56 (sept, $^3J_{HH}$ = 7.2 Hz, C*H*(CH$_3$)$_2$), 2.32 (m, 2H, C*H*$_2$), 1.57 (dd, 6H, $^3J_{HH}$ = 7.4 Hz, $^3J_{HP}$ = 15.7 Hz, CH(C*H*$_3$)$_2$), 1.48 (dd, 6H, $^3J_{HH}$ = 7.4 Hz, $^3J_{HP}$ = 15.7 Hz, CH(C*H*$_3$)$_2$), 1.42 (dd, 6H, $^3J_{HH}$ = 7.4 Hz, $^3J_{HP}$ = 15.7 Hz, CH(C*H*$_3$)$_2$), 1.35 (dd, 6H, $^3J_{HH}$ = 7.4 Hz, $^3J_{HP}$ = 15.7 Hz, CH(C*H*$_3$)$_2$) ppm.

^{31}P{^{1}H} NMR ($CDCl_3$, 121.48 MHz): δ = 15.4 ppm.

5.3.30 Synthesis of [($^{i\text{Pr}}$P$^{\text{H}}$NP)OsCl$_3$] (**37**) and [($^{\text{Imine}}$PNP)OsCl$_3$] (**38**)

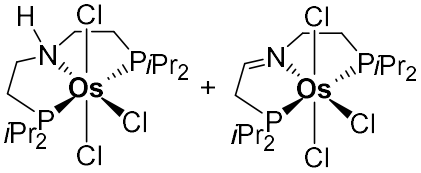

$OsCl_3 \cdot 3H_2O$ (180.0 mg, 513.3 µmol, 1.00 eq.) is finely powdered and $^{i\text{Pr}}$P$^{\text{H}}$NP (159.9 mg, 523.5 µmol, 1.02 eq.) dissolved in 5 mL toluene were added. The reaction mixture is heated to 115 °C for 3 days and afterwards 15 mL of pentane are added. The suspension is filtered, washed with pentane (3 x 5 mL), diethylether (3 x 5 mL) and cold (–40 °C) toluene (1 x 2 mL) and extracted with dichloromethane. Recrystallization from dichloromethane/diethylether furnishes [($^{i\text{Pr}}$P$^{\text{H}}$NP)OsCl$_3$] and [($^{\text{Imine}}$PNP)OsCl$_3$] as brown crystals (276.9 mg, 90%). Despite numerous attempts, the two species could not be separated. A sample suitable for elemental analysis is obtained by recrystallization from chloroform / diethylether and subsequent filtration of a dichloromethane solution through a silica plug. Single crystals suitable for X-ray crystallography are obtained by slow diffusion of diethylether into a saturated dichloromethane solution.

IR: (ATR, cm^{-1}) = 3171 (w, N*H*), 1613 (m, N=C).

EA: Anal. calcd. for $C_{16}H_{37}Cl_3N_1Os_1P_2$: C, 31.92; H, 6.20; N 2.33; found: C, 32.43; H, 6.38; N, 2.30.

MS: LIFDI: *m/z* = 602.0 (100%, [M]$^+$), calcd. for $C_{16}H_{35}Cl_3NNaOsP_2$ (602.1).

^{1}H NMR (CD_2Cl_2, 300.1 MHz): δ = –5.85 (br s), –7.89 (br s), –8.60 (br s), –8.91 (br s), –9.20 (br s), –13.8 (br s) ppm.

5.3.31 Synthesis of [(^{Imine}PNP)$OsCl_3$] (**38**)

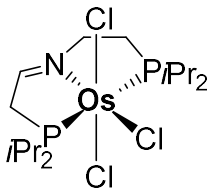

[(^{iPr}PNP)$OsCl_3$] and [(^{Imine}PNP)$OsCl_3$] (20 mg, 33.3 µmol, 1.00 eq.) are dissolved in 5 mL dichloromethane and a solution of TEMPO (5.2 mg, 33.3 µmol, 1.00 eq.) in 2 mL dichloromethane added dropwise over the course of approximately 3 minutes. The solution is stirred at room temperature for 27 hours and subsequently filtered through a short silica plug. Recrystallization from dichloromethane/pentane yields [(^{Imine}PNP)$OsCl_3$] as yellow-brown crystals (15.5 mg, 77%), which is sufficiently pure for further synthesis. Single crystals suitable for X-ray crystallography can be obtained by slow diffusion of pentane into a saturated dichloromethane solution of [(^{Imine}PNP)$OsCl_3$].

IR: (ATR, cm^{-1}): 1611 (m, C=N).

MS: ESI: *m/z* = 623.1 ([M] + Na^+), calcd. for $C_{16}H_{35}Cl_3NNaOsP_2$ (623.1).

^{1}H NMR ($CDCl_3$, 300.1 MHz): δ = –5.74 (br s), –6.37 (br s), –7.68 (br s), –8.49 (br s), –11.57 (br s), –14.00 (br s), –32.97 (br s) ppm.

Magnetic susceptibility (Evans' method): μ_{eff} = 1.77 ± 0.1 μ_B.

5.3.32 Synthesis of *trans*-[($^{iPr}P^{H}$NP)$OsCl_2(N_2)$] and *trans*-[(^{Imine}PNP)$OsCl_2(N_2)$] (*trans*-**39**) and (*trans*-**40**)

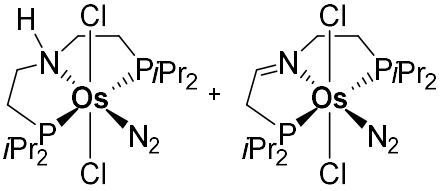

[($^{iPr}P^{H}$NP)$OsCl_3$] and [(^{Imine}PNP)$OsCl_3$] (50 mg, 83.1 µmol, 1.00 eq.) are dissolved in 5 mL of THF and 1.121 g (1.0 eq.) Na/Hg alloy (1 M) added in an N_2-glovebox. The suspension is stirred vigorously for

10 minutes at room temperature, filtered and subsequently the solvent removed. The residue is extracted with diethylether and after evaporation of the solvent washed with cold pentane (–80 °C, 2 x 5 mL), to obtain a yellow solid (38.4 mg, 64.6 µmol, 77%), which consists out of a mixture of *trans*-[($^{i\text{Pr}}$P$^{\text{H}}$NP)OsCl$_2$(N$_2$)] and *trans*-[($^{\text{Imine}}$PNP)OsCl$_2$(N$_2$)] in a ratio of 64%/36% according to ^{31}P{^{1}H} NMR integration. Single crystals of both complexes suitable for X-ray crystallography were obtained by slow evaporation of a saturated diethylether solution.

IR: (ATR, cm^{-1}) = 3161 (m, N*H*), 2066 (s, N$_2$).

MS: HRMS-ESI (tetrahydrofuran): 618.1326 (100%, [M+Na$^+$]), calcd. for $C_{16}H_{37}Cl_2N_3OsP_2Na$ (618.1327).

^{1}H NMR (THF-d$_8$, 400.25 MHz): δ = 4.47 (m, 1H, N*H*), 2.99 (m, 4H, C*H*(CH$_3$)$_2$), 2.89 (m, 4H, 2 x NC*H*$_2$), 2.30 (m, 2H, PC*H*$_2$), 1.57 (m, 2H, PC*H*$_2$), 1.41-1.32 (m, 24H, 4 x CH(C*H*$_3$)$_2$) ppm. Only the signals for the amine complex are denoted, for the imine complex see its independent synthesis below.

^{31}P NMR (C$_6$D$_6$, 121.49 MHz): δ = 25.5 (d, 1P, *J* = 303 Hz, *P*$_{\text{Imine}}$), 17.7 (d, 1P, *J* = 303 Hz, *P*$_{\text{Imine}}$), 16.7 (s, 2P, *P*$_{\text{Amine}}$) ppm.

5.3.33 Synthesis of *trans*-[($^{\text{Imine}}$PNP)OsCl$_2$(N$_2$)] (*trans*-**40**)

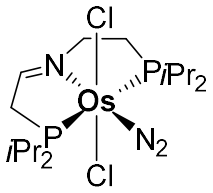

0.5 mL THF-d$_8$ is condensed onto [($^{\text{Imine}}$PNP)OsCl$_3$] (5.4 mg, 9.0 µmol, 1.00 eq.) and CoCp$^*_2$ (3.0 mg, 9.1 µmol, 1.01 eq.). Afterwards the *J*-Young NMR tube is filled with an atmosphere of N$_2$ upon thawing of the solvent. The reaction mixture is stirred at room temperature for three hours, after which a reaction control *via* ^{1}H-NMR indicated the full consumption of the starting material. The solvent is removed under reduced pressure, the residue extracted with benzene and filtered over a short silica plug. Lyophilization of the benzene extract yields *trans*-[($^{\text{Imine}}$PNP)OsCl$_2$(N$_2$)] (4.2 mg, 7.1 µmol, 79%) as a lemon yellow solid. The compound is crystallographically characterized as the co-crystallizing component of *trans*-[($^{i\text{Pr}}$P$^{\text{H}}$NP)OsCl$_2$(N$_2$)].

MS: HRMS-ESI (tetrahydrofuran): 530.1517 (100%, [M – N$_2$ – Cl]), calcd. for $C_{16}H_{35}ClNOsP_2$ (530.1532).

IR: (ATR, cm^{-1}) = 2073 (s, N$_2$), 1622 (m, C=N).

^{1}H NMR (C_6D_6, 300.13 MHz): δ = 8.33 (m, 1H, *H*C=N), 3.83 (m, 2H, C*H*$_2$), 3.04 – 2.98 (m, 4H, 4 x C*H*(CH$_3$)$_2$), 2.94 – 2.91 (m, 4H, 2 x CH$_2$), 1.43 – 1.34 (m, 24H, 4 x CH(C*H*$_3$)$_2$) ppm.

^{31}P{^{1}H} NMR (THF-d$_8$, 121.49 MHz): δ = 26.1 (d, 1P, J = 303 Hz, P_{Imine}), 18.1 (d, 1P, J = 303 Hz, P_{Imine}) ppm.

5.3.34 Synthesis of [PPN][($^{i\text{Pr}}$P=N=P)OsCl$_3$] (**$^{\text{PPN}}$41**)

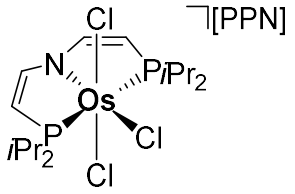

[($^{i\text{Pr}}$P$^{\text{H}}$NP)OsCl$_3$] and [($^{\text{Imine}}$PNP)OsCl$_3$] (20.0 mg, 33.2 µmol, 1.00 eq.) and PPNN$_3$ (19.2 mg, 33.1 µmol, 1.00 eq.) are suspended in 3 mL THF and stirred for 24 hours at 65 °C. Afterwards the solvent is removed and the residue washed with cold toluene (–40 °C, 3 x 1 mL) and extracted with THF. [PPN][($^{i\text{Pr}}$P=N=P)OsCl$_3$] (18.0 mg, 15.9 µmol, 48%) is obtained as a green powder upon removal of the solvent and subsequent recrystallization from THF/pentane. Emerald-green single crystals suitable for X-ray crystallography are obtained from a reaction mixture in THF after cooling to room temperature.

MS: HRMS-ESI (negative mode): *m/z* = 597.0661 (100%), calcd. for $C_{16}H_{32}Cl_3NOsP_2$ (597.0668).

^{1}H NMR (THF-d$_8$, 400.3 MHz): δ = –3.59 (br s), –5.77 (br s) ppm.

5.3.35 Synthesis of [($^{i\text{Pr}}$PNP)OsCl$_3$] (**43**) and [($^{\text{Imine}}$PNP)OsCl$_3$] (**38**)

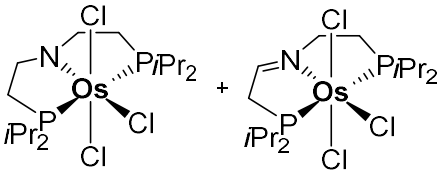

[($^{i\text{Pr}}$P$^{\text{H}}$NP)OsCl$_3$] and [($^{\text{Imine}}$PNP)OsCl$_3$] (40.4 mg, 67.1 µmol, 1.00 eq.) are dissolved in 10 mL dichloromethane and 3.6 mg 1,4-benzoquinone (33.3 µmol, 0.50 eq.) dissolved in 2 mL dichloromethane are added dropwise over the course of 3 minutes. The light brown solution is stirred for one hour at room temperature upon which a distinct darkening of the solution is observed. The solvent is removed under reduced pressure and the residue washed with diethylether (3 x 3 mL) and benzene (1 x 3 mL)

and extracted with dichloromethane. Recrystallization from dichloromethane/diethylether furnishes [($^{i\text{Pr}}$PNP)OsCl$_3$] as brown crystals (18.2 mg, 45%), which are contaminated with [($^{\text{Imine}}$PNP)OsCl$_3$] even after multiple recrystallization attempts. Single crystals suitable for X-ray crystallography are obtained by slow diffusion of pentane into a saturated THF solution.

^{1}H NMR ($CDCl_3$, 400.3 MHz): δ = 4.40 (m, 4H, (C*H*$_2$)$_2$), 3.05 (m, 4 H, C*H*(CH$_2$)$_2$), 2.29 (m, 4H, (C*H*$_2$)$_2$), 1.66 (dd, 12H, $^3J_{HH}$ = 7.3 Hz, $^3J_{HP}$ = 16.2 Hz, 2 x (CH(C*H*$_3$)$_2$), 1.58 (dd, 12H, $^3J_{HH}$ = 7.3 Hz, $^3J_{HP}$ = 16.2 Hz, 2 x (CH(C*H*$_3$)$_2$) ppm.

^{31}P{^{1}H} NMR ($CDCl_3$, 162.01 MHz): δ = –39.8 ppm.

5.3.36 Synthesis of [($^{i\text{Pr}}$P=N=P)OsCl$_3$] (**44**)

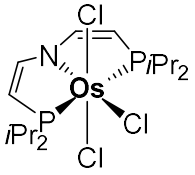

[($^{i\text{Pr}}$P$^{\text{H}}$NP)OsCl$_3$] and [($^{\text{Imine}}$PNP)OsCl$_3$] (13.9 mg, 23.1 µmol, 1.00 eq.) and 2,4,6-tri*tert*butyl phenoxy radical (66.0 mg, 252.4 µmol, 10.9 eq.) are dissolved in 5 mL benzene and heated to 65 °C for 24 hours. The solvent is removed under reduced pressure and the dark residue is washed with pentane (3 x 2 mL) and diethylether (3 x 2 mL) and extracted with tetrahydrofuran. The solvent is removed to obtain [($^{i\text{Pr}}$P=N=P)OsCl$_3$] (12.6 mg, 21.1 µmol, 92%) as a dark green powder. Single crystals suitable for X-ray crystallography can be obtained from a saturated solution of P=N=POsCl$_3$ in acetonitrile at –40 °C.

MS: LIFDI: *m/z* = 597.0 (100%), calcd. for $C_{16}H_{32}Cl_3NOsP_2$ (597.1).

^{1}H NMR (C_6D_6, 300.1 MHz): δ = 9.39 (m, 2H, 2 x PC*H*CHN), 5.59 (m, 4H, C*H*(CH$_3$)$_2$), 3.93 (dd, 12 H, $^3J_{HP}$ = 14.6 Hz, $^3J_{HH}$ = 7.2 Hz, 2 x (CH(C*H*$_3$)$_2$)), –11.80 (d, 2H, $^3J_{HP}$ = 6.5 Hz, 2 x PCHC*H*N) ppm.

^{31}P{^{1}H} (C_6D_6, 162.01 MHz): δ = –280.6 ppm.

5.3.37 Synthesis of [(^{Ph}PNP)Re(NO)(NOB(C_6F_5)$_3$)] (**47**)

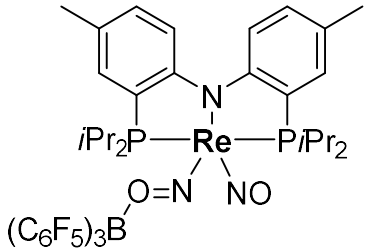

[(^{Ph}PNP)Re(NO)$_2$] (2.3 mg, 3.4 µmol, 1.00 eq.) and 1.7 mg B(C_6F_5)$_3$ were dissolved in toluene and the mixture stirred for one hour at room temperature. Afterwards, the solution was filtered and layered with pentane at −80 °C. Single crystals of [(^{Ph}PNP)Re(NO)(NOB(C_6F_5)$_3$)] suitable for X-ray crystallography were obtained over night.

5.4 Computational Appendix

For all independently performed calculations the ORCA 4.2.1 program package was used on full model complexes with no truncation.[499,500] The DFT calculations were performed using the PBE,[501] PBE0[502],BP86[503] and ωB97X-D[504] functionals. The double-ζ, triple-ζ and quadruple-ζ (def2-SVP, def2-TZVP, def2-QZVP) basis sets of *Ahlrich* were used for all elements, except for Osmium and Rhenium, for which the effective core potentials (ECP) with the Stuttgart-Dresden 60 parameter sets were used (replacing the *1s-4f* electrons).[505,506] For DFT calculations with the PBE and BP86 functionals the RI-*J*[507][508] approximation and for the hybrid functionals PBE0 and ωB97X-D the RIJCOSX[509] approximation were used with the def2/J auxiliary basis sets, to save computational cost, while maintaining reasonable numerical accuracy.[510] The energies were further corrected for dispersion interactions with *Grimme's* D3 model[511] and with the *Becke-Johnson* damping, using the implemented D3BJ command.[512]

TIGHTOPT and TIGHTSCF convergence criteria of ORCA were applied for geometry optimizations. Analytical frequency calculations were performed at the same level of DFT as the geometry optimization and analysis of the vibrational frequencies confirmed the structure to be a local minimum (no imaginary vibrational frequency) or transition-state (one imaginary vibrational frequency). The frequency calculations employed *Grimme's* quasi RRHO approach for vibrational frequencies below 35 cm^{-1}.[513] Solvent effects for BDFE calculations utilized the CPCM continuum solvation models.[514] The output files of DFT calculations were analyzed and the obtained geometries / orbitals plotted using the *ChemCraft* or *Avogadro* programs.

Natural bond orbital (NBO) analyses were performed with the NBO 7.0 program[515,516] using PBE0/def2-TZVP(Re,Cl,P,O,N);def2-SVP orbitals.

5.4.1 Calculation of Infrared Spectra

For the calculation of infrared spectra an initial benchmarking of different functionals and basis sets was conducted. The mononitrosyl complex *cis*-[(^{Ph}PNP)Re(NO)Cl_2] was employed as experimental benchmark (ν_{NO} = 1702 cm^{-1}).

In a first step, the X-ray crystallographically determined solid-state structure was taken as input for geometry optimizations for the functional/basis-set combinations. The optimized geometries were then compared with the solid-state structural parameters (Table 5.2 and Table 5.3) after verifying them as minima with the aid of a frequency calculation. Optimization and frequency calculation of both possible backbone conformations on PBE0/def2-TZVP confirmed both isomers to be isoenergetic ($\Delta E = 0.02$ kcal·mol^{-1}) within DFT error and therefore only one conformation was calculated.

Table 5.2: Comparison of structural parameters of optimized geometries on different levels of DFT with X-ray crystallographic parameters. Axial and equatorial refers to the plane defined by the pincer ligand (Part 1). Smallest deviation from experimental values is highlighted in bold.

bonds [Å]	exp.	PBE0/ def2-TZVP	PBE0/ def2-TZVP;SVP*	PBE/ def2-TZVP	PBE/ def2-TZVP;SVP*
Re-N_{NO}	1.797	1.752	1.753	1.776	1.776
N-O	1.184	1.168	1.168	1.189	**1.188**
Re-$Cl_{ax.}$	2.354	**2.411**	**2.411**	2.422	2.419
Re-$Cl_{eq.}$	2.394	2.366	2.366	2.390	2.389
Re-N_{PNP}	2.050	**2.097**	2.098	2.103	2.108
$Ø\Delta_{exp,DFT}$	-	0.039	0.039	0.030	0.031

* def2-TZVP(Re,Cl,P,N,O);def2-SVP(C,H).

Table 5.3: Comparison of structural parameters of optimized geometries on different levels of DFT with X-ray crystallographic parameters. Axial and equatorial refers to the plane defined by the pincer ligand (Part 2). Smallest deviation from experimental values is highlighted in bold.

bonds [Å]	exp.	BP86/def2-TZVP;SVP*	BP86/def2-QZVP;SVP**	B3LYP/def2-TZVP;SVP	ωB97X-D/def2-TZVP;SVP*	ωB97X-D/def2-SVP
Re-N_{NO}	1.797	**1.777**	1.774	1.763	1.740	1.745
N-O	1.184	1.189	1.190	1.176	1.172	1.170
Re-$Cl_{ax.}$	2.354	2.419	2.419	2.436	2.459	2.468
Re-$Cl_{eq.}$	2.394	2.389	2.389	**2.394**	2.374	2.385
Re-N_{PNP}	2.050	2.106	2.103	2.112	2.118	2.112
$Ø\Delta_{exp,DFT}$	-	0.030	0.030	0.037	0.052	0.050

* def2-TZVP(Re,Cl,P,N,O);def2-SVP(C,H) **def2-QZVP(Re,Cl,P,N,O); def2-SVP(C,H)

The structural parameters of the first coordination sphere of the rhenium, as well as the nitrosyl ligand were taken to compare the different levels of DFT. Interestingly, hybrid functionals perform worse than functionals without Hartree-Fock exchange. For example the BP86 functional shows smaller deviations from experimental data (ØΔ = 0.030 Å), compared to hybrid functionals like B3LYP (ØΔ = 0.037 Å), PBE0 (ØΔ = 0.039 Å) or ωB97X-D (ØΔ = 0.051 Å). BP86 and PBE perform similarly well, especially the bond parameters of the nitrosyl ligand are in good agreement with the experimental data on these functionals.

A similar picture arises from the frequency calculations and the vibrational spectroscopic data derived thereof. The vibrational frequency of the N-O stretch was compared to the experimentally data derived by infrared spectroscopy (ν_{NO} = 1702 cm^{-1}). The BP86 functional in combination with the diffuse def2-QZVP basis set on the heavy atoms (Re,Cl,P,N,O) and less diffuse def2-SVP basis set on carbon and hydrogen atoms showed the best agreement (ν_{NO} = 1731 cm^{-1}) with the experimental data. A similarly good agreement was achieved with the PBE functional (ν_{NO} = 1742 cm^{-1}). For both functionals a strong dependence on the basis-set was observed (Table 5.4 and Table 5.5).

Table 5.4: Comparison of vibrational and electronic parameters of experimentally determined values for *cis*-[(^{Ph}PNP)Re(NO)Cl$_2$] and different functional/basis-set combinations. The best agreement is highlighted in bold. Computational cost in cores and gigabytes of RAM.

	exp.	PBE/def2-QZVP;SVP*	PBE/def2-TZVP	PBE/def2-SVP	BP86/def2-QZVP;SVP*	BP86/def2-TZVP;SVP**
ν_{NO} [cm]	1702	1742	1748	1811	**1731**	1738
<S^2>	-	0.76	0.76	0.76	0.76	0.76
comp. cost	-	5h 2min 16c/40GB	15h 30 min 16c/40GB	3h 12min 16c/40GB	6h 2min 16c/54GB	4h 43min 16c/40GB

*def2-QZVP(Re,Cl,P,N,O); def2-SVP(C,H) **def2-TZVP(Re,Cl,P,N,O);def2-SVP(C,H)

Table 5.5: Comparison of vibrational and electronic parameters of experimentally determined values for *cis*-[(^{Ph}PNP)Re(NO)Cl$_2$] and different functional/basis-set combinations. The best agreement is highlighted in bold. Computational cost in cores and gigabytes of RAM.

	exp.	PBE0/def2-TZVP	PBE0/def2-TZVP;SVP*	PBE0/SVP	B3LYP/def2-TZVP;SVP*	ωB97X-D3/def2-TZVP
ν_{NO} [cm]	1702	1846	1850	1920	1784	1858
<S^2>	-	0.78	0.78	0.78	0.77	0.79
comp. cost	-	8h 28min 32c/80GB	2h 55min 48c/168GB	4h 20min 16c/56GB	7h 19min 16c/40GB	1h 37min 32c/112GB

*def2-QZVP(Re,Cl,P,N,O); def2-SVP(C,H)

Interestingly, the hybrid functionals performed considerably worse. For example, the PBE0 functional showed deviations of more than 140 cm^{-1}, which increased up to 218 cm^{-1} for the less diffuse basis-set def2-SVP on all atoms. The range-separated hybrid-functional ωB97X-D3 performed similarly to PBE0. B3LYP showed less deviation from the experimental IR stretch, however, still worse than the non-hybrid functionals. Especially taking the computational cost into account, the BP86 functional shows the best compromise of structural and vibrational parameters with relatively low computational cost. This general trend with regard to hybrid and non-hybrid functionals could be reproduced for the dinitrosyl complex *cis*-[(^{Ph}PNP)Re(NO)$_2$Cl]. As a consequence, the IR calculations for the various rhenium and

osmium complexes were performed using the BP86/def2-QZVP;def2-SVP level of theory (Table 5.6).

Table 5.6: Comparison of calculated and experimentally determined IR stretches for specified ligands in complexes.

complex	*trans*-[(^{Py}PNP)OsCl$_2$(N$_2$)]*	*cis*-[(^{Ph}PNP)Re(NCO)Cl$_2$]	*cis*-[(^{Ph}PNP)Re(NS)Cl$_2$]	*cis*-[(^{Ph}PNP)Re(NO)$_2$Cl]
$\nu_{exp.}$ [cm^{-1}]	2081 (N$_2$)	2206 (NCO)	1176 (NS)	1694,1633 (NO)
ν_{DFT} [cm^{-1}]	2095 (N$_2$)	2245 (NCO)	1227 (NS)	1719, 1675 (NO)
Δ [cm^{-1}]	14	39	49	25,42

complex	*cis*-[(^{Ph}PNP)Re(NO)Cl$_2$]	[(^{Imine}PNP)OsCl$_2$(N$_2$)] / [(^{iPr}P^{H}NP)OsCl$_2$(N$_2$)]
$\nu_{exp.}$ [cm^{-1}]	1702 (NO)	2066 (N$_2$)
ν_{DFT} [cm^{-1}]	1731 (NO)	2081, 2100 (N$_2$)
Δ [cm^{-1}]	29	15,34

* presumed complex/isomer

The deviation between calculated and experimentally determined IR-stretches for selected ligands in rhenium and osmium complexes using the BP86/def2-QZVP;SVP level of theory is in the range between 14 and 49 cm^{-1}, which is a good agreement with the experimental data.

Table 5.7: XYZ coordinates of the complexes in Table 5.6.

	x	y	z		x	y	z
***trans*-[(^{Py}PNP)OsCl$_2$(N$_2$)]**				***cis*-[(^{Ph}PNP)Re(NCO)Cl$_2$]**			
C	1,83586	-2,31041	-4,46766	C	-4,92789	-0,22667	-3,46807
C	-0,20985	-2,54039	-2,95589	C	-2,58482	0,71656	-3,12594
C	1,26154	-2,11566	-3,05745	C	-3,67664	-0,03471	-2,64695
C	2,28244	-5,2438	-2,95448	C	2,3595	-0,48106	-2,50143
C	4,01911	-2,35385	-2,09675	C	-1,40683	0,87123	-2,37858
C	2,20245	-4,62039	-1,55039	C	4,7116	-0,38567	-1,59931
C	6,23227	-2,58643	-0,8736	C	-3,54514	-0,64325	-1,3768
C	4,87634	-2,23193	-0,87053	C	3,29592	-0,9306	-1,36928
C	0,88921	-5,04179	-0,86077	C	-1,28565	0,26496	-1,11209
C	3,40949	-5,10034	-0,71868	C	1,10745	3,85724	-0,44286
C	6,99074	-2,44869	0,29549	C	-2,37326	-0,51676	-0,62463
C	4,92462	1,44102	0,8054	C	0,24937	2,75554	-0,56908
C	6,36822	-1,94899	1,44518	C	3,37035	4,89994	0,09244
C	5,01053	-1,60018	1,40951	C	2,46355	3,70781	-0,08694
C	2,78191	2,7075	1,13738	C	0,72735	1,44695	-0,34155
C	3,7674	1,71581	1,79158	C	-2,67211	-3,84383	0,10162
C	4,3064	-1,05684	2,62096	C	2,93658	2,39596	0,14246
C	4,37803	2,34922	3,05523	C	2,09593	1,28297	0,03288
C	1,83923	0,21137	3,69542	C	-3,04295	-2,80582	1,16619
C	0,98463	1,48997	3,59917	C	4,01786	-0,49451	1,47196
C	0,87084	-0,98192	3,78376	C	4,48351	-1,95856	1,56561
C	2,69311	0,22155	4,97902	C	-2,44027	1,40757	1,79242
H	1,2541	-1,69141	-5,18258	C	-4,35131	-0,16039	2,27399
H	1,77819	-3,35791	-4,81828	C	-2,82576	-0,0284	2,18208
H	2,89029	-1,98097	-4,54388	C	-2,82646	-3,34897	2,58877
H	-0,8236	-1,92247	-3,64281	C	3,63347	0,05564	2,85058
H	1,38552	-5,02106	-3,56259	H	-4,95327	-1,23775	-3,92961
H	3,17756	-4,90968	-3,51744	H	-2,64993	1,18579	-4,12045

H	-0,36017	-3,59999	-3,24428	H	-4,9958	0,51328	-4,28926
H	4,46465	-3,05305	-2,82877	H	2,72155	-0,89222	-3,46538
H	2,34935	-6,34815	-2,85526	H	-5,84159	-0,13443	-2,84586
H	3,9369	-1,34991	-2,56419	H	5,05555	-0,66022	-2,61798
H	-0,61391	-2,40101	-1,93457	H	2,3468	0,62367	-2,58529
H	6,68045	-2,97134	-1,80014	H	-0,56358	1,44169	-2,79173
H	0,00675	-4,75818	-1,45378	H	1,32381	-0,83573	-2,35289
H	4,37014	-4,92253	-1,24067	H	4,72673	0,72233	-1,53745
H	0,8764	-6,14632	-0,74486	H	2,99177	5,78763	-0,45121
H	3,31999	-6,19514	-0,55665	H	3,31121	-2,04098	-1,34429
H	8,05473	-2,72708	0,30979	H	-4,3792	-1,24422	-0,98115
H	0,80679	-4,58731	0,14429	H	5,45495	-0,78299	-0,88254
H	4,57361	0,93997	-0,11459	H	-2,74453	-3,43643	-0,92479
H	3,44107	-4,61181	0,2736	H	0,70357	4,86819	-0,61099
H	5,36871	2,41457	0,51057	H	-0,80961	2,91228	-0,81524
H	2,2728	2,25248	0,26797	H	4,3982	4,68843	-0,26575
H	3,35221	3,58757	0,77172	H	-3,35483	-4,71472	0,18105
H	5,73165	0,83906	1,2645	H	-1,63517	-4,20145	0,24338
H	6,92535	-1,82298	2,38396	H	3,98898	2,24932	0,43177
H	2,02195	3,07884	1,84596	H	3,45269	5,18023	1,16527
H	4,96235	3,2443	2,75342	H	4,81794	-2,3644	0,59094
H	3,80026	-1,90533	3,12812	H	-4,10709	-2,51261	1,03179
H	0,42214	1,533	2,6454	H	4,82833	0,13208	1,04039
H	5,02869	-0,59912	3,32283	H	-2,94312	1,70375	0,85074
H	0,20542	-1,04632	2,90492	H	-4,8234	-0,01383	1,28036
H	5,07781	1,66606	3,57755	H	3,657	-2,59963	1,93448
H	3,61449	2,68948	3,77887	H	5,33156	-2,04402	2,27506
H	1,39622	-1,94864	3,86366	H	-1,3529	1,53218	1,65024
H	1,57803	2,41711	3,698	H	-4,68078	-1,13783	2,67409
H	0,24071	1,48379	4,42292	H	-3,4093	-4,28131	2,73275
H	0,23751	-0,84799	4,68631	H	-1,75384	-3,57995	2,75144
H	3,22773	-0,73792	5,12009	H	-2,75976	2,10907	2,58858
H	3,43391	1,03883	5,01146	H	3,23673	1,08748	2,79826
H	2,01983	0,34649	5,85367	H	-4,75455	0,62498	2,94621
Cl	2,49798	0,45857	-1,36892	H	-3,13969	-2,63128	3,37225
Cl	2,06706	-3,22485	1,80773	H	-2,36469	-0,26793	3,16398
N	4,28054	-1,74888	0,26216	H	4,52528	0,06441	3,50997
N	0,35869	-0,99334	0,32021	H	2,86501	-0,58464	3,32306
N	-0,75276	-0,79015	0,33557	Cl	0,33573	-2,73654	-0,95396
Os	2,2332	-1,32997	0,28021	Cl	0,91538	-3,07954	2,30012
P	2,2664	-2,7399	-1,62112	N	0,4395	-0,0058	2,40158
P	2,9009	0,04857	2,11939	N	-0,10196	0,30572	-0,34224
H	1,31244	-1,02795	-2,83464	P	2,59145	-0,45051	0,29885
***cis*-[(^{Ph}PNP)Re(NS)Cl$_2$]**				P	-2,04506	-1,25863	1,00643
H	-2,86134	-0,60726	-2,84138	Re	0,37581	-1,24811	0,85709
H	4,01753	1,58549	-2,16865	C	0,47412	0,78709	3,30517
H	-2,8893	0,95181	-1,95821	O	0,51369	1,57391	4,20574
H	3,44223	-1,01254	-1,67368	***cis*-[(^{Ph}PNP)Re(NO)$_2$Cl]**			
H	-1,37076	-0,01189	-2,05147	C	1,683	4,6647	-3,53925
H	-4,82597	-1,33008	-1,53102	C	1,15056	3,47503	-2,7775
H	4,75645	-1,85661	-0,78074	C	-0,23552	3,19923	-2,72456
H	-0,63962	4,31117	-0,80191	C	4,21869	-0,38902	-2,60758
H	3,04342	-2,00933	-0,25361	C	1,84306	-1,23725	-2,6897
H	-2,44467	-1,84606	-0,71543	C	-3,22577	-1,42819	-2,28587
H	-4,86362	0,09921	-0,46193	C	2,00414	2,60763	-2,06919
H	4,79666	0,54002	-0,16391	C	-2,05763	-0,68494	-2,08678

H	-5,2278	5,33726	0,35714
H	4,54884	3,16736	-0,11699
H	-5,81467	3,89325	1,24539
H	-4,77388	-1,55243	0,23956
H	2,08531	3,99732	0,09726
H	5,30368	-1,18079	1,6418
H	-4,40282	1,89412	1,45024
H	5,25342	2,18809	1,21426
H	-4,78017	5,09545	2,06757
H	1,0174	3,32082	1,36673
H	4,72333	3,8654	1,51766
H	3,5774	-1,14633	2,13626
H	2,31378	4,46212	1,81543
H	-3,28488	-2,71024	1,45064
H	4,60279	0,30645	2,34947
H	-4,18469	-0,4178	2,05042
H	3,02655	2,16242	2,40056
H	-1,86886	-2,43294	2,51149
H	-2,7485	1,13958	3,49043
H	-3,51131	-2,58176	3,22182
H	-1,66029	-0,23367	3,83651
H	-3,36111	-0,2843	4,39664
Cl	0,48638	-1,35322	-0,88955
Cl	0,88626	-1,76855	2,35954
N	-0,17308	1,65101	-0,30531
N	0,18552	1,16605	2,46989
P	2,50558	0,96411	0,39312
P	-2,13145	-0,05348	0,83572
Re	0,30313	0,12029	1,0358
S	0,15378	2,06958	3,74312
H	-2,7121	5,53006	-0,18172

cis-[(^{Ph}PNP)Re(NO)Cl$_2$]

C	1,58945	4,72611	-3,48782
C	1,07558	3,51693	-2,74523
C	-0,30668	3,22209	-2,69897
C	4,12968	-0,33103	-2,68803
C	1,77738	-1,25	-2,6899
C	-3,14772	-1,52717	-2,34796
C	1,9473	2,65103	-2,0534
C	-2,00428	-0,75072	-2,1308
C	-0,80826	2,12107	-1,99648
C	-5,06362	-2,99975	-1,54826
C	2,98741	-0,87573	-1,81903
C	-3,84646	-2,14656	-1,28659
C	1,46649	1,54412	-1,33884
C	0,0674	1,25392	-1,29855
C	-1,5065	-0,5551	-0,82051
C	-3,34603	-1,95629	0,01778
C	4,03846	1,12077	0,11603
C	-2,19941	-1,18584	0,2572
C	4,93435	0,04019	0,7446
C	3,74166	2,25207	1,1067
C	-2,50283	1,7404	1,43444
C	-1,33298	-3,56571	2,60137
C	-2,46444	0,63574	2,50184
C	-1,89415	-2,21326	3,05328
C	-0,75519	2,11579	-2,00826
C	-5,16736	-2,85773	-1,46299
C	3,03489	-0,90438	-1,77745
C	-3,91564	-2,04967	-1,21957
C	1,50208	1,51936	-1,33802
C	0,10159	1,2376	-1,29687
C	-1,51281	-0,52118	-0,78875
C	-3,3706	-1,89977	0,06995
C	4,04573	1,119	0,15439
C	-2,19461	-1,16533	0,28828
C	4,92948	0,05823	0,83056
C	3,72497	2,27957	1,10273
C	-2,50907	1,68679	1,52141
C	-1,33201	-3,63022	2,51508
C	-2,39552	0,58684	2,58915
C	-1,82199	-2,27743	3,04208
C	-3,78561	0,20683	3,11664
C	-1,22725	-1,95025	4,42193
H	1,32159	4,67334	-4,58902
H	2,79061	4,66826	-3,564
H	4,45089	-1,11872	-3,41036
H	1,35717	5,62298	-3,07998
H	-0,93521	3,86965	-3,25006
H	-3,60826	-1,54712	-3,31286
H	3,96763	0,5714	-3,10362
H	2,13104	-2,05044	-3,3861
H	1,55314	-0,3537	-3,29171
H	-1,53678	-0,24533	-2,94861
H	-5,95987	-2,24882	-1,94782
H	5,14275	-0,24463	-2,01596
H	3,08953	2,79654	-2,08208
H	-4,97169	-3,7216	-2,13366
H	-1,84155	1,95535	-1,97197
H	0,96631	-1,57837	-2,1114
H	3,31728	-1,82063	-1,21706
H	-5,58273	-3,25736	-0,5169
H	4,56753	1,51833	-0,74194
H	5,19208	-0,77592	0,1513
H	3,01422	3,00108	0,65776
H	-3,87242	-2,38512	0,92208
H	-3,16926	1,35792	0,69532
H	5,87501	0,51673	1,18449
H	4,65685	2,82298	1,35984
H	-1,53496	1,96188	1,08248
H	-1,70725	-3,83996	1,49624
H	4,41392	-0,37812	1,70902
H	3,28171	1,90755	2,04582
H	-2,94809	2,59863	1,97324
H	-4,39641	-0,26332	2,31845
H	-0,2282	-3,66332	2,4655
H	-1,68061	-4,43551	3,19418
H	-2,93049	-2,30474	3,12109
H	-4,32293	1,1198	3,44609
H	-1,76633	0,96322	3,42381
H	-3,74988	-0,48435	3,98031
H	-0,12271	-1,88403	4,36554

C	-3,88524	0,26818	2,95033
C	-1,38097	-1,82542	4,45014
H	1,20491	4,75988	-4,52853
H	2,69607	4,73512	-3,53427
H	4,35788	-1,05781	-3,49494
H	1,26863	5,6699	-2,99628
H	-1,01498	3,8896	-3,21599
H	-3,50096	-1,67498	-3,38136
H	3,83883	0,6206	-3,17991
H	2,07968	-2,02789	-3,42027
H	1,41367	-0,37131	-3,25905
H	-1,46605	-0,31282	-2,98288
H	-5,82894	-2,45045	-2,13587
H	5,06709	-0,15956	-2,12497
H	3,02958	2,85614	-2,07113
H	-4,80311	-3,90914	-2,13129
H	-1,89138	1,93975	-1,95728
H	0,94704	-1,65578	-2,08493
H	3,3167	-1,78143	-1,26699
H	-5,5368	-3,33366	-0,60409
H	4,53439	1,54305	-0,78503
H	5,20139	-0,76257	0,02983
H	3,02072	2,98896	0,70448
H	-3,86253	-2,43704	0,86362
H	-3,09521	1,41507	0,55635
H	5,87797	0,4949	1,10914
H	4,6813	2,7871	1,35343
H	-1,49875	2,02879	1,07861
H	-1,64893	-3,83072	1,57483
H	4,4226	-0,43174	1,60845
H	3,32856	1,84803	2,05056
H	-2,9856	2,64545	1,855
H	-4,45846	-0,18932	2,11745
H	-0,22694	-3,55779	2,61351
H	-1,68758	-4,35633	3,29483
H	-3,00517	-2,26755	3,06695
H	-4,42956	1,18425	3,25984
H	-1,87883	1,00322	3,37172
H	-3,90169	-0,43062	3,80848
H	-0,27861	-1,70307	4,43469
H	-1,82511	-0,88271	4,8262
H	-1,62766	-2,62567	5,17721
Cl	0,87393	-2,58	0,30707
Cl	2,05964	-1,1448	3,01648
N	-0,35326	0,17105	-0,52608
N	0,76234	1,31602	1,85328
O	0,73541	2,39421	2,356
P	2,48427	0,31248	-0,47051
P	-1,48695	-0,83533	1,88866
Re	0,78686	-0,32112	1,17038

[(^{iPr}P^{H}NP)OsCl$_2$(N$_2$)]

Os	7,14053	5,30543	10,87974
Cl	8,02415	6,64825	9,04187
Cl	5,87923	4,20555	12,64911
P	6,15231	3,86419	9,30144
P	7,65129	7,06863	12,35482
H	-1,60237	-0,99342	4,83533
H	-1,48112	-2,75166	5,14483
Cl	0,87287	-2,60581	0,23229
N	1,85359	-1,06985	2,57152
N	-0,3361	0,17029	-0,5163
N	0,72922	1,33986	1,84361
P	2,50934	0,30287	-0,45871
P	-1,4498	-0,87233	1,90508
Re	0,84147	-0,36006	1,20952
O	2,49726	-1,63352	3,40253
O	0,64845	2,44087	2,30185

[(^{1mine}PNP)OsCl$_2$(N$_2$)]

Os	1,63043	10,14383	15,10917
Cl	3,64888	9,12875	14,19554
Cl	-0,33077	11,07022	16,24082
P	2,88276	11,34613	16,70128
P	0,23899	8,56856	14,05927
N	1,73605	8,70495	16,58495
N	1,57083	11,43262	13,69658
N	1,55328	12,1726	12,84385
C	2,09685	8,9657	17,7995
H	2,15976	8,14291	18,53596
C	2,40134	10,36654	18,21379
H	3,12605	10,40051	19,04994
H	1,45519	10,82428	18,56991
C	2,57307	13,14377	17,10984
H	3,57728	13,55181	17,35531
C	1,65453	13,3724	18,31704
H	0,65643	12,92329	18,14243
H	1,51274	14,46202	18,47355
H	2,07491	12,9571	19,25442
C	2,04556	13,85975	15,85721
H	2,70864	13,71563	14,98356
H	1,96359	14,94962	16,04807
H	1,0435	13,47334	15,58852
C	4,72869	11,21272	16,61174
H	4,88613	10,14085	16,36335
C	5,46527	11,56657	17,90737
H	6,55969	11,4438	17,76897
H	5,16874	10,92077	18,75748
H	5,29274	12,62134	18,20764
C	5,21723	12,04039	15,41287
H	4,67888	11,75507	14,48854
H	6,29827	11,863	15,24146
H	5,0827	13,12825	15,58429
C	1,44712	7,31705	16,18775
H	1,40014	6,66326	17,08382
H	2,29787	6,99276	15,55378
C	0,14468	7,2772	15,38772
H	-0,70383	7,55727	16,04398
H	-0,04395	6,26219	14,98996
C	-1,54177	9,03435	13,82653
H	-1,78369	9,46921	14,82046
C	-2,46569	7,84281	13,54939
H	-3,52308	8,17967	13,52611
H	-2,38901	7,05353	14,32325

N	5,37191	6,49353	10,49898
N	8,69926	4,2752	11,17576
N	9,62266	3,64542	11,36186
C	4,21359	5,68019	10,04339
H	3,36211	6,34664	9,78275
H	3,91269	5,04449	10,89845
C	4,63294	4,82908	8,84702
H	4,90148	5,48409	7,99278
H	3,80006	4,17769	8,51976
C	5,49424	2,24589	9,92397
H	4,79939	2,59731	10,71903
C	4,71396	1,40508	8,9068
H	3,96274	1,99284	8,34189
H	4,17117	0,589	9,42785
H	5,39169	0,92761	8,17182
C	6,59189	1,43395	10,62833
H	7,34905	1,05629	9,91442
H	6,14187	0,55676	11,1367
H	7,10495	2,04082	11,39646
C	7,04011	3,65769	7,68818
H	7,38297	4,70557	7,5329
C	6,19803	3,2367	6,47646
H	6,78889	3,37841	5,54721
H	5,27272	3,8362	6,36774
H	5,90653	2,17001	6,51956
C	8,29513	2,79075	7,85862
H	8,94558	2,8843	6,96504
H	8,03894	1,71812	7,97136
H	8,89031	3,09735	8,73997
C	5,03627	7,41478	11,61676
H	4,71677	6,78445	12,46916
H	4,18483	8,06853	11,32562
C	6,27065	8,2438	11,96718
H	6,05428	8,9472	12,79349
H	6,57661	8,84136	11,0868
C	7,46089	6,7219	14,16809
H	6,48451	6,19429	14,21447
C	7,42014	7,96338	15,06519
H	8,37328	8,53159	15,03486
H	7,25536	7,66299	16,12092
H	6,60414	8,66232	14,79371
H	5,71136	7,06022	9,70198
C	8,53905	5,71929	14,60473
H	8,53932	4,82465	13,95331
H	8,34896	5,38097	15,64352
H	9,55203	6,17069	14,58321
C	9,2496	8,02759	12,23857
H	9,46518	8,35603	13,27815
C	9,16045	9,27304	11,34643
H	8,86335	8,99747	10,31498
H	10,15446	9,76386	11,29199
H	8,4433	10,02248	11,73588
C	10,37369	7,08562	11,77866
H	10,19217	6,74791	10,74028
H	10,4534	6,1841	12,41431
H	11,34881	7,61398	11,81203
H	-2,25296	7,37405	12,56615
C	-1,70047	10,15096	12,78728
H	-1,49837	9,78937	11,75874
H	-1,02435	11,00101	12,99765
H	-2,74015	10,53728	12,80265
C	0,72736	7,70978	12,48035
H	-0,21958	7,30621	12,05922
C	1,70108	6,54334	12,70136
H	1,95635	6,08062	11,72545
H	1,27266	5,74508	13,33922
H	2,64172	6,90466	13,16145
C	1,31296	8,74448	11,50447
H	1,5039	8,27176	10,51899
H	2,27101	9,13701	11,8968
H	0,63662	9,60404	11,34183

5.4.2 Calculation of Spin Densities and Mulliken Population Analysis

Spin densities were derived using the PBE0 functional, using the unrestricted Kohn-Sham orbital formalism. For Rhenium the zeroth order all-electron scalar relativistic basis set reported by *Neese* and coworkers (SARC-Zora-TZVP) and the SARC/J auxiliary basis set were used.[517] For all other atoms the def2-TZVP basis set was employed. The resulting Mulliken population analysis was examined and the spin density plotted using the *ChemCraft* software.

Table 5.8: XYZ coordinates and Mulliken population analysis of open-shell species (PBE0/SARC-Zora-TZVP(Re);def2-TZVP). Excess alpha spin density is represented in red isosurfaces and excess beta spin is represented in blue isosurfaces.

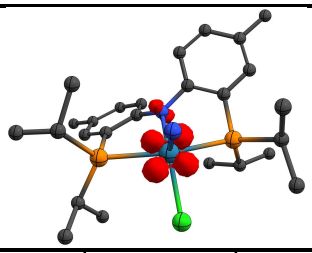

[(^{Ph}PNP)Re(N)Cl]$^+$
$\langle S^2 \rangle$ = 0.76

	x	y	z	atomic charge	spin population
C	-0,92537	-1,69305	-5,5213	-0,41896	-0,00373
C	-0,65911	-1,33749	-4,09378	0,12863	0,04747
C	0,64426	-1,23986	-3,60534	-0,10395	-0,02517
C	-1,69368	-1,09533	-3,19944	-0,26346	-0,01739
C	-4,27103	1,27983	-2,14762	-0,42572	-4,93E-4
C	0,91379	-0,89152	-2,29652	-0,35515	0,04184
C	-1,44575	-0,74345	-1,87856	-0,21008	0,03343
C	-0,12944	-0,6123	-1,41067	0,28964	-0,01313
C	-4,0487	-1,71424	-0,96391	-0,13072	0,01315
C	-3,5144	-3,13945	-0,96746	-0,40348	0,00162
C	-3,42774	1,19289	-0,88336	-0,06074	0,00171
C	-2,3194	2,23703	-0,88635	-0,41256	-0,00108
C	2,00117	1,23229	-0,44205	-0,3621	0,03643
C	-5,19127	-1,51985	0,02505	-0,39155	1,44E-4
C	3,20393	1,74113	0,00565	-0,09796	-0,0217
C	1,3114	0,2917	0,32198	0,27333	-0,01314
C	1,18213	-3,33167	0,83528	-0,39386	-1,88E-4
C	3,7701	1,343	1,21893	0,17522	0,05249
C	5,07907	1,90306	1,67463	-0,4168	-0,00381
C	1,85161	-0,09455	1,55712	-0,10765	0,04949
C	3,06609	0,42454	1,98715	-0,30481	-0,02808
C	1,35125	-2,91921	2,29188	-0,04696	0,0021
C	2,77447	-3,13707	2,78308	-0,41537	-2,97E-4
C	0,97774	-0,74799	4,28923	-0,11498	0,00513
C	0,61506	0,70724	4,5428	-0,39322	-8,8E-5
C	0,16252	-1,69766	5,15843	-0,39459	3,48E-4
H	-0,68904	-0,85422	-6,18206	0,15554	0,00305
H	-0,31099	-2,53742	-5,84014	0,15075	0,00209
H	-1,97187	-1,95493	-5,67907	0,14082	1,33E-4
H	1,47461	-1,45696	-4,26881	0,14436	0,00118
H	-2,71736	-1,19862	-3,543	0,16146	0,00129

H	-3,67223	1,07215	-3,03767	0,14715	9,5E-5
H	-4,65877	2,29593	-2,24741	0,15778	-2,3E-5
H	-5,12615	0,60351	-2,13484	0,1533	8E-6
H	-4,40472	-1,47272	-1,9718	0,13111	0,00104
H	1,93951	-0,84809	-1,95465	0,16551	-0,00185
H	-2,70081	-3,27025	-1,6823	0,15446	-1,82E-4
H	-4,31995	-3,82166	-1,2475	0,15282	3,77E-4
H	-1,64545	2,08574	-1,7328	0,13791	2,76E-4
H	1,58079	1,5756	-1,37895	0,16029	-0,00181
H	-2,76439	3,22874	-0,98803	0,15281	-2,01E-4
H	-5,98962	-2,22958	-0,20098	0,15276	6,1E-4
H	3,71677	2,4825	-0,5977	0,14682	0,00106
H	-4,06125	1,34859	-0,00345	0,13895	2,08E-4
H	-5,61806	-0,51658	-0,02451	0,14537	4E-6
H	-3,16171	-3,4319	0,02175	0,1576	2,9E-4
H	-1,73575	2,22427	0,03362	0,17604	5,46E-4
H	1,78638	-2,71007	0,17103	0,136	1,28E-4
H	1,50683	-4,36651	0,70989	0,15876	-1,36E-4
H	-4,86054	-1,70391	1,04862	0,15986	0,00121
H	0,1407	-3,27598	0,50864	0,14952	2,6E-4
H	5,88239	1,63034	0,9855	0,15345	0,0027
H	5,04594	2,99444	1,71425	0,15452	0,00294
H	3,48396	-2,5306	2,2153	0,14836	1,3E-5
H	3,05055	-4,18464	2,64419	0,15736	-5,6E-5
H	5,34722	1,53663	2,66551	0,14095	1,1E-5
H	3,47229	0,12028	2,9458	0,15084	0,00185
H	0,6533	-3,50264	2,90232	0,14097	6,56E-4
H	2,89176	-2,90629	3,84297	0,14992	-1,1E-5
H	1,17229	1,39245	3,90278	0,15337	-1,68E-4
H	-0,44927	0,88068	4,37965	0,16587	2,56E-4
H	2,04411	-0,89129	4,50124	0,12526	-2,65E-4
H	0,47875	-2,73694	5,05875	0,14401	-5E-5
H	-0,90027	-1,63823	4,9157	0,16073	4,64E-4
H	0,84196	0,95366	5,58206	0,15313	-8,2E-5
H	0,28333	-1,41548	6,2061	0,15445	5,12E-4
Cl	-2,42293	-2,36923	2,37969	0,09817	0,098166
N	0,07853	-0,25791	-0,07089	-0,0508	0,09624
N	-1,60466	0,7571	2,13445	-0,48763	-0,09225
P	-2,72273	-0,49276	-0,63842	0,17863	-0,02695
P	0,79406	-1,18724	2,52233	0,17063	-0,04114
Re	-1,28537	-0,64823	1,35926	0,79048	0,790483

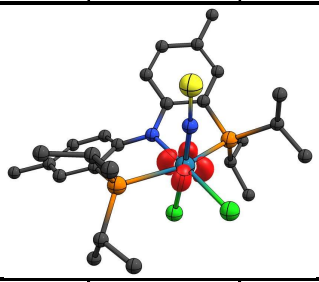

***cis*-[(^{Ph}PNP)Re(NS)Cl$_2$]**
$\langle S^2 \rangle = 0.81$

	x	y	z	atomic charge	spin population
C	-0,43285	-1,24169	-4,3083	-0,42371	3,7E-5
C	-1,91388	0,74198	-4,61506	-0,38833	-6,5E-4
C	-0,53706	0,26922	-4,16302	-0,08545	0,01286
C	4,8173	-0,7269	-3,67989	-0,42955	-0,0042

C	1,10012	3,15544	-3,29043	-0,41719	-2,63E-4
C	-1,31724	3,36909	-2,60606	-0,39963	3,49E-4
C	2,4992	-0,01	-3,00736	-0,32432	-0,02793
C	-0,00277	2,6274	-2,38642	-0,06829	-4,96E-4
C	3,73972	-0,52266	-2,66098	0,18605	0,04805
C	1,49576	0,18009	-2,06455	-0,05374	0,04439
C	3,94067	-0,85662	-1,32068	-0,14294	-0,02592
C	1,71229	-0,14138	-0,71337	0,22672	-0,01884
C	2,96077	-0,67596	-0,36786	-0,3333	0,04206
C	-2,56788	-3,47736	1,58231	-0,42087	0,00117
C	0,92304	0,25431	1,52972	0,22948	-0,01994
C	-4,2499	-0,48994	2,05857	-0,38871	-3,59E-4
C	-1,3361	-2,73064	2,07657	-0,04811	1,58E-4
C	2,06266	0,92969	1,98682	-0,35144	0,04047
C	-0,00435	-0,17881	2,4925	-0,00361	0,04017
C	-2,9616	-0,39906	2,86945	-0,09801	0,01435
C	2,29486	1,09703	3,33493	-0,13583	-0,02455
C	-0,95043	-3,14757	3,4861	-0,42647	-3,1E-5
C	-2,85924	0,97711	3,51275	-0,39081	-8,2E-5
C	0,26263	-0,01689	3,84818	-0,37181	-0,02465
C	1,41365	0,60829	4,30068	0,1852	0,0446
C	1,69469	0,7735	5,76186	-0,43034	-0,00399
H	-0,52573	-1,50666	-5,36478	0,12745	2,18E-4
H	-2,12471	0,32327	-5,60251	0,12353	6E-4
H	0,22972	0,74866	-4,78387	0,10181	0,0018
H	4,46796	-0,46956	-4,68084	0,13131	6,5E-5
H	0,8588	3,00654	-4,34644	0,11995	-2,8E-5
H	0,50963	-1,64166	-3,93557	0,15487	-7,85E-4
H	-1,98608	1,82461	-4,69028	0,1188	-1,9E-5
H	-1,5188	3,50713	-3,6694	0,1082	1E-5
H	2,30925	0,23989	-4,04617	0,14108	0,0016
H	1,21111	4,23187	-3,134	0,137	-2,52E-4
H	-1,24316	-1,7332	-3,76879	0,16454	4,55E-4
H	5,69326	-0,10904	-3,46287	0,1368	0,00227
H	5,15334	-1,76714	-3,69974	0,13844	0,0024
H	-2,68793	0,39306	-3,92854	0,16678	0,00272
H	2,06303	2,68577	-3,0861	0,15673	-4,6E-5
H	-1,24548	4,3618	-2,15583	0,129	1,38E-4
H	-2,16395	2,86168	-2,14507	0,1829	4,07E-4
H	0,28882	2,77	-1,33994	0,13975	1,8E-5
H	4,88825	-1,29287	-1,02011	0,12011	0,00124
H	3,14403	-0,97956	0,65457	0,15141	-0,00199
H	-2,88427	-3,14095	0,59349	0,18147	-1,09E-4
H	-2,34275	-4,54431	1,51392	0,13291	-1,53E-4
H	-4,26927	0,28896	1,29604	0,1679	0,00205
H	2,76096	1,33635	1,26665	0,14802	-0,00184
H	-0,50417	-2,97076	1,40386	0,12141	-8,16E-4
H	-4,37562	-1,44576	1,55211	0,12127	2,1E-5
H	-3,40553	-3,36	2,27386	0,11787	-1,5E-5
H	-5,10271	-0,34261	2,72665	0,12323	7,24E-4
H	-2,85575	1,75523	2,75135	0,16048	3,06E-4
H	-0,81926	-4,23263	3,51887	0,13613	-2,8E-5
H	-2,98528	-1,15806	3,66148	0,09824	0,00201
H	3,18377	1,63409	3,65121	0,11884	0,00116
H	-0,01596	-2,68724	3,80711	0,15757	-4,3E-5
H	-3,73421	1,12292	4,1527	0,11963	5,5E-4

H	-1,72719	-2,89578	4,21355	0,12293	-3,2E-5
H	-1,96781	1,10329	4,12355	0,15112	-4E-6
H	-0,45091	-0,38404	4,57785	0,15374	0,00149
H	2,58684	0,2162	6,06195	0,13606	0,00222
H	1,86853	1,82213	6,01758	0,13819	0,00215
H	0,86048	0,4158	6,36722	0,13136	7,4E-5
N	-0,89618	-1,87882	-1,06727	-0,3847	-0,13698
Cl	-1,71346	1,9406	0,40494	0,00952	0,009520
Cl	-3,45867	-0,2796	-1,33118	0,10516	0,105161
N	0,66703	0,02303	0,18811	-0,03182	0,06718
P	-0,16251	0,79249	-2,43872	0,19822	-0,02884
P	-1,51275	-0,91265	1,83194	0,20595	-0,03046
Re	-1,26072	-0,26152	-0,5166	1,01438	1,014383
S	-0,51727	-3,33296	-1,4456	-0,08344	-0,15727

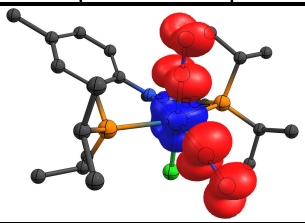

***cis*-[(^{Ph}PNP)Re(NO)$_2$Cl]**
$\langle S^2 \rangle = 0.84$

	x	y	z	atomic charge	spin population
C	-1,06823	3,30713	-5,03488	-0,425	2,3E-4
C	-0,98993	2,49105	-3,78165	0,12126	-0,00229
C	-1,96796	1,54506	-3,47211	-0,1017	0,00128
C	0,06268	2,6248	-2,88842	-0,24912	0,0012
C	3,42663	1,4849	-2,3826	-0,4032	-9,56E-4
C	-1,91221	0,77373	-2,32892	-0,43286	-7,57E-4
C	0,14293	1,85382	-1,73563	-0,1404	-0,003
C	-0,81613	-3,051	-1,44761	-0,40263	0,00111
C	3,00466	2,4752	-1,30948	-0,11407	-0,00203
C	-0,85515	0,91097	-1,41761	0,35737	0,00131
C	4,09228	2,63293	-0,25284	-0,39624	-4,4E-5
C	-0,05912	-3,57048	-0,23033	-0,06984	-0,00335
C	1,33657	4,77346	-0,03271	-0,41088	5,8E-5
C	-0,69673	-4,86435	0,25598	-0,42059	-1,59E-4
C	-3,06055	0,19042	0,41661	-0,44301	-0,00388
C	-1,7875	-0,3942	0,39362	0,36363	0,00496
C	0,94007	3,42941	0,56307	-0,07383	-8,99E-4
C	-0,56155	3,40483	0,82687	-0,39744	1,57E-4
C	-4,08987	-0,37594	1,14153	-0,09986	0,00263
C	-1,60934	-1,56173	1,16168	-0,12702	-0,00579
C	-3,92241	-1,54458	1,88427	0,11661	-0,00409
C	-2,66009	-2,1198	1,87731	-0,25895	0,00271
C	1,81406	-3,79073	2,49444	-0,40016	-1,8E-4
C	-5,04951	-2,12962	2,67803	-0,42529	3,83E-4
C	0,43191	-3,15963	2,62466	-0,11977	-9,79E-4
C	0,33184	-2,31159	3,88192	-0,38482	3,95E-4
H	-1,03757	2,67441	-5,92659	0,13521	-1,42E-4
H	-1,99683	3,88275	-5,07973	0,13335	-9E-5
H	-0,23692	4,01102	-5,09927	0,12615	-7E-6
H	-2,79393	1,39539	-4,16102	0,11356	-1,58E-4
H	0,8476	3,343	-3,10607	0,136	-6,8E-5
H	2,63502	1,29438	-3,10795	0,15174	-8E-5
H	4,29446	1,87874	-2,918	0,12957	-9E-5

H	-0,73188	-3,77675	-2,26	0,12859	3,5E-5
H	-2,67991	0,03331	-2,14444	0,15124	1,28E-4
H	3,71565	0,53109	-1,94042	0,15273	1,22E-4
H	2,8133	3,44638	-1,77812	0,11299	-4,05E-4
H	-0,44004	-2,09703	-1,81028	0,17859	-0,0024
H	-1,87488	-2,92748	-1,2105	0,13238	-2,07E-4
H	0,87111	4,92355	-1,01082	0,13654	-1E-5
H	5,01442	2,98597	-0,72112	0,13089	-5E-5
H	-0,77963	-5,56161	-0,58192	0,13534	-1,17E-4
H	0,98062	-3,76034	-0,5178	0,11977	-2,19E-4
H	2,41397	4,90063	-0,13975	0,13774	1E-6
H	-3,23024	1,1153	-0,11955	0,15271	1,11E-4
H	4,30543	1,67496	0,22548	0,15822	-6,66E-4
H	-1,11589	3,61829	-0,08974	0,12451	6E-6
H	3,82165	3,34214	0,53113	0,13648	3,2E-5
H	0,97468	5,57125	0,62124	0,13608	4,4E-5
H	-1,70855	-4,685	0,62947	0,14158	-1,8E-5
H	-0,12105	-5,35886	1,03868	0,14234	-4E-6
H	-5,05668	0,11846	1,146	0,11193	-3,1E-5
H	1,46038	3,26415	1,51171	0,13056	1,37E-4
H	-0,88989	2,44787	1,22713	0,18392	-1,51E-4
H	-0,80489	4,17877	1,55928	0,12362	-3E-6
H	1,90409	-4,43925	1,62081	0,13287	-4E-6
H	-5,92542	-2,31722	2,05117	0,13157	-1,72E-4
H	-2,48972	-3,01851	2,46229	0,14163	-1,01E-4
H	2,58444	-3,02048	2,42472	0,16025	-6,85E-4
H	-0,31815	-3,95608	2,68076	0,11134	-1,18E-4
H	-4,75854	-3,07613	3,13658	0,12558	-1,1E-5
H	2,02598	-4,39404	3,38055	0,1322	-2,3E-5
H	-5,36488	-1,45605	3,48025	0,13633	-2,01E-4
H	1,10355	-1,54343	3,90079	0,1616	-6,37E-4
H	-0,63015	-1,80569	3,9627	0,14922	1E-6
H	0,46152	-2,95861	4,7542	0,11896	-7,5E-5
Cl	0,5239	0,70249	2,50388	0,00712	0,007122
N	1,72633	-0,98791	-1,17621	-0,05805	0,38813
N	-0,70309	0,13815	-0,27976	-0,04713	0,00127
N	2,88122	-0,49304	1,2378	-0,02608	0,45088
O	2,00358	-1,48398	-2,20406	-0,3387	0,27857
O	3,84139	-0,5785	1,90422	-0,30983	0,32309
P	1,4357	1,98984	-0,49167	0,19783	0,00936
P	0,04502	-2,25459	1,07515	0,19853	0,00246
Re	1,27647	-0,2679	0,40196	-0,44256	-0,442558

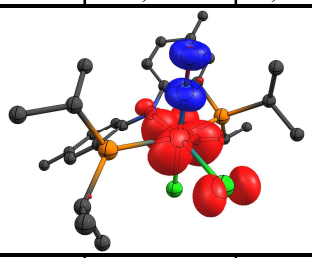

***cis*-[(^{Ph}PNP)Re(NO)Cl$_2$]**
$\langle S^2 \rangle = 0.77$

	x	y	z	atomic charge	spin population
C	1,56031	4,64428	-3,52677	-0,42452	-0,0027
C	1,05429	3,45749	-2,76697	0,12845	0,03081
C	-0,30926	3,16807	-2,70573	-0,10324	-0,01572
C	4,16748	-0,34816	-2,62569	-0,41169	-2,28E-4

C	1,84513	-1,25168	-2,69307	-0,39996	-2,9E-4
C	-3,14992	-1,46937	-2,32101	-0,09415	-0,01392
C	1,91543	2,61246	-2,08016	-0,25213	-0,01888
C	-2,01112	-0,71832	-2,10512	-0,42039	0,02428
C	-0,8008	2,0911	-1,99522	-0,40619	0,02707
C	-5,06402	-2,90922	-1,53943	-0,4251	-0,00229
C	3,00991	-0,87189	-1,78616	-0,07464	1E-4
C	-3,84527	-2,07965	-1,27764	0,12676	0,02519
C	1,44375	1,52537	-1,35748	-0,13487	0,02817
C	0,06548	1,23778	-1,30097	0,31961	-0,01037
C	-1,51023	-0,53712	-0,81185	0,32988	-0,00588
C	-3,34608	-1,90593	0,00632	-0,2603	-0,01379
C	3,9958	1,15473	0,10689	-0,10927	0,01172
C	-2,20305	-1,15729	0,24487	-0,13714	0,0199
C	4,89917	0,11788	0,76665	-0,39717	-2,9E-5
C	3,69431	2,29795	1,0624	-0,41325	7,3E-5
C	-2,50382	1,72988	1,50099	-0,4025	-8,67E-4
C	-1,32029	-3,56404	2,552	-0,39145	-2,63E-4
C	-2,44183	0,60568	2,52775	-0,06944	9E-6
C	-1,88449	-2,22738	3,00484	-0,12394	0,01674
C	-3,84863	0,24042	2,98065	-0,41961	-3,74E-4
C	-1,39513	-1,8733	4,40527	-0,39926	-3,29E-4
H	1,20745	4,63592	-4,56128	0,13463	0,0011
H	2,65095	4,66536	-3,54498	0,12869	7,9E-5
H	4,40864	-1,08471	-3,39666	0,13541	-3,1E-5
H	1,21766	5,5804	-3,07628	0,13788	0,00187
H	-1,01077	3,81974	-3,21751	0,11646	7,7E-4
H	-3,50122	-1,60357	-3,33949	0,11459	6,3E-4
H	3,89228	0,57735	-3,13919	0,13578	-1,1E-5
H	2,17006	-2,0436	-3,37273	0,12491	-1,03E-4
H	1,53363	-0,39661	-3,29753	0,12217	2,89E-4
H	-1,48293	-0,28757	-2,94628	0,14757	-0,00101
H	-5,81986	-2,34565	-2,09278	0,13291	9,85E-4
H	5,07463	-0,16719	-2,04916	0,14	9E-6
H	2,98178	2,81489	-2,10538	0,13996	0,00105
H	-4,82162	-3,79475	-2,13396	0,13842	0,00148
H	-1,86835	1,91665	-1,9514	0,14666	-0,00131
H	0,99165	-1,62113	-2,12862	0,18201	3,7E-4
H	3,31657	-1,76012	-1,22456	0,13204	5,16E-4
H	-5,51667	-3,25017	-0,6071	0,12788	6,1E-5
H	4,48981	1,555	-0,78525	0,11017	0,00281
H	5,16974	-0,69654	0,09272	0,13019	1E-6
H	2,97213	3,00616	0,65409	0,1462	-2,6E-4
H	-3,85673	-2,3814	0,83795	0,14247	8,35E-4
H	-3,11121	1,43089	0,64386	0,12907	3,42E-4
H	5,82276	0,59703	1,10102	0,12612	2,11E-4
H	4,61856	2,84014	1,27831	0,12928	8E-5
H	-1,5241	2,02678	1,13373	0,17113	6,9E-4
H	-1,61168	-3,81397	1,53182	0,14629	7,9E-5
H	4,40588	-0,31769	1,6385	0,17065	0,00268
H	3,30479	1,91978	2,00782	0,16553	2,14E-4
H	-2,97171	2,60613	1,95614	0,13009	-1,33E-4
H	-4,42746	-0,17903	2,15334	0,14132	5E-5
H	-0,23148	-3,55928	2,58958	0,16971	8,25E-4
H	-1,68913	-4,34544	3,22248	0,11954	6,78E-4
H	-2,97891	-2,28821	3,00908	0,10847	0,00353

H	-4,36637	1,14301	3,31565	0,13456	-1,16E-4
H	-1,85583	0,9484	3,38764	0,12384	2,92E-4
H	-3,86023	-0,47091	3,80663	0,14341	1,8E-5
H	-0,30941	-1,75523	4,41064	0,16989	0,00244
H	-1,84106	-0,95501	4,79153	0,12839	1,2E-5
H	-1,65132	-2,68265	5,09331	0,12772	5,06E-4
Cl	0,87338	-2,56393	0,2739	-0,344310	0,011623
Cl	2,04032	-1,17578	2,96577	-0,345028	0,112507
N	-0,35348	0,16991	-0,52267	-0,03714	0,02233
N	0,76131	1,2687	1,8694	-0,05693	-0,09979
O	0,74079	2,31056	2,3987	-0,36166	-0,07849
P	2,46892	0,32595	-0,48286	0,21742	-0,013
P	-1,49044	-0,84127	1,86695	0,21892	-0,0125
Re	0,783141	-0,324721	1,158547	0,572254	0,936665

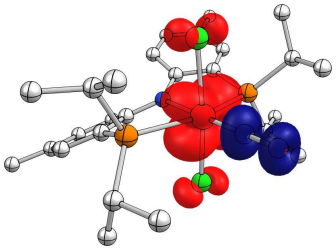

***trans*-**
[(^{Ph}PNP)Re(NO)Cl$_2$]
$\langle S^2 \rangle = 0.78$

	x	y	z	atomic charge	spin population
C	0,13141	-1,21784	-4,42687	-0,35598	3,12E-4
C	-2,09492	-0,12525	-4,16388	-0,39741	-3,27E-4
C	-0,58523	0,07997	-4,08103	-0,07696	0,00633
C	4,96864	-0,12341	-3,61619	-0,42337	-2,3E-4
C	0,88219	3,16127	-3,60959	-0,41551	-5E-4
C	-1,57062	3,11927	-3,03524	-0,40533	2,64E-4
C	2,58881	0,33967	-2,93629	-0,40005	-0,00193
C	-0,17872	2,63151	-2,65909	-0,05652	0,01045
C	3,85295	-0,12175	-2,61794	0,19005	0,00214
C	1,54726	0,35548	-2,00979	-0,02428	0,00551
C	4,03289	-0,61491	-1,32383	-0,14708	-9,17E-4
C	1,75839	-0,05625	-0,67875	0,26173	0,00155
C	3,02644	-0,58867	-0,38485	-0,36818	0,00114
C	-3,00184	-3,18032	1,5211	-0,40459	2,6E-4
C	1,00005	0,09372	1,59584	0,26131	0,0015
C	-4,16646	0,05165	2,07286	-0,39798	-3,56E-4
C	-1,67218	-2,65859	2,04708	-0,0584	0,01036
C	2,17693	0,66289	2,11404	-0,36895	0,00116
C	0,04591	-0,33652	2,53955	-0,02402	0,00553
C	-2,90938	-0,12751	2,91876	-0,0767	0,00631
C	2,42134	0,70642	3,46814	-0,1468	-9,36E-4
C	-1,37853	-3,16969	3,44793	-0,41484	-4,99E-4
C	-2,57034	1,17909	3,62266	-0,35505	2,77E-4
C	0,32673	-0,30316	3,90474	-0,39919	-0,00194
C	1,51741	0,1948	4,40157	0,19003	0,00216
C	1,8157	0,21426	5,8685	-0,42338	-2,29E-4
H	-0,21626	-1,55764	-5,4066	0,11927	0,0012
H	-2,37075	-0,37518	-5,19173	0,12838	1,2E-4
H	-0,29196	0,85031	-4,80411	0,08935	1,6E-5
H	4,61133	0,16116	-4,60732	0,12606	7E-6
H	0,74425	2,79019	-4,62911	0,11665	1,25E-4
H	1,21313	-1,10928	-4,46908	0,13112	-2,9E-5

H	-2,66718	0,75295	-3,86632	0,14419	-6,3E-5
H	-1,83265	2,83496	-4,05721	0,12618	2,2E-5
H	2,40103	0,68447	-3,94766	0,17051	1,18E-4
H	0,81265	4,25164	-3,65313	0,13458	8,74E-4
H	-0,09963	-1,99312	-3,69685	0,15125	0,00229
H	5,75834	0,57964	-3,33463	0,13414	9,8E-5
H	5,43062	-1,11095	-3,69743	0,13381	1,16E-4
H	-2,39583	-0,95538	-3,5232	0,15341	6,74E-4
H	1,8889	2,90344	-3,28141	0,16201	-2,5E-5
H	-1,59844	4,21044	-2,9823	0,13129	3,94E-4
H	-2,33183	2,73469	-2,35492	0,17109	9,05E-4
H	0,04296	2,98473	-1,64713	0,13049	0,00175
H	4,99075	-1,04679	-1,04956	0,11349	5,7E-5
H	3,20725	-1,00756	0,5958	0,15561	-4,4E-5
H	-3,21323	-2,80995	0,51695	0,171	9,01E-4
H	-2,96912	-4,27157	1,47286	0,13126	3,87E-4
H	-4,03363	0,88226	1,3782	0,15355	7,25E-4
H	2,8962	1,09686	1,43272	0,15547	-4,3E-5
H	-0,88169	-3	1,37134	0,13054	0,00177
H	-4,42558	-0,83342	1,49263	0,14452	-6,6E-5
H	-3,82891	-2,90711	2,18084	0,12635	2E-5
H	-5,01179	0,28762	2,72454	0,12833	1,15E-4
H	-2,32067	1,95465	2,89907	0,15151	0,0023
H	-1,43304	-4,26178	3,4503	0,1346	8,72E-4
H	-3,09693	-0,89948	3,67451	0,08951	5E-6
H	3,34061	1,16691	3,81761	0,11352	5,7E-5
H	-0,38244	-2,88421	3,78569	0,16194	-2,5E-5
H	-3,44741	1,50894	4,18667	0,11946	0,00117
H	-2,10872	-2,81052	4,1787	0,11649	1,24E-4
H	-1,73652	1,08597	4,31516	0,12996	-2,1E-5
H	-0,4182	-0,6638	4,6062	0,17064	1,19E-4
H	2,62356	-0,47903	6,12156	0,13429	1E-4
H	2,12896	1,20809	6,1991	0,13371	1,13E-4
H	0,93986	-0,07215	6,45318	0,12606	8E-6
Cl	-0,83416	-2,20996	-1,17422	-0,323687	0,090241
Cl	-1,43045	2,17539	0,42222	-0,323952	0,089815
N	-2,95787	-0,0439	-0,98607	-0,02261	-0,12638
N	0,72577	0,00936	0,24136	-0,03739	-0,01475
O	-4,06334	-0,06029	-1,35536	-0,35097	-0,10109
P	-0,1401	0,80124	-2,43259	0,15464	-0,05359
P	-1,54801	-0,82659	1,87277	0,15514	-0,05339
Re	-1,29022	-0,01968	-0,42932	0,540675	1,104513

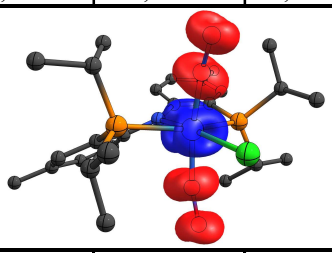

***trans*-[(^{Ph}PNP)Re(NO)$_2$Cl]**
$\langle S^2 \rangle$ = 1.13

	x	y	z	atomic charge	spin population
C	-1,03159	3,18863	-5,11615	-0,42423	7,67E-4
C	-0,97266	2,40733	-3,83997	0,13723	-0,00623
C	-1,95264	1,46481	-3,52365	-0,11234	0,00228
C	0,0648	2,56875	-2,93343	-0,2666	0,00366

C	3,48583	1,47218	-2,23149	-0,42446	1,92E-4
C	-1,91276	0,71945	-2,36261	-0,40704	-0,00392
C	0,12904	1,82252	-1,76374	-0,14989	-0,00543
C	-0,71366	-2,90688	-1,56108	-0,39455	0,0033
C	2,96345	2,50424	-1,24482	-0,09787	-0,01127
C	-0,86889	0,88378	-1,44085	0,29254	5,82E-4
C	3,98613	2,78369	-0,1494	-0,4063	-3,57E-4
C	-0,11361	-3,49	-0,28832	-0,06808	-0,00326
C	0,99129	4,71616	-0,10472	-0,42048	-3,77E-4
C	-0,89943	-4,71866	0,14866	-0,41983	-3,6E-4
C	-3,09418	0,23538	0,39672	-0,40744	-0,00399
C	-1,82632	-0,36334	0,38868	0,29155	6,09E-4
C	0,8419	3,36668	0,58402	-0,06731	-0,0033
C	-0,59342	3,17196	1,0549	-0,3951	0,00331
C	-4,12589	-0,30686	1,1365	-0,11205	0,00231
C	-1,65963	-1,52075	1,17256	-0,14951	-0,0055
C	-3,96731	-1,46105	1,90525	0,13741	-0,00625
C	-2,71344	-2,05474	1,90248	-0,26642	0,00373
C	1,71889	-3,86156	2,40401	-0,40766	-3,23E-4
C	-5,09643	-2,01185	2,72025	-0,42452	7,65E-4
C	0,39362	-3,12828	2,5768	-0,09823	-0,0114
C	0,43722	-2,19821	3,77879	-0,42419	2,61E-4
H	-0,95297	2,53444	-5,98931	0,13616	-3,64E-4
H	-1,97405	3,73538	-5,20673	0,13327	-3,22E-4
H	-0,21847	3,91406	-5,17186	0,12792	-1,8E-5
H	-2,76702	1,29681	-4,22202	0,11447	-7,8E-5
H	0,8514	3,28359	-3,15508	0,13786	-1,44E-4
H	2,72847	1,16782	-2,95602	0,14331	-2,21E-4
H	4,33253	1,89223	-2,78039	0,12878	-1,83E-4
H	-0,68187	-3,66032	-2,35179	0,13015	3,04E-4
H	-2,68132	-0,01873	-2,17215	0,14853	2,28E-4
H	3,83648	0,58431	-1,70537	0,17436	-6,91E-4
H	2,73539	3,43274	-1,7807	0,10823	-0,00345
H	-0,18145	-2,02469	-1,91179	0,1654	-0,00406
H	-1,75855	-2,63134	-1,40089	0,12579	-4,56E-4
H	0,39538	4,75499	-1,02055	0,142	-2,3E-5
H	4,93144	3,09031	-0,60401	0,1257	-1,29E-4
H	-0,95966	-5,42508	-0,68334	0,13493	-3,13E-4
H	0,92741	-3,76866	-0,4846	0,12581	-3,82E-4
H	2,02558	4,95389	-0,35505	0,14197	1,4E-5
H	-3,2577	1,1466	-0,16434	0,14865	2,33E-4
H	4,16833	1,88167	0,44037	0,18089	-8,4E-5
H	-1,28542	3,23073	0,21168	0,12581	-4,57E-4
H	3,66965	3,57906	0,52759	0,12608	4E-5
H	0,62305	5,50376	0,55778	0,13496	-3,18E-4
H	-1,9229	-4,44959	0,42303	0,14188	-2,4E-5
H	-0,44133	-5,23972	0,9898	0,14144	1,3E-5
H	-5,08891	0,19482	1,13167	0,11441	-8E-5
H	1,5074	3,3204	1,45289	0,1255	-3,94E-4
H	-0,74736	2,21635	1,55247	0,16577	-0,00413
H	-0,85234	3,96705	1,75828	0,13026	2,94E-4
H	1,68843	-4,6033	1,60405	0,12601	4,4E-5
H	-5,99851	-2,14176	2,11692	0,13302	-2,88E-4
H	-2,55188	-2,94754	2,49877	0,13681	-1,46E-4
H	2,52144	-3,15206	2,18652	0,1814	-6,7E-5
H	-0,415	-3,85578	2,71201	0,10824	-0,00344

H	-4,83729	-2,98171	3,1479	0,12808	-2,2E-5
H	1,96869	-4,38338	3,33119	0,12601	-1,32E-4
H	-5,3547	-1,3441	3,54762	0,13684	-3,93E-4
H	1,31342	-1,55168	3,72854	0,17468	-6,93E-4
H	-0,4523	-1,57023	3,85305	0,14294	-2,54E-4
H	0,51139	-2,79216	4,69332	0,12889	-1,8E-4
N	0,99612	0,52891	2,15993	-0,06806	0,52998
N	1,94167	-1,0738	-0,98455	-0,06865	0,52874
N	-0,72792	0,14304	-0,28174	-0,07228	0,01481
Cl	3,47151	-0,64661	1,38074	-0,393935	0,007213
O	2,59426	-1,67673	-1,74562	-0,28277	0,41513
P	1,38483	1,96128	-0,48898	0,19896	-0,00185
P	-0,00746	-2,20983	1,04239	0,20178	-0,00185
Re	1,22284	-0,22489	0,48909	0,749250	-0,847514
O	1,12171	0,98289	3,23074	-0,28212	0,4163

5.4.3 Calculation of EPR parameters

EPR parameters[518] of selected species were obtained with the ADF program,[519] using single-point calculations on preoptimized structures on the PBE0/def2-TZVP;SVP level of theory. For the ADF calculations, the implemented Zora formalism[520] was utilized together with the PBE0 hybrid functional and TZP Slater type orbital basis set.[521]

Table 5.9: Calculated EPR parameters for selected open-shell species and comparison with experimental data.

	cis-[(^{Ph}PNP)Re(NO)$_2$Cl]	*cis*-[(^{Ph}PNP)Re(NO)Cl$_2$]	*trans*-[(^{Ph}PNP)Re(NO)Cl$_2$]	[(^{Ph}PNP)Re(N)Cl]$^+$
$g_{iso,DFT}$	2.025	1.999	2.025	1.983
$g_{iso,exp.}$*	2.009	1.996	2.049	1.97
$A_{iso,DFT}$ ($^{185/187}$Re)	191.3 MHz	–626.1 MHz	–699.3 MHz	–637.5 MHz
$A_{iso,exp.}$* ($^{185/187}$Re)	140 MHz	782 MHz	967 MHz	780 MHz
A_{iso}($^{14}N_{NO}$)	24.6 / 27.8 MHz	–8.8 MHz	–8.8 MHz	-
A_{iso}(^{31}P)	18.8 / 19.0 MHz	–44.6 / –46.5 MHz	–68.2 / –68.8 MHz	–44.8 / –52.6 MHz
A_{iso}($^{14}N_{nitride}$)	-	-	-	5.8 MHz

* derived from simulation of the experimental X-band EPR spectra.

5.4.4 Calculation of the Nitride Transfer Reaction Mechanism

To obtain a reaction mechanism within reasonable computational cost the PBE functional was utilized. The valence triple-zeta polarization basis-set (def2-TZVP) was employed for Re,Cl,P,N,O atoms and split valence polarization (def2-SVP) for carbon and hydrogen atoms as a compromise to reduce computational cost significantly. To reduce the number of potential isomers only one pincer-backbone conformer was considered throughout the mechanism. Comparison of the energies of the conformers for some of the complexes showed differences

in energy smaller than 3 kcal·mol^{-1} and mostly below 1 kcal ·mol^{-1}. Thus, it was expected that reactivity is not significantly influenced by the different backbone conformations, however, *Ison* and coworkers proposed in their calculations regarding CO addition to methyl nitride [(^{Ph}PNP)Re(N)Me] a non-negligible energetic difference of 4.4 kcal·mol^{-1} of the two backbone conformations and an isomerization barrier of 15.6 kcal·mol^{-1} (M06/SDD+f(Re);6-31G(d,p)).[168]

For complexes with three different ligands in addition to the pincer ligand there are up to three coordination isomers possible and they were all evaluated. No reactivity of more than one equivalent of NO in one structure or of the $(NO)_2$ dimer was considered. Finally, transition-states were – if one could be found – located with relaxed surface scans and the local maximum verified with a frequency calculation and exactly one imaginary vibrational frequency. The first part of the calculated mechanism is displayed in Figure 5.15.

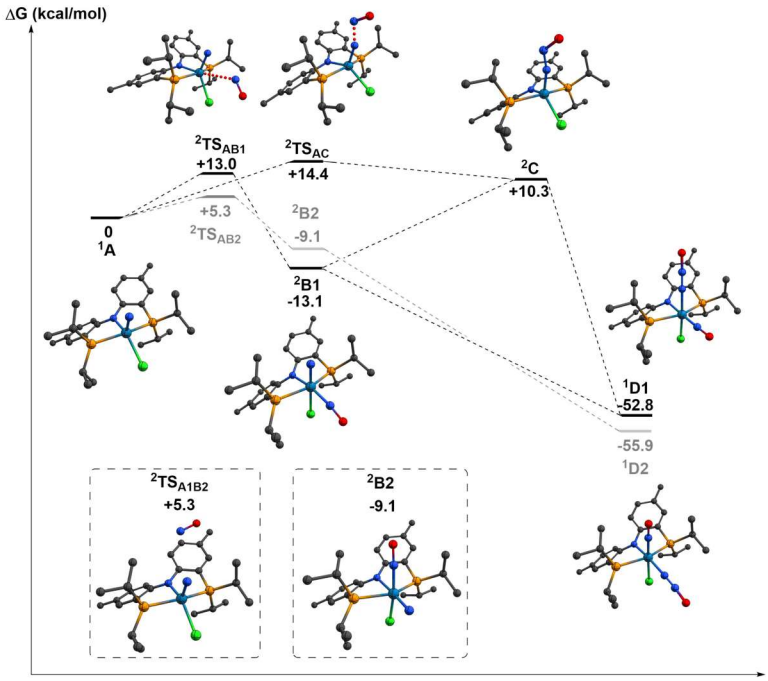

Figure 5.15: Part 1 of the DFT calculated (PBE/def2-TZVP(Re,Cl,P,N,O);def2-SVP) reaction mechanism of Re^V nitride [(^{Ph}PNP)Re(N)Cl] with nitric oxide.

The addition of nitric oxide to singlet ground state nitride **^{1}A** can result in four different complexes, three coordination isomers of [(^{Ph}PNP)Re(N)(NO)(Cl)] (**B1** – **B3**) and direct addition to the nitride to form nitrous oxide complex **C**. From the coordination isomers the one with the nitrosyl ligand in the virtual pincer plane **B1** was computed as lowest in energy (–13.1 kcal·mol^{-1}), followed by the isomer with the nitride ligand in the pincer plane **B2** (–9.1 kcal·mol^{-1}). Both isomers **B1** and **B2** were found to have doublet ground states with almost no spin

contamination. A transition state towards **B1** was located ($d_{Re\text{-}NO}$ = 2.98 Å), imposing a barrier of +13.0 kcal·mol^{-1} for binding of NO to five-coordinate nitride **A**. The barrier towards isomer **B2** is smaller (+5.3 kcal·mol^{-1}), but leads to the higher-energy product. The other conceivable product, complex **C** is computed to be endergonic (+10.3 kcal·mol^{-1}) and a transition state for the interaction of the nitride ligand with nitric oxide (+14.4 kcal·mol^{-1}, d($N_{nitride}$-N_{NO}) = 1.67 Å) could be located with the aid of a relaxed surface scan. The high energy for the five-coordinate product **C** is in good agreement with the observed tendency of (^{Ph}PNP)Re complexes to favor octahedral over five-fold coordination environments and is in its conclusion in agreement with the higher-level calculations. Interestingly, the N_2O ligand in **C** is strongly bent ($\sphericalangle_{N\text{-}N\text{-}O}$ = 122.7°), implying a small bond order between the two nitrogen atoms of N_2O (d_{NN} = 1.29 Å). Finally, **C** can be formed upon insertion of the nitride ligand of **B1** into the Re-N_{NO} bond, however, this process would be highly endergonic (+23.4 kcal·mol^{-1}) and no transition state could be located for this reaction.

Starting from the complexes **B1** and **C**, addition of another equivalent of nitric oxide would lead to the formation of the nitrosyl-nitrous oxide complex **D1**. From **B1** the nitric oxide would bind to the nitride nitrogen atom in a strongly exergonic process (–39.7 kcal·mol^{-1}), for which no transition state could be located. Singlet ground state **D1** can furthermore be formed upon binding of NO to the five-coordinate complex **C** in an even more exergonic (–63.1 kcal·mol^{-1}) reaction. The coordination isomer **D2** can be formed from **B2** in an exergonic (–43.7 kcal·mol^{-1}) reaction and is slightly lower in energy relative to **D1** (–3.1 kcal·mol^{-1}). This strongly exergonic and barrierless binding of a second NO equivalent could be an explanation, why no nitride-nitrosyl complexes (**B**) could be observed experimentally. Furthermore, the strong decrease in energy upon addition of the second NO for the complexes **B** could indicate that coordination of NO to a five-coordinate nitride might induce an ambiphilic character of the rhenium nitride moiety, resulting in facilitated reactivity towards NO.

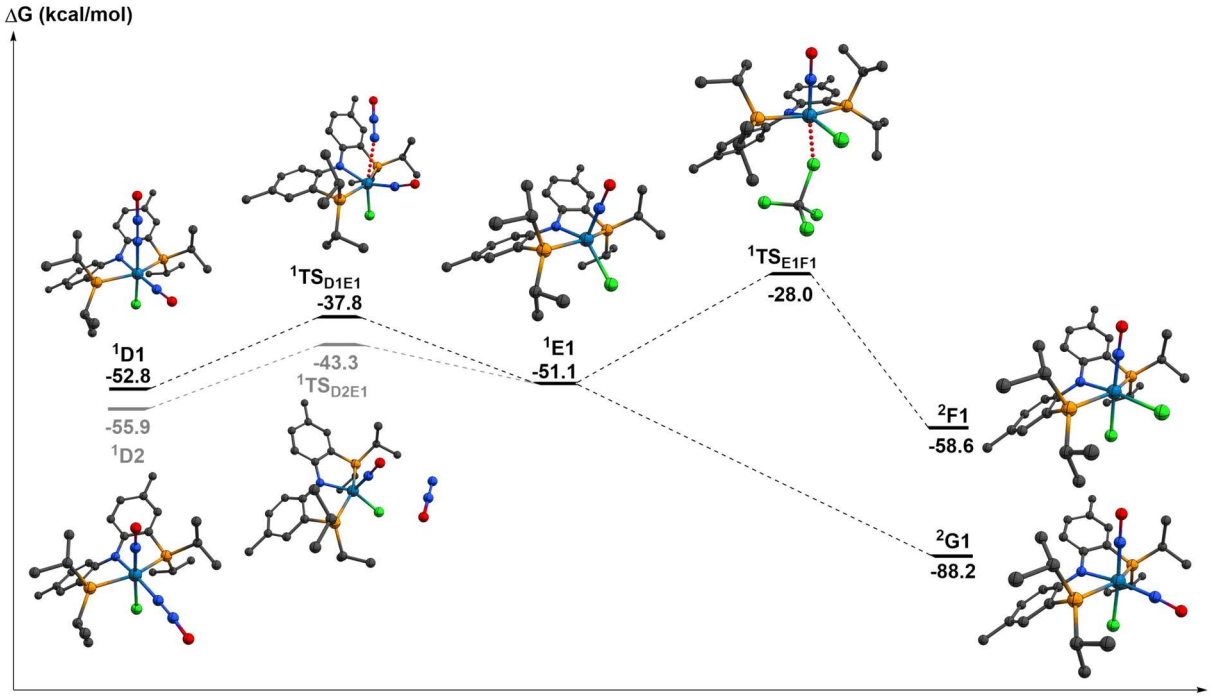

Figure 5.16: Part 2 of the DFT calculated (PBE/def2-TZVP(Re,Cl,P,N,O);def2-SVP) reaction mechanism of Re^{V} nitride [(^{Ph}PNP)Re(N)Cl] with nitric oxide.

From **D1** and **D2** nitrous oxide loss forms five-coordinate nitrosyl complex **E1**. This loss is for both species slightly endergonic (**D1**: +1.7 kcal·mol^{-1}, **D2**: +4.8 kcal·mol^{-1}) and for both reactions a similar transition state barrier could be found (**D1**: 15.0 kcal·mol^{-1}, **D2**: 12.6 kcal·mol^{-1}). Singlet ground state **E1** is assumed to be the central intermediate for the formation of both final reaction products **F1** and **G1**, which are formed upon chlorine atom and nitric oxide addition, respectively. For the exergonic chlorine atom addition to **E1** (–7.5 kcal·mol^{-1}) a high barrier upon chlorine atom abstraction from CCl_4 was found (+22.9 kcal·mol^{-1}), which is not in agreement with the experimental observation that the reaction is very fast at room temperature and still proceeds at –20 °C to the final product in presence of CCl_4. Therefore the barrier is likely overestimated, as it otherwise would allow for isolation of **E1** at low temperature or react with another NO to **G1**. The addition of NO to **E1** is energetically strongly downhill (–37.1 kcal·mol^{-1}), as well as barrierless and leads to dinitrosyl complex **G1**.

Overall, in comparison to the higher-level calculations for this reaction mechanism (see chapter 2.5.5) it can be derived, that barriers with the PBE/def2-TZVP;SVP level of theory are often substantially over- or underestimated or no transition-state could be found. This is especially critical for the decisive bond-formation step from **B** to **D**, for which on the PBE/def2-TZVP;SVP level of theory no TS could be located. Nevertheless, these calculations can give

an initial insight into possible reaction pathways and can identify potentially isolable intermediates.

Table 5.10: XYZ coordinates of calculated structures for the reaction mechanism (PBE/def2-TZVP;SVP).

	A				B1		
	x	**y**	**z**		**x**	**y**	**z**
C	1,86967	4,28512	-4,19271	C	1,60989	4,5025	-3,82393
C	1,27132	3,29185	-3,22935	C	1,08487	3,38255	-2,96234
C	-0,1272	3,17345	-3,07437	C	-0,30356	3,14772	-2,8334
C	4,0563	-0,59829	-2,36019	C	4,42821	-0,45652	-2,39355
C	1,8918	-1,78391	-1,73775	C	2,03905	-1,22032	-2,72532
C	-3,28886	-1,14254	-2,32143	C	-3,28638	-1,37621	-2,28699
C	2,07541	2,45698	-2,43067	C	1,94431	2,53944	-2,23673
C	-2,12372	-0,40643	-2,09054	C	-2,11409	-0,64461	-2,07883
C	-0,70286	2,24811	-2,1975	C	-0,81432	2,11588	-2,043
C	-5,28447	-2,5209	-1,53587	C	-5,25032	-2,77838	-1,47909
C	3,07851	-0,94968	-1,23689	C	3,13194	-0,88827	-1,69897
C	-4,00814	-1,76213	-1,2763	C	-3,99392	-1,98468	-1,22647
C	1,51627	1,53296	-1,53244	C	1,44913	1,50405	-1,42491
C	0,10481	1,38398	-1,41881	C	0,05062	1,24774	-1,32703
C	-1,60636	-0,23743	-0,77853	C	-1,58013	-0,4772	-0,77689
C	-3,47203	-1,63908	0,01767	C	-3,45633	-1,83947	0,06506
C	3,89474	1,52738	0,21414	C	3,9327	1,3018	0,1857
C	-2,29566	-0,91223	0,27448	C	-2,27451	-1,11557	0,29224
C	4,75776	0,6941	1,17075	C	4,76714	0,36795	1,07369
C	3,44504	2,85036	0,84191	C	3,51647	2,57759	0,92258
C	-2,59864	1,74973	2,10515	C	-2,38173	1,76551	1,74015
C	-1,17201	-3,57413	1,85265	C	-1,39996	-3,6749	2,41729
C	-2,48495	0,43545	2,88626	C	-2,39118	0,55821	2,68606
C	-1,75689	-2,44983	2,71669	C	-1,87368	-2,33814	2,99302
C	-3,86343	-0,08904	3,29979	C	-3,8186	0,20765	3,12145
C	-1,1316	-2,4058	4,11758	C	-1,29433	-2,07614	4,39093
Cl	1,98049	-1,77852	2,11686	H	1,29134	4,38715	-4,88148
N	-0,41578	0,45363	-0,49265	H	2,71655	4,5427	-3,80948
N	0,74032	1,38141	2,22957	H	4,72671	-1,23844	-3,12192
P	2,43086	0,53425	-0,32742	H	1,23347	5,49045	-3,48353
P	-1,49449	-0,80673	1,8971	H	-1,00986	3,80955	-3,36065
Re	0,66338	0,03705	1,2425	H	-3,65689	-1,49824	-3,3178
H	1,45903	5,30442	-4,03668	H	4,28999	0,48335	-2,96756
H	1,65177	4,01113	-5,24724	H	2,3759	-2,07072	-3,35227
H	2,97038	4,34424	-4,08551	H	1,84268	-0,35519	-3,38971
H	-0,78933	3,84151	-3,64891	H	-1,57963	-0,22004	-2,93985
H	4,41878	-1,52451	-2,85254	H	-6,03646	-2,15809	-1,95923
H	4,94662	-0,04964	-1,9942	H	5,27645	-0,31733	-1,69613
H	3,56509	0,02151	-3,13808	H	3,03187	2,70641	-2,2983
H	2,25969	-2,68436	-2,27055	H	-5,06045	-3,63589	-2,15888
H	1,25729	-1,20756	-2,44138	H	-1,90176	1,98642	-1,9528
H	1,25195	-2,13038	-0,90189	H	1,0967	-1,52168	-2,23047
H	-3,64584	-1,25376	-3,35829	H	3,30599	-1,79181	-1,07637
H	3,1712	2,55258	-2,49618	H	-5,671	-3,18448	-0,53851
H	-1,58761	0,02654	-2,9456	H	4,52946	1,58306	-0,70907
H	-1,7957	2,20978	-2,08878	H	5,04493	-0,5761	0,56426
H	-5,27912	-2,99986	-2,53563	H	2,95732	3,27235	0,26757
H	-6,17097	-1,85005	-1,50416	H	-3,96665	-2,32546	0,91187
H	-5,45048	-3,31342	-0,77913	H	-2,95019	1,54764	0,81348

H	3,59542	-1,52744	-0,44005	H	5,70428	0,87359	1,38346
H	-3,97454	-2,15519	0,85133	H	4,42184	3,10123	1,29288
H	4,47177	1,74339	-0,7124	H	-1,35309	2,06242	1,46132
H	4,16932	0,36895	2,0521	H	-1,78918	-3,85204	1,39727
H	5,6144	1,30081	1,52888	H	4,20805	0,09918	1,99175
H	5,16789	-0,2161	0,691	H	2,86783	2,34699	1,79097
H	2,83202	2,66985	1,74756	H	-2,86549	2,62851	2,24154
H	2,84014	3,45742	0,14073	H	-4,42695	-0,13106	2,25761
H	4,33409	3,44474	1,1363	H	-0,29687	-3,71755	2,34904
H	-1,60486	2,15767	1,84264	H	-1,7481	-4,49642	3,07737
H	-3,132	2,50403	2,71908	H	-2,98367	-2,3537	3,06156
H	-3,17563	1,6027	1,16932	H	-4,31222	1,11056	3,53595
H	-1,63734	-3,60794	0,84827	H	-1,77196	0,80405	3,57539
H	-1,3451	-4,55428	2,34344	H	-3,85669	-0,5758	3,9029
H	-0,07849	-3,44378	1,72945	H	-0,18922	-1,99951	4,35376
H	-1,86021	0,60857	3,78839	H	-1,68533	-1,1485	4,85311
H	-2,85556	-2,59681	2,80517	H	-1,54807	-2,91914	5,06518
H	-4,48186	-0,33391	2,41192	Cl	0,79971	-2,68136	0,07752
H	-4,40441	0,69533	3,86846	N	1,82017	-1,23668	2,46019
H	-3,8099	-0,98696	3,94539	N	-0,39644	0,2127	-0,50134
H	-0,04453	-2,19859	4,04935	N	0,7934	1,23119	1,91065
H	-1,26416	-3,38322	4,62551	P	2,48066	0,36193	-0,47741
H	-1,59142	-1,62935	4,76109	P	-1,50016	-0,88895	1,90509
B2				Re	0,79127	-0,3258	1,18748
C	1,73558	4,66819	-3,61144	O	2,42026	-1,99733	3,14448
C	1,17487	3,48622	-2,8621	**C1**			
C	-0,20964	3,19895	-2,8755	C	-5,00627	0,24338	-3,26435
C	4,23942	-0,41423	-2,50249	C	-2,59396	1,00058	-2,98828
C	1,88034	-1,29919	-2,61204	C	-3,71863	0,31257	-2,48404
C	-3,29885	-1,44561	-2,31825	C	2,26434	-1,19989	-2,16621
C	1,99575	2,63367	-2,10152	C	-1,39404	1,08176	-2,2746
C	-2,13841	-0,68646	-2,15563	C	4,65088	-0,68311	-1,47706
C	-0,75641	2,11868	-2,1792	C	-3,56967	-0,32963	-1,2407
C	-5,20774	-2,87896	-1,43298	C	3,28795	-1,21167	-1,02337
C	3,03529	-0,89685	-1,6842	C	-1,26429	0,47533	-1,00197
C	-3,95545	-2,06485	-1,2299	C	1,36694	3,94235	-0,80192
C	1,46641	1,54728	-1,38512	C	-2,3685	-0,27653	-0,51346
C	0,06457	1,24626	-1,41051	C	0,43448	2,8994	-0,72173
C	-1,55208	-0,4973	-0,87274	C	3,74057	4,85551	-0,7097
C	-3,37475	-1,90177	0,04061	C	2,74364	3,73194	-0,58618
C	3,98585	1,22122	0,18285	C	0,84937	1,58532	-0,41457
C	-2,19808	-1,15469	0,2248	C	-2,54495	-3,55376	-0,40487
C	4,85773	0,21029	0,94101	C	3,14859	2,42434	-0,24713
C	3,65533	2,441	1,04782	C	2,2291	1,37011	-0,14561
C	-2,65626	1,6547	1,44545	C	-2,94036	-2,80664	0,87441
C	-1,43573	-3,63972	2,45199	C	3,96648	-0,17555	1,67593
C	-2,43221	0,60278	2,54194	C	4,40953	-1,5839	2,09417
C	-1,82221	-2,26	2,99269	C	-2,54381	1,25774	2,24512
C	-3,76729	0,20628	3,18262	C	-4,42478	-0,42846	2,40166
C	-1,16114	-1,97313	4,34845	C	-2,90709	-0,22786	2,36868
H	1,48327	4,62678	-4,69246	C	-2,64892	-3,62612	2,13959
H	2,83948	4,71839	-3,52617	C	3,56093	0,67742	2,88234
H	4,49602	-1,18599	-3,25686	H	-4,85573	-0,2291	-4,25798
H	1,32776	5,627	-3,22647	H	-2,65494	1,48121	-3,97803
H	-0,88577	3,86051	-3,44209	H	-5,42209	1,25562	-3,45214
H	-3,70771	-1,57576	-3,33385	H	2,65701	-1,77339	-3,03055

H	4,00439	0,5163	-3,06	H	-5,77725	-0,34224	-2,72701
H	2,2081	-2,13933	-3,25768	H	5,00872	-1,26325	-2,35304
H	1,59264	-0,45473	-3,26973	H	2,05782	-0,16633	-2,51147
H	-1,64649	-0,24936	-3,03617	H	-0,53783	1,60859	-2,71718
H	-6,02278	-2,2723	-1,88226	H	1,30394	-1,66219	-1,86664
H	5,14583	-0,23619	-1,89361	H	4,58561	0,37932	-1,78997
H	3,07785	2,83744	-2,05786	H	4,0742	4,98493	-1,76242
H	-5,03336	-3,7354	-2,11855	H	3,38404	-2,25683	-0,6564
H	-1,84319	1,9542	-2,19629	H	-4,41321	-0,91447	-0,84096
H	0,99046	-1,62909	-2,04654	H	5,42632	-0,76429	-0,69058
H	3,31517	-1,77561	-1,06532	H	-2,78069	-2,97075	-1,31605
H	-5,58515	-3,2891	-0,47628	H	1,00628	4,95961	-1,0234
H	4,52359	1,56155	-0,72882	H	-0,63276	3,11514	-0,86771
H	5,13894	-0,66571	0,32436	H	4,64719	4,66628	-0,10173
H	2,95563	3,13736	0,54717	H	-3,09697	-4,51483	-0,46232
H	-3,85187	-2,38764	0,9067	H	-1,46137	-3,78159	-0,41031
H	-3,41293	1,29935	0,71855	H	4,21153	2,23706	-0,02676
H	5,79419	0,69758	1,27919	H	3,30742	5,8234	-0,38728
H	4,58821	2,99379	1,27983	H	4,80087	-2,17874	1,24574
H	-1,73858	1,89541	0,88066	H	-4,02541	-2,56889	0,83293
H	-1,84591	-3,82751	1,44203	H	4,79942	0,32918	1,1387
H	4,32388	-0,16753	1,83663	H	-2,99302	1,69995	1,33281
H	3,20505	2,13189	2,01062	H	-4,89571	-0,11161	1,4482
H	-3,03186	2,59196	1,90308	H	3,56341	-2,1456	2,53949
H	-4,41632	-0,32812	2,45785	H	5,21144	-1,51705	2,85731
H	-0,33771	-3,74971	2,3879	H	-1,4506	1,41795	2,20679
H	-1,82906	-4,41749	3,13911	H	-4,71942	-1,47644	2,60346
H	-2,92634	-2,22476	3,11464	H	-3,18952	-4,59425	2,10392
H	-4,31154	1,12151	3,49431	H	-1,56441	-3,84152	2,22098
H	-1,76101	1,0259	3,31903	H	-2,93259	1,81128	3,1236
H	-3,64874	-0,42761	4,08187	H	3,14324	1,65837	2,58245
H	-0,05652	-1,96448	4,24792	H	-4,86433	0,19717	3,20613
H	-1,46744	-0,99868	4,77852	H	-2,96115	-3,1016	3,0649
H	-1,43828	-2,76213	5,07742	H	-2,46117	-0,61708	3,30876
Cl	0,96263	-2,53715	0,40357	H	4,4491	0,86488	3,51991
N	1,8268	-0,78057	2,72463	H	2,8093	0,15883	3,50978
N	-0,38915	0,20115	-0,63422	Cl	0,90293	-3,23818	0,64548
N	0,64157	1,47069	1,77136	N	0,42956	-0,34092	2,73804
P	2,46318	0,37271	-0,44032	N	-0,05537	0,49724	-0,25494
P	-1,4685	-0,84814	1,84705	P	2,58366	-0,31046	0,45023
Re	0,89964	-0,31064	1,35678	P	-2,03419	-1,19313	1,02267
O	0,43618	2,62489	1,96856	Re	0,35505	-0,97357	1,064
D1				N	0,1819	0,15797	3,89757
C	1,71915	4,635	-3,56946	O	0,75625	-0,23247	4,94003
C	1,17909	3,45172	-2,80709	**D2**			
C	-0,20678	3,18519	-2,75344	C	1,63154	4,56951	-3,78037
C	4,28592	-0,40213	-2,57979	C	1,11497	3,41746	-2,95656
C	1,92894	-1,29756	-2,67619	C	-0,2666	3,12867	-2,88625
C	-3,26714	-1,38295	-2,29135	C	4,33131	-0,33964	-2,53405
C	2,02604	2,57851	-2,09774	C	1,99361	-1,27268	-2,64276
C	-2,0817	-0,66808	-2,09736	C	-3,24556	-1,42857	-2,28198
C	-0,73166	2,1037	-2,03858	C	1,97665	2,59561	-2,20744
C	-5,2398	-2,7565	-1,45676	C	-2,07172	-0,69493	-2,09489
C	3,09937	-0,91797	-1,75777	C	-0,76904	2,07049	-2,12475
C	-3,96709	-1,98329	-1,22135	C	-5,20952	-2,80658	-1,4314
C	1,52101	1,492	-1,36601	C	3,1389	-0,84427	-1,71351

C	0,11881	1,21771	-1,32867	C	-3,94819	-2,01285	-1,20407
C	-1,52681	-0,51484	-0,80228	C	1,49317	1,53448	-1,42355
C	-3,40988	-1,84763	0,06372	C	0,09826	1,23023	-1,37828
C	4,04616	1,13221	0,16566	C	-1,52804	-0,50078	-0,79848
C	-2,21316	-1,14494	0,27853	C	-3,40044	-1,84252	0,08
C	4,94253	0,09956	0,8649	C	4,0149	1,32651	0,11675
C	3,72759	2,31295	1,08753	C	-2,21278	-1,12164	0,29039
C	-2,63839	1,61704	1,57262	C	4,94783	0,3709	0,87273
C	-1,44151	-3,69684	2,40975	C	3,6381	2,54122	0,96963
C	-2,39849	0,53828	2,64067	C	-2,50083	1,73032	1,57508
C	-1,82633	-2,33619	2,99616	C	-1,43586	-3,62932	2,46386
C	-3,72676	0,14818	3,29825	C	-2,37987	0,61278	2,62111
C	-1,16033	-2,09649	4,35949	C	-1,87346	-2,2695	3,01505
H	1,36642	4,63874	-4,62195	C	-3,76439	0,24979	3,16965
H	2,82664	4,6372	-3,58546	C	-1,2857	-2,00549	4,40844
H	4,53858	-1,14373	-3,3658	H	1,34388	4,46978	-4,84835
H	1,39049	5,59617	-3,1191	H	2,73613	4,63809	-3,73586
H	-0,90289	3,85984	-3,27801	H	4,60893	-1,10622	-3,28693
H	-3,65647	-1,49448	-3,31647	H	1,22144	5,54049	-3,42943
H	4,03377	0,54594	-3,09883	H	-0,97676	3,76884	-3,43481
H	2,24753	-2,1125	-3,35789	H	-3,62323	-1,56958	-3,30788
H	1,61867	-0,43352	-3,29766	H	4,07178	0,5832	-3,09296
H	-1,5542	-0,24379	-2,96307	H	2,33574	-2,11158	-3,28274
H	-6,01507	-2,12951	-1,94561	H	1,69189	-0,43709	-3,30576
H	5,20136	-0,23725	-1,97956	H	-1,54269	-0,2868	-2,9672
H	3,11221	2,7646	-2,11096	H	-5,99168	-2,19784	-1,93246
H	-5,06945	-3,62963	-2,12194	H	5,23348	-0,13621	-1,92594
H	-1,81951	1,95125	-2,00431	H	3,05842	2,80502	-2,22652
H	1,05611	-1,65739	-2,10107	H	-5,02645	-3,68825	-2,08194
H	3,39135	-1,81939	-1,17761	H	-1,85404	1,904	-2,07678
H	-5,66521	-3,13808	-0,50802	H	1,10739	-1,61599	-2,07872
H	4,56659	1,51652	-0,7379	H	3,4366	-1,72115	-1,09938
H	5,21078	-0,74948	0,20661	H	-5,63326	-3,17806	-0,47783
H	3,0398	3,04209	0,61672	H	4,5264	1,68055	-0,80392
H	-3,9206	-2,32145	0,91738	H	5,24869	-0,50623	0,26697
H	-3,42286	1,28775	0,86269	H	2,89278	3,18991	0,47082
H	5,88624	0,57734	1,19911	H	-3,91054	-2,30637	0,93949
H	4,66342	2,84857	1,34817	H	-3,18004	1,42329	0,7548
H	-1,73927	1,84294	0,97087	H	5,87219	0,89976	1,18298
H	-1,88727	-3,8638	1,41108	H	4,54208	3,1502	1,17697
H	4,44047	-0,31806	1,7605	H	-1,53246	2,00605	1,12131
H	3,27454	1,96263	2,03578	H	-1,82316	-3,81022	1,44344
H	-2,98091	2,55662	2,0515	H	4,45634	-0,01017	1,79046
H	-4,39864	-0,35527	2,57254	H	3,21527	2,23196	1,94454
H	-0,34563	-3,78822	2,29373	H	-2,92451	2,63871	2,04952
H	-1,79595	-4,49902	3,09037	H	-4,40043	-0,20143	2,38019
H	-2,92993	-2,30569	3,12388	H	-0,3337	-3,70508	2,40889
H	-4,25198	1,06139	3,64764	H	-1,8112	-4,43462	3,12926
H	-1,71283	0,94442	3,41579	H	-2,98248	-2,25713	3,08728
H	-3,6018	-0,51467	4,17559	H	-4,27922	1,16936	3,51705
H	-0,0562	-2,11537	4,26577	H	-1,73486	0,97313	3,45127
H	-1,44313	-1,12622	4,81469	H	-3,72663	-0,44842	4,02766
H	-1,45136	-2,89654	5,07044	H	-0,1777	-1,99057	4,37094
Cl	0,9752	-2,64869	0,30673	H	-1,61984	-1,04259	4,84298
N	1,8146	-0,79133	2,63116	H	-1,58379	-2,81189	5,10912
N	-0,32852	0,15452	-0,54	Cl	1,003	-2,56954	0,34565

N	0,64291	1,52308	1,73847	N	1,93475	-0,99874	2,69055
P	2,51632	0,28331	-0,44672	N	-0,34047	0,19193	-0,5522
P	-1,43387	-0,89666	1,89509	N	0,73324	1,32005	1,92384
Re	0,83766	-0,39622	1,1781	P	2,51634	0,39416	-0,45311
O	2,46496	-1,03024	3,59626	P	-1,43912	-0,84601	1,90389
N	0,54195	2,63876	1,97502	Re	0,8039	-0,28422	1,15144
O	0,39963	3,79948	2,26577	O	0,69379	2,34594	2,52795
E1				N	2,58548	-1,47961	3,49855
C	-5,16171	0,29959	-3,23904	O	3,18547	-1,99908	4,40325
C	-2,73567	1,01999	-2,98309	**F1**			
C	-3,8605	0,33299	-2,47856	C	1,58892	4,69122	-3,54312
C	2,57138	-1,05602	-2,28874	C	1,07665	3,49362	-2,78515
C	-1,51987	1,0635	-2,29212	C	-0,3051	3,20326	-2,7273
C	4,84053	-0,8831	-1,19071	C	4,19196	-0,34381	-2,65588
C	-3,70073	-0,34214	-1,25317	C	1,84906	-1,27283	-2,69269
C	3,37986	-1,30665	-1,00872	C	-3,17676	-1,4998	-2,34362
C	-1,36811	0,40896	-1,04601	C	1,94736	2,63294	-2,0882
C	1,33585	3,79486	-0,76133	C	-2,0235	-0,73986	-2,12822
C	-2,48445	-0,32515	-0,55187	C	-0,80488	2,11099	-2,01268
C	0,38887	2,76862	-0,70999	C	-5,112	-2,94126	-1,54155
C	3,71726	4,67943	-0,60004	C	3,03538	-0,87747	-1,80208
C	2,70867	3,56167	-0,525	C	-3,88232	-2,1093	-1,28239
C	0,77045	1,43236	-0,42277	C	1,46851	1,53365	-1,35957
C	-2,77238	-3,66424	-0,29489	C	0,07006	1,24458	-1,3111
C	3,07962	2,24738	-0,19069	C	-1,51758	-0,54973	-0,81934
C	2,14291	1,2008	-0,11527	C	-3,37445	-1,9279	0,01902
C	-3,14496	-2,80151	0,91598	C	4,03605	1,16137	0,11305
C	3,80749	-0,31595	1,76982	C	-2,2157	-1,17462	0,25751
C	4,15168	-1,72026	2,28515	C	4,94657	0,11284	0,7697
C	-2,04088	1,1162	2,38699	C	3,73111	2,31684	1,07032
C	-4,28596	-0,06838	2,33708	C	-2,52073	1,73802	1,49131
C	-2,76496	-0,23641	2,36093	C	-1,38407	-3,60049	2,5577
C	-2,97714	-3,55943	2,23938	C	-2,4624	0,61779	2,5389
C	3,31136	0,60637	2,89005	C	-1,90738	-2,2436	3,03547
H	-5,03838	-0,16988	-4,23804	C	-3,87434	0,25174	3,01085
H	-2,80802	1,52609	-3,95948	C	-1,38215	-1,8951	4,43605
H	-5,55782	1,322	-3,41398	H	1,20528	4,70975	-4,58429
H	2,98834	-1,65948	-3,12053	H	2,69528	4,70218	-3,58878
H	-5,93747	-0,27246	-2,69371	H	4,43359	-1,08308	-3,44731
H	5,26687	-1,38814	-2,08232	H	1,26532	5,64131	-3,06643
H	2,62267	0,01248	-2,57998	H	-1,01484	3,86826	-3,24539
H	-0,66338	1,58725	-2,73825	H	-3,53349	-1,64215	-3,37649
H	1,50523	-1,32581	-2,17563	H	3,91017	0,59918	-3,16892
H	4,92405	0,20954	-1,36422	H	2,17155	-2,06689	-3,3968
H	3,80552	5,07967	-1,63268	H	1,49983	-0,40873	-3,29323
H	3,33684	-2,39055	-0,76781	H	-1,48322	-0,31002	-2,98334
H	-4,54893	-0,91829	-0,85005	H	-5,87293	-2,37618	-2,11933
H	5,47932	-1,14711	-0,32591	H	5,1198	-0,16393	-2,08026
H	-2,82285	-3,09564	-1,24392	H	3,02974	2,83731	-2,11219
H	0,99366	4,81926	-0,98126	H	-4,86966	-3,84886	-2,13454
H	-0,67074	3,007	-0,87424	H	-1,88899	1,93635	-1,9662
H	4,72412	4,34015	-0,28741	H	1,00267	-1,66695	-2,10143
H	-3,46818	-4,52476	-0,37328	H	3,35801	-1,77368	-1,22991
H	-1,74659	-4,0689	-0,19808	H	-5,58372	-3,27634	-0,59739
H	4,13464	2,0405	0,0503	H	4,52911	1,56537	-0,79801
H	3,43178	5,53349	0,04939	H	5,22832	-0,70506	0,07819

H	4,54129	-2,38083	1,48471	H	2,99896	3,03421	0,65258
H	-4,20116	-2,46871	0,81318	H	-3,89619	-2,40323	0,86484
H	4,70791	0,13731	1,30135	H	-3,12624	1,42611	0,61672
H	-2,2118	1,68584	1,4511	H	5,88228	0,59352	1,1213
H	-4,61681	0,44996	1,41379	H	4,66695	2,86999	1,29158
H	3,25315	-2,20324	2,7194	H	-1,52413	2,03961	1,1242
H	4,92644	-1,66012	3,07707	H	-1,7184	-3,8436	1,53142
H	-0,94769	0,99858	2,52234	H	4,44347	-0,34366	1,64662
H	-4,82469	-1,03419	2,4011	H	3,33203	1,93994	2,03121
H	-3,53465	-4,51764	2,20264	H	-3,00189	2,63318	1,93512
H	-1,90875	-3,78954	2,42879	H	-4,46761	-0,19407	2,18581
H	-2,41629	1,72913	3,23183	H	-0,2782	-3,62296	2,5576
H	3,08719	1,62494	2,51825	H	-1,75228	-4,39132	3,24393
H	-4,61328	0,54888	3,19956	H	-3,01923	-2,2745	3,05571
H	-3,35362	-2,98473	3,10817	H	-4,40645	1,1687	3,33813
H	-2,45475	-0,81109	3,26093	H	-1,85969	0,9722	3,40311
H	4,08859	0,69263	3,67759	H	-3,87936	-0,45338	3,86372
H	2,39564	0,19657	3,35962	H	-0,27779	-1,79412	4,42104
N	0,47927	-2,6363	-0,26697	H	-1,80658	-0,95251	4,83446
Cl	0,44908	-1,64116	3,18655	H	-1,64308	-2,70608	5,14612
N	-0,1546	0,37043	-0,32015	Cl	0,88449	-2,58759	0,30712
P	2,52133	-0,4877	0,44149	Cl	2,06546	-1,15093	3,01434
P	-2,10731	-1,26931	0,95421	N	-0,35497	0,16741	-0,52969
Re	0,29126	-1,28296	0,82751	N	0,76553	1,30513	1,86261
O	0,6439	-3,58817	-0,98253	O	0,74254	2,37541	2,3782
G1				P	2,49362	0,32064	-0,47234
C	1,69102	4,60799	-3,63675	P	-1,4917	-0,84703	1,88937
C	1,15692	3,43812	-2,85014	Re	0,79039	-0,32958	1,16905
C	-0,22953	3,17062	-2,78453				
C	4,32042	-0,43835	-2,52941				
C	1,93832	-1,25102	-2,69337				
C	-3,26212	-1,38114	-2,28281				
C	2,00688	2,58232	-2,12661				
C	-2,0809	-0,66124	-2,08589				
C	-0,74979	2,10388	-2,04703				
C	-5,23147	-2,76449	-1,45593				
C	3,09279	-0,9074	-1,74022				
C	-3,96315	-1,98634	-1,21555				
C	1,50444	1,51024	-1,37035				
C	0,10392	1,23197	-1,32189				
C	-1,52941	-0,50101	-0,7887				
C	-3,40903	-1,84979	0,07022				
C	4,0383	1,18369	0,15773				
C	-2,21705	-1,13908	0,28788				
C	4,91712	0,17661	0,91407				
C	3,70455	2,40302	1,02109				
C	-2,55973	1,66869	1,61408				
C	-1,43297	-3,68837	2,42053				
C	-2,39042	0,55302	2,65536				
C	-1,83013	-2,33047	3,00536				
C	-3,74966	0,16584	3,24996				
C	-1,17932	-2,08544	4,37503				
H	1,32187	4,60025	-4,6833				
H	2,79861	4,60553	-3,67029				
H	4,57074	-1,19908	-3,29723				
H	1,37218	5,57631	-3,19478				

H	-0,92817	3,83617	-3,31745
H	-3,64682	-1,49464	-3,30959
H	4,1184	0,50972	-3,07012
H	2,24345	-2,09279	-3,34792
H	1,69011	-0,38604	-3,34078
H	-1,55161	-0,23876	-2,95131
H	-6,01389	-2,13527	-1,93109
H	5,22171	-0,29534	-1,90364
H	3,09275	2,77105	-2,14317
H	-5,0595	-3,62659	-2,1349
H	-1,83765	1,95354	-2,00195
H	1,02994	-1,56218	-2,14563
H	3,33876	-1,81466	-1,14778
H	-5,64921	-3,16198	-0,51081
H	4,57577	1,52566	-0,7535
H	5,17461	-0,71415	0,30835
H	3,00446	3,09703	0,51751
H	-3,91601	-2,33114	0,92172
H	-3,27471	1,35941	0,82662
H	5,86667	0,65755	1,22408
H	4,6353	2,95885	1,25519
H	-1,61183	1,94861	1,1218
H	-1,8614	-3,85327	1,41412
H	4,40641	-0,18092	1,82996
H	3,24882	2,09953	1,98273
H	-2,96441	2,5761	2,10669
H	-4,40459	-0,29735	2,48276
H	-0,33527	-3,78035	2,32455
H	-1,79827	-4,49256	3,0928
H	-2,93523	-2,30543	3,12291
H	-4,26765	1,07751	3,61263
H	-1,72303	0,91886	3,46474
H	-3,66915	-0,52975	4,10704
H	-0,07415	-2,09999	4,29325
H	-1,47349	-1,11623	4,8245
H	-1,47672	-2,8855	5,08388
Cl	0,87649	-2,59989	0,22811
N	1,85506	-1,06072	2,56187
N	-0,3433	0,17988	-0,52332
N	0,71666	1,3443	1,84445
P	2,5183	0,32288	-0,45484
P	-1,45347	-0,88826	1,90609
Re	0,83728	-0,35299	1,2011
O	2,50262	-1,6217	3,38944
O	0,6306	2,43988	2,31127

5.4.5 Calculation of BDFE's

For the calculation of BDFE's the PBE0 functional and the def2-TZVP basis set were employed, together with the RIJCOSX approximation. The optimized gas-phase geometries were verified as minima by an analytical frequency calculation. For BDFE's in THF the CPCM solvent model as implemented in ORCA was utilized.[514] Thermodynamic data were calculated by applying *Grimme*'s quasi-RRHO approach.[513] The free energies were corrected for standard solution conditions (1 mol·L^{-1}, 298.15 K) by adding 1.89 kcal·mol^{-1} and if the BDFE was calculated for THF 3.38 kcal·mol^{-1}, to account for their concentrations in the pure solvent. The free energy correction of the H-atom was derived from the electronic and translational partition function (–4.78 kcal·mol^{-1})[522].

Table 5.11: XYZ geometries relevant for the BDFE calculations (PBE0/def2-TZVP).

[(^{Ph}P^{H}NP)ReCl$_3$]				[(^{Ph}PNP)ReCl$_3$]			
	x	**y**	**z**		**x**	**y**	**z**
C	-5,02147	0,15383	-3,14042	C	-4,82105	-0,2279	-3,45673
C	-2,8028	1,24788	-2,67239	C	-2,50196	0,687	-3,09446
C	-3,82444	0,39759	-2,27383	C	-3,57873	-0,06926	-2,63619
C	3,22539	-0,53856	-2,49818	C	2,29602	-0,5021	-2,52404
C	-1,66378	1,42367	-1,89869	C	-1,34628	0,8415	-2,35017
C	4,85862	-1,53088	-0,89627	C	4,65134	-0,44104	-1,72125
C	-3,65502	-0,29781	-1,07995	C	-3,44441	-0,68984	-1,39878
C	3,38856	-1,22982	-1,14947	C	3,24477	-0,94146	-1,41505
C	-1,51903	0,72553	-0,71492	C	-1,22227	0,23072	-1,10079
C	1,40783	3,98782	-0,79793	C	1,06743	3,83927	-0,36842
C	-2,50628	-0,18123	-0,31099	C	-2,29116	-0,55878	-0,64143
C	0,42318	3,08503	-0,4501	C	0,2451	2,73482	-0,51457
C	3,79369	4,54172	-1,36223	C	3,27934	4,92283	0,15237
C	2,72615	3,57012	-0,96754	C	2,41485	3,71543	-0,04614
C	0,73165	1,74273	-0,26618	C	0,75054	1,44849	-0,33599
C	-2,58557	-3,50424	-0,72857	C	-2,72067	-3,85099	0,13146
C	3,02062	2,23607	-0,72929	C	2,92225	2,42614	0,10872
C	2,05061	1,30792	-0,34995	C	2,11566	1,30866	-0,01438
C	-2,9799	-2,90868	0,61417	C	-3,06412	-2,78993	1,1634
C	3,77565	-0,04803	1,55257	C	4,09102	-0,50875	1,3556
C	3,82485	-1,26402	2,47382	C	4,53867	-1,96938	1,38846
C	-2,8344	0,80089	2,64805	C	-2,53912	1,41072	1,71535
C	-4,46684	-1,06001	2,5435	C	-4,40554	-0,16335	2,11663
C	-2,98323	-0,71004	2,51508	C	-2,89066	-0,02098	2,10427
C	-2,73293	-3,90723	1,74091	C	-2,89978	-3,32384	2,58377
C	3,57619	1,23298	2,35165	C	3,80661	-0,0218	2,76914
H	-4,76603	-0,51895	-3,96468	H	-4,61891	-0,7884	-4,37396
H	-2,88385	1,78081	-3,6138	H	-2,56622	1,16539	-4,06672
H	-5,39657	1,07908	-3,58298	H	-5,22837	0,74136	-3,75569
H	3,58178	-1,21176	-3,28343	H	2,60244	-0,97692	-3,45974
H	-5,8314	-0,31141	-2,57679	H	-5,59423	-0,76387	-2,90474
H	5,22867	-2,179	-1,69529	H	4,93945	-0,77565	-2,72178

H	3,81683	0,37765	-2,55786	H	2,34458	0,58066	-2,66334
H	-0,87837	2,07649	-2,2525	H	-0,52324	1,42287	-2,74708
H	2,18626	-0,2921	-2,70957	H	1,26472	-0,78861	-2,32829
H	5,46831	-0,62352	-0,91129	H	4,68932	0,65216	-1,72052
H	3,78124	4,72456	-2,44094	H	3,74064	5,24807	-0,78588
H	2,84606	-2,17769	-1,20308	H	3,23707	-2,03511	-1,36271
H	-4,42164	-1,00422	-0,78066	H	-4,26274	-1,29655	-1,02401
H	5,03587	-2,04684	0,04747	H	5,40114	-0,81168	-1,02324
H	-2,73246	-2,80448	-1,55104	H	-2,8259	-3,4802	-0,88932
H	1,15175	5,03351	-0,93119	H	0,63654	4,82949	-0,47705
H	-0,59742	3,42313	-0,30948	H	-0,80986	2,87075	-0,71635
H	4,78316	4,16579	-1,09786	H	4,08623	4,71933	0,85782
H	-3,19644	-4,39187	-0,91765	H	-3,39475	-4,70245	0,25939
H	-1,53639	-3,8009	-0,73502	H	-1,69655	-4,20293	0,25421
H	4,05371	1,91156	-0,80272	H	3,96765	2,30084	0,37347
H	3,6522	5,50442	-0,86747	H	2,69755	5,76107	0,54073
H	3,94549	-2,2024	1,92969	H	4,81936	-2,35471	0,40737
H	-4,04461	-2,65447	0,5865	H	-4,10259	-2,4768	1,01226
H	4,72809	0,03012	1,02182	H	4,8737	0,10967	0,90268
H	-3,2611	1,31426	1,78192	H	-2,95887	1,65855	0,73735
H	-4,98618	-0,64424	1,67557	H	-4,81897	-0,0252	1,11359
H	2,90034	-1,34176	3,04677	H	3,73915	-2,59761	1,78895
H	4,65842	-1,16444	3,17517	H	5,40596	-2,06909	2,04567
H	-1,79556	1,10203	2,7818	H	-1,46682	1,59083	1,69833
H	-4,66306	-2,13075	2,57981	H	-4,75074	-1,11987	2,50828
H	-3,30655	-4,81937	1,55659	H	-3,5167	-4,21658	2,7134
H	-1,67437	-4,17064	1,79052	H	-1,85824	-3,59412	2,77462
H	-3,37937	1,14625	3,53077	H	-2,97974	2,09229	2,447
H	3,6691	2,12539	1,7327	H	3,44139	1,00569	2,79677
H	-4,92529	-0,61437	3,43072	H	-4,83109	0,62128	2,74736
H	-3,02523	-3,51879	2,71851	H	-3,20442	-2,59814	3,34018
H	-2,4769	-1,17807	3,36525	H	-2,48367	-0,22161	3,10031
H	4,34119	1,28379	3,13237	H	4,72837	-0,08062	3,35398
H	2,60262	1,25076	2,83837	H	3,05779	-0,65376	3,24725
Cl	0,15508	-1,66191	-1,48876	Cl	0,40285	-2,75992	-0,78952
Cl	0,93637	-3,31668	1,44885	Cl	0,99602	-2,8741	2,51254
Cl	0,42772	-0,08317	2,92179	Cl	0,47565	0,33421	2,71879
N	-0,33071	0,82805	0,13734	N	-0,06021	0,30313	-0,31946
P	2,47463	-0,37783	0,25737	P	2,62448	-0,41221	0,25247
P	-2,05573	-1,36291	1,0199	P	-2,04157	-1,26712	1,00672
Re	0,31389	-1,17513	0,82223	Re	0,4093	-1,18231	0,94208
H	-0,65726	1,16426	1,0443				

[($^{i\mathrm{Pr}}$P$^{\mathrm{H}}$NP)OsCl$_3$]				**[($^{i\mathrm{Pr}}$PNP)OsCl$_3$]**			
C	1,28862	1,87727	-1,75705	C	3,26237	-1,65326	-2,24279
C	2,4975	0,97218	-1,68178	C	0,89614	0,95686	-2,53121
C	-2,38362	0,99534	-1,67031	C	-1,49065	0,88699	-2,17565
C	-4,57267	-1,29139	-1,36064	C	2,20547	1,30594	-1,86019
C	-1,16515	1,8875	-1,7525	C	-2,55784	1,17143	-1,14434
C	4,7308	-1,24019	-1,28504	C	3,50692	-1,13196	-0,83183
C	-3,27697	-1,52548	-0,59146	C	-4,66164	-1,35717	-0,46448
C	3,36861	-1,55747	-0,67967	C	3,43038	-2,24379	0,20664
C	-3,49824	-2,42947	0,61064	C	-3,17793	-1,49355	-0,15825
C	-4,6856	1,25198	0,83487	C	4,77004	1,74911	0,11884
C	3,49232	-2,57715	0,4394	C	-4,44987	1,56974	1,37101
C	3,48508	2,27792	1,02018	C	3,43396	1,35145	0,72989
C	3,50506	0,75823	1,09483	C	-2,9263	-2,61035	0,84633

C	-3,21562	0,97996	1,12076	C	-3,10498	0,92846	1,68767
C	3,17201	0,29119	2,50745	C	3,61571	0,77833	2,12669
C	-3,02794	0,44051	2,53464	C	-3,20502	0,06821	2,94097
H	1,25947	2,40949	-2,71279	H	-1,45844	1,67759	-2,92973
H	2,48346	0,27677	-2,5275	H	3,42237	-0,88359	-3,0003
H	-2,38689	0,30114	-2,51656	H	3,96981	-2,4612	-2,45186
H	-1,13592	2,41904	-2,70846	H	0,97877	0,02622	-3,1101
H	4,68056	-0,51047	-2,09555	H	0,59944	1,74218	-3,23107
H	-4,93054	-2,24662	-1,75814	H	-1,6938	-0,05283	-2,71027
H	-4,44882	-0,61809	-2,21082	H	2,25439	-2,05376	-2,35524
H	0,05509	0,39626	-2,3803	H	3,03862	1,2205	-2,55855
H	3,41903	1,5504	-1,75496	H	-3,55206	1,08625	-1,5843
H	5,16823	-2,154	-1,69907	H	-2,43777	2,19274	-0,77409
H	-3,29571	1,59083	-1,73376	H	-4,8872	-0,53062	-1,14039
H	-2,56975	-2,02824	-1,26188	H	4,51496	-0,70431	-0,81171
H	1,28767	2,61397	-0,95292	H	2,16399	2,3413	-1,51139
H	2,72368	-1,98363	-1,45516	H	-5,01513	-2,27383	-0,94693
H	5,4278	-0,85996	-0,53383	H	-2,65552	-1,76922	-1,08168
H	-5,36058	-0,88824	-0,72448	H	4,143	-3,03334	-0,0492
H	-1,15505	2,62555	-0,94933	H	4,67894	2,14126	-0,8971
H	-3,86337	-3,40427	0,27211	H	5,47123	0,91138	0,09934
H	3,77359	2,65826	0,03902	H	2,42919	-2,67508	0,23913
H	-4,87239	1,59422	-0,18508	H	-4,41823	2,21398	0,49063
H	3,895	-3,51189	0,03639	H	-5,24846	-1,22313	0,44597
H	-5,29724	0,36639	1,01603	H	3,67131	-1,88762	1,20855
H	4,51817	0,42578	0,84458	H	-3,20923	-3,5665	0,39531
H	-2,57704	-2,58231	1,1776	H	5,22782	2,53323	0,72893
H	-4,25239	-2,01724	1,28475	H	-5,23118	0,82391	1,21938
H	2,50077	2,67156	1,27369	H	-4,75329	2,19194	2,21823
H	4,20164	2,67797	1,74378	H	2,80295	2,24153	0,81542
H	4,18328	-2,23414	1,21382	H	-1,87774	-2,66745	1,14195
H	2,52798	-2,7863	0,90728	H	-2,37928	1,72707	1,87911
H	-5,04507	2,03325	1,51158	H	4,32058	-0,05665	2,12911
H	-2,66644	1,92657	1,06326	H	-3,53134	-2,47775	1,74446
H	-3,65115	-0,43762	2,71305	H	2,67051	0,42914	2,54591
H	3,2827	-0,7863	2,632	H	4,02634	1,54842	2,78578
H	-1,99142	0,16569	2,73207	H	-3,98396	-0,69026	2,83883
H	3,8448	0,78077	3,21818	H	-2,26356	-0,43457	3,17391
H	2,14556	0,55238	2,76915	H	-3,48317	0,70136	3,78907
H	-3,32825	1,2041	3,25839	Cl	-0,00179	-2,13801	-0,92504
Cl	0,04255	-2,00418	-1,47919	Cl	0,18499	2,04123	1,34822
Cl	0,02204	1,78791	1,38853	Cl	0,39309	-1,19823	2,20767
Cl	0,05471	-1,60793	2,00974	N	-0,17446	0,75732	-1,56136
N	0,05836	1,07319	-1,61578	Os	0,08839	0,01498	0,12962
Os	0,05405	-0,20576	0,09473	P	2,40474	0,27272	-0,36359
P	2,41433	-0,06539	-0,15754	P	-2,29295	0,05913	0,27954
P	-2,30964	-0,025	-0,13669				
[(^{Imine}PNP)OsCl$_3$]				**[(P=NP)OsCl$_3$]**			
C	3,10196	0,28841	-2,5659	C	3,29388	-1,6619	-2,25049
C	-3,47127	0,74444	-2,32526	C	0,86544	0,95877	-2,50873
C	3,22769	0,92786	-1,18678	C	-1,45002	1,2362	-1,93592
C	-3,47835	-2,54252	-0,81655	C	2,19067	1,29071	-1,8572
C	4,68258	1,24476	-0,86914	C	-2,55124	0,99031	-1,21343
C	-3,52185	1,03599	-0,83156	C	3,52001	-1,14659	-0,83462
C	-3,20604	2,50023	-0,55731	C	-4,66809	-1,40316	-0,42799
C	3,60151	-2,39781	-0,49104	C	3,43715	-2,2644	0,19699

C	-3,39481	-1,64664	0,41004	C	-3,18845	-1,55779	-0,11502
C	3,25583	-1,47286	0,66547	C	4,75687	1,7533	0,09162
C	-4,77168	-1,40103	1,01234	C	-4,43366	1,59929	1,30092
C	4,48538	-1,17228	1,51682	C	3,4342	1,33916	0,7208
C	1,08263	2,02381	1,4948	C	-2,94491	-2,64939	0,91889
C	2,28185	1,09723	1,57101	C	-3,10572	0,93849	1,64018
C	-2,38848	0,63099	1,80466	C	3,64121	0,7675	2,11446
C	-1,1637	1,4327	1,98789	C	-3,2264	0,10292	2,90958
H	3,39409	1,01518	-3,32986	H	3,45761	-0,88805	-3,00281
H	-4,18729	1,38622	-2,84635	H	4,00798	-2,46497	-2,4554
H	3,76402	-0,57303	-2,66834	H	0,91799	-0,0011	-3,03908
H	-2,47616	0,95621	-2,72009	H	0,58819	1,72342	-3,23716
H	-3,72467	-0,28951	-2,56373	H	2,28983	-2,068	-2,37659
H	2,08282	-0,03843	-2,77381	H	3,00974	1,19206	-2,57013
H	5,05563	1,98071	-1,58789	H	-4,87197	-0,59726	-1,13531
H	-4,15777	-2,13576	-1,56913	H	4,52554	-0,71436	-0,79951
H	-2,50062	-2,68655	-1,28047	H	2,16951	2,32723	-1,51006
H	2,66103	1,86567	-1,21589	H	-5,03982	-2,33026	-0,87552
H	-3,86404	3,12528	-1,16819	H	-2,66525	-1,85481	-1,03019
H	4,39934	-1,97856	-1,10805	H	4,16105	-3,04595	-0,05129
H	5,3127	0,35831	-0,96218	H	4,64581	2,14875	-0,921
H	-3,87103	-3,52014	-0,5199	H	5,46605	0,92283	0,05699
H	2,73711	-2,59492	-1,12903	H	2,43983	-2,7057	0,21094
H	-2,1767	2,74191	-0,82664	H	-4,37702	2,22367	0,40759
H	-4,5326	0,8327	-0,46176	H	-5,25296	-1,22148	0,4755
H	3,96507	-3,35236	-0,09799	H	3,65827	-1,91148	1,20475
H	4,82679	1,66536	0,12833	H	-3,2411	-3,61198	0,49041
H	-3,37647	2,78021	0,48401	H	5,21553	2,53977	0,69786
H	-5,45921	-0,97615	0,27668	H	-5,23241	0,86952	1,16189
H	5,29302	-0,73141	0,93215	H	-4,72571	2,24633	2,13324
H	1,18047	2,70657	0,64616	H	2,79343	2,2216	0,81451
H	-2,76619	-2,15385	1,15052	H	-1,89505	-2,71191	1,20961
H	-5,19924	-2,35181	1,34512	H	-2,36692	1,72673	1,81939
H	2,51893	-1,97986	1,29889	H	4,34759	-0,06623	2,10588
H	3,20099	1,67696	1,66906	H	-3,54192	-2,49128	1,81808
H	4,86284	-2,10739	1,94257	H	2,70405	0,41778	2,55086
H	-4,74996	-0,73579	1,87794	H	4,0611	1,5394	2,76535
H	-3,27687	1,20189	2,07787	H	-4,01403	-0,64775	2,81882
H	4,27203	-0,50303	2,35211	H	-2,29297	-0,40551	3,16242
H	0,97459	2,61688	2,40584	H	-3,50123	0,75808	3,74174
H	2,19034	0,4543	2,45071	Cl	0,00551	-2,12294	-0,98738
H	-2,32674	-0,21537	2,5011	Cl	0,16167	1,98836	1,36011
H	-1,13412	2,19443	2,76608	Cl	0,41412	-1,25318	2,20471
Cl	-0,01614	1,57913	-1,75981	N	-0,19391	0,82635	-1,51007
Cl	0,01315	-1,86155	-1,91029	Os	0,0999	-0,03514	0,15099
Cl	-0,07936	-1,84973	1,54939	P	2,40789	0,24979	-0,36464
N	-0,12505	1,23505	1,27215	P	-2,28944	0,0053	0,27277
Os	-0,06479	-0,21452	-0,19404	H	-1,48568	1,76077	-2,88601
P	-2,41628	-0,11119	0,11008	H	-3,51522	1,3287	-1,57226
P	2,28931	-0,00915	0,09879	C			
[(^{Imine}PN=P)OsCl$_3$]				**[(P=N=P)OsCl$_3$]**			
C	3,23493	-0,32032	-2,72724	C	-2,92219	-1,06192	-2,86125
C	-3,48304	1,09901	-2,13186	C	3,5102	-0,26814	-2,08087
C	3,2578	0,67618	-1,57671	C	-2,92288	-1,66916	-1,4663
C	-3,68052	-2,255	-1,21409	C	-3,51536	1,90107	-1,05439
C	4,68074	1,12083	-1,27454	C	-4,24253	-2,36948	-1,1742

C	-3,51955	1,13373	-0,60922	C	3,54058	-0,59744	-0,59399
C	-3,20239	2,53501	-0,09934	C	3,30044	2,78466	-0,60287
C	3,52661	-2,42332	0,06659	C	4,95658	-0,56931	-0,04017
C	-3,39605	-1,70468	0,1773	C	-3,51552	0,90264	0,09548
C	3,2113	-1,16494	0,86338	C	-4,92504	0,49589	0,49629
C	-4,67377	-1,58468	0,99419	C	2,90777	2,08717	0,69391
C	4,43346	-0,66276	1,6197	C	3,9704	2,21023	1,77212
C	1,11875	1,74665	1,64707	C	-2,35077	-1,39853	1,35368
C	2,2552	1,49336	1,00636	C	2,27746	-0,47343	1,95697
C	-2,2828	0,31767	1,89427	C	-1,18933	-1,46417	2,01338
C	-1,07039	1,11509	2,12687	C	1,10369	-1,00466	2,31327
H	3,62768	0,16284	-3,62731	H	-3,10891	-1,853	-3,59421
H	-4,21596	1,80808	-2,52708	H	-3,71496	-0,32156	-2,98075
H	3,86771	-1,18486	-2,51619	H	-1,9697	-0,5838	-3,09851
H	-2,49683	1,38821	-2,49667	H	3,98667	-1,08031	-2,63658
H	-3,72337	0,11765	-2,53985	H	2,49208	-0,15203	-2,45192
H	2,22671	-0,68342	-2,93514	H	-4,08476	1,53106	-1,90937
H	5,07801	1,66483	-2,13689	H	-4,32493	-3,24912	-1,81959
H	-4,44926	-1,66906	-1,72262	H	4,06111	0,6466	-2,3041
H	-2,78293	-2,26802	-1,83501	H	-2,50456	2,13411	-1,394
H	2,6656	1,54817	-1,87591	H	-2,12007	-2,41372	-1,42673
H	-3,84508	3,25387	-0,61607	H	-3,9874	2,82988	-0,72084
H	4,34424	-2,25845	-0,6384	H	-5,09617	-1,72701	-1,39415
H	5,33583	0,26423	-1,1052	H	4,23939	2,3976	-1,00404
H	-4,05874	-3,27843	-1,13295	H	5,57013	-1,29405	-0,58367
H	2,65747	-2,78396	-0,48742	H	2,53002	2,67708	-1,3698
H	-2,16706	2,80903	-0,31068	H	3,13539	-1,60798	-0,4749
H	-4,52649	0,86486	-0,27146	H	3,44462	3,85175	-0,41159
H	3,84399	-3,21469	0,75215	H	-4,32817	-2,71633	-0,14259
H	4,7526	1,78492	-0,41107	H	-5,49554	0,12914	-0,35833
H	-3,39096	2,64629	0,97042	H	5,42151	0,40909	-0,17418
H	-5,39947	-0,92417	0,51288	H	-5,45157	1,36912	0,89324
H	5,27008	-0,43914	0,95763	H	5,00374	-0,83087	1,0192
H	-2,70716	-2,38767	0,68656	H	-3,03618	1,39211	0,95006
H	-5,1421	-2,56963	1,07922	H	4,91243	1,73717	1,49156
H	2,44386	-1,42745	1,60013	H	-4,94143	-0,27118	1,27322
H	4,7646	-1,4422	2,31265	H	1,99743	2,56399	1,07002
H	-4,50016	-1,21783	2,00789	H	4,17549	3,27097	1,9481
H	-3,16673	0,80205	2,30988	H	-3,2284	-1,87517	1,77267
H	4,22029	0,22759	2,21404	H	3,63548	1,78138	2,71869
H	-2,14928	-0,63414	2,42687	H	3,14136	-0,60411	2,5966
H	-1,02453	1,80113	2,97136	H	-1,08615	-1,9769	2,96465
Cl	-0,03998	1,821	-1,56262	H	0,97424	-1,56478	3,23427
Cl	-0,2044	-1,49079	-2,31836	Cl	0,07235	1,27104	-2,22177
Cl	-0,0301	-2,1494	1,05014	Cl	0,4776	-1,93151	-1,30359
N	-0,0405	0,99743	1,36368	Cl	-0,4769	2,09496	0,97479
Os	-0,07904	-0,21013	-0,32206	N	-0,03208	-0,86862	1,51381
P	-2,40181	-0,1532	0,105	Os	0,00128	0,07683	-0,1568
P	2,27596	0,08353	-0,13579	P	-2,32461	-0,4733	-0,19462
H	1,01169	2,518	2,40409	P	2,30347	0,37592	0,3681
H	3,13371	2,08222	1,2418				

5.4.6 Frontier molecular orbitals of $[Ru(NH_3)_5(N_2)]^{2+}$ and $[Ru(NH_3)_5(NO)]^{3+}$

The molecular orbitals of the prototypical $[Ru(NH_3)_5(N_2)]^{2+}$ complex were computed, to derive a general overview of the ordering of the MO's in terminal dinitrogen complexes. The complex was optimized using the PBE0 functional together with the def2-TZVP basis set and the RIJCOSX approximation. Energy levels are relative to the non-bonding d_{xy} metal orbital (Figure 5.17).

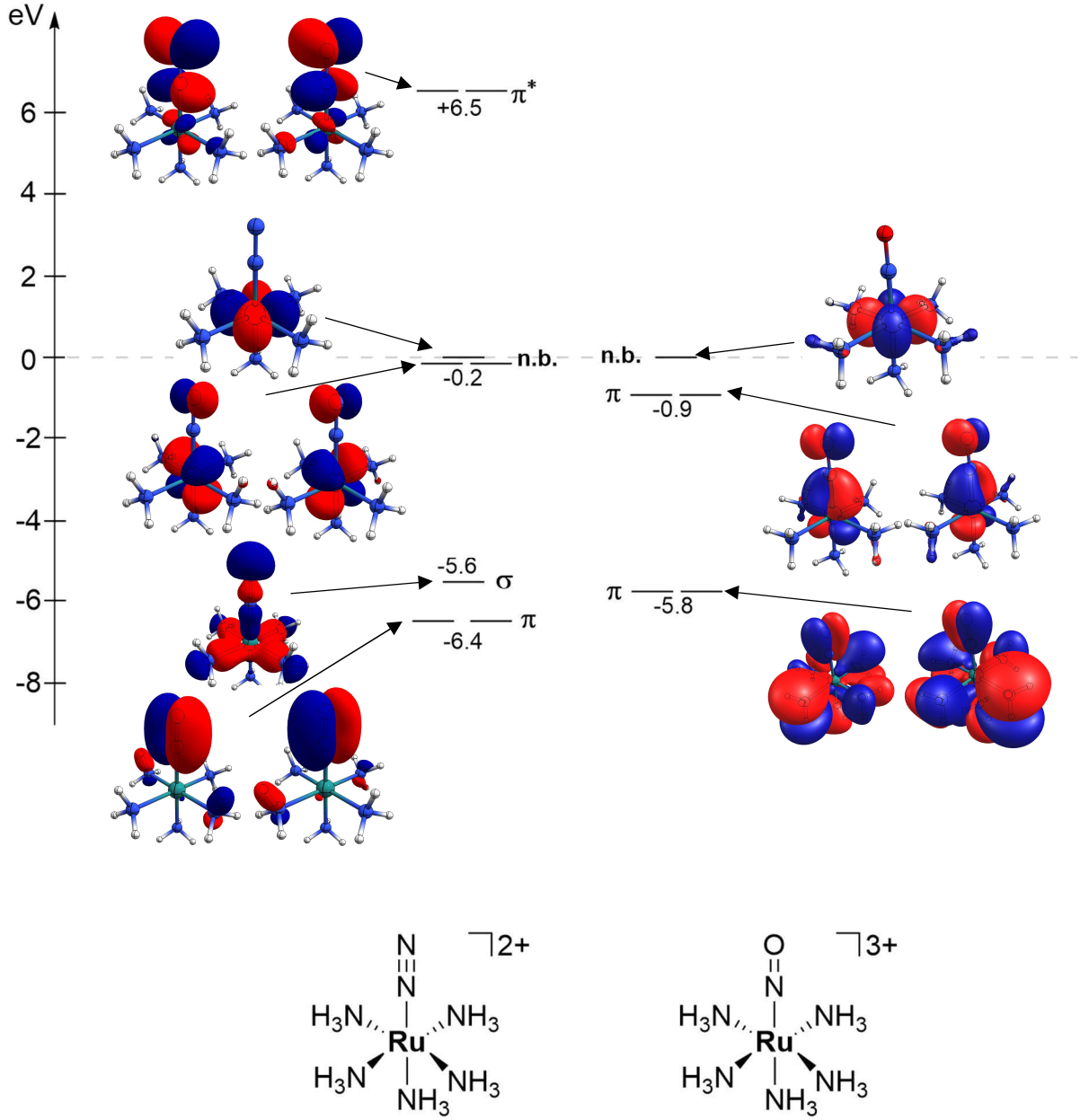

Figure 5.17: Schematic representation of selected molecular orbitals of $[Ru(NH_3)_5(N_2)]^{2+}$ and $[Ru(NH_3)_5(NO)]^{3+}$ (PBE0/def2-TZVP).

From the calculated MO's it can be derived that the two-fold degenerate orbitals, which represent the π-backbonding interaction are very close in energy (–0.2 eV) to the metal-centered d_{xy} MO and therefore essentially non-bonding, as apparent from the nodal-plane through the nitrogen atom bonding to the metal. For comparison, the MO's of the isoelectronic nitrosyl complex $[Ru(NH_3)_5(NO)]^{3+}$ were calculated on the same level of theory. The π-backbonding MO's are considerably lower in energy and can be considered bonding. This is well-represented by considerable contribution of the metal-bound nitrogen atom in this complex.

5.5 Crystallographic Appendix

X-ray Single-Crystal Structure Analysis of [(^{Ph}PNP)OsCl$_3$] (1)

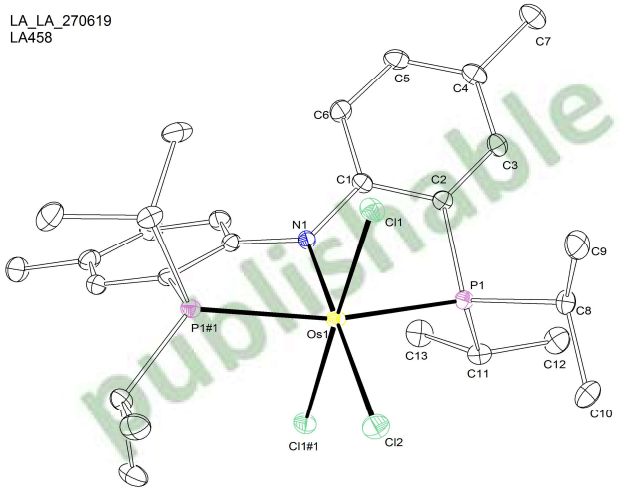

Figure 5.18: Thermal ellipsoid plot of [(^{Ph}PNP)OsCl$_3$] with the anisotropic displacement parameters drawn at the 50% probability level. The asymmetric unit contains only a half complex molecule.

Table 5.12: Crystal data and structure refinement for [(^{Ph}PNP)OsCl$_3$].

Identification code	mo_LA_LA_270619_0m_a	
Empirical formula	$C_{26}H_{40}Cl_3NOsP_2$	
Formula weight	725.08	
Temperature	101(2) K	
Wavelength	0.71073 Å	
Crystal system	Monoclinic	
Space group	P2/n	
Unit cell dimensions	a = 11.1838(5) Å	α= 90°
	b = 9.5444(4) Å	β= 100.430(2)°
	c = 13.0835(6) Å	γ = 90°
Volume	1373.49(11) Å^3	
Z	2	
Density (calculated)	1.753 Mg/m^3	
Absorption coefficient	5.067 mm^{-1}	
F(000)	720	
Crystal size	0.155 x 0.071 x 0.051 mm^3	
Crystal shape and color	Block,	clear intense brown
Theta range for data collection	2.207 to 28.373°	
Index ranges	-14<=h<=14, -12<=k<=12, -17<=l<=17	
Reflections collected	43967	
Independent reflections	3441 [R (int) = 0.0335]	
Completeness to theta = 25.242°	100.0 %	
Refinement method	Full-matrix least-squares on F^2	

Data / restraints / parameters	3441 / 0 / 156	
Goodness-of-fit on F^2	1.126	
Final R indices [I>2sigma(I)]	R1 = 0.0150,	wR2 = 0.0353
R indices (all data)	R1 = 0.0176,	wR2 = 0.0368
Largest diff. peak and hole	1.482 and -0.556 eÅ^{-3}	

X-ray Single-Crystal Structure Analysis of [((^{Py}PNP)OsCl$_2$)$_2$(μ-N$_2$)] (3)

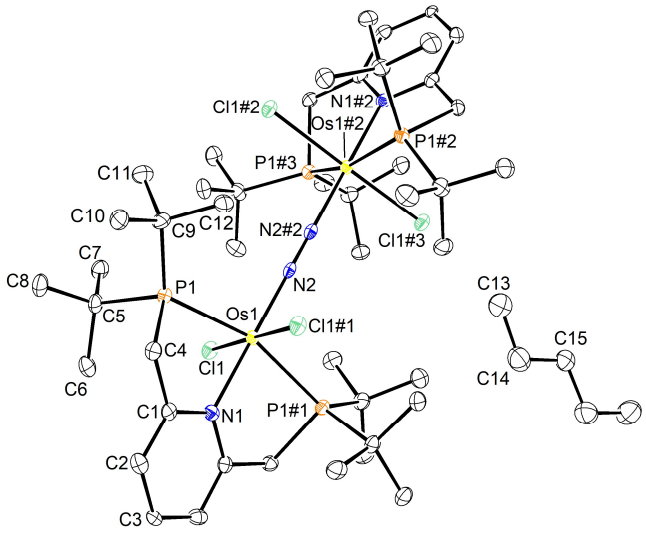

Figure 5.19: Thermal ellipsoid plot of [((^{Py}PNP)OsCl$_2$)$_2$(μ-N$_2$)] with the anisotropic displacement parameters drawn at the 50% probability level. The asymmetric unit contains a quarter complex molecule and half a pentane solvent molecule.

Table 5.13: Crystal data and structure refinement for [((^{Py}PNP)OsCl$_2$)$_2$(μ-N$_2$)].

Identification code	mo_LA_LA_131219_0m_a (LA784)	
Empirical formula	$C_{56}H_{110}Cl_4N_4Os_2P_4$	
Formula weight	1485.55	
Temperature	100(2) K	
Wavelength	0.71073 Å	
Crystal system	Tetragonal	
Space group	$I4_1/a$	
Unit cell dimensions	a = 12.4027(6) Å	α= 90°
	b = 12.4027(6) Å	β= 90°
	c = 42.496(3) Å	γ = 90°
Volume	6537.0(8) Å^3	
Z	4	
Density (calculated)	1.509 Mg/m^3	
Absorption coefficient	4.182 mm^{-1}	
F(000)	3016	
Crystal size	0.242 x 0.241 x 0.142 mm^3	
Crystal shape and color	block,	clear intense red
Theta range for data collection	2.183 to 30.582°	

Index ranges	-17<=h<=17, -17<=k<=17, -60<=l<=60	
Reflections collected	138892	
Independent reflections	5025 [R(int) = 0.1142]	
Completeness to theta = 25.242°	99.9 %	
Refinement method	Full-matrix least-squares on F^2	
Data / restraints / parameters	5025 / 0 / 168	
Goodness-of-fit on F^2	0.834	
Final R indices [I>2sigma(I)]	R1 = 0.0298,	wR2 = 0.0597
R indices (all data)	R1 = 0.0563,	wR2 = 0.0721
Largest diff. peak and hole	0.979 and -0.672 eÅ^{-3}	

X-ray Single-Crystal Structure Analysis of [(^{Py}PNP)OsCl$_2$OTf] (6)

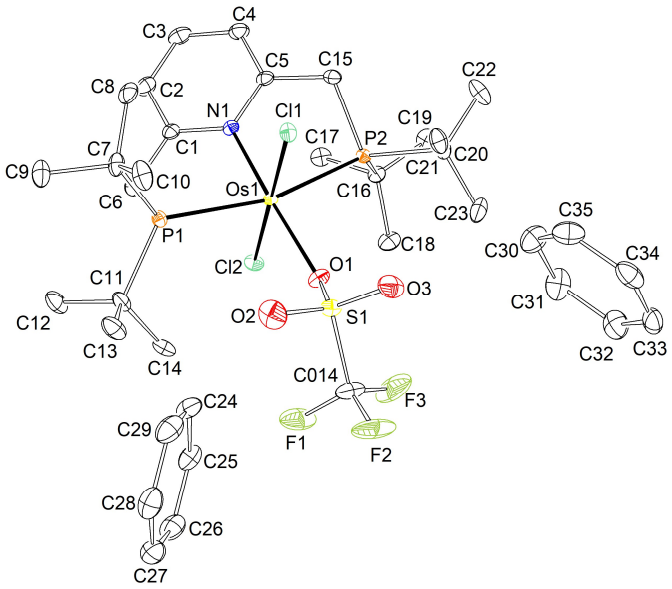

Figure 5.20: Thermal ellipsoid plot of [(^{Py}PNP)OsCl$_2$OTf] with the anisotropic displacement parameters drawn at the 50% probability level. The asymmetric unit contains one complex molecule and two benzene solvent molecules.

Table 5.14: Crystal data and structure refinement for [(^{Py}PNP)OsCl$_2$OTf].

Identification code	mo_LA_LA_090320_0m_a	
Empirical formula	$C_{36}H_{55}Cl_2F_3NO_3OsP_2S$	
Formula weight	961.91	
Temperature	100(2) K	
Wavelength	0.71073 Å	
Crystal system	Triclinic	
Space group	P-1	
Unit cell dimensions	a = 12.2039(7) Å	α= 97.740(3)°
	b = 13.3746(8) Å	β= 111.389(3)°
	c = 14.3517(9) Å	γ = 107.508(3)°
Volume	1999.8(2) Å^3	

Z	2	
Density (calculated)	1.597 Mg/m^3	
Absorption coefficient	3.503 mm^{-1}	
F(000)	970	
Crystal size	0.872 x 0.474 x 0.216 mm^3	
Crystal shape and color	block,	clear intense orange
Theta range for data collection	2.324 to 26.372°	
Index ranges	-15<=h<=15, -16<=k<=16, -17<=l<=17	
Reflections collected	110180	
Independent reflections	8167 [R(int) = 0.0905]	
Completeness to theta = 25.242°	99.9 %	
Refinement method	Full-matrix least-squares on F^2	
Data / restraints / parameters	8167 / 0 / 454	
Goodness-of-fit on F^2	0.847	
Final R indices [I>2sigma(I)]	R1 = 0.0240,	wR2 = 0.0594
R indices (all data)	R1 = 0.0289,	wR2 = 0.0636
Largest diff. peak and hole	1.276 and -1.327 eÅ^{-3}	

X-ray Single-Crystal Structure Analysis of [(^{Py}PNPN)OsCl$_3$] (8)

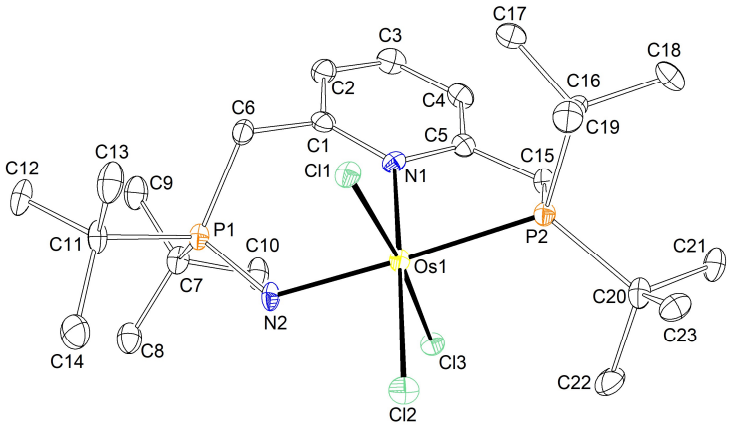

Figure 5.21: Thermal ellipsoid plot of [(^{Py}PNPN)OsCl$_3$] with the anisotropic displacement parameters drawn at the 50% probability level. The asymmetric unit contains one disordered complex molecule.

Table 5.15: Crystal data and structure refinement for [(^{Py}PNPN)OsCl$_3$].

Identification code	SJKF_LA_03062020_a	
Empirical formula	$C_{23}H_{43}Cl_3N_2OsP_2$	
Formula weight	706.08	
Temperature	100(2) K	
Wavelength	0.71073 Å	
Crystal system	Monoclinic	
Space group	$P2_1/c$	
Unit cell dimensions	a = 15.1185(12) Å	α= 90°
	b = 13.3487(10) Å	β= 111.083(4)°

	c = 14.7724(12) Å	γ = 90°
Volume	2781.7(4) Å^3	
Z	4	
Density (calculated)	1.686 Mg/m^3	
Absorption coefficient	5.002 mm^{-1}	
F(000)	1408	
Crystal size	0.458 x 0.291 x 0.214 mm^3	
Crystal shape and color	block,	clear intense brown
Theta range for data collection	2.250 to 25.121°	
Index ranges	-18<=h<=18, -15<=k<=15, -17<=l<=17	
Reflections collected	93405	
Independent reflections	4960 [R(int) = 0.0762]	
Completeness to theta = 25.121°	99.9 %	
Refinement method	Full-matrix least-squares on F^2	
Data / restraints / parameters	4960 / 0 / 292	
Goodness-of-fit on F^2	1.089	
Final R indices [I>2sigma(I)]	R1 = 0.0281,	wR2 = 0.0584
R indices (all data)	R1 = 0.0387,	wR2 = 0.0660
Largest diff. peak and hole	2.596 and -1.263 eÅ^{-3}	

X-ray Single-Crystal Structure Analysis of [(^{Ph}PNP)ReCl$_3$] (9)

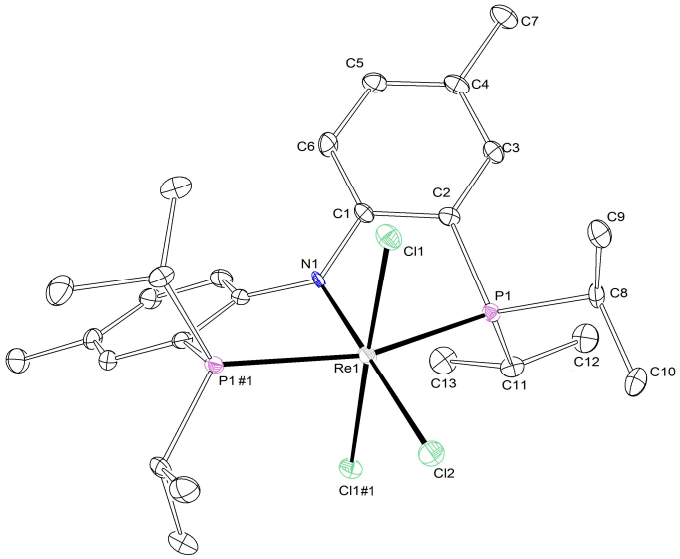

Figure 5.22: Thermal ellipsoid plot of [(^{Ph}PNP)ReCl$_3$] with the anisotropic displacement parameters drawn at the 50% probability level. The asymmetric unit contains only a half complex molecule.

Table 5.16: Crystal data and structure refinement for [(^{Ph}PNP)ReCl$_3$].

Identification code	mo_LA_LA_240619_0m_a
Empirical formula	$C_{26}H_{40}Cl_3NP_2Re$
Formula weight	721.08
Temperature	100(2) K

Wavelength	0.71073 Å	
Crystal system	Monoclinic	
Space group	P2/n	
Unit cell dimensions	a = 11.2602(7) Å	α= 90°
	b = 9.5880(6) Å	β= 99.940(2)°
	c = 13.0629(8) Å	γ = 90°
Volume	1389.14(15) $Å^3$	
Z	2	
Density (calculated)	1.724 Mg/m^3	
Absorption coefficient	4.794 mm^{-1}	
F(000)	718	
Crystal size	0.533 x 0.284 x 0.238 mm^3	
Crystal shape and color	Plate,	clear intense brown
Theta range for data collection	2.208 to 26.490°	
Index ranges	-14<=h<=14, -12<=k<=12, -16<=l<=16	
Reflections collected	59231	
Independent reflections	2874 [R(int) = 0.0776]	
Completeness to theta = 25.242°	100.0 %	
Refinement method	Full-matrix least-squares on F^2	
Data / restraints / parameters	2874 / 0 / 156	
Goodness-of-fit on F^2	1.097	
Final R indices [I>2sigma(I)]	R1 = 0.0198,	wR2 = 0.0431
R indices (all data)	R1 = 0.0262,	wR2 = 0.0456
Largest diff. peak and hole	1.232 and -0.964 $eÅ^{-3}$	

X-ray Single-Crystal Structure Analysis of [(^{Ph}PNP)$ReCl_3$][BF_4] (10^+)

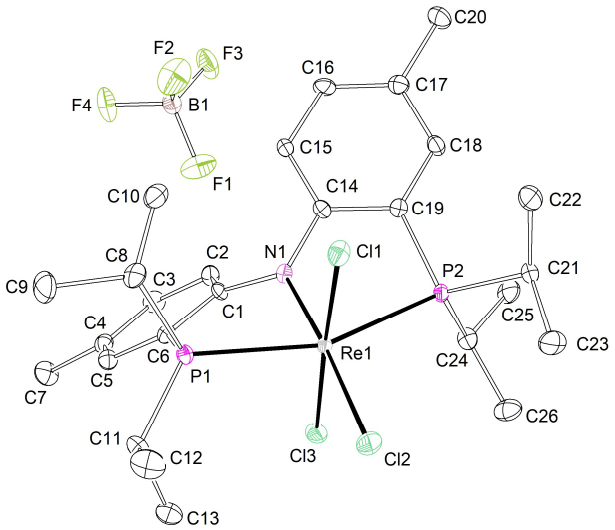

Figure 5.23: Thermal ellipsoid plot of [(^{Ph}PNP)$ReCl_3$][BF_4] with the anisotropic displacement parameters drawn at the 50% probability level. The asymmetric unit contains one complex molecule and one BF_4 anion. The solvent molecule (acetonitrile) was removed using the SQUEEZE procedure. The reflections 1 0 7, -3 3 9, 1 0 4, -4 0 3, -1 0 3, 1 3 0, -2 -6 2, -2 -3 1, 1 0 2, -3 -3 1, 1 3 6, -2 0 2, -1 11 1, 2 -6 4, 0 3 7, -6 -3 4, 6 -3 4, 6 8 5, 0 11 0, 3 11 8, -2 -3 3, 5 0 7, 4 0 5 and 1 -3 5 are removed from the refinement using the OMIT commands.

Table 5.17: Crystal data and structure refinement for of [(^{Ph}PNP)$ReCl_3$][BF_4].

Identification code	mo_LA_040321_LA_2 (PNPReCl3BF4)	
Empirical formula	$C_{26}H_{40}BCl_3F_4NP_2Re$	
Formula weight	807.89	
Temperature	100(2) K	
Wavelength	0.71073 Å	
Crystal system	Triclinic	
Space group	P-1	
Unit cell dimensions	a = 8.0525(3) Å	α= 81.7380(10)°
	b = 12.9984(4) Å	β= 89.8810(10)°
	c = 16.0529(5) Å	γ = 89.9440(10)°
Volume	1662.81(10) Å^3	
Z	2	
Density (calculated)	1.614 Mg/m^3	
Absorption coefficient	4.031 mm^{-1}	
F(000)	800	
Crystal size	0.096 x 0.184 x 0.482 mm^3	
Crystal shape and color	block,	clear intense purple
Theta range for data collection	2.176 to 26.371°.	
Index ranges	-10<=h<=10, -16<=k<=16, -20<=l<=20	
Reflections collected	95477	
Independent reflections	6742 [R(int) = 0.0347]	
Completeness to theta = 25.242°	99.3 %	
Refinement method	Full-matrix least-squares on F^2	
Data / restraints / parameters	6742 / 0 / 353	
Goodness-of-fit on F^2	1.303	
Final R indices [I>2sigma(I)]	R1 = 0.0285,	wR2 = 0.0762
R indices (all data)	R1 = 0.0285,	wR2 = 0.0762
Largest diff. peak and hole	1.655 and -2.410 eÅ^{-3}	

X-ray Single-Crystal Structure Analysis of *cis*-[(^{Ph}PNP)Re(CO)Cl$_2$]

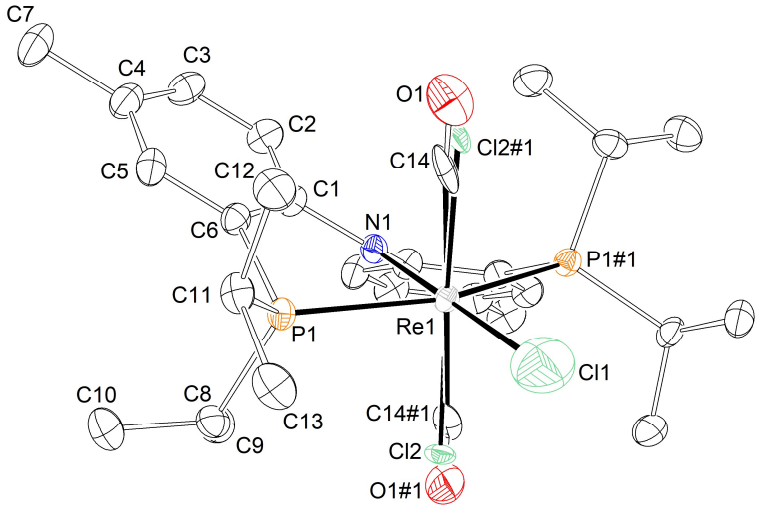

Figure 5.24: Thermal ellipsoid plot of *cis*-[(^{Ph}PNP)Re(CO)Cl$_2$] with the anisotropic displacement parameters drawn at the 50% probability level. The asymmetric unit contains only a half complex molecule. The CO moiety was refined with some restraints (RIGU).

Table 5.18: Crystal data and structure refinement for *cis*-[(^{Ph}PNP)Re(CO)Cl$_2$].

Identification code	t4_a	
Empirical formula	$C_{27}H_{40}Cl_2NOP_2Re$	
Formula weight	713.64	
Temperature	100(2) K	
Wavelength	0.71073 Å	
Crystal system	Monoclinic	
Space group	P2/n	
Unit cell dimensions	a = 11.273(4) Å	α= 90°
	b = 9.701(4) Å	β= 100.128(10)°
	c = 13.094(4) Å	γ = 90°
Volume	1409.6(8) Å^3	
Z	2	
Density (calculated)	1.681 Mg/m^3	
Absorption coefficient	4.634 mm^{-1}	
F(000)	712	
Crystal size	0.435 x 0.230 x 0.163 mm^3	
Crystal color and shape	block,	clear intense purple
Theta range for data collection	2.099 to 28.425°	
Index ranges	-15<=h<=15, -12<=k<=12, -17<=l<=17	
Reflections collected	48777	
Independent reflections	3526 [R(int) = 0.0904]	
Completeness to theta = 25.242°	100.0 %	
Refinement method	Full-matrix least-squares on F^2	
Data / restraints / parameters	3526 / 5 / 174	
Goodness-of-fit on F^2	0.975	

Final R indices [I>2sigma(I)]	R1 = 0.0320,	wR2 = 0.0754
R indices (all data)	R1 = 0.0387,	wR2 = 0.0793
Largest diff. peak and hole	2.155 and -1.868 eÅ^{-3}	

X-ray Single-Crystal Structure Analysis of *trans*-[(^{Ph}PNP)ReCl$_2$(py)] (*trans*-13)

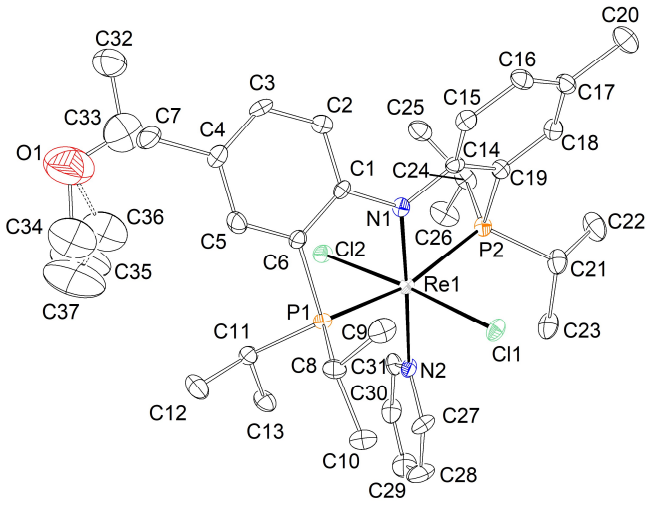

Figure 5.25: Thermal ellipsoid plot of *trans*-[(^{Ph}PNP)ReCl$_2$(py)] with the anisotropic displacement parameters drawn at the 50% probability level. The asymmetric unit contains one complex molecule and one disorder diethylether solvent molecule. The disordered solvent molecule was refined with population of 0.50 on the main domain using some restraints and constraints (SADI, EADP).

Table 5.19: Crystal data and structure refinement for *trans*-[(^{Ph}PNP)ReCl$_2$(py)].

Identification code	t5_a_pl	
Empirical formula	$C_{35}H_{55}Cl_2N_2OP_2Re$	
Formula weight	838.27	
Temperature	100(2) K	
Wavelength	0.71073 Å	
Crystal system	Orthorhombic	
Space group	Pbca	
Unit cell dimensions	a = 18.005(5) Å	α= 90°
	b = 17.044(6) Å	β= 90°
	c = 24.784(9) Å	γ = 90°
Volume	7606(4) Å^3	
Z	4	
Density (calculated)	1.464 Mg/m^3	
Absorption coefficient	3.448 mm^{-1}	
F(000)	3404	
Crystal size	0.156 x 0.178 x 0.351 mm^3	
Crystal shape and color	block,	clear intense red
Theta range for data collection	1.839 to 25.349°	
Index ranges	-21<=h<=21, -20<=k<=20, -29<=l<=29	

Reflections collected	209254	
Independent reflections	6966 [R(int) = 0.1649]	
Completeness to theta = 25.242°	100.0 %	
Refinement method	Full-matrix least-squares on F^2	
Data / restraints / parameters	6966 / 1 / 408	
Goodness-of-fit on F^2	1.009	
Final R indices [I>2sigma(I)]	R1 = 0.0304,	wR2 = 0.0556
R indices (all data)	R1 = 0.0517,	wR2 = 0.0625
Largest diff. peak and hole	1.028 and -1.008 eÅ^{-3}	

X-ray Single-Crystal Structure Analysis of [(^{Ph}PNP)Re(N)Cl] (15)

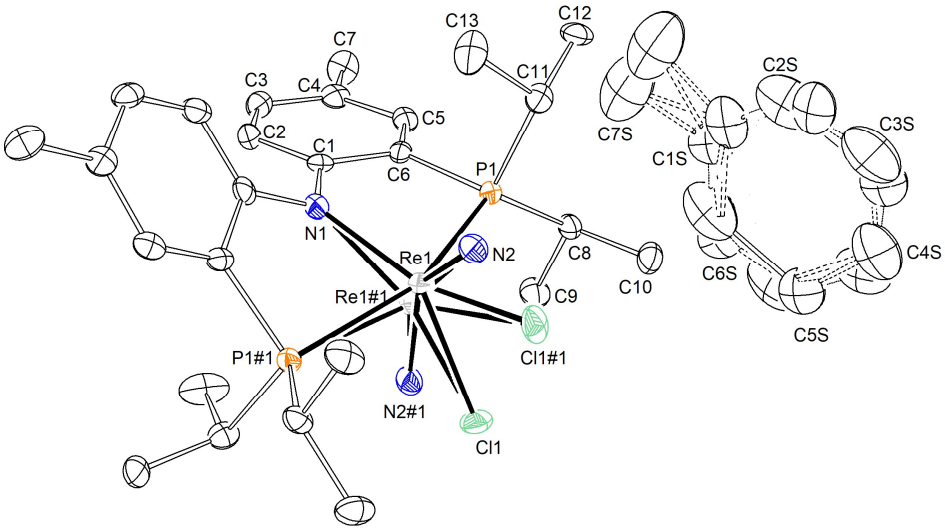

Figure 5.26: Thermal ellipsoid plot of [(^{Ph}PNP)Re(N)Cl] with the anisotropic displacement parameters drawn at the 50% probability level. The asymmetric unit contains only a half complex molecule and half toluene solvent molecule.

Table 5.20: Crystal data and structure refinement for [(^{Ph}PNP)Re(N)Cl].

Identification code	mo_SJKF_LA_16062020_0m_a	
Empirical formula	$C_{33}H_{48}ClN_2P_2Re$	
Formula weight	756.32	
Temperature	100(2) K	
Wavelength	0.71073 Å	
Crystal system	Monoclinic	
Space group	P2/n	
Unit cell dimensions	a = 11.514(13) Å	α= 90°
	b = 9.631(2) Å	β= 91.860(3)°
	c = 14.714(3) Å	γ = 90°
Volume	1630.6(2) Å^3	
Z	2	
Density (calculated)	1.540 Mg/m^3	

Absorption coefficient	3.931 mm^{-1}	
F(000)	764	
Crystal size	0.396 x 0.248 x 0.203 mm^3	
Crystal shape and color	block,	clear intense orange
Theta range for data collection	2.211 to 27.963°	
Index ranges	-14<=h<=15, -12<=k<=12, -19<=l<=19	
Reflections collected	69817	
Independent reflections	3915 [R(int) = 0.1155]	
Completeness to theta = 25.242°	100.0 %	
Refinement method	Full-matrix least-squares on F^2	
Data / restraints / parameters	3915 / 122 / 228	
Goodness-of-fit on F^2	1.118	
Final R indices [I>2sigma(I)]	R1 = 0.0401,	wR2 = 0.0588
R indices (all data)	R1 = 0.0619,	wR2 = 0.0639
Largest diff. peak and hole	0.573 and -0.488 $eÅ^{-3}$	

X-ray Single-Crystal Structure Analysis of [(^{Ph}PNP)ReBr$_3$] (16)

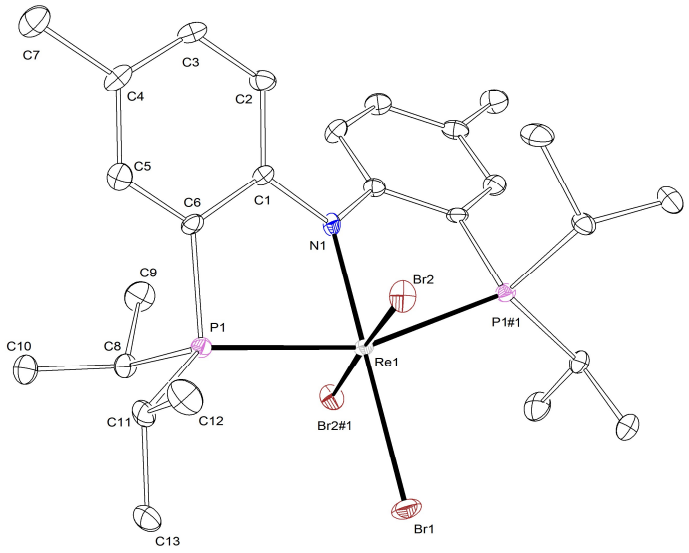

Figure 5.27: Thermal ellipsoid plot of [(^{Ph}PNP)ReBr$_3$] with the anisotropic displacement parameters drawn at the 50% probability level. The asymmetric unit contains only half a complex molecule.

Table 5.21: Crystal data and structure refinement for [(^{Ph}PNP)ReBr$_3$].

Identification code	mo_LA_LA_211119_2
Empirical formula	$C_{26}H_{40}Br_3NP_2Re$
Formula weight	854.46
Temperature	100(2) K
Wavelength	0.71073 Å
Crystal system	Monoclinic
Space group	P2/n

Unit cell dimensions	a = 11.3558(6) Å	α= 90°
	b = 9.7363(6) Å	β= 100.192(2)°
	c = 13.3823(7) Å	γ = 90°
Volume	1456.25(14) Å^3	
Z	2	
Density (calculated)	1.949 Mg/m^3	
Absorption coefficient	8.414 mm^{-1}	
F(000)	826	
Crystal size	0.407 x 0.197 x 0.170 mm^3	
Crystal shape and color	block,	clear intense green
Theta range for data collection	2.590 to 30.616°	
Index ranges	-16<=h<=16, -13<=k<=13, -19<=l<=19	
Reflections collected	77966	
Independent reflections	4489 [R(int) = 0.0986]	
Completeness to theta = 25.242°	99.9 %	
Refinement method	Full-matrix least-squares on F^2	
Data / restraints / parameters	4489 / 0 / 156	
Goodness-of-fit on F^2	1.046	
Final R indices [I>2sigma(I)]	R1 = 0.0281, wR2 = 0.0496	
R indices (all data)	R1 = 0.0466, wR2 = 0.0562	
Largest diff. peak and hole	1.700 and -1.368 eÅ^{-3}	

X-ray Single-Crystal Structure Analysis of [(^{Ph}PNP)ReI$_3$] (18)

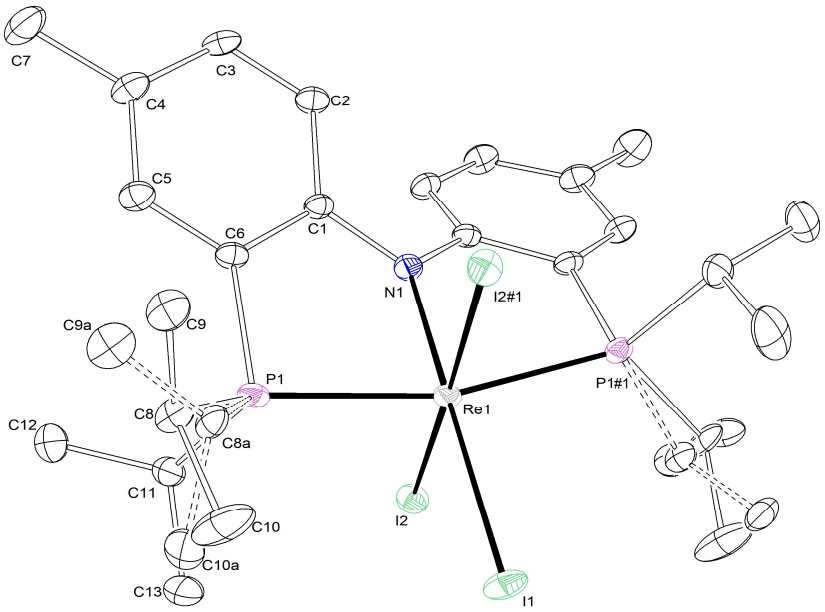

Figure 5.28: Thermal ellipsoid plot of [(^{Ph}PNP)ReI$_3$] with the anisotropic displacement parameters drawn at the 50% probability level. The asymmetric unit contains only a half disordered complex molecule. The disordered complex molecule was refined with population of 0.51 on the main domain.

Table 5.22: Crystal data and structure refinement for [(^{Ph}PNP)ReI$_3$].

Identification code	mo_LA_LA_211119_0m_a	
Empirical formula	$C_{26}H_{40}I_3NP_2Re$	
Formula weight	995.43	
Temperature	100(2) K	
Wavelength	0.71073 Å	
Crystal system	Monoclinic	
Space group	C2/c	
Unit cell dimensions	a = 15.3083(8) Å	α= 90°
	b = 10.5073(5) Å	β= 92.353(2)°
	c = 18.7392(10) Å	γ = 90°
Volume	3011.6(3) Å^3	
Z	4	
Density (calculated)	2.195 Mg/m^3	
Absorption coefficient	7.232 mm^{-1}	
F(000)	1868	
Crystal size	0.412 x 0.315 x 0.228 mm^3	
Crystal shape and color	Block,	clear intense black
Theta range for data collection	2.352 to 31.617°	
Index ranges	-22<=h<=22, -15<=k<=15, -27<=l<=27	
Reflections collected	87738	
Independent reflections	5074 [R(int) = 0.0613]	
Completeness to theta = 25.242°	100.0 %	
Refinement method	Full-matrix least-squares on F^2	
Data / restraints / parameters	5074 / 0 / 186	
Goodness-of-fit on F^2	1.083	
Final R indices [I>2sigma(I)]	R1 = 0.0276,	wR2 = 0.0617
R indices (all data)	R1 = 0.0382,	wR2 = 0.0675
Largest diff. peak and hole	1.902 and -1.614 eÅ^{-3}	

X-ray Single-Crystal Structure Analysis of [(^{Ph}PNP)Re(N)I] (19)

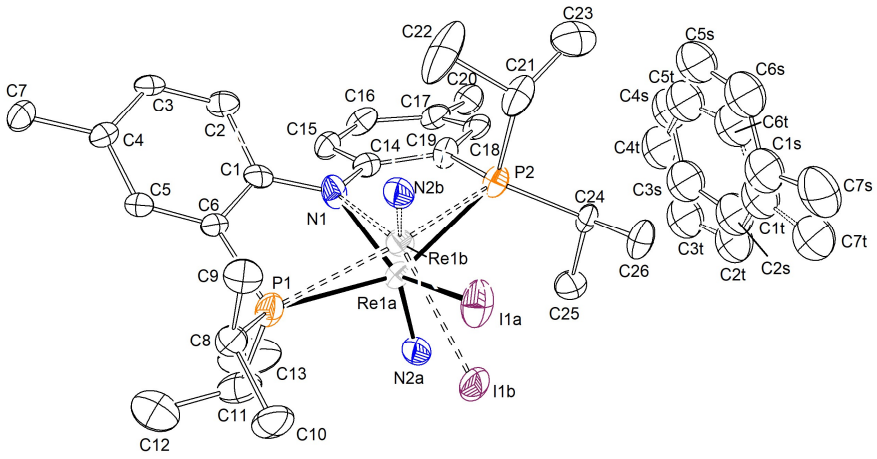

Figure 5.29: Thermal ellipsoid plot of [(^{Ph}PNP)Re(N)I] with the anisotropic displacement parameters drawn at the 50% probability level. The asymmetric unit contains one disordered complex molecule. The disordered complex molecule was refined with population of 0.628(6) on the main domain using some restraints and constraints (RIGU, SADI, EADP). The structure was refined as inversion twin using the twin law -100 0-10 00-1 (BASF: 0.49(2)). The SQUEEZE algorithm was used to omit a disordered toluene molecule from the refinement.

Table 5.23: Crystal data and structure refinement for [(^{Ph}PNP)Re(N)I].

Identification code	mo_LA_170221_LA_0m_b	
Empirical formula	$C_{33}H_{48}IN_2P_2Re$	
Formula weight	847.77	
Temperature	100(2) K	
Wavelength	0.71073 Å	
Crystal system	Orthorhombic	
Space group	$Pna2_1$	
Unit cell dimensions	a = 20.259(3) Å	α= 90°
	b = 14.608(2) Å	β= 90°
	c = 11.332(2) Å	γ = 90°
Volume	3353.6(9) Å^3	
Z	4	
Density (calculated)	1.498 Mg/m^3	
Absorption coefficient	4.663 mm^{-1}	
F(000)	1672	
Crystal size	0.232 x 0.208 x 0.160 mm^3	
Crystal shape and color	block,	clear intense orange
Theta range for data collection	2.012 to 30.555°.	
Index ranges	-28<=h<=28, -20<=k<=20, -16<=l<=16	
Reflections collected	127136	
Independent reflections	10285 [R(int) = 0.1283]	
Completeness to theta = 25.242°	100.0 %	
Refinement method	Full-matrix least-squares on F^2	
Data / restraints / parameters	10285 / 954 / 449	

Goodness-of-fit on F^2	1.104	
Final R indices [I>2sigma(I)]	R1 = 0.0556,	wR2 = 0.1039
R indices (all data)	R1 = 0.0858,	wR2 = 0.1175
Absolute structure parameter	0.47(2)	
Largest diff. peak and hole	1.068 and -1.099 eÅ^{-3}	

X-ray Single-Crystal Structure Analysis of [(^{Ph}PNP)Re(N)Cl][BF$_4$] (20$^+$)

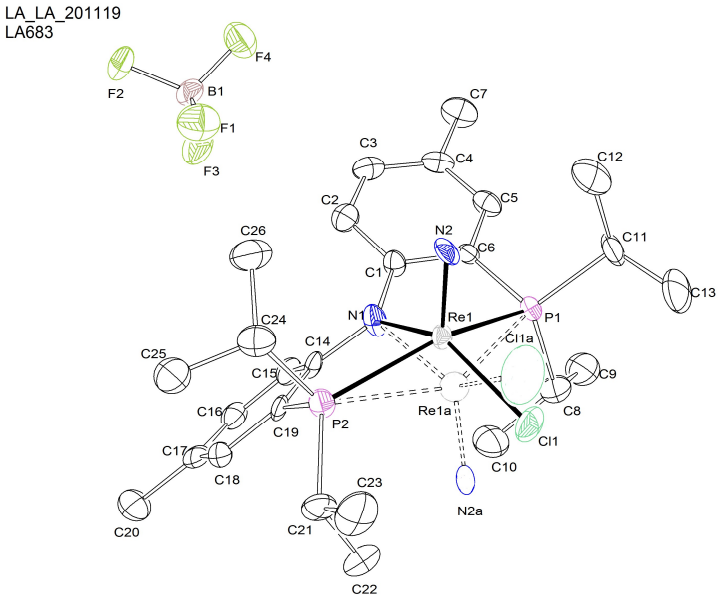

Figure 5.30: Thermal ellipsoid plot of [(^{Ph}PNP)Re(N)Cl][BF$_4$] with the anisotropic displacement parameters drawn at the 50% probability level. The asymmetric unit contains one disordered complex molecule and one BF$_4^-$ anion. The disordered complex molecule was refined with population of 0.850(2) on the main domain using some restraints (RIGU, SIMU, SADI).

Table 5.24: Crystal data and structure refinement for [(^{Ph}PNP)Re(N)Cl][BF$_4$].

Identification code	mo_LA_LA_201119_0m_a	
Empirical formula	$C_{26}H_{40}BClF_4N_2P_2Re$	
Formula weight	751.00	
Temperature	100(2) K	
Wavelength	0.71073 Å	
Crystal system	Orthorhombic	
Space group	Pbca	
Unit cell dimensions	a = 12.5787(6) Å	α= 90°
	b = 17.9177(7) Å	β= 90°
	c = 26.8153(11) Å	γ = 90°
Volume	6043.7(4) Å^3	
Z	8	
Density (calculated)	1.651 Mg/m^3	

Absorption coefficient	4.259 mm^{-1}	
F(000)	2984	
Crystal size	0.227 x 0.218 x 0.170 mm^3	
Crystal shape and color	Plate,	clear light red
Theta range for data collection	2.220 to 25.384°	
Index ranges	-15<=h<=15, -21<=k<=19, -32<=l<=32	
Reflections collected	59762	
Independent reflections	5546 [R(int) = 0.0719]	
Completeness to theta = 25.242°	99.9 %	
Refinement method	Full-matrix least-squares on F^2	
Data / restraints / parameters	5546 / 44 / 372	
Goodness-of-fit on F^2	1.292	
Final R indices [I>2sigma(I)]	R1 = 0.0539,	wR2 = 0.1174
R indices (all data)	R1 = 0.0629,	wR2 = 0.1206
Largest diff. peak and hole	1.667 and -1.922 $eÅ^{-3}$	

X-ray Single-Crystal Structure Analysis of [(^{Ph}PNP)Re(N)Cl][BF_4]

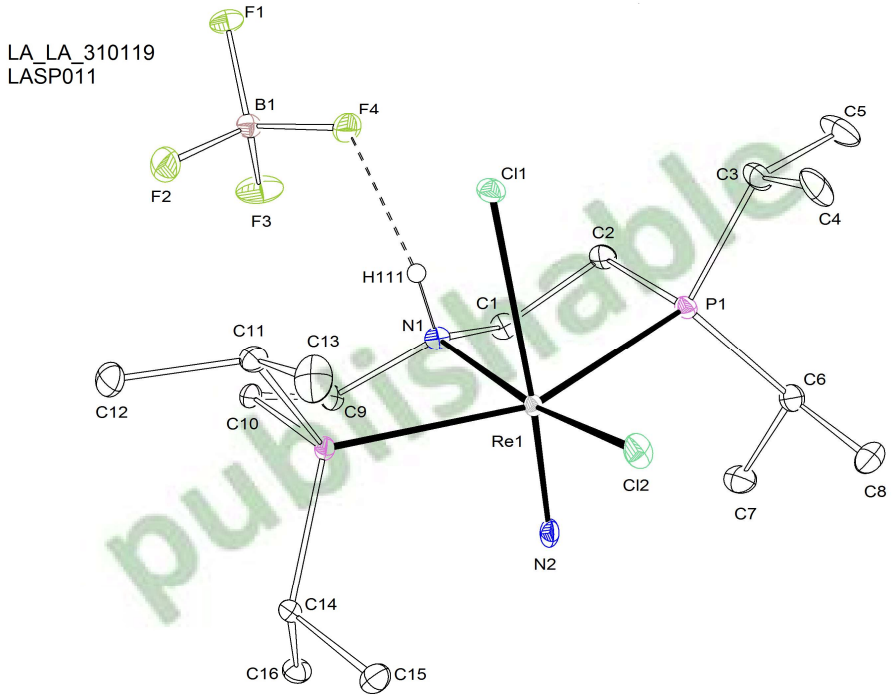

Figure 5.31: Thermal ellipsoid plot of [(^{Ph}PNP)Re(N)Cl][BF_4] with the anisotropic displacement parameters drawn at the 50% probability level. The asymmetric unit contains one complex molecule and one BF_4^- anion. The N-H hydrogen atom was found from the residual density map and isotropically refined.

Table 5.25: Crystal data and structure refinement for [(^{Ph}PNP)Re(N)Cl][BF_4].

Identification code	mo_LA_LA_310119_0m_a (LASP011)	
Empirical formula	$C_{16}H_{37}BCl_2F_4N_2P_2Re$	
Formula weight	663.32	
Temperature	100(2) K	
Wavelength	0.71073 Å	
Crystal system	Orthorhombic	
Space group	Pbca	
Unit cell dimensions	a = 11.4113(8) Å	α= 90°
	b = 14.7633(12) Å	β= 90°
	c = 29.129(2) Å	γ = 90°
Volume	4907.4(6) Å^3	
Z	8	
Density (calculated)	1.796 Mg/m^3	
Absorption coefficient	5.336 mm^{-1}	
F(000)	2616	
Crystal size	0.336 x 0.326 x 0.216 mm^3	
Crystal shape and color	Plate,	lustrous intense red
Theta range for data collection	2.267 to 28.385°	
Index ranges	-15<=h<=15, -19<=k<=19, -38<=l<=38	
Reflections collected	88243	
Independent reflections	6139 [R(int) = 0.0577]	
Completeness to theta = 25.242°	100.0 %	
Refinement method	Full-matrix least-squares on F^2	
Data / restraints / parameters	6139 / 0 / 265	
Goodness-of-fit on F^2	1.076	
Final R indices [I>2sigma(I)]	R1 = 0.0260,	wR2 = 0.0444
R indices (all data)	R1 = 0.0373,	wR2 = 0.0479
Largest diff. peak and hole	1.146 and -0.931 eÅ^{-3}	

X-ray Single-Crystal Structure Analysis of [(^{Ph}PNP)Re(NBArF$_{18}$)Cl] (21)

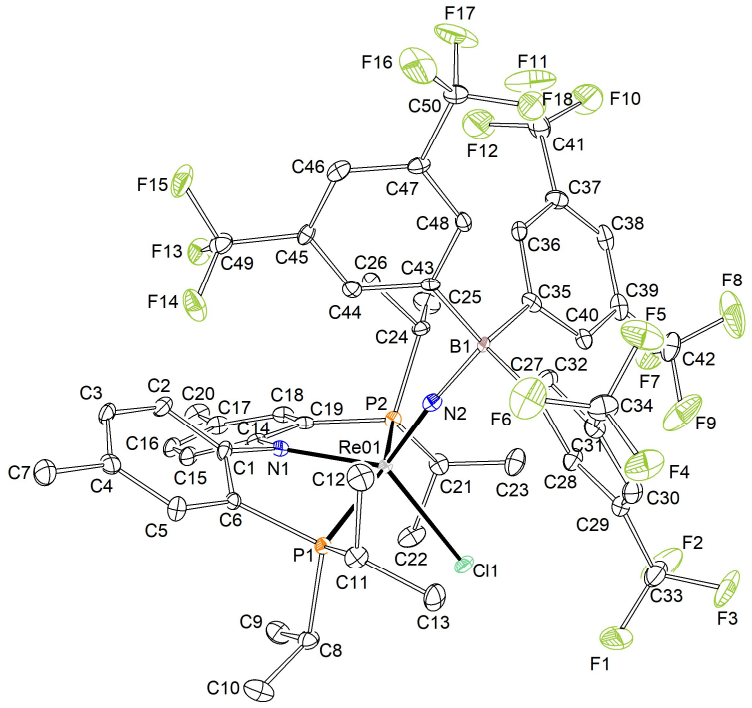

Figure 5.32: Thermal ellipsoid plot of [(^{Ph}PNP)Re(NBArF$_{18}$)Cl] with the anisotropic displacement parameters drawn at the 50% probability level. The asymmetric unit contains one complex molecule. The complex molecule was refined as an inversion twin using the twin law -1 0 0 0 -1 0 0 0 -1 and BASF 0.006(6). A disordered toluene solvent molecule was removed from refinement using the SQUEEZE algorithm. The reflections 0 0 4, 0 1 4, 0 2 0, 2 0 3 and 0 3 6 were omitted from the refinement using the OMIT command.

Table 5.26: Crystal data and structure refinement for [(^{Ph}PNP)Re(NBArF$_{18}$)Cl].

Identification code	mo_sjkf_la_23072020_0m_a	
Empirical formula	$C_{50}H_{49}BClF_{18}N_2P_2Re$	
Formula weight	1314.31	
Temperature	100(2) K	
Wavelength	0.71073 Å	
Crystal system	Orthorhombic	
Space group	$P2_12_12_1$	
Unit cell dimensions	a = 11.4620(18) Å	α= 90°
	b = 17.364(3) Å	β= 90°
	c = 28.535(4) Å	γ = 90°
Volume	5679.1(14) Å^3	
Z	4	
Density (calculated)	1.537 Mg/m^3	
Absorption coefficient	2.337 mm^{-1}	
F(000)	2608	
Crystal size	0.223 x 0.149 x 0.078 mm^3	
Crystal shape and color	block,	clear intense orange

Theta range for data collection	2.246 to 26.372°	
Index ranges	-12<=h<=14, -21<=k<=21, -35<=l<=35	
Reflections collected	164392	
Independent reflections	11576 [R(int) = 0.1220]	
Completeness to theta = 25.242°	99.8 %	
Refinement method	Full-matrix least-squares on F^2	
Data / restraints / parameters	11576 / 0 / 687	
Goodness-of-fit on F^2	1.017	
Final R indices [I>2sigma(I)]	R1 = 0.0283,	wR2 = 0.0578
R indices (all data)	R1 = 0.0364,	wR2 = 0.0604
Absolute structure parameter	0.006(6)	
Largest diff. peak and hole	0.523 and -0.728 eÅ^{-3}	

X-ray Single-Crystal Structure Analysis of *cis*-[($^{t\text{Bu}}$PNP)Re(CO)Cl$_2$]

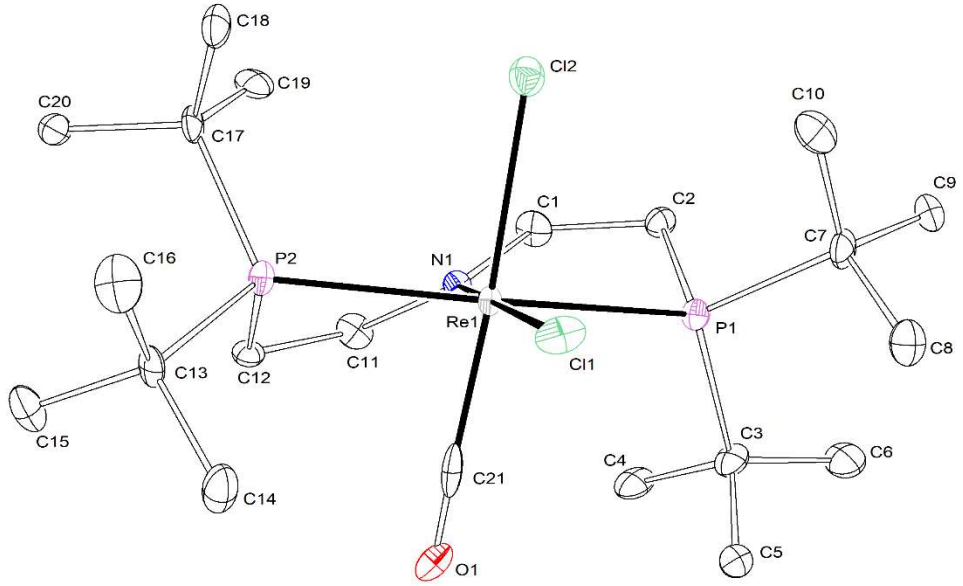

Figure 5.33: Thermal ellipsoid plot of *cis*-[($^{t\text{Bu}}$PNP)Re(CO)Cl$_2$] with the anisotropic displacement parameters drawn at the 50% probability level. The asymmetric unit contains one complex molecule.

Table 5.27: Crystal data and structure refinement for *cis*-[($^{t\text{Bu}}$PNP)Re(CO)Cl$_2$].

Identification code	mo_CW_LA_090517_2_0m_a (LA-B004K2)	
Empirical formula	$C_{21}H_{44}Cl_2NOP_2Re$	
Formula weight	645.61	
Temperature	100(2) K	
Wavelength	0.71073 Å	
Crystal system	Monoclinic	
Space group	C2/c	
Unit cell dimensions	a = 30.7099(14) Å	α= 90°
	b = 12.8064(6) Å	β= 111.463(2)°
	c = 14.2870(6) Å	γ = 90°

Volume	5229.2(4) Å^3	
Z	8	
Density (calculated)	1.640 Mg/m^3	
Absorption coefficient	4.987 mm^{-1}	
F(000)	2592	
Crystal size	0.180 x 0.120 x 0.052 mm^3	
Crystal shape and color	Plate,	clear intense green
Theta range for data collection	2.486 to 26.450°	
Index ranges	-38<=h<=38, -16<=k<=16, -17<=l<=17	
Reflections collected	88105	
Independent reflections	5382 [R(int) = 0.1671]	
Completeness to theta = 25.242°	99.9 %	
Refinement method	Full-matrix least-squares on F^2	
Data / restraints / parameters	5382 / 0 / 265	
Goodness-of-fit on F^2	1.037	
Final R indices [I>2sigma(I)]	R1 = 0.0371,	wR2 = 0.0626
R indices (all data)	R1 = 0.0607,	wR2 = 0.0681
Largest diff. peak and hole	1.436 and -1.305 eÅ^{-3}	

X-ray Single-Crystal Structure Analysis of *cis*-[(^{Ph}PNP)Re(NCO)Cl$_2$] (*cis*-24)

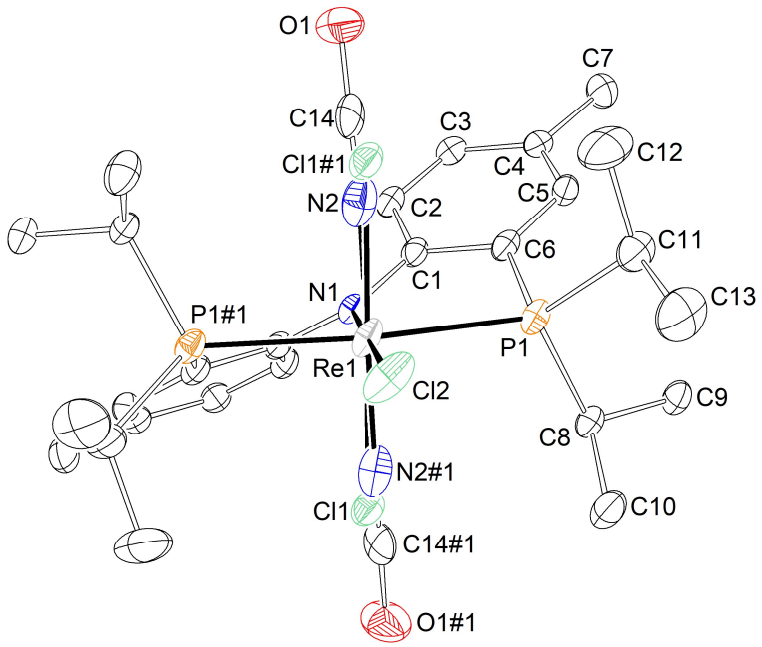

Figure 5.34: Thermal ellipsoid plot of *cis*-[(^{Ph}PNP)Re(NCO)Cl$_2$] with the anisotropic displacement parameters drawn at the 50% probability level. The asymmetric unit contains half a disordered complex molecule. The disordered complex molecule was refined with population of 0.50 on the main domain.

Table 5.28: Crystal data and structure refinement for *cis*-[(^{Ph}PNP)Re(NCO)Cl_2].

Identification code	mo_LA_220621_LA_0m_a (LA1455)	
Empirical formula	$C_{27}H_{40}Cl_2N_2OP_2Re$	
Formula weight	727.65	
Temperature	100(2) K	
Wavelength	0.71073 Å	
Crystal system	Monoclinic	
Space group	C2/c	
Unit cell dimensions	a = 15.4010(9) Å	α= 90°
	b = 9.8242(6) Å	β= 90.991(2)°
	c = 18.9417(11) Å	γ = 90°
Volume	2865.5(3) Å^3	
Z	4	
Density (calculated)	1.687 Mg/m^3	
Absorption coefficient	4.562 mm^{-1}	
F(000)	1452	
Crystal size	0.445 x 0.167 x 0.164 mm^3	
Crystal shape and color	block,	clear intense purple
Theta range for data collection	2.151 to 28.323°	
Index ranges	-20<=h<=20, -13<=k<=13, -25<=l<=25	
Reflections collected	44995	
Independent reflections	3570 [R(int) = 0.0398]	
Completeness to theta = 25.242°	100.0 %	
Refinement method	Full-matrix least-squares on F^2	
Data / restraints / parameters	3570 / 0 / 183	
Goodness-of-fit on F^2	1.295	
Final R indices [I>2sigma(I)]	R1 = 0.0240,	wR2 = 0.0496
R indices (all data)	R1 = 0.0253,	wR2 = 0.0499
Largest diff. peak and hole	1.409 and -2.191 eÅ^{-3}	

X-ray Single-Crystal Structure Analysis of *cis*-[(^{Ph}PNP)Re(NS)Cl$_2$] (*cis*-25)

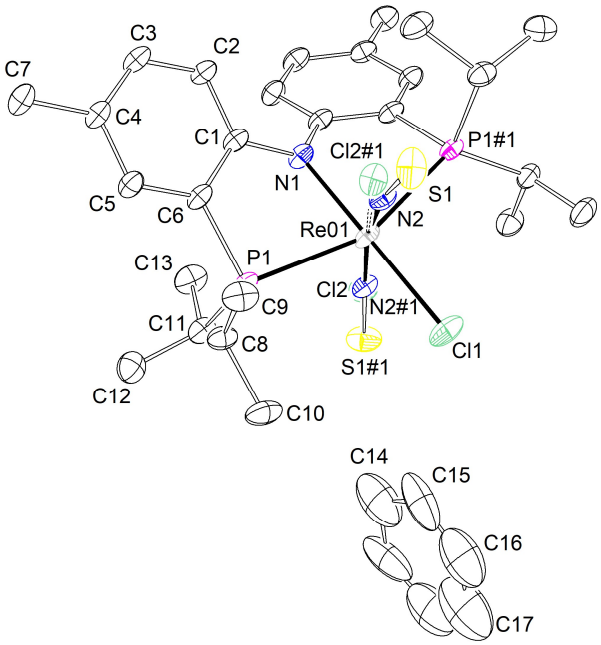

Figure 5.35: Thermal ellipsoid plot of *cis*-[(^{Ph}PNP)Re(NS)Cl$_2$] with the anisotropic displacement parameters drawn at the 50% probability level. The asymmetric unit contains half a disordered complex molecule. The disordered complex molecule was refined with population of 0.50 on the main domain using PART commands. The reflection 1 1 0 was omitted from the refinement using the OMIT command.

Table 5.29: Crystal data and structure refinement for *cis*-[(^{Ph}PNP)Re(NS)Cl$_2$].

Identification code	mo_LA_160621_LA_0m_a	
Empirical formula	$C_{32}H_{46}Cl_2N_2P_2ReS$	
Formula weight	809.81	
Temperature	100(2) K	
Wavelength	0.71073 Å	
Crystal system	Orthorhombic	
Space group	Pccn	
Unit cell dimensions	a = 11.3995(7) Å	α= 90°
	b = 14.8087(9) Å	β= 90°
	c = 20.1670(12) Å	γ = 90°
Volume	3404.4(4) Å^3	
Z	4	
Density (calculated)	1.580 Mg/m^3	
Absorption coefficient	3.906 mm^{-1}	
F(000)	1628	
Crystal size	0.992 x 0.704 x 0.422 mm^3	
Crystal shape and color	block,	clear intense green
Theta range for data collection	2.020 to 33.249°.	
Index ranges	-17<=h<=17, -22<=k<=22, -31<=l<=31	

Reflections collected	167652
Independent reflections	6547 [R(int) = 0.0802]
Completeness to theta = 25.242°	99.9 %
Refinement method	Full-matrix least-squares on F^2
Data / restraints / parameters	6547 / 15 / 202
Goodness-of-fit on F^2	1.250
Final R indices [I>2sigma(I)]	R1 = 0.0433, wR2 = 0.0953
R indices (all data)	R1 = 0.0544, wR2 = 0.1015
Largest diff. peak and hole	1.816 and -1.959 eÅ^{-3}

X-ray Single-Crystal Structure Analysis of [(^{Ph}PNP)Re(NO)$_2$Cl] (26)

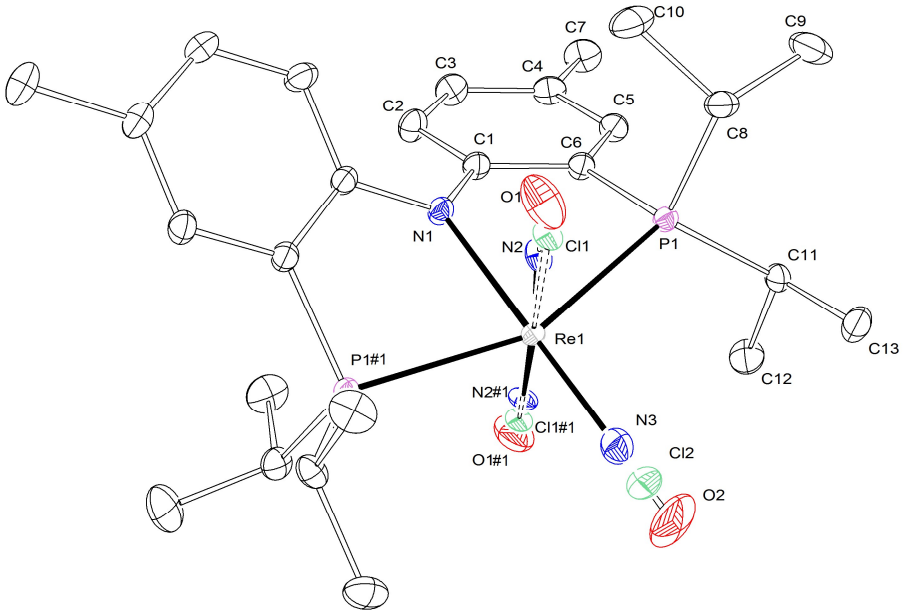

Figure 5.36: Thermal ellipsoid plot of [(^{Ph}PNP)Re(NO)$_2$Cl] with the anisotropic displacement parameters drawn at the 50% probability level. The asymmetric unit contains only a half disordered complex molecule. The disordered complex was refined with occupation factors of 0.75 for N(2)-O(1), 0.6 for Cl(1), 0.5 for N(3)-O(2) and 0.2 for Cl(2).

Table 5.30: Crystal data and structure refinement for [(^{Ph}PNP)Re(NO)$_2$Cl].

Identification code	SJKF_LA_12082020_0m_a (LA999)	
Empirical formula	$C_{26}H_{40}Cl_{1.14}N_{2.78}O_{1.78}P_2Re$	
Formula weight	708.38	
Temperature	100(2) K	
Wavelength	0.71073 Å	
Crystal system	Monoclinic	
Space group	P2/n	
Unit cell dimensions	a = 11.1999(13) Å	α= 90°
	b = 9.7936(11) Å	β= 100.646(5)°

	c = 13.0179(15) Å	γ = 90°
Volume	1403.3(3) Å^3	
Z	2	
Density (calculated)	1.676 Mg/m^3	
Absorption coefficient	4.579 mm^{-1}	
F(000)	708	
Crystal size	0.757 x 0.253 x 0.184 mm^3	
Crystal shape and color	Block,	clear intense green orange
Theta range for data collection	2.207 to 33.517°	
Index ranges	-17<=h<=17, -15<=k<=15, -20<=l<=20	
Reflections collected	123543	
Independent reflections	5474 [R(int) = 0.1034]	
Completeness to theta = 25.242°	100.0 %	
Refinement method	Full-matrix least-squares on F^2	
Data / restraints / parameters	5474 / 0 / 185	
Goodness-of-fit on F^2	1.053	
Final R indices [I>2sigma(I)]	R1 = 0.0250,	wR2 = 0.0507
R indices (all data)	R1 = 0.0320,	wR2 = 0.0528
Largest diff. peak and hole	1.509 and -1.709 eÅ^{-3}	

X-ray Single-Crystal Structure Analysis of SJKF_LA_12082020 (LA999) (Solution in P_n)

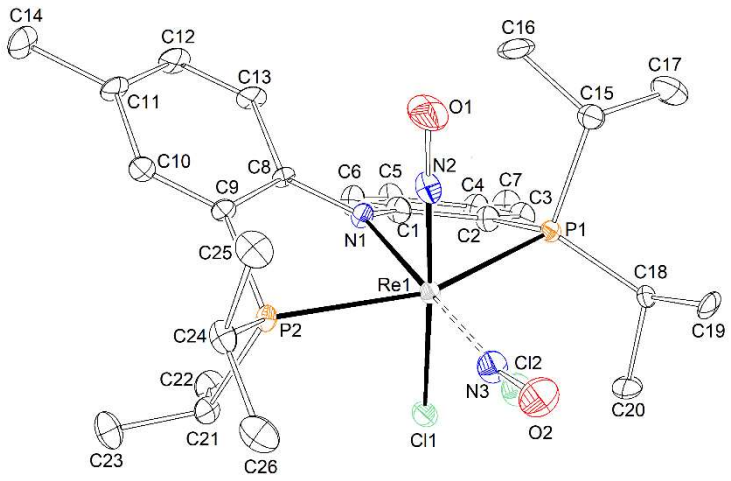

Figure 5.37: Thermal ellipsoid plot of SJKF_LA_12082020 refined in space group *Pn* with the anisotropic displacement parameters drawn at the 50% probability level.

X-ray Single-Crystal Structure Analysis of *cis*-[(^{Ph}PNP)Re(NO)$_2$Cl][Al(OC(CF$_3$)$_3$)$_4$] (*cis*-27**$^+$)**

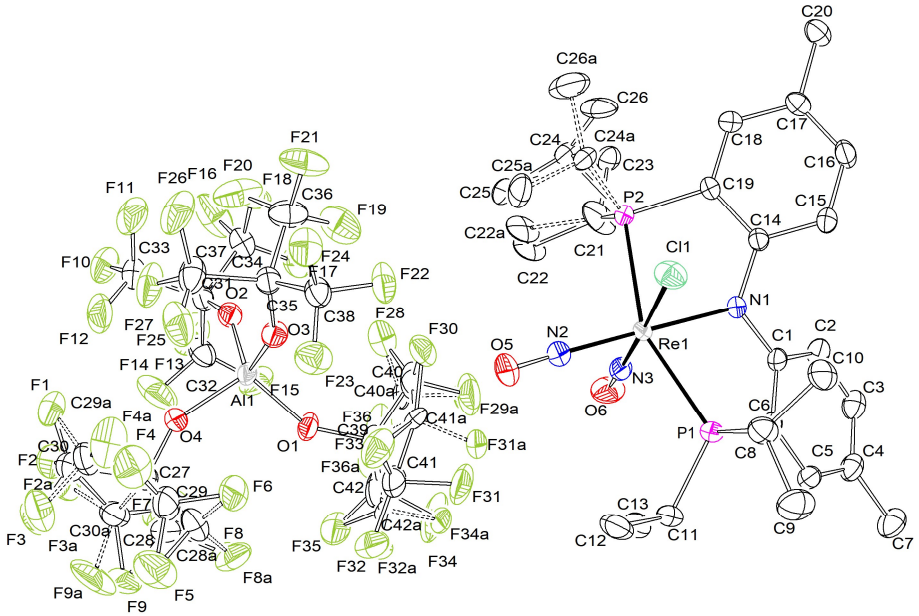

Figure 5.38: Thermal ellipsoid plot of *cis*-[(^{Ph}PNP)Re(NO)$_2$Cl][Al(OC(CF$_3$)$_3$)$_4$] with the anisotropic displacement parameters drawn at the 50% probability level. The asymmetric unit contains one disordered complex molecule and one disordered [Al(OC(CF$_3$)$_3$)$_4$] anion. The disordered complex molecule and the [Al(OC(CF$_3$)$_3$)$_4$] anion were refined with population of 0.69 on the main domain using some restraints (SADI,RIGU) and constraints (EADP).

Table 5.31: Crystal data and structure refinement for *cis*-[(^{Ph}PNP)Re(NO)$_2$Cl][Al(OC(CF$_3$)$_3$)$_4$].

Identification code	mo_LA_050321_LA_0m_a [cisPNPReNO2Cl)(Al(OC(CF$_3$)$_3$)$_4$]	
Empirical formula	$C_{41.69}H_{39.06}AlClF_{36}N_3O_6P_2Re$	
Formula weight	1672.63	
Temperature	100(2) K	
Wavelength	0.71073 Å	
Crystal system	Monoclinic	
Space group	$P2_1/c$	
Unit cell dimensions	a = 13.7973(5) Å	α= 90°
	b = 11.8103(4) Å	β= 96.6270(10)°
	c = 35.8531(12) Å	γ = 90°
Volume	5803.2(3) Å^3	
Z	4	
Density (calculated)	1.914 Mg/m^3	
Absorption coefficient	2.374 mm^{-1}	
F(000)	3269	
Crystal size	0.271 x 0.142 x 0.112 mm^3	
Crystal shape and color	Block,	clear intense brown
Theta range for data collection	1.977 to 26.434°	
Index ranges	-17<=h<=17, -14<=k<=14, -44<=l<=44	
Reflections collected	334589	
Independent reflections	11935 [R(int) = 0.0490]	

Completeness to theta = 25.242°	100.0 %
Refinement method	Full-matrix least-squares on F^2
Data / restraints / parameters	11935 / 21 / 1021
Goodness-of-fit on F^2	1.193
Final R indices [I>2sigma(I)]	R1 = 0.0419, wR2 = 0.0855
R indices (all data)	R1 = 0.0434, wR2 = 0.0861
Largest diff. peak and hole	2.141 and -2.064 eÅ^{-3}

X-ray Single-Crystal Structure Analysis of [(^{Ph}PNP)Re(NO)$_2$] (28)

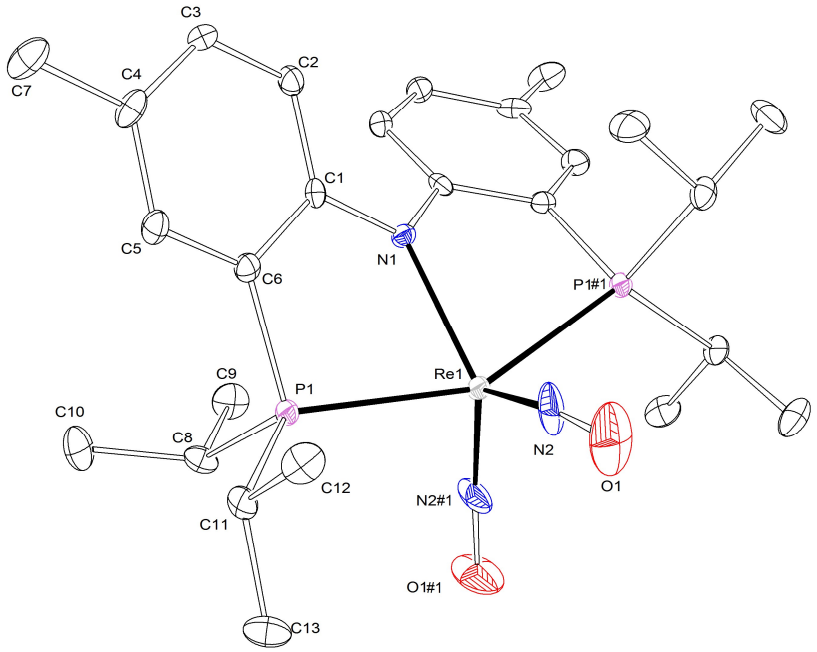

Figure 5.39: Thermal ellipsoid plot of [(^{Ph}PNP)Re(NO)$_2$] with the anisotropic displacement parameters drawn at the 50% probability level. The asymmetric unit contains only a half complex molecule.

Table 5.32: Crystal data and structure refinement for [(^{Ph}PNP)Re(NO)$_2$].

Identification code	MO_LA_220620_0m_a (LA1004)	
Empirical formula	$C_{26}H_{40}N_3O_2P_2Re$	
Formula weight	674.75	
Temperature	100(2) K	
Wavelength	0.71073 Å	
Crystal system	Monoclinic	
Space group	P2/n	
Unit cell dimensions	a = 11.200(3) Å	α= 90°
	b = 9.272(3) Å	β= 97.023(9)°
	c = 13.062(3) Å	γ = 90°
Volume	1346.3(6) Å^3	
Z	2	

Density (calculated)	1.665 Mg/m^3	
Absorption coefficient	4.660 mm^{-1}	
F(000)	676	
Crystal size	0.200 x 0.094 x 0.088 mm^3	
Crystal shape and color	Block,	clear intense orange
Theta range for data collection	2.196 to 28.384°	
Index ranges	-14<=h<=13, -12<=k<=12, -17<=l<=17	
Reflections collected	42271	
Independent reflections	3382 [R(int) = 0.1333]	
Completeness to theta = 25.242°	100.0 %	
Refinement method	Full-matrix least-squares on F^2	
Data / restraints / parameters	3382 / 0 / 160	
Goodness-of-fit on F^2	1.023	
Final R indices [I>2sigma(I)]	R1 = 0.0320,	wR2 = 0.0549
R indices (all data)	R1 = 0.0469,	wR2 = 0.0584
Largest diff. peak and hole	0.969 and -1.351 eÅ^{-3}	

X-ray Single-Crystal Structure Analysis of [(^{Ph}PNP)Re(NO)(NOB(C$_6$F$_5$)$_3$] (47)

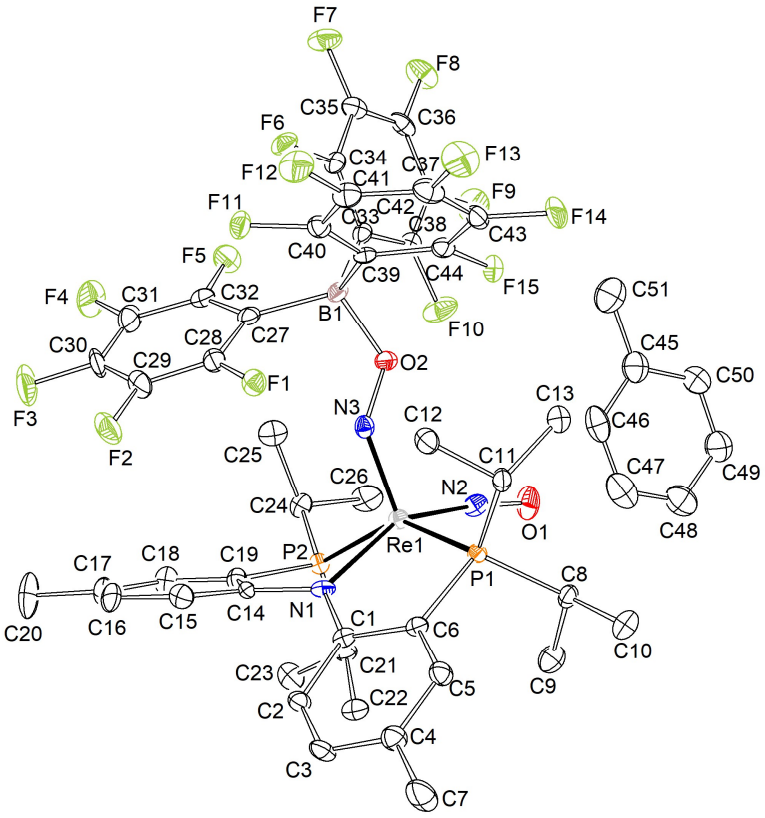

Figure 5.40: Thermal ellipsoid plot of [(^{Ph}PNP)Re(NO)(NOB(C$_6$F$_5$)$_3$] with the anisotropic displacement parameters drawn at the 50% probability level. The asymmetric unit contains one complex molecule and one toluene solvent molecule.

Table 5.33: Crystal data and structure refinement for [(^{Ph}PNP)Re(NO)(NOB(C_6F_5)$_3$].

Identification code	mo_LA_LA_121020_0m_a	
Empirical formula	$C_{51}H_{48}BF_{15}N_3O_2P_2Re$	
Formula weight	1278.87	
Temperature	100(2) K	
Wavelength	0.71073 Å	
Crystal system	Triclinic	
Space group	P-1	
Unit cell dimensions	a = 12.0992(11) Å	α= 116.065(5)°
	b = 15.3203(14) Å	β= 99.263(5)°
	c = 16.3726(15) Å	γ = 103.108(5)°
Volume	2534.6(4) Å^3	
Z	2	
Density (calculated)	1.676 Mg/m^3	
Absorption coefficient	2.560 mm^{-1}	
F(000)	1272	
Crystal size	0.424 x 0.240 x 0.159 mm^3	
Crystal shape and color	block,	clear intense orange
Theta range for data collection	2.291 to 25.350°	
Index ranges	-14<=h<=14, -18<=k<=18, -19<=l<=19	
Reflections collected	120894	
Independent reflections	9031 [R(int) = 0.1395]	
Completeness to theta = 25.242°	97.2 %	
Refinement method	Full-matrix least-squares on F^2	
Data / restraints / parameters	9031 / 0 / 687	
Goodness-of-fit on F^2	0.959	
Final R indices [I>2sigma(I)]	R1 = 0.0333,	wR2 = 0.0713
R indices (all data)	R1 = 0.0506,	wR2 = 0.0796
Largest diff. peak and hole	2.345 and -1.411 eÅ^{-3}	

X-ray Single-Crystal Structure Analysis of *cis*-[(^{Ph}PNP)Re(NO)Cl$_2$] (*cis*-14)

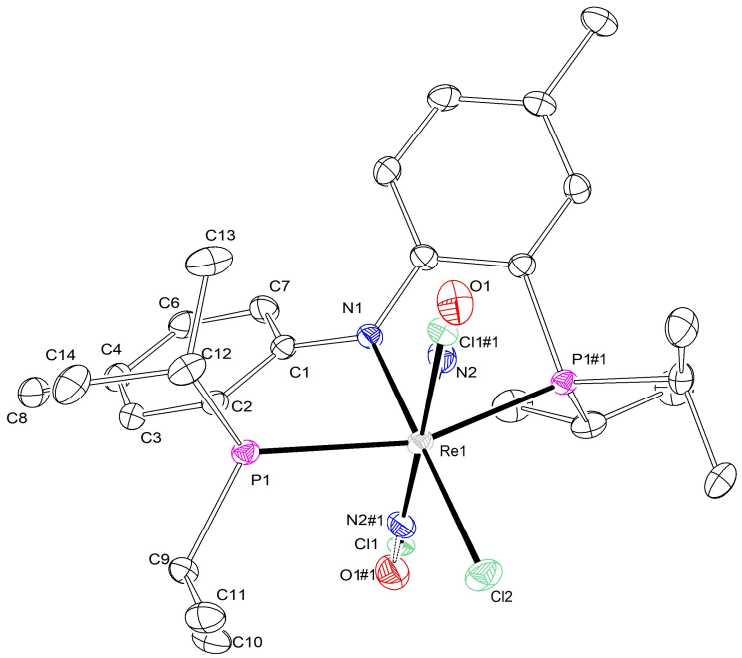

Figure 5.41: Thermal ellipsoid plot of *cis*-[(^{Ph}PNP)Re(NO)Cl$_2$] with the anisotropic displacement parameters drawn at the 50% probability level. The asymmetric unit contains half a disordered complex molecule. The disordered complex molecule was refined with population of 0.55 on the main domain using a restraint (DELU).

Table 5.34: Crystal data and structure refinement for *cis*-[(^{Ph}PNP)Re(NO)Cl$_2$].

Identification code	mo_LA_LA_031220_0m_a (cisPNPReNOCl2)	
Empirical formula	$C_{26}H_{40}Cl_2N_2OP_2Re$	
Formula weight	715.64	
Temperature	100(2) K	
Wavelength	0.71073 Å	
Crystal system	Monoclinic	
Space group	P2/n	
Unit cell dimensions	a = 11.2687(3) Å	α = 90°.
	b = 9.6049(3) Å	β = 100.1050(10)°.
	c = 13.1225(3) Å	γ = 90°.
Volume	1398.28(7) Å^3	
Z	2	
Density (calculated)	1.700 Mg/m^3	
Absorption coefficient	4.673 mm^{-1}	
F(000)	714	
Crystal size	0.291 x 0.277 x 0.086 mm^3	
Crystal shape and color	block,	clear intense green
Theta range for data collection	2.120 to 28.279°.	
Index ranges	-15<=h<=15, -12<=k<=12, -17<=l<=17	

Reflections collected	90457	
Independent reflections	3470 [R(int) = 0.0890]	
Completeness to theta = 25.242°	100.0 %	
Refinement method	Full-matrix least-squares on F^2	
Data / restraints / parameters	3470 / 1 / 176	
Goodness-of-fit on F^2	1.112	
Final R indices [I>2sigma(I)]	R_1 = 0.0196,	wR_2 = 0.0436
R indices (all data)	R_1 = 0.0225,	wR_2 = 0.0447
Largest diff. peak and hole	0.966 and -0.783 eÅ^{-3}	

X-ray Single-Crystal Structure Analysis of *cis*-[(^{Ph}PNP)Re(NO)Cl$_2$][OTf] (*cis*-29$^+$)

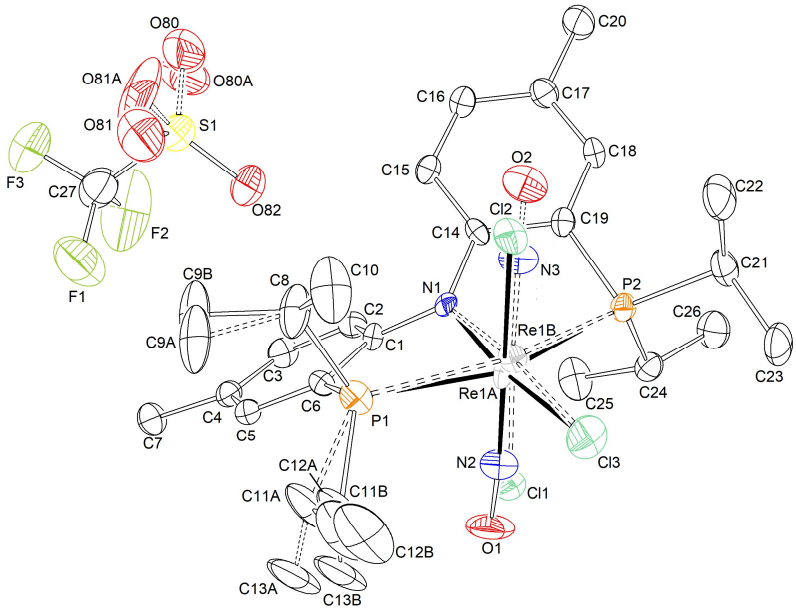

Figure 5.42: Thermal ellipsoid plot of *cis*-[(^{Ph}PNP)Re(NO)Cl$_2$][OTf] with the anisotropic displacement parameters drawn at the 50% probability level. The asymmetric unit contains one disordered complex molecule and a triflate counterion. The disordered complex molecule was refined with population of 0.61(1) on the main domain using some restraints and constraints (SADI, DELU, EADP).

Table 5.35: Crystal data and structure refinement for *cis*-[(^{Ph}PNP)Re(NO)Cl$_2$][OTf].

Identification code	mo_LA_LA_181120_0m_a	
Empirical formula	$C_{27}H_{40}Cl_2F_3N_2O_4P_2ReS$	
Formula weight	864.71	
Temperature	100(2) K	
Wavelength	0.71073 Å	
Crystal system	Monoclinic	
Space group	$P2_1/c$	
Unit cell dimensions	a = 14.113(2) Å	α= 90°
	b = 14.787(2) Å	β= 91.586(8)°
	c = 16.065(3) Å	γ = 90°

Volume	3351.3(9) Å^3	
Z	4	
Density (calculated)	1.714 Mg/m^3	
Absorption coefficient	3.995 mm^{-1}	
F(000)	1720	
Crystal size	0.366 x 0.228 x 0.172 mm^3	
Crystal shape and color	block,	clear intense purple
Theta range for data collection	2.343 to 25.347°	
Index ranges	-16<=h<=16, -17<=k<=17, -19<=l<=19	
Reflections collected	101211	
Independent reflections	6135 [R(int) = 0.0633]	
Completeness to theta = 25.242°	100.0 %	
Refinement method	Full-matrix least-squares on F^2	
Data / restraints / parameters	6135 / 189 / 455	
Goodness-of-fit on F^2	1.179	
Final R indices [I>2sigma(I)]	R1 = 0.0473,	wR2 = 0.0974
R indices (all data)	R1 = 0.0621,	wR2 = 0.1110
Largest diff. peak and hole	2.316 and -1.916 eÅ^{-3}	

X-ray Single-Crystal Structure Analysis of [(^{Ad}PNP)ReCl$_2$]

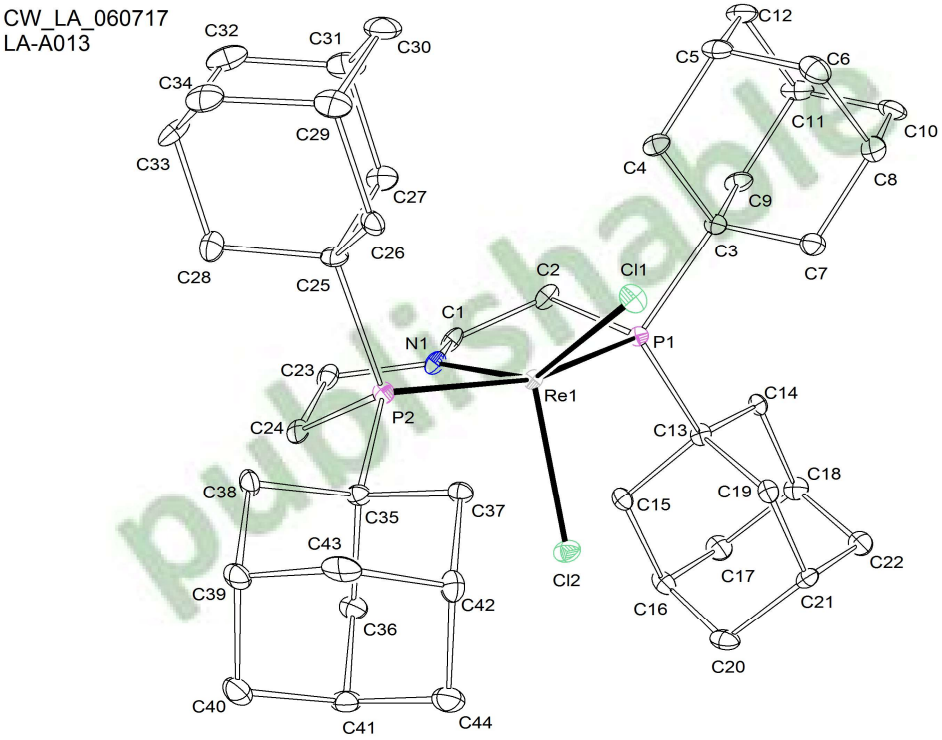

Figure 5.43: Thermal ellipsoid plot of [(^{Ad}PNP)ReCl$_2$] with the anisotropic displacement parameters drawn at the 50% probability level. The asymmetric unit contains one complex molecule.

Table 5.36: Crystal data and structure refinement for [(^{Ad}PNP)ReCl$_2$].

Identification code	mo_CW_LA_060717_0m_a (LA-A013)	
Empirical formula	$C_{44}H_{68}Cl_2NP_2Re$	
Formula weight	930.03	
Temperature	100(2) K	
Wavelength	0.71073 Å	
Crystal system	Monoclinic	
Space group	$P2_1/c$	
Unit cell dimensions	a = 7.3692(4) Å	α= 90°
	b = 19.4689(9) Å	β= 92.222(2)°
	c = 27.7853(12) Å	γ = 90°
Volume	3983.4(3) Å^3	
Z	4	
Density (calculated)	1.551 Mg/m^3	
Absorption coefficient	3.298 mm^{-1}	
F(000)	1912	
Crystal size	0.166 x 0.155 x 0.151 mm^3	
Crystal shape and color	block,	dark violet
Theta range for data collection	2.217 to 28.406°	
Index ranges	-9<=h<=9, -26<=k<=26, -37<=l<=37	
Reflections collected	107395	
Independent reflections	9964 [R(int) = 0.1241]	
Completeness to theta = 25.242°	99.9 %	
Refinement method	Full-matrix least-squares on F^2	
Data / restraints / parameters	9964 / 0 / 451	
Goodness-of-fit on F^2	1.033	
Final R indices [I>2sigma(I)]	R1 = 0.0373,	wR2 = 0.0540
R indices (all data)	R1 = 0.0645,	wR2 = 0.0591
Largest diff. peak and hole	0.953 and -0.963 eÅ^{-3}	

X-ray Single-Crystal Structure Analysis of *trans*-[(^{Ph}PNP)Re(NO)Cl$_2$] (*trans*-14)

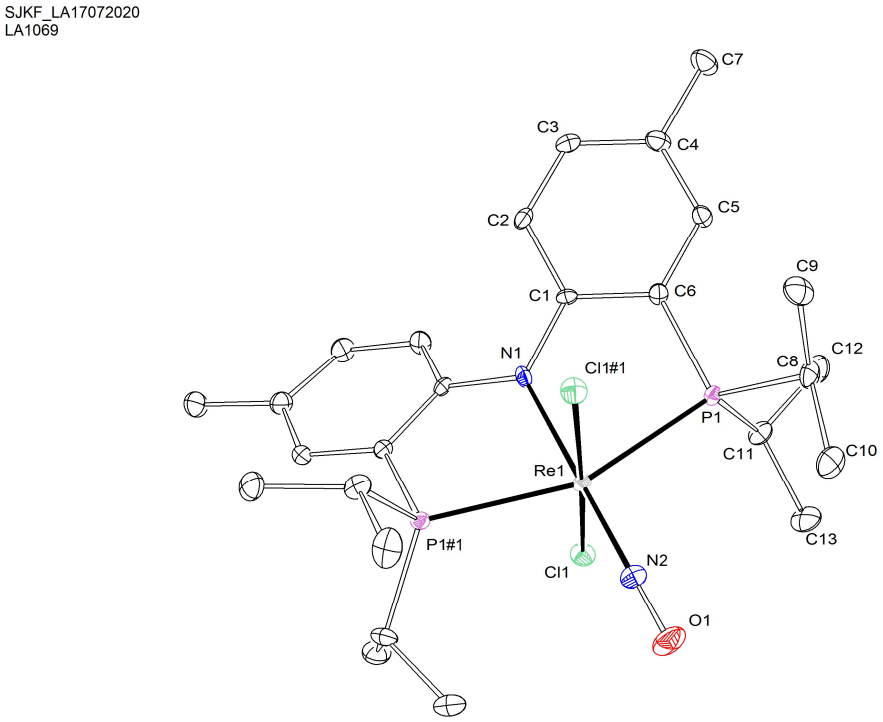

Figure 5.44: Thermal ellipsoid plot of *trans*-[(^{Ph}PNP)Re(NO)Cl$_2$] with the anisotropic displacement parameters drawn at the 50% probability level. The asymmetric unit contains only a half complex molecule. The structure was refined as an inversion twin using the twin law -100 0-10 00-1 (BASF: 0.105(8)).

Table 5.37: Crystal data and structure refinement for *trans*-[(^{Ph}PNP)Re(NO)Cl$_2$].

Identification code	SJKF_LA17072020_b	
Empirical formula	$C_{26}H_{40}Cl_2N_2OP_2Re$	
Formula weight	715.64	
Temperature	100(2) K	
Wavelength	0.71073 Å	
Crystal system	Orthorhombic	
Space group	Fdd2	
Unit cell dimensions	a = 15.3371(11) Å	α= 90°
	b = 34.485(2) Å	β= 90°
	c = 10.6889(7) Å	γ = 90°
Volume	5653.3(7) Å^3	
Z	8	
Density (calculated)	1.682 Mg/m^3	
Absorption coefficient	4.623 mm^{-1}	
F(000)	2856	
Crystal size	0.295 x 0.394 x 0.494 mm^3	
Crystal shape and color	block,	clear intense green
Theta range for data collection	2.362 to 33.239°	
Index ranges	-23<=h<=23, -53<=k<=52, -16<=l<=16	

Reflections collected	39369	
Independent reflections	5400 [R(int) = 0.0688]	
Completeness to theta = 25.242°	100.0 %	
Refinement method	Full-matrix least-squares on F^2	
Data / restraints / parameters	5400 / 1 / 162	
Goodness-of-fit on F^2	1.051	
Final R indices [I>2sigma(I)]	R1 = 0.0277,	wR2 = 0.0460
R indices (all data)	R1 = 0.0366,	wR2 = 0.0479
Absolute structure parameter	0.105(8)	
Largest diff. peak and hole	0.616 and -1.192 eÅ^{-3}	

X-ray Single-Crystal Structure Analysis of *trans*-[($^{i\mathrm{Pr}}$P$^{\mathrm{H}}$NP)OsCl$_2$(PPh$_3$)] (*trans*-34)

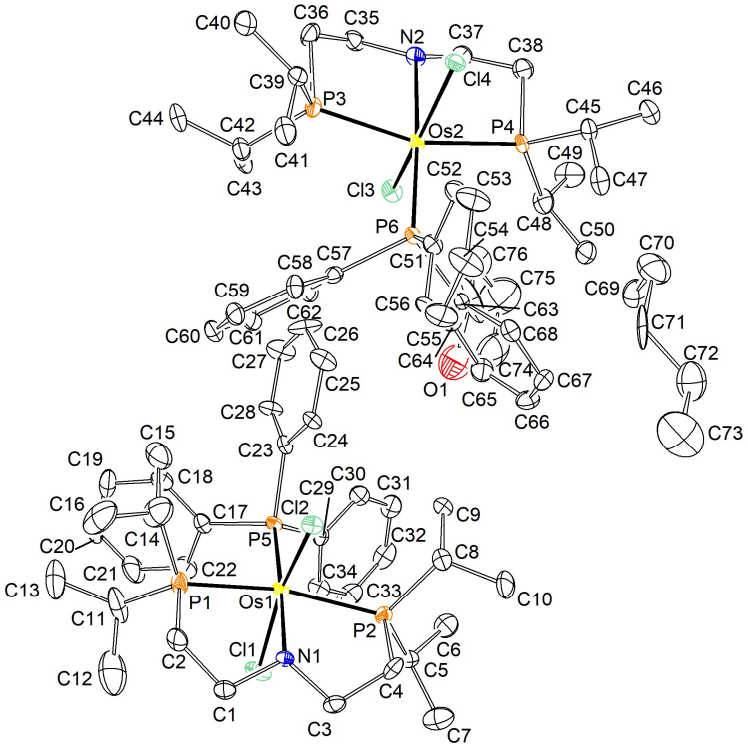

Figure 5.45: Thermal ellipsoid plot of *trans*-[($^{i\mathrm{Pr}}$P$^{\mathrm{H}}$NP)OsCl$_2$(PPh$_3$)] with the anisotropic displacement parameters drawn at the 50% probability level. The asymmetric unit contains two complex molecules, one pentane and one THF solvent molecule. The reflections -1 3 1, 2 -1 1, 2 1 1, 0 -16 15, 0 -1 2, 0 2 0, -2 15 13, 8 12 9, -1 -1 1 and 8 -1 15 are removed from the refinement using OMIT commands. The solvent molecules were refined using some restraints (RIGU).

Table 5.38: Crystal data and structure refinement for *trans*-[($^{i\mathrm{Pr}}$P$^{\mathrm{H}}$NP)OsCl$_2$(PPh$_3$)].

Identification code	mo_LA_LA_070119_0m_a
Empirical formula	$C_{145}H_{224}Cl_8N_4OOs_4P_{12}$
Formula weight	3455.31
Temperature	100(2) K
Wavelength	0.71073 Å

Crystal system	Triclinic	
Space group	P-1	
Unit cell dimensions	a = 12.2428(13) Å	α= 89.290(4)°
	b = 18.1377(18) Å	β= 73.399(4)°
	c = 18.954(2) Å	γ = 81.085(4)°
Volume	3982.4(8) Å^3	
Z	1	
Density (calculated)	1.441 Mg/m^3	
Absorption coefficient	3.482 mm^{-1}	
F(000)	1750	
Crystal size	0.349 x 0.296 x 0.284 mm^3	
Crystal shape and color	block,	clear intense orange
Theta range for data collection	2.240 to 25.350°	
Index ranges	-14<=h<=14, -21<=k<=21, -22<=l<=22	
Reflections collected	167056	
Independent reflections	13995 [R(int) = 0.0984]	
Completeness to theta = 25.242°	95.9 %	
Refinement method	Full-matrix least-squares on F^2	
Data / restraints / parameters	13995 / 36 / 847	
Goodness-of-fit on F^2	1.037	
Final R indices [I>2sigma(I)]	R1 = 0.0404,	wR2 = 0.0935
R indices (all data)	R1 = 0.0540,	wR2 = 0.0989
Largest diff. peak and hole	1.727 and -1.421 eÅ^{-3}	

X-ray Single-Crystal Structure Analysis of [($^{i\mathrm{Pr}}$P$^{\mathrm{H}}$NP)OsCl$_3$] (37)

LA_LA_220219
LA313

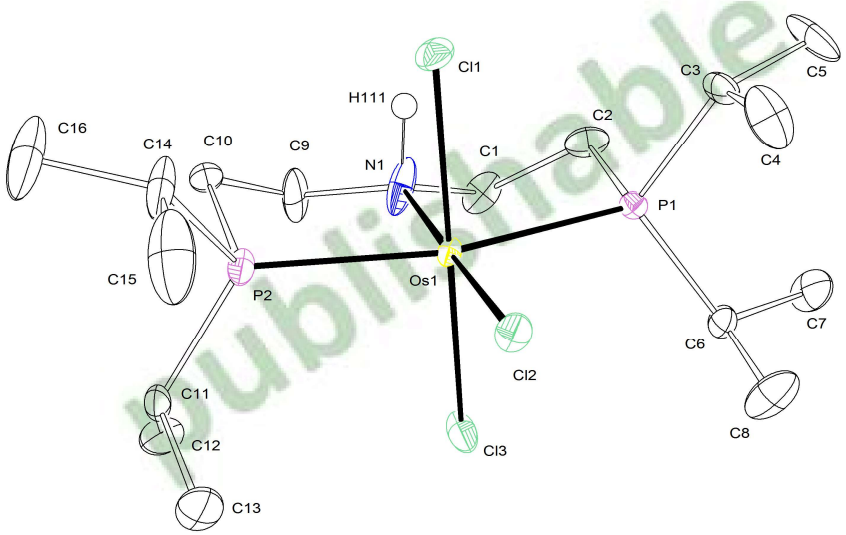

Figure 5.46: Thermal ellipsoid plot of [($^{i\mathrm{Pr}}$P$^{\mathrm{H}}$NP)OsCl$_3$] with the anisotropic displacement parameters drawn at the 50% probability level. The asymmetric unit contains one complex molecule. The structure was refined as an inversion twin using the twin law -100 0-10 00-1 (BASF: 0.024(8)). The N-H hydrogen atom was found from the residual density map and constrained to 1.2 U_{eq} of the connected N-atom.

Table 5.39: Crystal data and structure refinement for [($^{i\text{Pr}t}$P^{H}NP)OsCl$_3$].

Identification code	mo_LA_LA_220219_0m_b	
Empirical formula	$C_{16}H_{37}Cl_3NOsP_2$	
Formula weight	601.95	
Temperature	100(2) K	
Wavelength	0.71073 Å	
Crystal system	Orthorhombic	
Space group	$P2_12_12_1$	
Unit cell dimensions	a = 7.3459(5) Å	α= 90°
	b = 12.9600(8) Å	β= 90°
	c = 23.5463(14) Å	γ = 90°
Volume	2241.7(2) Å^3	
Z	4	
Density (calculated)	1.784 Mg/m^3	
Absorption coefficient	6.188 mm^{-1}	
F(000)	1188	
Crystal size	0.103 x 0.073 x 0.013 mm^3	
Crystal shape and color	Plate,	clear light yellow
Theta range for data collection	2.337 to 28.394°	
Index ranges	-9<=h<=9, -17<=k<=17, -31<=l<=31	
Reflections collected	74657	
Independent reflections	5600 [R(int) = 0.0956]	
Completeness to theta = 25.242°	99.9 %	
Refinement method	Full-matrix least-squares on F^2	
Data / restraints / parameters	5600 / 0 / 217	
Goodness-of-fit on F^2	1.081	
Final R indices [I>2sigma(I)]	R1 = 0.0271,	wR2 = 0.0453
R indices (all data)	R1 = 0.0328,	wR2 = 0.0465
Absolute structure parameter	0.024(8)	
Largest diff. peak and hole	0.584 and -1.147 eÅ^{-3}	

X-ray Single-Crystal Structure Analysis of *trans*-[($^{i\text{Pr}}$P$^{\text{H}}$NP)OsCl$_2$(N$_2$)] (*trans*-39) and *trans*-[($^{\text{Imine}}$PNP)OsCl$_2$(N$_2$)] (*trans*-40)

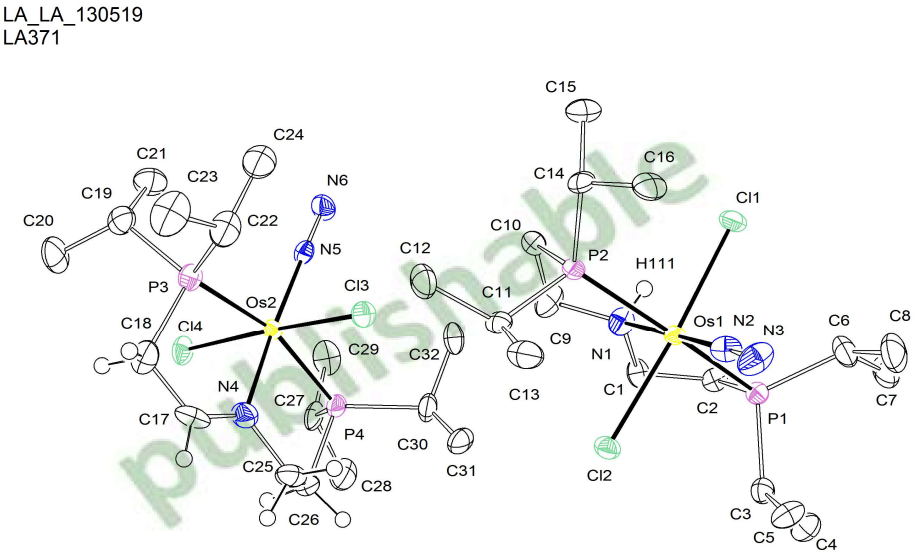

Figure 5.47: Thermal ellipsoid plots of [($^{i\text{Pr}}$P$^{\text{H}}$NP)OsCl$_2$(N$_2$)] and [($^{\text{Imine}}$PNP)OsCl$_2$(N$_2$)] with the anisotropic displacement parameters drawn at the 50% probability level. The asymmetric unit contains two complex molecules. The N-H hydrogen atom was found from the residual density map and isotropically refined.

Table 5.40: Crystal data and structure refinement for [($^{i\text{Pr}}$P$^{\text{H}}$NP)OsCl$_2$(N$_2$)] and [($^{\text{Imine}}$PNP)OsCl$_2$(N$_2$)].

Identification code	mo_LA_LA_130519_0m_a (LA371)	
Empirical formula	$C_{32}H_{72}Cl_4N_6Os_2P_4$	
Formula weight	1187.03	
Temperature	103(2) K	
Wavelength	0.71073 Å	
Crystal system	Monoclinic	
Space group	$P2_1/n$	
Unit cell dimensions	a = 17.1817(13) Å	α= 90°
	b = 15.1017(11) Å	β= 106.801(4)°
	c = 17.9346(13) Å	γ = 90°
Volume	4454.9(6) Å^3	
Z	4	
Density (calculated)	1.770 Mg/m^3	
Absorption coefficient	6.113 mm^{-1}	
F(000)	2344	
Crystal size	0.202 x 0.134 x 0.105 mm^3	
Crystal shape and color	block,	clear intense yellow
Theta range for data collection	2.368 to 26.442°	
Index ranges	-21<=h<=21, -18<=k<=17, -22<=l<=22	
Reflections collected	54865	
Independent reflections	9085 [R(int) = 0.1091]	
Completeness to theta = 25.242°	99.2 %	

Refinement method	Full-matrix least-squares on F^2	
Data / restraints / parameters	9085 / 0 / 453	
Goodness-of-fit on F^2	1.023	
Final R indices [I>2sigma(I)]	R1 = 0.0396,	wR2 = 0.0762
R indices (all data)	R1 = 0.0692,	wR2 = 0.0870
Largest diff. peak and hole	1.226 and -1.393 eÅ^{-3}	

X-ray Single-Crystal Structure Analysis of [PPN][(P=N=P)OsCl$_3$] (^{PPN}41)

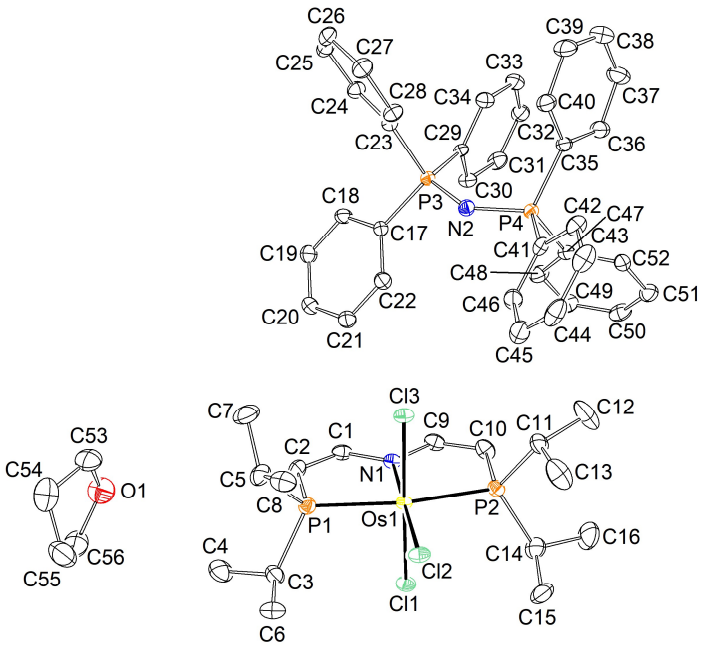

Figure 5.48: Thermal ellipsoid plot of [PPN][(P=N=P)OsCl$_3$] with the anisotropic displacement parameters drawn at the 50% probability level. The asymmetric unit contains one complex molecule, a PPN cation and a THF solvent molecule.

Table 5.41: Crystal data and structure refinement for [PPN][(P=N=P)OsCl$_3$].

Identification code	mo_LA_230221_LA_a	
Empirical formula	$C_{56}H_{70}Cl_3N_2OOsP_4$	
Formula weight	1207.57	
Temperature	100(2) K	
Wavelength	0.71073 Å	
Crystal system	Triclinic	
Space group	P-1	
Unit cell dimensions	a = 9.1157(3) Å	α= 96.815(2)°
	b = 13.7899(5) Å	β= 97.402(2)°
	c = 22.0701(8) Å	γ = 90.359(2)°
Volume	2731.10(17) Å^3	
Z	2	
Density (calculated)	1.468 Mg/m^3	

Absorption coefficient	2.639 mm^{-1}	
F(000)	1230	
Crystal size	0.189 x 0.116 x 0.095 mm^3	
Crystal shape and color	block,	clear intense green
Theta range for data collection	1.851 to 33.142°	
Index ranges	-14<=h<=14, -21<=k<=21, -33<=l<=33	
Reflections collected	261371	
Independent reflections	20793 [R(int) = 0.1207]	
Completeness to theta = 25.242°	100.0 %	
Refinement method	Full-matrix least-squares on F^2	
Data / restraints / parameters	20793 / 0 / 612	
Goodness-of-fit on F^2	1.075	
Final R indices [I>2sigma(I)]	R1 = 0.0416,	wR2 = 0.0821
R indices (all data)	R1 = 0.0608,	wR2 = 0.0897
Largest diff. peak and hole	1.549 and -2.630 $eÅ^{-3}$	

X-ray Single-Crystal Structure Analysis of [(^{iPr}PNP)$OsCl_3$] (43)

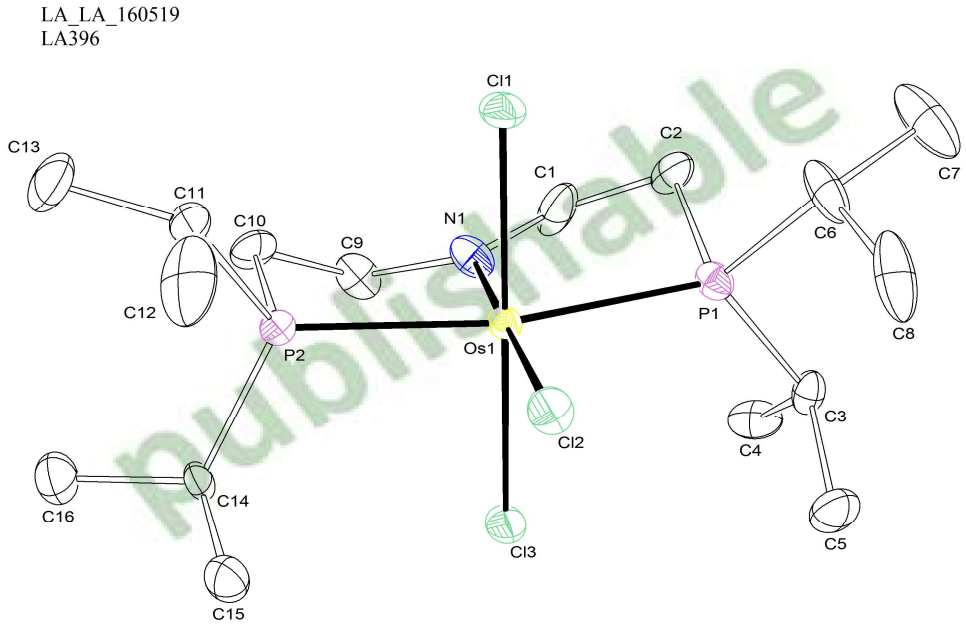

Figure 5.49: Thermal ellipsoid plot of [(^{iPr}PNP)$OsCl_3$] with the anisotropic displacement parameters drawn at the 50% probability level. The asymmetric unit contains one complex molecule. The structure was refined as an inversion twin using the twin law -100 0-10 00-1 (BASF: 0.023(8)).

Table 5.42: Crystal data and structure refinement for [(^{iPr}PNP)$OsCl_3$].

Identification code	mo_LA_LA_160519_0m_b	(LA396)
Empirical formula	$C_{16}H_{36}Cl_3NOsP_2$	
Formula weight	600.95	
Temperature	104(2) K	

Wavelength	0.71073 Å	
Crystal system	Orthorhombic	
Space group	$P2_12_12_1$	
Unit cell dimensions	a = 7.3334(7) Å	α= 90°
	b = 12.6637(11) Å	β= 90°
	c = 24.004(2) Å	γ = 90°
Volume	2229.2(3) Å^3	
Z	4	
Density (calculated)	1.791 Mg/m^3	
Absorption coefficient	6.223 mm^{-1}	
F(000)	1184	
Crystal size	0.337 x 0.227 x 0.209 mm^3	
Crystal shape and color	block,	clear intense yellow
Theta range for data collection	2.338 to 28.379°	
Index ranges	-9<=h<=9, -16<=k<=16, -30<=l<=32	
Reflections collected	33592	
Independent reflections	5560 [R(int) = 0.0663]	
Completeness to theta = 25.242°	99.8 %	
Refinement method	Full-matrix least-squares on F^2	
Data / restraints / parameters	5560 / 0 / 217	
Goodness-of-fit on F^2	1.031	
Final R indices [I>2sigma(I)]	R1 = 0.0277,	wR2 = 0.0510
R indices (all data)	R1 = 0.0351,	wR2 = 0.0530
Absolute structure parameter	0.023(8)	
Largest diff. peak and hole	1.321 and -1.332 eÅ^{-3}	

X-ray Single-Crystal Structure Analysis of [(^{Imine}PNP)OsCl$_3$] (38)

LA_LA_020419
LA338

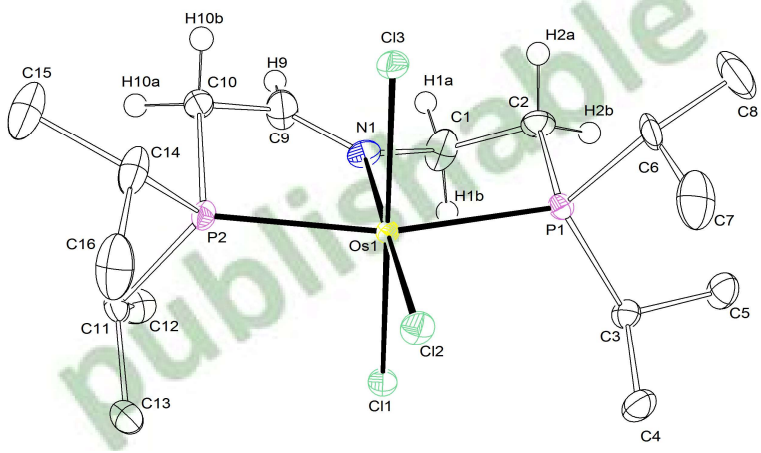

Figure 5.50: Thermal ellipsoid plot of [(^{Imine}PNP)OsCl$_3$] with the anisotropic displacement parameters drawn at the 50% probability level. The asymmetric unit contains one complex molecule. The structure was refined as an inversion twin using the twin law -100 0-10 00-1 (BASF: 0.027(6)).

Table 5.43: Crystal data and structure refinement for [(^{Imine}PNP)$OsCl_3$].

Identification code	mo_LA_LA_020419_0m_d	(LA338)
Empirical formula	$C_{16}H_{35}Cl_3NOsP_2$	
Formula weight	599.94	
Temperature	100(2) K	
Wavelength	0.71073 Å	
Crystal system	Orthorhombic	
Space group	$P2_12_12_1$	
Unit cell dimensions	a = 7.2705(5) Å	α= 90°
	b = 12.4671(8) Å	β= 90°
	c = 24.2081(15) Å	γ = 90°
Volume	2194.3(2) $Å^3$	
Z	4	
Density (calculated)	1.816 Mg/m^3	
Absorption coefficient	6.322 mm^{-1}	
F(000)	1180	
Crystal size	0.456 x 0.201 x 0.178 mm^3	
Crystal shape and color	block,	clear intense brown
Theta range for data collection	2.345 to 30.590°	
Index ranges	-10<=h<=10, -17<=k<=17, -34<=l<=34	
Reflections collected	44936	
Independent reflections	6703 [R(int) = 0.0388]	
Completeness to theta = 25.242°	99.9 %	
Refinement method	Full-matrix least-squares on F^2	
Data / restraints / parameters	6703 / 0 / 217	
Goodness-of-fit on F^2	1.057	
Final R indices [I>2sigma(I)]	R1 = 0.0206,	wR2 = 0.0423
R indices (all data)	R1 = 0.0254,	wR2 = 0.0438
Absolute structure parameter	0.027(6)	
Largest diff. peak and hole	1.226 and -0.951 $eÅ^{-3}$	

X-ray Single-Crystal Structure Analysis of [(P=N=P)OsCl$_3$] (44)

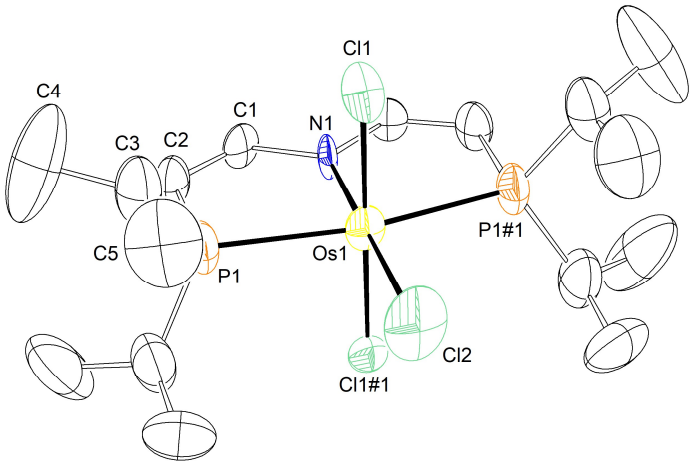

Figure 5.51: Thermal ellipsoid plot of [(P=N=P)OsCl$_3$] with the anisotropic displacement parameters drawn at the 50% probability level. The asymmetric unit contains one quarter complex molecule. The complex molecule was refined as a twin using the TWIN command and a BASF of 0.58(4) and some restraints (DELU).

Table 5.44: Crystal data and structure refinement for [(P=N=P)OsCl$_3$].

Identification code	mo_LA_LA_290519_0m_a	
Empirical formula	$C_{16}H_{32}Cl_3NOsP_2$	
Formula weight	596.91	
Temperature	100(2) K	
Wavelength	0.71073 Å	
Crystal system	Tetragonal	
Space group	P-42$_1$m	
Unit cell dimensions	a = 11.3822(2) Å	α= 90°
	b = 11.3822(2) Å	β= 90°
	c = 8.4217(4) Å	γ = 90°
Volume	1091.07(6) Å^3	
Z	2	
Density (calculated)	1.817 Mg/m^3	
Absorption coefficient	6.357 mm^{-1}	
F(000)	584	
Crystal size	0.271 x 0.172 x 0.116 mm^3	
Crystal shape and color	block,	clear intense green
Theta range for data collection	2.418 to 30.485°	
Index ranges	-16<=h<=16, -16<=k<=16, -11<=l<=12	
Reflections collected	15865	
Independent reflections	1768 [R(int) = 0.0522]	
Completeness to theta = 25.242°	100.0 %	
Refinement method	Full-matrix least-squares on F^2	
Data / restraints / parameters	1768 / 7 / 67	

Goodness-of-fit on F^2	1.147	
Final R indices [I>2sigma(I)]	R1 = 0.0423,	wR2 = 0.0950
R indices (all data)	R1 = 0.0571,	wR2 = 0.1051
Absolute structure parameter	0.58(4)	
Largest diff. peak and hole	1.899 and -1.822 $eÅ^{-3}$	

Part VI: References

[1] X. Zhang, B. B. Ward, D. M. Sigman, *Chem. Rev.* **2020**, *120*, 5308–5351.
[2] M. Sorai, N. Yoshida, M. Ishikawa, *J. Geophys. Res.* **2007**, *112*, G01006.
[3] B. Johnson, C. Goldblatt, *Earth-Science Rev.* **2015**, *148*, 150–173.
[4] J. G. Chen, R. M. Crooks, L. C. Seefeldt, K. L. Bren, R. M. Bullock, M. Y. Darensbourg, P. L. Holland, B. Hoffman, M. J. Janik, A. K. Jones, et al., *Science* **2018**, *360*, eaar6611.
[5] C. Ferousi, S. H. Majer, I. M. DiMucci, K. M. Lancaster, *Chem. Rev.* **2020**, *120*, 5252–5307.
[6] A. E. Shilov, *Russ. Chem. Bull.* **2003**, *52*, 2555–2562.
[7] F. Masero, M. A. Perrin, S. Dey, V. Mougel, *Chem. Eur. J.* **2021**, *27*, 3892–3928.
[8] B. M. Hoffman, D. Lukoyanov, Z.-Y. Yang, D. R. Dean, L. C. Seefeldt, *Chem. Rev.* **2014**, *114*, 4041–4062.
[9] S. E. McGlynn, E. S. Boyd, J. W. Peters, V. J. Orphan, *Front. Microbiol.* **2012**, *3*, 1–8.
[10] P. C. Dos Santos, Z. Fang, S. W. Mason, J. C. Setubal, R. Dixon, *BMC Genomics* **2012**, *13*, 162.
[11] D. E. Canfield, A. N. Glazer, P. G. Falkowski, *Science* **2010**, *330*, 192–196.
[12] N. Gruber, J. N. Galloway, *Nature* **2008**, *451*, 293–296.
[13] J. B. Howard, D. C. Rees, *Chem. Rev.* **1996**, *96*, 2965–2982.
[14] L. C. Seefeldt, B. M. Hoffman, D. R. Dean, *Curr. Opin. Chem. Biol.* **2012**, *16*, 19–25.
[15] B. K. Burgess, D. J. Lowe, *Chem. Rev.* **1996**, *96*, 2983–3012.
[16] C. Van Stappen, L. Decamps, G. E. Cutsail, R. Bjornsson, J. T. Henthorn, J. A. Birrell, S. DeBeer, *Chem. Rev.* **2020**, *120*, 5005–5081.
[17] J. Kim, D. C. Rees, *Science* **1992**, *257*, 1677–1682.
[18] J. Kirn, D. C. Rees, *Nature* **1992**, *360*, 553–560.
[19] M. Chan, J. Kim, D. C. Rees, *Science* **1993**, *260*, 792–794.
[20] T. Spatzal, M. Aksoyoglu, L. Zhang, S. L. A. Andrade, E. Schleicher, S. Weber, D. C. Rees, O. Einsle, *Science* **2011**, *334*, 940.
[21] K. M. Lancaster, M. Roemelt, P. Ettenhuber, Y. Hu, M. W. Ribbe, F. Neese, U. Bergmann, S. DeBeer, *Science* **2011**, *334*, 974–977.
[22] R. R. Eady, *Chem. Rev.* **1996**, *96*, 3013–3030.
[23] L. C. Seefeldt, Z. Yang, D. A. Lukoyanov, D. F. Harris, D. R. Dean, S. Raugei, B. M. Hoffman, *Chem. Rev.* **2020**, *120*, 5082–5106.
[24] S. Shaw, D. Lukoyanov, K. Danyal, D. R. Dean, B. M. Hoffman, L. C. Seefeldt, *J. Am. Chem. Soc.* **2014**, *136*, 12776–12783.
[25] L. C. Seefeldt, Z.-Y. Yang, S. Duval, D. R. Dean, *Biochim. Biophys. Acta Bioenerg.* **2013**, *1827*, 1102–1111.
[26] C. C. Lee, Y. Hu, M. W. Ribbe, *Science* **2010**, *329*, 642–642.
[27] Y. Hu, C. C. Lee, M. W. Ribbe, *Science* **2011**, *333*, 753–755.
[28] L. C. Seefeldt, M. E. Rasche, S. A. Ensign, *Biochemistry* **1995**, *34*, 5382–5389.
[29] H. Bortels, *Arch. Mikrobiol.* **1930**, *1*, 333–342.
[30] J. Chatt, G. J. Leigh, *Chem. Soc. Rev.* **1972**, *1*, 121.
[31] A. D. Allen, R. O. Harris, B. R. Loescher, J. R. Stevens, R. N. Whiteley, *Chem. Rev.* **1973**, *73*, 11–20.
[32] D. Sellmann, *Angew. Chem. Int. Ed. Engl.* **1974**, *13*, 639–649.
[33] A. D. Allen, C. V Senoff, *Chem. Commun.* **1965**, 621.
[34] A. D. Allen, F. Bottomley, R. O. Harris, V. P. Reinsalu, C. V. Senoff, *J. Am. Chem. Soc.* **1967**, *89*, 5595–5599.
[35] Y. Nishibayashi (Ed.), *Transition Metal-Dinitrogen Complexes*, Wiley-VCH Verlag GmbH & Co. KGaA, Weinheim, Germany, **2019**.
[36] B. A. MacKay, M. D. Fryzuk, *Chem. Rev.* **2004**, *104*, 385–401.
[37] A. Poveda, I. C. Perilla, C. R. Pérez, *J. Coord. Chem.* **2001**, *54*, 427–440.
[38] J. E. Weber, F. Hasanayn, M. Fataftah, B. Q. Mercado, R. H. Crabtree, P. L. Holland, *Inorg.*

Chem. **2021**, *60*, 6115–6124.
[39] S. J. K. Forrest, B. Schluschaß, E. Y. Yuzik-Klimova, S. Schneider, *Chem. Rev.* **2021**, *121*, 6522–6587.
[40] M. J. Chalkley, M. W. Drover, J. C. Peters, *Chem. Rev.* **2020**, *120*, 5582–5636.
[41] J. Chatt, A. J. Pearman, R. L. Richards, *Nature* **1975**, *253*, 39–40.
[42] J. Chatt, J. R. Dilworth, R. L. Richards, *Chem. Rev.* **1978**, *78*, 589–625.
[43] J. Chatt, J. R. Dilworth, *J. Chem. Soc., Chem. Commun.* **1974**, 517–518.
[44] J. Chatt, G. A. Heath, R. L. Richards, *J. Chem. Soc., Dalton Trans.* **1974**, 2074.
[45] J. Chatt, A. J. Pearman, R. L. Richards, *J. Chem. Soc., Dalton Trans.* **1978**, 1766.
[46] J. Chatt, A. J. Pearman, R. L. Richards, *J. Chem. Soc., Dalton Trans.* **1976**, 1520.
[47] J. Chatt, A. J. Pearman, R. L. Richards, *J. Organomet. Chem.* **1975**, *101*, C45–C47.
[48] A. Galindo, A. Hills, D. L. Hughes, R. L. Richards, M. Hughes, J. Mason, *J. Chem. Soc., Dalton Trans.* **1990**, 283.
[49] J. Chatt, A. J. Pearman, R. L. Richards, *J. Chem. Soc., Dalton Trans.* **1977**, 1852.
[50] J. Chatt, A. J. Pearman, R. L. Richards, *J. Chem. Soc., Dalton Trans.* **1977**, 2139.
[51] T. E. Glassman, M. G. Vale, R. R. Schrock, *J. Am. Chem. Soc.* **1992**, *114*, 8098–8109.
[52] B. M. Barney, J. McClead, D. Lukoyanov, M. Laryukhin, T.-C. Yang, D. R. Dean, B. M. Hoffman, L. C. Seefeldt, *Biochemistry* **2007**, *46*, 6784–6794.
[53] P. S. Wagenknecht, J. R. Norton, *J. Am. Chem. Soc.* **1995**, *117*, 1841–1842.
[54] D. V. Yandulov, R. R. Schrock, *Science* **2003**, *301*, 76–78.
[55] D. V. Yandulov, R. R. Schrock, *Inorg. Chem.* **2005**, *44*, 1103–1117.
[56] G. C. Stephan, C. Sivasankar, F. Studt, F. Tuczek, *Chem. Eur. J.* **2008**, *14*, 644–652.
[57] F. Studt, F. Tuczek, *Angew. Chem. Int. Ed.* **2005**, *44*, 5639–5642.
[58] R. R. Schrock, *Angew. Chem. Int. Ed.* **2008**, *47*, 5512–5522.
[59] F. Neese, *Angew. Chem. Int. Ed.* **2006**, *45*, 196–199.
[60] W. Thimm, C. Gradert, H. Broda, F. Wennmohs, F. Neese, F. Tuczek, *Inorg. Chem.* **2015**, *54*, 9248–9255.
[61] A. Sharma, M. Roemelt, M. Reithofer, R. R. Schrock, B. M. Hoffman, F. Neese, *Inorg. Chem.* **2017**, *56*, 6906–6919.
[62] V. Ritleng, D. V. Yandulov, W. W. Weare, R. R. Schrock, A. S. Hock, W. M. Davis, *J. Am. Chem. Soc.* **2004**, *126*, 6150–6163.
[63] W. W. Weare, R. R. Schrock, A. S. Hock, P. Müller, *Inorg. Chem.* **2006**, *45*, 9185–9196.
[64] J. M. Chin, R. R. Schrock, P. Müller, *Inorg. Chem.* **2010**, *49*, 7904–7916.
[65] M. R. Reithofer, R. R. Schrock, P. Müller, *J. Am. Chem. Soc.* **2010**, *132*, 8349–8358.
[66] N. C. Smythe, R. R. Schrock, P. Müller, W. W. Weare, *Inorg. Chem.* **2006**, *45*, 7111–7118.
[67] N. C. Smythe, R. R. Schrock, P. Müller, W. W. Weare, *Inorg. Chem.* **2006**, *45*, 9197–9205.
[68] K. Arashiba, Y. Miyake, Y. Nishibayashi, *Nat. Chem.* **2011**, *3*, 120–125.
[69] K. Arashiba, K. Sasaki, S. Kuriyama, Y. Miyake, H. Nakanishi, Y. Nishibayashi, *Organometallics* **2012**, *31*, 2035–2041.
[70] S. Kuriyama, K. Arashiba, K. Nakajima, H. Tanaka, N. Kamaru, K. Yoshizawa, Y. Nishibayashi, *J. Am. Chem. Soc.* **2014**, *136*, 9719–9731.
[71] H. Tanaka, K. Arashiba, S. Kuriyama, A. Sasada, K. Nakajima, K. Yoshizawa, Y. Nishibayashi, *Nat. Commun.* **2014**, *5*, 3737.
[72] J. S. Anderson, J. Rittle, J. C. Peters, *Nature* **2013**, *501*, 84–87.
[73] S. E. Creutz, J. C. Peters, *J. Am. Chem. Soc.* **2014**, *136*, 1105–1115.
[74] J. Rittle, J. C. Peters, *J. Am. Chem. Soc.* **2016**, *138*, 4243–4248.
[75] N. B. Thompson, M. T. Green, J. C. Peters, *J. Am. Chem. Soc.* **2017**, *139*, 15312–15315.
[76] T. J. Del Castillo, N. B. Thompson, J. C. Peters, *J. Am. Chem. Soc.* **2016**, *138*, 5341–5350.
[77] J. Fajardo, J. C. Peters, *J. Am. Chem. Soc.* **2017**, *139*, 16105–16108.
[78] M. J. Chalkley, T. J. Del Castillo, B. D. Matson, J. P. Roddy, J. C. Peters, *ACS Cent. Sci.* **2017**, *3*, 217–223.
[79] M. J. Chalkley, P. H. Oyala, J. C. Peters, *J. Am. Chem. Soc.* **2019**, *141*, 4721–4729.
[80] Y. Ashida, K. Arashiba, K. Nakajima, Y. Nishibayashi, *Nature* **2019**, *568*, 536–540.
[81] S. S. Kolmar, J. M. Mayer, *J. Am. Chem. Soc.* **2017**, *139*, 10687–10692.

[82] T. V. Chciuk, R. A. Flowers, *J. Am. Chem. Soc.* **2015**, *137*, 11526–11531.
[83] T. V. Chciuk, W. R. Anderson, R. A. Flowers, *J. Am. Chem. Soc.* **2016**, *138*, 8738–8741.
[84] T. V. Chciuk, W. R. Anderson, R. A. Flowers, *J. Am. Chem. Soc.* **2018**, *140*, 15342–15352.
[85] K. A. Brown, D. F. Harris, M. B. Wilker, A. Rasmussen, N. Khadka, H. Hamby, S. Keable, G. Dukovic, J. W. Peters, L. C. Seefeldt, et al., *Science* **2016**, *352*, 448–450.
[86] S. Kim, F. Loose, P. J. Chirik, *Chem. Rev.* **2020**, *120*, 5637–5681.
[87] J. Chatt, G. A. Heath, G. J. Leigh, *J. Chem. Soc., Chem. Commun.* **1972**, *0*, 444.
[88] A. A. Diamantis, J. Chatt, G. J. Leigh, G. A. Heath, *J. Organomet. Chem.* **1975**, *84*, C11–C12.
[89] P. C. Bevan, J. Chatt, G. J. Leigh, E. G. Leelamani, *J. Organomet. Chem.* **1977**, *139*, C59–C62.
[90] C. J. Pickett, G. J. Leigh, *J. Chem. Soc., Chem. Commun.* **1981**, 1033.
[91] J. C. Peters, J.-P. F. Cherry, J. C. Thomas, L. Baraldo, D. J. Mindiola, W. M. Davis, C. C. Cummins, *J. Am. Chem. Soc.* **1999**, *121*, 10053–10067.
[92] H. Tanaka, A. Sasada, T. Kouno, M. Yuki, Y. Miyake, H. Nakanishi, Y. Nishibayashi, K. Yoshizawa, *J. Am. Chem. Soc.* **2011**, *133*, 3498–3506.
[93] S. Kuriyama, K. Arashiba, K. Nakajima, H. Tanaka, K. Yoshizawa, Y. Nishibayashi, *Eur. J. Inorg. Chem.* **2016**, *2016*, 4856–4861.
[94] Q. Liao, A. Cavaillé, N. Saffon-Merceron, N. Mézailles, *Angew. Chem. Int. Ed.* **2016**, *55*, 11212–11216.
[95] Q. Liao, N. Saffon-Merceron, N. Mézailles, *Angew. Chem. Int. Ed.* **2014**, *53*, 14206–14210.
[96] Q. Liao, N. Saffon-Merceron, N. Mézailles, *ACS Catal.* **2015**, *5*, 6902–6906.
[97] M. Kol, R. R. Schrock, R. Kempe, W. M. Davis, *J. Am. Chem. Soc.* **1994**, *116*, 4382–4390.
[98] J. B. Geri, J. P. Shanahan, N. K. Szymczak, *J. Am. Chem. Soc.* **2017**, *139*, 5952–5956.
[99] A. Simonneau, R. Turrel, L. Vendier, M. Etienne, *Angew. Chem. Int. Ed.* **2017**, *56*, 12268–12272.
[100] M.-A. Légaré, G. Bélanger-Chabot, R. D. Dewhurst, E. Welz, I. Krummenacher, B. Engels, H. Braunschweig, *Science* **2018**, *359*, 896–900.
[101] M.-A. Légaré, C. Pranckevicius, H. Braunschweig, *Chem. Rev.* **2019**, *119*, 8231–8261.
[102] M.-A. Légaré, M. Rang, G. Bélanger-Chabot, J. I. Schweizer, I. Krummenacher, R. Bertermann, M. Arrowsmith, M. C. Holthausen, H. Braunschweig, *Science* **2019**, *363*, 1329–1332.
[103] C. Smith, A. K. Hill, L. Torrente-Murciano, *Energy Environ. Sci.* **2020**, *13*, 331–344.
[104] R. Schlögl, *Angew. Chem. Int. Ed.* **2003**, *42*, 2004–2008.
[105] G. Ertl, *Catal. Rev.* **1980**, *21*, 201–223.
[106] J. Bendix, K. Meyer, T. Weyhermüller, E. Bill, N. Metzler-Nolte, K. Wieghardt, *Inorg. Chem.* **1998**, *37*, 1767–1775.
[107] J. H. Enemark, R. D. Feltham, *Coord. Chem. Rev.* **1974**, *13*, 339–406.
[108] I. M. Treitel, M. T. Flood, R. E. Marsh, H. B. Gray, *J. Am. Chem. Soc.* **1969**, *91*, 6512–6513.
[109] D. F. Harrison, E. Weissberger, H. Taube, *Science* **1968**, *159*, 320–322.
[110] J. Chatt, R. C. Fay, R. L. Richards, *J. Chem. Soc. A* **1971**, 702–704.
[111] R. D. Sanner, J. M. Manriquez, R. E. Marsh, J. E. Bercaw, *J. Am. Chem. Soc.* **1976**, *98*, 8351–8357.
[112] C. E. Laplaza, M. J. A. Johnson, J. C. Peters, A. L. Odom, E. Kim, C. C. Cummins, G. N. George, I. J. Pickering, *J. Am. Chem. Soc.* **1996**, *118*, 8623–8638.
[113] I. Klopsch, E. Y. Yuzik-Klimova, S. Schneider, *Topics in Organometallic Chemistry*, Elsevier **2017**, Vol. 60, 71–112.
[114] R. M. Badger, *J. Chem. Phys.* **1934**, *2*, 128–131.
[115] M. D. Fryzuk, S. A. Johnson, *Coord. Chem. Rev.* **2000**, *200–202*, 379–409.
[116] D. H. Woen, G. P. Chen, J. W. Ziller, T. J. Boyle, F. Furche, W. J. Evans, *J. Am. Chem. Soc.* **2017**, *139*, 14861–14864.
[117] D. J. Mindiola, K. Meyer, J.-P. F. Cherry, T. A. Baker, C. C. Cummins, *Organometallics* **2000**, *19*, 1622–1624.
[118] J. J. Curley, T. R. Cook, S. Y. Reece, P. Müller, C. C. Cummins, *J. Am. Chem. Soc.* **2008**, *130*, 9394–9405.
[119] L. R. Doyle, A. J. Wooles, L. C. Jenkins, F. Tuna, E. J. L. McInnes, S. T. Liddle, *Angew. Chem. Int. Ed.* **2018**, *57*, 6314–6318.
[120] L. R. Doyle, A. J. Wooles, S. T. Liddle, *Angew. Chem. Int. Ed.* **2019**, *58*, 6674–6677.

[121] G. A. Silantyev, M. Förster, B. Schluschaß, J. Abbenseth, C. Würtele, C. Volkmann, M. C. Holthausen, S. Schneider, *Angew. Chem. Int. Ed.* **2017**, *56*, 5872–5876.
[122] B. Schluschaß, J. Abbenseth, S. Demeshko, M. Finger, A. Franke, C. Herwig, C. Würtele, I. Ivanovic-Burmazovic, C. Limberg, J. Telser, S. Schneider, *Chem. Sci.* **2019**, *10*, 10275–10282.
[123] I. Klopsch, M. Finger, C. Würtele, B. Milde, D. B. Werz, S. Schneider, *J. Am. Chem. Soc.* **2014**, *136*, 6881–6883.
[124] B. M. Lindley, R. S. van Alten, M. Finger, F. Schendzielorz, C. Würtele, A. J. M. Miller, I. Siewert, S. Schneider, *J. Am. Chem. Soc.* **2018**, *140*, 7922–7935.
[125] K. Shih, R. R. Schrock, R. Kempe, *J. Am. Chem. Soc.* **1994**, *116*, 8804–8805.
[126] M. Pucino, F. Allouche, C. P. Gordon, M. Wörle, V. Mougel, C. Copéret, *Chem. Sci.* **2019**, *10*, 6362–6367.
[127] R. Ferguson, E. Solari, C. Floriani, A. Chiesi-Villa, C. Rizzoli, *Angew. Chemie Int. Ed. Engl.* **1993**, *32*, 396–397.
[128] R. Ferguson, E. Solari, C. Floriani, D. Osella, M. Ravera, N. Re, A. Chiesi-Villa, C. Rizzoli, *J. Am. Chem. Soc.* **1997**, *119*, 10104–10115.
[129] N. Re, M. Rosi, A. Sgamellotti, C. Floriani, E. Solari, *Inorg. Chem.* **1994**, *33*, 4390–4397.
[130] L. Alig, M. Fritz, S. Schneider, *Chem. Rev.* **2019**, *119*, 2681–2751.
[131] M. J. Bezdek, S. Guo, P. J. Chirik, *Inorg. Chem.* **2016**, *55*, 3117–3127.
[132] C. E. Laplaza, C. C. Cummins, *Science* **1995**, *268*, 861–863.
[133] J. C. Peters, J. P. F. Cherry, J. C. Thomas, L. Baraldo, D. J. Mindiola, W. M. Davis, C. C. Cummins, *J. Am. Chem. Soc.* **1999**, *121*, 10053–10067.
[134] Q. Cui, D. G. Musaev, M. Svensson, S. Sieber, K. Morokuma, *J. Am. Chem. Soc.* **1995**, *117*, 12366–12367.
[135] N. J. Brookes, D. C. Graham, G. Christian, R. Stranger, B. F. Yates, *J. Comput. Chem.* **2009**, *30*, 2146–2156.
[136] G. Christian, R. Stranger, B. F. Yates, *Chem. Eur. J.* **2009**, *15*, 646–655.
[137] J. S. Figueroa, N. A. Piro, C. R. Clough, C. C. Cummins, *J. Am. Chem. Soc.* **2006**, *128*, 940–950.
[138] K. Arashiba, A. Eizawa, H. Tanaka, K. Nakajima, K. Yoshizawa, Y. Nishibayashi, *Bull. Chem. Soc. Jpn.* **2017**, *90*, 1111–1118.
[139] A. Yamamoto, K. Arashiba, S. Naniwa, K. Kato, H. Tanaka, K. Yoshizawa, Y. Nishibayashi, H. Yoshida, *Phys. Chem. Chem. Phys.* **2020**, *22*, 12368–12372.
[140] Y. Tanabe, Y. Sekiguchi, H. Tanaka, A. Konomi, K. Yoshizawa, S. Kuriyama, Y. Nishibayashi, *Chem. Commun.* **2020**, *56*, 6933–6936.
[141] T. J. Hebden, R. R. Schrock, M. K. Takase, P. Müller, *Chem. Commun.* **2012**, *48*, 1851.
[142] Q. Liao, A. Cavaillé, N. Saffon-Merceron, N. Mézailles, *Angew. Chem. Int. Ed.* **2016**, *55*, 11212–11216.
[143] M. L. Besmer, H. Braband, S. Schneider, B. Spingler, R. Alberto, *Inorg. Chem.* **2021**, *60*, 6696–6701.
[144] F. Meng, S. Kuriyama, H. Tanaka, A. Egi, K. Yoshizawa, Y. Nishibayashi, *Angew. Chem. Int. Ed.* **2021**, *60*, 13906–13912.
[145] I. Klopsch, M. Kinauer, M. Finger, C. Würtele, S. Schneider, *Angew. Chem. Int. Ed.* **2016**, *55*, 4786–4789.
[146] R. S. van Alten, F. Wätjen, S. Demeshko, A. J. M. Miller, C. Würtele, I. Siewert, S. Schneider, *Eur. J. Inorg. Chem.* **2020**, *2020*, 1402–1410.
[147] I. Klopsch, F. Schendzielorz, C. Volkmann, C. Würtele, S. Schneider, *Z. Anorg. Allg. Chem.* **2018**, *644*, 916–919.
[148] A. Katayama, T. Ohta, Y. Wasada-Tsutsui, T. Inomata, T. Ozawa, T. Ogura, H. Masuda, *Angew. Chem. Int. Ed.* **2019**, *58*, 11279–11284.
[149] V. Krewald, *Dalton Trans.* **2018**, *47*, 10320–10329.
[150] E. Solari, C. Da Silva, B. Iacono, J. Hesschenbrouck, C. Rizzoli, R. Scopelliti, C. Floriani, *Angew. Chem. Int. Ed.* **2001**, *40*, 3907–3909.
[151] A. S. Huss, J. J. Curley, C. C. Cummins, D. A. Blank, *J. Phys. Chem. B* **2013**, *117*, 1429–1436.
[152] F. Schendzielorz, M. Finger, J. Abbenseth, C. Würtele, V. Krewald, S. Schneider, *Angew. Chem.*

Int. Ed. **2019**, *58*, 830–834.
[153] Q. J. Bruch, G. P. Connor, C.-H. Chen, P. L. Holland, J. M. Mayer, F. Hasanayn, A. J. M. Miller, *J. Am. Chem. Soc.* **2019**, *141*, 20198–20208.
[154] H. Kunkely, A. Vogler, *Angew. Chem. Int. Ed.* **2010**, *49*, 1591–1593.
[155] V. Krewald, L. González, *Chem. Eur. J.* **2018**, *24*, 5112–5123.
[156] H. Kunkely, A. Vogler, *Z. Naturforsch. B* **2012**, *67*, 488–490.
[157] H. Kunkely, A. Vogler, *Inorg. Chim. Acta* **2012**, *391*, 229–231.
[158] S. Pavlidis, "Synthese Und Funktionalisierung Eines Rhenium (VI)-Nitrid-PNP-Pinzetten Komplexes," Georg-August Universität Göttingen, **2019**.
[159] R. S. van Alten, "Electrochemical N2-Splitting and Functionalisation in the Coordination Sphere of Rhenium," Georg-August Universität Göttingen, **2021**.
[160] L. Fan, B. M. Foxman, O. V. Ozerov, *Organometallics* **2004**, *23*, 326–328.
[161] B. C. Bailey, J. C. Huffman, D. J. Mindiola, W. Weng, O. V. Ozerov, *Organometallics* **2005**, *24*, 1390–1393.
[162] J. C. DeMott, C. Guo, B. M. Foxman, D. V. Yandulov, O. V. Ozerov, *Mendeleev Commun.* **2007**, *17*, 63–65.
[163] U. J. Kilgore, C. A. Sengelaub, M. Pink, A. R. Fout, D. J. Mindiola, *Angew. Chem. Int. Ed.* **2008**, *47*, 3769–3772.
[164] J. D. Masuda, K. C. Jantunen, O. V. Ozerov, K. J. T. Noonan, D. P. Gates, B. L. Scott, J. L. Kiplinger, *J. Am. Chem. Soc.* **2008**, *130*, 2408–2409.
[165] T. Cantat, B. L. Scott, D. E. Morris, J. L. Kiplinger, *Inorg. Chem.* **2009**, *48*, 2114–2127.
[166] J. Cheng, T. Shima, Z. Hou, *Angew. Chem. Int. Ed.* **2011**, *50*, 1857–1860.
[167] A. V. Zabula, Y. Qiao, A. J. Kosanovich, T. Cheisson, B. C. Manor, P. J. Carroll, O. V. Ozerov, E. J. Schelter, *Chem. Eur. J.* **2017**, *23*, 17923–17934.
[168] N. S. Lambic, R. D. Sommer, E. A. Ison, *Dalton Trans.* **2018**, *47*, 758–768.
[169] L. S. Yamout, M. Ataya, F. Hasanayn, P. L. Holland, A. J. M. Miller, A. S. Goldman, *J. Am. Chem. Soc.* **2021**, *143*, 9744–9757.
[170] A. T. Radosevich, J. G. Melnick, S. A. Stoian, D. Bacciu, C.-H. Chen, B. M. Foxman, O. V. Ozerov, D. G. Nocera, *Inorg. Chem.* **2009**, *48*, 9214–9221.
[171] W. Weng, C. Guo, C. Moura, L. Yang, B. M. Foxman, O. V. Ozerov, *Organometallics* **2005**, *24*, 3487–3499.
[172] W. Weng, C. Guo, R. Çelenligil-Çetin, B. M. Foxman, O. V. Ozerov, *Chem. Commun.* **2006**, 197–199.
[173] J. J. Davidson, J. C. Demott, C. Douvris, C. M. Fafard, N. Bhuvanesh, C. H. Chen, D. E. Herbert, C. I. Lee, B. J. McCulloch, B. M. Foxman, et al., *Inorg. Chem.* **2015**, *54*, 2916–2935.
[174] W. Weng, L. Yang, B. M. Foxman, O. V. Ozerov, *Organometallics* **2004**, *23*, 4700–4705.
[175] S. Gatard, C. Guo, B. M. Foxman, O. V. Ozerov, *Organometallics* **2007**, *26*, 6066–6075.
[176] J. Chatt, G. J. Leigh, D. M. P. Mingos, *J. Chem. Soc. A Inorganic, Phys. Theor.* **1969**, 1674.
[177] J. Abbenseth, M. Diefenbach, S. C. Bete, C. Würtele, C. Volkmann, S. Demeshko, M. C. Holthausen, S. Schneider, *Chem. Commun.* **2017**, *53*, 5511–5514.
[178] K. Arashiba, Y. Miyake, Y. Nishibayashi, *Nat. Chem.* **2011**, *3*, 120–125.
[179] N. Lease, E. M. Pelczar, T. Zhou, S. Malakar, T. J. Emge, F. Hasanayn, K. Krogh-Jespersen, A. S. Goldman, *Organometallics* **2018**, *37*, 314–326.
[180] G. A. Silantyev, M. Förster, B. Schluschaß, J. Abbenseth, C. Würtele, C. Volkmann, M. C. Holthausen, S. Schneider, *Angew. Chem. Int. Ed.* **2017**, *56*, 5872–5876.
[181] S. J. K. Forrest, B. Schluschaß, E. Y. Yuzik-Klimova, S. Schneider, *Chem. Rev.* **2021**, *121*, 6522–6587.
[182] H. Kunkely, A. Vogler, *Angew. Chem. Int. Ed.* **2010**, *49*, 1591–1593.
[183] I. Klopsch, M. Kinauer, M. Finger, C. Würtele, S. Schneider, *Angew. Chem. Int. Ed.* **2016**, *55*, 4786–4789.
[184] I. Klopsch, F. Schendzielorz, C. Volkmann, C. Würtele, S. Schneider, *Z. Anorg. Allg. Chem.* **2018**, *644*, 916–919.
[185] K. D. Demadis, T. J. Meyer, P. S. White, *Inorg. Chem.* **1997**, *36*, 5678–5679.
[186] K. D. Demadis, E.-S. El-Samanody, G. M. Coia, T. J. Meyer, *J. Am. Chem. Soc.* **1999**, *121*, 535–

544.
[187] K. D. Demadis, C. M. Hartshorn, T. J. Meyer, *Chem. Rev.* **2001**, *101*, 2655–2685.
[188] M. B. Robin, P. Day, in *Adv. Inorg. Chem. Radiochem.*, **1968**, pp. 247–422.
[189] W. P. Griffith, D. Pawson, *J. Chem. Soc. Dalton Trans.* **1973**, 1315.
[190] F. Wätjen, "Rhenium and Osmium PNP Pincer Complexes for Nitrogen Fixation and Nitride Transfer," Georg-August Universität Göttingen, **2019**.
[191] M. H. V. Huynh, P. S. White, K. D. John, T. J. Meyer, *Angew. Chem. Int. Ed.* **2001**, *40*, 4049.
[192] G. M. Coia, P. S. White, T. J. Meyer, D. A. Wink, L. K. Keefer, W. M. Davis, *J. Am. Chem. Soc.* **1994**, *116*, 3649–3650.
[193] B. J. Charette, J. W. Ziller, A. F. Heyduk, *Inorg. Chem.* **2021**, *60*, 1579–1589.
[194] B. J. Charette, J. W. Ziller, A. F. Heyduk, *Inorg. Chem.* **2021**, *60*, 5367–5375.
[195] G. R. Fulmer, A. J. M. Miller, N. H. Sherden, H. E. Gottlieb, A. Nudelman, B. M. Stoltz, J. E. Bercaw, K. I. Goldberg, *Organometallics* **2010**, *29*, 2176–2179.
[196] K. Knox, C. E. Coffey, *J. Am. Chem. Soc.* **1959**, *81*, 5–7.
[197] Q. J. Bruch, G. P. Connor, N. D. McMillion, A. S. Goldman, F. Hasanayn, P. L. Holland, A. J. M. Miller, *ACS Catal.* **2020**, *10*, 10826–10846.
[198] N. G. Connelly, W. E. Geiger, *Chem. Rev.* **1996**, *96*, 877–910.
[199] N. S. Lambic, R. D. Sommer, E. A. Ison, *Dalton Trans.* **2018**, *47*, 758–768.
[200] F. Schendzielorz, M. Finger, J. Abbenseth, C. Würtele, V. Krewald, S. Schneider, *Angew. Chem. Int. Ed.* **2019**, *58*, 830–834.
[201] Q. J. Bruch, G. P. Connor, C.-H. Chen, P. L. Holland, J. M. Mayer, F. Hasanayn, A. J. M. Miller, *J. Am. Chem. Soc.* **2019**, *141*, 20198–20208.
[202] G. P. Connor, B. Q. Mercado, H. M. C. Lant, J. M. Mayer, P. L. Holland, *Inorg. Chem.* **2019**, *58*, 10791–10801.
[203] I. Klopsch, "N2 Splitting and Functionalization in the Coordination Sphere of Rhenium," Georg-August Universität Göttingen, **2016**.
[204] B. M. Lindley, R. S. Van Alten, M. Finger, F. Schendzielorz, C. Würtele, A. J. M. Miller, I. Siewert, S. Schneider, *J. Am. Chem. Soc.* **2018**, *140*, 7922–7935.
[205] T. I. Al-Salih, C. J. Pickett, *J. Chem. Soc., Dalton Trans.* **1985**, 1255.
[206] S. Kim, F. Loose, P. J. Chirik, *Chem. Rev.* **2020**, *120*, 5637–5681.
[207] M. Anand, C. S. Abraham, J. K. Nørskov, *Chem. Sci.* **2021**, *12*, 6442–6448.
[208] R. Eikey, A.-O. M. M., *Coord. Chem. Rev.* **2003**, *243*, 83–124.
[209] C. J. Ballhausen, H. B. Gray, *Inorg. Chem.* **1962**, *1*, 111–122.
[210] R. Hoffmann, *Angew. Chemie Int. Ed. Engl.* **1982**, *21*, 711–724.
[211] J. M. Smith, in *Prog. Inorg. Chem.*, **2014**, 417–470.
[212] J. F. Berry, *Comments Inorg. Chem.* **2009**, *30*, 28–66.
[213] B. K. Bennett, T. J. Crevier, D. D. Dumez, Y. Matano, W. S. McNeil, J. M. Mayer, *J. Organomet. Chem.* **1999**, *591*, 96–103.
[214] A. Walstrom, M. Pink, X. Yang, J. Tomaszewski, M.-H. Baik, K. G. Caulton, *J. Am. Chem. Soc.* **2005**, *127*, 5330–5331.
[215] M. G. Scheibel, B. Askevold, F. W. Heinemann, E. J. Reijerse, B. De Bruin, S. Schneider, *Nat. Chem.* **2012**, *4*, 552–558.
[216] F. S. Schendzielorz, M. Finger, C. Volkmann, C. Würtele, S. Schneider, *Angew. Chem. Int. Ed.* **2016**, *55*, 11417–11420.
[217] J. Schöffel, A. Y. Rogachev, S. D. B. George, P. Burger, *Angew. Chem. Int. Ed.* **2009**, *48*, 4734–4738.
[218] D. E. Wigley, in *Prog. Inorg. Chem. Vol. 42*, **2007**, pp. 239–482.
[219] W. A. Nugent, R. J. McKinney, R. V. Kasowski, F. A. Van-Catledge, *Inorg. Chim. Acta* **1982**, *65*, L91–L93.
[220] E. D. Hedegård, J. Bendix, S. P. A. Sauer, *J. Mol. Struct. THEOCHEM* **2009**, *913*, 1–7.
[221] U. Abram, E. Schulz Lang, S. Abram, J. Wegmann, J. R. Dilworth, R. Kirmse, J. D. Woollins, *J. Chem. Soc., Dalton Trans.* **1997**, 623–630.
[222] W.-H. Leung, J. L. C. Chim, I. D. Williams, W.-T. Wong, *Inorg. Chem.* **1999**, *38*, 3000–3005.
[223] U. Abram, B. Schmidt-Brücken, S. Ritter, *Polyhedron* **1999**, *18*, 831–838.

[224] B. Schmidt-Brücken, U. Abram, *Z. Anorg. Allg. Chem.* **2001**, *627*, 1714–1716.
[225] K. Frick, U. Ziener, M. Hanack, *Eur. J. Inorg. Chem.* **1999**, *1999*, 1309–1313.
[226] S. Ritter, U. Abram, *Z. Anorg. Allg. Chem.* **1996**, *622*, 965–973.
[227] S. Ritter, U. Abram, *Inorg. Chim. Acta* **1995**, *231*, 245–248.
[228] U. Abram, A. Hagenbach, A. Voigt, R. Kirmse, *Z. Anorg. Allg. Chem.* **2001**, *627*, 955–964.
[229] L. H. Doerrer, A. J. Graham, M. L. H. Green, *J. Chem. Soc., Dalton Trans.* **1998**, *2*, 3941–3946.
[230] U. Abram, *Z. Anorg. Allg. Chem.* **1999**, *625*, 839–841.
[231] U. Abram, A. Voigt, R. Kirmse, *Polyhedron* **2000**, *19*, 1741–1748.
[232] W. Leung, E. Y. Y. Chan, T. C. Y. Lai, W. Wong, *J. Chem. Soc., Dalt. Trans.* **2000**, *4*, 51–56.
[233] U. Abram, S. Ritter, *Z. Anorg. Allg. Chem.* **1994**, *620*, 1223–1228.
[234] M. W. Bishop, J. Chatt, J. R. Dilworth, *J. Chem. Soc., Dalton Trans.* **1979**, 1.
[235] B. W. Tsang, J. Reibenspies, A. E. Martell, *Inorg. Chim. Acta* **1993**, *211*, 23–26.
[236] K. Frick, S. Verma, J. Sundermeyer, M. Hanack, *Eur. J. Inorg. Chem.* **2000**, *2000*, 1025–1030.
[237] I. Klopsch, M. Finger, C. Würtele, B. Milde, D. B. Werz, S. Schneider, *J. Am. Chem. Soc.* **2014**, *136*, 6881–6883.
[238] W.-L. Man, W. W. Y. Lam, S.-M. Yiu, T.-C. Lau, S.-M. Peng, *J. Am. Chem. Soc.* **2004**, *126*, 15336–15337.
[239] R. W. Marshman, J. M. Shusta, S. R. Wilson, P. A. Shapley, *Organometallics* **1991**, *10*, 1671–1676.
[240] D. Sellmann, M. W. Wemple, W. Donaubauer, F. W. Heinemann, *Inorg. Chem.* **1997**, *36*, 1397–1402.
[241] J. L. Koch, P. A. Shapley, *Organometallics* **1997**, *16*, 4071–4076.
[242] T. J. Crevier, B. K. Bennett, J. D. Soper, J. A. Bowman, A. Dehestani, D. A. Hrovat, S. Lovell, W. Kaminsky, J. M. Mayer, *J. Am. Chem. Soc.* **2001**, *123*, 1059–1071.
[243] T. J. Crevier, J. M. Mayer, *Angew. Chem. Int. Ed.* **1998**, *37*, 1891–1893.
[244] C. F. Leung, T. W. Wong, T. C. Lau, W. T. Wong, *Eur. J. Inorg. Chem.* **2005**, 773–778.
[245] T. J. Crevier, J. M. Mayer, *J. Am. Chem. Soc.* **1998**, *120*, 5595–5596.
[246] A. G. Maestri, K. S. Cherry, J. J. Toboni, S. N. Brown, *J. Am. Chem. Soc.* **2001**, *123*, 7459–7460.
[247] S. N. Brown, *J. Am. Chem. Soc.* **1999**, *121*, 9752–9753.
[248] A. G. Maestri, S. D. Taylor, S. M. Schuck, S. N. Brown, *Organometallics* **2004**, *23*, 1932–1946.
[249] M. H. V Huynh, P. S. White, C. A. Carter, T. J. Meyer, *Angew. Chem. Int. Ed.* **2001**, *40*, 3037–3039.
[250] M. H. V. Huynh, T. J. Meyer, R. T. Baker, *J. Am. Chem. Soc.* **2003**, *125*, 2832–2833.
[251] J. Xiang, W.-L. Man, S.-M. Yiu, S.-M. Peng, T.-C. Lau, *Chem. Eur. J.* **2011**, *17*, 13044–13051.
[252] K. D. Demadis, T. J. Meyer, P. S. White, *Inorg. Chem.* **1998**, *37*, 3610–3619.
[253] K. D. Demadis, E.-S. El-Samanody, T. J. Meyer, P. S. White, *Inorg. Chem.* **1998**, *37*, 838–839.
[254] M. H. V Huynh, R. T. Baker, D. L. Jameson, A. Labouriau, T. J. Meyer, *J. Am. Chem. Soc.* **2002**, *124*, 4580–4582.
[255] M. H. V. Huynh, E.-S. El-Samanody, K. D. Demadis, P. S. White, T. J. Meyer, *Inorg. Chem.* **2000**, *39*, 3075–3085.
[256] M. H. V. Huynh, E.-S. El-Samanody, K. D. Demadis, T. J. Meyer, P. S. White, *J. Am. Chem. Soc.* **1999**, *121*, 1403–1404.
[257] M. R. McCarthy, T. J. Crevier, B. Bennett, A. Dehestani, J. M. Mayer, *J. Am. Chem. Soc.* **2000**, *122*, 12391–12392.
[258] Q.-F. Zhang, K.-K. Lau, J. L. C. Chim, T. K. T. Wong, W.-T. Wong, I. D. Williams, W.-H. Leung, *J. Chem. Soc. Dalton Trans.* **2000**, 3027–3033.
[259] W. Leung, E. Y. Y. Chan, T. C. Y. Lai, W. Wong, *J. Chem. Soc. Dalton Trans.* **2000**, *4*, 51–56.
[260] T.-W. Wong, T.-C. Lau, W.-T. Wong, *Inorg. Chem.* **1999**, *38*, 6181–6186.
[261] K. D. Demadis, M. Bakir, B. G. Klesczewski, D. S. Williams, P. S. White, T. J. Meyer, *Inorg. Chim. Acta* **1998**, *270*, 511–526.
[262] T. J. Crevier, S. Lovell, J. M. Mayer, A. L. Rheingold, I. A. Guzei, *J. Am. Chem. Soc.* **1998**, *120*, 6607–6608.
[263] G.-S. Fang, J.-S. Huang, N. Zhu, C.-M. Che, *Eur. J. Inorg. Chem.* **2004**, *2004*, 1341–1348.
[264] M. H. V. Huynh, P. S. White, T. J. Meyer, *Inorg. Chem.* **2000**, *39*, 2825–2830.

[265] D. S. Williams, T. J. Meyer, P. S. White, *J. Am. Chem. Soc.* **1995**, *117*, 823–824.
[266] T. J. Meyer, M. H. V. Huynh, *Inorg. Chem.* **2003**, *42*, 8140–8160.
[267] "'Nitric Acid,'" can be found under https://essentialchemicalindustry.org/chemicals/nitric-acid.html, **2016**.
[268] M. S. Stark, J. T. H. Harrison, C. Anastasi, *J. Geophys. Res. Atmos.* **1996**, *101*, 6963–6969.
[269] B. S. Patil, Q. Wang, V. Hessel, J. Lang, *Catal. Today* **2015**, *256*, 49–66.
[270] L. Y. Stein, *Curr. Opin. Chem. Biol.* **2019**, *49*, 9–15.
[271] M. A. H. J. van Kessel, D. R. Speth, M. Albertsen, P. H. Nielsen, H. J. M. Op den Camp, B. Kartal, M. S. M. Jetten, S. Lücker, *Nature* **2015**, *528*, 555–559.
[272] H. Daims, E. V. Lebedeva, P. Pjevac, P. Han, C. Herbold, M. Albertsen, N. Jehmlich, M. Palatinszky, J. Vierheilig, A. Bulaev, et al., *Nature* **2015**, *528*, 504–509.
[273] W. G. Zumft, *Microbiol. Mol. Biol. Rev.* **1997**, *61*, 533–616.
[274] J. A. McCleverty, *Chem. Rev.* **2004**, *104*, 403–418.
[275] J. Hartung, *Chem. Rev.* **2009**, *109*, 4500–4517.
[276] M. W. Siegel, R. J. Celotta, J. L. Hall, J. Levine, R. A. Bennett, *Phys. Rev. A* **1972**, *6*, 607–631.
[277] D. Teillet-Billy, F. Fiquet-Fayard, *J. Phys. B At. Mol. Phys.* **1977**, *10*, L111–L117.
[278] A. J. Deeming, *Annu. Rep. Prog. Chem., Sect. A Inorg. Chem.* **1980**, *77*, 269–301.
[279] H. L. Johnston, W. F. Giauque, *J. Am. Chem. Soc.* **1929**, *51*, 3194–3214.
[280] J. Mason, *J. Chem. Educ.* **1975**, *52*, 445.
[281] L. Zhang, G. Spezzati, V. Muravev, M. A. Verheijen, B. Zijlstra, I. A. W. Filot, Y. Su, M. Chang, E. J. M. Hensen, *ACS Catal.* **2021**, 5614–5627.
[282] C. Sun, L. Yang, M. A. Ortuño, A. M. Wright, T. Chen, A. R. Head, N. López, M. Dincă, *Angew. Chem. Int. Ed.* **2021**, *60*, 7845–7850.
[283] Y. Shiro, *Biochim. Biophys. Acta Bioenerg.* **2012**, *1817*, 1907–1913.
[284] T. Hino, Y. Matsumoto, S. Nagano, H. Sugimoto, Y. Fukumori, T. Murata, S. Iwata, Y. Shiro, *Science* **2010**, *330*, 1666–1670.
[285] W. G. Zumft, *J. Inorg. Biochem.* **2005**, *99*, 194–215.
[286] P. C. Ford, I. M. Lorkovic, *Chem. Rev.* **2002**, *102*, 993–1018.
[287] G. C. Dousmanis, *Phys. Rev.* **1955**, *97*, 967–970.
[288] J. Chatt, L. A. Duncanson, *J. Chem. Soc.* **1953**, 2939.
[289] J. Chatt, L. A. Duncanson, L. M. Venanzi, *J. Chem. Soc.* **1955**, 4456.
[290] T. W. Hayton, P. Legzdins, W. B. Sharp, *Chem. Rev.* **2002**, *102*, 935–992.
[291] A. E. Crease, P. Legzdins, *J. Chem. Soc., Dalton Trans.* **1973**, 1501.
[292] A. E. Crease, P. Legzdins, *J. Chem. Soc., Chem. Commun.* **1972**, *0*, 268.
[293] A. Llamazares, H. W. Schmalle, H. Berke, *Organometallics* **2001**, *20*, 5277–5288.
[294] K. E. Lee, A. M. Arif, J. A. Gladysz, *Inorg. Chem.* **1990**, *29*, 2885–2887.
[295] K. E. Lee, A. M. Arif, J. A. Gladysz, *Chem. Ber.* **1991**, *124*, 309–320.
[296] W. B. Sharp, P. Legzdins, B. O. Patrick, *J. Am. Chem. Soc.* **2001**, *123*, 8143–8144.
[297] D. Gusev, A. Llamazares, G. Artus, H. Jacobsen, H. Berke, *Organometallics* **1999**, *18*, 75–89.
[298] Y. Jiang, W. Huang, H. W. Schmalle, O. Blacque, T. Fox, H. Berke, *Organometallics* **2013**, *32*, 7043–7052.
[299] Y. Jiang, B. Schirmer, O. Blacque, T. Fox, S. Grimme, H. Berke, *J. Am. Chem. Soc.* **2013**, *135*, 4088–4102.
[300] Y. Jiang, W. Huang, H. W. Schmalle, O. Blacque, T. Fox, H. Berke, *Eur. J. Inorg. Chem.* **2014**, *2014*, 140–147.
[301] H. Jacobsen, K. Heinze, A. Llamazares, H. W. Schmalle, G. Artus, H. Berke, *J. Chem. Soc. Dalton Trans.* **1999**, *2*, 1717–1728.
[302] J. Böhmer, G. Haselhorst, K. Wieghardt, B. Nuber, *Angew. Chem. Int. Ed. Engl.* **1994**, *33*, 1473–1476.
[303] M. L. H. Green, J. T. James, J. F. Sanders, *Chem. Commun.* **1996**, 1343.
[304] J. S. Southern, M. T. Green, G. L. Hillhouse, I. A. Guzei, A. L. Rheingold, *Inorg. Chem.* **2001**, *40*, 6039–6046.
[305] A. L. Odom, C. C. Cummins, J. D. Protasiewicz, *J. Am. Chem. Soc.* **1995**, *117*, 6613–6614.
[306] P. Legzdins, S. J. Rettig, K. J. Ross, J. E. Veltheer, *J. Am. Chem. Soc.* **1991**, *113*, 4361–4363.

[307] P. Legzdins, S. J. Rettig, K. J. Ross, R. J. Batchelor, F. W. B. Einstein, *Organometallics* **1995**, *14*, 5579–5587.
[308] D. Sellmann, B. Seubert, *Angew. Chem. Int. Ed. Engl.* **1992**, *31*, 205–207.
[309] H. Berke, R. Hoffmann, *J. Am. Chem. Soc.* **1978**, *100*, 7224–7236.
[310] W. P. Weiner, M. A. White, R. G. Bergman, *J. Am. Chem. Soc.* **1981**, *103*, 3612–3614.
[311] M. D. Seidler, R. G. Bergman, *Organometallics* **1983**, *2*, 1897–1899.
[312] S. Niu, M. B. Hall, *J. Phys. Chem. A* **1997**, *101*, 1360–1365.
[313] S. Niu, M. B. Hall, *J. Am. Chem. Soc.* **1997**, *119*, 3077–3086.
[314] W. P. Weiner, R. G. Bergman, *J. Am. Chem. Soc.* **1983**, *105*, 3922–3929.
[315] P. Legzdins, B. Wassink, F. W. B. Einstein, A. C. Willis, *J. Am. Chem. Soc.* **1986**, *108*, 317–318.
[316] S. H. Lin, G. H. Lee, S. M. Peng, R. S. Liu, *Organometallics* **1993**, *12*, 2591–2599.
[317] C. M. Frech, O. Blacque, H. W. Schmalle, H. Berke, *Chem. Eur. J.* **2006**, *12*, 5199–5209.
[318] Y. Wang, J. J. R. Fraústo da Silva, A. J. L. Pombeiro, M. A. Pellinghelli, A. Tiripicchio, *J. Organomet. Chem.* **1994**, *476*, C9–C11.
[319] Z. Assefa, D. M. Stanbury, *J. Am. Chem. Soc.* **1997**, *119*, 521–530.
[320] B. Mondal, H. Paul, V. G. Puranik, G. K. Lahiri, *J. Chem. Soc., Dalton Trans.* **2001**, *1*, 481–487.
[321] H. Nagao, K. Ito, N. Tsuboya, D. Ooyama, N. Nagao, F. Scott Howell, M. Mukaida, *Inorg. Chim. Acta* **1999**, *290*, 113–119.
[322] M. Weidemann, S. Sievertsen, H. Homborg, *Z. Anorg. Allg. Chem.* **1998**, *624*, 909–918.
[323] P. Kumar, Y.-M. Lee, Y. J. Park, M. A. Siegler, K. D. Karlin, W. Nam, *J. Am. Chem. Soc.* **2015**, *137*, 4284–4287.
[324] S. G. Clarkson, F. Basolo, *Inorg. Chem.* **1973**, *12*, 1528–1534.
[325] J. L. Schneider, S. M. Carrier, C. E. Ruggiero, V. G. Young, W. B. Tolman, *J. Am. Chem. Soc.* **1998**, *120*, 11408–11418.
[326] A. J. Timmons, M. D. Symes, *Chem. Soc. Rev.* **2015**, *44*, 6708–6722.
[327] A. K. Bar, M. J. Heras Ojea, J. Tang, R. A. Layfield, *J. Am. Chem. Soc.* **2020**, *142*, 4104–4107.
[328] C.-H. Chuang, W.-F. Liaw, C.-H. Hung, *Angew. Chem. Int. Ed.* **2016**, *55*, 5190–5194.
[329] A. R. Ravishankara, J. S. Daniel, R. W. Portmann, *Science* **2009**, *326*, 123–125.
[330] D. Fowler, C. E. Steadman, D. Stevenson, M. Coyle, R. M. Rees, U. M. Skiba, M. A. Sutton, J. N. Cape, A. J. Dore, M. Vieno, et al., *Atmos. Chem. Phys.* **2015**, *15*, 13849–13893.
[331] V. N. Parmon, G. I. Panov, A. Uriarte, A. S. Noskov, *Catal. Today* **2005**, *100*, 115–131.
[332] K. Severin, *Chem. Soc. Rev.* **2015**, *44*, 6375–6386.
[333] J. G. Andino, U. J. Kilgore, M. Pink, A. Ozarowski, J. Krzystek, J. Telser, M. H. Baik, D. J. Mindiola, *Chem. Sci.* **2010**, *1*, 351–356.
[334] U. J. Kilgore, C. A. Sengelaub, H. Fan, J. Tomaszewski, J. A. Karty, M.-H. Baik, D. J. Mindiola, *Organometallics* **2009**, *28*, 843–852.
[335] A. Reinholdt, D. Pividori, A. L. Laughlin, I. M. DiMucci, S. N. MacMillan, M. G. Jafari, M. R. Gau, P. J. Carroll, J. Krzystek, A. Ozarowski, et al., *Inorg. Chem.* **2020**, *59*, 17834–17850.
[336] C. E. Laplaza, A. L. Odom, W. M. Davis, C. C. Cummins, J. D. Protasiewicz, *J. Am. Chem. Soc.* **1995**, *117*, 4999–5000.
[337] J. P. Reeds, B. L. Yonke, P. Y. Zavalij, L. R. Sita, *J. Am. Chem. Soc.* **2011**, *133*, 18602–18605.
[338] A. G. Tskhovrebov, E. Solari, M. D. Wodrich, R. Scopelliti, K. Severin, *Angew. Chem. Int. Ed.* **2012**, *51*, 232–234.
[339] M. Falcone, L. Barluzzi, J. Andrez, F. Fadaei Tirani, I. Zivkovic, A. Fabrizio, C. Corminboeuf, K. Severin, M. Mazzanti, *Nat. Chem.* **2019**, *11*, 154–160.
[340] S. Ghosh, S. I. Gorelsky, S. DeBeer George, J. M. Chan, I. Cabrito, D. M. Dooley, J. J. G. Moura, I. Moura, E. I. Solomon, *J. Am. Chem. Soc.* **2007**, *129*, 3955–3965.
[341] C. C. Mokhtarzadeh, C. Chan, C. E. Moore, A. L. Rheingold, J. S. Figueroa, *J. Am. Chem. Soc.* **2019**, *141*, 15003–15007.
[342] W. B. Tolman, *Angew. Chem. Int. Ed.* **2010**, *49*, 1018–1024.
[343] J. N. Armor, H. Taube, *J. Am. Chem. Soc.* **1969**, *91*, 6874–6876.
[344] F. Paulat, T. Kuschel, C. Näther, V. K. K. Praneeth, O. Sander, N. Lehnert, *Inorg. Chem.* **2004**, *43*, 6979–6994.

[345] N. A. Piro, M. F. Lichterman, W. H. Harman, C. J. Chang, *J. Am. Chem. Soc.* **2011**, *133*, 2108–2111.
[346] C. B. Pamplin, E. S. F. Ma, N. Safari, S. J. Rettig, B. R. James, *J. Am. Chem. Soc.* **2001**, *123*, 8596–8597.
[347] M. R. Gyton, B. Leforestier, A. B. Chaplin, *Angew. Chem. Int. Ed.* **2019**, *58*, 15295–15298.
[348] V. Zhuravlev, P. J. Malinowski, *Angew. Chem. Int. Ed.* **2018**, *57*, 11697–11700.
[349] B. M. Puerta Lombardi, C. Gendy, B. S. Gelfand, G. M. Bernard, R. E. Wasylishen, H. M. Tuononen, R. Roesler, *Angew. Chem. Int. Ed.* **2021**, *60*, 7077–7081.
[350] A. Walstrom, M. Pink, H. Fan, J. Tomaszewski, K. G. Caulton, *Inorg. Chem.* **2007**, *46*, 7704–7706.
[351] L. Hartung, "Chemische Transformation von Stickstoff Zu Nitroxiden Mittels Eines Rhenium-PNP- Pinzetten Komplexes," Georg-August Universität Göttingen, **2021**.
[352] A. J. Kosanovich, W.-C. Shih, R. Ramírez-Contreras, O. V. Ozerov, *Dalton Trans.* **2016**, *45*, 18532–18540.
[353] B. Schluschaß, J. Borter, S. Rupp, S. Demeshko, C. Herwig, C. Limberg, N. A. Maciulis, J. Schneider, C. Würtele, V. Krewald, D. Schwarzer, S. Schneider, *JACS Au* **2021**, *1*, 879–894.
[354] K. Omura, D. Swern, *Tetrahedron* **1978**, *34*, 1651–1660.
[355] L. Mohammadkhani, M. M. Heravi, *ChemistrySelect* **2019**, *4*, 6309–6337.
[356] S. V. F. Hansen, T. Ulven, *Org. Lett.* **2015**, *17*, 2832–2835.
[357] J. . Morton, K. . Preston, *J. Magn. Reson.* **1978**, *30*, 577–582.
[358] M. G. Scheibel, I. Klopsch, H. Wolf, P. Stollberg, D. Stalke, S. Schneider, *Eur. J. Inorg. Chem.* **2013**, *2013*, 3836–3839.
[359] P. J. Blower, J. R. Dilworth, G. J. Leigh, B. D. Neaves, F. B. Normanton, J. Hutchinson, J. A. Zubieta, *J. Chem. Soc., Dalton Trans.* **1985**, 2647.
[360] H.-Y. Ng, W.-M. Cheung, E. Kwan Huang, K.-L. Wong, H. H. Y. Sung, I. D. Williams, W.-H. Leung, *Dalton Trans.* **2015**, *44*, 18459–18468.
[361] S. F. Vyboishchikov, G. Frenking, *Theor. Chem. Accounts Theory, Comput. Model. (Theoretica Chim. Acta)* **1999**, *102*, 300–308.
[362] B. Machura, *Coord. Chem. Rev.* **2005**, *249*, 2277–2307.
[363] B. Machura, R. Kruszynski, *J. Coord. Chem.* **2006**, *59*, 445–456.
[364] T. J. Bartczak, W. Czurak, J. O. Dzięgielewski, B. MacHura, A. Jankowska, J. Kusz, J. Warczewski, *Polyhedron* **1999**, *18*, 2313–2320.
[365] A. C. Merkle, N. L. Fry, P. K. Mascharak, N. Lehnert, *Inorg. Chem.* **2011**, *50*, 12192–12203.
[366] G. Monsch, P. Klüfers, *Angew. Chem. Int. Ed.* **2019**, *58*, 8566–8571.
[367] A. T. Radosevich, J. G. Melnick, S. A. Stoian, D. Bacciu, C.-H. Chen, B. M. Foxman, O. V. Ozerov, D. G. Nocera, *Inorg. Chem.* **2009**, *48*, 9214–9221.
[368] A. Klein, C. Vogler, W. Kaim, *Organometallics* **1996**, *15*, 236–244.
[369] T. Scheiring, A. Klein, W. Kaim, *J. Chem. Soc. Perkin Trans. 2* **1997**, 2569–2572.
[370] F. A. Cotton, B. F. G. Johnson, *Inorg. Chem.* **1964**, *3*, 1609–1612.
[371] M. Keilwerth, J. Hohenberger, F. W. Heinemann, J. Sutter, A. Scheurer, H. Fang, E. Bill, F. Neese, S. Ye, K. Meyer, *J. Am. Chem. Soc.* **2019**, *141*, 17217–17235.
[372] T. M. Scherer, I. Hartenbach, F. Lissner, B. Schwederski, R. Hübner, J. Fiedler, S. Záliš, B. Sarkar, W. Kaim, *Z. Anorg. Allg. Chem.* **2021**, *647*, 867–875.
[373] C. M. Frech, O. Blacque, H. W. Schmalle, H. Berke, *Dalton Trans.* **2006**, 4590.
[374] A. J. Kosanovich, W.-C. Shih, O. V. Ozerov, *J. Organomet. Chem.* **2019**, *897*, 1–6.
[375] S. Amabilino, M. Tasse, P. G. Lacroix, S. Mallet-Ladeira, V. Pimienta, J. Akl, I. Sasaki, I. Malfant, *New J. Chem.* **2017**, *41*, 7371–7383.
[376] V. Bukhanko, P. G. Lacroix, I. Sasaki, M. Tassé, S. Mallet-Ladeira, Z. Voitenko, I. Malfant, *Inorg. Chim. Acta* **2018**, *482*, 195–205.
[377] A. W. Shaw, A. J. Vosper, *J. Chem. Soc. Faraday Trans. 1 Phys. Chem. Condens. Phases* **1977**, *73*, 1239.
[378] P.-H. Chan, S.-P. Chen, K.-W. Yeung, K.-C. Cheung, S. Hong, S.-G. Sun, K.-Y. Wong, *Electrochem. Commun.* **2005**, *7*, 1244–1248.
[379] E. S. El-Samanody, K. D. Demadis, T. J. Meyer, P. S. White, *Inorg. Chem.* **2001**, *40*, 3677–

3686.
[380] T.-C. Lau, J. Xiang, P. Ming, P. Yi, L.-J. Luo, S.-C. Cheng, X. Jin, S.-M. Yiu, W.-L. Man, C.-C. Ko, et al., *Chem. Sci.* **2021**, *68*, 42–61.
[381] C. J. Moulton, B. L. Shaw, *J. Chem. Soc., Dalton Trans.* **1976**, 1020–1024.
[382] M. Albrecht, G. van Koten, *Angew. Chem. Int. Ed.* **2001**, *40*, 3750–3781.
[383] E. Peris, R. H. Crabtree, *Chem. Soc. Rev.* **2018**, *47*, 1959–1968.
[384] J. R. Khusnutdinova, D. Milstein, *Angew. Chem. Int. Ed.* **2015**, *54*, 12236–12273.
[385] J. Choi, A. H. R. MacArthur, M. Brookhart, A. S. Goldman, *Chem. Rev.* **2011**, *111*, 1761–1779.
[386] O. R. Luca, R. H. Crabtree, *Chem. Soc. Rev.* **2013**, *42*, 1440–1459.
[387] H. Valdés, M. A. García-Eleno, D. Canseco-Gonzalez, D. Morales-Morales, *ChemCatChem* **2018**, *10*, 3136–3172.
[388] M. E. O'Reilly, A. S. Veige, *Chem. Soc. Rev.* **2014**, *43*, 6325–6369.
[389] S. Schneider, J. Meiners, B. Askevold, *Eur. J. Inorg. Chem.* **2012**, *2012*, 412–429.
[390] C. Gunanathan, D. Milstein, *Chem. Rev.* **2014**, *114*, 12024–12087.
[391] D. Benito-Garagorri, K. Kirchner, *Acc. Chem. Res.* **2008**, *41*, 201–213.
[392] F. Schneck, M. Finger, M. Tromp, S. Schneider, *Chem. Eur. J.* **2017**, *23*, 33–37.
[393] K. Ray, T. Petrenko, K. Wieghardt, F. Neese, *Dalton Trans.* **2007**, 1552–1566.
[394] S. C. E. Stieber, C. Milsmann, J. M. Hoyt, Z. R. Turner, K. D. Finkelstein, K. Wieghardt, S. Debeer, P. J. Chirik, *Inorg. Chem.* **2012**, *51*, 3770–3785.
[395] V. Lyaskovskyy, B. De Bruin, *ACS Catal.* **2012**, *2*, 270–279.
[396] K. Hindson, B. de Bruin, *Eur. J. Inorg. Chem.* **2012**, 340.
[397] T. K. Mukhopadhyay, C. L. Rock, M. Hong, D. C. Ashley, T. L. Groy, M. H. Baik, R. J. Trovitch, *J. Am. Chem. Soc.* **2017**, *139*, 4901–4915.
[398] M. W. Bouwkamp, S. C. Bart, E. J. Hawrelak, R. J. Trovitch, E. Lobkovsky, P. J. Chirik, *Chem. Commun.* **2005**, 3406–3408.
[399] T. M. Kooistra, Q. Knijnenburg, J. M. M. Smits, A. D. Horton, P. H. M. Budzelaar, A. W. Gal, *Angew. Chemie* **2001**, *113*, 4855–4858.
[400] J. M. Darmon, S. C. E. Stieber, K. T. Sylvester, I. Fernández, E. Lobkovsky, S. P. Semproni, E. Bill, K. Wieghardt, S. Debeer, P. J. Chirik, *J. Am. Chem. Soc.* **2012**, *134*, 17125–17137.
[401] R. J. Trovitch, E. Lobkovsky, P. J. Chirik, *J. Am. Chem. Soc.* **2008**, *130*, 11631–11640.
[402] D. Zhu, I. Thapa, I. Korobkov, S. Gambarotta, P. H. M. Budzelaar, *Inorg. Chem.* **2011**, *50*, 9879–9887.
[403] S. C. Bart, K. Chłopek, E. Bill, M. W. Bouwkamp, E. Lobkovsky, F. Neese, K. Wieghardt, P. J. Chirik, *J. Am. Chem. Soc.* **2006**, *128*, 13901–13912.
[404] J. M. Hoyt, K. T. Sylvester, S. P. Semproni, P. J. Chirik, *J. Am. Chem. Soc.* **2013**, *135*, 4862–4877.
[405] Q. Knijnenburg, S. Gambarotta, P. H. M. Budzelaar, *J. Chem. Soc., Dalton Trans.* **2006**, 5442–5448.
[406] D. Enright, S. Gambarotta, G. P. A. Yap, P. H. M. Budzelaar, *Angew. Chem. Int. Ed.* **2002**, *41*, 3873–3876.
[407] A. M. Tondreau, J. M. Darmon, B. M. Wile, S. K. Floyd, E. Lobkovsky, P. J. Chirik, *Organometallics* **2009**, *28*, 3928–3940.
[408] S. C. Bart, E. Lobkovsky, P. J. Chirik, *J. Am. Chem. Soc.* **2004**, *126*, 13794–13807.
[409] S. Monfette, Z. R. Turner, S. P. Semproni, P. J. Chirik, *J. Am. Chem. Soc.* **2012**, *134*, 4561–4564.
[410] C. Hamacher, N. Hurkes, A. Kaiser, A. Klein, A. Schüren, *Inorg. Chem.* **2009**, *48*, 9947–9951.
[411] T. J. Anderson, G. D. Jones, D. A. Vicic, *J. Am. Chem. Soc.* **2004**, *126*, 8100–8101.
[412] G. Desimoni, G. Faita, P. Quadrelli, *Chem. Rev.* **2003**, *103*, 3119–3154.
[413] G. Desimoni, G. Faita, K. A. Jørgensen, *Chem. Rev.* **2006**, *106*, 3561–3651.
[414] R. Noyori, T. Ohkuma, *Angew. Chem. Int. Ed.* **2001**, *40*, 40–73.
[415] T. Ohkuma, T. Hattori, H. Ooka, T. Inoue, R. Noyori, *Org. Lett.* **2004**, *6*, 2681–2683.
[416] C. A. Sandoval, T. Ohkuma, K. Muñiz, R. Noyori, *J. Am. Chem. Soc.* **2003**, *125*, 13490–13503.
[417] Y. Shvo, D. Czarkie, Y. Rahamim, D. F. Chodosh, *J. Am. Chem. Soc.* **1986**, *108*, 7400–7402.
[418] B. L. Conley, M. K. Pennington-Boggio, E. Boz, T. J. Williams, *Chem. Rev.* **2010**, *110*, 2294–2312.

[419] Y. Blum, D. Czarkie, Y. Rahamim, Y. Shvo, *Organometallics* **1985**, *4*, 1459–1461.
[420] C. P. Casey, H. Guan, *J. Am. Chem. Soc.* **2007**, *129*, 5816–5817.
[421] H.-J. Knölker, E. Baum, H. Goesmann, R. Klauss, *Angew. Chem. Int. Ed.* **1999**, *38*, 2064–2066.
[422] R. Langer, G. Leitus, Y. Ben-David, D. Milstein, *Angew. Chem. Int. Ed.* **2011**, *50*, 2120–2124.
[423] D. Milstein, *Phil. Trans. R. Soc. A* **2015**, *373*, 20140189.
[424] M. Vogt, A. Nerush, M. A. Iron, G. Leitus, Y. Diskin-Posner, L. J. W. Shimon, Y. Ben-David, D. Milstein, *J. Am. Chem. Soc.* **2013**, *135*, 17004–17018.
[425] M. Vogt, A. Nerush, Y. Diskin-Posner, Y. Ben-David, D. Milstein, *Chem. Sci.* **2014**, *5*, 2043–2051.
[426] J. Zhang, G. Leitus, Y. Ben-David, D. Milstein, *Angew. Chemie* **2006**, *118*, 1131–1133.
[427] A. Anaby, M. Feller, Y. Ben-David, G. Leitus, Y. Diskin-Posner, L. J. W. Shimon, D. Milstein, *J. Am. Chem. Soc.* **2016**, *138*, 9941–9950.
[428] E. Ben-Ari, G. Leitus, L. J. W. Shimon, D. Milstein, *J. Am. Chem. Soc.* **2006**, *128*, 15390–15391.
[429] L. Schwartsburd, M. A. Iron, L. Konstantinovski, E. Ben-Ari, D. Milstein, *Organometallics* **2011**, *30*, 2721.
[430] M. Vogt, O. Rivada-Wheelaghan, M. A. Iron, G. Leitus, Y. Diskin-Posner, L. J. W. Shimon, Y. Ben-David, D. Milstein, *Organometallics* **2013**, *32*, 300–308.
[431] M. Feller, E. Ben-Ari, M. A. Iron, Y. Diskin-Posner, G. Leitus, L. J. W. Shimon, L. Konstantinovski, D. Milstein, *Inorg. Chem.* **2010**, *49*, 1615–1625.
[432] X. Yang, *Inorg. Chem.* **2011**, *50*, 12836–12843.
[433] N. Gorgas, B. Stöger, L. F. Veiros, E. Pittenauer, G. Allmaier, K. Kirchner, *Organometallics* **2014**, *33*, 6905–6914.
[434] R. Langer, M. A. Iron, L. Konstantinovski, Y. Diskin-Posner, G. Leitus, Y. Ben-David, D. Milstein, *Chem. Eur. J.* **2012**, *18*, 7196–7209.
[435] A. Bruneau-Voisine, D. Wang, T. Roisnel, C. Darcel, J.-B. Sortais, *Catal. Commun.* **2017**, *92*, 1–4.
[436] F. Kallmeier, T. Irrgang, T. Dietel, R. Kempe, *Angew. Chem. Int. Ed.* **2016**, *55*, 11806–11809.
[437] F. Kallmeier, R. Kempe, *Angew. Chem. Int. Ed.* **2018**, *57*, 46–60.
[438] S. Rösler, J. Obenauf, R. Kempe, *J. Am. Chem. Soc.* **2015**, *137*, 7998–8001.
[439] T. Zell, Y. Ben-David, D. Milstein, *Catal. Sci. Technol.* **2015**, *5*, 822–826.
[440] N. Gorgas, B. Stöger, L. F. Veiros, K. Kirchner, *ACS Catal.* **2016**, *6*, 2664–2672.
[441] J. A. Garg, S. Chakraborty, Y. Ben-David, D. Milstein, *Chem. Commun.* **2016**, *52*, 5285–5288.
[442] A. Mukherjee, D. Srimani, S. Chakraborty, Y. Ben-David, D. Milstein, *J. Am. Chem. Soc.* **2015**, *137*, 8888–8891.
[443] T. Zell, Y. Ben-David, D. Milstein, *Angew. Chem. Int. Ed.* **2014**, *53*, 4685–4689.
[444] N. A. Espinosa-Jalapa, A. Kumar, G. Leitus, Y. Diskin-Posner, D. Milstein, *J. Am. Chem. Soc.* **2017**, *139*, 11722–11725.
[445] F. Bertini, N. Gorgas, B. Stöger, M. Peruzzini, L. F. Veiros, K. Kirchner, L. Gonsalvi, *ACS Catal.* **2016**, *6*, 2889–2893.
[446] F. Bertini, M. Glatz, N. Gorgas, B. Stöger, M. Peruzzini, L. F. Veiros, K. Kirchner, L. Gonsalvi, *Chem. Sci.* **2017**, *8*, 5024–5029.
[447] N. Meyer, A. J. Lough, R. H. Morris, *Chem. Eur. J.* **2009**, *15*, 5605–5610.
[448] P. E. Sues, A. J. Lough, R. H. Morris, *Organometallics* **2011**, *30*, 4418–4431.
[449] W. Zuo, A. J. Lough, Y. F. Li, R. H. Morris, *Science* **2013**, *342*, 1080–1083.
[450] G. Zhang, B. L. Scott, S. K. Hanson, *Angew. Chem. Int. Ed.* **2012**, *51*, 12102–12106.
[451] G. Zhang, K. V. Vasudevan, B. L. Scott, S. K. Hanson, *J. Am. Chem. Soc.* **2013**, *135*, 8668–8681.
[452] S. Chakraborty, P. O. Lagaditis, M. Förster, E. A. Bielinski, N. Hazari, M. C. Holthausen, W. D. Jones, S. Schneider, *ACS Catal.* **2014**, *4*, 3994–4003.
[453] P. O. Lagaditis, P. E. Sues, J. F. Sonnenberg, K. Y. Wan, A. J. Lough, R. H. Morris, *J. Am. Chem. Soc.* **2014**, *136*, 1367–1380.
[454] S. Elangovan, C. Topf, S. Fischer, H. Jiao, A. Spannenberg, W. Baumann, R. Ludwig, K. Junge, M. Beller, *J. Am. Chem. Soc.* **2016**, *138*, 8809–8814.
[455] S. A. M. Smith, P. O. Lagaditis, A. Lüpke, A. J. Lough, R. H. Morris, *Chem. Eur. J.* **2017**, *23*,

7212–7216.
[456] M. B. Widegren, G. J. Harkness, A. M. Z. Slawin, D. B. Cordes, M. L. Clarke, *Angew. Chem. Int. Ed.* **2017**, *56*, 5825–5828.
[457] M. Garbe, K. Junge, S. Walker, Z. Wei, H. Jiao, A. Spannenberg, S. Bachmann, M. Scalone, M. Beller, *Angew. Chem. Int. Ed.* **2017**, *56*, 11237–11241.
[458] F. Schneck, M. Assmann, M. Balmer, K. Harms, R. Langer, *Organometallics* **2016**, *35*, 1931–1943.
[459] U. Jayarathne, Y. Zhang, N. Hazari, W. H. Bernskoetter, *Organometallics* **2017**, *36*, 409–416.
[460] K. Dong, S. Elangovan, R. Sang, A. Spannenberg, R. Jackstell, K. Junge, Y. Li, M. Beller, *Nat. Commun.* **2016**, *7*, 12075.
[461] C. Bornschein, S. Werkmeister, B. Wendt, H. Jiao, E. Alberico, W. Baumann, H. Junge, K. Junge, M. Beller, *Nat. Commun.* **2014**, *5*, 1–11.
[462] S. Chakraborty, H. Dai, P. Bhattacharya, N. T. Fairweather, M. S. Gibson, J. A. Krause, H. Guan, *J. Am. Chem. Soc.* **2014**, *136*, 7869–7872.
[463] S. Elangovan, B. Wendt, C. Topf, S. Bachmann, M. Scalone, A. Spannenberg, H. Jiao, W. Baumann, K. Junge, M. Beller, *Adv. Synth. Catal.* **2016**, *358*, 820–825.
[464] Y. Zhang, A. D. MacIntosh, J. L. Wong, E. A. Bielinski, P. G. Williard, B. Q. Mercado, N. Hazari, W. H. Bernskoetter, *Chem. Sci.* **2015**, *6*, 4291–4299.
[465] M. R. Mills, C. L. Barnes, W. H. Bernskoetter, *Inorg. Chem.* **2018**, *57*, 1590–1597.
[466] E. A. Bielinski, P. O. Lagaditis, Y. Zhang, B. Q. Mercado, C. Würtele, W. H. Bernskoetter, N. Hazari, S. Schneider, *J. Am. Chem. Soc.* **2014**, *136*, 10234–10237.
[467] Y. Li, L. Maser, L. Alig, Z. Ke, R. Langer, *Dalton Trans.* **2021**, *50*, 954-959.
[468] N. Deibl, R. Kempe, *Angew. Chem. Int. Ed.* **2017**, *56*, 1663–1666.
[469] F. Huang, Z. Liu, Z. Yu, *Angew. Chem. Int. Ed.* **2016**, *55*, 862–875.
[470] G. Zhang, Z. Yin, S. Zheng, *Org. Lett.* **2016**, *18*, 300–303.
[471] A. Bruneau-Voisine, D. Wang, V. Dorcet, T. Roisnel, C. Darcel, J.-B. Sortais, *J. Catal.* **2017**, *347*, 57–62.
[472] S. Elangovan, J. Neumann, J.-B. Sortais, K. Junge, C. Darcel, M. Beller, *Nat. Commun.* **2016**, *7*, 12641.
[473] F. Schneck, M. Finger, M. Tromp, S. Schneider, *Chem. Eur. J.* **2017**, *23*, 33–37.
[474] F. Schneck, J. Ahrens, M. Finger, A. C. Stückl, C. Würtele, D. Schwarzer, S. Schneider, *Nat. Commun.* **2018**, *9*, 1161.
[475] F. Schneck, F. Schendzielorz, N. Hatami, M. Finger, C. Würtele, S. Schneider, *Angew. Chem. Int. Ed.* **2018**, *57*, 14482-14487.
[476] G. Rouschias, G. Wilkinson, *J. Chem. Soc. A Inorganic, Phys. Theor.* **1967**, 993.
[477] J. J. Warren, T. A. Tronic, J. M. Mayer, *Chem. Rev.* **2010**, *110*, 6961–7001.
[478] J. Meiners, A. Friedrich, E. Herdtweck, S. Schneider, *Organometallics* **2009**, *28*, 6331–6338.
[479] B. Boduszek, H. J. Shine, *J. Org. Chem.* **1988**, *53*, 5142–5143.
[480] N. A. Yakelis, R. G. Bergman, *Organometallic* **2005**, *24*, 3579–3581.
[481] A. Martinsen, J. Songstad, R. Larsson, M. Pouchard, P. Hagenmuller, A. F. Andresen, *Acta Chem. Scand.* **1977**, *31a*, 645–650.
[482] V. W. Manner, T. F. Markle, J. H. Freudenthal, J. P. Roth, J. M. Mayer, *Chem. Commun.* **2008**, *246*, 256–258.
[483] A. K. Hijazi, Z. A. Taha, A. Ajlouni, N. Radhakrishnan, B. Voit, F. E. Kühn, *J. Organomet. Chem.* **2014**, *763–764*, 65–68.
[484] J. R. Shapley, D. J. Santure, A. P. Sattelberger, F. A. Cotton, W. Wang, *Inorg. Synth.*, John Wiley & Sons, Inc., Hoboken, NJ, USA, **1989**.
[485] N. A. Giffin, M. Makramalla, A. D. Hendsbee, K. N. Robertson, C. Sherren, C. C. Pye, J. D. Masuda, J. A. C. Clyburne, *Org. Biomol. Chem.* **2011**, *9*, 3672.
[486] S. K. Sur, *J. Magn. Reson.* **1989**, 169.
[487] E. Bill, *MpView.1.4.1, Program for Viewing and Data Import for Files from MPMS3 SQUID Magnetometer*, Mülheim/Ruhr, **2021**.
[488] W. Haberditzl, *Angew. Chemie Int. Ed. Engl.* **1966**, *5*, 288–298.
[489] E. Bill, *JulX, Program for Simulation of Molecular Magnetic Data*, Max-Planck Institute For

Chemical Energy Conversion, Mülheim/Ruhr, **2008**.
[490] O. Kahn, *Molecular Magnetism*, VCH Publishers Inc., New York, **1993**.
[491] N. Elgrishi, K. J. Rountree, B. D. McCarthy, E. S. Rountree, T. T. Eisenhart, J. L. Dempsey, *J. Chem. Educ.* **2018**, *95*, 197–206.
[492] S. Stoll, A. Schweiger, *J. Magn. Reson.* **2006**, *178*, 42–55.
[493] *APEX3 V2016.9-0 (SAINT/SADABS/SHELXT/SHELXL)*, Bruker AXS Inc., Madison, WI, USA, **2016**.
[494] L. Krause, R. Herbst-Irmer, G. M. Sheldrick, D. Stalke, *J. Appl. Crystallogr.* **2015**, *48*, 3–10.
[495] G. M. Sheldrick, *Acta Crystallogr.* **2015**, *A71*, 3–8.
[496] G. M. Sheldrick, *Acta Crystallogr.* **2015**, *C71*, 3–8.
[497] G. M. Sheldrick, *Acta Crystallogr.* **2008**, *A64*, 112–122.
[498] J. Abbenseth, M. Diefenbach, A. Hinz, L. Alig, C. Würtele, J. M. Goicoechea, M. C. Holthausen, S. Schneider, *Angew. Chem. Int. Ed.* **2019**, *58*, 10966–10970.
[499] F. Neese, *WIREs Comput. Mol. Sci.* **2012**, *2*, 73–78.
[500] F. Neese, *WIREs Comput. Mol. Sci.* **2018**, *8*, 4–9.
[501] J. P. Perdew, K. Burke, M. Ernzerhof, *Phys. Rev. Lett.* **1996**, *77*, 3865–3868.
[502] J. P. Perdew, M. Ernzerhof, K. Burke, *J. Chem. Phys.* **1996**, *105*, 9982–9985.
[503] A. D. Becke, *Phys. Rev. A* **1988**, *38*, 3098–3100.
[504] J.-D. Chai, M. Head-Gordon, *Phys. Chem. Chem. Phys.* **2008**, *10*, 6615.
[505] F. Weigend, R. Ahlrichs, *Phys. Chem. Chem. Phys.* **2005**, *7*, 3297.
[506] D. Andrae, U. Häusermann, M. Dolg, H. Stoll, H. Preuß, *Theor. Chim. Acta* **1990**, *77*, 123–141.
[507] O. Treutler, R. Ahlrichs, *J. Chem. Phys.* **1995**, *102*, 346–354.
[508] K. Eichkorn, O. Treutler, H. Öhm, M. Häser, R. Ahlrichs, *Chem. Phys. Lett.* **1995**, *242*, 652–660.
[509] F. Neese, F. Wennmohs, A. Hansen, U. Becker, *Chem. Phys.* **2009**, *356*, 98–109.
[510] F. Weigend, *Phys. Chem. Chem. Phys.* **2006**, *8*, 1057.
[511] S. Grimme, J. Antony, S. Ehrlich, H. Krieg, *J. Chem. Phys.* **2010**, *132*, 154104.
[512] S. Grimme, S. Ehrlich, L. Goerigk, *J. Comput. Chem.* **2011**, *32*, 1456–1465.
[513] S. Grimme, *Chem. Eur. J.* **2012**, *18*, 9955–9964.
[514] V. Barone, M. Cossi, *J. Phys. Chem. A* **1998**, *102*, 1995–2001.
[515] E. D. Glendening, C. R. Landis, F. Weinhold, *J. Comput. Chem.* **2019**, *40*, jcc.25873.
[516] E. D. Glendening, C. R. Landis, F. Weinhold, *WIREs Comput. Mol. Sci.* **2012**, *2*, 1–42.
[517] D. A. Pantazis, X.-Y. Chen, C. R. Landis, F. Neese, *J. Chem. Theory Comput.* **2008**, *4*, 908–919.
[518] E. van Lenthe, P. E. S. Wormer, A. van der Avoird, *J. Chem. Phys.* **1997**, *107*, 2488–2498.
[519] G. te Velde, F. M. Bickelhaupt, E. J. Baerends, C. Fonseca Guerra, S. J. A. van Gisbergen, J. G. Snijders, T. Ziegler, *J. Comput. Chem.* **2001**, *22*, 931–967.
[520] E. van Lenthe, E. J. Baerends, J. G. Snijders, *J. Chem. Phys.* **1993**, *99*, 4597–4610.
[521] E. Van Lenthe, E. J. Baerends, *J. Comput. Chem.* **2003**, *24*, 1142–1156.
[522] F. Schneck, M. Finger, I. Siewert, S. Schneider, *Z. Anorg. Allg. Chem.* **2021**, *647*, 1478–1485.
[523] D. C. Ware, H. Taube, *Inorg. Chem.* **1991**, *30*, 4605–4610.

Publication List

1. **L. Alig**, K. A. Eisenlohr, Y. Zelenkova, S. Rosendahl, R. Herbst-Irmer, S. Demeshko, M. C. Holthausen, S. Schneider,
Rhenium-mediated Conversion of Dinitrogen and Nitric Oxide to Nitrous Oxide
Angew. Chem. Int. Ed. **2022**, *61*, e202113340.

2. W. Xu, L. Maser, **L. Alig**, R. Langer,
Rhodium carbonyl complexes featuring carbodiphosphorane-based pincer ligands
Polyhedron **2021**, *196*, 115018.

3. Y. Li, L. Maser, **L. Alig**, Z. Ke, R. Langer,
From carbones to carbenes and ylides in the coordination sphere of iridium
Dalton Trans. **2021**, *50*, 954-959.

4. L. Maser, C. Schneider, **L. Alig**, R. Langer,
Comparing the acidity of $(R_3P)_2BH$-based donor groups in iridium pincer complexes
Inorganics **2019**, *7*, 61.

5. J. Abbenseth, M. Diefenbach, A. Hinz, **L. Alig**, C. Würtele, J. M. Goicoechea, M. C. Holthausen, S. Schneider,
Oxidative Coupling of Terminal Rhenium Pnictide Complexes
Angew. Chem. Int. Ed. **2019**, *58*, 10966-10970.

6. L. Maser, C. Schneider, L. Vondung, **L. Alig**, R. Langer,
Quantifying the Donor Strength of Ligand-Stabilized Main Group Fragments
J. Am. Chem. Soc. **2019**, *141*, 7596-7604.

7. **L. Alig**, M. Fritz, S. Schneider,
First-Row Transition Metal (De)Hydrogenation Catalysis Based on Functional Pincer Ligands
Chem. Rev. **2019**, *119*, 2681-2751.

8. L. Vondung, **L. Alig**, M. Ballmann, R. Langer,
Umpolung at Boron: Ancillary-Ligand-Induced Formation of Boron-Based Donor Ligands from Phosphine-Boranes
Chem. Eur. J. **2018**, *24*, 12346-12353.

9. L. Vondung, N. Frank, M. Fritz, **L. Alig**, R. Langer,
Phosphine-Stabilized Borylenes and Boryl Anions as Ligands? Redox Reactivity in Boron-Based Pincer Complexes
Angew. Chem. Int. Ed. **2016**, *55*, 14450-14454.